Fuxue Zhang Wei Zhang Guosheng Wang

Non-driven Micromechanical Gyroscopes and Their Applications





Non-driven Micromechanical Gyroscopes and Their Applications

Fuxue Zhang · Wei Zhang Guosheng Wang

Non-driven Micromechanical Gyroscopes and Their Applications





Fuxue Zhang
Beijing Information Science and Technology
University
Beijing
China

Guosheng Wang Academy of Armored Forces Engineering Beijing China

Wei Zhang
Beijing Information Science and Technology
University
Beijing
China

ISBN 978-3-662-54043-5 ISBN 978-3-662-54045-9 (eBook) https://doi.org/10.1007/978-3-662-54045-9

Jointly published with National Defense Industry Press

The print edition is not for sale in China Mainland. Customers from China Mainland please order the print book from: National Defense Industry Press.

Library of Congress Control Number: 2017955248

© National Defense Industry Press and Springer-Verlag GmbH Germany 2018

This work is subject to copyright. All rights are reserved by the Publishers, whether the whole or part of the material is concerned, specifically the rights of translation, reprinting, reuse of illustrations, recitation, broadcasting, reproduction on microfilms or in any other physical way, and transmission or information storage and retrieval, electronic adaptation, computer software, or by similar or dissimilar methodology now known or hereafter developed.

The use of general descriptive names, registered names, trademarks, service marks, etc. in this publication does not imply, even in the absence of a specific statement, that such names are exempt from the relevant protective laws and regulations and therefore free for general use.

The publishers, the authors and the editors are safe to assume that the advice and information in this book are believed to be true and accurate at the date of publication. Neither the publishers nor the authors or the editors give a warranty, express or implied, with respect to the material contained herein or for any errors or omissions that may have been made. The publishers remains neutral with regard to jurisdictional claims in published maps and institutional affiliations.

Printed on acid-free paper

This Springer imprint is published by the registered company Springer-Verlag GmbH, DE part of Springer Nature

The registered company address is: Heidelberger Platz 3, 14197 Berlin, Germany

Preface

According to their working principle, gyroscopes can be divided into either electromechanical gyroscopes or optical gyroscopes. Electromechanical gyroscopes include the ball bearing gyroscope, the liquid floated gyroscope, the flexible gyroscope, the electrostatic gyroscope, the piezoelectric gyroscope, the airstream gyroscope and the micromechanical gyroscope, while optical gyroscopes include the laser gyroscope and the optical fiber gyroscope. At present the laser gyroscope and the optical fiber gyroscope have seen the fastest development.

Electromechanical gyroscopes can be also be divided into two type according to their structure, namely driven gyroscopes and non-driven gyroscopes. The former have been successively developed and put into use in developed countries such as the United States, Japan and in China, while the latter has fewer patent and reports at home and abroad. Non-driven micromechanical gyroscope appears such that the gyroscope is expanded from a kind of driven structure to two kinds of the driven structure and the non-driven structure.

A non-driven micromechanical gyroscope has a simple structure, low cost and high reliability. Its biggest advantage is that it can perceive the transverse angular velocity and the rolling angular velocity of the rotating flight carrier simultaneously, that is, it has the function of two driven micromechanical gyroscopes, which greatly reduces cost. Over the last ten years, the non-driven micromechanical gyroscope has been successfully developed and used for rotating carriers in China. A total of 29 invention patents has been licensed relating to the non-driven micromechanical gyroscope in China, Britain, France, Germany and America. It has won one first prizes and five second prizes on the Provincial Technological Invention Awards, 149 papers have been published in domestic and foreign academic journals and at academic conferences. This book describes this gyroscope and its application in detail.

During the writing of this book, Wang Jiaguang of China Aerospace Science and Technology Corporation carefully reviewed the revised book and Prof. Li Yaozong provided the translation of the foreign sources in Part 1. My doctoral candidates, namely Yan Qingwen, Wang Hongwei, Mao Xu, Wu Lifeng, Liu Yu, Zhao Hui, Zhang Zengping and Wang Ling, and my postgraduates, namely Zhang Nan, Xu

vi Preface

Xiaosong, Sun Chengxiang, Xu Hongzhuo, Liu Hailin, Wen Jiangchuan, Ye Qing, Yue Guannan, bright, Jiang Shiyu, Wang Ling, Zhao Qifeng, Lin Xia, Qin Shengjie and Yu Xiaolong talk, Dan Yanfeng, Guo Heng, Wan Pinjun, Meng Dong, happy, Ma section, Gao Yinjuan, Zhang Ning, Liu, Yuan Min, Xu Hongwei, Qiao Li and Zhao Haixiao, have participated in the development of non-driven micromechanical gyroscopes and their applications or the proofreading of the manuscript and the fruits of their labor are included in this book. I would like to express my deep gratitude to them.

Many technical problems relating to non-driven micromechanical gyroscopes and their applications still need to be addressed and solved. If there are some defective descriptions, I hope the readers of this book do not hesitate to offer their valuable advice.

Beijing, China October 2013 Fuxue Zhang Wei Zhang

About the Book

This book comprehensively and systematically introduces the theories, structures, performances and applications of non-driven mechanical gyroscopes and non-driven micromechanical gyroscopes.

This book comprises three parts. The first part includes four chapters and mainly discusses mathematic models, precision, performance and the operating error of non-driven mechanical gyroscopes. The second part includes five chapters covering operating theory, error, phase shift and performance tests of non-driven micromechanical gyroscopes in rotating flight carriers. The third part includes two sections and mainly focuses on the applications of non-driven micromechanical gyroscopes in the control system of a rotating flight carrier.

This book can be used by the scientific and technological personnel in development department working on the use of inertial devices and automatic control systems of rotating flight carriers, and can also be used as a teaching reference book for bachelors, graduate students and teachers of related majors in colleges and universities.

Contents

Part I Non-driven Mechanical Gyroscopes 1 Operating Theory of a Non-driven Mechanical Gyroscope 3 3 1.1 1.2 Motion Equation for the Sensitive Elements in a Non-driven 9 Performance of the Gyroscope as the Aircraft Rotates 1.3 16 Choice of System Scheme for a Non-driven Mechanical 1.4 19 1.5 Dynamic Performance Regulation of the System..... 27 1.6 Stability of a Non-driven Mechanical Gyroscope with 35 Technical Performance of a Non-driven Mechanical 1.7 56 Precision of a Non-driven Mechanical Gyroscope 2 with Negative Velocity Feedback..... 59 2.1 Measurement Precision of a Constant Angular Velocity 59 2.2 Regulation of a Non-driven Mechanical Gyroscope..... 80 3 Performances of Non-driven Mechanical Gyroscope in the Condition of an Alternating Angular Velocity 85 Performance of Non-driven Mechanical Gyroscope 3.1 86 3.2 Output Signal of Non-driven Mechanical Gyroscope

x Contents

	3.3		rement Accuracy of the Harmonic Angular	
			ty for the Aircraft	105
	3.4		nance of Non-driven Mechanical Gyroscope	
		in a Ci	rcumferential Vibration	129
4	The	Operation	ng Errors of a Non-driven Mechanical Gyroscope	137
	4.1	Error (Caused by Static Unbalance of the Framework	137
	4.2	Error (Caused by Angular Vibration and Circumferential	
		Vibrati	on	141
	4.3	Error (Caused by Imprecise Installation	143
	4.4	Error (Caused by Change of Environmental Temperature	146
Part	t II	Non-driv	ven Micromechanical Gyroscopes	
5			echanical Accelerometer and the Micromechanical	
	•	_		153
	5.1		icromechanical Accelerometer	153
		5.1.1	Basic Principle, Technology Type and Applications	
			of a Micromechanical Accelerometer	153
		5.1.2	The Working Principle of a Micromechanical	
			Accelerometer	156
		5.1.3	The Micromechanical Accelerometer Manufactured	
		~ 1 <i>1</i>	by a Bulk Micromachining Process	157
		5.1.4	The Micromechanical Accelerometer Manufactured	1.61
			by a Surface Micromachining Process	161
		5.1.5	Force Feedback	166
	<i>-</i> 2	5.1.6	The Resonant Micromechanical Accelerometer	168
	5.2		icromechanical Gyroscope	171
		5.2.1	The Structural Basis of a Micromechanical	1.7.1
		5.0.0	Gyroscope	171
		5.2.2	The Basic Principle of a Micromechanical	170
		<i>5</i> 2 2	Gyroscope	173
		5.2.3	Frequency Bandwidth	176
		5.2.4	Thermal Mechanical Noise	179
		5.2.5	Types of Micromechanical Gyroscope	180
6			g Principle of a Non-Driven Micromechanical	
				187
	6.1		ructure Principle	187
	6.2		ynamic Model	188
		6.2.1	The Mass Vibrational Model	188
		6.2.2	The Solution of the Angular Vibrational Equation	193
	6.3	-	is and Calculation of Kinetic Parameters	196
		6.3.1	Torsion Stiffness of the Elastic Supporting Beam	196
		6.3.2	Parameter Calculation of the Flexible Joints	197

Contents xi

		6.3.3 The Damping Coefficient of Angular Vibration for the Vibrating Element	199
		6.3.4 Relationship Between the Angular Vibration Natural	1//
		Frequency, the Angular Vibration Amplitude and the	
		Measured Angular Velocity	201
	6.4	Signal Detection	202
		6.4.1 The Relationship Between the Output Voltage and	
		The Swing Angle	203
		6.4.2 Signal Processing Circuit	205
	6.5	ANSYS Simulation and Analogy	210
		6.5.1 Modal Analysis	210
		6.5.2 Frequency Response Analysis	211
7	Erro	r of a Non-driven Micromechanical Gyroscope	213
	7.1	Motion Equations of a Vibratory Gyroscope	213
	7.2	Error Principle of a Vibratory Gyroscope	224
	7.3	Error Calculation of a Non-driven Micromechanical	
		Gyroscope	230
	7.4	Error of a Non-driven Micromechanical Gyroscope	233
8	Phas	e Shift of a Non-driven Micromechanical Gyroscope	237
	8.1	Phase Shift Calculation of a Non-driven Micromechanical	
		Gyroscope	237
	8.2	Phase Shift of a Non-driven Micromechanical Gyroscope	241
	8.3	Feasibility of Adjusting the Position to Compensate the Phase	
		Shift of the Output Signal	243
	8.4	Characteristic Calculation of a Non-driven Micromechanical	
		Gyroscope in the Angular Vibration Table	247
9	Stati	c Performance Test of a Non-driven Micromechanical	
	Gyro	oscope	251
	9.1	Performance of the Prototype of a Non-driven	
		Micromechanical Gyroscope	251
		9.1.1 Temperature Performance of the Prototype	251
		9.1.2 Performance of the Prototype	254
		9.1.3 Temperature Stability of the Prototype	256
	9.2	Performance of a CJS-DR-WB01 Type Silicon	
	0.5	Micromechanical Gyroscope	257
	9.3	Performance of a CJS-DR-WB02 Type Silicon	250
	0.4	Micromechanical Gyroscope	258
	9.4	Performance Test of CJS-DR-WB03 Type Silicon Micromechanical Gyroscope	258
		Mileromechanical L-Wroscone	, , , , ,

xii Contents

Part	t III	Applications of Non-driven Micromechanical Gyroscopes	
10	Signa	al Processing	285
	10.1	Inhibiting the Influence of a Change in Rolling Angular	
		Velocity of the Rotating Body on the Stability	
		of the Output Signal	285
		10.1.1 Influence of a Change in Rolling Angular Velocity	
		of the Rotating Body on the Output Signal	285
		10.1.2 Method for Inhibiting the Influence of a Change	
		in Rolling Angular Velocity on the Output Signal	285
		10.1.3 Validation of Inhibiting Influence Method	288
	10.2	The Attitude Demodulation Method of a Micromechanical	
		Gyroscope Based on Phase Difference	292
		10.2.1 Study of the Phase Difference Between the Output	
		Signal and the Reference Signal of the Gyroscope	292
		10.2.2 Factors Influencing Phase Difference	300
		10.2.3 Phase Difference Compensating Method	307
	10.3	Posture Demodulation of the Rotating Body Based on the	
		Micromechanical Gyroscope	310
		10.3.1 Demodulation Method	310
		10.3.2 Simulation Experiment	321
11	Annl	lications in the Flight Attitude Control System	325
	11.1		325
	11.1	11.1.1 Calculation Method and Software	325
		11.1.2 Computer Software Design	325
	11.2	•	323
	11.2	as Three Axes Move Simultaneously	329
	11.3	DSP Digital Output of the Gyroscope	330
	11.5	11.3.1 Hardware Circuit Design	330
		11.3.2 Algorithm and Software Realization	331
		11.3.3 Test Results	334
	11.4	Attitude Sensing System for Single Channel Control of the	55.
		Rotating Flight Carrier	337
	11.5	Three Channels Attitude Sensing System of the Rotating	557
	11.0	Flight Carrier Through the Rectangular Coordinate	
		Transformation	340
	11.6		5.10
	11.0	Through the Polar Coordinate Transformation	344
		11.6.1 Method for Obtaining the Transverse Angular	577
		Velocity Relative to the Rotating Coordinate System	
		of the Rotating Flight Carrier	346
		11.6.2 Method for Obtaining the Rolling Angular	J+0
		Velocity Relative to the Coordinate System	
		of the Quasi-Rotating Flight Carrier	348
		of the Quasi-Notating Flight Carret	240

Contents xiii

11.6.3 Method for Obtaining the Pitch Angular Velocity and	
the Yaw Angular Velocity Relative to the Coordinate	
System of the Quasi-Rotating Flight Carrier	350
11.7 Applications in the Non-rotating Flight Carrier	351
References	353

Author's Introduction

Zhang Fuxue, born in 1939, Xuanwei City of Yunnan province. A piezoelectric and sensing technology expert, Professor, Ph.D. supervisor, Beijing Information Science and Technology University.

In 1960s, he invented the piezoelectric ceramic with the high mechanical quality factors and high mechanical and electrical coupling coefficients before the inventions of the United States and Japan. In 1970s, by using the aforementioned ceramic piezoelectric gyroscope, in China he firstly achieved the assumption of solidified inertial device through the new theory and the new technology proposed by Tsien Hsueshen. In 1980s, he found the "gas pendulum" phenomenon, proposed the new concept of "gas pendulum", and established the gas pendulum theory, which formed a new subject branch of the inertial technology—the gas pendulum inertia technology. Based on this theory, he invented 1-D, 2-D and omnibearing level posture sensor than those of the United States similar as early as three years. In 1990s, because there is no constant temperature environment in the use of the weapon's accelerometer and level posture sensor, the standard period is twelve years, and the error of the standard scale factor is less than 1/1000, he invented the piezoelectric accelerometer and the level posture sensor. In the early twenty-first Century, he found the gyroscope effect of silicon pendulum, invented the carrier-driven gyroscope, and pioneered a new field of the carrier-driven gyroscope.

He won the second prize of state technological invention twice, the third prize of state technological invention twice, the second prize of national scientific and technological progress once, and the first prize and the second prize of the province and the minister 25 times; He won 50 invention patents (including 18 patents of the United States, Britain, France and Germany). His inventions were widely used in missiles, ships and robots, and his research results and academic thoughts have important guiding significance for the development of the technology of the piezoelectric and inertial technology in China. He published 25 books, where "the piezoelectricity", "the robot technology and its applications", and "the modern

xvi Author's Introduction

piezoelectric" were awarded the second prize of national outstanding science and technology books in 1988, the second prize of Chinese Book Award in 2002 and the second prize of the electronic information science and technology in 2008. He was awarded the "National advanced science and technology worker" and "the national labor model".

Part I Non-driven Mechanical Gyroscopes

Chapter 1 Operating Theory of a Non-driven Mechanical Gyroscope

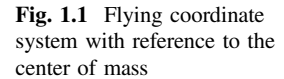
1.1 Characteristics of a Flying Aircraft

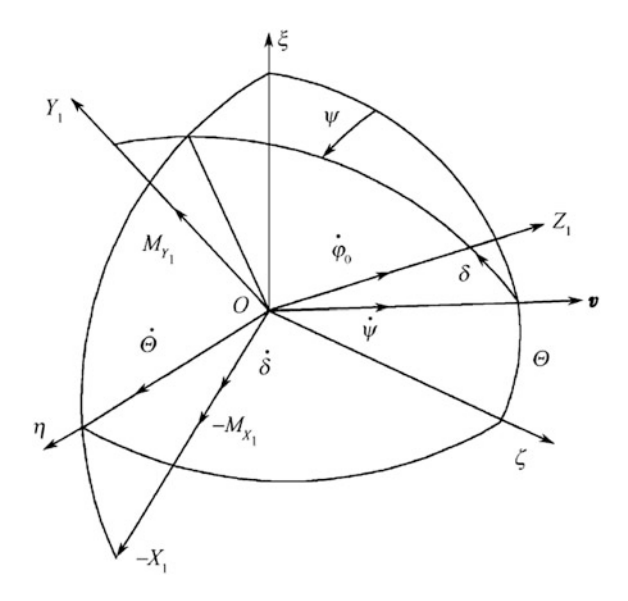
Before the performance of gyroscopes on the rotating carrier under different flying conditions can be studied in detail, the movement characteristics of the flying carrier must be studied.

The non-driven mechanical gyroscope of a rotating state aircraft is the angular velocity sensor. Therefore, when studying the performance of the rotating state aircraft in detail, it is necessary to study the possible motions around the center of mass. Accurate measurement of the motion parameters of the aircraft's rotating state is not the purpose of this section. Qualitative research on the motion characteristics of the center of mass is the main task of our work.

The instrument was originally dedicated to generating the damping torque in the control channel of the automatic steering and rotating carrier around the longitudinal axis. The first task of the flying carrier rotating around its longitudinal axis is to ensure its flying stability. This kind of self-rotating motion can reduce the influence of rotational torque around the center of mass of the rotating flight carrier on its motion characteristics. For example, some rotating torque is produced by the drawbacks (the engine of the rotating flight carrier is tilted on the vertical axis) of the processing technology of its shell. The average effect of these drawbacks on the rotation of the rotating flight carrier can improve the influence of the disturbance torque.

It is not necessary to use the inclined gyroscope in the automatic steering and rotating carriers, because the flying process is realized in the coordinate system which is connected to the rotating flight carrier so the automatic steering task can be achieved at any angle, or in other words it is not related to the dip angle whether the angle is constant or changes with time. Therefore, the self-rotating velocity of the rotating flight carrier can be changed in a certain range (e.g. 10–20 Hz) and have "no effect".





In order to determine the flying characteristics of the rotating flight carrier with reference to the center of mass, the motion equation of a rotating flight carrier with reference to the center of mass is given when the rotating flight carrier is rotating around its longitudinal axis with a rotating frequency 10–20 Hz.

Under the influence of tilting moment $-M_{X_1}$, the motion around its longitudinal axis of the rotating flight carrier with reference to the center of mass is shown in Fig. 1.1.

With the help of the second Lagrange differential equations the motion equation of the rotating flight carrier with reference to the center of mass can be obtained as

$$\frac{\mathrm{d}}{\mathrm{d}t} \left(\frac{\partial E_k}{\partial q_i} \right) - \frac{\partial E_k}{\partial q_i} = Q_i \tag{1.1}$$

where E_k is the rotating kinetic energy of the rotating flight carrier; q_i is the generalized coordinate; and Q_i is the generalized force.

It is generally believed that the center of mass of the rotating flying carrier is fixed, while the rotating flight carrier is rotating with reference to a fixed point under the action of the various aerodynamic, controlled and harmful (such as the process technology) moments. In this case, the motion of the rotating flight carrier will have three degrees of freedom (Fig. 1.1). In this figure, $O\xi\eta\zeta$ is an absolutely immovable coordinate system and $OX_1Y_1Z_1$ is the aircraft's implicated coordinate system.

In the inertial space (i.e. the absolute coordinate system of $O\xi\eta\zeta$) the position of the rotating flight carrier (i.e. the coordinate system $OX_1Y_1Z_1$ is connected with the rotating flight carrier) is determined by three Euler angles: δ is the nutation angle between the longitudinal axis of the aircraft and the vector \overline{v} (the velocity of the

center of mass) in the rotating plane OY_1Z_1 ; φ is the rotating angle produced by the aircraft's rotation around its longitudinal axis; ψ is the precession angle produced by the rotating plane's rotation around the vector \overline{v} ; and Θ is the angle of the rotating flight carrier's curvature characteristic (between the vector \overline{v} and the horizon).

In flight, the moment is applied to the rotating flight carrier along all three axes of the absolute coordinate system and the tilting moment applied to the rotating flight carrier is projected on the equatorial plane which is perpendicular to the longitudinal axis of the rotating flight carrier. Thus, it is assumed that there is an inclined moment M_{X_1} acting on the rotating flight carrier.

Simultaneously, the projection of the moment M_{X_1} on the three basic rotating axes (corresponding to the three Euler angles) is the generalized force Q in the Lagrange's equation: $Q_{\varphi} = 0$; $Q_{\psi} = 0$; $Q_{\delta} = -M_{X_1}$. The kinetic energy of the aircraft is expressed as follows:

$$E_k = \frac{1}{2} (J_{X_1} \Omega_{X_1}^2 + J_{Y_1} \Omega_{Y_1}^2 + J_{Z_1} \Omega_{Z_1}^2)$$
 (1.2)

where Ω_{X_1} , Ω_{Y_1} and Ω_{Z_1} are the projections of instantaneous angular velocity of the rotating flight carrier on the three axes of the implicated coordinate system.

For a rotating flight carrier, two moments of inertia can be considered as equivalent to the axis of the equatorial plane, that is, $J_{Y_1} = J_{X_1}$. Thus there holds

$$E_k = \frac{1}{2} \left[J_{Z_1} \Omega_{Z_1}^2 + J_{X_1} \left(\Omega_{X_1}^2 + \Omega_{Y_1}^2 \right) \right]$$
 (1.3)

Now, we are analyzing the motion characteristics and features on the ballistic section with a small curvature of the rotating flight carrier and if the angle Θ changes slightly the instantaneous velocity of the rotating flight carrier with sufficient precision is recorded by

$$\mathbf{\Omega} = \dot{\boldsymbol{\varphi}} + \dot{\boldsymbol{\delta}} + \dot{\boldsymbol{\psi}} \tag{1.4}$$

or from Fig. 1.1, we can obtain

$$\begin{cases}
\Omega_{X_1} = -\dot{\delta} \\
\Omega_{Y_1} = -\dot{\psi}\sin\delta \\
\Omega_{Z_1} = \dot{\varphi} + \dot{\psi}\cos\delta
\end{cases}$$
(1.5)

Thus Eq. (1.3) can be expressed as

$$E_{k} = \frac{1}{2} \left[J_{Z_{1}} (\dot{\phi} + \dot{\psi} \cos \delta)^{2} + J_{X_{1}} (\dot{\delta}^{2} + \dot{\psi}^{2} \sin^{2} \delta) \right]$$
(1.6)

Using the second Lagrange equation, the expression of each coordinate of the generalized coordinate system can be expressed as follows:

(1) For the coordinate φ :

$$\frac{\mathrm{d}}{\mathrm{d}t} \left(\frac{\partial E_k}{\partial \dot{\varphi}} \right) - \frac{\partial E_k}{\partial \varphi} = Q_{\varphi} \tag{1.7}$$

$$\frac{\mathrm{d}}{\mathrm{d}t} \left[J_{Z_1} (\dot{\varphi} + \dot{\psi} \cos \delta) \right] = 0 \tag{1.8}$$

Thus there holds

$$\dot{\phi} + \dot{\psi}\cos\delta \approx \dot{\phi}_{\text{initial}} - \text{cons}t \tag{1.9}$$

In other words, the rotating angular velocity around the longitudinal axis of the rotating flight carrier can be considered to be fixed (without considering the damping). However Eq. (1.9) shows that even though we do not consider the effect of damping that is rotating around the longitudinal axis, the rotating velocity value of the rotating flight carrier is not constant and is related to the change of the precession velocity and the nutation angle of the rotating flight carrier. The reason being that the value of Eq. (1.9) is fixed in any condition so in the zero condition it is fixed too, thus at the initial time it can be considered to be equal to the self-rotating frequency of the rotating flight carrier.

(2) For the coordinate ψ :

$$\frac{\mathrm{d}}{\mathrm{d}t} \left(\frac{\partial E_k}{\partial \dot{\psi}} \right) - \frac{\partial E_k}{\partial \psi} = Q_{\psi} \tag{1.10}$$

$$\frac{\mathrm{d}}{\mathrm{d}t} \left[J_{Z_1} (\dot{\varphi} + \dot{\psi} \cos \delta) \cos \delta + J_{X_1} \dot{\psi} \sin^2 \delta \right] = 0 \tag{1.11}$$

$$J_{Z_1}(\dot{\varphi} + \dot{\psi}\cos\delta)\cos\delta + J_{X_1}\dot{\psi}\sin^2\delta = C - \text{const}$$
 (1.12)

From the initial condition we can obtain $J_{Z_1}\dot{\varphi}_{\text{initial}} = C$, and from (1.9), we can obtain

$$\begin{cases} J_{Z_1} \dot{\varphi}_{\text{initial}} \cos \delta + J_{X_1} \dot{\psi} \sin^2 \delta = J_{Z_1} \dot{\varphi}_{\text{initial}} \\ J_{X_1} \dot{\psi} \sin^2 \delta = J_{Z_1} \dot{\varphi}_{\text{initial}} (1 - \cos \delta) \\ \dot{\psi} = \frac{J_{Z_1} \dot{\varphi}_{\text{initial}} (1 - \cos \delta)}{J_{X_1} \sin^2 \delta} \end{cases}$$
(1.13)

or because the nutation angle δ is very small, and when $\dot{\varphi}_{\rm initial}$ has remained constant there holds

$$\dot{\psi} = \frac{J_{Z_1} \dot{\varphi}_{\text{initial}}}{2J_{X_1}} = \dot{\psi}_{\text{initial}} - \text{const}$$
 (1.14)

In this case, the precession angle $\psi = \psi_{\text{initial}} + \dot{\psi}t$.

Because of the relationship between the axial and the equator of the inertia moment of the rotating flight carrier, $J_{Z_1} \approx 0.1 J_{X_1}$, we can approximately obtain

$$\dot{\psi} = 0.05 \dot{\varphi}_{\text{initial}} \approx 0.05 \dot{\varphi}_{0} \tag{1.15}$$

In the working condition, the maximum value of the self-rotating frequency which the rotating flight carrier is rotating around the longitudinal axis is 20 Hz. Thus in the condition of a small nutation angle the maximum precession velocity of the rotating flight carrier is 1 Hz. If we consider the actual nutation angles and the relationship between the axial and the equator of the inertia moment of the rotating flight carrier, the appropriate maximum precession velocity must be selected to be close to 2–2.5 Hz.

(3) For the coordinate δ :

$$\frac{\mathrm{d}}{\mathrm{d}t} \left(\frac{\partial E_k}{\partial \dot{\delta}} \right) - \frac{\partial E_k}{\partial \delta} = Q_{\delta} \tag{1.16}$$

Thus there holds

$$\begin{split} \frac{\mathrm{d}}{\mathrm{d}t}(J_{X_1}\dot{\delta}) - J_{Z_1}(\dot{\varphi} + \dot{\psi}\cos\delta)\dot{\psi}\sin\delta - J_{X_1}\dot{\psi}^2\sin\delta\cos\delta &= -M_{X_1}\\ \ddot{\delta} - \dot{\psi}^2\sin\delta\cos\delta + \frac{J_{Z_1}}{J_{X_1}}(\dot{\varphi} + \dot{\psi}\cos\delta)\dot{\psi}\sin\delta &= -\frac{M_{X_1}}{J_{X_1}} \end{split}$$

Assuming that the nutation angle is small and considering the condition of Eq. (1.9), we obtain

$$\ddot{\delta} + \left(\frac{J_{Z_1}}{J_{X_1}}\dot{\phi}_{\text{inital}}\dot{\psi} - \dot{\psi}^2\right)\delta = -\frac{M_{X_1}}{J_{X_1}}$$
(1.17)

The solution of Eq. (1.17) can be expressed as follows

$$\delta = C \sin \left[\left(\sqrt{\frac{J_{Z_1}}{J_{X_1}} \dot{\varphi}_{\text{inital}} \dot{\psi} - \dot{\psi}^2} \right) t + \beta \right] - \frac{M_{X_1}}{J_{X_1} \left(\frac{J_{Z_1}}{J_{X_1}} \dot{\varphi}_{\text{inital}} \dot{\psi} - \dot{\psi}^2 \right)}$$
(1.18)

Denote

$$\omega_0^2 = \frac{J_{Z_1}}{J_{X_1}} \dot{\varphi}_{\text{inital}} \dot{\psi} - \dot{\psi}^2 = \dot{\psi}^2 \left(\frac{J_{Z_1}}{J_{X_1}} \frac{\dot{\varphi}_{\text{inital}}}{\dot{\psi}} - 1 \right) = \dot{\psi}^2 K_{\sigma}$$
 (1.19)

Thus Eq. (1.18) has the following expression:

$$\delta = C\sin(\dot{\psi}\sqrt{K_{\sigma}t} + \beta) - \frac{M_{X_1}}{J_{X_1}\dot{\psi}^2 K_{\sigma}}$$
 (1.20)

Assuming that there exists the initial angle velocity $\dot{\delta}_{\text{initial}}$, we can obtain

$$\begin{cases} C \sin \beta - \frac{M_{X_1}}{J_{X_1} \dot{\psi}^2 K_{\sigma}} = 0\\ C \dot{\psi} \sqrt{K_{\sigma}} \cos \beta = \dot{\delta}_{\text{initial}} \end{cases}$$
(1.21)

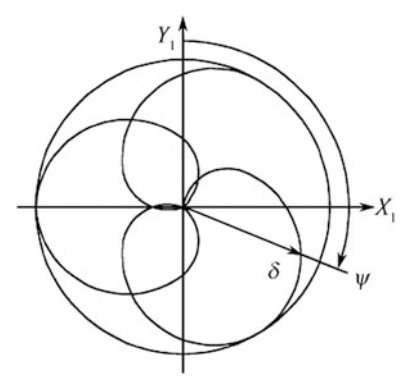
$$C = \frac{\sqrt{M_{X_1}^2 + J_{X_1}^2 \dot{\psi}^2 K_{\sigma} \dot{\delta}_{\text{initial}}^2}}{J_{X_1} \dot{\psi}^2 K_{\sigma}} = \sqrt{\frac{M_{X_1}^2}{J_{X_1}^2 \dot{\psi}^4 K_{\sigma}^2} + \frac{\dot{\delta}_{\text{initial}}^2}{\dot{\psi}^2 K_{\sigma}}}$$
(1.22)

$$\beta = \arctan\left(\frac{M_{X_1}}{J_{X_1}\dot{\psi}\sqrt{K_\sigma}\dot{\delta}_{\text{initial}}}\right) \tag{1.23}$$

Equation (1.20) shows that the nutation motion has the harmonic oscillation characteristic with cycle $T = \frac{2\pi}{\omega_0} = \frac{2\pi}{\dot{\psi}\sqrt{K_\sigma}}$, and the amplitude of the relative constant nutation angle is small.

The precession is a circular oscillation while the nutation movement is in essence an angular oscillation around the lateral axis of the rotating flight carrier. Thus we can obtain the space motion of the rotating flight carrier in complex polar coordinates as shown in Fig. 1.2.

Fig. 1.2 Rotating motion trajectory of the craft's shaft end



When the coefficient K_{σ} is negative, Eq. (1.20) has the following different expression:

$$\delta = C \sin\left(\dot{\psi}\sqrt{|K_{\sigma}|}t + \beta\right) - \frac{M_{X_1}}{J_{X_1}\dot{\psi}^2|K_{\sigma}|}$$
(1.24)

In Eq. (1.24) the nutation angle is expressed by the hyperbola function. Obviously, the nutation angle will increase without a limitation. Thus, K_{σ} is the criterion to determine the rotating stability of a rotating flight carrier. When Eq. (1.24) is applied and $K_{\sigma} = 1 > 0$, the value of the nutation angle is determined by Eq. (1.20).

When the state and the reference center of mass of the rotating flight carrier in the flight are qualitatively studied, both in the state of a constant velocity measurement and in the condition of the angular and circular oscillations of the rotating flight carrier, normal operation of the rotor-type vibratory gyroscope can be guaranteed. For the aerial rotating flight carrier, the angle of oscillation amplitude is less than 5° and the frequency lies in the range of 2–10 Hz.

By rotating around its longitudinal axis of the rotating flight carrier, its flight can get rid of the torque disturbance caused by many technical problems. These torques are caused by some problems such as the inhomogeneous mass distribution of the rotating flight carrier. However, the inhomogeneous mass distribution of the rotating flight carrier can also result in the longitudinal axis of the rotating flight carrier (structure) not coinciding with its self-rotating axis. Therefore, it is necessary to introduce some additional corrective measures into its structure and the detailed method is related to increasing the swing angle of the sensitive element as presented in the following sections.

It is noted that when the performance of a rotor-type vibratory gyroscope mounted on a rotating state aircraft is studied, the performance and characteristics of the rotating flight carrier in flight must be considered under all possible motion states of the rotating flight carrier (the movement state with a constant velocity angle oscillation and a circular oscillation) so that the technical requirements of the instrument's performance parameters can be guaranteed.

1.2 Motion Equation for the Sensitive Elements in a Non-driven Mechanical Gyroscope

In order to obtain the motion equation of the gyroscope's sensitive element the complete expression of the projection of the craft's absolute angular velocity on the coordinates of the absolute coordinate system is defined.

According to the motion characteristics of the rotating flight caa rrier (taking the centroid as the reference), the projections of the craft's angular velocity on the axes $O\xi$, $O\eta$ and $O\zeta$ have the following expressions

$$\begin{cases}
\Omega_{\zeta} = \Omega_{\zeta}^{0} + \Omega_{\zeta}^{\psi} + \Omega_{\zeta}^{v} \\
\Omega_{\eta} = \Omega_{\eta}^{0} + \Omega_{\eta}^{\psi} + \Omega_{\eta}^{v} \\
\Omega_{\zeta} = \Omega_{\zeta}^{0} + \Omega_{\zeta}^{\psi} + \Omega_{\zeta}^{v}
\end{cases} (1.25)$$

Figure 1.3 is a coordinate system to derive the motion equation of the sensitive element in a non-driven mechanical gyroscope: $O\xi\eta\zeta$ is an absolute coordinate system; $OX_0Y_0Z_0$ is an implicated coordinate system of a non-driven mechanical gyroscope and craft, and it does not rotate around the axis Z_0 ; $OX_1Y_1Z_1$ is an implicated coordinate system of a non-driven mechanical gyroscope and craft, and it rotates around the axis Z_0 ; OXYZ is an implicated coordinate system. Figure 1.4 is the projection of the craft's angular velocity on the axis of the absolute coordinate system.

From Fig. 1.4, the projections Ω_{ζ}^0 , Ω_{η}^0 and Ω_{ζ}^0 of the constant angular velocities on the axes O_{ζ}^{ζ} , O_{η} and O_{ζ}^{ζ} are obtained as

Fig. 1.3 Coordinate system to derive the motion equation of the sensitive element in a rotor type non-driven mechanical gyroscope

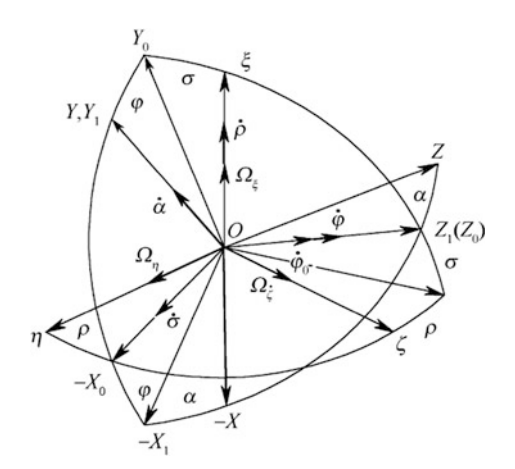
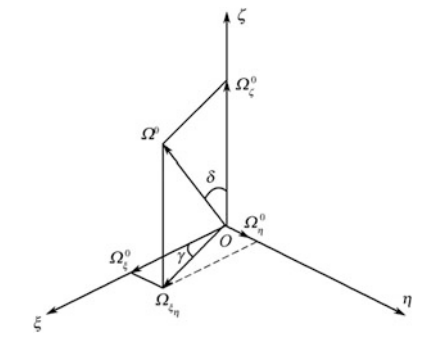


Fig. 1.4 Projection of the craft's angular velocity on the axis of the absolute coordinate system



$$\begin{cases} \Omega_{\xi}^{0} = \Omega^{0} \sin \delta \cos \gamma \\ \Omega_{\eta}^{0} = \Omega^{0} \sin \delta \sin \gamma \\ \Omega_{\zeta}^{0} = \Omega^{0} \cos \delta \end{cases}$$
 (1.26)

Denote Ω_{ζ}^{ν} , Ω_{η}^{ν} and Ω_{ζ}^{ν} as the projections of the harmonic angular velocity Ω^{ν} cos νt (angular oscillation) on the axes $O\xi$, $O\eta$ and $O\zeta$:

$$\begin{cases} \Omega_{\zeta}^{\nu} = \Omega^{\nu} \sin \delta_{\nu} \cos \gamma_{\nu} \cos \nu t \\ \Omega_{\eta}^{\nu} = \Omega^{\nu} \sin \delta_{\nu} \sin \gamma_{\nu} \cos \nu t \\ \Omega_{\zeta}^{\nu} = \Omega^{\nu} \cos \delta_{\nu} \cos \nu t \end{cases}$$
(1.27)

Denote Ω_{η}^{ψ} and Ω_{ζ}^{ψ} as the projections of the circular oscillating angular velocity Ω^{ψ} on the plane $O\xi\eta$ and the axis $O\zeta$, respectively:

$$\begin{cases} \Omega_{\xi}^{\psi} = \Omega^{\psi} \sin \delta_{\psi} \cos(\psi t + \gamma_{\psi}) \\ \Omega_{\eta}^{\psi} = \Omega^{\psi} \sin \delta_{\psi} \sin(\psi t + \gamma_{\psi}) \\ \Omega_{\xi}^{\psi} = \Omega^{\psi} \cos \delta_{\psi} \end{cases}$$
(1.28)

Substituting Eqs. (1.26), (1.27) and (1.28) into Eq. (1.25), we can obtain the complete expressions Ω_{ξ} , Ω_{η} and Ω_{ζ} of the influence of the aircraft's circular vibration velocity:

$$\begin{cases} \Omega_{\xi} = \Omega^{0} \sin \delta \cos \gamma + \Omega^{\psi} \sin \delta_{\psi} \cos(\psi t + \gamma_{\psi}) + \Omega^{v} \sin \delta_{v} \cos \gamma_{v} \cos v t \\ \Omega_{\eta} = \Omega^{0} \sin \delta \sin \gamma + \Omega^{\psi} \sin \delta_{\psi} \sin(\psi t + \gamma_{\psi}) + \Omega^{v} \sin \delta_{v} \sin \gamma_{v} \cos v t \\ \Omega_{\zeta} = \Omega^{0} \cos \delta + \Omega^{\psi} \cos \delta_{\psi} + \Omega^{v} \cos \delta_{v} \cos v t \end{cases}$$

$$(1.29)$$

By using the dynamic non-generalized Euler equation, we can obtain the motion equation of the gyroscope's sensitive element:

$$B_1 \dot{\Omega}_Y - (C_1 - A_1) \Omega_X \Omega_Z = -D_\alpha \dot{\alpha} - K\alpha + M_{Y,\text{harmful}}$$
 (1.30)

where A_1, B_1 and C_1 are the inertia moments of the sensitive element which take OX, OY and OZ axes as the references; $-D_{\alpha}\dot{\alpha}$ is the damping torque; D_{α} is the damping coefficient; $\dot{\varphi}_0$ is the rotating angular velocity of the rotating flight carrier and the instrument frame rotating around the axis OZ_1 ; α is the rotation angle of the sensitive element around the axis OY; $-K\alpha$ is the flexibility torque; K is the flexibility coefficient (the angular rigidity); $M_{Y,\text{harmful}}$ is the disturbance (harmful) torque that is relative to the axis OY_1 (OY), which is caused by the unbalance of the sensitive element and other factors.

According to the requirement of Fig. 1.3, the values of $\dot{\Omega}_Y$, Ω_X and Ω_Z in (1.30) are regulated. Therefore, we can obtain the projections of the rocket's angular velocity on the axes OX, OY and OZ:

$$\begin{cases} \Omega_X = \dot{\rho}\cos\sigma\sin\varphi\cos\alpha - \dot{\sigma}\cos\varphi\cos\alpha - \dot{\varphi}\sin\alpha \\ \Omega_Z = \dot{\rho}\cos\sigma\sin\varphi\sin\alpha - \dot{\sigma}\cos\varphi\sin\alpha + \dot{\varphi}\cos\alpha \\ \Omega_Y = \dot{\rho}\cos\sigma\cos\varphi + \dot{\sigma}\sin\varphi + \dot{\alpha} \end{cases}$$
(1.31)

Multiplying Ω_X and Ω_Z in Eq. (1.31) and differentiating Ω_Y , we can obtain

$$\begin{cases} \Omega_{X}\Omega_{Z} = (\dot{\rho}\cos\sigma\sin\varphi - \dot{\sigma}\cos\varphi)^{2}\sin\alpha\cos\alpha - \dot{\varphi}^{2}\sin\alpha\cos\alpha + \\ (\dot{\rho}\cos\sigma\sin\varphi - \dot{\sigma}\cos\varphi)\dot{\varphi}(\cos^{2}\alpha - \sin^{2}\alpha) \\ \dot{\Omega}_{Y} = (\ddot{\rho}\cos\sigma - \dot{\rho}\dot{\sigma}\sin\sigma)\cos\varphi - \dot{\rho}\dot{\varphi}\cos\sigma\sin\varphi + \ddot{\sigma}\sin\varphi + \dot{\sigma}\dot{\varphi}\cos\varphi + \ddot{\alpha} \end{cases}$$

$$(1.32)$$

Because the angle a is small and the value of a^2 is ignored, we can obtain $\sin \alpha = \alpha$ and $\cos \alpha = 1$. Thus Eqs. (1.31) and (1.32) have the following expressions:

$$\begin{cases} \Omega_X = \dot{\rho} \cos \sigma \sin \varphi - \dot{\sigma} \cos \varphi - \dot{\varphi}\alpha \\ \Omega_Z = (\dot{\rho} \cos \sigma \sin \varphi - \dot{\sigma} \cos \varphi)\alpha + \dot{\varphi} \\ \Omega_Y = \dot{\rho} \cos \sigma \cos \varphi + \dot{\sigma} \sin \varphi + \dot{\alpha} \end{cases}$$
(1.33)

and

$$\begin{cases} \Omega_X \Omega_Z = (\dot{\rho} \cos \sigma \sin \varphi - \dot{\sigma} \cos \varphi)^2 \alpha - \dot{\varphi}^2 \alpha + (\dot{\rho} \cos \sigma \sin \varphi - \dot{\sigma} \cos \varphi) \dot{\varphi} \\ \dot{\Omega}_Y = (\ddot{\rho} \cos \sigma - \dot{\rho} \dot{\sigma} \sin \sigma) \cos \varphi - \dot{\rho} \dot{\varphi} \cos \sigma \sin \varphi + \ddot{\sigma} \sin \varphi + \dot{\sigma} \dot{\varphi} \cos \varphi + \ddot{\alpha} \end{cases}$$
(1.34)

Substituting Eqs. (1.33) and (1.34) into Eq. (1.30), and thinking that $M_{Y,\text{harmful}} = 0$, we can obtain

$$B_{1}[(\ddot{\rho}\cos\sigma - \dot{\rho}\dot{\sigma}\sin\sigma)\cos\varphi - \dot{\rho}\dot{\phi}\cos\sigma\sin\varphi + \ddot{\sigma}\sin\varphi + \dot{\sigma}\dot{\phi}\cos\varphi + \ddot{\alpha}]$$

$$-(C_{1} - A_{1})\{[(\dot{\rho}\cos\sigma\sin\varphi - \sigma\cos\varphi)^{2} - \dot{\phi}^{2}]\alpha$$

$$+(\dot{\rho}\cos\sigma\sin\varphi - \sigma\cos\varphi)\dot{\phi}\} = -D_{\alpha}\dot{\alpha} - K\alpha$$
(1.35)

After some simple transformations, Eq. (1.35) has the following expression:

$$B_{1}\ddot{\alpha} + D_{\alpha}\dot{\alpha} + [(C_{1} - A_{1})(\dot{\varphi}^{2} - (\dot{\rho}\cos\sigma\sin\varphi - \dot{\sigma}\cos\varphi)^{2}) + K]\alpha$$

$$= (C_{1} - A_{1} + B_{1})(\dot{\rho}\cos\sigma\sin\varphi - \dot{\sigma}\cos\varphi)\dot{\varphi}$$

$$- B_{1}[(\ddot{\rho}\cos\sigma - \dot{\rho}\dot{\sigma}\sin\sigma)\cos\varphi + \ddot{\sigma}\sin\varphi]$$
(1.36)

If the projection of the rotating flight carrier's angular velocity on the instrument's sensitive plane exists and is utilized to measure the inertial moment, the right side of Eq. (1.36) shows that: $C_1(\dot{\rho}\cos\sigma\sin\varphi-\dot{\sigma}\cos\varphi)\dot{\varphi}$ is the gyroscopic moment caused by the rotary and changed angular velocity around the lateral axis of the rotating flight carrier; $-A_1(\dot{\rho}\cos\sigma\sin\varphi-\dot{\sigma}\cos\varphi)\dot{\varphi}$ is the centrifugal moment caused by the rotary and changed angular velocity around the lateral axis of the rotating flight carrier; $B_1(\dot{\rho}\cos\sigma\sin\varphi-\dot{\sigma}\cos\varphi)\dot{\varphi}$ is the inertia moment caused by the change of the projections of the rotating carrier's angular velocity on the instrument's sensitive axis, where the change of the projections is restricted by the rotating velocity around the longitudinal axis of the rotating carrier flight; $-B_1[(\ddot{\rho}\cos\sigma-\dot{\rho}\dot{\sigma}\sin\sigma)\cos\varphi+\ddot{\sigma}\sin\varphi])$ is the component of the inertia moment caused by the change of the rotating carrier's angular velocity (the angular acceleration).

Denote

$$H_0 = (C_1 - A_1 + B_1)\dot{\varphi} \tag{1.37}$$

$$B_0 = (C_1 - A_1) \left[\dot{\varphi}^2 - (\dot{\rho}\cos\sigma\sin\varphi - \dot{\sigma}\cos\varphi)^2 \right] + K$$
 (1.38)

$$\omega_0 = \sqrt{\frac{B_0}{B_1}} = \sqrt{\frac{(C_1 - A_1)\left[\dot{\varphi}^2 - (\dot{\rho}\cos\sigma\sin\varphi - \dot{\sigma}\cos\varphi)^2\right] + K}{B_1}}$$
(1.39)

$$\xi = \frac{D_{\alpha}}{2B_{1}\omega_{0}} = \frac{D_{\alpha}}{2\sqrt{B_{1}\left\{ (C_{1} - A_{1})\left[\dot{\varphi}^{2} - (\dot{\rho}\cos\sigma\sin\varphi - \dot{\sigma}\cos\varphi)^{2}\right] + K\right\}}}$$
(1.40)

By using the above denotations, the motion equation of the instrument's sensitive element can be written in the differential equation form of the forced harmonic vibration:

$$\ddot{\alpha} + 2\xi\omega_0\dot{\alpha} + \omega_0^2\alpha = \frac{H_0}{B_1}(\dot{\rho}\cos\sigma\sin\varphi - \dot{\sigma}\cos\varphi) - [(\ddot{\rho}\cos\sigma - \dot{\sigma}\dot{\rho}\sin\sigma)\cos\varphi + \ddot{\sigma}\sin\varphi]$$
 (1.41)

In general, the vibration motion characteristic of the instrument's sensitive element is determined by the instrument's internal parameters such as the sensitive element's inertia moment, the damping coefficient and the aircraft's self-rotating velocity, which are also determined by the external forces acting on the velocity of the rotating flight carrier.

The angular velocity and the angular acceleration caused by some basic rotations in Fig. 1.3 can be expressed by the following equations:

$$\begin{cases} \dot{\rho} = \Omega_{\xi} \\ \dot{\sigma} = \Omega_{\eta} \cos \rho + \Omega_{\zeta} \sin \rho \\ \dot{\varphi} = \dot{\varphi}_{0} + \Omega_{\xi} \sin \sigma - \Omega_{\eta} \sin \rho \cos \sigma + \Omega_{\zeta} \cos \rho \cos \sigma \end{cases}$$
 (1.42)

$$\begin{cases} \ddot{\rho} = \dot{\Omega}_{\xi} \\ \ddot{\sigma} = \dot{\Omega}_{\eta} \cos \rho - \Omega_{\eta} \dot{\rho} \sin \rho + \dot{\Omega}_{\zeta} \sin \rho + \Omega_{\zeta} \dot{\rho} \cos \rho \end{cases}$$
 (1.43)

By differentiating Eq. (1.29), we can obtain the angular accelerations $\dot{\Omega}_{\xi}$, $\dot{\Omega}_{\eta}$ and $\dot{\Omega}_{\Gamma}$:

$$\begin{cases} \dot{\Omega}_{\xi} = -\Omega^{\psi} \psi \sin \delta_{\psi} \sin(\psi t + \gamma_{\psi}) - \Omega^{\nu} v \sin \delta_{\nu} \cos \gamma_{\nu} \sin v t \\ \dot{\Omega}_{\eta} = \Omega^{\psi} \psi \sin \delta_{\psi} \cos(\psi t + \gamma_{\psi}) - \Omega^{\nu} v \sin \delta_{\nu} \sin \gamma_{\nu} \sin v t \\ \dot{\Omega}_{\zeta} = -\Omega^{\nu} v \cos \delta_{\nu} \sin v t \end{cases}$$
(1.44)

The above expressions show that the instrument simultaneously measures the angular velocities with which the craft rotates around the axes OX_0 and OY_0 , and these angular velocities have the following forms:

$$\Omega_{X_0} = \dot{\sigma}$$

$$\Omega_{Y_0} = \dot{\rho}\cos\sigma$$

These angular velocities are proportional to the amplitude of the sensitive element's forced oscillation.

In order to analyze the instrument's working condition, another form of (1.41) is more convenient where the projections of the angular velocity vector on the plane OX_0Y_0 substitute those on the axes OX_0 and OY_0 :

$$\ddot{\alpha} + 2\xi\omega_0\dot{\alpha} + \omega_0^2\alpha = \frac{H_0}{B_1}\Omega\sin(\dot{\phi}t - \delta_1) - \dot{\Omega}\cos(\dot{\phi}t - \delta_2)$$
 (1.45)

$$\ddot{\alpha} + 2\xi\omega_0\dot{\alpha} + \omega_0^2\alpha = \frac{H_0}{B_1}\Omega\sin(\dot{\phi}t - \delta_1) - \dot{\Omega}\sin(\dot{\phi}t + \delta_2)$$
 (1.46)

where

$$\Omega = \sqrt{\left(\dot{\rho}\cos\sigma\right)^2 + \dot{\sigma}^2} \tag{1.47}$$

is the projection of the rotating flight carrier's angular velocity on the plane OX_0Y_0 ;

$$\dot{\Omega} = \sqrt{\left(\ddot{\rho}\cos\sigma - \dot{\sigma}\dot{\rho}\sin\sigma\right)^2 + \ddot{\sigma}^2} \tag{1.48}$$

is the projection of the angular acceleration on the plane OX_0Y_0 , while the phase shift angles δ_1 and δ_2 are the vector position's angles on the sensitive plane OX_0Y_0 of the rotating flight carrier's angular velocity and angular acceleration:

$$\delta_1 = \arctan\left(\frac{\dot{\sigma}}{\dot{\rho}\cos\sigma}\right) \tag{1.49}$$

$$\delta_2 = \arctan\left(\frac{\ddot{\rho}\cos\sigma - \dot{\sigma}\dot{\rho}\sin\sigma}{\ddot{\sigma}}\right) \tag{1.50}$$

In this case, Eqs. (1.39) and (1.40) are changed as

$$\omega_0 = \sqrt{\frac{B_0}{B_1}} = \sqrt{\frac{(C_1 - A_1)[\dot{\varphi}^2 - \Omega^2 \sin^2(\dot{\varphi}t - \delta_1)] + K}{B_1}}$$
 (1.51)

$$\xi = \frac{D_{\alpha}}{2B_{1}\omega_{0}} = \frac{D_{\alpha}}{2\sqrt{B_{1}\{(C_{1} - A_{1})[\dot{\varphi}^{2} - \Omega^{2}\sin^{2}(\dot{\varphi}t - \delta_{1})] + K\}}}$$
(1.52)

Therefore, the motion equation of the sensitive element of the rotating state aircraft's non-driving mechanical gyroscope in the aircraft's implicated coordinate system is expressed as

$$\ddot{\alpha} + \frac{D_{\alpha}}{B_{1}}\dot{\alpha} + \frac{(C_{1} - A_{1})\left[\dot{\varphi}^{2} - \Omega^{2}\sin^{2}(\dot{\varphi}t - \delta_{1})\right] + K}{B_{1}}\alpha$$

$$= \frac{C_{1} - A_{1} + B_{1}}{B_{1}}\left[\Omega\dot{\varphi}\sin(\dot{\varphi}t - \delta_{1}) - \dot{\Omega}\sin(\dot{\varphi}t + \delta_{2})\right]$$
(1.53)

or

$$\ddot{\alpha} + \frac{D_{\alpha}}{B_{1}}\dot{\alpha} + \frac{(C_{1} - A_{1})[\dot{\varphi}^{2} - (\dot{\rho}^{2}\cos^{2}\sigma - \dot{\sigma}^{2})]\sin\left[\dot{\varphi}t - \arctan\left(\frac{\dot{\sigma}}{\dot{\rho}\cos\sigma}\right)\right] + K}{B_{1}}\alpha$$

$$= \frac{C_{1} - A_{1} + B_{1}}{B_{1}}\dot{\varphi}\sqrt{\dot{\rho}^{2}\cos^{2}\sigma + \dot{\sigma}^{2}}\sin\left[\dot{\varphi}t - \arctan\left(\frac{\dot{\sigma}}{\dot{\rho}\cos\sigma}\right)\right]$$

$$-\sqrt{(\ddot{\rho}\cos\sigma - \dot{\sigma}\dot{\rho}\sin\sigma)^{2} + \ddot{\sigma}^{2}}\sin\left[\dot{\varphi}t + \arctan\left(\frac{\ddot{\rho}\cos\sigma - \dot{\sigma}\dot{\rho}\sin\sigma}{\ddot{\sigma}}\right)\right]$$

$$(1.54)$$

From Eqs. (1.51) and (1.52), the undamped vibration's natural frequency and the attenuation coefficient of the non-driving mechanical gyroscope's sensitive element used in the rotating state aircraft have a complex relationship with the amplitude and the phase of the measured angular velocity.

The motion equation of a rotor-type vibratory gyroscope can be obtained as:

$$\begin{split} B_1 \ddot{\alpha} + D_\alpha \dot{\alpha} + (C_1 - A_1) [\dot{\varphi}^2 - (\dot{\rho}\cos\sigma\sin\varphi - \dot{\sigma}\cos\varphi)^2] \alpha \\ &= (C_1 - A_1 + B_1) (\dot{\rho}\cos\sigma\sin\varphi - \dot{\sigma}\cos\varphi) \dot{\varphi} \\ &- B_1 [(\ddot{\rho}\cos\sigma - \dot{\rho}\dot{\sigma}\sin\sigma)\cos\varphi + \ddot{\sigma}\sin\varphi] + M_{T,\text{inertia}} \end{split}$$

where

$$\begin{split} \dot{\rho} &= \Omega_{\xi}; \dot{\sigma} = \Omega_{\eta} \cos \rho + \Omega_{\zeta} \sin \rho \\ \dot{\varphi} &= \dot{\varphi}_{0} + \Omega_{\xi} \sin \sigma - \Omega_{\eta} \sin \rho \cos \sigma + \Omega_{\zeta} \cos \rho \cos \sigma \\ \ddot{\rho} &= \dot{\Omega}_{\xi}; \ddot{\sigma} = \dot{\Omega}_{\eta} \cos \rho - \Omega_{\eta} \dot{\rho} \sin \rho + \dot{\Omega}_{\zeta} \sin \rho + \Omega_{\zeta} \dot{\rho} \cos \rho \\ \ddot{\alpha} &+ 2\xi \omega_{0} \dot{\alpha} + \omega_{0}^{2} \alpha = \frac{H_{0}}{B_{1}} \Omega \sin(\dot{\varphi}t - \delta_{1}) - \dot{\Omega} \sin(\dot{\varphi}t + \delta_{2}) \\ H_{0} &= (C_{1} - A_{1} + B_{1}) \dot{\varphi}; B_{0} = (C_{1} - A_{1}) [\dot{\varphi}^{2} - (\dot{\rho} \cos \sigma \sin \varphi - \dot{\sigma} \cos \varphi)^{2}] \\ \Omega &= \sqrt{(\dot{\rho} \cos \sigma)^{2} + \dot{\sigma}^{2}}; \dot{\Omega} = \sqrt{(\ddot{\rho} \cos \sigma - \dot{\sigma} \dot{\rho} \sin \sigma)^{2} + \ddot{\sigma}^{2}} \\ \delta_{1} &= \arctan\left(\frac{\dot{\sigma}}{\dot{\rho} \cos \sigma}\right); \delta_{2} = \arctan\left(\frac{\ddot{\rho} \cos \sigma - \dot{\sigma} \dot{\rho} \sin \sigma}{\ddot{\sigma}}\right) \end{split}$$

The condition of tuning resonance is

$$\mu = \sqrt{\frac{C_1 - A_1}{B_1}} = \frac{\omega_0}{\dot{\varphi}_0} = 1$$

The vibration state is established as

$$\alpha = \frac{(C_1 - A_1 + B_1)\Omega \sin \left[\dot{\varphi}_0 t - \gamma - \arctan\left(\frac{2D_{\alpha}}{(C_1 - A_1 - B_1)\dot{\varphi}_0}\right)\right]}{\sqrt{\left[(C_1 - A_1 - B_1)\dot{\varphi}_0\right]^2 + D_{\alpha}^2}}$$

When precisely tuned, there holds

$$\alpha = -\frac{2B_1}{D_{\alpha}}\Omega\cos(\dot{\varphi}_0 t - \gamma)$$

1.3 Performance of the Gyroscope as the Aircraft Rotates With a Constant Angular Velocity

Under the following conditions, the solution of the sensitive element's motion Eq. (1.46) is analyzed:

$$\Omega^{\psi} = 0; \Omega^{\nu} = 0; \delta = (0; \pi/2); \gamma = (0; \pi/2)$$
(1.55)

Equation (1.25) has the following form:

$$\begin{cases}
\Omega_{\xi} = \Omega_{\xi}^{0} = \Omega^{0} \sin \delta \cos \gamma \\
\Omega_{\eta} = \Omega_{\eta}^{0} = \Omega^{0} \sin \delta \sin \gamma \\
\Omega_{\zeta} = \Omega_{\zeta}^{0} = \Omega^{0} \cos \delta
\end{cases}$$
(1.56)

It is the case that the angular velocity of the inertia space whose space changes and whose time is constant acts on the rotating flight carrier. From Eq. (1.42), the basic unit rotating angular velocity is

$$\begin{cases} \dot{\rho} = \Omega_{\xi}^{0} = \Omega^{0} \sin \delta \cos \gamma \\ \dot{\sigma} = \Omega_{\eta}^{0} \cos \rho + \Omega_{\zeta}^{0} \sin \rho = \Omega^{0} \sin \delta \sin \gamma \cos \rho + \Omega^{0} \cos \delta \sin \rho \\ \dot{\varphi} = \dot{\varphi}_{0} + \Omega_{\xi}^{0} \sin \sigma - \Omega_{\eta}^{0} \sin \rho \cos \sigma + \Omega_{\zeta}^{0} \cos \rho \cos \sigma \\ = \dot{\varphi}_{0} + \Omega^{0} \sin \delta \cos \gamma \sin \sigma - \Omega^{0} \sin \delta \sin \gamma \sin \rho \cos \sigma + \Omega^{0} \cos \delta \cos \rho \cos \sigma \end{cases}$$

$$(1.57)$$

Under the action of the constant angular velocity, the angles ρ and σ are very small, while the self-rotating angular velocity of the carrier around the longitudinal axis is many times bigger than that of the carrier around the absolute coordinate system's axis, that is, $\dot{\varphi}_0 \gg \Omega_{\xi}$, Ω_{η} and Ω_{ζ} . Thus Eq. (1.57) is changed into the following form:

$$\begin{cases} \dot{\rho} = \Omega_{\xi}^{0} = \Omega^{0} \sin \delta \cos \gamma \\ \dot{\sigma} = \Omega_{\eta}^{0} + \Omega_{\zeta}^{0} \rho = \Omega^{0} \sin \delta \sin \gamma + \Omega^{0} \rho \cos \delta \approx \Omega_{\eta}^{0} = \Omega^{0} \sin \delta \sin \gamma \\ \dot{\varphi} = \dot{\varphi}_{0} + \Omega_{\xi}^{0} \sigma + \Omega_{\zeta}^{0} - \Omega_{\eta}^{0} \rho = \dot{\varphi}_{0} + \Omega^{0} \sigma \sin \delta \cos \gamma - \Omega^{0} \rho \sin \delta \sin \gamma + \Omega^{0} \cos \delta \approx \dot{\varphi}_{0} \end{cases}$$

$$(1.58)$$

In this case the basic unit rotation angular acceleration is zero:

$$\begin{cases} \ddot{\rho} = 0\\ \ddot{\sigma} = 0 \end{cases} \tag{1.59}$$

Since the gyroscope measures the angular velocity that is located on the sensitive plane of the instrument, from Fig. 1.3, the instrument will deal with the value of the projection Ω^0 on the sensitive plane:

$$\Omega = \Omega^0 \sin \delta \tag{1.60}$$

It is noted that the instrument only measures the aircraft's angular velocity component located on the measured plane. Therefore, substituting Eq. (1.58) into Eqs. (1.47), (1.48) and (1.49), obtains

$$\Omega = \sqrt{(\dot{\rho}\cos\sigma)^2 + \dot{\sigma}^2} \approx \sqrt{\dot{\rho}^2 + \dot{\sigma}^2} = \sqrt{\Omega_{\xi}^2 + \Omega_{\eta}^2} = \Omega^0 \sin\delta$$
 (1.61)

$$\dot{\Omega} = 0 \tag{1.62}$$

$$\delta_1 = \arctan\left(\frac{\dot{\sigma}}{\dot{\rho}\cos\sigma}\right) = \arctan\left(\frac{\Omega_{\eta}^0}{\Omega_{\xi}^0}\right) = \gamma \tag{1.63}$$

Therefore, under the action of the constant angular velocity, the sensitive element's motion Eq. (1.46) has the following form:

$$\ddot{\alpha} + 2\xi\omega_0\dot{\alpha} + \omega_0^2\alpha = \frac{H_0}{B_1}\Omega\sin(\dot{\varphi}_0t - \delta_1)$$
 (1.64)

or

$$\ddot{\alpha} + 2\xi\omega_0\dot{\alpha} + \omega_0^2\alpha = \frac{H_0}{B_1}\Omega^0\sin\delta\sin(\dot{\varphi}_0t - \gamma)$$
 (1.65)

By solving Eq. (1.64), we can obtain the sensitive element's vibration expression:

$$\alpha = Ce^{-\xi\omega_0 t} \sin\left[\left(\omega_0 \sqrt{1-\xi^2}\right)t + \beta\right] + \lambda \frac{H_0}{B_0} \Omega \sin(\dot{\varphi}_0 t - \gamma + x)$$
 (1.66)

where C and β are the definite integrals under the given initial condition; ξ is the vibration attenuation coefficient under the action of the constant velocity and $\dot{\varphi}_0 \gg \Omega$:

$$\xi = \frac{D_{\alpha}}{2B_{1}\omega_{0}} = \frac{D_{\alpha}}{2\sqrt{B_{1}\left[(C_{1} - A_{1})\dot{\varphi}_{0}^{2} + K\right]}}$$
(1.67)

 ω_0 is the natural frequency of the undamped vibration under the same assumption:

$$\omega_0 = \sqrt{\frac{B_0}{B_1}} = \sqrt{\frac{(C_1 - A_1)\dot{\varphi}_0^2 + K}{B_1}}$$
 (1.68)

 λ is a dynamic coefficient:

$$\lambda = \frac{1}{\sqrt{\left(1 - \frac{\dot{\varphi}_0^2}{\omega_0^2}\right)^2 + \left(2\xi\frac{\dot{\varphi}_0}{\omega_0}\right)^2}} = \frac{\omega_0^2}{\sqrt{\left(\omega_0^2 - \dot{\varphi}_0^2\right)^2 + \left(2\xi\dot{\varphi}_0\omega_0\right)^2}}$$
(1.69)

Considering Eqs. (1.67) and (1.68), obtains

$$\lambda = \frac{(C_1 - A_1)\dot{\varphi}_0^2 + K}{\sqrt{\left[(C_1 - A_1 - B_1)\dot{\varphi}_0^2 + K\right]^2 + (D_\alpha\dot{\varphi}_0)^2}}$$
(1.70)

 χ is the gyroscope's phase shift:

$$\chi = -\arctan\left(\frac{2\xi\dot{\varphi}_0/\omega_0}{1-\dot{\varphi}_0^2/\omega_0^2}\right) = -\arctan\left(\frac{2\xi\dot{\varphi}_0\omega_0}{\omega_0^2-\dot{\varphi}_0^2}\right) \tag{1.71}$$

Substituting Eqs. (1.67) and (1.68) into Eq. (1.71), obtains

$$\chi = -\arctan\left[\frac{D_{\alpha}\dot{\varphi}_{0}}{(C_{1} - A_{1} - B_{1})\dot{\varphi}_{0}^{2} + K}\right]$$
(1.72)

Equations (1.65) and (1.66) show that when the frequency $\dot{\varphi}_0$ coincides with the rotating frequency of the carrier around the longitudinal axis, the sensitive element's vibration amplitude is proportional to the vector mode of the projection of the rotating flight carrier's angular velocity on the measured plane, while the vibration phase is dependent on the vector position's angle α in the measured plane of the rotating flight carrier's angular velocity.

1.4 Choice of System Scheme for a Non-driven Mechanical Gyroscope

The choice of the instrument system scheme depends on the size of the instrument, the technical requirements and the kinematic scheme proposed in the technical task. The determination of the instrument parameters should be realized through calculation, so that it not only satisfies the requirements of the technical task and the appearance size of the instrument, but also ensure the quality and stability of the adjustment, and the accuracy and stability of the output signal. It should be kept in mind that the decision to choose the instrument system's scheme is its working state.

In reviewing Eq. (1.66) the oscillating state has been established for the sensitive element. For the established state the oscillation characteristic has the following form:

$$\alpha = \lambda \frac{H_0}{B_0} \Omega \sin(\dot{\varphi}_0 t - \gamma + \chi) = \frac{(C_1 - A_1 + B_1)\dot{\varphi}_0 \Omega}{\sqrt{\left[(C_1 - A_1 - B_1)\dot{\varphi}_0^2 + K\right]^2 + (D_\alpha \dot{\varphi}_0)^2}} \times \sin\left\{\dot{\varphi}_0 t - \gamma - \arctan\left[\frac{D_\alpha \dot{\varphi}_0}{(C_1 - A_1 - B_1)\dot{\varphi}_0^2 + K}\right]\right\}$$
(1.73)

Now, the advantages and the disadvantages of two possible working states of the instrument are analyzed: the two working states are non-resonant and resonant. According to the non-driving mechanical gyroscope used in the rotating flight carrier, two working states are considered. The basic idea and the focus should be placed on the factors which lead to the instability of the instrument, namely the instability of the rotating velocity of the aircraft and the instability of the temperature characteristic.

In the non-resonant working state, the output signal of the instrument adopts the following form:

$$\alpha = \frac{(C_1 - A_1 + B_1)\dot{\varphi}_0 \Omega}{(C_1 - A_1 - B_1)\dot{\varphi}_0^2 + K}\sin(\dot{\varphi}_0 t - \gamma)$$
 (1.74)

When the elastic coefficient is large enough:

$$\alpha = \frac{(C_1 - A_1 + B_1)\dot{\varphi}_0 \Omega}{K} \sin(\dot{\varphi}_0 t - \gamma)$$
(1.75)

The advantage of the non-resonant working state is that the resonance adjustment is not required, but in order to achieve a tuning, some special methods are needed such that the output signal phase shift is equal to zero and the temperature stability is higher. The disadvantage is that the output signal has a linear relationship with the self-rotating velocity instability of the craft, and the sensitivity is low.

One of the most unstable factors in the non-resonant working state is the instability of the self-rotating angular velocity $\dot{\varphi}_0$ of the aircraft. The instrument with the resonant state can not only improve the sensitivity of the instrument, but can also eliminate the influence of the rotating angular velocity of the aircraft on the amplitude of the output signal. The condition for the resonant tuning is

$$\dot{\varphi}_0 = \omega_0$$

From a similar equation, the tuning can be achieved:

$$\omega_0 = \sqrt{\frac{(C_1 - A_1)\dot{\varphi}_0^2 + K}{B_1}} = \dot{\varphi}_0 \tag{1.76}$$

$$\frac{\omega_0}{\dot{\varphi}_0} = \sqrt{\frac{(C_1 - A_1) + K/\dot{\varphi}_0^2}{B_1}} = 1 \tag{1.77}$$

Thus Eq. (1.73) has the following form:

$$\alpha = \frac{(C_1 - A_1 + B_1)}{D_{\alpha}} \Omega \sin\left(\dot{\varphi}_0 t - \gamma - \frac{\pi}{2}\right)$$
 (1.78)

Therefore, the instrument with the resonant state can rule out the dependence of the output signal on the rotating velocity of the aircraft. The instrument parameters should be optimized to ensure that the instrument is adjusted to a resonant state.

Equation (1.77) is actually the condition of the resonant adjustment. This condition can be changed into the following form:

$$K = (B_1 + A_1 - C_1)\dot{\varphi}_0^2 \tag{1.79}$$

Thus the condition of the resonance adjustment is directly related to the rotating frequency of the aircraft, and the influence of the instability of $\dot{\varphi}_0$ is reduced.

In summary, the advantages of the resonant working state of a non-driven mechanical gyroscope are its high sensitivity and fact that the stability of the instrument phase shift is independent of the rotating velocity of the craft. The disadvantages are the need to ensure the stability of the damping work of the instrument, and the resonance adjustment work is complex.

There are some defects in these two working states of a non-driven mechanical gyroscope. Some special measures have to be taken to eliminate the defects in the instrument. The choice of the working state should be based on a variety of possible ways to compensate for or reduce the existing defects of the method.

One of the disadvantages of the non-resonant state is that the sensitivity of the instrument is low. The dependency of the output signal on the self-rotating angular velocity of the craft and can be easily eliminated by the method of integrating the output signal. While the sensitivity of the instrument can be improved by reducing the elastic coefficient K, this will result in reducing the damping effect of the instrument or this will lead to the amplitude conversion of the output signal of the gyroscope, and as the conversion is related to the square number of the aircraft's self-rotating angular velocity, it will also cause instability of the output signal. The damping effect of the instrument is reduced such that there is a negative effect on the adjustment of the quality of the instrument.

In the resonance working state, the stability of the output signal is basically dependent on the stability of the damping effect, and the velocity feedback method is used to establish the damping effect in the instrument and is able to meet the required accuracy. Under the resonant working state there is the angular velocity which is passed from the craft's rotation around the horizontal axis, while the produced inertia moment mainly relies on the damping torque to maintain a balance, and unlike the elastic torque has an effect on the non-resonant working state. However, the static elastic stiffness of the instrument faces a very serious problem in the precise adjustment of the resonant state, because the condition of the resonant tuning is related to the instability of the rotating velocity of the craft. Due to some of the above factors, in the resonant working state of a non-driven mechanical gyroscope some static elastic components of the rotating state aircraft should be fully discarded.

There are three ways to eliminate the static elasticity of the instrument:

- ① If the known instruments are the same then a sliding bearing with a small friction coefficient is used. In this case, the static elasticity is only determined by the stiffness of the elastic rod, and the signal transmission between the sensing element and the shell can be realized by the elastic rod.
- ② The angular vibration of the sensitive element is compensated by the positive feedback of the elastic moment of the torsion bar.
- 3 An elastic torsion bar with a small angle rigidity is used.

In this case, the condition of the resonant tuning takes the following form:

$$\sqrt{(B_1 - C_1 + A_1)}\dot{\varphi}_0 = 0 \tag{1.80}$$

or

$$\sqrt{\frac{C_1 - A_1}{B_1}} = 1 \tag{1.81}$$

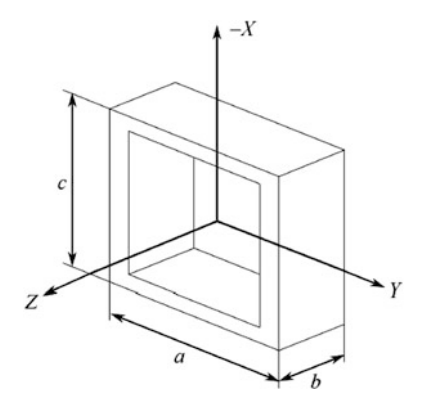
and no matter whether the condition is related to the angular velocity of rotation around the longitudinal axis of the rocket, it cannot in fact be realized.

From Fig. 1.5, the tuning condition of the resonance point can be recorded by the frame's geometry size:

$$\sqrt{\frac{C_1 - A_1}{B_1}} = \sqrt{\frac{\frac{abc(a^2 + c^2)}{12} - \frac{abc(a^2 + b^2)}{12}}{\frac{abc(b^2 + c^2)}{12}}} = \frac{c^2 - b^2}{c^2 + b^2} = 1 \ (b = 0)$$

This result is virtually impossible to achieve. In the case that the dimension b is arbitrary, the instrument works in the non-resonant region and the smaller the size of b is, the closer the working state of the instrument is to the resonance state. In

Fig. 1.5 Relationship between the frame's geometry and tuning



fact, the value of $\sqrt{\frac{C_1-A_1}{B_1}}$ can be very close to 1, and may reach 0.9–0.98. As a result, we can think that the instrument works in the near-resonant area which is close to the resonant point, and is directly close to the resonant point. Under the condition of the existence of the elastic torsion bar, although the resonance adjustment is not very accurate, it has the most important outstanding performance difference from the resonance point tuning, namely its stability is independent of the aircraft's self-rotating velocity.

Therefore, according to the technical tasks and the possibility of a non-driven mechanical gyroscope's working state to complete the task, we can draw the conclusion that the most suitable condition is resonance status with velocity feedback, and in order to ensure the stable damping performance in the instrument, the inelastic non-inertia effect is needed.

Within the range of the permissible outline dimensions of the instrument, the more appropriate choice of the geometric dimensions of the sensitive components can be more accurate to ensure the condition of the resonant tuning work, as shown in Eq. (1.81); reducing the choice of the static elastic method, first of all depends on the accuracy of easily realizing the elastic positive feedback compensation, and the possibility of ensuring that the torsion angle stiffness is as little as possible.

The sliding bearing structure is relatively simple and cheap. As shown in Eq. (1.78), the vibration angle of the instrument's sensitive elements is independent of the rotating angular velocity $\dot{\varphi}_0$ (in fact, when making a non-precise tuning, the oscillation angle is nonlinear and small (see Sect. 2.1), and is independent of $\dot{\varphi}_0$). Therefore, the input angular velocity of the rotating flight carrier is measured by the vibration angle of the sensitive element.

However, the angle sensor which is used to measure the angle position has many intrinsic defects.

- (1) A non-driven mechanical gyroscope with a hall sensor (Fig. 1.6). The hall sensor is a semiconductor device with four pieces of thin film generated by metal evaporation deposition (Fig. 1.6a), where two pole pieces constitute the input pole of the sensor and two pole pieces are used for signal detection. When the sensor is placed in a magnetic field, it generates a signal proportional to the intensity of the magnetic induction on the output end of the sensor. At this time, the instrument structure along the thickness direction is not a uniform gap of the magnetic system (Fig. 1.6b). Because the hall sensors on the sensitive element are placed in a magnetic field, the magnetic induction varies with the height of the pole and is proportional to the angle of the instrument frame. A hall sensor's fault is that its output signal is considerably dependent on the temperature. The disadvantage of the circuit scheme is that the magnetic measurement system is too complicated. There is a linear relationship between the magnetic flux in the magnetic system gap and the rotating angle of the sensing element.
- (2) A non-driven mechanical gyroscope with an inductance angle sensor (Fig. 1.7). The temperature characteristic of the output signal of an inductance angle sensor is unstable. In addition, the oscillator must be set to ensure that there is

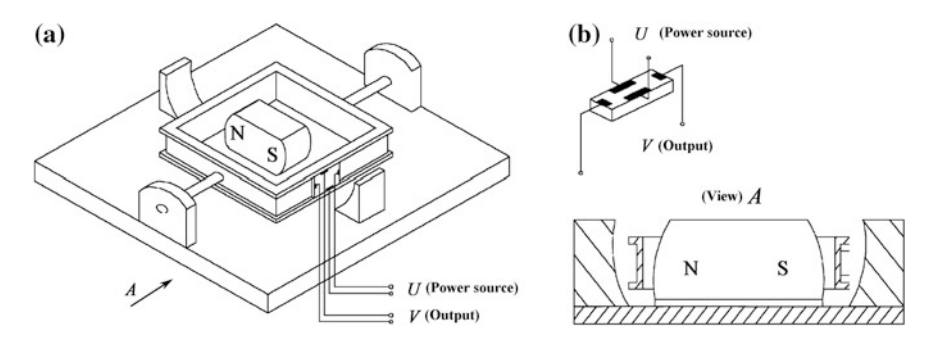
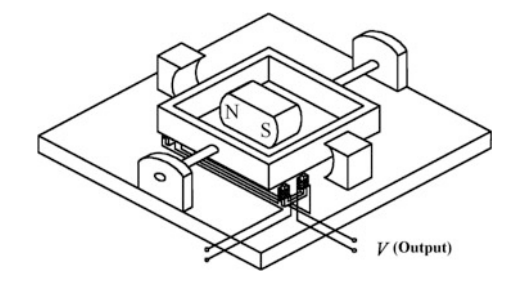


Fig. 1.6 Non-driven mechanical gyroscope with a hall sensor

Fig. 1.7 Non-driven mechanical gyroscope with an inductance angle sensor



the power of the sensor work. In a non-driven mechanical gyroscope with an inductance angle sensor, the range of oscillation angle of the sensitive element is limited. The dependent characteristic of a large temperature cannot be eliminated and the eddy current has considerable damping.

(3) A non-driven mechanical gyroscope with an eddy current angle sensor (Fig. 1.8). The working principle of this kind of sensor is based on the use of an eddy current, and the effect of an eddy current on the magnetic flux of the electromagnet flowing along the magnetic circuit is proportional to the size of the flat plate as the flat plate is rotating (Fig. 1.8a). In order to carry out the transmission and measure the information, the sensor uses a bridge circuit (Fig. 1.8b).

An eddy angle sensor also has the disadvantage of an inductance angle sensor. In order to obtain the normal operation of the vortex angle sensor, the oscillator must be equipped with. In terms of the vibration angle of a sensitive element, the eddy current angle sensor has the problem of working scope, and the output signal of the eddy current angle sensor is strongly dependent on the temperature due to the impact of the plate conductivity change.

It is obvious that the dependence of the output signal on the temperature is a common defect in all kinds of angle sensor.

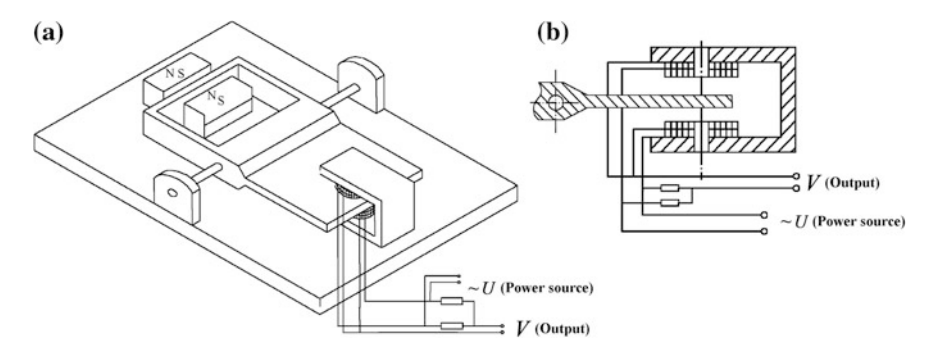
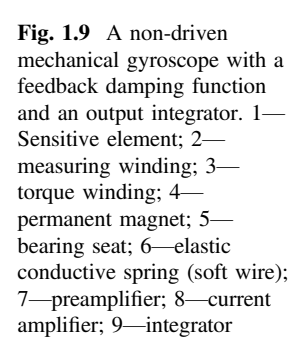
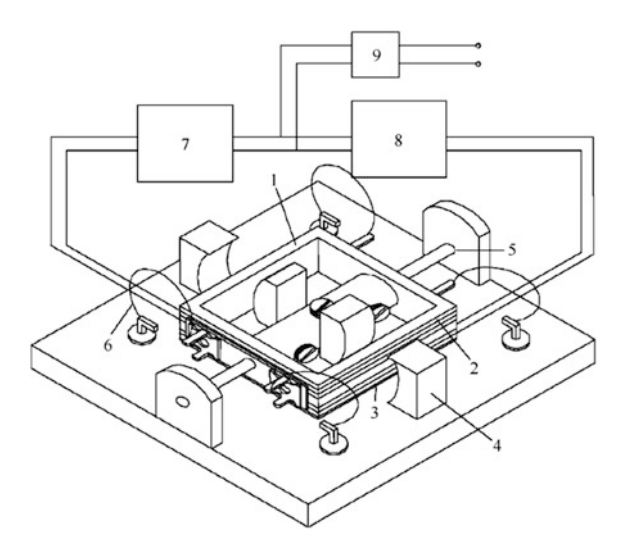


Fig. 1.8 A non-driven mechanical gyroscope with an eddy current angle sensor, a Principle diagram of the sensor; b Bridge circuit of the sensor





For the design of the temperature performance, the most stable design scheme is shown in Fig. 1.9.

In the condition of inserting an integral part at the output end of the instrument and using the electronic components with small temperature coefficients, when the temperature changes in the operating temperature range, this approach provides a fairly stable phase shift. As stated in the preface, this is most important, and its importance is even greater than the magnitude of the phase shift itself. Without a doubt, the integral part not only increases the transition process but also has a negative influence on regulating the quality of the instrument, and more detailed studies can be seen in Sect. 2.2.

However, these negative components which are related to an integral part at the output end of the instrument in working conditions are not mentioned; their effects

are less than many of the problems that are generated from all the sensor solutions using the angle sensor.

From the structural point of view or from the design of the error caused by the program itself, there is no doubt that the angular velocity output signal measurement of the sensitive element vibration is the most realistic and feasible solution. Similar design schemes of signal measurement can limit the negative effect of the friction torque in the sliding bearing. In this case, the influence of the sliding bearing friction torque does not show in the output signal and is only the threshold value of the instrument's sensitivity. Therefore, in order to reduce the sensitivity threshold, sliding bearings with low friction coefficient materials must be adopted.

The temperature of the output signal, which is determined by the signal detection circuit, is unstable. Under this condition it is dependent only on the temperature of the magnet, the minimum value can be achieved by selecting a magnetic material with small temperature coefficients.

The instability damping effect, which is caused by the vortex and produced in the conductive material of the sensitive component shell can be eliminated by using non-conductive materials in the sensitive component's shell, or by adopting a more reasonable approach such as the structure scheme of the sensitive component without a shell.

As was put forward previously, the damping effect of the instrument is of decisive significance, and is directly related to the sensitivity, accuracy, and stability of the output signal. It is advantageous to obtain the signal by measuring the vibration angular velocity of the instrument's sensitive element. Through the velocity feedback with the current amplifier, the damping structure in the instrument can again be confirmed as suitable and the temperature dependency of the damping effect can be eliminated (see Sect. 1.6). It should be pointed out that the use of velocity feedback will lead to the following consequences:

- ① Some changes are needed to the design: if components with feedback electronics are adopted, then in the condition of increasing the mechanical structure of the instrument, the total size of the instrument must be relaxed accurately.
- ② The torque distribution in the framework of the sensor can be changed: The simplest and most convenient solution to this problem is to change the winding mode of the sensor on the sensitive element, and the same sensitive winding should be applied to the same sensitive element. Two windings overlap on the same frame and it is inevitable that mutual inductance will be produced. In Sect. 1.6, the effect of the two windings' mutual inductance on the stability and the reading of the instrument will be studied.

According to the requirements of precision and sensitivity, we should weigh the advantages and disadvantages of the compromise in order to help select the damping of the instrument. A small attenuation coefficient ξ can cause both the instrument sensitivity and the settling time to increase. Due to the instability of the

rotating flight carrier's angular velocity $\dot{\varphi}_0$ around the longitudinal axis, the output signal will be unstable. As has been pointed out, it is impossible to accurately tune the resonance. The larger the attenuation is, the lower the instrument sensitivity is.

According to the structure of the instrument circuit, we can draw the following conclusion: The instrument's sensitive element is arranged without a skeleton hanger frame and with a single degree of freedom. The plane of the frame is perpendicular to the aircraft rotation axis. Two groups of windings are wound around the frame and located in the same magnetic field of the permanent magnet. The magnetic lines of the windings are parallel to the plane of the frame. One set of windings is the sensitive winding which is designed to measure the vibration angular velocity $\dot{\alpha}$ of the sensitive element and the other set is the torque winding used to ensure the torque effect and this is proportional to the vibration velocity. The two sets of windings are connected by the current amplifier and the front amplifier. According to the vibration angle of the framework, the output information is measured by the integrator, which is connected to the output end of the current pre-amplifier. Thus it can be ensured that the output signal is independent on the angular velocity $\dot{\phi}_0$ of the aircraft.

1.5 Dynamic Performance Regulation of the System

Under the condition of the existence of the constant rotating angular velocity of the craft around the horizontal axis and regardless of the principle to establish the damping force and the elastic force of the instrument, the regulation quality of the rotor vibrating gyroscope used in rotating aircraft is analyzed. Therefore, we first study the transition process of the instrument, namely the complete solution of the differential equation of the motion of the sensing element:

$$\ddot{\alpha} + 2\xi\omega_0\dot{\alpha} + \omega_0^2\alpha = \frac{H_0}{B_1}\Omega\sin(\dot{\phi}t - \gamma)$$
 (1.82)

Equation (1.66) is a complete solution of Eq. (1.82):

$$\alpha = C^* e^{-\zeta \omega_0 t} \sin \left[\left(\omega_0 \sqrt{1 - \zeta^2} \right) t + \beta^* \right] + \lambda \frac{H_0}{B_0} \Omega \sin(\dot{\varphi}_0 t - \gamma + x)$$

According to the initial condition $\alpha(0) = 0$ and $\dot{\alpha}(0) = 0$, the constants C^* and β^* can be obtained:

$$\begin{split} \dot{\alpha} &= -\xi \omega_0 C^* e^{-\xi \omega_0 t} \sin \left[\left(\omega_0 \sqrt{1 - \xi^2} \right) t + \beta^* \right] \\ &+ C^* e^{-\xi \omega_0 t} \omega_0 \sqrt{1 - \xi^2} \cos \left[\left(\omega_0 \sqrt{1 - \xi^2} \right) t + \beta^* \right] \\ &+ \lambda \frac{H_0}{R_0} \Omega \dot{\varphi}_0 \cos (\dot{\varphi}_0 t - \gamma + x) \end{split} \tag{1.83}$$

$$\begin{cases} C^* \sin \beta^* + \lambda \frac{\mu_0}{B_0} \Omega \sin(\chi - \gamma) = 0 \\ -\xi \omega_0 C^* \sin \beta^* + \omega_0 \sqrt{1 - \xi^2} C^* \cos \beta^* + \lambda \frac{\mu_0}{B_0} \Omega \dot{\phi}_0 \cos(\chi - \gamma) = 0 \end{cases}$$
 (1.84)

Therefore,

$$\beta^* = \arctan\left(\frac{\omega_0 \sqrt{1 - \xi^2}}{\sqrt{\xi^2 \omega_0^2 + \dot{\varphi}_0^2} \cdot \sin\left[x - \gamma + \arctan\left(\frac{\dot{\varphi}_0}{\xi\omega_0}\right)\right]}\right)$$
(1.85)

$$C^* = -\frac{\lambda H_0 \Omega \sin(x - \gamma)}{B_0 \omega_0 \sqrt{1 - \xi^2}} \sqrt{\omega_0^2 (1 - \xi^2) + (\xi^2 \omega_0^2 + \dot{\varphi}_0^2) \sin^2 \left[x - \gamma + \arctan \left(\frac{\dot{\varphi}_0}{\xi \omega_0} \right) \right]}$$
(1.86)

From Eqs. (1.37), (1.67), (1.68), (1.70) and (1.72), we can obtain

$$\beta^* = \arctan\left(\frac{\sqrt{\frac{\left[(C_1 - A_1)\dot{\varphi}_0^2 + K\right]}{B_1} - \frac{D_{\alpha}^2}{4B_1^2}}}{\sqrt{\frac{D_{\alpha}^2}{4B_1^2} + \dot{\varphi}_0^2} \cdot \sin\left[\arctan\left(\frac{2B_1\dot{\varphi}_0}{D_{\alpha}}\right) - \arctan\left(\frac{2D_{\alpha}\dot{\varphi}_0}{(C_1 - A_1 - B_1)\dot{\varphi}_0^2 + K}\right) - \gamma\right]}\right)$$
(1.87)

$$C^{*} = \frac{(C_{1} - A_{1} + B_{1})\dot{\varphi}_{0}\Omega \sin\left[\gamma + \arctan\left(\frac{2D_{x}\dot{\varphi}_{0}}{(C_{1} - A_{1} - B_{1})\dot{\varphi}_{0}^{2} + K}\right)\right]}{\sqrt{\left\{\left[(C_{1} - A_{1} - B_{1})\dot{\varphi}_{0}^{2} + K\right]^{2} + (D_{x}\dot{\varphi}_{0})^{2}\right\}}}$$

$$\times \sqrt{1 + \frac{(4B_{1}^{2}\dot{\varphi}_{0}^{2} + D_{x}^{2})\sin^{2}\left[\arctan\left(\frac{2B_{1}\dot{\varphi}_{0}}{D_{x}}\right) - \gamma - \arctan\left(\frac{2D_{x}\dot{\varphi}_{0}}{(C_{1} - A_{1} - B_{1})\dot{\varphi}_{0}^{2} + K}\right)\right]}}{4B_{1}\left[(C_{1} - A_{1})\dot{\varphi}_{0}^{2} + K\right] - D_{x}^{2}}$$

$$(1.88)$$

In this case, Eq. (1.66) has the following form:

$$\begin{split} &\alpha = \lambda \frac{H_0}{B_0} \Omega \, \sin(\dot{\varphi}_0 t + x - \gamma) \\ &- \frac{\lambda H_0 \Omega \, \sin(x - \gamma)}{B_0 \omega_0 \sqrt{1 - \xi^2}} \sqrt{\omega_0^2 \big(1 - \xi^2\big) + \big(\xi^2 \omega_0^2 + \dot{\varphi}_0^2\big) \sin^2 \left[x - \gamma + \arctan\left(\frac{\dot{\varphi}_0}{\xi \omega_0}\right)\right]} \\ &\times e^{-\xi \omega_0 t} \sin \left[\left(\omega_0 \sqrt{1 - \xi^2}\right) t + \arctan\left(\frac{\omega_0 \sqrt{1 - \xi^2}}{\sqrt{\xi^2 \omega_0^2 + \dot{\varphi}_0} \cdot \sin\left[x - \gamma + \arctan\left(\frac{\dot{\varphi}_0}{\xi \omega_0}\right)\right]} \right) \right] \end{split}$$

or

$$\alpha = \frac{\lambda H_0}{B_0} \Omega \left\{ \sin(\dot{\varphi}_0 t + x - \gamma) - \frac{\sin(x - \gamma)}{\omega_0 \sqrt{1 - \xi^2}} \sqrt{\omega_0^2 (1 - \xi^2) + (\xi^2 \omega_0^2 + \dot{\varphi}_0^2) \sin^2 \left[x - \gamma + \arctan\left(\frac{\dot{\varphi}_0}{\xi \omega_0}\right) \right]} \right\}$$

$$\times e^{-\xi \omega_0 t} \sin \left[\left(\omega_0 \sqrt{1 - \xi^2} \right) t + \arctan\left(\frac{\omega_0 \sqrt{1 - \xi^2}}{\sqrt{\xi^2 \omega_0^2 + \dot{\varphi}_0 \cdot \sin \left[x - \gamma + \arctan\left(\frac{\dot{\varphi}_0}{\xi \omega_0}\right) \right]} \right) \right] \right\}$$

$$(1.89)$$

Under the condition of the existence of the constant rotating angular velocity of the craft around the horizontal axis, Eq. (1.89) is the transition process of the rotor vibration gyroscope used in the rotating state aircraft.

The numerical value obtained in the transition process is in the form of

$$\alpha_{\text{stable}} = \alpha_{t \to \infty} = \lambda \frac{H_0}{R_0} \Omega \sin(\dot{\varphi}_0 t - \gamma + \chi)$$
 (1.90)

The form of the transition process can be observed obviously when considering the instrument's reaction to the constant input action of the aircraft in the implicated coordinate system. In this case, the rotation angular velocity $\dot{\varphi}_0$ of the rotating flight carrier around the longitudinal axis can be considered as constant (stable).

The value of the right part of the motion equation of the sensitive element is unchanged (in the condition that the measured angular velocity is sine constant), when the angle $\dot{\varphi}_0 t - \gamma$ is constant. In the case of a circular oscillation, this angle is constant and the frequency of the circumferential oscillation is coincident with the rotating frequency of the rotating flight carrier, that is, $\gamma = \dot{\varphi}_0 t - \gamma_1$, where γ_1 is a constant angle. In this case, the phenomenon of superposition of two periodic signals which are similar in frequency does not occur, as shown in Eq. (1.89), and it is also shown by the fact that the result of the decay component of the transition process is produced.

Then from Eq. (1.66), we have

$$\begin{cases} \alpha = Ce^{-\xi\omega_0 t} \sin\left[\left(\omega_0\sqrt{1-\xi^2}\right)t + \beta\right] + \lambda \frac{\mu_0}{\mu_0}\Omega \sin(\gamma_1 + x) \\ \dot{\alpha} = -\xi\omega_0 Ce^{-\xi\omega_0 t} \sin\left[\left(\omega_0\sqrt{1-\xi^2}\right) + \beta\right] + C\omega_0\sqrt{1-\xi^2} \cos\left[\left(\omega_0\sqrt{1-\xi^2}\right)t + \beta\right] \end{cases}$$

$$(1.91)$$

$$\begin{cases} C \sin \beta + \frac{H_0}{B_0} \Omega \sin(\gamma_1 + x) = 0\\ -\xi \omega_0 C \sin \beta + \omega_0 \sqrt{1 - \xi^2} C \cos \beta = 0 \end{cases}$$
 (1.92)

Thus we have

$$\beta = \arctan\left(\frac{\sqrt{1-\xi^2}}{\xi}\right) = \arctan\left(\frac{\sqrt{4B_1\left[(C_1 - A_1)\dot{\varphi}_0^2 + K\right] - D_\alpha^2}}{D_\alpha}\right)$$
(1.93)

$$C = -\frac{\lambda H_0}{B_0 \sqrt{1 - \xi^2}} \Omega \sin(\gamma_1 + \chi) = -\frac{(C_1 - A_1 + B_1) \dot{\varphi}_0 \Omega \sin(\gamma_1 + \chi)}{\left[(C_1 - A_1) \dot{\varphi}_0^2 + K \right] \sqrt{1 - \frac{D_x^2}{4B_1 \left[(C_1 - A_1) \dot{\varphi}_0^2 + K \right]}}}$$
(1.94)

Therefore, Eq. (1.91) has the form of

$$\alpha = -\frac{\lambda H_0 \sin(\gamma_1 + \chi)}{B_0 \sqrt{1 - \xi^2}} \Omega e^{-\xi \omega_0 t} \sin \left[\left(\omega_0 \sqrt{1 - \xi^2} \right) t + \arctan \left(\frac{\sqrt{1 - \xi^2}}{\xi} \right) \right]$$

$$+ \lambda \frac{H_0}{B_0} \Omega \sin(\gamma_1 + \chi)$$

$$= \frac{\lambda H_0 \sin(\gamma_1 + \chi)}{B_0} \Omega \left\{ 1 - \frac{e^{-\xi \omega_0 t}}{\sqrt{1 - \xi^2}} \sin \left[\left(\omega_0 \sqrt{1 - \xi^2} \right) t + \arctan \left(\frac{\sqrt{1 - \xi^2}}{\xi} \right) \right] \right\}$$

$$(1.95)$$

Equation (1.95) is a transition process under the condition that the constant disturbance acts on the sensitive element in the implicated coordinate system of the aircraft. The stable numerical form of the vibration angle α of the sensitive element is

$$\alpha_{\text{stable}} = \alpha_{t \to \infty} = \lambda \frac{H_0}{B_0} \Omega \sin(\gamma_1 + \chi)$$
 (1.96)

where α_{stable} is the vibration angle of the sensitive element with some stable states; λ is a dynamic coefficient; χ is a phase shift.

It should be noted that this is different from Eq. (1.90) in that the angle value determined by Eq. (1.96) is constant. The loop scheme and the parameters of the above selected gyroscope are discussed, but the method of establishing the damping function in the instrument is not considered. The parameters are

$$H_0 = (C_1 - A_1 + B_1)\dot{\varphi}_0 \tag{1.97}$$

$$B_0 = (C_1 - A_1)\dot{\varphi}_0^2 \tag{1.98}$$

$$\omega_0 = \dot{\varphi}_0 \sqrt{\frac{C_1 - A_1}{B_1}} \tag{1.99}$$

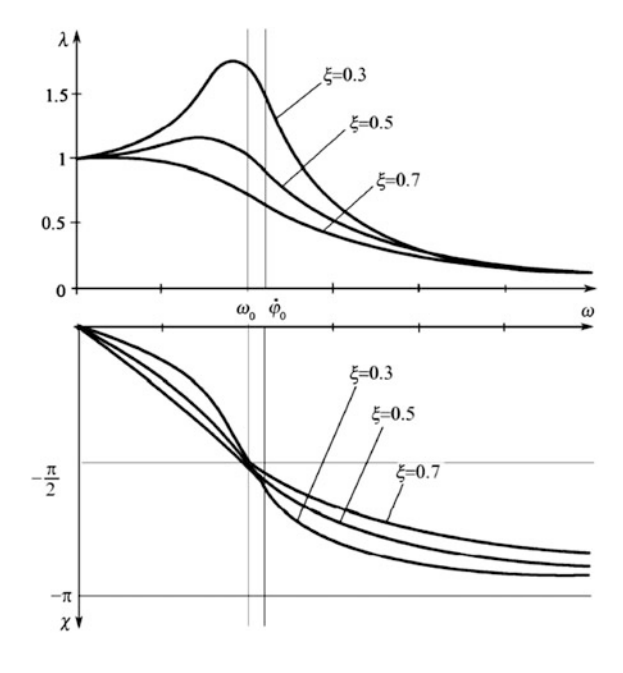
$$\xi = \frac{D_{\alpha}}{2\dot{\varphi}_{0}\sqrt{B_{1}(C_{1} - A_{1})}} \tag{1.100}$$

At this time, the expression of the gyroscope transition process will not change in nature. However, from Eqs. (1.99) and (1.100), both λ and χ are changing. In the implicated coordinate system of the aircraft, if there is a constant force then these values will not affect the transition process of the instrument. However, if there is a constant force in the inertia space, their direct effects show up in the transition process and the stable oscillation of the sensitive elements.

The dynamic coefficient λ and the phase shift χ affect the frequency characteristic curves of the amplitude and the phase of the oscillation loop, as shown in Fig. 1.10. From the curves in Fig. 1.10, we can see that the instrument works in the near-resonance region and is directly approaching the near-resonance point.

Because of the objectivity of the curves in Fig. 1.10, they are suitable for determining the parameters of the instrument. From Eq. (1.99), it is known that the

Fig. 1.10 Frequency characteristics of the amplitude and phase of the sensitive element with different attenuation coefficients



inertia moment of the sensitive element can be adjusted to the working point of the curves in Fig. 1.10, but this will happen in the near-resonance region.

Thus, each point of these characteristic curves has the feature of the inertial torque of each group and Eq. (1.81) shows more accurately that the inherent non-attenuation vibration frequency is closer to the rotating frequency around the aircraft's longitudinal axis.

There is a close relationship between the inherent frequency of non-damped oscillation in the instrument and the natural frequency of the rotating flight carrier around the longitudinal axis. By using the numerical values of the inertia moment and the vibration attenuation coefficient of the sensitive element, Eqs. (1.69) and (1.71) can be simplified and determined. Therefore, from the damping value constructed in the instrument, the values of λ and γ can be determined by

$$\lambda = \frac{C_1 - A_1}{\sqrt{(C_1 - A_1 - B_1)^2 + 4\xi^2 B_1 (C_1 - A_1)}}$$
(1.101)

$$\chi = -\arctan\left(\frac{2\xi\sqrt{B_1(C_1 - A_1)}}{C_1 - A_1 - B_1}\right) \tag{1.102}$$

By substituting Eq. (1.100), Eqs. (1.101) and (1.102) can be simplified as

$$\lambda = \frac{(C_1 - A_1)\dot{\varphi}_0}{\sqrt{(C_1 - A_1 - B_1)^2 \dot{\varphi}_0^2 + D_a^2}}$$
(1.103)

$$\chi = -\arctan\left(\frac{D_a}{(C_1 - A_1 - B_1)\dot{\varphi}_0}\right) \tag{1.104}$$

When the instrument is working in the resonant state, Eqs. (1.103) and (1.104) can be determined by

$$\lambda = \frac{(C_1 - A_1)\dot{\varphi}_0}{D_{\alpha}} \tag{1.105}$$

$$\chi = -\frac{\pi}{2} \tag{1.106}$$

The curves in Fig. 1.10 are drawn using the different vibration attenuation coefficients. When the value of ξ increases, the peak value on the λ curve will decrease and move to the left along the frequency axis.

The instrument is adjusted to be resonant such that the unstable rotating velocity of the rotating flight carrier around the longitudinal axis is independent of the output signal and increases the sensitivity of the instrument.

The increase of the instrument's sensitivity is related to the sharp increase of the amplitude-frequency characteristic in the natural frequency of the non-damped

oscillation of the oscillating loop (the dynamic coefficient). Subsequent facts prove that this phenomenon is correct only when ξ is small, because only in the case of a small value of ξ , does the amplitude-frequency characteristic of the oscillating loop (dynamic coefficient) in the natural frequency of the non-damped vibration have a maximum value. Therefore, in the case of a big attenuation coefficient ($\xi > 0.3$), the instrument is adjusted to a resonant state, but the maximum value of the sensitivity will not be adjusted simultaneously. In other words, the frequency at the maximum value of the instrument sensitivity and the instrument output signal are independent of the rotating velocity frequency around the vertical axis of the rotating flight carrier and they are different from each other, but in the case of $\xi < 0.3$, the two frequencies actually overlap.

The dynamic coefficients with the maximum frequency can be expressed by the following formula:

$$\dot{\varphi}_M = \omega_0 \sqrt{1 - 2\xi^2} \tag{1.107}$$

At the frequency $\dot{\varphi}_M$, the sensitivity has a maximum value. When the instrument is adjusted according to the frequency $\dot{\varphi}_M$, there holds

$$\dot{\varphi}_0 = \dot{\varphi}_M = \omega_0 \sqrt{1 - \frac{D_\alpha^2}{2B_1(C_1 - A_1)\dot{\varphi}_0^2}}$$
(1.108)

Denote the mistuning coefficient of the instrument by

$$\mu = \sqrt{\frac{C_1 - A_1}{B_1}} = \frac{\omega_0}{\dot{\varphi}_0} \tag{1.109}$$

Then

$$\dot{\varphi}_0 = \sqrt{\omega_0^2 - \frac{D_\alpha^2}{2B_1(C_1 - A_1)}\mu^2} = \sqrt{\omega_0^2 - \frac{D_\alpha^2}{2B_1^2}}$$

Thus we can calculate the condition that the instrument is tuned to the frequency $\dot{\phi}_M$ as

$$2B_1^2\dot{\varphi}_0^2 = 2B_1^2\omega_0^2 - D_2^2$$

From the above equation, we have

$$D_{\alpha} = B_1 \sqrt{2(\omega_0^2 - \dot{\varphi}_0^2)} = \dot{\varphi}_0 B_1 \sqrt{2(\mu^2 - 1)}$$
 (1.110)

From Eq. (1.110), the following conclusion can be drawn:

- (1) Because the rotating angular velocity around the longitudinal axis of the aircraft is not stable, the instrument cannot be precisely tuned through $\dot{\varphi}_M$. Thus the similar tuning method is not appropriate to improve the sensitivity. Comparing Eq. (1.81) with Eqs. (1.110) and (1.81) is more meaningful for the detected instrument.
- (2) Obviously, when the detuning coefficient $\mu \ge 1$, Eq. (1.110) can be achieved. However, as previously noted, μ cannot actually be achieved. This situation can be explained in that the instrument works in the back resonant region, while if the maximum value of the dynamic coefficient $\xi \ge 0$, the instrument always works in the front of the resonant region.

In the coordinate system connected with the craft, a constant force acts on the sensitive element. Substituting the simplified formula of the dynamic coefficient and the phase shift, the following expressions for the definite integral can be obtained:

$$\beta = \arctan\left(\frac{\sqrt{4B_1(C_1 - A_1)\dot{\varphi}_0^2 - D_a^2}}{D_{\alpha}}\right)$$
 (1.111)

$$C = -\frac{(C_1 - A_1 + B_1)\Omega \sin \gamma_1}{(C_1 - A_1)\dot{\varphi}_0 \sqrt{1 - \frac{D_a^2}{4B_1(C_1 - A_1)\dot{\varphi}_0^2}}}$$
(1.112)

In the case of resonance, the definite integral can be reduced to the following form:

$$\beta = \arctan\left(\frac{\sqrt{4B_1^2\dot{\varphi}_0^2 - D_\alpha^2}}{D_\alpha}\right) \tag{1.113}$$

$$C = \frac{4B_1 \Omega \sin \gamma_1}{\sqrt{(4B_1^2 \dot{\varphi}_0^2 - D_\alpha^2)}}$$
 (1.114)

In the case that the accuracy is resonant, the transition process can be described by the following expressions:

$$\alpha = \frac{2\Omega \sin \gamma_1}{\dot{\varphi}_0} \left\{ 1 - \frac{2B_1 \dot{\varphi}_0 e^{-\frac{D_2}{2B}t}}{\sqrt{4B_1^2 \dot{\varphi}_0^2 - D_{\alpha}^2}} \sin \left[\frac{\sqrt{4B_1^2 \dot{\varphi}_0^2 - D_{\alpha}^2}}{2B_1} t + \arctan \left(\frac{\sqrt{4B_1^2 \dot{\varphi}_0^2 - D_{\alpha}^2}}{D_{\alpha}} \right) \right] \right\}$$
(1.115)

When the instrument is working on the direct approximation of the resonance point, the value of the transition process has the following form:

$$\alpha_{\text{tran}} = \frac{2\Omega}{\dot{\varphi}_0} \sin \gamma_1 \tag{1.116}$$

Fig. 1.11 Transition process of the sensitive element

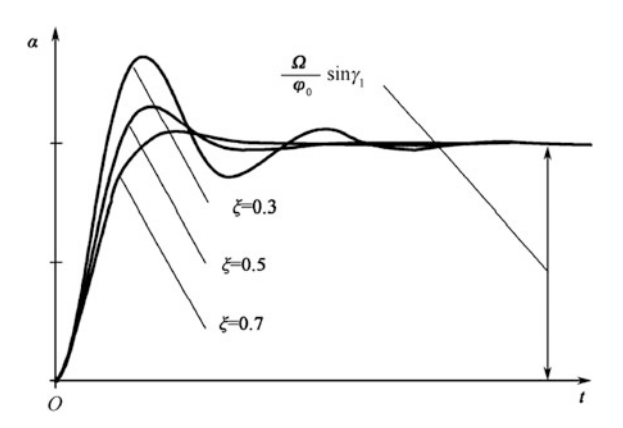


Figure 1.11 gives the transition process of the selected gyroscope and is consistent with Eq. (1.115). Therefore, in the implicated coordinate system of the aircraft, corresponding to every point on the time axis, the constant angular velocity Ω of the rotating flight carrier will enable the small framework to generate a deflection angle α_{stable} . Moreover, when the self-rotating velocity $\dot{\varphi}_0$ of the craft around the longitudinal axis increases, the settling time is not reduced because the time constant $\frac{1}{\dot{\zeta}\omega_0} = \frac{2B_1}{D_2}$ of the damped oscillation in the transition process is independent on the self-rotating velocity around the longitudinal axis of the craft. In this case, the sensitivity of the instrument is also reduced.

From all the facts mentioned above, the following conclusions can be drawn:

- (1) In order to obtain high sensitivity, in the case that μ is known, ξ must be reduced. It should be kept in mind that the damping coefficient is mainly determined by the size of the damping effect of the instrument, and if the damping effect is reduced, the stability of the instrument will deteriorate.
- (2) A reasonable choice of $\xi = 0.5 \sim 0.7$ can guarantee that the transition process, regulation quality, and the stability of the instrument will all be improved.

1.6 Stability of a Non-driven Mechanical Gyroscope with Negative Velocity Feedback

The steady state motion equation of the instrument sensitive element:

$$\alpha = \lambda \frac{H_0}{B_0} \Omega \sin(\dot{\varphi}_0 t - \gamma + \chi) \tag{1.117}$$

In general, the steady-state motion of the framework is the oscillation of frequency 0. The amplitude and phase of the vibration are determined by the motion

parameters of the rotating carrier, the characteristics and parameters of the instrument, and the feedback velocity. We have determined the influence of feedback and its rationality and necessity. At the same time, we also take into account the fact that the damping function in the instrument depends on the sum of the feedback damping effect and the natural damping effect (basically aerodynamic), that is, $D_{\alpha} = D_0 + D_{\text{feedback}}$, where D_0 is the aerodynamic damping effect and D_{feedback} is the feedback damping effect.

In order to constitute the block diagram of the instrument, where the inputs are the angular velocities Ω_{ξ} and Ω_{η} , and the output is the oscillating angle of the sensitive element, the motion equation of the sensitive element is rewritten as

$$B_1\ddot{\alpha} + D_\alpha\dot{\alpha} + B_0\alpha = H_0\left(\Omega_\xi\sin\varphi - \Omega_\eta\cos\varphi\right) - B_1\left(\dot{\Omega}_\xi\cos\varphi + \dot{\Omega}_\eta\sin\varphi\right)$$
(1.118)

$$B_1\ddot{\alpha} + D_\alpha\dot{\alpha} + B_0\alpha = (H_0\Omega_{\xi} - B_1\dot{\Omega}_{\eta})\sin\varphi - (H_0\Omega_{\eta} + B_1\dot{\Omega}_{\xi})\cos\varphi \qquad (1.119)$$

Substituting (1.37), we can obtain

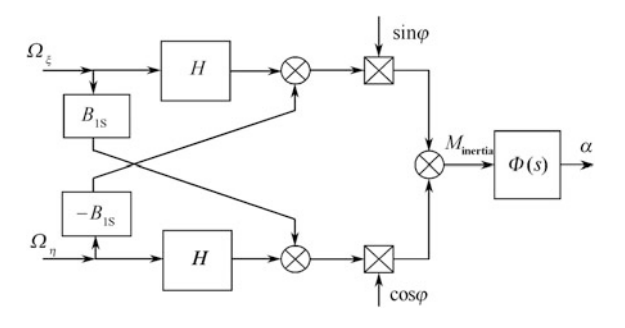
$$B_1\ddot{\alpha} + D_{\alpha}\dot{\alpha} + B_0\alpha = \left[(C_1 - A_1 + B_1)\dot{\varphi}\Omega_{\xi} - B_{1s}\dot{\Omega}_{\eta} \right] \sin\varphi - \left[(C_1 - A_1 + B_1)\dot{\varphi}\Omega_{\eta} + B_{1s}\dot{\Omega}_{\xi} \right] \cos\varphi$$
 (1.120)

The block diagram of Fig. 1.12 is in accord with Eq. (1.120), and is the series circuit diagram consisting of a dual channel network and a single channel network. The dual channel network is a soft connection non-symmetric line with a cut-through by means of rotating around the longitudinal axis of the aircraft, and the resulting input force exhibits the modulation characteristic. The single channel network is the transfer function of this instrument.

In the case of constant angular velocity, the dual channel network in Fig. 1.12 shows a change, and has the form shown in Fig. 1.13, while the single channel network does not change.

The double channel network of the diagram is disconnected, while the modulation function is set up by rotating around the longitudinal axis of the craft. In order to examine the stability of the instrument, the single channel network, which is limited to the block diagram, is studied as shown in Fig. 1.13.

Fig. 1.12 Block diagram of a non-driven mechanical gyroscope



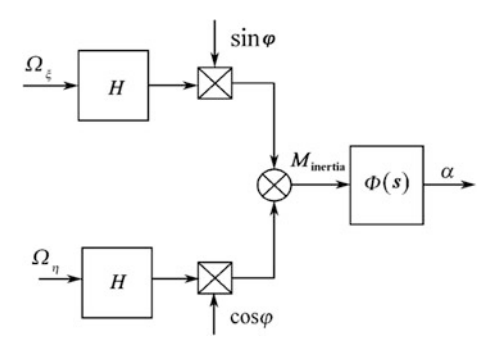


Fig. 1.13 Block diagram of a non-driven mechanical gyroscope under constant angular velocity

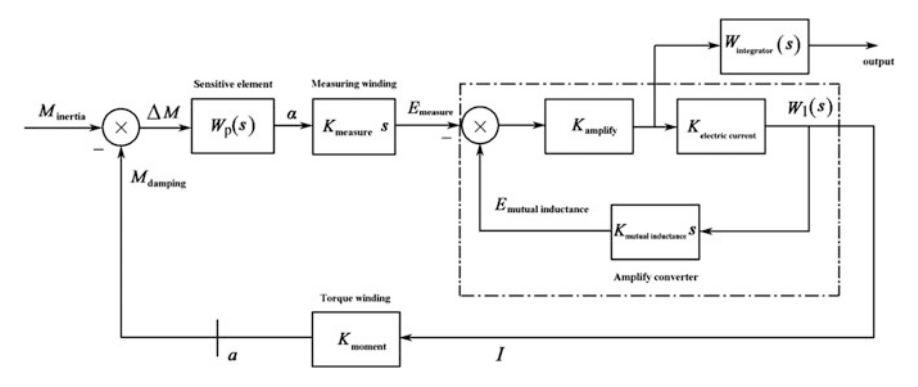


Fig. 1.14 Block diagram of a non-driven mechanical gyroscope with velocity feedback (a single channel network)

For the above reasons, if the single channel network is stable, the whole instrument is stable. Therefore, the single channel network diagram (Fig. 1.14) can be separately investigated.

In Fig. 1.14, M_{inertia} is the moment inertia, that is, the moment is produced by the angular velocity rotating around the horizontal axis of the aircraft; M_{damping} is the damping moment, that is, the moment is established by the feedback; $W_P(s)$ is the transfer function of the sensitive element; α is the oscillation angle of the sensitive element; K_{measure} is the measuring winding transfer coefficient of the sensitive element; E_{measure} is the induction electromotive force in sensitive windings; K_{amplify} is the amplify coefficient of the preamplifier; $K_{\text{electric current}}$ is the amplification coefficient of the current amplifier; $K_{\text{mutualinductance}}$ is the mutual inductance coefficient; $E_{\text{mutualinductance}}$ is the induced electromotive force due to the mutual inductance of the winding and the torque winding; K_{moment} is the moment winding transfer coefficient of the sensitive element; $W_{\text{integrator}}(s)$ is the transfer function of the integrator.

Because some characteristics of the instrument such as the natural frequency of non-damped oscillation are dependent on the frequency that is rotating around the longitudinal axis of the aircraft, it should be noted that the frequency of the inertia moment $M_{\rm inertiamoment}$ may change when the amplitude frequency characteristic and the phase frequency characteristic are investigated. Because of changes in the frequency of rotation around the longitudinal axis of the aircraft, the vibration frequency of the sensitive element also changes. When the aircraft has a circular oscillation, no matter what the other reasons are, the vibration frequency of the sensitive elements will not be changed.

Therefore, the stability of the instrument should be considered by two block diagrams. The two transfer functions of the sensitive elements are used, and these functions satisfy the following description.

(1) The frequency change of the external action causes the damping oscillation frequency of the sensitive element. In this case, the transfer function of the sensitive element is

$$W_{P}'(s) = \frac{\alpha(s)}{\Delta M(s)} = \frac{1}{B_{1}s^{2} + D_{0}s + B_{0}} = \frac{1}{B_{1}s^{2} + D_{0}s - (C_{1} - A_{1})(j\dot{\varphi}_{0})^{2}}$$

$$= \frac{1}{(B_{1} - C_{1} + A_{1})s^{2} + D_{0}s} = \frac{1}{D_{0}s} \frac{1}{\frac{B_{1} - C_{1} + A_{1}}{D_{0}}s + 1} = \frac{1}{K_{P}'s} \frac{1}{T's + 1}$$
(1.121)

where K'_P is the reciprocal of the amplification coefficient for the transfer function of the sensitive element, $K'_P = D_0$, which is the aerodynamic damping coefficient; T' is the time constant of the transient process of the sensitive element, i.e.,

$$T' = \frac{B_1 - C_1 + A_1}{D_0} \tag{1.122}$$

(2) The frequency change of the external force will not cause the frequency change of the non-damping vibration. At this time, the transfer function of the sensitive element of the instrument is

$$W_p(s) = \frac{\alpha(s)}{\Delta M(s)} = \frac{1}{B_1 s^2 + D_0 s + B_0} = \frac{1}{K_P} \frac{1}{T_0 s^2 + 2\xi_0 T_0 s + 1}$$
(1.123)

where K_P is the equivalent elastic angular stiffness for the sensitive element, i.e.,

$$K_p = (C_1 - A_1)\dot{\varphi}_0^2 = B_0 \tag{1.124}$$

 T_0 is the oscillation time constant for the sensitive element, i.e.,

$$T_0 = \frac{1}{\omega_0} = \sqrt{\frac{B_1}{B_0}} = \frac{1}{\dot{\varphi}_0} \sqrt{\frac{B_1}{C_1 - A_1}} = \frac{1}{\mu \dot{\varphi}_0}$$
 (1.125)

 ξ_0 is the relative vibration attenuation coefficient of the instrument under the action of aerodynamic damping:

$$\xi_0 = \frac{D_0}{2\omega_0 B_1} = \frac{D_0}{2\sqrt{B_0 B_1}} = \frac{D_0}{2\dot{\varphi}_0 \sqrt{(C_1 - A_1)B_1}}$$
(1.126)

It should be noted that the aerodynamic damping effect is small and ξ_0 is no more than 0.05.

The transfer function of the amplifier—converter is

$$W_{1}(s) = \frac{K_{\text{amplify}}K_{\text{electric current}}}{1 + K_{\text{amplify}}K_{\text{electric current}}K_{\text{mutual inductance}}s} = \frac{K_{\text{amplify}}K_{\text{electric current}}}{1 + T_{\text{amplify}}s} \quad (1.127)$$

where

$$T_{\text{amplify}} = K_{\text{amplify}} K_{\text{electric current}} K_{\text{mutual inductance}}$$
 (1.128)

Because the harmonic of frequency $\dot{\varphi}_0$ is the output signal of the instrument, a non-periodic loop with a large time constant $T_{\rm inertia}$ can be selected as an integrator. Thus

$$W_{\text{integrator1}}(s) = \frac{W_{\text{integrator1}}}{1 + T_{\text{integrator}}s}$$
(1.129)

The integrators studied in this book have two kinds of deformation: one kind has already been mentioned with a large time constant of a non-periodic loop and the other kind is the combination of a differential loop and the vibration loop with the following transfer function:

$$W_{\text{integrator2}}(s) = K_{\text{integrator2}} \frac{T_1 s + 1}{T_2^2 s^2 + 2\xi_{\text{integrator}} T_2 s + 1}$$
(1.130)

For the integrator with the transfer function in Eq. (1.130), in the range of 10–20 Hz rotation frequency around the vertical axis of the aircraft, then by means of changing the transfer function parameters (time constant and attenuation coefficient) the high stability of the phase shift influenced by this integrator is better than that of the integrator with the transfer function in Eq. (1.129).

Three kinds of instrument electronic circuits—no integrator at the instrument output, integrator with the transfer function in Eq. (1.129) and integrator with the transfer function in Eq. (1.130)—are compared. However, the fourth possible

circuit that uses the integrator directly of the feedback can make the velocity feedback into the auxiliary elasticity, and its negative impacts on the instrument are pointed out in Sect. 1.4.

The transfer function of the system is now analyzed. The open-loop system which is disconnected at I is:

$$W(s) = W_p(s)K_{\text{measure}}sW_1(s) \tag{1.131}$$

Consider Eqs. (1.121), (1.122) and (1.123):

$$W'(s) = W'_{p}(s)K_{\text{measure}}sW_{1}(s)K_{\text{moment}}$$

$$= \frac{K_{\text{moment}}K_{\text{measure}}K_{\text{amplify}}K_{\text{electric current}}}{K'_{p}} \frac{1}{(T's+1)(T_{\text{amplify}}s+1)}$$
(1.132)

$$W(s) = \frac{K_{\text{moment}}K_{\text{measure}}K_{\text{amplify}}K_{\text{electric current}}}{K_p} \frac{s}{(T_0^2s^2 + 2\xi_0T_0s + 1)(T_{\text{amplify}}s + 1)}$$
(1.133)

Introduce the following denotations:

$$K = \frac{K_{\text{moment}}K_{\text{measure}}K_{\text{amplify}}K_{\text{electric current}}}{K_{D}} = \frac{D_{\text{feedback}}}{B_{0}} = 2\xi T_{0}$$
 (1.134)

$$K' = \frac{K_{\text{moment}}K_{\text{measure}}K_{\text{amplify}}K_{\text{electric current}}}{K'_{n}} = \frac{D_{\text{feedback}}}{D_{0}}$$
(1.135)

Substituting Eqs. (1.134) and (1.135) into (1.132) and (1.133) respectively, obtains

$$W'(s) = \frac{K'}{(T's+1)(T_{\text{amplify}}s+1)}$$
(1.136)

$$W(s) = \frac{Ks}{(T_0^2 s^2 + 2\xi_0 T_0 s + 1)(T_{\text{amplify}} s + 1)}$$
(1.137)

The closed-loop transfer functions of the output before the integrator (U_0) and after the integrator (U) have the following forms respectively,

$$\Phi_0'(s) = \frac{W'(s)}{1 + W'(s)} \frac{1}{K_{\text{moment}}} \frac{1}{K_{\text{electric current}}} = \frac{U_0(s)}{M_{\text{Lat}}(s)}$$
(1.138)

$$\Phi_0(s) = \frac{W(s)}{1 + W(s)} \frac{1}{K_{\text{moment}}} \frac{1}{K_{\text{electric current}}} = \frac{U_0(s)}{M_{\text{Lat}}(s)}$$
(1.139)

$$\Phi'(s) = \frac{W'(s)}{1 + W'(s)} \frac{1}{K_{\text{moment}}} \frac{1}{K_{\text{electric current}}} W_{\text{integrator}}(s) = \frac{U(s)}{M_{\text{Lat}}(s)}$$
(1.140)

$$\Phi(s) = \frac{W(s)}{1 + W(s)} \frac{1}{K_{\text{moment}}} \frac{1}{K_{\text{electric current}}} W_{\text{integrator}}(s) = \frac{U(s)}{M_{\text{Lat}}(s)}$$
(1.141)

Substituting Eqs. (1.129), (1.130), (1.136) and (1.137) into Eqs. (1.138)–(1.141), obtains

$$\Phi_0'(s) = \frac{K'}{K_{\text{moment}} K_{\text{electric current}}} \frac{1}{T_{\text{amplify}} T' s^2 + (T' + T_{\text{amplify}}) s + 1 + K'}$$
(1.142)

$$\Phi_0(s) = \frac{K}{K_{\text{moment}}K_{\text{electric current}}} \frac{s}{T_0^2 T_{\text{amplify}} s^3 + (T_0^2 + 2\xi_0 T_0 T_{\text{amplify}}) s^2 + (T_{\text{amplify}} + 2\xi_0 T_0 + K) s + 1}$$

$$(1.143)$$

$$\Phi_{1}'(s) = \frac{K'K_{\text{integrator1}}}{K_{\text{moment}}K_{\text{electric current}}} \frac{1}{1 + T_{\text{integrator}}s} \frac{1}{T_{\text{amplify}}T's^{2} + (T' + T_{\text{amplify}})s + 1 + K'}$$

$$(1.144)$$

$$\Phi_2'(s) = \frac{K'K_{\text{integrator2}}}{K_{\text{amplify}}K_{\text{electric current}}} \frac{T_1 s + 1}{T_2^2 s^2 + 2\xi_{\text{integrator}} T_2 s + 1} \frac{s}{T_{\text{amplify}} T' s^2 + (T' + T_{\text{amplify}}) s + 1 + K'}$$

$$(1.145)$$

$$\begin{split} \Phi_{1}(s) &= \frac{KK_{\text{integrator1}}}{K_{\text{moment}}K_{\text{electric current}}} \\ &= \frac{1}{1 + T_{\text{integrator}}s} \frac{s}{T_{0}^{2}T_{\text{amplify}}s^{3} + (T_{0}^{2} + 2\xi_{0}T_{0}T_{\text{amplify}})s^{2} + (T_{\text{amplify}} + 2\xi_{0}T_{0} + K)s + 1} \\ &= (1.146) \end{split}$$

$$\begin{split} \Phi_{2}(s) &= \frac{KK_{\text{integrator2}}}{K_{\text{moment}}K_{\text{electric current}}} \frac{T_{1}s+1}{T_{2}^{2}s^{2}+2\xi_{\text{integrator}}T_{2}s+1} \\ &\times \frac{T_{0}^{2}T_{\text{amplify}}s^{3}+(T_{0}^{2}+2\xi_{0}T_{0}T_{\text{amplify}})s^{2}+(T_{\text{amplify}}+2\xi_{0}T_{0}+K)s+1}{(1.147)} \end{split}$$

The stability of the system is now studied.

(1) Based on the transfer function in Eq. (1.136). The frequency characteristic curve is in accordance with the transfer function in Eq. (1.136), as shown in Fig. 1.15.

Fig. 1.15 The frequency characteristic curve in accordance with Eq. (1.136) for a non-driven structure mechanical gyroscope with a velocity feedback

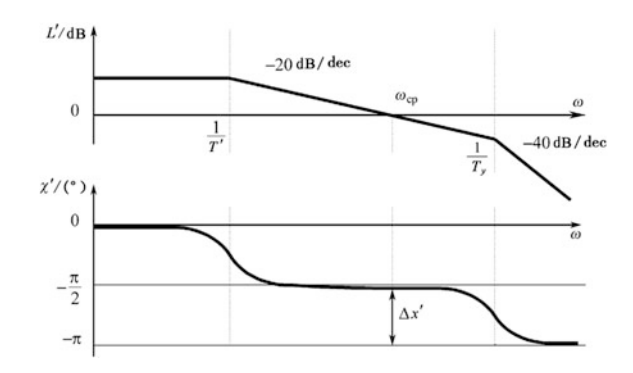


Figure 1.15 shows that the system with a velocity feedback of Eq. (1.136) is stable and has phase stability with a large enough margin. At the same time, the crossover frequency is closer to the frequency $1/T_{\rm amplify}$, the smaller the phase stability margin is. So, in order to increase the phase margin, the coefficient K' must be increased, that is, the damping effect is increased or the time constant $T_{\rm amplify}$ is reduced.

(2) Based on the transfer function in Eq. (1.137), then in order to study the stability, the denominator of Eq. (1.137) is transformed to be similar to Eqs. (1.146) and (1.147):

$$W(s) = \frac{Ks}{T_0^2 T_{\text{amplify}} s^3 + (T_0^2 + 2\xi_0 T_0 T_{\text{amplify}}) s^2 + (T_{\text{amplify}} + 2\xi_0 T_0) s + 1}$$
 (1.148)

In order to study the stability, the last two summands are moved away from the molecular to the denominator. Then the characteristic polynomial $\frac{W(s)}{1+W(s)}$ of the closed-loop system is unchanged. Thus the equivalent transfer function $W_1(s)$ can be obtained as

$$W_1(s) = \frac{(T_{\text{amplify}} + 2\xi_0 T_0 + K)s + 1}{s^2 \left[T_0^2 T_{\text{amplify}} s + (T_0^2 + 2\xi_0 T_0 T_{\text{amplify}}) \right]}$$
(1.149)

In the condition of a small ξ_0 , it can only be determined by the aerodynamic resistance $(\xi_0 \leq \xi)$,and the following expressions are correct: $2\xi_0 T_0 \leq K = 2\xi T_0$; $2\xi_0 T_{\text{amplify}} \leq T_0$. Thus the expression (1.149) can be simplified as

$$W_1(s) = \frac{(T_{\text{amplify}} + K)s + 1}{T_0^2 s^2 (T_{\text{amplify}} s + 1)}$$
(1.150)

It should be noted that T_{amplify} is basically determined by the mutual inductance of the winding and the value is small enough, while K is determined by a large

enough damping effect, and the value is large. This damping effect is guaranteed by a velocity feedback. The frequency characteristic curve is satisfied with the transfer function in Eq. (1.150) as shown in Fig. 1.16.

From Fig. 1.16, we know that the size of the constant T_{amplify} affects the margin of coefficient stability, and as mentioned above, the increase of T_{amplify} will reduce the phase margin, but the system will still remain stable.

Assume that the denominator of the transfer function $\frac{W(s)}{1+W(s)}$ is zero, and obtain the characteristic equation as

$$T_0^2 T_{\text{amplify}} s^3 + (T_0^2 + 2\xi_0 T_0 T_{\text{amplify}}) s^2 + (T_{\text{amplify}} + 2\xi_0 T_0 + K) s + 1 = 0$$

or

$$T_0^2 T_{\text{amplify}} s^3 + (T_0^2 + 2\xi_0 T_0 T_{\text{amplify}}) s^2 + \left[T_{\text{amplify}} + 2(\xi_0 + \xi) T_0 \right] s + 1 = 0 \quad (1.151)$$

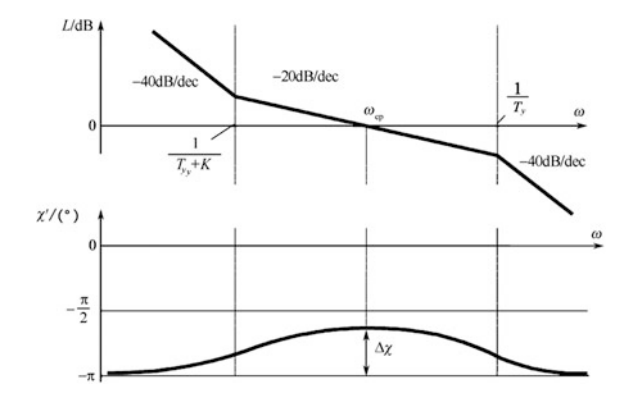
Since the whole terms of the equation are positive, the stability condition should be in the following form:

$$(T_0^2 + 2\xi_0 T_0 T_{\text{amplify}}) [T_{\text{amplify}} + 2(\xi + \xi_0) T_0] > T_0^2 T_{\text{amplify}}$$

When $\xi_0 = 0$, we can obtain that $T_0^2 T_{\text{amplify}} + 2\xi T_0^3 > T_0^2 T_{\text{amplify}} \Rightarrow 2\xi T_0^3 > 0$. So, when $\xi_0 = 0$, the system is stable.

The amplitude and phase characteristics satisfy the transfer functions in Eqs. (1.136) and (1.137). After all the symbols are substituted, they coincide completely. In order to use the instruments to measure the angular velocity of the aircraft, the two expressions can be used to study the accuracy analysis. However, when considering the circumferential vibration and the angular vibration of the craft, the transfer function in Eq. (1.137) is more reasonable. The reason is that the change of the circumferential vibration frequency and the angular vibration frequency of the aircraft are caused by changes of the external torque, and the input signal of the sensitive elements does not affect the natural frequency of non-damped

Fig. 1.16 Frequency characteristics of a non-driven mechanical gyroscope with a velocity feedback



oscillations. Therefore, in order to make the work more comprehensive and generalized, Eq. (1.137) will be used to determine the transfer function (Fig. 1.16).

Then, from Eq. (1.150), the phase frequency characteristic should have the following form:

$$x = -\pi + \arctan\left[(T_{\text{amplify}} + K)\omega \right] - \arctan(T_{\text{amplify}}\omega) = -\pi + \arctan$$

$$\left[\left(K_{\text{amplify}} K_{\text{electric current}} K_{\text{mutual inductance}} + \frac{K_{\text{moment}} K_{\text{measure}} K_{\text{amplify}} K_{\text{electric current}}}{(C_1 - A_1)\dot{\varphi}_0^2} \right) \omega \right] - \arctan\left(K_{\text{amplify}} K_{\text{electric current}} K_{\text{mutual inductance}}\omega \right)$$

$$(1.152)$$

From Eq. (1.152), the phase stability margin is related not only with the time constant T_{amplify} but also with the rotating velocity around the longitudinal axis of the craft. As mentioned earlier, the system is unstable over a large enough range (10-20 Hz). The margin of the phase stability is

$$\Delta \chi = \arctan[(T_{\text{amplify}} + K)\omega_{cp}] - \arctan(T_{\text{amplify}}\omega_{cp})$$
 (1.153)

where ω_{cp} is the crossover frequency of the log amplitude frequency characteristic curve.

Equation (1.153) shows that due to the small time constant T_{amplify} , the phase stability margin is essentially determined by K, which is approximately equal to

$$\Delta \chi = \arctan(K\omega_{cp}) \tag{1.154}$$

However, the influence of the instability of the rotating velocity around the longitudinal axis of the craft on the size of the phase stability margin effect is estimated.

It is well known that the crossover frequency of the frequency characteristic curve is the frequency of the intersection point between the log amplitude frequency characteristic curve and the zero line, i.e.,

$$\begin{split} &\lg\left(\frac{\sqrt{1+(T_{\text{amplify}}+K)^2\omega_{cp}^2}}{T_0^2\omega_{cp}^2\sqrt{1+T_{\text{amplify}}^2\omega_{cp}^2}}\right)=0\\ &\frac{\sqrt{1+(T_{\text{amplify}}+K)^2\omega_{cp}^2}}{T_0^2\omega_{cp}^2\sqrt{1+T_{\text{amplify}}^2\omega_{cp}^2}}=1 \end{split}$$

It should be noted that the change of the crossover frequency can only take into account changes in K. The value of K increases such that the crossover frequency will correspondingly increase. From Eq. (1.134), it is known that the change of K can only take into account the damping change due to feedback.

Assume that $T_{\text{amplify}} \leq K$ and $T_{\text{amplify}}^2 \omega_{cp}^2 \leq 1$, where ω_{cp} is the frequency associated with the phase $\Delta \gamma$ (Fig. 1.16). There holds

$$T_0^4 \omega_{cp}^4 - K^2 \omega_{cp}^2 - 1 = 0$$

Substituting Eq. (1.134), obtains

$$\omega_{cp}^{2} = \frac{K^{2} + \sqrt{K^{4} + 4T_{0}^{4}}}{2T_{0}^{4}} = \frac{4\xi^{2}T_{0}^{2} + T_{0}^{2}\sqrt{16\xi^{4} + 4}}{2T_{0}^{4}}$$

$$\omega_{cp} = \frac{\sqrt{2\xi^{2} + \sqrt{4\xi^{4} + 1}}}{T_{0}}$$
(1.155)

From Eq. (1.134) the attenuation coefficient of the instrument oscillation can be obtained through the damping effect produced by the feedback and its form is

$$\xi = \frac{D_{\text{feedback}}}{2T_0 B_0} = \frac{D_{\text{feedback}}}{2\dot{\varphi}_0 \sqrt{(C_1 - A_1)B_1}}$$
(1.156)

Substituting Eqs. (1.125) and (1.155) obtains

$$\omega_{cp} = \frac{\sqrt{\frac{D_{\text{feedback}}^{2}}{2\dot{\varphi}_{0}^{2}B_{1}(C_{1}-A_{1})} + \sqrt{\frac{D_{\text{feedback}}^{4}}{4\dot{\varphi}_{0}^{4}B_{1}^{2}(C_{1}-A_{1})^{2}} + 1}}}{\sqrt{\frac{B_{1}}{(C_{1}-A_{1})\dot{\varphi}_{0}^{2}}}}$$

$$= \sqrt{\frac{D_{\text{feedback}}^{2}}{2B_{1}^{2}} + \sqrt{\frac{D_{\text{feedback}}^{4}}{4B_{1}^{4}} + \frac{(C_{1}-A_{1})^{2}}{B_{1}^{2}}\dot{\varphi}_{0}^{4}}}}$$
(1.157)

Equation (1.157) shows that the crossover frequency depends on the inertia moment, the damping of the sensitive element and the rotating velocity around the longitudinal axis of the aircraft, so it is unstable.

According to the adjustment principle, the decrease $\pi/2$ of the phase frequency characteristic of the system at the logarithm amplitude frequency characteristics with a slope of -40 dB/dec is smaller than the decrease $\pi/2$ of the phase frequency characteristics of the original system at the logarithm amplitude frequency characteristics with a slope of -20 dB/dec. In other words, in the frequency ranges $0 \sim \frac{1}{T_{amplify} + K}$ and $\frac{1}{T_{amplify}} \sim \infty$, the phase stability margin is less than that in the frequency range $\left(\frac{1}{T_{amplify} + K} \sim \frac{1}{T_{amplify}}\right)$, as shown in Fig. 1.16. Thus, when selecting the crossover frequency, its value must be in the frequency range $\left(\frac{1}{T_{amplify} + K} \sim \frac{1}{T_{amplify}}\right)$. According to the above situation, the minimum value of the damping effect in the instrument is determined by:

$$\frac{1}{T_{\text{amplify}} + K} < \omega_{cp} \tag{1.158}$$

or according to $T_{\text{amplify}} \ll K$, there holds

$$\frac{1}{K} < \omega_{cp} \tag{1.159}$$

Substituting Eqs. (1.134) and (1.155) obtains

$$\frac{1}{2\xi T_0} < \frac{\sqrt{2\xi^2 + \sqrt{4\xi^4 + 1}}}{T_0} \tag{1.160}$$

Solving the inequality equation obtains

$$\xi > \frac{1}{2 \times \sqrt[4]{2}} = 0.42 \tag{1.161}$$

When selecting the size of the damping in the instrument, the condition in Eq. (1.161) must be guaranteed. At this time, substituting Eqs. (1.134) and (1.155), the stability margin will only be determined by the vibration attenuation coefficient of the sensitive element, and takes the following form:

$$\Delta\chi = \arctan(2\xi\sqrt{2\xi^2 + \sqrt{4\xi^4 + 1}}) \tag{1.162}$$

Substituting Eq. (1.156) obtains

$$\Delta \chi = \arctan \left[\frac{D_{\text{feedback}}}{\dot{\varphi}_0 \sqrt{(C_1 - A_1)B_1}} \sqrt{\frac{1}{2} \left(\frac{D_{\text{feedback}}}{\dot{\varphi}_0 \sqrt{(C_1 - A_1)B_1}} \right)^2 + \sqrt{\frac{1}{4} \left(\frac{D_{\text{feedback}}}{\dot{\varphi}_0 \sqrt{(C_1 - A_1)B_1}} \right)^4 + 1} \right]$$

Using the detuning coefficient μ [see Eq. (1.109)] and D_{feedback} , Eq. (1.154) can be simplified as

$$\Delta \chi = \arctan \left[\frac{K_{\text{moment}} K_{\text{measure}} K_{\text{amplify}} K_{\text{electric current}}}{\dot{\varphi}_0 \mu B_1} \right. \\ \left. \sqrt{\frac{1}{2} \left(\frac{K_{\text{moment}} K_{\text{measure}} K_{\text{amplify}} K_{\text{electric current}}}{\dot{\varphi}_0 \mu B_1} \right)^2 + \sqrt{\frac{1}{4} \left(\frac{K_{\text{moment}} K_{\text{measure}} K_{\text{amplify}} K_{\text{electric current}}}{\dot{\varphi}_0 \mu B_1} \right)^4 + 1} \right]}$$

$$(1.163)$$

From Eq. (1.153), the phase stability margin decreases with the decrease of K, and it is equal to zero when K=0. In this case, it is possible only when the damping effect of the feedback is present. It can be concluded that in order to increase the stability margin, K must be increased. But it should be noted that an increase of K will lead to an increase of the crossover frequency, this frequency is close to the frequency $\frac{1}{T_{amplify}}$. The second term in Eq. (1.153) exerts a greater influence on the stability margin and the phase stability margin begins to decrease, as shown in Fig. 1.16.

Reducing the time constant $T_{\rm amplify}$ or increasing the frequency of the crossover frequency method can be taken to increase the phase stability margin. However, increasing K and ω_{cp} will lead to an increase of the damping effect of the instrument.

From Eq. (1.163), we know that an increase of the rotating velocity of the aircraft will reduce the phase stability margin. However, increasing the rotating velocity of the aircraft is advantageous to improving the stability of the aircraft. At the same time, for the conventional loop scheme of the rotor vibration gyroscope, it is necessary to form a larger stiffness of the gyroscope. It can be seen that not increasing $\dot{\varphi}_0$ can keep it stable. Under the condition that $\dot{\varphi}_0$ is unstable (10–20 Hz), the change of the phase stability margin will be two times larger than the original value. However, it will not have taken the instrument out of the stable state.

From the summary regarding the phase stability margin, the conclusion can be drawn that in order to increase the phase stability margin, a method of increasing the damping effect or decreasing the time constant T_{amplify} must be used.

1. A method of decreasing T_{amplify}

Obviously, because $T_{\rm amplify}$ is small and furtherly reduced, the change of the phase stability margin will not have a significant effect. Even so, some basic ways to reduce $T_{\rm amplify}$ have been developed.

- (1) Because $T_{\text{amplify}} = K_{\text{amplify}} K_{\text{electric current}} K_{\text{mutual inductance}}$, reducing the transfer coefficient K_{amplify} of the preamplifier and the current amplification factor $K_{\text{electric current}}$, can decrease T_{amplify} , but this will decrease K to an undesirable situation. This is because the decrease of K leads to an opposite phenomenon, namely the stability margin is reduced. This reason for this is that the impact of K on the stability margin is significantly greater than that of T_{amplify} . Although reducing K by reducing K_{amplify} or D_{feedback} will increase the sensitivity of the instrument, the same problems occur so in the scheme of ensuring stability, it is still undesirable.
- (2) T_{amplify} can be reduced by reducing $K_{\text{mutual inductance}}$. As has been said before, a similar method of reducing T_{amplify} clearly cannot increase the phase stability

margin if the influence of the winding mutual inductance of the instrument on the output signal is decreased.

Substituting the transfer function (1.164) of the amplifier converter into the positive feedback to partially compensate, the effect of the mutual inductance can be reduced (Fig. 1.17):

$$W_k(s) = \frac{T_k s}{1 + T_k s} \tag{1.164}$$

In this case, the transmission characteristic form of the amplifier is

$$W_1'(s) = \frac{K_{\text{amplify}} K_{\text{electric current}}}{1 + K_{\text{amplify}} K_{\text{electric current}} s \left(K_{\text{mutual inductance}} - \frac{K_k}{1 + T_k s}\right)}$$
(1.165)

or

$$W_{1}'(s) = \frac{K_{\text{amplify}}K_{\text{electric current}}(1+T_{k}s)}{1+T_{k}s+K_{\text{amplify}}K_{\text{electric current}}K_{\text{mutual inductance}}s(1+T_{k}s)-K_{\text{amplify}}K_{\text{electric current}}K_{k}s}$$

$$(1.166)$$

Substituting Eq. (1.127), obtains

$$W_{1}'(s) = \frac{K_{\text{amplify}}K_{\text{electric current}}(1 + T_{k}s)}{T_{\text{amplify}}T_{k}s + (T_{k} + T_{\text{amplify}} - K_{\text{amplify}}K_{\text{electric current}}T_{k})s + 1}$$
(1.167)

The difference term $T_{\text{amplify}} - K_{\text{amplify}} K_{\text{electric current}} K_k$ is changed into the following form:

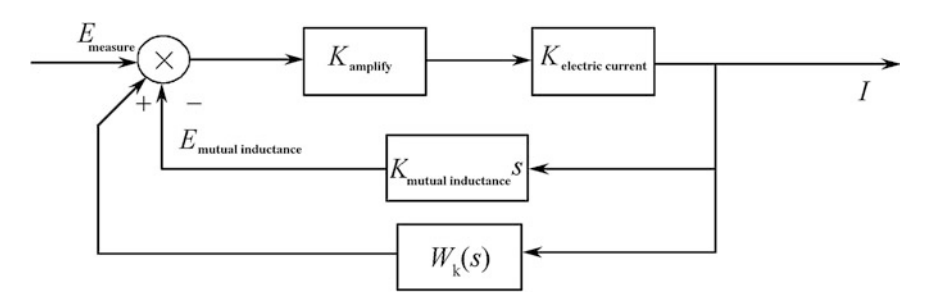


Fig. 1.17 Block diagram of the mutual inductance compensation

 $T_{
m amplify} - K_{
m amplify} K_{
m electric \, current} K_k = K_{
m amplify} K_{
m electric \, current} K_{
m mutual \, inductance} - K_{
m amplify} K_{
m electric \, current} K_k$ $= K_{
m amplify} K_{
m electric \, current} (K_{
m mutual \, inductance} - K_k) = K_{
m amplify} K_{
m electric \, current} \Delta K$

Substituting the above equation into Eq. (1.167), obtains

$$W_1'(s) = \frac{K_{\text{amplify}} K_{\text{electric current}} (1 + T_k s)}{T_{\text{amplify}} T_k s^2 + (T_k + K_{\text{amplify}} K_{\text{electric current}} \Delta K) s + 1}$$
(1.168)

How the stability is affected by the introduction of a similar loop is now analyzed. The most suitable mutual compensation type is $\Delta K = 0$.

From Eq. (1.168), we can see that when any value of every parameter is used in the transfer function, the phase frequency characteristic is always more than $-\pi$. Thus when $\Delta K = 0$ and T_k is selected as any value, the amplifier still remains stable. T_k should be selected as a small value to exclude the effect of the output signal and the amplitude frequency characteristics in the operating frequency range.

It should be pointed out that exact compensation cannot actually be achieved. Therefore, the residual uncompensated polarity should be determined. The reason for this is that when T_k is small, the polarity change of ΔK will enable the phase polarity of the amplifier converter to change, which will cause the instrument to deviate from the calculated parameters and the characteristic curve. In order to avoid the occurrence of this situation, the optimization coefficient n of the compensation precision is introduced. If $\Delta K = nK_{\text{mutual inductance}} > 0$, Eq. (1.168) is changed into

$$W_1'(s) = \frac{K_{\text{amplify}} K_{\text{electric current}} (1 + T_k s)}{T_{\text{amplify}} T_k s^2 + (T_k + n T_{\text{amplify}}) s + 1}$$
(1.169)

It is very difficult to make n small. Thus $T_k \le nT_{\text{amplify}}$ and there holds

$$W_1'(s) = \frac{K_{\text{amplify}} K_{\text{electric current}}}{n T_{\text{amplify}} s + 1}$$
(1.170)

In this case the optimization coefficient must be positive. Thus $W_1'(s)$ will be replaced by $W_1(s)$.

2. Increasing *K*

As has been pointed out previously, reducing $T_{\rm amplify}$ cannot increase the stability margin, because the phase margin is basically determined by K, and the stability margin increases with the increase of K. In order to ensure that the phase stability has a larger margin, it is necessary to increase the value of K. According to Eq. (1.134), increasing $D_{\rm feedback}$ or reducing B_0 can make K increase.

(1) Reducing B_0 . Because $B_0 = (C_1 - A_1)\dot{\varphi}_0$, reducing B_0 is related to three kinds of situation. Firstly, it is related to reducing the craft's rotation frequency.

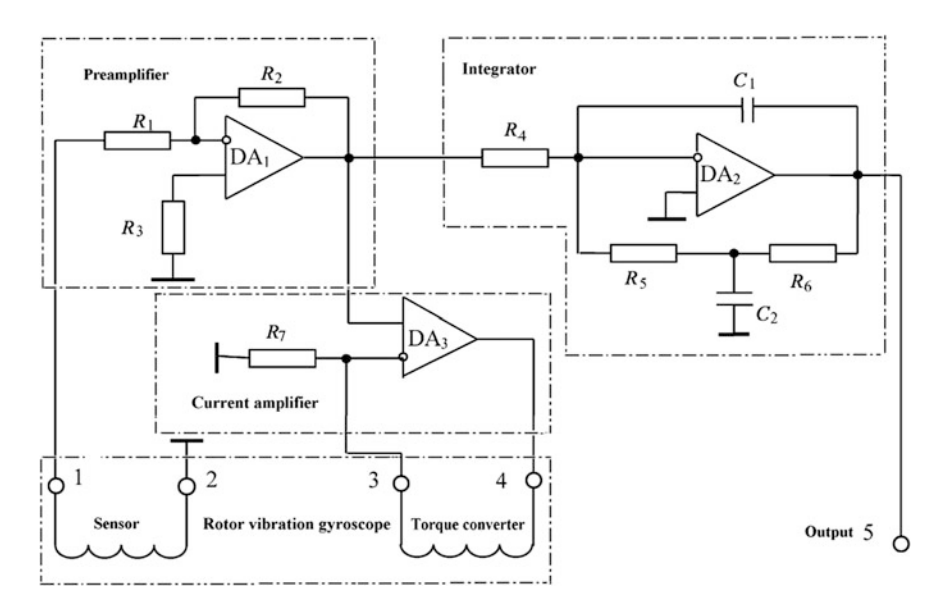


Fig. 1.18 Feedback circuit of a non-driven mechanical gyroscope

Secondly, it is related to changing the geometric shape and size of the sensitive elements of the instrument, which in turn is restricted by the technical requirements and the tuning technology conditions, and it is also related to the structural change of the instrument. But in the instrument design stage, it should be noted that reducing the difference $C_1 - A_1$ of the inertia moment will increase the stability margin. At this time, reducing the difference $C_1 - A_1$ will inevitably result in three cases: Firstly, the inertia moment B_1 must be reduced as shown in Fig. 1.18. As a result, ensuring the tuning condition more accurately is a problem that must be solved. Secondly, the attenuation coefficient ξ is increased by Eq. (1.156) and thirdly, the sensitivity of the instrument is decreased. Therefore, when selecting the inertia moment of the sensitive element, it is necessary to seek a compromise solution to satisfy all required conditions as far as possible.

(2) Increasing D_{feedback} . Because $D_{\text{feedback}} = K_{\text{amplify}} K_{\text{electric current}} K_{\text{moment}} K_{\text{measure}}$, when D_{feedback} increases, K_{amplify} and $K_{\text{electric current}}$ will decrease. Although the latter will make T_{amplify} increase, the phase stability margin will eventually increase. In this case, the impact of increasing K on the stability margin is greater than that of increasing T_{amplify} , and will result in the increase of the phase stability margin. K_{amplify} and $K_{\text{electric current}}$ are determined only by the feedback parameters. Therefore, when selecting these numbers, it should be considered that the larger these numbers are, the larger the phase stability margin is, but the higher the damping effect is, the smaller the instrument sensitivity is. As with reducing B_0 , we must seek a compromise solution.

For K_{moment} and K_{measure} , similar situations exist. The increase of two coefficients is generally related to the change of the geometric size of the instrument and the magnetic system characteristics of the measured information.

The feedback circuit of a non-driven mechanical gyroscope is shown in Fig. 1.18. The feedback loop consists of two circuits: a preamplifier and a current amplifier.

As has been mentioned before, the damping coefficient of a non-driven mechanical gyroscope with a negative velocity feedback for the rotating state craft is determined by four parameters: the transconductance K_{measure} of the measuring winding, the transfer coefficient K_{ampify} of the preamplifier, the amplification coefficient $K_{\text{electric current}}$ of the current amplifier and the transconductance K_{moment} of the torque winding of the instrument. The integrator in the circuit (Fig. 1.18) uses the integrator with the transfer function (1.130). Within the working frequency range, its phase frequency characteristic is better than that of the non-periodic loop.

From (1.105), the amplitude of the oscillating angle of the sensitive element is inversely proportional to the damping coefficient of the instrument, and the oscillating angle of the sensitive element is constrained by the geometry and size of the instrument itself, and this constraint is added to the possible minimum damping coefficient. According to Eq. (1.78), the instrument works near the continuous resonant point. The angle deviation range of the sensitive element is recorded, and Eq. (1.81) is considered. Then there holds

$$\alpha_{\text{amplitude}} = \frac{2B_1\Omega}{D_{\alpha}}$$

The maximum amplitude of the harmonic oscillation of the sensitive element is derived from the maximum value of the angular velocity. In this case, there holds

$$lpha_{
m amplitude,\,max} = rac{2B_1\Omega_{
m max}}{D_lpha}$$

At this time, it should be noted that there are some constant torques (the dynamic unbalance torques) in the coordinates connected to the sensitive element and the deflection angle of the sensitive element caused by the inaccurate installation of the instrument, where this deflection angle is caused by a number of great harmonic deviations (see Sect. 4.3).

$$\alpha_{amplitude,\,max} = \alpha_{max} - \alpha_0$$

where α_{max} is the maximum swing angle of the sensitive element and α_0 is the constant deflection angle of the sensitive element.

At this moment, the maximum value of the damping coefficient is determined by the possible swing angle of the sensitive element:

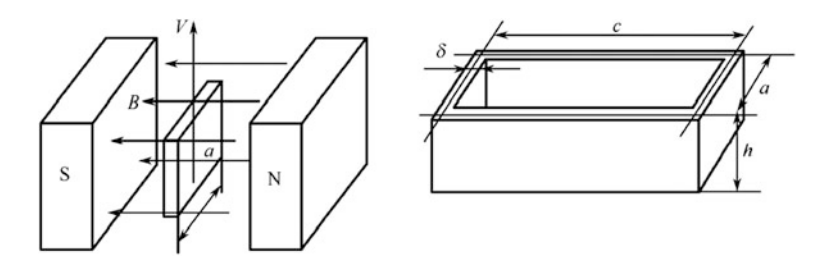


Fig. 1.19 Determination of the winding transfer coefficient

$$D_{\text{feedback}} \approx D_{\alpha} = \frac{2B_1 \Omega_{\text{max}}}{\alpha_{\text{max}} - \alpha_0}$$
 (1.171)

When the damping coefficient of the instrument is less than the value calculated by Eq. (1.171), or in other words, when the sensitive element has some relatively large angle, the sensitive element begins to hit its base and this phenomenon is not allowed. In addition, the oscillation of the sensitive element preferably occurs in the central part of the magnetic gap, where the magnetic induction is relatively stable, the magnetic field is perpendicular to the motion direction of the sensitive element, and there is no magnetic field distortion. If the sensitive element has a sufficiently large deflection angle, it can be out of the center range and this must be reflected in the instrument readings.

The measurement principle of the oscillation angular velocity of the sensitive element uses the law of electromagnetic induction. Its essence is that when the conductor moves at a velocity of v in a magnetic field with the magnetic induction intensity B, the electromotive force is produced in a conductor as E = vBa (Fig. 1.19):

$$E = vB_a = BN_{\text{measure}}ac\dot{\alpha} = K_{\text{measure}}\dot{\alpha}$$
 (1.172)

where N_{measure} is the number of turns of the measuring winding:

$$K_{\text{measure}} = BN_{\text{measure}}ac$$
 (1.173)

The transfer coefficient of the preamplifier is

$$K_{\text{amplify}} = \frac{R_2}{R_1} \tag{1.174}$$

and the voltage at the output of the preamplifier is determined by the following expression:

$$U = EK_{\text{amplify}} = K_{\text{amplify}}K_{\text{measure}}\dot{\alpha} = BN_{\text{measure}}ac\frac{R_2}{R_1}\dot{\alpha}$$
 (1.175)

The amplification factor of the current amplifier is calculated by the following formula:

$$K_{\text{electric current}} = \frac{1}{R_7}$$
 (1.176)

But the current in the torque winding of the instrument is determined by the following expression:

$$I = UK_{\text{electric current}} = K_{\text{measure}} K_{\text{amplify}} K_{\text{measure}} \dot{\alpha} = BN_{\text{measure}} ac \frac{R_2}{R_1 R_7} \dot{\alpha} \qquad (1.177)$$

According to the Ampere's law, a charged conductor in a magnetic field is subjected to a force that is opposite to the velocity vector and the force is $F_A = IBN_{\text{moment}}ac$, where N_{moment} is the number of turns of the torque winding. When the sensitive element is moving in a magnetic field, the magnitude of the torque acting on it is

$$M_{
m damping} = Fc = IBN_{
m moment}ac = K_{
m moment}I = K_{
m moment}K_{
m measure}K_{
m amplify}K_{
m electric \, current}\dot{\alpha}$$

$$= B^2N_{
m measure}N_{
m moment}a^2c^2\frac{R_2}{R_1R_2}\dot{\alpha} = D_{
m feedback}\dot{\alpha}$$

where

$$K_{\text{measure}} = BN_{\text{moment}}ac$$
 (1.178)

Thus, the damping coefficient has the following form:

$$D_{\text{feedback}} = K_{\text{moment}} K_{\text{measure}} K_{\text{amplify}} K_{\text{electric current}} = B^2 N_{\text{measure}} N_{\text{moment}} a^2 c^2 \frac{R_2}{R_1 R_7}$$
(1.179)

From Eq. (1.179), it is concluded that the stability of the damping coefficient produced by the feedback mode, and the stability of the output signal of the instrument are determined by the stability of the resistances R_1 , R_2 and R_7 and the stability of the magnetic induction in the magnetic gap of the magnetic system. The stability of this magnetic system is also determined by the temperature stability of the permanent magnet and the heterogeneity of the magnetic field along the height distribution in the magnetic gap of the magnetic system.

Therefore, the change and adjustment of the damping is realized by selecting R_1 , R_2 and R_7 of the instrument.

With the feedback loop of the instrument, the influences of the mutual action of the measuring winding and the torque winding can be assessed. The magnetic flux generated by the torque winding is

$$\Phi_{\text{moment}} = IL = K_{\text{measure}} K_{\text{amplify}} K_{\text{electric current}} \dot{\alpha} \mu_0 N_0^2 \frac{S_c}{I_c}
= BN_{\text{measure}} ac \frac{R_2}{R_1 R_7} \dot{\alpha} \mu_0 N_{\text{moment}}^2 \frac{S_{\text{moment}}}{I_{\text{moment}}}$$
(1.180)

The alternating magnetic flux of the torque winding acts on the measuring coil and produces the electromotive force, whose amplitude is directly proportional to that of the oscillating angular acceleration of the sensitive element. The phase is also proportional to that of the angular acceleration:

$$\begin{split} E_{\text{mutual inductance}} &= -N_{\text{measure}} \frac{\text{d} \varPhi_{\text{moment}}}{\text{d} t} = -\mu_0 N_{\text{measure}} N_{\text{moment}}^2 \frac{S_{\text{moment}} \text{d} I}{I_{\text{moment}} \text{d} t} \\ &= -K_{\text{measure}} K_{\text{amplify}} K_{\text{electric current}} \ddot{\alpha} \mu_0 N_{\text{moment}}^2 \frac{S_{\text{moment}}}{I_{\text{moment}}} \\ &= -B N_{\text{measure}}^2 a c \frac{R_2}{R_1 R_7} \ddot{\alpha} \mu_0 N_{\text{moment}}^2 \frac{S_{\text{moment}}}{I_{\text{moment}}} \\ &E_{\text{mutual inductance}} = -K_{\text{mutual inductance}} \frac{\text{d} I}{\text{d} t} \end{split} \tag{1.182}$$

where S_{moment} is the area of the torque winding; I_{moment} is the current of the torque winding and the mutual inductance is

$$K_{\text{mutual inductance}} = \mu_0 N_{\text{measure}} N_{\text{moment}}^2 \frac{S_{\text{moment}}}{I_{\text{moment}}}$$
(1.183)

The relative influence of the mutual inductance of the winding on the output signal of the instrument is determined by the following expression:

$$\frac{E_{\text{mutual inductance amplitude}}}{E_{\text{measure, amplitude}}} = \frac{K_{\text{measure}} K_{\text{amplify}} K_{\text{electric current}} \ddot{\alpha}_{\text{amplitude}} \mu_0 N_{\text{moment}}^2 S_{\text{moment}}}{K_{\text{measure}} \dot{\alpha}_{\text{amplitude}} I_{\text{moment}}} \\ = K_{\text{amplify}} K_{\text{electric current}} \dot{\phi}_0 \mu_0 N_{\text{moment}}^2 \frac{S_{\text{moment}}}{I_{\text{moment}}} \\ \tag{1.184}$$

The error value is not more than one thousand when calculating the parameters of the mechanical gyroscope prototype with negative feedback. However, according to the circuit and method in the references used to study the design of similar instruments, when encountering the large effect of winding mutual inductance (such

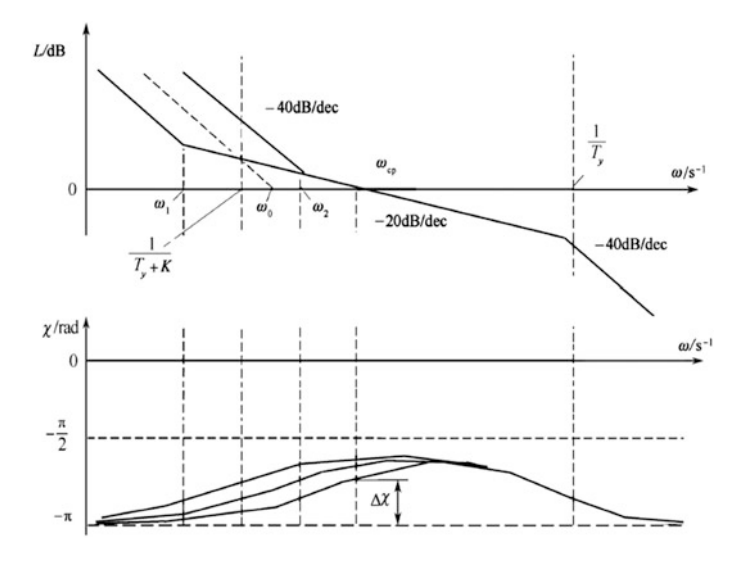


Fig. 1.20 Logarithmic frequency characteristic of a non-driven mechanical gyroscope with negative feedback

as a large number of turns of the gyroscope winding, another kind of the proportional relationship between the conductor length of winding and cross-section, the larger transfer coefficients of the amplifier converter and the current amplifier), several measures should be taken to reduce the time constant T_{amplify} , and the time constant is mainly determined by the coefficient size of the mutual inductance.

For Fig. 1.20, the open-loop transfer function of a non-driven mechanical gyroscope with negative feedback is

$$\begin{split} W_p(s) &= \frac{1}{B_0(T_0s^2 + 2\xi_0T_0s + 1)} \\ W_y(s) &= \frac{K_{\text{amplify}}K_{\text{electric current}}}{1 + T_{\text{amplify}}s} \\ K &= \frac{K_{\text{moment}}K_{\text{measure}}K_{\text{amplify}}K_{\text{electric current}}}{B_0} \\ W(s) &= \frac{Ks}{(T_0^2s^2 + 2\xi_0T_0s + 1)(T_{\text{amplify}}s + 1)} \Rightarrow W_1(s) = \frac{(T_{\text{amplify}} + K)s + 1}{T_0^2s^2(T_{\text{amplify}}s + 1)} \end{split}$$

1.7 Technical Performance of a Non-driven Mechanical Gyroscope

The technical requirements and use conditions of a non-driven mechanical gyroscope for a rotating aircraft are shown in Table 1.1.

Table 1.1	Technical requirements and use conditions of a non-drive	n mechanical gyroscope for a				
rotating aircraft						

Technical requirements		Use conditions		
Measuring angular velocity range/(°/s)		Outline dimensions/mm	ϕ 30 × 15	
Sensitivity threshold (°/s) 1.		Rotating angular velocity of aircraft/(r/s)	10–20	
Scale factor [mV/(°/s)]	30	Acceleration in any direction	10 g	
Scale factor stability (%)	8	Acceleration along the axis of rotation	75 g	
Zero bias signal (°/s)	0.6	Ambient temperature/°C	-40 to +75	
Quality (g)	40			

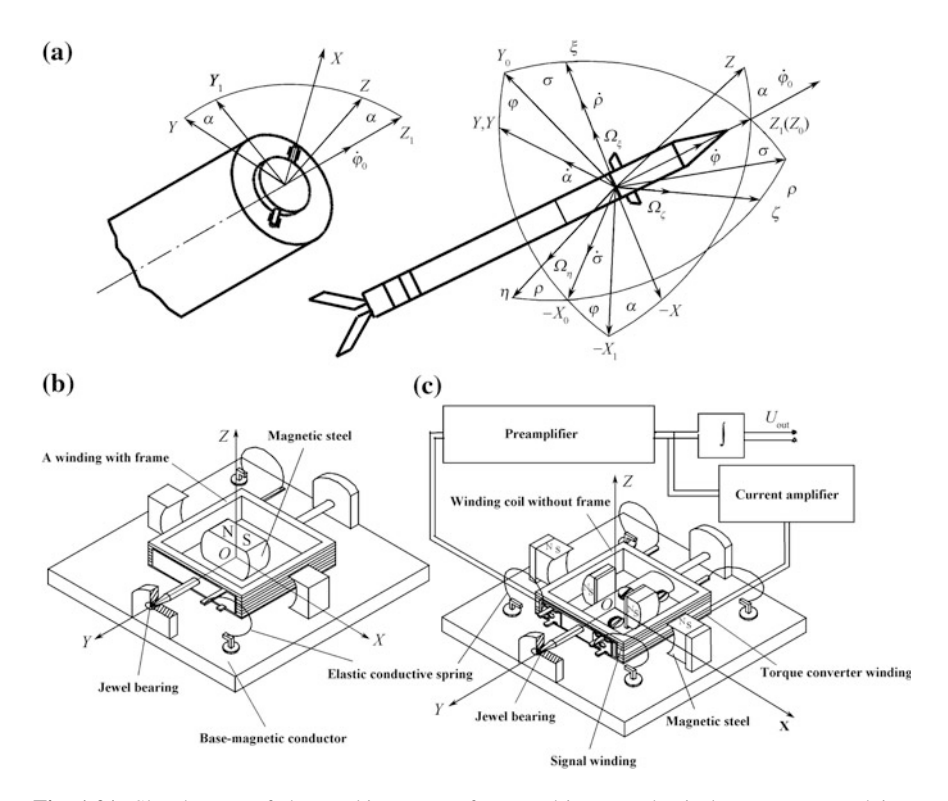


Fig. 1.21 Sketch map of the working state of a non-driven mechanical gyroscope used in a rotating aircraft, $\bf a$ Rotating flight carrier; $\bf b$ Gyroscope; $\bf c$ Non-driven mechanical gyroscope with a negative velocity feedback

Table 1.2 Performance of a non-driven gyroscope used in a rotating aircraft

Instrument parameters	9M39 gyroscope	Non-driven mechanical gyroscope with negative feedback	Instrument parameters	9M39 gyroscope	Non-driven mechanical gyroscope with negative feedback
Measuring angular velocity range (°/s)	300	300	Zero bias signal (3σ)/ (°/s)	1	0.6
Sensitivity threshold (°/s)	1.5	1.5	Outline dimension/ mm	φ 30 × 15	φ 30 × 15
Scale factor [mV/ (°/s)]	1	30	Quality/g	40	40
Instability (3σ)/ (%)	60	7			

The working state of a non-driven gyroscope used in a rotating aircraft is shown in Fig. 1.21, and its performance is detailed in Table 1.2.

Chapter 2 Precision of a Non-driven Mechanical Gyroscope with Negative Velocity Feedback

2.1 Measurement Precision of a Constant Angular Velocity Rotating Around The Horizontal Axis

The output signal is connected with the angular velocity by the scale factor: $U_{\text{out,amplitude}} = K_{\text{SF}}\Omega$. So the study of the measurement precision of a constant angular velocity rotating around the horizontal axis of the aircraft is ultimately attributed to the stability of the calibration scale factor of the instrument. In this chapter, the precision of the gyroscope is studied based on the dynamic characteristics of the instrument. Therefore, the closed-loop transfer function expressions (1–143), (1–146) and (1–147) are used, and nT_{amplify} replaces T_{amplify} :

$$\begin{split} \Phi_{0}(s) &= \frac{K}{K_{\text{moment}}K_{\text{electric current}}} \\ &\times \frac{s}{T_{0}^{2}nT_{\text{amplify}}s^{3} + \left(T_{0}^{2} + 2\xi_{0}T_{0}nT_{\text{amplify}}\right)s^{2} + \left(nT_{\text{amplify}} + 2\xi_{0}T_{0} + K\right)s + 1} \end{split} \tag{2.1}$$

$$\Phi_{1}(s) = \frac{KK_{\text{integrator1}}}{K_{\text{moment}}K_{\text{electric current}}} \times \frac{1}{1 + T_{\text{integrator}}s} \times \frac{1}{s} \times \frac{1}{T_{0}^{2}nT_{\text{amplify}}s^{3} + \left(T_{0}^{2} + 2\xi_{0}T_{0}nT_{\text{amplify}}\right)s^{2} + \left(nT_{\text{amplify}} + 2\xi_{0}T_{0} + K\right)s + 1}$$

$$(2.2)$$

$$\Phi_{2}(s) = \frac{KK_{\text{integrator2}}}{K_{\text{moment}}K_{\text{electric current}}} \times \frac{T_{1}s + 1}{T_{2}^{2}s^{2} + 2\xi_{\text{integrator}}T_{2}s + 1} \times \frac{T_{1}s + 1}{s} \times \frac{T_{1}s + 1}{s} \times \frac{T_{2}s^{2} + 2\xi_{\text{integrator}}T_{2}s + 1}{s} \times \frac{T_{1}s + 1}{s} \times \frac{T_{1}s + 1}{s} \times \frac{T_{2}s^{2} + 2\xi_{\text{integrator}}T_{2}s + 1}{s} \times \frac{T_{1}s + 1}{s} \times \frac{$$

Because $U_{\text{out}}(s) = \Phi(s) M_{\text{inertia}}(s)$ and $M_{\text{inertia}}(s)$ changes by the harmonic law, U_{out} is determined as

$$U_{\text{out}} = |\Phi(j\omega)| H_0 \Omega \sin \left\{ \dot{\varphi}_0 t + \arg \left[\Phi(j\omega) \atop \omega = \dot{\varphi}_0 \right] \right\}$$
 (2.4)

$$\begin{cases}
U_{\text{amplitude}} = H_0 \Omega |\Phi(j\omega)| = (C_1 - A_1 + B_1) \dot{\varphi}_0 \Omega |\Phi(j\omega)| \\
\omega = \dot{\varphi}_0 \\
\chi = \arg \Phi(j\omega) \\
\omega = \dot{\varphi}_0
\end{cases}$$
(2.5)

From Eqs. (2.1), (2.2) and (2.3) the amplitude of the output signal is

$$U_{\text{amplitude0}} = (C_1 - A_1 + B_1)\dot{\varphi}_0^2 \Omega \frac{K}{K_{\text{moment}}K_{\text{electric current}}} \times \frac{1}{\sqrt{\left\{ \left[nT_{\text{amplify}} + 2T_0(\xi_0 + \xi) \right] \dot{\varphi}_0 - T_0^2 nT_{\text{amplify}} \dot{\varphi}_0^3 \right\}^2 + \left[1 - \left(T_0^2 + 2\xi_0 T_0 nT_{\text{amplify}} \right) \dot{\varphi}_0^2 \right]^2}}$$

$$(2.6)$$

$$\begin{split} U_{\text{amplitude1}} &= (C_1 - A_1 + B_1) \dot{\varphi}_0^2 \Omega \frac{K K_{\text{integrator 1}}}{K_{\text{moment}} K_{\text{electric current}}} \times \frac{1}{\sqrt{1 + T_{\text{integrator}}^2 \dot{\varphi}_0^2}} \times \\ &\qquad \frac{1}{\sqrt{\left\{ \left[n T_{\text{amplify}} + 2 T_0 (\xi_0 + \xi) \right] \dot{\varphi}_0 - T_0^2 n T_{\text{amplify}} \dot{\varphi}_0^3 \right\}^2 + \left[1 - \left(T_0^2 + 2 \xi_0 T_0 n T_{\text{amplify}} \right) \dot{\varphi}_0^2 \right]^2}} \end{split}$$

$$\begin{split} U_{\text{amplitude2}} &= (C_1 - A_1 + B_1) \dot{\varphi}_0^2 \Omega \frac{K K_{\text{integrator2}}}{K_{\text{moment}} K_{\text{electric current}}} \times \frac{\sqrt{1 + T_1^2 \dot{\varphi}_0^2}}{\sqrt{\left(1 - T_2^2 \dot{\varphi}_0^2\right)^2 + \left(2 \xi_{\text{integrator}} T_2 \dot{\varphi}_0\right)^2}} \times \\ & \frac{1}{\sqrt{\left\{\left[n T_{\text{amplify}} + 2 T_0 (\xi_0 + \xi)\right] \dot{\varphi}_0 - T_0^2 n T_{\text{amplify}} \dot{\varphi}_0^3\right\}^2 + \left[1 - \left(T_0^2 + 2 \xi_0 T_0 n T_{\text{amplify}}\right) \dot{\varphi}_0^2\right]^2}} \end{split}$$

When the integrator is ideal ($T_{\rm integrator}$ is very large) and the ideal compensation of the influence of the mutual inductance (n=0) is considered, because $nT_{\rm amplify}$ and ξ_0 are small and can therefore be ignored, from Eq. (2.7) we can obtain

$$U_{\text{amplitude1}} = (C_1 - A_1 + B_1)\dot{\varphi}_0^2 \Omega \frac{KK_{\text{integrator1}}}{K_{\text{moment}}K_{\text{electric current}}} \times \frac{1}{T_{\text{integrator}}\dot{\varphi}_0 \sqrt{\left(1 - T_0^2 \dot{\varphi}_0^2\right)^2 + \left(2\xi T_0 \dot{\varphi}_0\right)^2}}$$
(2.9)

When the instrument is operating at close to the resonant point, $T_0^2 \dot{\varphi}_0^2 \approx 1$ and $C_1 - A_1 = B_1$.

$$U_{\text{amplitude1}} = \frac{2B_1 \Omega K K_{\text{integrator1}}}{K_{\text{moment}} K_{\text{electric current}} T_{\text{integrator}} 2\xi T_0}$$

$$= \frac{2B_1 \Omega K_{\text{integrator1}}}{K_{\text{moment}} K_{\text{electric current}} T_{\text{integrator}}} \text{ (in the close to ideal condition)} \quad (2.10)$$

In the close to ideal condition, the output signals of the instrument are determined only by the transfer coefficients of the torque winding of the torque converter, a current amplifier and the integrator. The measurement result of the stability of the above parameters is a percentage, and can satisfy the high precision requirement of the angular velocity measurement of the rotating flight carrier.

When the integrator with the transfer function (1–130) is used, then where this function is in the ideal integral condition, T_1 and T_2 are relatively large. Assume that n=0 and $\xi_0=0$, there holds

$$U_{\text{amplitude2}} = (C_1 - A_1 + B_1) \dot{\varphi}_0^2 \Omega \frac{KK_{\text{integrator2}}}{K_{\text{moment}} K_{\text{electric current}}} \times \frac{T_1 \dot{\varphi}_0}{T_2^2 \dot{\varphi}_0^2 \sqrt{\left(1 - T_0^2 \dot{\varphi}_0^2\right)^2 + \left(2\xi T_0 \dot{\varphi}_0\right)^2}}$$
(2.11)

But in the case of the resonance, there holds

$$U_{\text{amplitude2}} = \frac{2B_1 K K_{\text{integrator2}} T_1}{K_{\text{moment}} K_{\text{electric current}} T_2^2 2\xi T_0} \Omega = \frac{2B_1 K_{\text{integrator2}} T_1}{K_{\text{moment}} K_{\text{electric current}} T_2^2} \Omega$$
 (2.12)

When $\frac{T_2^2}{T_1} = T_{\text{integrator}}$, Eq. (2.12) corresponds to Eq. (2.10).

When there is no integrator and no assumption $(n = 0, \xi_0 = 0)$, at the output end of the instrument, from Eq. (2.6), we can obtain

$$U_{\text{amplitude0}} = (C_1 - A_1 + B_1)\dot{\varphi}_0^2 \Omega \frac{K}{K_{\text{moment}}K_{\text{electric current}}} \times \frac{1}{\sqrt{\left(1 - T_0^2 \dot{\varphi}_0^2\right)^2 + \left(2\xi T_0 \dot{\varphi}_0\right)^2}}$$
(2.13)

In the case of resonance, there holds

$$U_{\text{amplitude0}} = \frac{2B_1 K \dot{\varphi}_0}{K_{\text{moment}} K_{\text{electric current}} 2 \xi T_0} \Omega = \frac{2B_1 \dot{\varphi}_0}{K_{\text{moment}} K_{\text{electric current}}} \Omega \tag{2.14}$$

Comparing Eqs. (2.10), (2.12) and (2.14) shows that if there is no integrator at the output end of the instrument, the output signal of the instrument will be unstable. This is because there is a linear relationship between the stability of the

output signal and the angular velocity rotating around the longitudinal axis of the aircraft. The integrator at the output end of the instrument, as shown in Eqs. (2.10) and (2.12) can eliminate the dependency between the output signal and the rotational angular velocity around the longitudinal axis of the aircraft. Therefore, the integrator can significantly improve the stability of the output signal.

As has been discussed before, in the case of non-precise tuning, for example in the case of $\mu=0.9$, there is instability between the amplitude of the output signal and the angular velocity rotating around the longitudinal axis of the aircraft. When $T_{\rm damping}$ is smaller, for these loops, $\xi=\frac{D_{\rm fredback}}{2\phi_0\mu B_1}$ can be substituted into Eq. (2.11) and $\dot{\varphi}_0$ is replaced by $\dot{\varphi}_0^0\pm\Delta\dot{\varphi}_0$.

$$\begin{split} U_{\text{amplitude2}} &= \frac{(\mu^2 + 1)D_{\text{feedback}}K_{\text{integrator2}}T_1\Omega}{\left(\dot{\varphi}_0^0 \pm \Delta\dot{\varphi}_0\right)K_{\text{moment}}K_{\text{electric current}}T_2^2\sqrt{(\mu^2 - 1)^2 + \left[\frac{D_{\text{feedback}}}{\left(\dot{\varphi}_0^0 \pm \Delta\dot{\varphi}_0\right)B_1}\right]^2}} \\ &= \frac{(\mu^2 + 1)B_1D_{\text{feedback}}K_{\text{integrator2}}T_1\Omega}{K_{\text{moment}}K_{\text{electric current}}T_2^2\sqrt{\left[\left(\dot{\varphi}_0^0 \pm \Delta\dot{\varphi}_0\right)B_1(\mu^2 - 1\right)\right]^2 + D_{\text{feedback}}^2}} \end{split}$$

In order to obtain the general result, the effect of the instability of the angular velocity rotating around the longitudinal axis on the amplitude of the output signal is in the form of a relative value:

$$\frac{U_{\text{amplitude}}}{U_{\text{amplitude}}(\Delta \dot{\varphi}_0 = 0)} = \sqrt{\frac{\left[\dot{\varphi}_0^0 B_1(\mu^2 - 1)\right]^2 + D_{\text{feedback}}^2}{\left[\left(\dot{\varphi}_0^0 \pm \Delta \dot{\varphi}_0\right) B_1(\mu^2 - 1)\right]^2 + D_{\text{feedback}}^2}}$$
(2.16)

The coefficient K is introduced to denote the ratio of the unstable value of the angular velocity rotating around the longitudinal axis of the aircraft to the average value of this angular velocity, i.e., $\Delta \dot{\varphi}_0 = K \varphi_0^0$. In this case Eq. (2–16) has the following form:

$$\frac{U_{\text{amplitude}}}{U_{\text{amplitude}}(\Delta \dot{\varphi}_0 = 0)} = \sqrt{\frac{(\mu^2 - 1)^2 + (2\xi^0 \mu)^2}{(1 \pm K)^2 (\mu^2 - 1)^2 + (2\xi^0 \mu)^2}}$$
(2.17)

where $\xi^0 = \frac{D_{\text{feedback}}}{2\phi_0^0 \mu B_1}$ is the attenuation coefficient, which has nothing to do with the instability of the angular velocity rotating around the longitudinal axis of the aircraft.

The curve corresponding to Eq. (2.17) is shown in Fig. 2.1.

Obviously, in the case of the precise tuning the amplitude ratio in Eq. (2.17) is equal to 1 and has no relationship with $\Delta \dot{\varphi}_0$ which is confirmed by Fig. 2.1a. It is worth noting that the enhanced damping effect of the instrument will lead to the

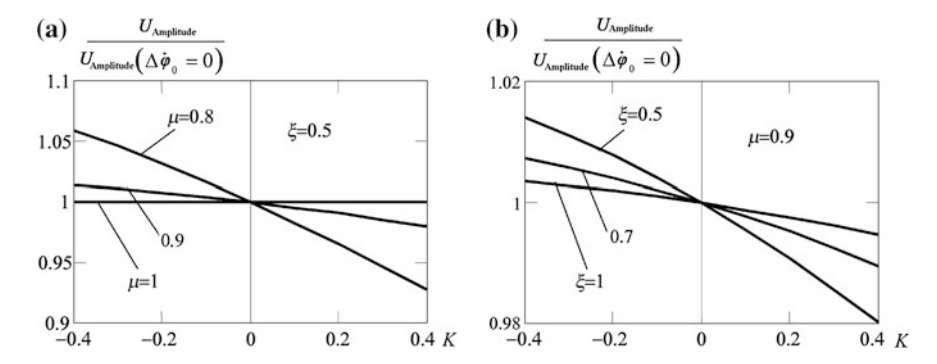


Fig. 2.1 Effect of instability of the angular velocity rotating around the longitudinal axis of the aircraft on the output signal amplitude of a non-driven mechanical gyroscope, **a** Variation of the detuning coefficient; **b** Variation of the damping coefficient

decrease of the dependency in Eq. (2.17), which is proved by Fig. 2.1b. When the angular velocity rotating around the longitudinal axis of the aircraft varies in the whole range (10–20 Hz) as well as in the case of $\mu = 0.9$ and $\xi = 0.5$, the relative error of the amplitude of the output signal value is 3.8%, that is, the ratio associated with the average amplitude is $\pm 1.9\%$.

Because the instantaneous value of the output signal is used in the instrument, the phase of the output signal and the phase stability should be noted accurately.

Corresponding to Eq. (2.5) there holds

$$\chi_0 = \frac{\pi}{2} - \arctan\left(\frac{\left[nT_{\text{amplify}} + 2T_0(\xi_0 + \xi)\right]\dot{\varphi}_0 - T_0^2 nT_{\text{amplify}}\dot{\varphi}_0^3}{1 - \left(T_0^2 + 2\xi_0 T_0 nT_{\text{amplify}}\right)\dot{\varphi}_0^2}\right)$$
(2.18)

$$\begin{split} \chi_1 &= \frac{\pi}{2} - \arctan\left(T_{\text{integrator}} \dot{\varphi}_0\right) \\ &- \arctan\left\{\frac{\left[nT_{\text{amplify}} + 2T_0(\xi_0 + \xi)\right] \dot{\varphi}_0 - T_0^2 n T_{\text{amplify}} \dot{\varphi}_0^3}{1 - \left(T_0^2 + 2\xi_0 T_0 n T_{\text{amplify}}\right) \dot{\varphi}_0^2}\right\} \end{split} \tag{2.19}$$

$$\begin{split} \chi_{2} &= \frac{\pi}{2} + \arctan\left(T_{1}\dot{\varphi}_{0}\right) - \arctan\left(\frac{2\xi_{\text{integrator}}T_{2}\dot{\varphi}_{0}}{1 - T_{2}^{2}\dot{\varphi}_{0}^{2}}\right) \\ &- \arctan\left\{\frac{\left[nT_{\text{amplify}} + 2T_{0}(\xi_{0} + \xi)\right]\dot{\varphi}_{0} - T_{0}^{2}nT_{\text{amplify}}\dot{\varphi}_{0}^{3}}{1 - \left(T_{0}^{2} + 2\xi_{0}T_{0}nT_{\text{amplify}}\right)\dot{\varphi}_{0}^{2}}\right\} \end{split} \tag{2.20}$$

Under the above conditions, n = 0, $\xi_0 = 0$, T_1 , T_2 and $T_{\text{integrator}}$ are very large.

$$\chi_0 = \frac{\pi}{2} - \arctan\left(\frac{2\xi T_0 \dot{\varphi}_0}{1 - T_0^2 \dot{\varphi}_0^2}\right)$$
 (2.21)

$$\chi_1 = -\arctan\left(\frac{2\xi T_0 \dot{\varphi}_0}{1 - T_0^2 \dot{\varphi}_0^2}\right) \tag{2.22}$$

$$\chi_2 = -\arctan\left(\frac{2\xi T_0 \dot{\varphi}_0}{1 - T_0^2 \dot{\varphi}_0^2}\right) \tag{2.23}$$

It can be seen that under the condition of using the circuit with the different integrators, the phase shifts are equal and the phase difference between the circuit with the different integrators and the circuit without the integrators is 90°.

In order to determine the stability of these values, Eqs. (2.21), (2.22) and (2.23) have the following form:

$$\chi_0 = \Delta \chi_0$$

$$\chi_1 = -\frac{\pi}{2} - \Delta \chi_1$$

$$\chi_2 = -\frac{\pi}{2} - \Delta \chi_2$$

Because χ_1 , χ_0 and χ_2 can be described by the same method, only χ_1 is studied and obtained as

$$\tan \chi_{1} = \tan \left(-\Delta \chi_{1} - \frac{\pi}{2}\right) = \cot \Delta \chi_{1} = \frac{1}{\tan \Delta \chi_{1}}$$

$$\tan \Delta \chi_{1} = \frac{1}{\tan \chi_{1}} = \frac{T_{0}^{2} \dot{\varphi}_{0}^{2} - 1}{2 \xi T_{0} \dot{\varphi}_{0}}$$
(2.24)

In this case, substituting Eqs. (1.124), (1.125) and (1.134) obtains

$$\tan \Delta \chi_1 = \frac{\frac{B_1}{C_1 - A_1} - 1}{\frac{K_{\text{moment}} K_{\text{amplify}} K_{\text{measure}} K_{\text{electric current}}}{(C_1 - A_1)\dot{\phi}_0}} = \frac{[B_1 - (C_1 - A_1)]\dot{\phi}_0}{K_{\text{moment}} K_{\text{amplify}} K_{\text{measure}} K_{\text{electric current}}}$$
(2.25)

and there holds

$$\chi_1 = -\frac{\pi}{2} - \arctan\left\{\frac{[B_1 - (C_1 - A_1)]\dot{\varphi}_0}{K_{\text{moment}}K_{\text{amplify}}K_{\text{measure}}K_{\text{electric current}}}\right\}$$
(2.26)

Because the tuning factor $\mu < 1$, there holds $(C_1 - A_1) < B_1$ and the symbol term "arctan" in the expression is positive.

Equation (2.26) shows that because the signal phase does not exceed $-\frac{\pi}{2}$, the instrument works outside the resonance point. And because

$$\dot{\varphi}_0 = \dot{\varphi}_0^0 \pm \Delta \dot{\varphi}_0 \tag{2.27}$$

where $\dot{\varphi}_0^0$ is the average angular velocity rotating around the longitudinal axis of the aircraft (here it is 15 Hz) and $\Delta\dot{\varphi}_0$ is the unstable value of the angular velocity rotating around the longitudinal axis of the aircraft (here it is the maximum value $\Delta\dot{\varphi}_0 = 5$ Hz).

Combining this with Eq. (2.26), it is known that the phase shift of the instrument is unstable because it has a dependent relationship with the unstable angular velocity rotating around the longitudinal axis of the aircraft.

Substituting Eq. (2.27) into Eq. (2.26) obtains

$$\chi_{1} = -\frac{\pi}{2} - \arctan\left\{\frac{\left[B_{1} - (C_{1} - A_{1})\right]\left(\dot{\varphi}_{0}^{0} \pm \triangle \dot{\varphi}_{0}\right)}{K_{\text{moment}}K_{\text{amplify}}K_{\text{measure}}K_{\text{electric current}}}\right\}$$
(2.28)

Because the value of the expression "arctan" is small, there holds

$$\chi_1 = -\frac{\pi}{2} - \arctan\left\{\frac{[B_1 - (C_1 - A_1)](\dot{\varphi}_0^0 \pm \Delta \dot{\varphi}_0)}{K_{\text{moment}} K_{\text{amplify}} K_{\text{measure}} K_{\text{electric current}}}\right\} = \chi_{10} \pm \Delta \chi_{10} \quad (2.29)$$

where

$$\chi_{10} = -\frac{\pi}{2} - \frac{[B_1 - (C_1 - A_1)]\dot{\varphi}_0^0}{K_{\text{moment}}K_{\text{amplify}}K_{\text{measure}}K_{\text{electric current}}}$$
(2.30)

When the instrument is mounted to the machine body, the angle is compensated by the method of rotating the instrument or when the output signal of the instrument is furtherly processed, the angle is compensated in the aircraft. χ_{10} is a constant and does not have a dependent relationship with the unstable value $\Delta \dot{\phi}_0$.

 $\Delta\chi_{10}$ is caused by the instability of the angular velocity rotating around the longitudinal axis of the aircraft and is the unstable phase value of the output signal of the instrument. It should be noted that $\Delta\dot{\phi}_0$ is quite large, so the phase error is relatively large.

$$\Delta \chi_{10} = \frac{[B_1 - (C_1 - A_1)]\Delta \dot{\varphi}_0}{K_{\text{moment}} K_{\text{amplify}} K_{\text{measure}} K_{\text{electric current}}}$$
(2.31)

Similar to Eq. (2.29), for the circuit without the integrators and the circuit with the integrators, the expressions of the output signal phase are obtained as follows:

$$\chi_0 = \frac{\pi}{2} - \arctan\left\{\frac{[B_1 - (C_1 - A_1)](\dot{\varphi}_0^0 \pm \Delta \dot{\varphi}_0)}{K_{\text{moment}} K_{\text{amplify}} K_{\text{measure}} K_{\text{electric current}}}\right\} = \chi_{00} \pm \Delta \chi_{00} \qquad (2.32)$$

$$\chi_2 = -\frac{\pi}{2} - \arctan\left\{\frac{[B_1 - (C_1 - A_1)](\dot{\varphi}_0^0 \pm \Delta \dot{\varphi}_0)}{K_{\text{moment}} K_{\text{amplify}} K_{\text{measure}} K_{\text{electric current}}}\right\} = \chi_{20} \pm \Delta \chi_{20} \quad (2.33)$$

We will estimate how the unstable phase value of the output signal affects its instantaneous value. As the output signal of the instrument is in the form of

$$U_{\rm out} = U_{\rm amplitude} \sin \left(\dot{\varphi}_0 t + \chi \right)$$

then

$$U_{\rm out} = U_{\rm amplitude} \sin \left\{ (\dot{\varphi}_0 \pm \Delta \dot{\varphi}_0) t \mp \frac{[B_1 - (C_1 - A_1)] \Delta \dot{\varphi}_0}{K_{\rm moment} K_{\rm amplify} K_{\rm measure} K_{\rm electric \, current}} \right\} \quad (2.34)$$

The angle χ_0 in Eq. (2.30) is considered as a compensation in Eq. (2.34). $(\dot{\varphi}_0 \pm \Delta \dot{\varphi}_0)t$ will no longer calculate the unstable value of the angular velocity rotating around the longitudinal axis of the rotating flight carrier. Therefore, as this unstable value affects the steering engine of the rotating flight carrier and does not affect the processing precision of the input signal, then

$$U_{\rm out} = U_{\rm amplitude} \sin \left\{ \dot{\varphi}_0 t \mp \frac{[B_1 - (C_1 - A_1)] \Delta \dot{\varphi}_0}{K_{\rm moment} K_{\rm amplify} K_{\rm measure} K_{\rm electric \, current}} \right\}$$
(2.35)

When the output signal is the maximum or minimum value, the sensitive axis of the instrument is coincident with the vector direction of the measured angular velocity. Thus

$$\dot{\varphi}_0 t = \pm \frac{\pi}{2} \pm \pi k$$

The error of the instrument is small because Eq. (2.35) has the following form:

$$U_{\text{out}} = \pm U_{\text{amplitude}} \cos \left\{ \frac{[B_1 - (C_1 - A_1)]\Delta \dot{\varphi}_0}{K_{\text{moment}} K_{\text{amplify}} K_{\text{measure}} K_{\text{electric current}}} \right\}$$
(2.36)

Equation (2.36) shows that in the case of resonance, $\Delta \chi_{10} = 0$ in Eq. (2.31), then $U_{\text{out}} = \pm U_{\text{amplitude}}$, where the positive and negative symbols will determine the maximum or minimum value of the signal.

When the instrument is not in the resonant state but it is directly close to the resonant state, then because $\Delta\chi_{10}$ is determined and is small, the unstable value of the angular velocity rotating around the longitudinal axis of the aircraft will not significantly affect the maximum or minimum value of the instrument's output signal.

In this case, the output of the instrument is zero, which indicates that the instrument's sensitive axis is perpendicular to the vector direction of the measured angular velocity. Thus

$$\dot{\varphi}_0 t = 0 \pm \pi k$$

The form of the instrument's output signal is

$$U_{\text{out}} = \mp U_{\text{amplitude}} \sin \left\{ \frac{[B_1 - (C_1 - A_1)]\Delta \dot{\varphi}_0}{K_{\text{moment}} K_{\text{amplify}} K_{\text{measure}} K_{\text{electric current}}} \right\}$$
(2.37)

In this case, because the output signal is proportional to the sinusoidal value of $\Delta\chi_{10}$, its image is different. In the case of resonance, the output signal should be equal to zero but in the case of imprecise adjustment of the resonance because $\Delta\chi_{10}$ is very small, the output signal will be

$$U_{\text{out}} = \mp U_{\text{amplitude}} \left\{ \frac{[B_1 - (C_1 - A_1)] \triangle \dot{\varphi}_0}{K_{\text{moment}} K_{\text{amplify}} K_{\text{measure}} K_{\text{electric current}}} \right\}$$
(2.38)

Thus, in the above moment the signal error is, in essence, the cross error of the instrument and is proportional to the unstable value of the angular velocity rotating around the longitudinal axis of the aircraft. It should be pointed out that the size of $\Delta \chi_{10}$ can be up to a few degrees.

Under the condition that the integral time constant of the integral loop is not large enough, the influence degree of the integral loop at the output signal end on the phase stability of the output signal is measured. In Eqs. (2.19) and (2.20), assume that n=0 and $\xi_0=0$, then

$$\chi_1 = \frac{\pi}{2} - \arctan\left(T_{\text{integrator}}\dot{\varphi}_0\right) - \arctan\left(\frac{2T_0\xi\dot{\varphi}_0}{1 - T_0^2\dot{\varphi}_0^2}\right)$$
(2.39)

$$\chi_{2} = \frac{\pi}{2} + \arctan\left(T_{1}\dot{\varphi}_{0}\right) - \arctan\left(\frac{2\xi_{\text{integrator}}T_{2}\dot{\varphi}_{0}}{1 - T_{2}^{2}\dot{\varphi}_{0}^{2}}\right) - \arctan\left(\frac{2T_{0}\xi\dot{\varphi}_{0}}{1 - T_{0}^{2}\dot{\varphi}_{0}^{2}}\right)$$
(2.40)

According to the above calculations and obtains

$$\chi_{1} = -\frac{\pi}{2} + \Delta \chi_{\text{integrator1}} - \Delta \chi_{1}$$

$$\chi_{2} = -\frac{\pi}{2} - \Delta \chi_{\text{integrator2}1} + \Delta \chi_{\text{integrator2}2} - \Delta \chi_{2}$$

$$\tan \chi_{1} = \tan \left(-\Delta \chi_{1} + \Delta \chi_{\text{integrator1}} - \frac{\pi}{2} \right) = \cot \left(\Delta \chi_{1} - \Delta \chi_{\text{integrator1}} \right)$$

$$= \frac{1}{\tan \left(\Delta \chi_{1} - \Delta \chi_{\text{integrator2}1} \right)}$$

$$\tan \chi_{2} = \tan \left(-\Delta \chi_{2} - \Delta \chi_{\text{integrator2}1} + \Delta \chi_{\text{integrator2}2} - \frac{\pi}{2} \right)$$

$$= \frac{1}{\tan \left(\Delta \chi_{2} + \Delta \chi_{\text{integrator2}1} - \Delta \chi_{\text{integrator2}2} \right)}$$

$$\tan \left(\Delta \chi_{1} - \Delta \chi_{\text{integrator1}} \right) = \frac{1}{\tan \chi_{1}} = \tan \left[\arctan \left(T_{\text{integrator}} T_{0}^{2} \dot{\varphi}_{0}^{3} + 2 T_{0} \dot{\xi} \dot{\varphi}_{0} \right) \right]$$

$$= \frac{T_{\text{integrator}} \dot{\varphi}_{0} - T_{\text{integrator}} T_{0}^{2} \dot{\varphi}_{0}^{3} + 2 T_{0} \dot{\xi} \dot{\varphi}_{0}}{1 - T_{0}^{2} \dot{\varphi}_{0}^{2}} \right]$$

$$= \frac{T_{\text{integrator}} \dot{\varphi}_{0} - T_{\text{integrator}} T_{0}^{2} \dot{\varphi}_{0}^{3} + 2 T_{0} \dot{\xi} \dot{\varphi}_{0}}{1 - T_{0}^{2} \dot{\varphi}_{0}^{2}}$$

$$= \frac{T_{\text{integrator}} \dot{\varphi}_{0} - T_{\text{integrator}} T_{0}^{2} \dot{\varphi}_{0}^{3} + 2 T_{0} \dot{\xi} \dot{\varphi}_{0}}{1 - T_{0}^{2} \dot{\varphi}_{0}^{2}}$$

$$= \frac{T_{\text{integrator}} \dot{\varphi}_{0} - T_{\text{integrator}} T_{0}^{2} \dot{\varphi}_{0}^{3} + 2 T_{0} \dot{\xi} \dot{\varphi}_{0}^{2}}{1 - T_{0}^{2} \dot{\varphi}_{0}^{2}}$$

$$= \frac{T_{\text{integrator}} \dot{\varphi}_{0} - T_{\text{integrator}} T_{0}^{2} \dot{\varphi}_{0}^{3}}{1 - T_{0}^{2} \dot{\varphi}_{0}^{2}} + 2 T_{\text{integrator}} \chi_{\text{integrator}} \chi_{\text{integrator}} \chi_{\text{ensure}} \chi_{\text{electric current}} \chi_{\text{electric cu$$

In this case, even in the state of resonance, the phase of the output signal always maintains a complex relationship with the rotating angular velocity of the aircraft itself. The integral time constant is small and can be easily determined. The time constant causes the phase of the integral loop and the angular velocity rotating around the longitudinal axis of the aircraft to change, and make them keep very small dependency in the varying range of the above angular velocity. This condition is obtained by Eqs. (2.41) and (2.42), and the following two expressions are obtained, which show that the instrument is considered to be working in a resonant state.

$$\tan(\Delta \chi_1 - \Delta \chi_{\text{integrator1}}) = \frac{1}{T_{\text{integrator}} \dot{\varphi}_0}$$
 (2.43)

$$\tan(\Delta \chi_2 + \Delta \chi_{\text{integrator}21} - \Delta \chi_{\text{integrator}22}) = \frac{1 + \frac{2\xi_{\text{integrator}}T_2T_1\dot{\phi}_0^2}{1 - T_2^2\dot{\phi}_0^2}}{T_1\dot{\phi}_0 - \frac{2\xi_{\text{integrator}}T_2\dot{\phi}_0}{1 - T_3^2\dot{\phi}_0^2}}$$
(2.44)

where

$$\chi_1 = -\frac{\pi}{2} - \arctan\left[\frac{1}{T_{\text{integrator}}(\dot{\varphi}_0^0 \pm \Delta \dot{\varphi}_0)}\right]$$
(2.45)

$$\chi_{2} = -\frac{\pi}{2} - \arctan \left[\frac{1 + \frac{2\xi_{\text{integrator}}T_{2}T_{1}\left(\dot{\varphi}_{0}^{0} \pm \Delta\dot{\varphi}_{0}\right)^{2}}{1 - T_{2}^{2}\left(\dot{\varphi}_{0}^{0} \pm \Delta\dot{\varphi}_{0}\right)^{2}}}{T_{1}\left(\dot{\varphi}_{0}^{0} \pm \Delta\dot{\varphi}_{0}\right) - \frac{2\xi_{\text{integrator}}T_{2}\left(\dot{\varphi}_{0}^{0} \pm \Delta\dot{\varphi}_{0}\right)}{1 - T_{2}^{2}\left(\dot{\varphi}_{0}^{0} \pm \Delta\dot{\varphi}_{0}\right)^{2}}} \right]$$
(2.46)

Equations (2.29), (2.30), (2.45) and (2.46) show that the instability of the rotating angular velocity signal has a huge influence on the stability of the phase and the instantaneous value of the instrument output signal. Therefore, various measures must be taken to reduce the phase instability. Introducing the differential circuit in the integrator can achieve this purpose. Then, Eqs. (1.129) and (1.130) have the following form by some transformations:

$$W_{\text{integrator1}}(s) = K_{\text{integrator1}} \frac{1 + T_{\text{damping}}s}{1 + T_{\text{integrator}}s}$$
(2.47)

$$W_{\text{integrator2}}(s) = K_{\text{integrator2}} \frac{\left(1 + T_{\text{damping}}s\right)\left(1 + T_{\text{integrator}}s\right)}{T_2^2 s^2 + 2\xi_{\text{integrator}}T_2 s + 1}$$
(2.48)

The transfer function of the closed-loop system is described by the following expressions:

$$\begin{split} \Phi_{1}(s) &= \frac{KK_{\text{integrator1}}}{K_{\text{moment}}K_{\text{electric current}}} \times \frac{1 + T_{\text{damping}}s}{1 + T_{\text{integrator}}s} \\ &\times \frac{s}{T_{0}^{2}nT_{\text{amplify}}s^{3} + \left(T_{0}^{2} + 2\xi_{0}T_{0}nT_{\text{amplify}}\right)s^{2} + \left(nT_{\text{amplify}} + 2\xi_{0}T_{0} + K\right)s + 1} \end{split}$$

$$\Phi_{2}(s) = \frac{KK_{\text{integrator2}}}{K_{\text{moment}}K_{\text{electric current}}} \times \frac{(1+T_{1}s)\left(1+T_{\text{damping}}s\right)}{T_{2}^{2}s^{2}+2\xi_{\text{integrator}}T_{2}s+1} \times \frac{s}{T_{0}^{2}nT_{\text{amplify}}s^{3}+\left(T_{0}^{2}+2\xi_{0}T_{0}nT_{\text{amplify}}\right)s^{2}+\left(nT_{\text{amplify}}+2\xi_{0}T_{0}+K\right)s+1}$$
(2.50)

In this case, the amplitude and the phase of the output signal is also changed:

$$\begin{split} U_{\text{amplitude1}} &= (C_1 - A_1 + B_1) \dot{\phi}_0^2 \Omega \frac{K K_{\text{integrator1}}}{K_{\text{moment}} K_{\text{electric current}}} \times \frac{\sqrt{1 + T_{\text{damping}}^2 \dot{\phi}_0^2}}{\sqrt{1 + T_{\text{integrator}}^2 \dot{\phi}_0^2}} \\ &\times \frac{1}{\sqrt{\left\{ \left[n T_{\text{amplify}} + 2 T_0 (\xi_0 + \xi) \right] \dot{\phi}_0 - T_0^2 n T_{\text{amplify}} \dot{\phi}_0^3 \right\}^2 + \left[1 - \left(T_0^2 + 2 \xi_0 T_0 n T_{\text{amplify}} \right) \dot{\phi}_0^2 \right]^2}} \end{split}$$

$$\begin{split} U_{\text{amplitude2}} &= (C_1 - A_1 + B_1) \dot{\varphi}_0^2 \Omega \frac{K K_{\text{integrator2}}}{K_{\text{moment}} K_{\text{electric current}}} \frac{\sqrt{\left(1 + T_1^2 \dot{\varphi}_0^2\right) \left(1 + T_{\text{damping}}^2 \dot{\varphi}_0^2\right)}}{\sqrt{\left(1 - T_2^2 \dot{\varphi}_0^2\right)^2 + \left(2 \xi_{\text{integrator}} T_2 \dot{\varphi}_0\right)^2}} \\ &\times \frac{1}{\sqrt{\left\{ \left[n T_{\text{amplify}} + 2 T_0 (\xi_0 + \xi)\right] \dot{\varphi}_0 - T_0^2 n T_{\text{amplify}} \dot{\varphi}_0^3\right\}^2 + \left[1 - \left(T_0^2 + 2 \xi_0 T_0 n T_{\text{amplify}}\right) \dot{\varphi}_0^2\right]^2}} \end{split}$$

Under the assumption used previously and the assumption that $\xi_0=0$, $T_{\rm integrator}\dot{\phi}_0\geq 1$ and $T_{\rm damping}$ is very small $(T_{\rm damping}\dot{\phi}_0\leq 1)$, Eq. (2.51) is obtained as

$$U_{\text{amplitude 1}} = \frac{KK_{\text{integrator 1}}}{K_{\text{moment}}K_{\text{electric current}}} \frac{(C_1 - A_1 + B_1)\dot{\varphi}_0^2\Omega}{T_{\text{integrator}}\dot{\varphi}_0\sqrt{\left[\left(nT_{\text{amplify}} + 2\xi T_0\right)\dot{\varphi}_0 - T_0^2nT_{\text{amplify}}\dot{\varphi}_0^3\right]^2 + \left[1 - T_0^2\dot{\varphi}_0^2\right]^2}}$$

$$(2.53)$$

$$U_{\mathrm{amplitude1}} = \frac{KK_{\mathrm{integrator1}}}{K_{\mathrm{moment}}K_{\mathrm{electric \, current}}} \frac{(C_1 - A_1 + B_1)\Omega}{2\xi T_0 T_{\mathrm{integrator}} \sqrt{\left[1 + \frac{nT_{\mathrm{amplify}}}{2\xi T_0} \left(1 - T_0^2 \dot{\varphi}_0^2\right)\right]^2 + \left[\frac{1}{2\xi T_0} \left(1 - T_0^2 \dot{\varphi}_0^2\right)\right]^2}}$$

Equation (2.53) shows that the differential loop whose time constant is small enough, is introduced into the integrator and will not affect the amplitude of the output signal. When the instrument is working in the resonant state and nT_{amplify} is very small, Eq. (2.53) is in accordance with Eq. (2.10).

Next we will analyze the situation when the instrument is not working at the resonance point, but is very close to the resonance point. This situation is more realistic. At this time, $nT_{\rm amplify}$ is a very small constant but is not equal to zero. Because $nT_{\rm amplify}$ is very small and $\dot{\varphi}_0$ approaches ω_0 , $\frac{nT_{\rm amplify}}{2\xi T_0} \left(1 - T_0^2 \dot{\varphi}_0^2\right)$ is far less than 1 and its square value can be neglected when compared with 1. There holds

$$U_{\text{amplitude1}} = \frac{K_{\text{integrator1}}}{K_{\text{moment}}K_{\text{electric current}}} \frac{(C_1 - A_1 + B_1)\Omega}{T_{\text{integrator}}\sqrt{\frac{1 - T_0^2\dot{\varphi}_0^2}{2\xi T_0} \left[\frac{1 - T_0^2\dot{\varphi}_0^2}{2\xi T_0\dot{\varphi}_0^2} + 2nT_{\text{amplify}}\right] + 1}}$$

$$(2.54)$$

Substituting Eqs. (1.124), (1.125) and (1.134) obtains

$$\frac{U_{\text{amplitude1}} = \frac{K_{\text{integrator1}}}{K_{\text{moment}}K_{\text{electric current}}}}{(C_1 - A_1 + B_1)\Omega} \\ \frac{(C_1 - A_1 - B_1)\dot{\varphi}_0^2}{T_{\text{integrator}}\sqrt{\frac{(C_1 - A_1 - B_1)\dot{\varphi}_0^2}{K_{\text{moment}}K_{\text{amplify}}K_{\text{measure}}K_{\text{electric current}}}} \left[\frac{(C_1 - A_1 - B_1)\Omega}{K_{\text{moment}}K_{\text{amplify}}K_{\text{measure}}K_{\text{electric current}}} + 2nT_{\text{amplify}}\right] + 1}$$

$$(2.55)$$

When the influence of the mutual inductance effect is not completely compensated $(n \neq 0)$ and precisely tuned, the signal amplitude at the output end of the instrument will have a complex dependency on the angular velocity rotating around the longitudinal axis of the aircraft.

Equations (2.54) and (2.55) show that in the process of approaching the resonant point, not only is the influence of the angular velocity rotating around the longitudinal axis of the aircraft on the amplitude of the output signal decreased, but its influence on the time constant nT_{amplify} is also decreased. The effect of these parameters is reduced under the condition that the feedback damping function is enhanced.

Under the same assumptions, Eq. (2.52) can be obtained by analogy:

$$U_{\text{amplitude2}} = \frac{K_{\text{integrator2}}}{K_{\text{moment}}K_{\text{electric current}}} \frac{T_1(C_1 - A_1 + B_1)\Omega}{T_2\sqrt{\frac{(C_1 - A_1 - B_1)\dot{\varphi}_0^2}{K_{\text{moment}}K_{\text{amplify}}K_{\text{measure}}K_{\text{electric current}}}} \left[\frac{(C_1 - A_1 - B_1)\Omega}{K_{\text{moment}}K_{\text{amplify}}K_{\text{measure}}K_{\text{electric current}}} + 2nT_{\text{amplify}}\right] + 1}$$

$$(2.56)$$

When the integrator is introduced into the differential loop, the phase change of the output signal is obtained:

$$\begin{split} \chi_1 &= \frac{\pi}{2} + \arctan\left(T_{\text{damping}} \dot{\varphi}_0\right) - \arctan\left(T_{\text{integrator}} \dot{\varphi}_0\right) \\ &- \arctan\left\{\frac{\left[nT_{\text{amplify}} + 2T_0(\xi_0 + \xi)\right] \dot{\varphi}_0 - T_0^2 nT_{\text{amplify}} \dot{\varphi}_0^3}{1 - \left(T_0^2 + 2\xi_0 T_0 nT_{\text{amplify}}\right) \dot{\varphi}_0^2}\right\} \end{split} \tag{2.57}$$

$$\begin{split} \chi_{2} &= \frac{\pi}{2} + \arctan\left(T_{\text{damping}}\dot{\varphi}_{0}\right) + \arctan\left(T_{1}\dot{\varphi}_{0}\right) - \arctan\left(\frac{2\xi_{\text{integrator}}T_{2}\dot{\varphi}_{2}}{1 - T_{2}^{2}\dot{\varphi}_{0}^{2}}\right) \\ &- \arctan\left\{\frac{\left[nT_{\text{amplify}} + 2T_{0}(\xi_{0} + \xi)\right]\dot{\varphi}_{0} - T_{0}^{2}nT_{\text{amplify}}\dot{\varphi}_{0}^{3}}{1 - \left(T_{0}^{2} + 2\xi_{0}T_{0}nT_{\text{amplify}}\right)\dot{\varphi}_{0}^{2}}\right\} \end{split} \tag{2.58}$$

Because the damping of the air is small, and set $\xi_0 = 0$, there holds

$$\chi_{1} = \frac{\pi}{2} + \arctan\left(T_{\text{damping}}\dot{\varphi}_{0}\right) - \arctan\left(T_{\text{integrator}}\dot{\varphi}_{0}\right)$$
$$-\arctan\left(\frac{\dot{\varphi}_{0}\left[2\xi T_{0} + nT_{\text{amplify}}\left(1 - T_{0}^{2}\dot{\varphi}_{0}^{2}\right)\right]}{1 - T_{0}^{2}\dot{\varphi}_{0}^{2}}\right) \tag{2.59}$$

$$\begin{split} \chi_2 &= \frac{\pi}{2} + \arctan\left(T_{\text{damping}} \dot{\varphi}_0\right) + \arctan\left(T_1 \dot{\varphi}_0\right) - \arctan\left(\frac{2\xi_{\text{integrator}} T_2 \dot{\varphi}_0}{1 - T_2^2 \dot{\varphi}_0^2}\right) \\ &- \arctan\left\{\frac{\dot{\varphi}_0 \left[2\xi T_0 + nT_{\text{amplify}} \left(1 - T_0^2 \dot{\varphi}_0^2\right)\right]}{1 - T_0^2 \dot{\varphi}_0^2}\right\} \end{split} \tag{2.60}$$

Introducing the following symbols:

$$\chi_{\text{integrator}} = -\arctan\left(T_{\text{integrator}}\dot{\varphi}_0\right)$$
(2.61)

$$\chi_{\text{integrator1}} = \arctan\left(T_1 \dot{\varphi}_0\right)$$
(2.62)

$$\chi_{\rm integrator2} = -\arctan\left(\frac{2\xi_{\rm integrator}T_2\dot{\varphi}_0}{1 - T_2^2\dot{\varphi}_0^2}\right) \tag{2.63}$$

$$\chi_{\text{integrator0}} = -\arctan\left\{\frac{\dot{\varphi}_0\left[2\xi T_0 + nT_{\text{amplify}}\left(1 - T_0^2\dot{\varphi}_0^2\right)\right]}{1 - T_0^2\dot{\varphi}_0^2}\right\} \tag{2.64}$$

For larger values of $T_{integrator}$, T_1 , T_1 and the working state of approaching the resonant point, from transformations (2.22) and (2.23), Eqs. (2.61), (2.62), (2.63) and (2.64) can be transformed and rewritten as

$$\chi_{
m integrator} = -rac{\pi}{2} + \Delta \chi_{
m integrator}$$
 $\chi_{
m integrator1} = rac{\pi}{2} + \Delta \chi_{
m integrator1}$
 $\chi_{
m integrator2} = -\pi + \Delta \chi_{
m integrator2}$
 $\chi_{
m integrator0} = -rac{\pi}{2} + \Delta \chi_{
m integrator0}$

Because $\Delta \chi_{integrator}$, $\Delta \chi_{integrator1}$, $\Delta \chi_{integrator2}$ and $\Delta \chi_{integrator0}$ are small, there holds

$$\Delta \chi_{\rm integrator} = -\frac{1}{\tan \chi_{\rm integrator}} = \frac{1}{T_{\rm integrator} \dot{\varphi}_0}$$
 (2.65)

$$\Delta \chi_{\text{integrator1}} = -\frac{1}{\tan \chi_{\text{integrator1}}} = -\frac{1}{T_1 \dot{\varphi}_0}$$
 (2.66)

$$\Delta \chi_{\text{integrator2}} = \tan \chi_{\text{integrator2}} = -\frac{2\xi_{\text{integrator}} T_2 \dot{\varphi}_0}{1 - T_2^2 \dot{\varphi}_0^2} = \frac{2\xi_{\text{integrator}}}{T_2 \dot{\varphi}_0}$$
(2.67)

$$\Delta \chi_{\rm integrator0} = -\frac{1}{\tan \chi_{\rm integrator0}} = \frac{1 - T_0^2 \dot{\varphi}_0^2}{\dot{\varphi}_0 \left[2\xi T_0 + n T_{\rm amplify} \left(1 - T_0^2 \dot{\varphi}_0^2 \right) \right]} \tag{2.68}$$

For a small T_{damping} , $\arctan(T_{\text{damping}}\dot{\varphi}_0) = T_{\text{damping}}\dot{\varphi}_0$, then

$$\chi_{1} = -\frac{\pi}{2} + T_{\text{damping}} \dot{\varphi}_{0} + \frac{1}{T_{\text{integrator}} \dot{\varphi}_{0}} + \frac{1 - T_{0}^{2} \dot{\varphi}_{0}^{2}}{\dot{\varphi}_{0} \left[2\xi T_{0} + n T_{\text{amplify}} \left(1 - T_{0}^{2} \dot{\varphi}_{0}^{2} \right) \right]}$$
(2.69)

$$\chi_{2} = -\frac{\pi}{2} + T_{damping} \dot{\varphi}_{0} + \frac{2\xi_{integrator}}{T_{2} \dot{\varphi}_{0}} - \frac{1}{T_{1} \dot{\varphi}_{0}} + \frac{1 - T_{0}^{2} \dot{\varphi}_{0}^{2}}{\dot{\varphi}_{0} \left[2\xi T_{0} + n T_{amplify} \left(1 - T_{0}^{2} \dot{\varphi}_{0}^{2} \right) \right]}$$

$$(2.70)$$

The augments of the third term and the fourth term in Eq. (2.70) were synthesized as:

$$\chi_{2} = -\frac{\pi}{2} + T_{\text{damping}} \dot{\varphi}_{0} + \frac{2\xi_{\text{integrator}} T_{1} - T_{2}}{T_{2} T_{1} \dot{\varphi}_{0}} + \frac{1 - T_{0}^{2} \dot{\varphi}_{0}^{2}}{\dot{\varphi}_{0} \left[2\xi T_{0} + n T_{\text{amplify}} \left(1 - T_{0}^{2} \dot{\varphi}_{0}^{2} \right) \right]}$$
(2.71)

When $T_{\text{integrator}} = \frac{T_2 T_1}{2\xi_{\text{integrator}} T_1 - T_2}$, Eq. (2.71) is completely consistent with Eq. (2.69).

Figure 2.2 shows the frequency characteristic curves of two integrator schemes that have the transfer functions in Eq. (1.130). The frequency characteristic curves with different $\xi_{\text{integrator}}$ are drawn.

Comparing Eqs. (2.10) and (2.12) with (2.69) and (2.71), obtains two conditions in Eqs. (2.72) and (2.73). Under the above two conditions, the frequency characteristic curves for the integrator with the transfer function in Eq. (1.130) are in accord with the frequency characteristic curves of the non-periodic loop.

$$\frac{T_2^2}{T_1} = T_{\text{integrator}} \tag{2.72}$$

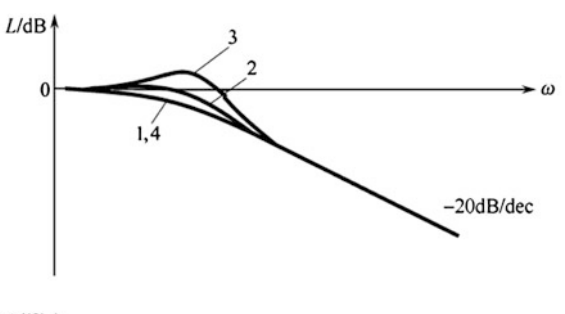
$$T_{\text{integrator}} = \frac{T_2 T_1}{2\xi_{\text{integrator}} T_1 - T_2}$$
 (2.73)

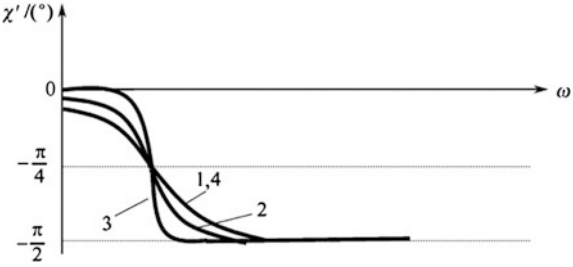
Because the three parameters of the integrator are only related to two equations, there are many groups of parameter solutions that satisfy the two equations.

The parameters of the frequency characteristics in the integrator are determined by Eqs. (2.72) and (2.73). It is recommended that these parameters are selected in the following order:

(1) Select a sufficiently large time constant $T_{\text{integrator}}$.

Fig. 2.2 Frequency characteristic curves of two integrators. 1—Integrator with the transfer function in Eq. (1.130), non-periodic loop; 2—Curve with $\xi_{\text{integrator}} = 0.8$; 3—Curve with $\xi_{\text{integrator}} = 0.5$; 4—Curve with $\xi_{\text{integrator}} = 1$





- (2) Select a sufficiently large time constant T_1 .
- (3) From (2.72), calculate the time constant T_2 .
- (4) From (2.73), determine the coefficient $\xi_{\text{integrator}}$. Under the condition of these parameters, calculate the requirement that the frequency characteristic curve of the integrator is fully in accord with that of the non-periodic loop.
- (5) As shown in Fig. 2.2, the coefficient $\xi_{\text{integrator}}$ is changed on the basis of the phase frequency characteristic curve. In the working frequency range, the required phase stability is obtained.

It should be noted that under the condition that the time constants T_1 and T_2 are large enough, then the change of $\xi_{\text{integrator}}$, within the working frequency range, does not actually affect the amplitude frequency characteristic curve.

According to the circuit shown in Fig. 1.18, the parameters of the integrator have the following forms:

$$K_{\text{integrator}} = \frac{R_5 + R_6}{R_4} \tag{2.74}$$

$$T_1 = \frac{C_2 R_5 R_6}{R_5 + R_6} \tag{2.75}$$

$$T_2 = \sqrt{C_1 C_2 R_5 R_6} \tag{2.76}$$

$$\xi_{\text{integrator}} = \frac{C_1(R_5 + R_6) + C_2 R_5}{2\sqrt{C_1 C_2 R_2 R_3}}$$
(2.77)

Review Eqs. (2.69) and (2.71), decompose $\frac{1}{T_{\text{integrator}}\dot{\phi}_0}$ and $\frac{2\xi_{\text{integrator}}T_1-T_2}{T_1T_2\dot{\phi}_0}$ into Taylor series, reject the two and higher powers of $(\dot{\phi}_0-\dot{\phi}_0^0)$ because of their small values, and substitute them into Eqs. (2.69) and (2.71)

$$\frac{1}{T_{\text{integrator}}\dot{\varphi}_0} = \frac{1}{T_{\text{integrator}}\dot{\varphi}_0^0} - \frac{\dot{\varphi}_0 - \dot{\varphi}_0^0}{T_{\text{integrator}}\left(\dot{\varphi}_0^0\right)^2} + \cdots$$
 (2.78)

$$\frac{2\xi_{\text{integrator}}T_{1}-T_{2}}{T_{\text{integrator}}\dot{\varphi}_{0}} = \frac{2\xi_{\text{integrator}}T_{1}-T_{2}}{T_{\text{integrator}}\dot{\varphi}_{0}^{0}} - \frac{\left(2\xi_{\text{integrator}}T_{1}-T_{2}\right)\left(\dot{\varphi}_{0}-\dot{\varphi}_{0}^{0}\right)}{T_{\text{integrator}}\left(\dot{\varphi}_{0}^{0}\right)^{2}} + \cdots$$

$$(2.79)$$

Substituting Eqs. (1.124), (1.125) and (1.134), Eqs. (2.69) and (2.71) are transformed into

$$\chi_{1} = -\frac{\pi}{2} + \frac{2}{T_{\text{integrator}}\dot{\varphi}_{0}^{0}} + \dot{\varphi}_{0} \left[T_{\text{damping}} - \frac{1}{T_{\text{integrator}}(\dot{\varphi}_{0}^{0})^{2}} + \frac{C_{1} - A_{1} - B_{1}}{K_{\text{moment}}K_{\text{amplify}}K_{\text{measure}}K_{\text{electric current}} + nT_{\text{amplify}}\dot{\varphi}_{0}^{2}(C_{1} - A_{1} - B_{1})} \right]$$
(2.80)

$$\chi_{2} = -\frac{\pi}{2} + \frac{2(2\xi_{\text{integrator}}T_{1} - T_{2})}{T_{1}T_{2}\dot{\varphi}_{0}^{0}} + \dot{\varphi}_{0} \left[T_{\text{damping}} - \frac{2\xi_{\text{integrator}}T_{1} - T_{2}}{T_{1}T_{2}(\dot{\varphi}_{0}^{0})^{2}}\right] + \frac{C_{1} - A_{1} - B_{1}}{K_{\text{moment}}K_{\text{amplify}}K_{\text{measure}}K_{\text{electric current}} + nT_{\text{amplify}}\dot{\varphi}_{0}^{2}(C_{1} - A_{1} - B_{1})}\right]$$
(2.81)

The conclusion can be drawn from Eqs. (2.80) and (2.81) that the differential loop with the time constant T_{damping} is used in the integrator, which can be a part of the compensation for the instability of the self-rotating angular velocity of the aircraft.

For χ_1 :

$$T_{\text{damping}} = \frac{1}{T_{\text{integrator}} (\dot{\varphi}_0^0)^2} - \frac{C_1 - A_1 - B_1}{K_{\text{moment}} K_{\text{amplify}} K_{\text{measure}} K_{\text{electric current}} + n T_{\text{amplify}} \dot{\varphi}_0^2 (C_1 - A_1 - B_1)}$$

$$(2.82)$$

For χ_2 :

$$T_{\text{damping}} = \frac{2\xi_{\text{integrator}}T_1 - T_2}{T_1T_2(\dot{\varphi}_0^0)^2} - \frac{C_1 - A_1 - B_1}{K_{\text{moment}}K_{\text{amplify}}K_{\text{measure}}K_{\text{electric current}} + nT_{\text{amplify}}\dot{\varphi}_0^2(C_1 - A_1 - B_1)}$$

$$(2.83)$$

Obviously, because of the relationship between Eqs. (2.82) and (2.83) and the rotating angular velocity around the longitudinal axis of the rotating flight carrier, it is not possible to achieve full compensation. However, the instrument approaches the working state of the resonance point, and the size of $T_{\rm damping}$ can be determined as follows:

For χ_1 :

$$T_{\text{damping}} = \frac{1}{T_{\text{integrator}} (\dot{\varphi}_0^0)^2}$$
 (2.84)

For χ_2 :

$$T_{\text{damping}} = \frac{2\xi_{\text{integrator}}T_1 - T_2}{T_1T_2(\dot{\varphi}_0^0)^2}$$
 (2.85)

Equations (2.84) and (2.85) point out that a larger integral time constant is required for a better quality of integral. And as has been discussed previously, for a small value of $T_{\rm damping}$, it is also required that the inconformity of the amplitude frequency characteristic does not produce a negative effect. For example, when $T_{\rm integrator} = 0.1$, the effect of the differential loop of the integrator on the amplitude of the output signal reaches $\pm 4\%$. However, if a larger $T_{\rm integrator}$ is selected, it should be kept in mind that the increase of $T_{\rm integrator}$ will lead to a decrease in the amplitude of the output signal and an increase in the phase lag of the output signal.

According to Eqs. (2.82) and (2.83), the effect evaluations of $\Delta \dot{\phi}_0$ on χ_1 and χ_2 can be obtained. For χ_1 , there holds

$$T_{\text{damping}} = \frac{1}{T_{\text{integrator}} (\dot{\varphi}_0^0)^2} - \frac{C_1 - A_1 - B_1}{D_{\text{feedback}} + nT_{\text{amplify}} (\dot{\varphi}_0^0)^2 (C_1 - A_1 - B_1)}$$
(2.86)

However for χ_2 , there holds

$$T_{\text{damping}} = \frac{2\xi_{\text{integrator}}T_1 - T_2}{T_1T_2(\dot{\varphi}_0^0)^2} - \frac{C_1 - A_1 - B_1}{D_{\text{feedback}} + nT_{\text{amplify}}(\dot{\varphi}_0^0)^2(C_1 - A_1 - B_1)} \quad (2.87)$$

Substituting Eqs. (2.86) and (2.87) into Eqs. (2.80) and (2.81) obtains

$$\begin{split} \chi_{1} &= -\frac{\pi}{2} + \frac{2}{T_{\text{integrator}} \dot{\phi}_{0}^{0}} + \left(\dot{\phi}_{0}^{0} \pm \Delta \dot{\phi}_{0}\right) \\ &\times \left[\frac{C_{1} - A_{1} - B_{1}}{D_{\text{feedback}} + nT_{\text{amplify}} \left(\dot{\phi}_{0}^{0} \pm \Delta \dot{\phi}_{0}\right)^{2} (C_{1} - A_{1} - B_{1})} - \frac{C_{1} - A_{1} - B_{1}}{D_{\text{feedback}} + nT_{\text{amplify}} \left(\dot{\phi}_{0}^{0}\right)^{2} (C_{1} - A_{1} - B_{1})} \right] \end{split}$$

$$(2.88)$$

$$\begin{split} \chi_{2} &= -\frac{\pi}{2} + \frac{2 \left(2 \xi_{\text{integrator}} T_{1} - T_{2} \right)}{T_{1} T_{2} \dot{\varphi}_{0}^{0}} + \left(\dot{\varphi}_{0}^{0} \pm \Delta \dot{\varphi}_{0} \right) \\ &\times \left[\frac{C_{1} - A_{1} - B_{1}}{D_{\text{feedback}} + n T_{\text{amplify}} \left(\dot{\varphi}_{0}^{0} \pm \Delta \dot{\varphi}_{0} \right)^{2} (C_{1} - A_{1} - B_{1})} - \frac{C_{1} - A_{1} - B_{1}}{D_{\text{feedback}} + n T_{\text{amplify}} \left(\dot{\varphi}_{0}^{0} \right)^{2} (C_{1} - A_{1} - B_{1})} \right] \end{split}$$

$$(2.89)$$

Select $\xi_{\text{integrator}} = 1$ and $T_1 = T_2 = T_{\text{integrator}}$, χ_2 can be obtained as

$$\chi_{2} = -\frac{\pi}{2} + \frac{2(2\xi_{\text{integrator}}T_{1} - T_{2})}{T_{1}T_{2}\dot{\phi}_{0}^{0}} + \frac{(\dot{\phi}_{0}^{0} \pm \Delta\dot{\phi}_{0})(C_{1} - A_{1} - B_{1})^{2}nT_{\text{amplify}}\left[\left(\dot{\phi}_{0}^{0}\right)^{2} - \left(\dot{\phi}_{0}^{0} \pm \Delta\dot{\phi}_{0}\right)^{2}\right]}{D_{\text{feedback}}^{2} + D_{\text{feedback}}^{2}nT_{\text{amplify}}(C_{1} - A_{1} - B_{1})\left[\left(\dot{\phi}_{0}^{0}\right)^{2} + \left(\dot{\phi}_{0}^{0} \pm \Delta\dot{\phi}_{0}\right)^{2}\right] + \left[nT_{\text{amplify}}(C_{1} - A_{1} - B_{1})\left(\dot{\phi}_{0}^{0} \pm \Delta\dot{\phi}_{0}\right)\dot{\phi}_{0}^{0}\right]^{2}}$$

$$(2.90)$$

Because all the augments in the denominator are compared with $D_{\rm feedback}^2$, they are very small and can be ignored. Then

$$\begin{split} \chi_{2} &= -\frac{\pi}{2} + \frac{2(2\xi_{\text{integrator}}T_{1} - T_{2})}{T_{1}T_{2}\dot{\varphi}_{0}^{0}} \\ &+ \frac{(C_{1} - A_{1} - B_{1})^{2}nT_{\text{amplify}}}{D_{\text{feedback}}^{2}} \left(\dot{\varphi}_{0}^{0} \pm \Delta\dot{\varphi}_{0}\right) \left(\mp 2\dot{\varphi}_{0}^{0}\Delta\dot{\varphi}_{0} - \Delta\dot{\varphi}_{0}^{2}\right) \\ &= -\frac{\pi}{2} + \frac{2(2\xi_{\text{integrator}}T_{1} - T_{2})}{T_{1}T_{2}\dot{\varphi}_{0}^{0}} \\ &- \frac{[B_{1} - (C_{1} - A_{1})]^{2}nT_{\text{amplify}}}{D_{\text{feedback}}^{2}} \left(\dot{\varphi}_{0}^{0} \pm \Delta\dot{\varphi}_{0}\right) \left(\Delta\dot{\varphi}_{0} + 2\dot{\varphi}_{0}^{0}\right)\Delta\dot{\varphi}_{0} \\ &= -\frac{\pi}{2} + \frac{2(2\xi_{\text{integrator}}T_{1} - T_{2})}{T_{1}T_{2}\dot{\varphi}_{0}^{0}} \\ &- \frac{[B_{1} - (C_{1} - A_{1})]^{2}nT_{\text{amplify}}}{D_{\text{feedback}}^{2}} \left(3\dot{\varphi}_{0}^{0}\Delta\dot{\varphi}_{0} \pm 2(\dot{\varphi}_{0}^{0})^{2} \pm \Delta\dot{\varphi}_{0}^{2}\right)\Delta\dot{\varphi}_{0} \end{split}$$

From Eq. (2.91), it can be clearly seen that the sign of the unstable value of the angular velocity around the longitudinal axis of the rotating flight carrier is changed and the sign of the second augment in the final parentheses is also changed. But even so, the output signal has higher phase stability due to the small coefficient of

the final bracket. When the coefficient is very small, the last term of Eq. (2.91) is comparable to the others and can be ignored.

When the working state of the instrument approaches the state of the resonant point, the integrity and accuracy influence of the compensation effect of $\Delta \dot{\varphi}_0$ increases. In the resonant state, the instability influence of the angular velocity rotating around the longitudinal axis of the aircraft does not exist.

But as has been mentioned earlier, in the state of the near-resonant point (when the detuning coefficient $\mu = 0.9$), the last term of Eq. (2.91) is negligible. At this time, Eq. (2.91) can be simplified and its expression without $\Delta \dot{\varphi}_0$ is obtained as

$$\chi_2 = -\frac{\pi}{2} + \frac{2(2\xi_{\text{integrator}}T_1 - T_2)}{T_1 T_2 \dot{\varphi}_0^0}$$
 (2.92)

And so on

$$\chi_1 = -\frac{\pi}{2} + \frac{2}{T_{\text{integrator}} \dot{\varphi}_0^0} \tag{2.93}$$

Equation (2.91) also shows that when the differential loop is introduced into the integrator, the influence of the angular velocity rotating around the longitudinal axis of the aircraft on the phase of the output signal decreases, and the damping effect guaranteed by the feedback increases and the compensation coefficient of the mutual inductance influence n decreases. Even when the resonant state is missed, but under the influence of a complete compensation of the mutual inductance winding (n = 0), and in the condition of using a non-periodic loop as the integrator, when Eq. (2.86) is implemented, or in the condition that the integrator with a transfer function (1–130) is used, when Eq. (2.87) is implemented, the phase has nothing to do with $\Delta \dot{\varphi}_0$.

At the output end of the instrument without an integrator, the output without an integrator, the impact of introducing the differentiator on the phase of the output signal would be determined.

$$\chi_{0} = \frac{\pi}{2} + \arctan(T_{\text{damping}}\dot{\varphi}_{0})
- \arctan\left(\frac{\left[nT_{\text{amplify}} + 2T_{0}(\xi_{0} + \xi)\right]\dot{\varphi}_{0} - T_{0}^{2}nT_{\text{amplify}}\dot{\varphi}_{0}^{3}}{1 - \left(T_{0}^{2} + 2\xi_{0}T_{0}nT_{\text{amplify}}\right)\dot{\varphi}_{0}^{2}}\right)$$
(2.94)

According to Eq. (2.69) the phase of the output signal of the instrument without an integrator can be written by the following expression:

$$\chi_0 = T_{\text{damping}} \dot{\varphi}_0 + \frac{1 - T_0^2 \dot{\varphi}_0^2}{\dot{\varphi}_0 \left[2\xi T_0 + n T_{\text{amplify}} \left(1 - T_0^2 \dot{\varphi}_0^2 \right) \right]}$$
(2.95)

Combining Eqs. (1.124), (1.125) and (1.134) obtains

$$\chi_0 = \dot{\varphi}_0 \left[T_{\text{damping}} + \frac{C_1 - A_1 - B_1}{K_{\text{moment}} K_{\text{amplify}} K_{\text{measure}} K_{\text{electric current}} + n T_{\text{amplify}} \dot{\varphi}_0^2 (C_1 - A_1 - B_1)} \right]$$

$$(2.96)$$

In this case, the time constant of the differential equation can be obtained by several other expressions. Unlike Eqs. (2.82) and (2.83), there is no added entry that determines the parameters of the integrator. The compensation accuracy is the same as that of the circuit with an integrator.

In order to ensure that the measurement accuracy of the angular velocity around the longitudinal axis of the aircraft is higher, two additional loops must be added to the velocity feedback loop to reduce the instability and mutual effect of the angular velocity around the longitudinal axis of the aircraft.

The basic formula for the amplitude of a rotor vibration gyroscope with negative feedback is as follows

$$\begin{split} \Phi(s) &= \frac{KK_{\text{integrator2}}}{K_{\text{moment}}K_{\text{electric current}}} \frac{(1+T_1s)(1+T_Ds)}{T_2^2s^2 + 2\xi_{\text{integrator}}T_2s + 1} \\ &\times \frac{s}{T_0^2nT_{\text{amplify}}s^3 + \left(T_0^2 + 2\xi_0T_0nT_{\text{amplify}}\right)s^2 + \left(nT_{\text{amplify}} + 2\xi_0T_0 + K\right)s + 1} \\ U_{\text{amplitude}} &= \frac{(C_1 - A_1 + B_1)\dot{\varphi}_0^2\Omega KK_{\text{integrator2}}\sqrt{\left(1 + T_1^2\dot{\varphi}_0^2\right)\left(1 + T_D^2\dot{\varphi}_0^2\right)}}{K_{\text{moment}}K_{\text{electric current}}\sqrt{\left(1 - T_2^2\dot{\varphi}_0^2\right)^2 + \left(2\xi_{\text{integrator}}T_2\dot{\varphi}_0\right)^2}} \times \\ &\times \frac{1}{\sqrt{\left\{\left[nT_{\text{amplify}} + 2T_0(\xi_0 + \xi)\right]\dot{\varphi}_0 - T_0^2nT_{\text{amplify}}\dot{\varphi}_0^3\right\}^2 + \left[1 - \left(T_0^2 + 2\xi_0T_0nT_{\text{amplify}}\right)\dot{\varphi}_0^2\right]^2}}} \\ \chi &= \frac{\pi}{2} + \arctan(T_D\dot{\varphi}_0) + \arctan(T_1\dot{\varphi}_0) - \arctan\left(\frac{2\xi_{\text{integrator}}T_2\dot{\varphi}_0}{1 - T_2^2\dot{\varphi}_0^2}\right) \\ &- \arctan\left(\frac{\left[nT_{\text{amplify}} + 2T_0(\xi_0 + \xi)\right]\dot{\varphi}_0 - T_0^2nT_{\text{amplify}}\dot{\varphi}_0^3}{1 - \left(T_0^2 + 2\xi_0T_0nT_{\text{amplify}}\right)\dot{\varphi}_0^2}\right) \end{split}$$

When nT_{amplify} , $T_{\text{integrator}}$ and ζ_o are small, and T_1 and T_2 are large, the measured amplitude of the constant angular velocity is

$$\begin{split} U_{\text{amplitude}} = & \frac{(C_1 - A_1 + B_1)T_1\Omega K_{\text{amplify}} K_{\text{integrator3}} K_{\text{integrator2}}}{T_2^2 \sqrt{\left(K_{\text{integrator3}} K_{\text{electric current}} K_{\text{moment}} K_{\text{amplify}}\right)^2 + \left(C_1 - A_1 - B_1\right)^2 \dot{\varphi}_0^2}} \\ \chi = & -\arctan\bigg(\frac{2\xi T_0 \dot{\varphi}_0}{1 - T_0^2 \dot{\varphi}_0^2}\bigg) \end{split}$$

In the case of precise tuning, there holds

$$U_{
m amplitude} = rac{2B_1K_{
m integrator2}T_1}{K_{
m moment}K_{
m electric \, current}T_2^2} \Omega$$
 $\chi = -rac{\pi}{2}$

2.2 Regulation of a Non-driven Mechanical Gyroscope

Compare the regulation quality of three instrument loops with a velocity feedback, which include the no integrator type, the integrator type with transfer function (1.129), and the integrator type with transfer function (1.130) at the output end of the instrument.

Comparing Sect. 1.4, the analogy method can be used to determine the response of the instrument to the constant input force in the implicated coordinate system. Therefore, according to Eqs. (2.1), (2.2) and (2.3), the differential loop in the integrator is designated as

$$\Phi_{0}(s) = \frac{K}{K_{\text{moment}}K_{\text{electric current}}} \times \frac{s\left(T_{\text{damping}}s+1\right)}{T_{0}^{2}nT_{\text{amplify}}s^{3} + \left(T_{0}^{2} + 2\xi_{0}T_{0}nT_{\text{amplify}}\right)s^{2} + \left(nT_{\text{amplify}} + 2\xi_{0}T_{0} + K\right)s + 1}$$

$$(2.97)$$

$$\begin{split} \Phi_{1}(s) &= \frac{KK_{\text{integrator1}}}{K_{\text{moment}}K_{\text{electric current}}} \times \frac{1}{1 + T_{\text{integrator}}s} \\ &\times \frac{s\left(T_{\text{damping}}s + 1\right)}{T_{0}^{2}nT_{\text{amplify}}s^{3} + \left(T_{0}^{2} + 2\xi_{0}T_{0}nT_{\text{amplify}}\right)s^{2} + \left(nT_{\text{amplify}} + 2\xi_{0}T_{0} + K\right)s + 1} \end{split}$$

$$\begin{split} \Phi_{2}(s) &= \frac{KK_{\text{integrator2}}}{K_{\text{moment}}K_{\text{electric current}}} \times \frac{T_{1}s + 1}{T_{2}^{2}s^{2} + 2\xi_{\text{integrator}}T_{2}s + 1} \\ &\times \frac{s\left(T_{\text{damping}}s + 1\right)}{T_{0}^{2}nT_{\text{amplify}}s^{3} + \left(T_{0}^{2} + 2\xi_{0}T_{0}nT_{\text{amplify}}\right)s^{2} + \left(nT_{\text{amplify}} + 2\xi_{0}T_{0} + K\right)s + 1} \end{aligned} \tag{2.99}$$

Because nT_{amplify} , ξ_0 and T_{damping} are very small, Eqs. (2.97), (2.98) and (2.99) are rewritten as

$$\Phi_0(s) = \frac{K}{K_{\text{moment}} K_{\text{electric current}}} \times \frac{s}{T_0^2 s^2 + K s + 1}$$
 (2.100)

$$\begin{split} \Phi_{1}(s) &= \frac{KK_{\text{integrator1}}}{K_{\text{moment}}K_{\text{electric current}}} \times \frac{1}{1 + T_{\text{integrator}}s} \\ &\times \frac{s}{T_{0}^{2}s^{2} + Ks + 1} = \frac{KK_{\text{integrator1}}}{K_{\text{moment}}K_{\text{electric current}}} \times \frac{\Phi_{0}(s)}{1 + T_{\text{integrator}}s} \end{split} \tag{2.101}$$

$$\begin{split} \Phi_{2}(s) &= \frac{KK_{\text{integrator2}}}{K_{\text{moment}}K_{\text{electric current}}} \times \frac{T_{1}s+1}{T_{2}^{2}s^{2}+2\xi_{\text{integrator}}T_{2}s+1} \times \frac{s}{T_{0}^{2}s^{2}+Ks+1} \\ &= \frac{KK_{\text{integrator2}}}{K_{\text{moment}}K_{\text{electric current}}} \times \frac{(T_{1}s+1)\Phi_{0}(s)}{T_{2}^{2}s^{2}+2\xi_{\text{integrator}}T_{2}s+1} \end{split}$$

$$(2.102)$$

Consider the expression (2.100) in Eq. (1.134), which is equivalent to the transfer function of the oscillation loop and is expressed by the angular velocity at the output end:

$$\Phi_0(s) = \frac{\alpha_0(s)}{M(s)}$$

where

$$\frac{\alpha_0(s)}{M(s)} = \frac{KK_{\rm integrator1}}{K_{\rm moment}K_{\rm electric \, current}} \times \frac{1}{T_0^2 s^2 + K s + 1}.$$

According to Eq. (1.91) and so on, when a constant force is acting on the instrument in the coordinate system which is connected to the aircraft, the transition process is expressed by the deflection angle of the sensitive element:

$$\alpha_0 = C_0 e^{-\xi \omega_0 t} \sin \left[\left(\omega_0 \sqrt{1 - \xi^2} \right) t + \beta_0 \right] + \frac{K K_{\text{integrator 1}}}{K_{\text{moment}} K_{\text{electric current}}} \times \frac{H_0}{B_0} \Omega \sin \gamma_1$$
(2.103)

According to Eqs. (1.93) and (1.94), the integral constant has the form of

$$\beta_0 = \arctan\left(\frac{\sqrt{1-\xi^2}}{\xi}\right) \tag{2.104}$$

$$C_0 = -\frac{KK_{\rm integrator1}}{K_{\rm moment}K_{\rm electric \, current}} \times \frac{H_0\Omega \, \sin\gamma_1}{B_0\sqrt{1-\xi^2}} = -\frac{K_{\rm integrator1}D_\alpha}{K_{\rm moment}K_{\rm electric \, current}} \times \frac{H_0\Omega \, \sin\gamma_1}{B_0^2\sqrt{1-\xi^2}}$$

$$(2.105)$$

It is obvious that there is no difference between the characteristics of the transition process of the gyroscope with a negative velocity feedback and the characteristics of the transition process of the gyroscope described in Eq. (1.95).

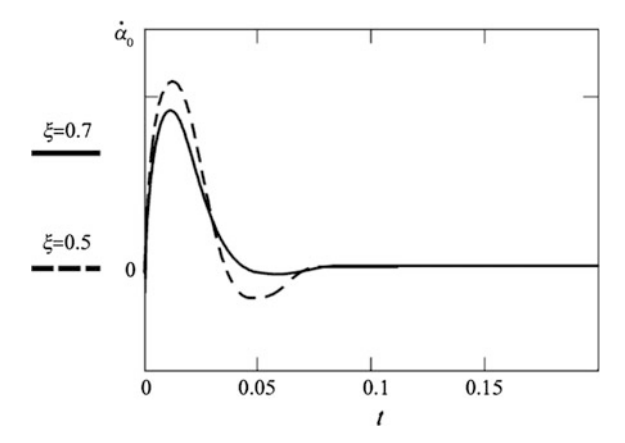
In order to obtain the impact of the different integrators on the transition process of the gyroscope, according to the oscillating angular velocity of the sensitive element, the transition process of the gyroscope without an integrator at the output end. When considering the complete expression of the integral constant, the transition process of the oscillating angular velocity of the sensitive element at the output of the preamplifier has the following form:

$$\begin{split} \dot{\alpha}_{0} &= \frac{H_{0}D_{\alpha}\sin\gamma_{1}\omega_{0}\mathrm{e}^{-\xi\omega_{0}t}}{K_{\mathrm{moment}}K_{\mathrm{electric\;current}}B_{0}^{2}\sqrt{1-\xi^{2}}}\Omega\,\sin\!\left[\left(\omega_{0}\sqrt{1-\xi^{2}}\right)t\right] \\ &= \dot{\alpha}_{0}\mathrm{e}^{-\xi\omega_{0}t}\sin\!\left[\left(\omega_{0}\sqrt{1-\xi^{2}}\right)t\right] \end{split} \tag{2.106}$$

The value of Eq. (2.106) is equal to zero, which is consistent with the value of the constant deviation angle of the sensitive element of the instrument determined by Eq. (1.106) in Sect. 1.4. Figure 2.3 shows the transition process of Eq. (2.106).

The effect of the integrator on the transition process is measured and the transition process of each integrator is added to the transient process of the sensitive element of a non-driven mechanical gyroscope used in a rotating state aircraft with negative velocity feedback. It can be seen that the transition process of each loop is the sum of the transient process of the sensitive element of a non-driven mechanical gyroscope used in a rotating state aircraft with a negative velocity feedback and the transient process of the integrator.

Fig. 2.3 Transition process of the sensitive element of a non-driven mechanical gyroscope used in a rotating state aircraft with velocity feedback (represented by the angular velocity)



$$\begin{split} &\alpha_1 = C' \mathrm{e}^{-\frac{1}{T_{\mathrm{integrator}}}} + \frac{D_{\alpha} K_{\mathrm{integrator}1} H \, \sin \gamma_1 \omega_0 \mathrm{e}^{-\xi \omega_0 t} \Omega \, \sin \left[\left(\omega_0 \sqrt{1 - \xi^2} \right) t - \arctan \left(T_{\mathrm{integrator}} \omega_0 \sqrt{1 - \xi^2} \right) \right] }{B_0^2 \sqrt{1 - \xi^2} K_{\mathrm{moment}} K_{\mathrm{electric \, current}} \sqrt{1 + T_{\mathrm{integrator}}^2 \omega_0^2 \left(1 - \xi^2 \right)} \\ = & C' \mathrm{e}^{-\frac{1}{T_{\mathrm{integrator}}}} + \frac{\dot{\alpha}_{0, \mathrm{amplitude}}}{\sqrt{1 + T_{\mathrm{integrator}}^2 \omega_0^2 \left(1 - \xi^2 \right)}} \mathrm{e}^{-\xi \omega_0 t} \sin \left[\left(\omega_0 \sqrt{1 - \xi^2} \right) t + \chi_{\mathrm{integrator}} \right] \end{aligned} \tag{2.107}$$

Under the initial condition of the zero position, the integral constant is equal to

$$C' = -\frac{\dot{\alpha}_{0,\text{amplitude}}}{\sqrt{1 + T_{\text{integrator}}^2 \omega_0^2 (1 - \xi^2)}} \sin(\chi_{\text{integrator}})$$
 (2.108)

The transient process of the integrator has the following form:

$$\alpha_{\text{integrator}} = -\frac{\dot{\alpha}_{0,\text{amplitude}} e^{-\frac{t}{T_b}}}{\sqrt{1 + T_{\text{integrator}}^2 \omega_0^2 (1 - \xi^2)}} \sin(\chi_{\text{integrator}})$$
 (2.109)

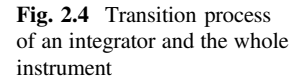
And the transition process of the whole gyroscope is

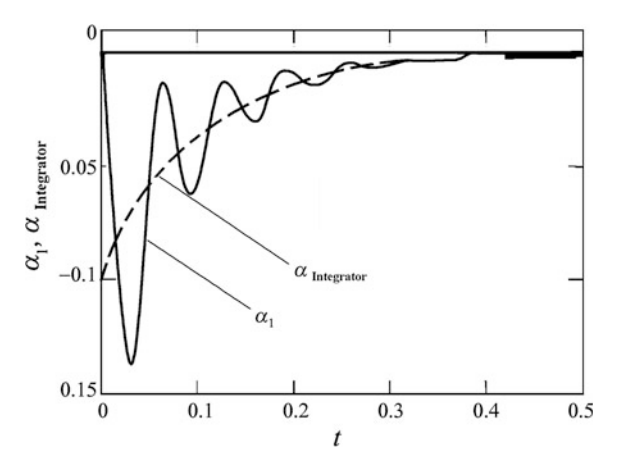
$$\begin{split} \alpha_1 = & \frac{\dot{\alpha}_{0,\text{amplitude}}}{\sqrt{1 + T_{\text{integrator}}^2 \omega_0^2 (1 - \xi^2)}} \left\{ e^{-\xi \omega_0 t} \sin \left[\left(\omega_0 \sqrt{1 - \xi^2} \right) t + \chi_{\text{integrator}} \right] \right. \\ & \left. - e^{-\frac{1}{T_{\text{integrator}}}} \sin \left(\chi_{\text{integrator}} \right) \right\} \end{split}$$

$$(2.110)$$

Thus, the existence of the integrator changes the transition process of the instrument. Unlike the transition process studied in Sect. 1.4, in the implicated coordinate system of the aircraft the transition process of the sensitive element of the instrument is equal to zero under the action of a constant force. That is to say, the friction moment, the dynamic unbalanced moment of the sensitive element of the instrument and the moment produced by the centrifugal acceleration of the aircraft due to the constant angular deviation of the sensitive element would not cause the change of the output signal of the instrument.

As described by Eq. (2.106), and unlike the transition process expressed by the angular velocity of the oscillation framework, the time of the transition process expressed by the deviation angle of the instrument with the integrator that satisfies Eq. (2.110) and has the integrator with the transfer function (1.129), is mainly determined by the settling time of the integrator and $T_{\text{integrator}}$ can be seen in Fig. 2.4.





Because the time constant of an integrator increases, the settling time of the instrument also increases, and every input force instantly changes with a frequency greater than $1/(3 \sim 4)$ $T_{\rm integrator}$, the instrument cannot react.

Because every force acting on the instrument in flight has different characteristics, the integrator at the output end of the instrument is not a major detriment to the work of the instrument.

Chapter 3 Performances of Non-driven Mechanical Gyroscope in the Condition of an Alternating Angular Velocity

In the condition of the following assumptions, the solution of Eq. (1.46) (the motion equation of the sensitive element of the instrument) is studied. The first assumption is that according to the accurate calculation results in Chap. 1, there are some harmonic components in the velocities Ω_{ξ} and Ω_{η} , and Ω_{ξ} that will not be considered in the calculation. The reason being that the projection of the sensitive plane is equal to zero. Then, in the first two equations of Eq. (1.29), the first added entry is zero. Thus there holds

$$\begin{cases}
\Omega_{\xi} = \Omega^{\psi} \sin \delta_{\psi} \cos(\psi t + \gamma_{\psi}) + \Omega^{v} \sin \delta_{v} \cos \gamma_{v} \cos vt \\
\Omega_{\eta} = \Omega^{\psi} \sin \delta_{\psi} \sin(\psi t + \gamma_{\psi}) + \Omega^{v} \sin \delta_{v} \sin \gamma_{v} \cos vt
\end{cases}$$
(3.1)

Items in Eq. (1.3) are analyzed one by one:

(1) The angular oscillation:

$$\begin{cases} \Omega_{\xi} = \Omega^{\nu} \sin \delta_{\nu} \cos \gamma_{\nu} \cos \nu t \\ \Omega_{\eta} = \Omega^{\nu} \sin \delta_{\nu} \sin \gamma_{\nu} \cos \nu t \end{cases}$$
(3.2)

(2) The circular oscillation:

$$\begin{cases}
\Omega_{\xi} = \Omega^{\psi} \sin \delta_{\psi} \cos(\psi t + \gamma_{\psi}) \\
\Omega_{\eta} = \Omega^{\psi} \sin \delta_{\psi} \sin(\psi t + \gamma_{\psi})
\end{cases}$$
(3.3)

3.1 Performance of Non-driven Mechanical Gyroscope in the Condition of an Angular Vibration

The case of an angular vibration of the aircraft is studied. In this case, the characteristic of the aircraft is that the angles σ and ρ are very small. Compared with its rotational velocity around the longitudinal axis of the aircraft, the angular velocity of the aircraft is also very small. Therefore, there is not only the projection of the angular velocity of the rotating flight carrier on the sensitive plane, but also the projection of the angular acceleration in the motion equation of the sensitive element of the instrument:

$$\begin{cases} \dot{\Omega}_{\xi} = -\Omega^{\nu} v \sin \delta_{\nu} \cos \gamma_{\nu} \sin \nu t \\ \dot{\Omega}_{\eta} = -\Omega^{\nu} v \sin \delta_{\nu} \sin \gamma_{\nu} \sin \nu t \end{cases}$$
(3.4)

In order to simplify the calculation, select $\delta_v = \frac{\pi}{2}$, and rewrite Eqs. (3.2) and (3.4) as:

$$\begin{cases}
\Omega_{\xi} = \Omega^{\nu} \cos \gamma_{\nu} \cos \nu t \\
\Omega_{\eta} = \Omega^{\nu} \sin \gamma_{\nu} \cos \nu t
\end{cases}$$
(3.5)

$$\begin{cases} \dot{\Omega}_{\xi} = -\Omega^{\nu} v \cos \gamma_{\nu} \sin \nu t \\ \dot{\Omega}_{\eta} = -\Omega^{\nu} v \sin \gamma_{\nu} \sin \nu t \end{cases}$$
(3.6)

Because the angular acceleration is negative, Eq. (1.46) takes the following form:

$$\ddot{\alpha} + 2\xi\omega_0\dot{\alpha} + \omega_0^2\alpha = \frac{H_0}{B_1}\Omega\sin(\dot{\varphi}_0t - \delta_1) + \dot{\Omega}\sin(\dot{\varphi}_0t + \delta_2)$$
(3.7)

where

$$\Omega = \sqrt{\Omega_{\xi}^2 + \Omega_{\eta}^2} = \Omega^{\nu} \cos \nu t \tag{3.8}$$

$$\dot{\Omega} = \sqrt{\dot{\Omega}_{\xi}^2 + \dot{\Omega}_{\eta}^2} = \Omega^{\nu} v \sin \nu t \tag{3.9}$$

$$\delta_1 = \arctan\left(\frac{\Omega_\eta}{\Omega_z}\right) = \gamma_v \tag{3.10}$$

$$\delta_2 = \arctan\left(\frac{\dot{\Omega}_{\xi}}{\dot{\Omega}_{\eta}}\right) = \frac{\pi}{2} - \gamma_{\nu} \tag{3.11}$$

$$\omega_0 = \sqrt{\frac{C_1 - A_1}{B_1}} \dot{\varphi}_0$$

In the case that $v \le \dot{\varphi}_0$, in order to determine the impact of the angular vibration frequency on the output signal of the instrument, the transfer characteristic of the complex amplitude can be determined by using second order system dynamic analysis (the envelope of the carrier frequency $\dot{\varphi}_0$). Note from Fig. 1.12 and Eq. (1.120), the right side of the expression (1.120) provides the external torque acting on the sensitive element of the instrument. The expression of the external torque is changed and the initial phase of the input angular velocity in this equation is selected as 90° to simplify the calculation. Then

$$M = (H_0 \Omega_{\xi} - B_1 \dot{\Omega}_{\eta}) \cos \varphi + (H_0 \Omega_{\eta} + B_1 \dot{\Omega}_{\xi}) \sin \varphi$$
 (3.12)

The complex amplitude of the external moment has the form:

$$M = M_{\text{damping}} + jM_M = \left(H_0\Omega_{\eta} + B_1\dot{\Omega}_{\xi}\right) + j\left(H_0\Omega_{\xi} - B_1\dot{\Omega}_{\eta}\right)$$
(3.13)

or

$$M = B_1(\dot{\Omega}_{\xi} - j\dot{\Omega}_{\eta}) + jH_0(\Omega_{\xi} - j\Omega_{\eta}) = (B_1s + jH_0)\Omega^*$$
(3.14)

where $\Omega^* = \Omega_{\xi} - j\Omega_{\eta}$.

It is well known that when the operator s is replaced by $s+\mathrm{j}\dot{\varphi}_0$, the complex amplitude (the envelope of the carrier frequency) can be obtained by the transfer function of the instantaneous value, which is expressed by the transfer function of a single-channel loop. In this case, only under the condition of $v\leq\dot{\varphi}_0$ proposed before is a similar replacement possible. In addition, under the condition of this replacement the transfer function for the complex amplitude is obtained and only shows the envelope amplitude of the output signal and the phase change characteristics.

After a similar replacement, the following equation can be obtained:

$$\frac{U}{M} = \Phi(s + j\dot{\varphi}_0). \tag{3.15}$$

Substituting (1.141), there holds

$$\frac{U}{\Omega^*} = (\mathbf{B}_1 s + \mathbf{j} H_0) \Phi(s + \mathbf{j} \dot{\varphi}_0) = (\mathbf{B}_1 s + \mathbf{j} H_0) \frac{W(s + \mathbf{j} \dot{\varphi}_0)}{1 + W(s + \mathbf{j} \dot{\varphi}_0)} \frac{W_{\text{integrator}}(s + \mathbf{j} \dot{\varphi}_0)}{K_{\text{moment}} K_{\text{electric current}}}$$
(3.16)

If the coefficient ξ_0 and the time constant nT_{amplify} are very small, there are

$$\frac{U}{\Omega^*} = \frac{\frac{K}{K_{\text{moment}} K_{\text{electric current}}} (\mathbf{B}_1 s + \mathbf{j} H_0)(s + \mathbf{j} \dot{\varphi}_0)}{T_0^2 (s + \mathbf{j} \dot{\varphi}_0)^2 + K(s + \mathbf{j} \dot{\varphi}_0) + 1} \frac{K_{\text{integrator}} [T_1 (s + \mathbf{j} \dot{\varphi}_0) + 1]}{T_2^2 (s + \mathbf{j} \dot{\varphi}_0)^2 + 2\xi_{\text{integrator}} T_2 (s + \mathbf{j} \dot{\varphi}_0) + 1}$$
(3.17)

The time constant of the integrator can be obtained equally, and the coefficient ξ_{η} can be selected approximately to be 1, then Eq. (3.17) can be rewritten as

$$\frac{U}{\Omega^*} = \frac{\frac{K}{K_{\text{moment}}K_{\text{electric current}}} \left(\mathbf{B}_1 s + \mathbf{j} H_0 \right) (s + \mathbf{j} \dot{\varphi}_0)}{T_0^2 (s + \mathbf{j} \dot{\varphi}_0)^2 + K(s + \mathbf{j} \dot{\varphi}_0) + 1} \frac{K_{\text{integrator}}}{T_2 (s + \mathbf{j} \dot{\varphi}_0) + 1}$$
(3.18)

The denominator and the numerator of Eq. (3.18) are changed into a single factor product, which is equivalent to the typical circuit of the second-order system. Then Eq. (3.18) can be changed as follows:

$$\frac{U}{\Omega^*} = \frac{\frac{KH_0\dot{\varphi}_0}{K_{\text{moment}}K_{\text{electric current}}} \left(\frac{B_1}{H_0}s + j\right) \left(\frac{1}{\dot{\varphi}_0}s + j\right)}{(\tau_1 s + j + \beta_1)(\tau_2 s + j + \beta_2)} \frac{\frac{K_{\text{integrator}}\tau_1\tau_2}{T_2\dot{\varphi}_0T_0^2}}{\left(\frac{1}{\dot{\varphi}_0}s + j + \frac{1}{T_2\dot{\varphi}_0}\right)}$$
(3.19)

where

$$\tau_{1} = \frac{T_{0}}{T_{0}\dot{\varphi}_{0} + \sqrt{1 - \xi^{2}}}; \quad \tau_{2} = \frac{T_{0}}{T_{0}\dot{\varphi}_{0} - \sqrt{1 - \xi^{2}}};
\beta_{1} = \frac{\xi}{T_{0}\dot{\varphi}_{0} + \sqrt{1 - \xi^{2}}}; \quad \beta_{2} = \frac{\xi}{T_{0}\dot{\varphi}_{0} - \sqrt{1 - \xi^{2}}}$$
(3.20)

Introduce the following symbol:

$$\tau_3 = \frac{B_1}{H} = \frac{1}{(1+\mu^2)\dot{\varphi}_0} \tag{3.21}$$

Take into account that T_2 is very large, and Eq. (3.19) takes the following form:

$$\begin{split} \frac{U}{\Omega^*} &= \frac{\frac{KH_0 \dot{\phi}_0}{K_{\text{moment}} K_{\text{electric current}}} (\tau_3 s + \mathbf{j}) \frac{K_{\text{integrator}}}{T_2 \dot{\phi}_0} \frac{\tau_1 \tau_2}{T_0^2}}{(\tau_1 s + \mathbf{j} + \beta_1) (\tau_2 s + \mathbf{j} + \beta_2)} \\ &= K_{\tau} \frac{\mu \xi (\mu^2 + 1)}{1 - \mu^2 (1 - \xi^2)} \frac{(\tau_3 s + \mathbf{j})}{(\tau_1 s + \mathbf{j} + \beta_1) (\tau_2 s + \mathbf{j} + \beta_2)} \end{split} \tag{3.22}$$

where

$$K_{\tau} = \frac{KH_0\dot{\varphi}_0}{K_{\text{moment}}K_{\text{electric current}}} \frac{K_{\text{integrator}}}{T_2\dot{\varphi}_0} \frac{\tau_1\tau_2}{T_0^2} = \frac{2B_1K_{\text{integrator}}}{K_{\text{moment}}K_{\text{electric current}}T_2}$$
(3.23)

It is obvious that the complex transfer function of a single-channel second-order angular velocity measuring instrument is the product of the transfer function of a second order system with three typical loops (namely a differential loop and two inertia loops with the complex coefficients).

The differential loop with the complex coefficient presents a double-channel loop with a straight-through asymmetric cross connection, and the inertia loop with the complex coefficients is a double-channel loop with a cross-asymmetrical feedback connection.

Figure 3.1 is an equivalent double-channel diagram of the instrument, which is a dual-channel series loop with three asymmetric cross connections. In Fig. 3.1, the values of $U_{\rm damping}$ and $U_{\rm M}$ are the real component and the imaginary component of the output signal respectively:

$$U = U_{
m damping} + {
m j} U_{
m M}$$
 $U = U_{
m damping} \sin arphi + U_{
m M} \cos arphi$

Equation (3.22) adopts the method of an automatic regulation second order system to study the dynamic problem of the instrument, and the logarithmic frequency characteristic method is one of the simplest and most convenient methods. It should be noted that only when the angular oscillation frequency is far less than the rotation frequency around the longitudinal axis of the aircraft can Fig. 1.12 be replaced by the equivalent block diagram in Fig. 3.1. In this case, the data results from the study of Fig. 3.1 and Eq. (3.22) can only be used for the judgment of the amplitude and phase of the output signal envelope, and the instantaneous voltage at

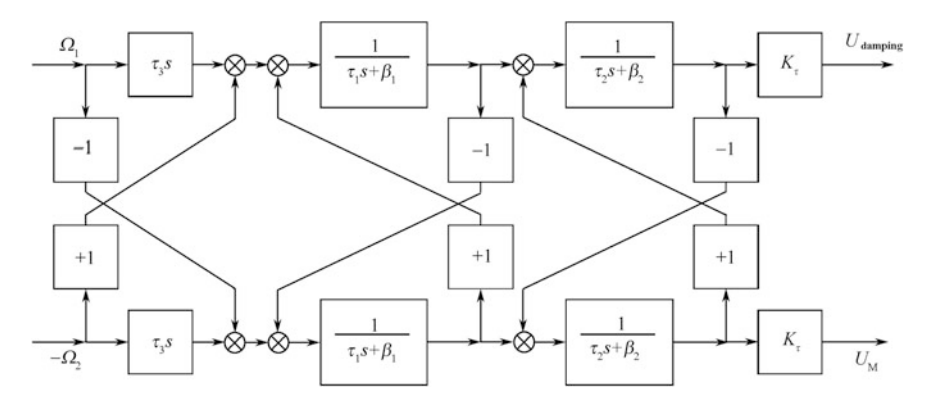


Fig. 3.1 Equivalent block diagram of a non-driven mechanical rotor gyroscope

the output end of the integrator output is the instantaneous output voltage of the instrument.

In Eq. (3.22), because $\tau_3 \approx \tau_1$ (almost equal), β_1 is very small (the attenuation coefficient is less than 0.5). Thus

$$\frac{\tau_3 s + \mathbf{j}}{\tau_1 s + \mathbf{j} + \beta_1} \approx 1$$

Therefore, Eq. (3.22) has the following form:

$$\frac{U}{\Omega^*} = K_{\tau} \frac{1}{\tau' s + \kappa' \mathbf{j} + \beta'} \tag{3.24}$$

where τ' and κ' are the equivalent time constant and the detuning frequency coefficient of the instrument:

$$\tau' = \frac{1}{\dot{\varphi}_0 \xi}; \quad \kappa' = \frac{1 - \mu \sqrt{1 - \xi^2}}{\xi}; \quad \beta' = \mu$$
 (3.25)

The double-channel block diagram with a rigid asymmetric feedback connection satisfies Eq. (3.24), and the frequency is detuned, that is, the rotation velocity around the longitudinal axis of the aircraft does not coincide with the resonant frequency of the sensitive element in Fig. 3.2.

The more accurate the resonance point of the instrument is, the smaller the value of κ' is, and when the tuning is very small, $\mu \to 0$, $\kappa' \to 0$.

The frequency characteristic curves of the amplitude and the phase of the instrument are shown in Fig. 3.3.

Fig. 3.2 Simplified equivalent loop diagram of the instrument

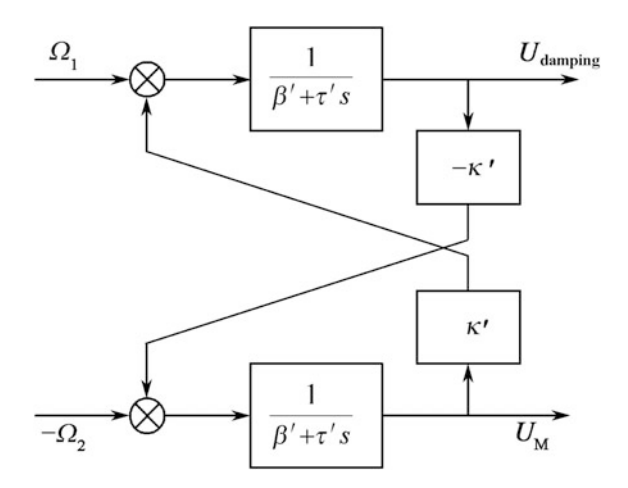
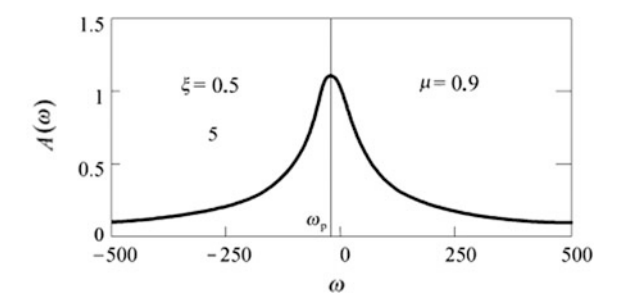
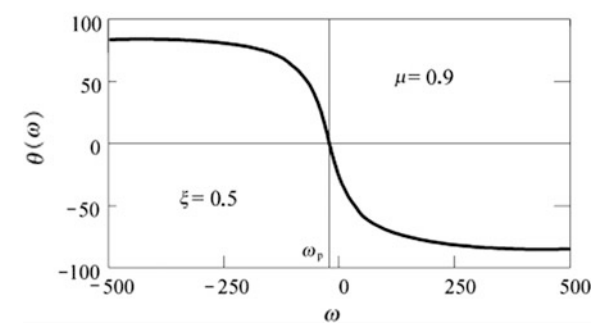


Fig. 3.3 Frequency characteristic curves of the amplitude and the phase of the instrument





$$A(\omega) = \frac{1}{\sqrt{(\beta')^2 + (\tau'\omega + \kappa')^2}}$$
(3.26)

$$\theta(\omega) = \arctan[-(\tau'\omega + \kappa')] \tag{3.27}$$

Because there are some complex coefficients in Eq. (3.24), the position of the maximum value of the amplitude frequency characteristic is moved from $\omega = 0$ to ω_p :

$$\omega_p = -\frac{\kappa'}{\tau'} = -\dot{\varphi}_0 \left(1 - \mu \sqrt{1 - \xi^2} \right) = \omega_0 \sqrt{1 - \xi^2} - \dot{\varphi}_0$$
 (3.28)

Obviously, when the attenuation coefficient is very small, the resonant frequency of the amplitude $A(\omega)$ is determined by the difference between the rotation velocity around the longitudinal axis of the aircraft and the undamped natural frequency. Consider Eq. (3.28) and the expression of the frequency characteristic can be rewritten as

$$A(\omega) = \frac{1}{\sqrt{\left(\beta'\right)^2 + \tau'^2 \left(\omega - \omega_p\right)^2}}$$
(3.29)

$$\theta(\omega) = \arctan\left[-\tau^{2}(\omega - \omega_{p})\right] \tag{3.30}$$

Obviously, the damping coefficient only affects the resonant frequency, while the detunding coefficient affects the resonance peak of the amplitude:

$$A(\omega_p) = \frac{1}{\beta'} \tag{3.31}$$

It can be seen that the instrument is a resonant loop with resonant frequency ω_p . The negative value of the resonance frequency can be explained by the complex coefficient and a 1/4 cycle of the phase shift of the input angular velocity.

When the attenuation coefficient is greater than 0.5, the expression is not Eq. (3.24). Equation (3.22) is more suitable and its resonant frequency is determined by Eq. (3.28), but the amplitude of the resonance point is slightly smaller.

The dynamic characteristics of the instrument can be studied from the logarithmic frequency characteristic curve, which unlike the single-channel loop must be drawn in the frequency range of $-\infty < \omega < \infty$.

The logarithmic frequency characteristic of the transfer function in Eq. (3.24) is shown in Fig. 3.4.

From Fig. 3.4 it can be seen that the reserve of the phase stability is large, but for a greater margin the coefficient K_{τ} must be reduced, or in other words the scale factor of the instrument must be reduced.

According to Eq. (3.23) K_{τ} may be reduced by the reducing coefficient $K_{\text{integrator}}$ or the increasing coefficients K_{moment} , $K_{\text{electric current}}$ and the time constant T_2 . Obviously, the increasing coefficients K_{moment} and $K_{\text{electric current}}$ will lead to an increase of damping and the sensitivity of the instrument will decrease. The damping coefficient is a selected tradeoff between the stability of the reserve and the sensitivity of the gyroscope. Increasing the time constant T_2 can lead to a decrease of the regulation quality of the instrument, and a decreasing $K_{\text{integrator}}$ can lead to a decrease of the scale factor.

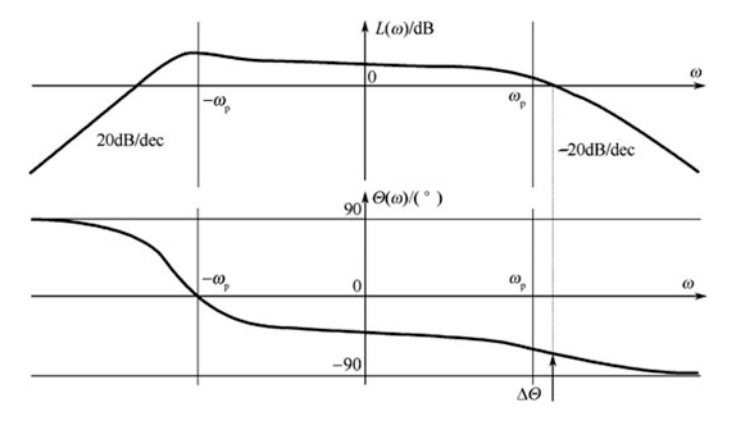


Fig. 3.4 Logarithmic frequency characteristic of the transfer function in Eq. (3.24)

From Eqs. (3.24) and Fig. 3.4, when the angular oscillation frequency is very small it is possible that the amplitude and phase of the output signal envelope can be calculated (for example, the minimum value $\dot{\varphi}_0/\nu > 10$. When $\dot{\varphi}_0/\nu < 10$, the complex transfer function is unreasonable.

Substituting Eqs. (3.8), (3.9) and (3.11) into (3.7), Eq. (3.7) can be rewritten as

$$\begin{split} \ddot{\alpha} + 2\xi\omega_0\dot{\alpha} + \omega_0^2\alpha &= \frac{H_0}{B_1}\Omega^{\nu}\cos(\nu t)\sin(\dot{\varphi}_0 t - \gamma_{\nu}) + \Omega^{\nu}\sin(\nu t)\cos(\dot{\varphi}_0 t - \gamma_{\nu}) \\ \ddot{\alpha} + 2\xi\omega_0\dot{\alpha} + \omega_0^2\alpha &= \frac{H_0}{2B_1}\Omega^{\nu}[\sin(\dot{\varphi}_0 t - \gamma_{\nu} + \nu t) + \sin(\dot{\varphi}_0 t - \gamma_{\nu} - \nu t)] \\ &+ \frac{\nu}{2}\Omega^{\nu}[\sin(\dot{\varphi}_0 t - \gamma_{\nu} + \nu t) - \sin(\dot{\varphi}_0 t - \gamma_{\nu} - \nu t)]; \end{split}$$

$$(3.32)$$

$$\ddot{\alpha} + 2\xi\omega_0\dot{\alpha} + \omega_0^2\alpha = \left(\frac{H_0}{2} + \frac{vB_1}{2}\right)\Omega^v\sin[(\dot{\varphi}_0 + v)t - \gamma_v] + \left(\frac{H_0}{2B_1} - \frac{v}{2}\right)\Omega^v\sin[(\dot{\varphi}_0 - v)t - \gamma_v]$$
(3.33)

Therefore, the external torque acting on the instrument sensing element is composed of two added entries:

$$M_{\text{inertia}} = M_1 + M_2 = \left(\frac{H_0}{2} + \frac{vB_1}{2}\right) \Omega^{\nu} \sin[(\dot{\varphi}_0 + v)t - \gamma_{\nu}] + \left(\frac{H_0}{2} - \frac{vB_1}{2}\right) \Omega^{\nu} \sin[(\dot{\varphi}_0 - v)t - \gamma_{\nu}]$$
(3.34)

where

$$\ddot{\alpha} + 2\xi\omega_0\dot{\alpha} + \omega_0^2\alpha = M_1 + M_2 \tag{3.35}$$

In this case, the output signal of the instrument is also composed of two added entries and according to $U_{\text{out}}(s) = \Phi(s)M_{\text{inertia}}(s)$, in the established working state the following expressions are determined:

$$U_{\text{out}}(t) = |\Phi(j\omega)| \Omega^{\nu} \left(\frac{H_0}{2} + \frac{\nu B_1}{2}\right) \sin\left\{ (\dot{\varphi}_0 + \nu)t - \gamma_{\nu} + \arg\left[\Phi(j\omega)\right] \right\}$$

$$+ |\Phi(j\omega)| \Omega^{\nu} \left(\frac{H_0}{2} - \frac{\nu B_1}{2}\right) \sin\left\{ (\dot{\varphi}_0 - \nu)t - \gamma_{\nu} + \arg\left[\Phi(j\omega)\right] \right\}$$

$$+ \omega = \dot{\varphi}_0 - \nu$$

$$(3.36)$$

Introduce the following symbols to simplify Eq. (3.36):

$$U_{+} = |\Phi(j\omega)| \Omega^{\nu} \left(\frac{H_0}{2} + \frac{\nu B_1}{2}\right)$$

$$(3.37)$$

$$U_{-} = |\Phi(j\omega)| \Omega^{\nu} \left(\frac{H_0}{2} - \frac{\nu B_1}{2}\right)$$

$$(3.38)$$

$$\chi_{+} = \arg \left[\Phi(j\omega) \right]_{\omega = \phi_0 + \nu} \tag{3.39}$$

$$\chi_{-} = \arg \left[\Phi(j\omega) \right]_{\omega = \phi_0 - \nu} \tag{3.40}$$

$$U_{\text{out}}(t) = U_{+} \sin[(\dot{\varphi}_{0} + v)t - \gamma_{v} + \chi_{+}] + U_{-} \sin\{(\dot{\varphi}_{0} - v)t - \gamma_{v} + \chi_{-}\}$$
 (3.41)

When the parameters of the integrator are correctly selected, the integrator with the transfer function (1.130) has a better performance. Therefore, when studying the role of the alternating angular velocity, the book adopts the integrator with the transfer function (1.130) as an integral loop.

Select $\xi_0 = 0$, and assume that the constant T_{damping} is very small, and the constants T_1 and T_2 are large. Then according to Eqs. (2.53) and (2.72) the following result can be obtained:

$$U_{+} = \frac{KK_{\text{integrator}} {}_{2}T_{1}[(C_{1} - A_{1} + B_{1})\dot{\varphi}_{0} + \nu B_{1}]\Omega^{\nu}}{2K_{\text{moment}}K_{\text{electric current}}T_{2}^{2}\sqrt{\left[\left(nT_{\text{amplify}} + 2\xi T_{0}\right)(\dot{\varphi}_{0} + \nu) - T_{0}^{2}nT_{\text{amplify}}(\dot{\varphi}_{0} + \nu)^{3}\right]^{2} + \left[1 - T_{0}^{2}(\dot{\varphi}_{0} + \nu)^{2}\right]^{2}}}$$

$$(3.42)$$

$$U_{-} = \frac{KK_{\text{integrator}} \,_{2}T_{1}[(C_{1} - A_{1} + B_{1})\dot{\phi}_{0} - \nu B_{1}]\Omega^{\nu}}{2K_{\text{moment}}K_{\text{electric current}}T_{2}^{2}\sqrt{\left[\left(nT_{\text{amplify}} + 2\xi T_{0}\right)(\dot{\phi}_{0} - \nu) - T_{0}^{2}nT_{\text{amplify}}(\dot{\phi}_{0} - \nu)^{3}\right]^{2} + \left[1 - T_{0}^{2}(\dot{\phi}_{0} - \nu)^{2}\right]^{2}}}$$

$$(3.43)$$

Assume that nT_{amplify} is very small, there holds

$$U_{+} = \frac{KK_{\rm integrator} {}_{2}T_{1}[(C_{1} - A_{1} + B_{1})\dot{\varphi}_{0} + \nu B_{1}]\Omega^{\nu}}{2K_{\rm moment}K_{\rm electric\; current}T_{2}^{2}\sqrt{\left[2\xi T_{0}(\dot{\varphi}_{0} + \nu)\right]^{2} + \left[1 - T_{0}^{2}(\dot{\varphi}_{0} + \nu)^{2}\right]^{2}}}$$
(3.44)

$$U_{-} = \frac{KK_{\text{integrator}} 2T_{1}[(C_{1} - A_{1} + B_{1})\dot{\varphi}_{0} - vB_{1}]\Omega^{v}}{2K_{\text{moment}}K_{\text{electric current}}T_{2}^{2}\sqrt{\left[2\xi T_{0}(\dot{\varphi}_{0} - v)\right]^{2} + \left[1 - T_{0}^{2}(\dot{\varphi}_{0} - v)^{2}\right]^{2}}}$$
(3.45)

Obviously, U_+ and U_- are related not only to the angular frequency v, but also to the velocity instability around the longitudinal axis of the aircraft and this

relationship is also present in the resonant condition. In the case of resonance, U_+ and U_- can be determined by the following equations:

$$U_{+} = \frac{KK_{\text{integrator}} 2T_{1}B_{1}(2\dot{\varphi}_{0} + \nu)\Omega^{\nu}}{2K_{\text{moment}}K_{\text{electric current}}T_{2}^{2}\sqrt{K^{2}(\dot{\varphi}_{0} + \nu)^{2} + \left(\frac{2\dot{\varphi}_{0}\nu + \nu^{2}}{\dot{\varphi}_{0}^{2}}\right)^{2}}}$$
(3.46)

$$U_{-} = \frac{KK_{\text{integrator 2}}T_{1}B_{1}(2\dot{\varphi}_{0} - \nu)\Omega^{\nu}}{2K_{\text{moment}}K_{\text{electric current}}T_{2}^{2}\sqrt{K^{2}(\dot{\varphi}_{0} - \nu)^{2} + \left(\frac{\nu^{2} - 2\dot{\varphi}_{0}\nu}{\dot{\varphi}_{0}^{2}}\right)^{2}}}$$
(3.47)

when the angular oscillation frequency v = 0, there holds

$$U_{
m amplitude} = U_{+} + U_{-} = rac{2K_{
m integrator}\,_{2}T_{1}B_{1}\Omega^{
m v}}{K_{
m moment}K_{
m electric \ current}T_{2}^{2}}$$

The above equation is the same as Eq. (2.12), which is in accordance with the case that a constant angular velocity acts on the instrument.

Note that $|\Phi(j\omega)|$ and the angular oscillation frequency ν are mainly determined by the dynamic coefficient and that Eqs. (3.44) and (3.45) can be simplified. The dynamic coefficients depend on the sum and difference frequency of the rotation frequency and the angular oscillation frequency around the longitudinal axis of the aircraft. Thus

$$\lambda_{+} = \frac{1}{\sqrt{\left[2\xi T_{0}(\dot{\varphi}_{0} + \nu)\right]^{2} + \left[1 - T_{0}^{2}(\dot{\varphi}_{0} + \nu)^{2}\right]^{2}}}$$
(3.48)

$$\lambda_{-} = \frac{1}{\sqrt{\left[2\xi T_0(\dot{\varphi}_0 - \nu)\right]^2 + \left[1 - T_0^2(\dot{\varphi}_0 - \nu)^2\right]^2}}$$
(3.49)

Equations (3.44) and (3.45) are transformed as

$$U_{+} = \frac{\lambda_{+} K K_{\text{integrator}} 2 T_{1} [(C_{1} - A_{1} + B_{1}) \dot{\varphi}_{0} + \nu B_{1}] \Omega^{\nu}}{2 K_{\text{moment}} K_{\text{electric current}} T_{2}^{2}}$$
(3.50)

$$U_{-} = \frac{\lambda_{-}KK_{\text{integrator}} {}_{2}T_{1}[(C_{1} - A_{1} + B_{1})\dot{\varphi}_{0} - \nu B_{1}]\Omega^{\nu}}{2K_{\text{moment}}K_{\text{electric current}}T_{2}^{2}}$$
(3.51)

It should be noted that the time constant $T_{\rm damping}$ selected by Eq. (2.85) is negligible in Eqs. (3.50) and (3.51) and in the case that the integrator time constant is 0.1 s and the angular oscillation frequency lies in the range of 0–8 Hz, it will cause the errors $\Delta U_{+} = \pm 5\%$ and $\Delta U_{-} = \pm 2\%$.

 ν and $\Delta \dot{\varphi}_0$ will not affect U_+ and U_- , thus it is reasonable to study the output signal.

Therefore, determine the phase shifts χ_+ and χ_- , and expand Eqs. (3.39) and (3.40):

$$\begin{split} \chi_{+} &= \frac{\pi}{2} + \arctan \big[T_{\text{damping}}(\dot{\phi}_{0} + \nu) \big] + \arctan [T_{1}(\dot{\phi}_{0} + \nu)] - \arctan \Bigg[\frac{2\xi_{\text{integrator}} T_{2}(\dot{\phi}_{0} + \nu)}{1 - T_{2}^{2}(\dot{\phi}_{0} + \nu)^{2}} \Bigg] \\ &- \arctan \Bigg\{ \frac{\big[nT_{\text{amplify}} + 2T_{0}(\xi_{0} + \xi) \big] (\dot{\phi}_{0} + \nu) - T_{0}^{2}nT_{\text{amplify}} (\dot{\phi}_{0} + \nu)^{3}}{1 - \big[T_{0}^{2} + 2\xi_{0}T_{0}nT_{\text{amplify}} \big] (\dot{\phi}_{0} + \nu)^{2}} \Bigg\} \end{split}$$
(3.52)

$$\begin{split} \chi_{-} = & \frac{\pi}{2} + \arctan \big[T_{\text{damping}}(\dot{\phi}_{0} - \nu) \big] + \arctan \big[T_{1}(\dot{\phi}_{0} - \nu) \big] - \arctan \left[\frac{2\xi_{\text{integrator}} T_{2}(\dot{\phi}_{0} - \nu)}{1 - T_{2}^{2}(\dot{\phi}_{0} - \nu)^{2}} \right] \\ & - \arctan \left\{ \frac{\big[nT_{\text{amplify}} + 2T_{0}(\xi_{0} + \xi) \big] (\dot{\phi}_{0} - \nu) - T_{0}^{2} nT_{\text{amplify}} (\dot{\phi}_{0} - \nu)^{3}}{1 - \big(T_{0}^{2} + 2\xi_{0}T_{0}nT_{\text{amplify}} \big) (\dot{\phi}_{0} - \nu)^{2}} \right\} \end{split}$$
(3.53)

Derive from Eq. (2.63):

$$\chi_{+} = -\frac{\pi}{2} + T_{\text{damping}}(\dot{\varphi}_{0} + \nu) + \frac{2\xi_{\text{integrator}}}{T_{2}(\dot{\varphi}_{0} + \nu)} - \frac{1}{T_{1}(\dot{\varphi}_{0} + \nu)} + \frac{1 - T_{0}^{2}(\dot{\varphi}_{0} + \nu)^{2}}{(\dot{\varphi}_{0} + \nu)\left\{2\xi T_{0} + nT_{\text{amplify}}\left[1 - T_{0}^{2}(\dot{\varphi}_{0} + \nu)\right]\right\}}$$
(3.54)

$$\chi_{-} = -\frac{\pi}{2} + T_{\text{damping}}(\dot{\varphi}_{0} - \nu) + \frac{2\xi_{\text{integrator}}}{T_{2}(\dot{\varphi}_{0} - \nu)} - \frac{1}{T_{1}(\dot{\varphi}_{0} - \nu)} + \frac{1 - T_{0}^{2}(\dot{\varphi}_{0} - \nu)^{2}}{(\dot{\varphi}_{0} - \nu)\left\{2\xi T_{0} + nT_{\text{amplify}}\left[1 - T_{0}^{2}(\dot{\varphi}_{0} - \nu)\right]\right\}}$$
(3.55)

It should be noted that only when the angular oscillation frequency lies in the range of 0–3 Hz can the simplified formula use Eqs. (3.54) and (3.55). Derived from Eq. (2.79), the phase shift of the integrator is broken down into a Taylor series of the average value of the rotation velocity around the longitudinal axis of the aircraft:

$$\begin{split} \frac{2\xi_{\text{integrator}}}{T_{2}(\dot{\varphi}_{0}+\nu)} - \frac{1}{T_{1}(\dot{\varphi}_{0}+\nu)} &= \frac{2\xi_{\text{integrator}}T_{1} - T_{2}}{T_{1}T_{2}(\dot{\varphi}_{0}+\nu)} = \frac{2\xi_{\text{integrator}}T_{1} - T_{2}}{T_{1}T_{2}\dot{\varphi}_{0}^{0}} \\ &- \frac{2\xi_{\text{integrator}}T_{1} - T_{2}}{T_{1}T_{2}} \frac{\dot{\varphi}_{0} + \nu - \dot{\varphi}_{0}^{0}}{\left(\dot{\varphi}_{0}^{0}\right)^{2}} \\ &= 2\frac{2\xi_{\text{integrator}}T_{1} - T_{2}}{T_{1}T_{2}\dot{\varphi}_{0}^{0}} - \frac{2\xi_{\text{integrator}}T_{1} - T_{2}}{T_{1}T_{2}} \frac{\dot{\varphi}_{0} + \nu}{\left(\dot{\varphi}_{0}^{0}\right)^{2}} \end{split}$$

$$(3.56)$$

$$\begin{split} \frac{2\xi_{\text{integrator}}}{T_{2}(\dot{\varphi}_{0}-v)} - \frac{1}{T_{1}(\dot{\varphi}_{0}-v)} &= \frac{2\xi_{\text{integrator}}T_{1}-T_{2}}{T_{1}T_{2}(\dot{\varphi}_{0}-v)} = \frac{2\xi_{\text{integrator}}T_{1}-T_{2}}{T_{1}T_{2}\dot{\varphi}_{0}^{0}} \\ &- \frac{2\xi_{\text{integrator}}T_{1}-T_{2}}{T_{1}T_{2}} \frac{\dot{\varphi}_{0}-v-\dot{\varphi}_{0}^{0}}{\left(\dot{\varphi}_{0}^{0}\right)^{2}} \\ &= 2\frac{2\xi_{\text{integrator}}T_{1}-T_{2}}{T_{1}T_{2}\dot{\varphi}_{0}^{0}} - \frac{2\xi_{\text{integrator}}T_{1}-T_{2}}{T_{1}T_{2}} \frac{\dot{\varphi}_{0}-v}{\left(\dot{\varphi}_{0}^{0}\right)^{2}} \end{split} \tag{3.57}$$

From (2.81) the relationship between the phase for the various components of the output signals and the frequency change of the instrument can be obtained and the change of the working frequency is caused by the fact that the rotation of the aircraft around the longitudinal axis has the angular oscillation and the velocity instability:

$$\chi_{+} = -\frac{\pi}{2} + \frac{2(2\xi_{\text{integrator}}T_{1} - T_{2})}{T_{1}T_{2}\dot{\varphi}_{0}^{0}} + (\dot{\varphi}_{0} + \nu) \left\{ T_{\text{damping}} - \frac{2\xi_{\text{integrator}}T_{1} - T_{2}}{T_{1}T_{2}(\dot{\varphi}_{0}^{0})^{2}} + \frac{\dot{\varphi}_{0}^{2}[(C_{1} - A_{1} - B_{1}) - (C_{1} - A_{1})(2\dot{\varphi}_{0} + \nu)\nu]}{(\dot{\varphi}_{0} + \nu)^{2} \left\{ D_{\text{feedback}} + nT_{\text{amplify}}\dot{\varphi}_{0}^{2}[(C_{1} - A_{1} - B_{1}) - (C_{1} - A_{1})(2\dot{\varphi}_{0} + \nu)\nu] \right\}} \right\}$$

$$(3.58)$$

$$\chi_{-} = -\frac{\pi}{2} + \frac{2(2\xi_{\text{integrator}}T_{1} - T_{2})}{T_{1}T_{2}\dot{\varphi}_{0}^{0}} + (\dot{\varphi}_{0} - v) \left\{ T_{\text{damping}} - \frac{2\xi_{\text{integrator}}T_{1} - T_{2}}{T_{1}T_{2}(\dot{\varphi}_{0}^{0})^{2}} + \frac{\dot{\varphi}_{0}^{2}[(C_{1} - A_{1} - B_{1}) - (C_{1} - A_{1})(-2\dot{\varphi}_{0} + v)v]}{(\dot{\varphi}_{0} - v)^{2} \left\{ D_{\text{feedback}} + nT_{\text{amplify}}\dot{\varphi}_{0}^{2}[(C_{1} - A_{1} - B_{1}) - (C_{1} - A_{1})(-2\dot{\varphi}_{0} + v)v] \right\} \right\}}$$
(3.59)

Obviously, when v = 0, Eqs. (3.58) and (3.59) are in accord with Eq. (2.81) and this equation determines the output signal phase of the instrument under the action of a constant angular velocity.

Therefore, Eqs. (3.58) and (3.59) show that even if the time constant T_{damping} in Eq. (2.83) is correctly selected, when the aircraft has an angular oscillation and the rotating velocity around the longitudinal axis of the aircraft is unstable, it is inevitable that the phase of the output signal is influenced. According to Eq. (2.83), when the time constant T_{damping} is calculated and substituted it into Eqs. (3.58) and (3.59), there holds

$$\begin{split} \chi_{+} &= -\frac{\pi}{2} + \frac{2\left(2\xi_{\text{integrator}}T_{1} - T_{2}\right)}{T_{1}T_{2}\dot{\phi}_{0}^{0}} + (\dot{\phi}_{0} + \nu) \left\{ \frac{(C_{1} - A_{1} - B_{1})}{D_{\text{feedback}} + nT_{\text{amplify}}\dot{\phi}_{0}^{2}(C_{1} - A_{1} - B_{1})} + \frac{\dot{\phi}_{0}^{2}}{\left(\dot{\phi}_{0} + \nu\right)^{2}} \left[(C_{1} - A_{1} - B_{1}) - (C_{1} - A_{1})(2\dot{\phi}_{0} + \nu)\nu \right]}{\left\{ D_{\text{feedback}} + nT_{\text{amplify}}\dot{\phi}_{0}^{2} \left[(C_{1} - A_{1} - B_{1}) - (C_{1} - A_{1})(2\dot{\phi}_{0} + \nu)\nu \right] \right\}} \end{split}$$

$$(3.60)$$

$$\begin{split} \chi_{-} &= -\frac{\pi}{2} + \frac{2\left(2\xi_{\text{integrator}}T_{1} - T_{2}\right)}{T_{1}T_{2}\dot{\varphi}_{0}^{0}} + (\dot{\varphi}_{0} - \nu)\left\{\frac{(C_{1} - A_{1} - B_{1})}{D_{\text{feedback}} + nT_{\text{amplify}}\dot{\varphi}_{0}^{2}(C_{1} - A_{1} - B_{1})} + \frac{\dot{\varphi}_{0}^{2}}{\left(\dot{\varphi}_{0} - \nu\right)^{2}}\left[(C_{1} - A_{1} - B_{1}) - (C_{1} - A_{1})(\nu - 2\dot{\varphi}_{0})\nu\right]}{\left\{D_{\text{feedback}} + nT_{\text{amplify}}\dot{\varphi}_{0}^{2}\left[(C_{1} - A_{1} - B_{1}) - (C_{1} - A_{1})(\nu - 2\dot{\varphi}_{0})\nu\right]\right\}} \end{split}$$

$$(3.61)$$

Equations (3.60) and (3.61) present the relationship between the phase of the output signal and the instability of the rotation velocity of the aircraft, and the relationship between the phase of the output signal and the angular oscillation frequency. Under the condition of the resonant working state and the complete compensation of the winding mutual inductance effect, the relationships are maintained:

$$\chi_{+} = -\frac{\pi}{2} + \frac{2(2\xi_{\text{integrator}}T_{1} - T_{2})}{T_{1}T_{2}\dot{\varphi}_{0}^{0}} - (\dot{\varphi}_{0} + \nu) \left\{ \frac{\dot{\varphi}_{0}^{2}[(C_{1} - A_{1})(2\dot{\varphi}_{0} + \nu)\nu]}{(\dot{\varphi}_{0} + \nu)^{2}D_{\text{feedback}}} \right\}$$
(3.62)

$$\chi_{-} = -\frac{\pi}{2} + \frac{2(2\xi_{\text{integrator}}T_{1} - T_{2})}{T_{1}T_{2}\dot{\varphi}_{0}^{0}} - (\dot{\varphi}_{0} - v) \left\{ \frac{\dot{\varphi}_{0}^{2}[(C_{1} - A_{1})(v - 2\dot{\varphi}_{0})v]}{(\dot{\varphi}_{0} - v)^{2}D_{\text{feedback}}} \right\}$$
(3.63)

If considering Eq. (2.27) then

$$\chi_{+} = -\frac{\pi}{2} + \frac{2(2\xi_{\text{integrator}}T_{1} - T_{2})}{T_{1}T_{2}\dot{\varphi}_{0}^{0}} - (\dot{\varphi}_{0}^{0} \pm \Delta\dot{\varphi}_{0} + \nu) \left\{ \frac{(\dot{\varphi}_{0}^{0} \pm \Delta\dot{\varphi}_{0})^{2}\{(C_{1} - A_{1})[2(\dot{\varphi}_{0}^{0} \pm \Delta\dot{\varphi}_{0}) + \nu]\nu\}}{(\dot{\varphi}_{0}^{0} \pm \Delta\dot{\varphi}_{0} + \nu)^{2}D_{\text{feedback}}} \right\}$$
(3.64)

$$\chi_{-} = -\frac{\pi}{2} + \frac{2(2\xi_{\text{integrator}}T_{1} - T_{2})}{T_{1}T_{2}\dot{\varphi}_{0}^{0}} - (\dot{\varphi}_{0}^{0} \pm \Delta\dot{\varphi}_{0} - v) \left\{ \frac{(\dot{\varphi}_{0}^{0} \pm \Delta\dot{\varphi}_{0})^{2} \{(C_{1} - A_{1}) [-2(\dot{\varphi}_{0}^{0} \pm \Delta\dot{\varphi}_{0}) + v]v\}}{(\dot{\varphi}_{0}^{0} \pm \Delta\dot{\varphi}_{0} - v)^{2} D_{\text{feedback}}} \right\}$$
(3.65)

Therefore, in the angular oscillation condition of the aircraft it is impossible that the instability of the rotation velocity around the longitudinal axis of the aircraft is compensated.

Now the relationship between the phase of the output signal and the instability of the rotation velocity around the longitudinal axis of the aircraft is studied, that is, in the condition of a constant angular oscillation frequency, the instability of the output signal phase.

In this case, the phase shift of the integrator is broken down into a Taylor series, $\frac{2\xi_{\text{integrator}}T_1-T_2}{T_1T_2(\dot{\phi}_0+\nu)}$ corresponds to $\dot{\phi}_0+\nu$, $\frac{2\xi_{\text{integrator}}T_1-T_2}{T_1T_2(\dot{\phi}_0-\nu)}$ corresponds to $\dot{\phi}_0-\nu$.

$$\frac{2\xi_{\text{integrator}}T_{1} - T_{2}}{T_{1}T_{2}(\dot{\varphi}_{0} + \nu)} = \frac{2\xi_{\text{integrator}}T_{1} - T_{2}}{T_{1}T_{2}(\dot{\varphi}_{0}^{0} + \nu)} - \frac{2\xi_{\text{integrator}}T_{1} - T_{2}}{T_{1}T_{2}} \frac{\dot{\varphi}_{0} - \dot{\varphi}_{0}^{0}}{\left(\dot{\varphi}_{0}^{0} + \nu\right)^{2}} \cdots = \frac{\left(2\xi_{\text{integrator}}T_{1} - T_{2}\right)\left(2\dot{\varphi}_{0}^{0} + \nu\right)}{T_{1}T_{2}\left(\dot{\varphi}_{0}^{0} + \nu\right)^{2}} - \frac{2\xi_{\text{integrator}}T_{1} - T_{2}}{T_{1}T_{2}} \frac{\dot{\varphi}_{0}}{\left(\dot{\varphi}_{0}^{0} + \nu\right)^{2}}.$$
(3.66)

$$\frac{2\xi_{\text{integrator}}T_{1} - T_{2}}{T_{1}T_{2}(\dot{\varphi}_{0} - v)} = \frac{2\xi_{\text{integrator}}T_{1} - T_{2}}{T_{1}T_{2}(\dot{\varphi}_{0}^{0} - v)} - \frac{2\xi_{\text{integrator}}T_{1} - T_{2}}{T_{1}T_{2}} \frac{\dot{\varphi}_{0} - \dot{\varphi}_{0}^{0}}{\left(\dot{\varphi}_{0}^{0} - v\right)^{2}} \cdots = \frac{\left(2\xi_{\text{integrator}}T_{1} - T_{2}\right)\left(2\dot{\varphi}_{0}^{0} - v\right)}{T_{1}T_{2}\left(\dot{\varphi}_{0}^{0} - v\right)^{2}} - \frac{2\xi_{\text{integrator}}T_{1} - T_{2}}{T_{1}T_{2}} \frac{\dot{\varphi}_{0}}{\left(\dot{\varphi}_{0}^{0} - v\right)^{2}}.$$
(3.67)

Substituting Eqs. (3.66) and (3.67) into Eqs. (3.54) and (3.55):

$$\chi_{+} = -\frac{\pi}{2} + \frac{\left(2\xi_{\text{integrator}}T_{1} - T_{2}\right)\left(2\dot{\varphi}_{0}^{0} + \nu\right)}{T_{1}T_{2}\left(\dot{\varphi}_{0}^{0} + \nu\right)^{2}} + \dot{\varphi}_{0} \left\{ T_{\text{damping}} - \frac{2\xi_{\text{integrator}}T_{1} - T_{2}}{T_{1}T_{2}\left(\dot{\varphi}_{0}^{0} + \nu\right)^{2}} + \frac{\dot{\varphi}_{0}\left[\left(C_{1} - A_{1} - B_{1}\right) - \left(C_{1} - A_{1}\right)\left(2\dot{\varphi}_{0} + \nu\right)\nu\right]}{\left(\dot{\varphi}_{0} + \nu\right)\left\{D_{\text{feedback}} + nT_{\text{amplify}}\dot{\varphi}_{0}^{2}\left[\left(C_{1} - A_{1} - B_{1}\right) - \left(C_{1} - A_{1}\right)\left(2\dot{\varphi}_{0} + \nu\right)\nu\right]\right\}} \right\}.$$
(3.68)

$$\chi_{-} = -\frac{\pi}{2} + \frac{\left(2\xi_{\text{integrator}}T_{1} - T_{2}\right)\left(2\dot{\varphi}_{0}^{0} - v\right)}{T_{1}T_{2}\left(\dot{\varphi}_{0}^{0} - v\right)^{2}} + \dot{\varphi}_{0} \left\{ T_{\text{damping}} - \frac{2\xi_{\text{integrator}}T_{1} - T_{2}}{T_{1}T_{2}\left(\dot{\varphi}_{0}^{0} - v\right)^{2}} + \frac{\dot{\varphi}_{0}\left[\left(C_{1} - A_{1} - B_{1}\right) - \left(C_{1} - A_{1}\right)\left(v - 2\dot{\varphi}_{0}\right)v\right]}{\left(\dot{\varphi}_{0} - v\right)\left\{D_{\text{feedback}} + nT_{\text{amplify}}\dot{\varphi}_{0}^{2}\left[\left(C_{1} - A_{1} - B_{1}\right) - \left(C_{1} - A_{1}\right)\left(v - 2\dot{\varphi}_{0}\right)v\right]\right\}} \right\}$$
(3.69)

when v = 0, Eqs. (3.68) and (3.69) are the same as Eqs. (2.80) and (2.81) respectively and they are the output signal phases when the constant angular velocity is applied to the instrument.

The time constant T_{amplify} in Eq. (2.83) is correctly selected, when the aircraft has the angular oscillation, the impact of the instability of the rotating velocity on the output signal phase is still not excluded.

When the angular oscillation frequency is larger (v > 3 Hz), Eqs. (3.52) and (3.53) are recommended. When ξ_0 and nT_{amplify} are small, the two expressions can be rewritten as

$$\chi_{+} = \frac{\pi}{2} + \arctan\left[T_{\text{damping}}(\dot{\varphi}_{0} + \nu)\right] + \arctan\left[T_{1}(\dot{\varphi}_{0} + \nu)\right]$$

$$- \arctan\left[\frac{2\xi_{\text{integrator}}T_{2}(\dot{\varphi}_{0} + \nu)}{1 - T_{2}^{2}(\dot{\varphi}_{0} + \nu)^{2}}\right] - \arctan\left[\frac{2\xi T_{0}(\dot{\varphi}_{0} + \nu)}{1 - T_{0}^{2}(\dot{\varphi}_{0} + \nu)^{2}}\right]$$

$$\chi_{-} = \frac{\pi}{2} + \arctan\left[T_{\text{damping}}(\dot{\varphi}_{0} - \nu)\right] + \arctan\left[T_{1}(\dot{\varphi}_{0} - \nu)\right]$$

$$- \arctan\left[\frac{2\xi_{\text{integrator}}T_{2}(\dot{\varphi}_{0} - \nu)}{1 - T_{2}^{2}(\dot{\varphi}_{0} - \nu)^{2}}\right] - \arctan\left[\frac{2\xi T_{0}(\dot{\varphi}_{0} - \nu)}{1 - T_{0}^{2}(\dot{\varphi}_{0} - \nu)^{2}}\right].$$

$$(3.71)$$

3.2 Output Signal of Non-driven Mechanical Gyroscope in the Condition of an Angular Vibration

As has been mentioned previously, the method for studying each frequency characteristic of two components of the output signal separately is not appropriate. Therefore, review (3.41) and obtain the transformed form:

$$\begin{split} U_{\text{out}} &= U_{+} \sin(\dot{\varphi}_{0}t - \gamma_{v}) \cos\left(vt + \chi_{+}\right) + U_{+} \cos(\dot{\varphi}_{0}t - \gamma_{v}) \sin\left(vt + \chi_{+}\right) \\ &+ U_{-} \sin(\dot{\varphi}_{0}t - \gamma_{v}) \cos(vt - \chi_{-}) - U_{-} \sin(vt - \chi_{-}) \cos(\dot{\varphi}_{0}t - \gamma_{v}) \\ &= \sin(\dot{\varphi}_{0}t - \gamma_{v}) \times (U_{+} \cos(vt) \cos\chi_{+} - U_{+} \sin(vt) \sin\chi_{+} \\ &+ U_{-} \cos(vt) \cos\chi_{-} + U_{-} \sin(vt) \sin\chi_{-}) + \cos(\dot{\varphi}_{0}t - \gamma_{v}) \\ &\times \left(U_{+} \sin(vt) \cos\chi_{+} + U_{+} \cos(vt) \sin\chi_{+} - U_{-} \sin(vt) \cos\chi_{-} + U_{-} \cos(vt) \sin\chi_{-}\right) \\ &= \sin(\dot{\varphi}_{0}t - \gamma_{v}) \left[\cos(vt) \left(U_{+} \cos\chi_{+} + U_{-} \cos\chi_{-}\right) - \sin(vt) \left(U_{+} \sin\chi_{+} - U_{-} \sin\chi_{-}\right)\right] \\ &+ \cos(\dot{\varphi}_{0}t - \gamma_{v}) \left[\cos(vt) \left(U_{+} \sin\chi_{+} + U_{-} \sin\chi_{-}\right) + \sin(vt) \left(U_{+} \cos\chi_{+} - U_{-} \cos\chi_{-}\right)\right] \end{split}$$

Introduce the following symbols:

$$\begin{cases} U_{C+} = U_{+} \cos \chi_{+} + U_{-} \cos \chi_{-} \\ U_{S+} = U_{+} \sin \chi_{+} + U_{-} \sin \chi_{-} \\ U_{C-} = U_{+} \cos \chi_{+} - U_{-} \cos \chi_{-} \\ U_{S-} = U_{+} \sin \chi_{+} - U_{-} \sin \chi_{-} \end{cases}$$

$$(3.72)$$

Then

$$U_{\text{out}} = \sin(\dot{\varphi}_0 t - \gamma_v) [U_{C+} \cos(vt) - U_{S-} \sin(vt)] + \cos(\dot{\varphi}_0 t - \gamma_v) [U_{S+} \cos(vt) + U_{C-} \sin(vt)]$$
(3.73)

that is,

$$U_{\text{out}} = \sqrt{U_{C+}^2 + U_{S-}^2} \sin(\dot{\varphi}_0 t - \gamma_v) \cos\left[vt + \arctan\left(\frac{U_{S-}}{U_{C+}}\right)\right] + \sqrt{U_{C-}^2 + U_{S+}^2} \cos(\dot{\varphi}_0 t - \gamma_v) \sin\left[vt + \arctan\left(\frac{U_{S+}}{U_{C-}}\right)\right]$$

$$(3.74)$$

Simultaneously,

$$\sqrt{U_{C+}^2 + U_{S-}^2} = \sqrt{U_{+}^2 + U_{-}^2 + 2U_{+}U_{-}\cos(\chi_{+} + \chi_{-})}$$
 (3.75)

$$\sqrt{U_{C-}^2 + U_{S+}^2} = \sqrt{U_{+}^2 + U_{-}^2 - 2U_{+}U_{-}\cos(\chi_{+} + \chi_{-})}$$
 (3.76)

Equation (3.74) can be written in a more convenient form:

$$U_{\text{out}} = U_{\text{m}} \sin(\dot{\varphi}_0 t - \gamma_v + \chi_{\text{m}}) \tag{3.77}$$

where

$$U_{\rm m} = \sqrt{\left(U_{C+}^2 + U_{S-}^2\right)\cos^2\left[vt + \arctan\left(\frac{U_{S-}}{U_{C+}}\right)\right] + \left(U_{C-}^2 + U_{S+}^2\right)\sin^2\left[vt + \arctan\left(\frac{U_{S+}}{U_{C-}}\right)\right]}$$
(3.78)

$$\chi_{\rm m} = \arctan \left\{ \frac{\sqrt{U_{C-}^2 + U_{S+}^2} \sin \left[vt + \arctan\left(\frac{U_{S+}}{U_{C-}}\right)\right]}{\sqrt{U_{C+}^2 + U_{S-}^2} \cos \left[vt + \arctan\left(\frac{U_{S-}}{U_{C+}}\right)\right]} \right\}$$
(3.79)

It is seen that the amplitude and phase of the output signal are related to the time in the complex form. Using Eqs. (3.72), (3.79) can be turned into the following form:

$$\chi_{\rm m} = \arctan \left\{ \frac{\sqrt{U_+^2 + U_-^2 - 2U_+ U_- \cos(\chi_+ + \chi_-)} \sin\left[vt + \arctan\left(\frac{U_+ \sin\chi_+ + U_- \sin\chi_-}{U_+ \cos\chi_+ - U_- \cos\chi_-}\right)\right]}{\sqrt{U_+^2 + U_-^2 + 2U_+ U_- \cos(\chi_+ + \chi_-)} \cos\left[vt + \arctan\left(\frac{U_+ \sin\chi_+ - U_- \sin\chi_-}{U_+ \cos\chi_+ + U_- \cos\chi_-}\right)\right]} \right\}$$
(3.80)

In order to simplify Eq. (3.78), by using Eqs. (3.75) and (3.76) the transformed form can be obtained:

$$\begin{split} U_{\rm m} &= \left\{ \left(U_{C+}^2 + U_{S-}^2 \right) \cos^2(\nu t) \cos^2 \left[\arctan \left(\frac{U_{S-}}{U_{C+}} \right) \right] + \left(U_{C+}^2 + U_{S-}^2 \right) \sin^2(\nu t) \sin^2 \left[\arctan \left(\frac{U_{S-}}{U_{C+}} \right) \right] \right. \\ &+ \left(U_{C-}^2 + U_{S+}^2 \right) \sin^2(\nu t) \cos^2 \left[\arctan \left(\frac{U_{S+}}{U_{C-}} \right) \right] + \left(U_{C-}^2 + U_{S+}^2 \right) \cos^2(\nu t) \sin^2 \left[\arctan \left(\frac{U_{S+}}{U_{C-}} \right) \right] \\ &- 2 \left(U_{C+}^2 + U_{S-}^2 \right) \cos(\nu t) \cos \left[\arctan \left(\frac{U_{S-}}{U_{C+}} \right) \right] \sin(\nu t) \sin \left[\arctan \left(\frac{U_{S-}}{U_{C+}} \right) \right] \\ &+ 2 \left(U_{C-}^2 + U_{S+}^2 \right) \sin(\nu t) \cos \left[\arctan \left(\frac{U_{S+}}{U_{C-}} \right) \right] \cos(\nu t) \sin \left[\arctan \left(\frac{U_{S+}}{U_{C-}} \right) \right] \right\}^{1/2} \end{split}$$

$$(3.81)$$

Consider

$$\cos\left[\arctan\left(\frac{U_{S-}}{U_{C+}}\right)\right] = \frac{U_{C+}}{\sqrt{U_{C+}^2 + U_{S-}^2}}$$
(3.82)

$$\sin\left[\arctan\left(\frac{U_{S-}}{U_{C+}}\right)\right] = \frac{U_{S-}}{\sqrt{U_{C+}^2 + U_{S-}^2}}$$
(3.83)

$$\cos\left[\arctan\left(\frac{U_{S+}}{U_{C-}}\right)\right] = \frac{U_{C-}}{\sqrt{U_{C-}^2 + U_{S+}^2}}$$
(3.84)

$$\sin\left[\arctan\left(\frac{U_{S+}}{U_{C-}}\right)\right] = \frac{U_{S+}}{\sqrt{U_{C-}^2 + U_{S+}^2}}$$
(3.85)

Substituting Eqs. (3.82)–(3.85) into Eq. (3.81) obtains

$$\begin{split} U_{\rm m} &= \left[U_{C+}^2 \cos^2(vt) + U_{S-}^2 \sin^2(vt) - 2U_{C+}U_{S-}\cos(vt) \sin(vt) \right. \\ &+ U_{C-}^2 \sin^2(vt) + U_{S+}^2 \cos^2(vt) + 2U_{C-}U_{S+}\cos(vt) \sin(vt) \right]^{1/2} \\ &= \sqrt{\left(U_{C+}^2 + U_{S+}^2 \right) \cos^2(vt) + \left(U_{S-}^2 + U_{C-}^2 \right) \sin^2(vt) + \sin(2vt) (U_{C-}U_{S+} - U_{C+}U_{S-})} \end{split}$$

Using Eq. (3.72) obtains

$$\begin{split} U_{\rm m} &= \left\{ \left[U_+^2 + U_-^2 + 2U_+ \, U_- \cos \left(\chi_+ - \chi_- \right) \right] \cos^2 (vt) \right. \\ &+ \left[U_+^2 + U_-^2 - 2U_+ \, U_- \cos \left(\chi_+ - \chi_- \right) \right] \sin^2 (vt) + 2U_+ \, U_- \sin \left(\chi_- - \chi_+ \right) \sin (2vt) \right\}^{1/2} \\ &= \sqrt{U_+^2 + U_-^2 + 2U_+ \, U_- \cos \left(\chi_+ - \chi_- \right) \cos (2vt) + 2U_+ \, U_- \sin \left(\chi_- - \chi_+ \right) \sin (2vt)} \end{split}$$

$$U_{\rm m} = \sqrt{U_+^2 + U_-^2 + 2U_+ U_- \cos(2vt - \chi_- + \chi_+)}$$
 (3.86)

Substituting Eqs. (3.50), (3.51), (3.70) and (3.71) into Eq. (3.86) and considering the impact of the differential loop on the integrator obtains

$$\begin{split} U_{\mathrm{m}} &= \frac{KK_{\mathrm{integrator}} 2T_{1}\Omega^{\nu}}{2K_{\mathrm{moment}}K_{\mathrm{electric \; current}}T_{2}^{2}} \left\{ \lambda_{+}^{2} \left[\dot{\varphi}_{0}(C_{1} - A_{1} + B_{1}) + \nu B_{1} \right]^{2} \left[1 + T_{\mathrm{damping}}^{2} (\dot{\varphi}_{0} + \nu)^{2} \right] \right. \\ &+ \lambda_{-}^{2} \left[\dot{\varphi}_{0}(C_{1} - A_{1} + B_{1}) - \nu B_{1} \right]^{2} \left[1 + T_{\mathrm{damping}}^{2} (\dot{\varphi}_{0} - \nu)^{2} \right] \\ &+ 2\lambda_{+}\lambda_{-} \left[\dot{\varphi}_{0}^{2}(C_{1} - A_{1} + B_{1})^{2} - \nu^{2}B_{1}^{2} \right] \left[1 + T_{\mathrm{damping}}^{2} (\dot{\varphi}_{0} + \nu)^{2} \right] \left[1 + T_{\mathrm{damping}}^{2} (\dot{\varphi}_{0} - \nu)^{2} \right] \\ &\times \cos\left(2\nu t + \arctan\left[T_{\mathrm{damping}}(\dot{\varphi}_{0} + \nu)\right] - \arctan\left[T_{\mathrm{damping}}(\dot{\varphi}_{0} - \nu)\right] + \arctan\left[T_{1}(\dot{\varphi}_{0} + \nu)\right] \\ &- \arctan\left[T_{1}(\dot{\varphi}_{0} - \nu)\right] - \arctan\left[\frac{2\xi_{\mathrm{integrator}}T_{2}(\dot{\varphi}_{0} + \nu)^{2}}{1 - T_{2}^{2}(\dot{\varphi}_{0} + \nu)^{2}} \right] + \arctan\left[\frac{2\xi_{\mathrm{integrator}}T_{2}(\dot{\varphi}_{0} - \nu)}{1 - T_{2}^{2}(\dot{\varphi}_{0} - \nu)^{2}} \right] \\ &- \arctan\left[\frac{2\xi T_{0}(\dot{\varphi}_{0} + \nu)}{1 - T_{0}^{2}(\dot{\varphi}_{0} + \nu)^{2}} \right] + \arctan\left[\frac{2\xi T_{0}(\dot{\varphi}_{0} - \nu)}{1 - T_{0}^{2}(\dot{\varphi}_{0} - \nu)^{2}} \right] \right) \right\}^{1/2} \end{split} \tag{3.87}$$

The differential loop is not considered. Equation (3.87) will have the following form:

$$\begin{split} U_{\mathrm{m}} &= \frac{K K_{\mathrm{integrator}} 2 T_{1} \Omega^{\nu}}{2 K_{\mathrm{moment}} K_{\mathrm{electric \, current}} T_{2}^{2}} \left\{ \lambda_{+}^{2} \left[\dot{\varphi}_{0} (C_{1} - A_{1} + B_{1}) + \nu B_{1} \right]^{2} + \lambda_{-}^{2} \left[\dot{\varphi}_{0} (C_{1} - A_{1} + B_{1}) - \nu B_{1} \right]^{2} \right. \\ &\quad + 2 \lambda_{+} \lambda_{-} \left[\dot{\varphi}_{0}^{2} (C_{1} - A_{1} + B_{1})^{2} - \nu^{2} B_{1}^{2} \right] \cos \{2 \nu t + \arctan[T_{1} (\dot{\varphi}_{0} + \nu)] \} \\ &\quad - \arctan[T_{1} (\dot{\varphi}_{0} - \nu)] - \arctan\left[\frac{2 \xi_{\mathrm{integrator}} T_{2} (\dot{\varphi}_{0} + \nu)}{1 - T_{2}^{2} (\dot{\varphi}_{0} + \nu)^{2}} \right] + \arctan\left[\frac{2 \xi_{\mathrm{integrator}} T_{2} (\dot{\varphi}_{0} - \nu)}{1 - T_{2}^{2} (\dot{\varphi}_{0} - \nu)^{2}} \right] \\ &\quad - \arctan\left[\frac{2 \xi T_{0} (\dot{\varphi}_{0} + \nu)}{1 - T_{0}^{2} (\dot{\varphi}_{0} + \nu)^{2}} \right] + \arctan\left[\frac{2 \xi T_{0} (\dot{\varphi}_{0} - \nu)}{1 - T_{0}^{2} (\dot{\varphi}_{0} - \nu)^{2}} \right] \right\}^{1/2} \end{split}$$

Equations (3.87) and (3.88) illustrate the complicated relationship between the amplitude of the output signal and the angular oscillation frequency of the aircraft. And the phase of the output signal also has a complicated relationship with the angular oscillation frequency. It should be noted that because in the expression of the output signal phase the amplitudes of the two components of the output signal have a ratio relationship, the coefficient $\frac{KK_{\text{integrator}} 2T_1\Omega^{\nu}}{2K_{\text{moment}}K_{\text{electric current}}T_2^2}$ does not affect the phase of the output signal. It shows that when the aircraft has an angular oscillation, the output signal phase will be independent of the angular velocity.

It can be seen that the amplitude of the output signal is related to the measured angular velocity.

The form of the output signal of a non-driven mechanical gyroscope under the action of harmonic angular velocity is shown in Fig. 3.5. From Eqs. (3.86), (3.87) and (3.88), the envelope value of the output signal can be determined.

In order to describe the output signal of the instrument the following parameters and symbols are introduced:

 U_0 Value of the envelope amplitude, which is equal to the maximum value of $U_{\rm H}$;

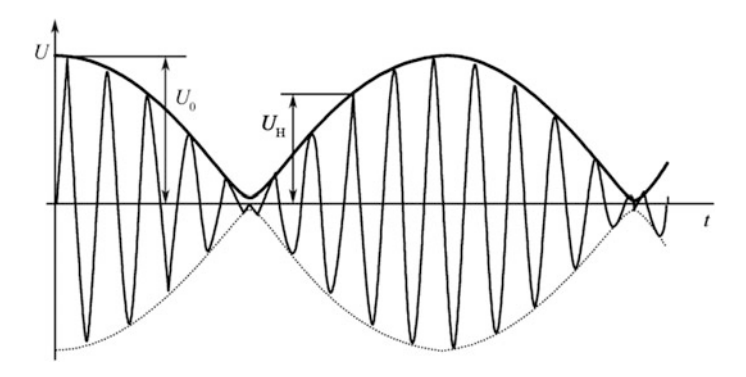


Fig. 3.5 Output signal of a non-driven mechanical gyroscope under the action of harmonic angular velocity

 $U_{\text{carrier wave}}$ Amplitude of the carrier wave;

 χ_0 Phase of the envelope;

 $\chi_{\text{carrier wave}}$ Phase of the carrier wave that corresponds to the envelope.

The relationship between $U_{\rm H}$ and time presents the amplitude characteristics of the carrier wave changing with time; the relationship between $U_{\rm H}$ and ν presents the envelope amplitude and the phase characteristics changing with the angular oscillation frequency; the relationship between $\chi_{\rm m}$ and the frequency ν presents the phase characteristics of the carrier wave changing with the angular oscillation frequency; and the relationship between $\chi_{\rm m}$ and the time presents the phase characteristics of the carrier wave changing with time.

The conclusion drawn from Fig. 3.5 is that the output signal of the instrument has a complex form of modulation and it is not appropriate that the output signal is regarded as the same as the harmonic signal of the input.

However, when research on the instrument is carefully performed, it is not important how the instrument deals with the harmonic signal input, but it is important how much the output signal of the instrument is in accord with the input signal of the aircraft's steering engine. It is necessary that this input signal accurately and reliably deals with the harmonic angular velocity and acts on the rotating flight carrier through the steering engine.

When the harmonic angular velocity acts on the rotating flight carrier, then in order to accurately and reliably deal with the harmonic angular velocity, the aircraft's steering engine must complete the oscillation of amplitude modulation, non-driven mechanical gyroscope and the rotating flight carrier rotate together. Thus, the oscillation of the aircraft's steering engine should correspond to the input harmonic angular velocity, which is modulated by the rotation of the aircraft, that is, it corresponds to the sensitive element of the instrument. In this way, the output signal of the instrument is connected with the modulated input signal and it is possible to study the instrument for processing the accuracy of the changing harmonic angular velocity. Because these two signals are modulated by the same envelope and frequency of the carrier wave, it is quite appropriate to compare them.

3.3 Measurement Accuracy of the Harmonic Angular Velocity for the Aircraft

For an aircraft limited by angular oscillation, the processing accuracy of the harmonic angular velocity of the instrument input is studied and when comparing the output signal and the input signal of the instrument, from Eq. (3.34) the input signal can be given by the following form:

$$M_{\text{inertia}} = M_{+} \sin[(\dot{\varphi}_{0} + v)t - \gamma_{v}] + M_{-} \sin[(\dot{\varphi}_{0} - v)t - \gamma_{v}]$$
(3.89)

where

$$M_{+} = \Omega^{\nu} \left(\frac{H_0}{2} + \frac{\nu B_1}{2} \right) \tag{3.90}$$

$$M_{-} = \Omega^{\nu} \left(\frac{H_0}{2} - \frac{\nu B_1}{2} \right) \tag{3.91}$$

Corresponding to Eqs. (3.32), (3.89) can be presented by another form:

$$M_{\text{intertia}} = (M_{+} + M_{-})\sin(\dot{\varphi}_{0}t - \gamma_{v})\cos(vt) + (M_{+} - M_{-})\cos(\dot{\varphi}_{0}t - \gamma_{v})\sin(vt)$$

$$= \Omega^{v}H_{0}\sin(\dot{\varphi}_{0}t - \gamma_{v})\cos(vt) + \Omega^{v}vB_{1}\cos(\dot{\varphi}_{0}t - \gamma_{v})\sin(vt)$$
(3.92)

$$\begin{split} M_{\text{intertia}} &= \sqrt{(M_{+} + M_{-})^{2} \cos^{2}(vt) + (M_{+} - M_{-})^{2} \sin^{2}(vt)x} \\ &\quad \sin \left\{ \dot{\varphi}_{0}t - \gamma_{v} + \arctan \left[\frac{M_{+} - M_{-}}{M_{+} + M_{-}} \tan(vt) \right] \right\} \\ &= \Omega^{v} \sqrt{H_{0}^{2} \cos^{2}(vt) + v^{2} B_{1}^{2} \sin^{2}(vt)} \sin \left\{ \dot{\varphi}_{0}t - \gamma_{v} + \arctan \left[\frac{vB_{1}}{H_{0}} \tan(vt) \right] \right\} \end{split}$$

$$(3.93)$$

Considering Eq. (1.37) obtains

$$M_{\text{intertia}} = \Omega^{\nu} \sqrt{\dot{\phi}_{0}^{2} (C_{1} - A_{1} + B_{1})^{2} \cos^{2}(\nu t) + \nu^{2} B_{1}^{2} \sin^{2}(\nu t)} \times \sin \left\{ \dot{\phi}_{0} t - \gamma_{\nu} + \arctan \left[\frac{\nu B_{1}}{\dot{\phi}_{0} (C_{1} - A_{1} + B_{1})} \tan(\nu t) \right] \right\}$$
(3.94)

Or compared with $U_{\rm m}$, $M_{\rm inertia}$ is changed into the 2 times angle 2vt:

$$\begin{split} M_{\text{intertia}} &= \Omega^{\nu} \sqrt{\frac{\dot{\varphi}_{0}^{2}(C_{1} - A_{1} + B_{1})^{2}}{2} + \frac{\nu^{2}B_{1}^{2}}{2} + \left[\frac{\dot{\varphi}_{0}^{2}(C_{1} - A_{1} + B_{1})^{2}}{2} - \frac{\nu^{2}B_{1}^{2}}{2}\right] \cos(2\nu t)} \\ &\times \sin\left\{\dot{\varphi}_{0}t - \gamma_{\nu} + \arctan\left[\frac{\nu B_{1}}{\dot{\varphi}_{0}(C_{1} - A_{1} + B_{1})} \tan(\nu t)\right]\right\} \\ &= \Omega^{\nu} \sqrt{\frac{H_{0}^{2}}{2} + \frac{\nu^{2}B_{1}^{2}}{2} + \left[\frac{H_{0}^{2}}{2} - \frac{\nu^{2}B_{1}^{2}}{2}\right] \cos(2\nu t)} \times \sin\left\{\dot{\varphi}_{0}t - \gamma_{\nu} + \arctan\left[\frac{\nu B_{1}}{H_{0}} \tan(\nu t)\right]\right\} \end{split}$$

$$(3.95)$$

From Eq. (3.95) the conclusion can be drawn that there is a relationship between the amplitude of the input signal and the time and the frequency changes with 2ν such as the amplitude of the output signal. Comparing with the output signal introduces the following symbols: $M_{\text{inp.envelope}}$ is the envelope amplitude of the input signal; $M_{\text{carrier wave}}$ is the amplitude of the carrier wave; $\chi_{\text{inp.envelope}}$ is the phase of the envelope and $\chi_{\text{inp.carrier wave}}$ is the phase of the carrier wave.

Similarly, compare with the output signal and write

$$M_{\text{intertia}} = M_{\text{m}} \sin(\dot{\varphi}_0 t - \gamma_v + \chi_{\text{inp,m}}) \tag{3.96}$$

where

$$M_{\rm m} = \Omega^{\rm v} \sqrt{\frac{H_0^2}{2} + \frac{v^2 B_1^2}{2} + \left[\frac{H_0^2}{2} - \frac{v^2 B_1^2}{2}\right] \cos(2vt)}$$
 (3.97)

$$\chi_{\text{inp,m}} = \arctan\left[\frac{vB_1}{H_0}\tan(vt)\right]$$
 (3.98)

Compare the output signal (3.77) and the input signal (3.96) and connect them:

$$\frac{U_{\text{out}}}{M_{\text{intertia}}} = \frac{U_{\text{m}}\sin(\dot{\varphi}_{0}t - \gamma_{\nu} + \chi_{\text{m}})}{M_{\text{m}}\sin(\dot{\varphi}_{0}t - \gamma_{\nu} + \chi_{\text{inp,m}})}$$
(3.99)

Next the amplitude, the phase and its instantaneous value will be compared.

1. Compare the amplitude

Assume that the phase of χ_m coincides with that of $\chi_{inp.m}$. In this case, Eq. (3.99) has the following form:

$$\frac{U_{\text{out}}}{M_{\text{intertia}}} = \frac{U_{\text{m}}}{M_{\text{m}}} = \frac{\sqrt{U_{+}^{2} + U_{-}^{2} + 2U_{+}U_{-}\cos(2vt + \chi_{+} - \chi_{-})}}{\Omega^{v}\sqrt{\frac{H_{0}^{2}}{2} + \frac{v^{2}B_{1}^{2}}{2} + \left(\frac{H_{0}^{2}}{2} - \frac{v^{2}B_{1}^{2}}{2}\right)\cos(2vt)}}$$
(3.100)

As has been noted previously, the amplitudes of the two signals are dependent on the time. Obviously, this relationship is not a pure harmonic type, but is a periodic relationship with twice the signal frequency 2vt. The envelop curves of the output and input signals of a non-driven mechanical gyroscope are shown in Fig. 3.6.

It is clear that when the angular oscillation frequencies of the two signals in Fig. 3.6 are consistent, the harmonic phase shifts in the radical sign of the expressions $U_{\rm m}$ and $M_{\rm m}$ are also consistent. Therefore, in order to evaluate the characteristics of these two values it is enough to compare the two amplitudes and phase frequencies.

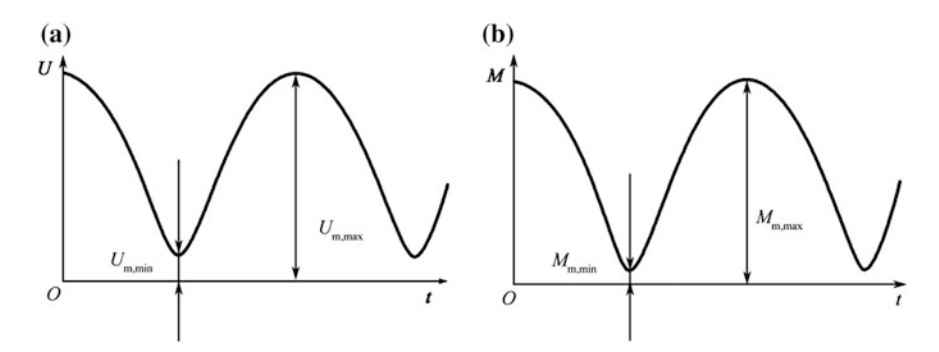


Fig. 3.6 The envelop curves of the output and input signals of non-driven mechanical gyroscope. **a** The output signal; **b** The input signal

Each value of Eq. (3.100) is analyzed in turn along with its relation.

1. The amplitude of the input signal

In order to determine the maximum and minimum values of the amplitude of the input signal, substituting Eq. (3.93) into Eq. (3.100) obtains

$$M_{\rm m} = \Omega^{\nu} \sqrt{H_0^2 \cos^2(\nu t) + \nu^2 B_1^2 \sin^2(\nu t)}$$
 (3.101)

When $vt = \frac{\pi}{2}n, n \in \mathbb{Z}$, because $H_0 > vB_1$, the following equation can be obtained

$$M_{\rm m,max} = H_0 \Omega^{\nu} \tag{3.102}$$

When $vt = \pi k$, $k \in \mathbb{Z}$:

$$M_{\rm m.min} = v B_1 \Omega^{\rm v} \tag{3.103}$$

When $vt = \frac{\pi}{2} + \pi k, k \in \mathbb{Z}$, the extreme value $M_{\rm m}$ equals zero.

Therefore, the possible instantaneous maximum value of the input signal envelope is independent of the frequency v. This situation can be explained as follows: when the input signal envelope has a maximum value, its measured harmonic angular velocity also has an instantaneous maximum value.

In this moment, the angular acceleration of the aircraft equals zero so it does not affect the envelope but when the envelope has a minimum value the angular velocity of the input end of the instrument is zero and the angular acceleration is maximum. Therefore, the angular acceleration only affects the minimum value of the envelope. Then it can be seen that with an increase in the angular vibration frequency, the minimum value of the input signal amplitude increases according to the linear relationship.

2. The amplitude of the output signal

Next determine the maximum value, the minimum value and the phase of $U_{\rm m}$. When $vt = \pi n - \frac{\chi_+ - \chi_-}{2}$, $n \in \mathbb{Z}$, the amplitude $U_{\rm m}$ is a maximum value;

When $vt = \pi \left(n + \frac{1}{2}\right) - \frac{\chi_+ - \chi_-}{2}$, the amplitude $U_{\rm m}$ is a minimum value. Thus, from (3.50) and (3.51), the maximum value and the minimum value of $U_{\rm m}$ have the following forms:

$$U_{\text{m,max}} = U_{+} + U_{-} = \frac{KK_{\text{integrator}} 2T_{1}\Omega^{\nu}}{2K_{\text{moment}}K_{\text{electric current}}T_{2}^{2}} \left\{ \lambda_{+} \left[\dot{\varphi}_{0}(C_{1} - A_{1} + B_{1}) + \nu B_{1} \right] \sqrt{1 + T_{\text{damping}}^{2} \left(\dot{\varphi}_{0} + \nu \right)^{2}} \right.$$

$$\left. + \lambda_{-} \left[\dot{\varphi}_{0}(C_{1} - A_{1} + B_{1}) - \nu B_{1} \right] \sqrt{1 + T_{\text{damping}}^{2} \left(\dot{\varphi}_{0} - \nu \right)^{2}} \right\}$$

$$V_{\text{m,min}} = U_{-} - U_{+} = \frac{KK_{\text{integrator}} 2T_{1}\Omega^{\nu}}{2K_{-}} \left\{ \lambda_{-} \left[\dot{\varphi}_{0}(C_{1} - A_{1} + B_{1}) - \nu B_{1} \right] \sqrt{1 + T_{\text{damping}}^{2} \left(\dot{\varphi}_{0} + \nu \right)^{2}} \right\}$$

$$\begin{split} U_{\rm m,min} &= U_{-} - U_{+} = \frac{K K_{\rm integrator\,2} T_{1} \Omega^{\nu}}{2 K_{\rm moment} K_{\rm electric\,\, current} T_{2}^{2}} \left\{ \lambda_{-} [\dot{\phi}_{0} (C_{1} - A_{1} + B_{1}) - \nu B_{1}] \sqrt{1 + T_{\rm damping}^{2} (\dot{\phi}_{0} + \nu)^{2}} \right. \\ & \left. - \lambda_{+} [\dot{\phi}_{0} (C_{1} - A_{1} + B_{1}) + \nu B_{1}] \sqrt{1 + T_{\rm damping}^{2} (\dot{\phi}_{0} - \nu)^{2}} \right\} \end{split}$$

$$(3.105)$$

or when T_{damping} is small:

$$U_{\rm m,max} = \frac{KK_{\rm integrator\,2}T_1\Omega^{\nu}}{2K_{\rm moment}K_{\rm electric\,\, current}T_2^2} \left[\dot{\varphi}_0(C_1 - A_1 + B_1)(\lambda_+ + \lambda_-) + \nu B_1(\lambda_+ - \lambda_-)\right] \tag{3.106}$$

$$U_{\text{m,min}} = \frac{KK_{\text{integrator }2}T_1\Omega^{\nu}}{2K_{\text{moment}}K_{\text{electric current}}T_2^2} [\dot{\varphi}_0(C_1 - A_1 + B_1)(\lambda_- - \lambda_+) - \nu B_1(\lambda_+ + \lambda_-)]$$
(3.107)

Like the analysis of the input signal, although the forms of Eqs. (3.106) and (3.107) are complex and have a relationship with the angular vibration frequency, due to $(\lambda_+ + \lambda_-) > (\lambda_+ - \lambda_-)$, the maximum amplitude of the output signal is mainly determined by the input angular velocity, while the minimum amplitude of the output signal is determined by the amplitude of the input angular acceleration.

Then analyze the dependency relationship between the values of $U_{\rm m,max}$ and $U_{\rm m}$, and the angular oscillation frequency. Compare them with $U_{\rm m,max}(\nu=0)$ and obtain the maximum value of the amplitude of the output signal:

$$\frac{U_{\text{m,max}}}{U_{\text{m,max}}(\nu=0)} = \frac{\dot{\varphi}_0(C_1 - A_1 + B_1)(\lambda_+ + \lambda_-) + \nu B_1(\lambda_+ - \lambda_-)}{2\dot{\varphi}_0(C_1 - A_1 + B_1)\lambda}$$
(3.108)

$$\frac{U_{\text{m,min}}}{U_{\text{m,max}}(\nu=0)} = \frac{\dot{\varphi}_0(C_1 - A_1 + B_1)(\lambda_- - \lambda_+) - \nu B_1(\lambda_+ + \lambda_-)}{2\dot{\varphi}_0(C_1 - A_1 + B_1)\lambda}$$
(3.109)

In order to find out the generality of this result, the coefficient m is introduced, which presents the angular vibration frequency characteristic value, then $v = m\dot{\phi}_0$. At this time, there are

$$\frac{U_{\text{m,max}}}{U_{\text{m,max}}(\nu=0)} = \frac{(\lambda_{+} + \lambda_{-})}{2\lambda} + \frac{m(\lambda_{+} - \lambda_{-})}{2(\mu^{2} + 1)\lambda}$$
(3.110)

$$\frac{U_{\rm m,min}}{U_{\rm m,max}(\nu=0)} = \frac{(\lambda_{-} - \lambda_{+})}{2\lambda} - \frac{m(\lambda_{+} + \lambda_{-})}{2(\mu^{2} + 1)\lambda}$$
(3.111)

Combine Eqs. (1.69), (3.48) and (3.49), and then from Eqs. (3.112) and (3.113) the relative frequency relationship between the maximum value and the minimum value of the output signal envelope can be described by the attenuation coefficient ξ , the detuning coefficient μ and the coefficient m:

$$\begin{split} \frac{U_{\rm m,max}(\nu=0)}{U_{\rm m,max}(\nu=0)} &= \frac{\sqrt{(\mu^2-1)^2+(2\xi\mu)^2}}{2\mu^2} \left[\frac{\mu^2}{\sqrt{\left[\mu^2-(1+m)^2\right]^2+\left[2\xi\mu(1+m)\right]^2}} \right. \\ &\quad + \frac{\mu^2}{\sqrt{\left[\mu^2-(1-m)^2\right]^2+\left[2\xi\mu(1-m)\right]^2}} + \frac{m}{\mu^2+1} \\ &\quad \times \left(\frac{\mu^2}{\sqrt{\left[\mu^2-(1+m)^2\right]^2+\left[2\xi\mu(1-m)\right]^2}} \right) \\ &\quad - \frac{\mu^2}{\sqrt{\left[\mu^2-(1-m)^2\right]^2+\left[2\xi\mu(1-m)\right]^2}} \right) \right] \\ \\ \frac{U_{\rm m,min}}{U_{\rm m,max}(\nu=0)} &= \frac{\sqrt{(\mu^2-1)^2+(2\xi\mu)^2}}{2\mu^2} \left[\frac{\mu^2}{\sqrt{\left[\mu^2-(1-m)^2\right]^2+\left[2\xi\mu(1-m)\right]^2}} \\ &\quad - \frac{\mu^2}{\sqrt{\left[\mu^2-(1+m)^2\right]^2+\left[2\xi\mu(1+m)\right]^2}} - \frac{m}{\mu^2+1} \right. \\ &\quad \times \left(\frac{\mu^2}{\sqrt{\left[\mu^2-(1+m)^2\right]^2+\left[2\xi\mu(1+m)\right]^2}} + \frac{\mu^2}{\sqrt{\left[\mu^2-(1-m)^2\right]^2+\left[2\xi\mu(1-m)\right]^2}} \right) \\ \end{split}$$

(3.113)

In Fig. 3.7, the curves present the relationship between Eqs. (3.112) and (3.113), and the coefficient m under the condition of different detuning coefficients and they also present the relationship with the angular oscillation frequency.

Figure 3.8 gives the relationship curves between Eqs. (3.112) and (3.113) and the coefficient m under the condition of different attenuation coefficients.

Figure 3.8 shows that increasing the damping of the instrument will result in the decrease of the error of the envelop amplitude but while there is angular acceleration of the aircraft the error will increase. Therefore, as has been pointed out previously, when selecting the feedback parameters of the instrument damping it is necessary to compromise and choose an oscillation attenuation coefficient that is close to 0.5. It should also be pointed out that with the increase of the angular oscillation frequency both the amplitude error of the envelope and the error caused by the angular acceleration of the aircraft will increase.

It should be noted that in Figs. 3.7b and 3.8b, on the curve of the characteristic value $\frac{U_{\text{m,min}}}{U_{\text{m,max}}(\nu=0)}$, there is the characteristic maximum value, which can be explained by the following method (Fig. 3.9).

From Fig. 3.9, it is clear that when the angular vibration frequency lies in the limit range of $\dot{\varphi}_0 - \dot{\varphi}_m$, the error $\lambda_- - \lambda_+$ will increase linearly and the increase is directly proportional to the angular vibration frequency. But when $\dot{\varphi}_0 - \nu < \dot{\varphi}_m$, the instrument will leave the line segment of the curve in Fig. 3.9, and the error growth in Figs. 3.7b and 3.8b will stop. Secondly, when $\dot{\varphi}_0 - \nu$ lies in the frequency range that is less than φ_m , the increase of the angular oscillation frequency will cause λ_+ and λ_- to decrease and the error will be reduced. Because $1 > m/(\mu^2 + 1)$, the impact of $\lambda_- - \lambda_+$ on the value of Eq. (3.113) is more powerful than that of $\lambda_- + \lambda_+$. At this time, the angular vibration frequency corresponding to the maximum point in Fig. 3.7b, and is determined by the following expression: $\nu_m = \dot{\varphi}_0 - \dot{\varphi}_m$, or taking into account Eqs. (1.107) and (1.109), there holds

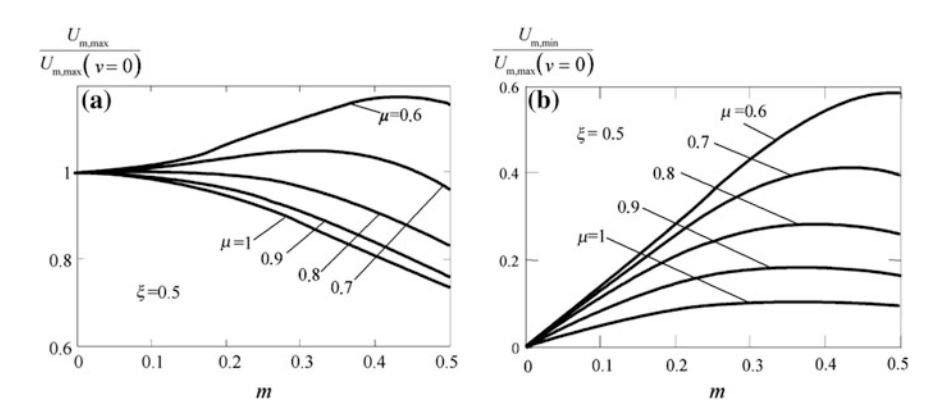


Fig. 3.7 Relationship curves between Eqs. (3.112) and (3.113) and the coefficient m under the condition of different detuning coefficients. **a** Relationship curves between Eq. (3.112) and the coefficient m; **b** Relationship curves between Eq. (3.113) and the coefficient m

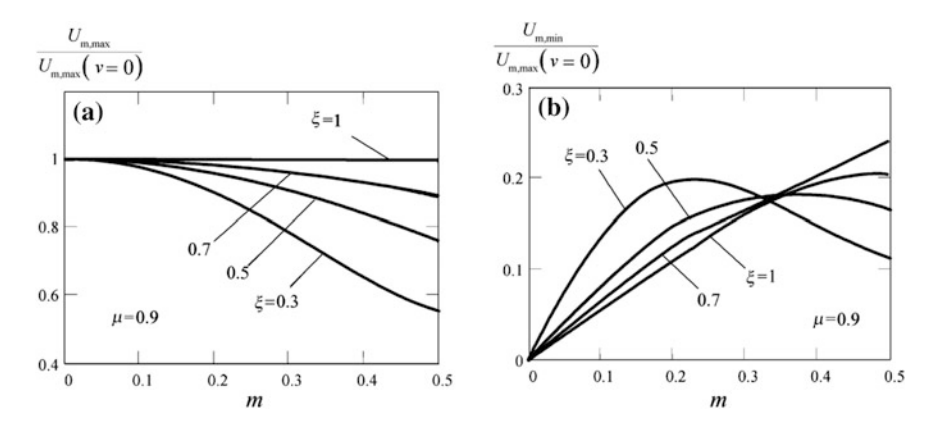
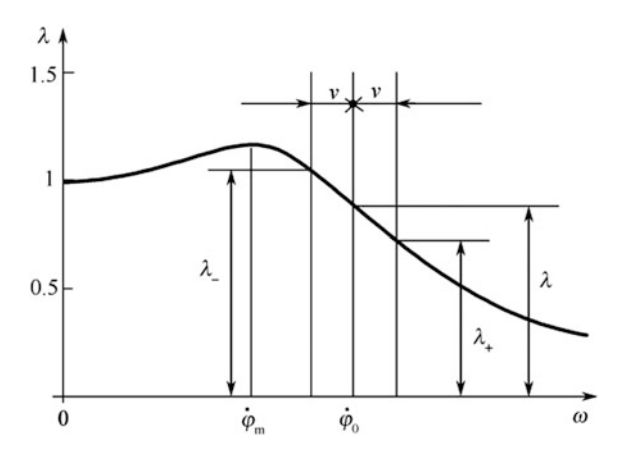


Fig. 3.8 Relationship curves between Eqs. (3.112) and (3.113) and the coefficient m under the condition of different attenuation coefficients. **a** Relationship curves between Eq. (3.112) and the coefficient m; **b** Relationship curves between Eq. (3.113) and the coefficient m

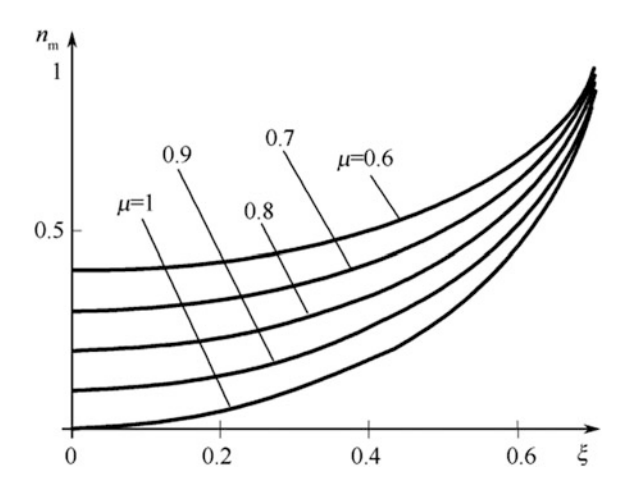
Fig. 3.9 Change of dynamic coefficients with increasing angular vibration frequency



$$v_{\rm m} = \dot{\varphi}_0 \left(1 - \sqrt{\frac{(C_1 - A_1)(1 - 2\xi^2)}{B_1}} \right) = \dot{\varphi}_0 \left(1 - \mu \sqrt{1 - 2\xi^2} \right)$$
 (3.114)

Using Eq. (1.156) obtains

Fig. 3.10 Relationship curve of Eq. (3.116)



$$v_{\rm m} = \dot{\varphi}_0 \left[1 - \sqrt{\frac{(C_1 - A_1)}{B_1}} \left(1 - \frac{D_{\rm feedback}^2}{2B_1(C_1 - A_1)\dot{\varphi}_0^2} \right) \right]$$

$$v_{\rm m} = \dot{\varphi}_0 - \sqrt{\omega_0^2 - \frac{D_{\rm feedback}^2}{2B_1^2}}$$
(3.115)

From Figs. 3.7b and 3.8b, it can be seen that the frequencies of the maximum point of the characteristic curve in these two figures change with the change of the attenuation coefficient. This conclusion can be drawn from Eq. (3.114). By using the coefficient m, from Eq. (3.114), we can obtain:

$$m_{\rm m} = 1 - \mu \sqrt{1 - 2\xi^2} \tag{3.116}$$

Figure 3.10 is the relationship curve of Eq. (3.116).

Only when the vibration attenuation coefficient is less than 0.7 is it reasonable to use Eq. (3.116) because in this range the square root of Eq. (3.116) is positive. When $\xi = 0.7$, in the condition that the instrument is tuned to the resonant point and the tuning coefficient is selected as any value, there holds $m_{\rm m} = 1$, i.e., $v_{\rm m} = \dot{\phi}_0$, the situation corresponds to $\dot{\phi}_{\rm m} = 0$.

When $\xi > 0.7$, the following equation is used:

$$m_{\rm m} = 1 + \mu \sqrt{2\xi^2 - 1} \tag{3.117}$$

Now analyze the phase of the output signal envelope. The phase of the output signal envelope is determined by $\chi_o = \frac{\chi_+ - \chi_-}{2}$. Combine Eqs. (3.70) and (3.71) and obtain

$$\begin{split} \chi_{\text{o}} &= \frac{1}{2} \left\{ \arctan \left[T_{\text{damping}}(\dot{\phi}_{0} + \nu) \right] + \arctan \left[T_{1}(\dot{\phi}_{0} + \nu) \right] \right. \\ &- \arctan \left[\frac{2\xi_{\text{integrator}} T_{2}(\dot{\phi}_{0} + \nu)}{1 - T_{2}^{2}(\dot{\phi}_{0} + \nu)^{2}} \right] - \arctan \left[\frac{2\xi T_{0}(\dot{\phi}_{0} + \nu)}{1 - T_{0}^{2}(\dot{\phi}_{0} + \nu)^{2}} \right] \\ &- \arctan \left[T_{\text{damping}}(\dot{\phi}_{0} - \nu) \right] - \arctan \left[T_{1}(\dot{\phi}_{0} - \nu) \right] \\ &+ \arctan \left[\frac{2\xi_{\text{integrator}} T_{2}(\dot{\phi}_{0} - \nu)}{1 - T_{2}^{2}(\dot{\phi}_{0} - \nu)^{2}} \right] + \arctan \left[\frac{2\xi T_{0}(\dot{\phi}_{0} - \nu)}{1 - T_{2}^{2}(\dot{\phi}_{0} - \nu)^{2}} \right] \right\} \\ \chi_{\text{o}} &= \frac{1}{2} \left\{ \arctan \left[T_{\text{damping}} \dot{\phi}_{0}(1 + m) \right] + \arctan \left[T_{1} \dot{\phi}_{0}(1 + m) \right] \right. \\ &- \arctan \left[\frac{2\xi_{\text{integrator}} T_{2} \dot{\phi}_{0}(1 + m)}{1 - T_{2}^{2} \dot{\phi}_{0}^{2}(1 + m)^{2}} \right] - \arctan \left[\frac{2\xi \mu (1 + m)}{\mu^{2} - (1 + m)^{2}} \right] \\ &- \arctan \left[T_{\text{damping}} \dot{\phi}_{0}(1 - m) \right] - \arctan \left[T_{1} \dot{\phi}_{0}(1 - m) \right] \\ &+ \arctan \left[\frac{2\xi_{\text{integrator}} T_{2} \dot{\phi}_{0}(1 - m)}{1 - T_{2}^{2} \dot{\phi}_{0}^{2}(1 - m)^{2}} \right] + \arctan \left[\frac{2\xi \mu (1 - m)}{\mu^{2} - (1 - m)^{2}} \right] \right\} \end{split}$$

Figure 3.11 shows the relationship curve between the phase of the output signal envelope and the angular vibration frequency of the aircraft in the condition of different time constants T_{damping} , T_1 and T_2 with different attenuation coefficients and different detuning coefficients.

When drawing the curve in Fig. 3.11, the following parameters are used: $T_{\rm damping} = 0.01$ s; $T_1 = 0.1$ s; $T_2 = 0.1$ s; $\xi_{\rm integrator} = 1$.

According to Eq. (3.119) and Fig. 3.11, in order to reduce the phase shift of the instrument output signal envelope due to the angular vibration frequency of the aircraft, the damping effect of feedback must be enhanced.

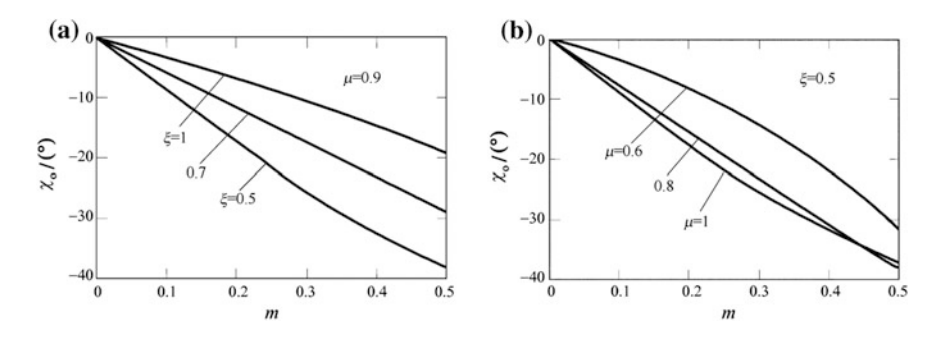


Fig. 3.11 Phase shift of the output signal envelope. a Different attenuation coefficients; b Different detuning coefficients

3. Ratio of the output signal amplitude and the input signal amplitude

The phase shift between the input signal and the output signal in Eq. (3.100) is determined only by the phase shift χ_0 of the output signal envelope. So, the maximum amplitude ratio of the output signal and the input signal (assume that χ_0 equals to zero):

$$\frac{U_{\rm m,max}}{M_{\rm m,max}} = \frac{U_1 + U_2}{H_0 \Omega^{\nu}}$$
 (3.120)

Obviously, because the denominator of this expression is constant, according to the characteristics and the form of the relationship curve the ratio in Eq. (3.120) corresponds to Figs. 3.7a and 3.8a respectively. It should be noted that in order to obtain the generality of the results Eq. (3.120) is replaced by the following equation:

$$\frac{U_{\text{m,max}}/U_{\text{m,max}}(v=0)}{M_{\text{m max}}/M_{\text{m max}}(v=0)} = \frac{U_{\text{m,max}}}{U_{\text{m max}}(v=0)}$$
(3.121)

This is entirely consistent with Eq. (3.112), Figs. 3.7a and 3.8a.

The comparison of the minimum amplitude of the output signal and the input signal is better carried out by using the relative value:

$$\frac{U_{\text{m,min}}/U_{\text{m,max}}(\nu=0)}{M_{\text{m,min}}/M_{\text{m,max}}(\nu=0)} = \frac{\frac{(\lambda-\lambda+)}{2\lambda} - m\frac{(\lambda+\lambda-)}{2(\mu^2+1)\lambda}}{\frac{m}{\mu^2+1}}$$
(3.122)

Consider Eq. (3.113), this equation has the following form:

$$\begin{split} \frac{U_{\text{m,min}}/U_{\text{m,max}}(\nu=0)}{M_{\text{m,min}}/M_{\text{m,max}}(\nu=0)} &= \frac{\sqrt{(\mu^2-1)^2+(2\xi\mu)^2}}{2\mu^2} \left[-\frac{\mu^2+1}{m} \right. \\ &\times \left(\frac{\mu^2}{\sqrt{\left[\mu^2-(1-m)^2\right]^2+\left[2\xi\mu(1-m)\right]^2}} + \frac{\mu^2}{\sqrt{\left[\mu^2-(1+m)^2\right]^2+\left[2\xi\mu(1+m)\right]^2}} \right) \\ &- \frac{\mu^2}{\sqrt{\left[\mu^2-(1+m)^2\right]^2+\left[2\xi\mu(1+m)\right]^2}} + \frac{\mu^2}{\sqrt{\left[\mu^2-(1-m)^2\right]^2+\left[2\xi\mu(1-m)\right]^2}} \\ &\left. (3.123) \right. \end{split}$$

The relationship curve of Eq. (3.123) and m is shown in Fig. 3.12. These curves are plotted in the condition of different vibration attenuation coefficients, detuning coefficients and m.

Because the aircraft has an angular acceleration, reducing the error of the instrument is related to the increase of the damping and the accuracy of tuning to the resonant point. At this time, with the increase of the angular vibration frequency the relative cross error will decrease. This phenomenon is explained by the fact that the growth rate of the cross component of the input signal is faster than that of the

cross component of the output signal. It should be noted that according to Eq. (3.123), when the angular vibration frequency of the aircraft is zero, namely when m = 0, although both the relative cross component of the output signal and the relative cross component of the input signal are equal to zero, because of its uncertainty their ratio can be taken as 1.

Because the phase shift and the amplitude in the output signal envelope are dependent on the angular vibration frequency of the aircraft, at each moment the relationship between the envelope values and these oscillation frequencies is determined like the impact of the angular oscillation frequency of the craft on the envelope amplitude and the phase shift of the output signal. At each moment, the envelope ratio of the input signal and the output signal is determined by (3.100). It is evident that this ratio is maximal when its numerator is a maximum value and when its numerator is a minimum value, this ratio is minimal.

Therefore, three frequency relations can be used to evaluate the envelope relationship between the output signal and the input signal.

- (1) The frequency relationship curves of the maximum value (Figs. 3.7a and 3.8a, Eq. (3.112)), will indicate the following features: how much the most likely value of the output signal corresponds to that of the input signal.
- (2) The frequency curves of the minimum value (Fig. 3.12, Eq. (3.123)) indicate the following features: only determined by the oscillation angular acceleration of the aircraft, that is, how much the most possible value of the output signal corresponds to that of the input signal determined only by the oscillation angular acceleration of the aircraft, and also indicates that the torque level caused by the instrument processing angular acceleration of the aircraft and naturely is the frequency characteristics of the instrument relative error caused by the angular acceleration of the aircraft.
- (3) The frequency relationship curves of the envelope phase (Fig. 3.11, Eq. (3.119)), indicate the phase shift characteristics between the envelopes of

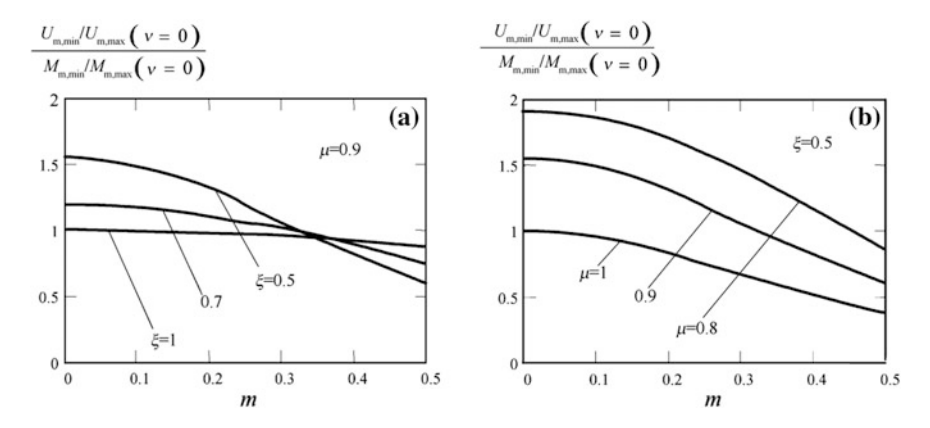


Fig. 3.12 Relationship curve between Eq. (3.123) and m. a Different attenuation coefficients; b Different detuning coefficients

the input signal and the output signal envelope and determine how long the input signal can find its reflected signal in the output signal.

If these three relationships are mastered, the envelope of the input signal can be completely transformed into the envelope relationship of the output signal.

However, in order to evaluate the working correctness of the instrument on the aircraft, the phase correctness of the carrier wave of the output signal must be determined, in other words the phase of the rotation frequency of the aircraft.

In order to describe the carrier wave of the output signal and compare it with the carrier wave of the input signal, a phase frequency relationship curve is added, which represents the difference characteristics of the carrier phase shift of the output signal with respect to the carrier phase shift of the input signal.

2. Phase comparison

For the envelope phase, it can be understood that the phase is within the limit range of v/2, the corresponding phase of the carrier wave lies in the period range of $1/\dot{\phi}_0$, so the phase of the carrier wave of the output signal is equal to $\chi_{\rm m}$, and the phase of the carrier wave of the input signal is equal to $\chi_{\rm inp.m.}$

The carrier wave phases of the input signal and the output signal are intricately connected with the time, however, it should be noted that the carrier wave phases Eqs. (3.79) and (3.98) are indirectly added into the envelope phase shift of two signals. The envelope phase shift of the input signal equals zero, while the envelope phase shift of the output signal depends on χ_+ and χ_- , and these two phases affect the carrier wave phase of the output signal by $\arctan\left(\frac{U_{S-}}{U_{C-}}\right)$ and $\arctan\left(\frac{U_{S+}}{U_{C+}}\right)$.

When considering χ_+ and χ_- , the influence of the phase shift of the carrier wave on the phase of the carrier wave of the output signal is excluded. In this case, Fig. 3.13 gives the amplitude and phase of the output signal and the input signal after the rotation frequency around its longitudinal axis of the aircraft is compensated by a constant phase shift, and when the instrument is mounted to the body of the aircraft, the compensation is performed by turning the instrument base. In this case, Fig. 3.13 can be transformed into Fig. 3.14.

It is obvious that the phases of the output signal and the input signal in Fig. 3.14 are changed by 180°. In order to agree with Fig. 3.14, two instantaneous time symbols are introduced:

- t_1 When the envelope of the input signal is at the moment of the maximum value;
- t_2 When the envelope of the input signal is at the moment of the minimum value.

Figure 3.14 shows the graphic similarity and some differences of the phase values of the input signal and the output signal. At this time, it should be considered that in order to make the output signal and the input signal have the amplitude modulation, the tangent value of the signal phase must remain constant. The only moment that satisfies the condition is t_1 , that is, the moment that the measured angular velocity is the maximum value and close to this value.

Fig. 3.13 Amplitude and the phase of the output signal and the input signal after being compensated by a constant phase shift χ_0

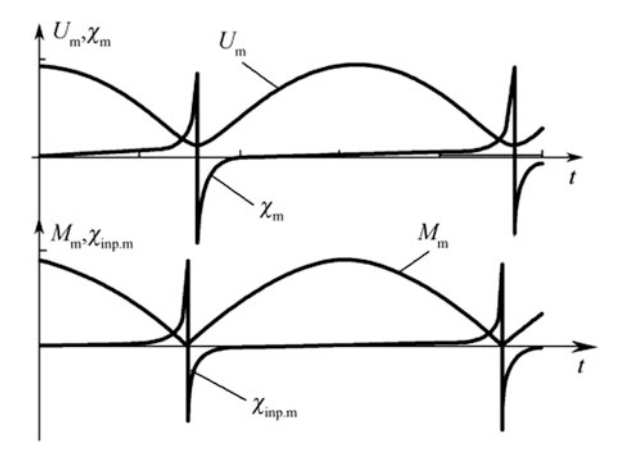
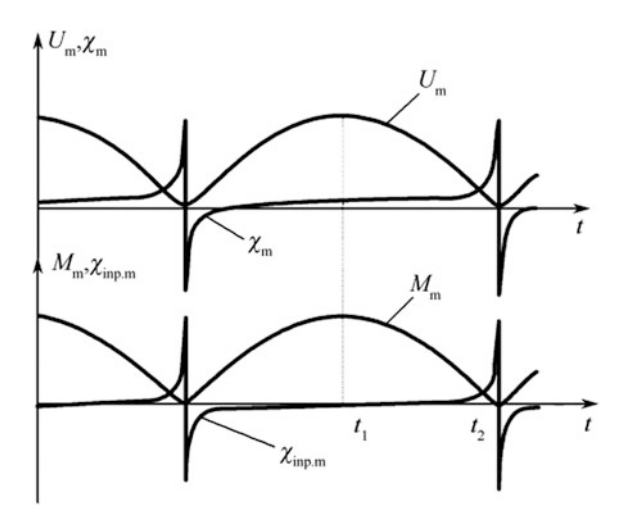


Fig. 3.14 Amplitude and phase of the output signal and the input signal after being compensated by a constant phase shift χ_0 and the envelope phase shift



Therefore, these signals are not pure amplitude modulations. It should be noted that the use of the instrument is to measure the angular velocity, and thus, when the measured angular velocity of the aircraft is at a maximum value, or in other words the carrier phase in the moment t_1 . The phase difference between the output and the input signal is determined by:

$$\begin{split} \chi_{\mathrm{m}} - \chi_{\mathrm{inp,m}} &= \arctan \left\{ \frac{\sqrt{U_{C-}^2 + U_{S+}^2} \sin \left[vt - \frac{\left(\chi_+ - \chi_-\right)}{2} + \arctan\left(\frac{U_{S+}}{U_{C-}}\right) \right]}{\sqrt{U_{C+}^2 + U_{S-}^2} \cos \left[vt - \frac{\left(\chi_+ - \chi_-\right)}{2} + \arctan\left(\frac{U_{S-}}{U_{C+}}\right) \right]} \right\} \\ &- \arctan\left[\frac{vB_1}{H} \tan(vt) \right] \end{split} \tag{3.124}$$

When T_{damping} and nT_{amplify} are very small, T_1 and T_2 are very large, the phase error in Eq. (3.124) is expressed by the detuning coefficient, the attenuation coefficient and the coefficient m:

$$\begin{split} \chi_{\rm m} - \chi_{\rm inp,m} &= \arctan \left\{ \sqrt{\frac{\left[(\mu^2+1) + m \right]^2 \lambda_+^2 + \left[(\mu^2+1) - m \right]^2 \lambda_-^2 - 2 \left[(\mu^2+1)^2 - m^2 \right] \lambda_+ \lambda_- \cos \left(\chi_+ + \chi_- \right)}{\left[(\mu^2+1) + m \right]^2 \lambda_+^2 + \left[(\mu^2+1) - m \right]^2 \lambda_-^2 + 2 \left[(\mu^2+1)^2 - m^2 \right] \lambda_+ \lambda_- \cos \left(\chi_+ + \chi_- \right)} \right. \\ &\times \frac{\sin \left[m \dot{\phi}_0 t - \frac{\chi_+ - \chi_-}{2} + \arctan \left(\frac{\left[(\mu^2+1) + m \right] \lambda_+ \sin \chi_+ + \left[(\mu^2+1) - m \right] \lambda_- \sin \chi_-}{\left[(\mu^2+1) + m \right] \lambda_+ \cos \chi_+ + \left[(\mu^2+1) - m \right] \lambda_- \cos \chi_-} \right) \right]}{\cos \left[m \dot{\phi}_0 t - \frac{\chi_+ - \chi_-}{2} + \arctan \left(\frac{\left[(\mu^2+1) + m \right] \lambda_+ \sin \chi_+ - \left[(\mu^2+1) - m \right] \lambda_- \sin \chi_-}{\left[(\mu^2+1) + m \right] \lambda_+ \cos \chi_+ + \left[(\mu^2+1) - m \right] \lambda_- \cos \chi_-} \right) \right]} \right\} \\ &- \arctan \left(\frac{m}{(\mu^2+1)} \tan (m \dot{\phi}_0 t) \right) \end{split}$$

Under different angular vibration frequencies, or different coefficients m, different attenuation coefficients and different detuning coefficients, the relationship between the phase difference in Eq. (3.125) and the time is shown in Fig. 3.15.

According to Fig. 3.15, it can be determined that in almost the entire half-cycle of the angular oscillation frequency, except the moment approaching t_2 (Fig. 3.15) that the phase difference of the carrier wave of the output signal and the input signal is actually constant (at the moment approaching t_1), and with the increase of the attenuation coefficients and the detuning harmonic coefficients, the variety degree of the dependent relationship of the phase difference and the time is small, and within the time range always presents a stable state, namely the peak values of the curves in Fig. 3.15a and b are squeezed and flattened. From Fig. 3.15b, it can clearly be seen that at the moment t_1 , the phase difference in Eq. (3.125) increases with the increase of the angular vibration frequency, however, it can be found that the peak value in the same curve decreases with the increase of the angular vibration frequency. The relationship curve of the phase difference between the carrier waves of the output signal and the input signal changes with the angular vibration frequency, the attenuation coefficient and the detuning coefficients and will be used later.

In order to describe Eq. (3.125) and the curve in Fig. 3.15, the phase difference of the carrier wave of the output signal and the input signal is broken down into two components. Of these two components, one is a constant component $\chi_{\text{carrier wave 0}}$ determined at the moment t_1 , and is also the phase shift of an effective signal, while

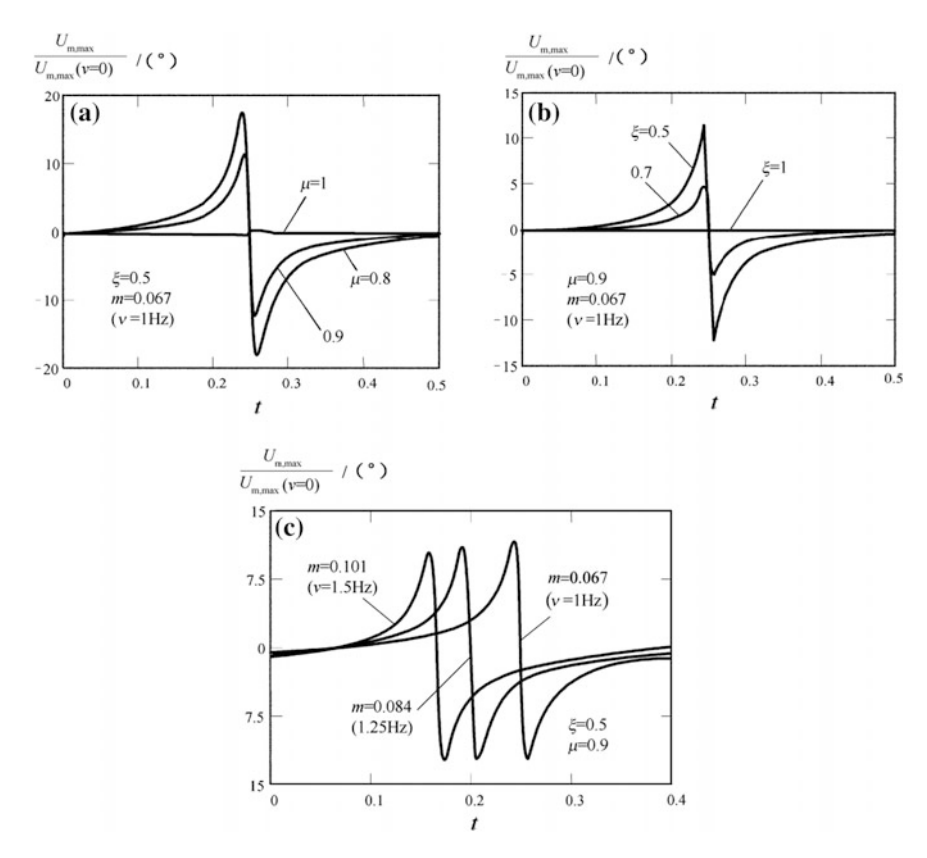
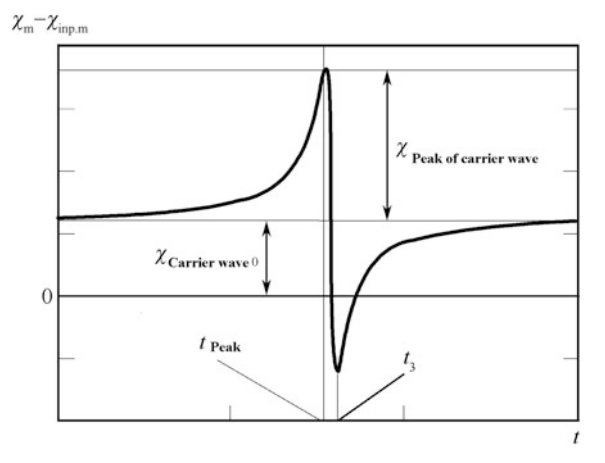


Fig. 3.15 Relationship curves between $\frac{U_{\text{in,max}}}{U_{\text{in,max}}(v_0)}$ and different coefficients (m, μ, ξ) . **a** Different detuning coefficients; **b** Different attenuation coefficients; **c** Different coefficients m

Fig. 3.16 Schematic diagram of the phase difference of the carrier wave broken down into two components



the other is a component $\chi_{\text{carrier wave peak}}$ with a peak shape change, which presents the phase difference in Eq. (3.107) at its peak moment surpassing the difference of the constant component (Fig. 3.16), which represents the phase shift characteristics of the output signal with respect to the input signal, while the phase shift, because the angular acceleration of the aircraft is subject to some constraints actually represents the phase shift characteristics of the instrument error due to the angular acceleration of the aircraft. When $m\dot{\phi}_0 t = 2\pi n, n \in Z$, i.e.,

$$t = \frac{2\pi n}{m\dot{\varphi}_0} \tag{3.126}$$

the value of $\chi_{carrier\ wave\ 0}$ is determined by Eq. (3.125).

From Fig. 3.16, the value of $\chi_{\text{carrier wave peak}}$ can be obtained by Eq. (3.125) at the moment t_{peak} . Now determine t_{peak} , $\chi_{\text{carrier wave 0}}$ and $\chi_{\text{carrier wave peak}}$.

Substituting Eq. (3.126) into Eq. (3.125) obtains

$$\begin{split} \chi_{\text{carrier wave 0}} &= \arctan \Bigg\{ \sqrt{\frac{\left[(\mu^2+1) + m \right]^2 \lambda_+^2 + \left[(\mu^2+1) - m \right]^2 \lambda_-^2 - 2 \left[(\mu^2+1)^2 - m^2 \right] \lambda_+ \lambda_- \cos \left(\chi_+ + \chi_- \right)}{\left[(\mu^2+1) + m \right]^2 \lambda_+^2 + \left[(\mu^2+1) - m \right]^2 \lambda_-^2 + 2 \left[(\mu^2+1)^2 - m^2 \right] \lambda_+ \lambda_- \cos \left(\chi_+ + \chi_- \right)} \\ &\times \frac{\sin \left[-\frac{\chi_+ - \chi_-}{2} + \arctan \left(\frac{\left[(\mu^2+1) + m \right] \lambda_+ \sin \chi_+ + \left[(\mu^2+1) - m \right] \lambda_- \sin \chi_-}{\left[(\mu^2+1) + m \right] \lambda_+ \cos \chi_+ - \left[(\mu^2+1) - m \right] \lambda_- \cos \chi_-} \right) \right]} \\ &\times \frac{\cos \left[-\frac{\chi_+ - \chi_-}{2} + \arctan \left(\frac{\left[(\mu^2+1) + m \right] \lambda_+ \sin \chi_+ - \left[(\mu^2+1) - m \right] \lambda_- \cos \chi_-}{\left[(\mu^2+1) + m \right] \lambda_+ \cos \chi_+ + \left[(\mu^2+1) - m \right] \lambda_- \cos \chi_-} \right) \right]} \\ & \\ &\times \frac{\cos \left[-\frac{\chi_+ - \chi_-}{2} + \arctan \left(\frac{\left[(\mu^2+1) + m \right] \lambda_+ \sin \chi_+ - \left[(\mu^2+1) - m \right] \lambda_- \sin \chi_-}{\left[(\mu^2+1) + m \right] \lambda_+ \cos \chi_+ + \left[(\mu^2+1) - m \right] \lambda_- \cos \chi_-} \right) \right]} \\ & \\ &\times \frac{\cos \left[-\frac{\chi_+ - \chi_-}{2} + \arctan \left(\frac{\left[(\mu^2+1) + m \right] \lambda_+ \sin \chi_+ - \left[(\mu^2+1) - m \right] \lambda_- \sin \chi_-}{\left[(\mu^2+1) + m \right] \lambda_+ \cos \chi_+ + \left[(\mu^2+1) - m \right] \lambda_- \cos \chi_-} \right) \right]} \\ & \\ &\times \frac{\cos \left[-\frac{\chi_+ - \chi_-}{2} + \arctan \left(\frac{\left[(\mu^2+1) + m \right] \lambda_+ \sin \chi_+ - \left[(\mu^2+1) - m \right] \lambda_- \sin \chi_-}{\left[(\mu^2+1) + m \right] \lambda_+ \cos \chi_+ + \left[(\mu^2+1) - m \right] \lambda_- \cos \chi_-} \right) \right]} \\ & \\ &\times \frac{\cos \left[-\frac{\chi_+ - \chi_-}{2} + \arctan \left(\frac{\left[(\mu^2+1) + m \right] \lambda_+ \sin \chi_+ - \left[(\mu^2+1) - m \right] \lambda_- \cos \chi_-}{\left[(\mu^2+1) + m \right] \lambda_+ \cos \chi_+ + \left[(\mu^2+1) - m \right] \lambda_- \cos \chi_-} \right) \right]} \\ & \\ &\times \frac{\sin \left[-\frac{\chi_+ - \chi_-}{2} + \arctan \left(\frac{\left[(\mu^2+1) + m \right] \lambda_+ \sin \chi_+ - \left[(\mu^2+1) - m \right] \lambda_- \cos \chi_-}{\left[(\mu^2+1) + m \right] \lambda_+ \cos \chi_+ + \left[(\mu^2+1) - m \right] \lambda_- \cos \chi_-} \right) \right]} \\ &\times \frac{\sin \left[-\frac{\chi_+ - \chi_-}{2} + \arctan \left(\frac{\left[(\mu^2+1) + m \right] \lambda_+ \sin \chi_+ - \left[(\mu^2+1) - m \right] \lambda_- \cos \chi_-}{\left[(\mu^2+1) + m \right] \lambda_+ \cos \chi_+ + \left[(\mu^2+1) - m \right] \lambda_- \cos \chi_-} \right) \right]} \\ &\times \frac{\sin \left[-\frac{\chi_+ - \chi_+}{2} + \arctan \left(\frac{\left[(\mu^2+1) + m \right] \lambda_+ \cos \chi_+}{\left[(\mu^2+1) + m \right] \lambda_+ \cos \chi_+} \right]} \\ &\times \frac{\sin \left[-\frac{\chi_+ - \chi_+}{2} + \arctan \left(\frac{\chi_+ - \chi_+}{2} + \frac{\chi_+ - \chi_+}{2} \right)} \\ &\times \frac{\sin \left[-\frac{\chi_+ - \chi_+}{2} + \frac{\chi_+ - \chi_+}{$$

Figure 3.17 gives the relationship curves between different tuning coefficients, attenuation coefficients and coefficient m respectively. From Fig. 3.17, it can be seen that with an increase of the instrument damping effect, $\chi_{\text{carrier wave 0}}$ decreases; with an increase of the angular oscillation frequency, $\chi_{\text{carrier wave 0}}$ increases; and when the tuning accuracy decreases, $\chi_{\text{carrier wave 0}}$ shows a small increase.

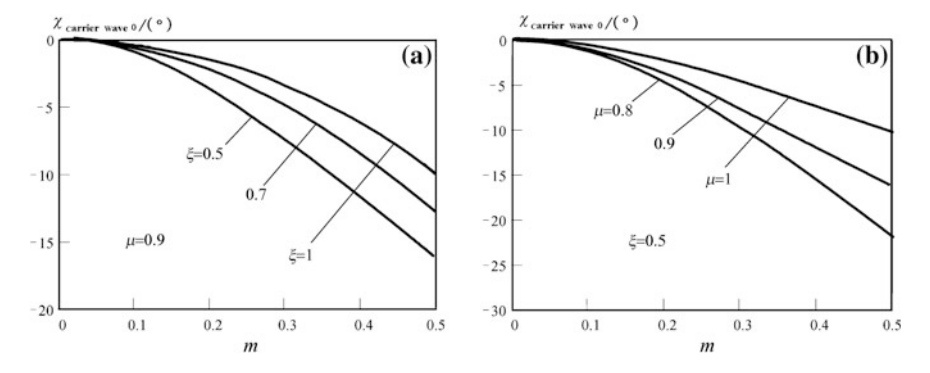


Fig. 3.17 Relationship curves of $\chi_{\text{carrier wave 0}}$ and m. a Different attenuation coefficients; b Different detuning coefficients

In order to compute the component $\chi_{\text{carrier wave peak}}$ with the change of peak shape, it is necessary to determine the instantaneous time t_{peak} which corresponds to the peak of the phase difference of the carrier wave. Obviously, t_{peak} corresponds to the instantaneous time that the phase curve slopes of the carrier waves of the output signal and the input signal are equal, or in other words when the derivative of the expression for the phase difference of the carrier wave is equal to zero. In order to simplify the calculation the shorter form is used. And from the phase difference of the carrier waves of the output signal and the input signal in Eq. (3.124), denote the symbol $\chi_p = \chi_m - \chi_{\text{inp.m}}$:

$$\left(\chi_{p}\right)' = \frac{\sqrt{\frac{U_{C-}^{2} + U_{S+}^{2}}{U_{C+}^{2} + U_{S-}^{2}}} v \cos\left[\arctan\left(\frac{U_{S+}}{U_{C-}}\right) - \arctan\left(\frac{U_{S-}}{U_{C+}}\right)\right]}{1 + \left\{\sqrt{\frac{U_{C-}^{2} + U_{S+}^{2}}{U_{C+}^{2} + U_{S-}^{2}}} \frac{\sin\left[vt - \frac{(x_{+} - x_{-})}{2} + \arctan\left(\frac{U_{S-}}{U_{C-}}\right)\right]}{\cos\left[vt - \frac{(x_{+} - x_{-})}{2} + \arctan\left(\frac{U_{S-}}{U_{C+}}\right)\right]}\right\}^{2}} - \frac{\frac{vB_{1}}{H}v\frac{1}{\cos^{2}(vt)}}{1 + \left[\frac{vB_{1}}{H}\tan(vt)\right]^{2}}$$

Rewrite the last expression:

$$(\chi_{p})' = \frac{\frac{\Lambda_{1} v \cos(\Lambda_{2} - \Lambda_{3})}{\cos^{2}(vt + \Lambda_{3})}}{1 + \left[\Lambda_{1} \frac{\sin(vt + \Lambda_{2})}{\cos(vt + \Lambda_{3})}\right]^{2}} - \frac{\Lambda_{4} v \frac{1}{\cos^{2}(vt)}}{1 + \left[\Lambda_{4} \tan(vt)\right]^{2}}$$
 (3.128)

where

$$\Lambda_1 = \sqrt{\frac{U_{C-}^2 + U_{S+}^2}{U_{C+}^2 + U_{S-}^2}}$$
 (3.129)

$$\Lambda_2 = -\frac{\left(\chi_+ - \chi_-\right)}{2} + \arctan\left(\frac{U_{S+}}{U_{C-}}\right) \tag{3.130}$$

$$\Lambda_3 = -\frac{\left(\chi_+ - \chi_-\right)}{2} + \arctan\left(\frac{U_{S-}}{U_{C+}}\right) \tag{3.131}$$

$$\Lambda_4 = \frac{\nu B_1}{H} \tag{3.132}$$

Set Eq. (3.128) to zero, and there holds

$$\frac{\Lambda_1 v \cos(\Lambda_2 - \Lambda_3)}{\cos^2(vt + \Lambda_3) + \Lambda_1^2 \sin^2(vt + \Lambda_2)} - \frac{\Lambda_4 v}{\cos^2(vt) + \Lambda_4^2 \sin^2(vt)} = 0$$

$$\frac{\Lambda_{1}v\cos(\Lambda_{2} - \Lambda_{3})}{(\cos\Lambda_{3} - \tan(vt)\sin\Lambda_{3})^{2} + \Lambda_{1}^{2}(\tan(vt)\cos\Lambda_{2} + \sin\Lambda_{2})^{2}} - \frac{\Lambda_{4}}{1 + \Lambda_{4}^{2}\tan^{2}(vt)} = 0$$

$$\begin{split} & \Lambda_{1}\cos(\Lambda_{2} - \Lambda_{3}) + \Lambda_{1}\cos(\Lambda_{2} - \Lambda_{3})\Lambda_{4}^{2}\tan^{2}(vt) = \Lambda_{4}\cos^{2}\Lambda_{3} \\ & - 2\Lambda_{4}\cos\Lambda_{3}\tan(vt)\sin\Lambda_{3} + \Lambda_{4}\tan^{2}(vt)\sin^{2}\Lambda_{3} + \Lambda_{4}\Lambda_{1}^{2}\tan^{2}(vt)\cos^{2}\Lambda_{2} \\ & + 2\Lambda_{4}\Lambda_{1}^{2}\tan(vt)\cos\Lambda_{2}\sin\Lambda_{2} + \Lambda_{4}\Lambda_{1}^{2}\sin^{2}\Lambda_{2}\left(\Lambda_{4}\Lambda_{1}^{2}\cos^{2}\Lambda_{2} + \Lambda_{4}\sin^{2}\Lambda_{3} - \Lambda_{1}\cos(\Lambda_{2} - \Lambda_{3})\Lambda_{4}^{2}\right)\tan^{2}(vt) + 2\Lambda_{4}\left(-\cos\Lambda_{3}\sin\Lambda_{3} + \Lambda_{1}^{2}\cos\Lambda_{2}\sin\Lambda_{2}\right)\tan(vt) \\ & + \left(\Lambda_{4}\cos^{2}\Lambda_{3} + \Lambda_{4}\Lambda_{1}^{2}\sin^{2}\Lambda_{2} - \Lambda_{1}\cos(\Lambda_{2} - \Lambda_{3})\right) = 0 \end{split}$$

$$(3.133)$$

Equation (3.133) is a second-order equation with the independent variable tan(vt). Next analyze the general form of Eq. (3.133) and the coefficient before the first order independent variable, and take into account Eqs. (3.82)–(3.85):

$$\begin{split} & 2 \mathcal{I}_{4} \Big(-\cos \mathcal{A}_{3} \sin \mathcal{A}_{3} + \mathcal{A}_{1}^{2} \cos \mathcal{A}_{2} \sin \mathcal{A}_{2} \Big) = \\ & 2 \frac{vB_{1}}{H} \left\{ -\left[\cos \left(\frac{\chi_{-} - \chi_{+}}{2} \right) \frac{U_{C+}}{\sqrt{U_{S-}^{2} + U_{C+}^{2}}} - \sin \left(\frac{\chi_{-} - \chi_{+}}{2} \right) \frac{U_{S-}}{\sqrt{U_{S-}^{2} + U_{C+}^{2}}} \right] \\ & \times \left[\sin \left(\frac{\chi_{-} - \chi_{+}}{2} \right) \frac{U_{C+}}{\sqrt{U_{S-}^{2} + U_{C+}^{2}}} + \cos \left(\frac{\chi_{-} - \chi_{+}}{2} \right) \frac{U_{S-}}{\sqrt{U_{S-}^{2} + U_{C+}^{2}}} \right] \\ & + \frac{U_{C-}^{2} + U_{S-}^{2}}{U_{C+}^{2} + U_{S+}^{2}} \left[\sin \left(\frac{\chi_{-} - \chi_{+}}{2} \right) \frac{U_{C-}}{\sqrt{U_{S+}^{2} + U_{C-}^{2}}} + \cos \left(\frac{\chi_{-} - \chi_{+}}{2} \right) \frac{U_{S+}}{\sqrt{U_{S+}^{2} + U_{C-}^{2}}} \right] \\ & \times \left[\cos \left(\frac{\chi_{-} - \chi_{+}}{2} \right) \frac{U_{C-}}{\sqrt{U_{S+}^{2} + U_{C-}^{2}}} - \sin \left(\frac{\chi_{-} - \chi_{+}}{2} \right) \frac{U_{S+}}{\sqrt{U_{S+}^{2} + U_{C-}^{2}}} \right] \right\} \end{split}$$

Obviously, substituting Eq. (3.72) into the obtained expression obtains that this equation is equal to zero. In this case, solve Eq. (3.133) and obtain

$$\tan(\nu t) = \sqrt{\frac{-\Lambda_4 \cos^2 \Lambda_3 - \Lambda_4 \Lambda_1^2 \sin^2 \Lambda_2 + \Lambda_1 \cos(\Lambda_2 - \Lambda_3)}{\Lambda_4 \Lambda_1^2 \cos^2 \Lambda_2 + \Lambda_4 \sin^2 \Lambda_3 - \Lambda_1 \cos(\Lambda_2 - \Lambda_3)\Lambda_4^2}}$$
(3.134)

Substitute Eqs. (3.129)–(3.132) into Eq. (3.134), and obtain

$$\begin{split} \tan(vt) &= \left[\left\{ -\frac{vB_1}{H} \left[\frac{U_{C+}}{\sqrt{U_{C+}^2 + U_{S-}^2}} \cos\left(\frac{\chi_- - \chi_+}{2}\right) - \frac{U_{S-}}{\sqrt{U_{C+}^2 + U_{S-}^2}} \sin\left(\frac{\chi_- - \chi_+}{2}\right) \right]^2 \right. \\ &- \frac{vB_1}{H} \frac{U_{S+}^2 + U_{C-}^2}{U_{C+}^2 + U_{S-}^2} \left[\frac{U_{S+}}{\sqrt{U_{C-}^2 + U_{S+}^2}} \cos\left(\frac{\chi_- - \chi_+}{2}\right) + \frac{U_{C-}}{\sqrt{U_{C-}^2 + U_{S+}^2}} \sin\left(\frac{\chi_- - \chi_+}{2}\right) \right]^2 \\ &+ \sqrt{\frac{U_{S+}^2 + U_{C-}^2}{U_{C+}^2 + U_{S-}^2}} \frac{U_{C+}U_{C-} - U_{S-}U_{S+}}{\left(U_{C+}^2 + U_{C-}^2\right)} \right\} / \left\{ \frac{vB_1}{H} \left[\frac{U_{S-}}{\sqrt{U_{C+}^2 + U_{S-}^2}} \cos\left(\frac{\chi_- - \chi_+}{2}\right) + \frac{U_{C+}^2}{2} \cos\left(\frac{\chi_- - \chi_+}{2}\right) \right] \right. \\ &+ \left. \frac{U_{C+}}{\sqrt{U_{C+}^2 + U_{S-}^2}} \sin\left(\frac{\chi_- - \chi_+}{2}\right) \right]^2 + \frac{vB_1}{H} \frac{U_{S+}^2 + U_{C-}^2}{U_{C+}^2 + U_{S-}^2} \left[\frac{U_{C-}}{\sqrt{U_{C-}^2 + U_{S+}^2}} \cos\left(\frac{\chi_- - \chi_+}{2}\right) - \frac{U_{S+}}{\sqrt{U_{C-}^2 + U_{S+}^2}} \sin\left(\frac{\chi_- - \chi_+}{2}\right) \right]^2 \\ &- \left. \frac{U_{S+}}{\sqrt{U_{C-}^2 + U_{S+}^2}} \sin\left(\frac{\chi_- - \chi_+}{2}\right) \right]^2 - \left(\frac{vB_1}{H}\right)^2 \sqrt{\frac{U_{S+}^2 + U_{C-}^2}{U_{C+}^2 + U_{S-}^2}} \frac{U_{C-}U_{C+} + U_{S-}U_{S+}}{\left(U_{C+}^2 + U_{S-}^2\right) \left(U_{S+}^2 + U_{C-}^2\right)} \right]^2 \end{split}$$

Transform Eq. (3.72) and obtain

$$\tan(\nu t) = \sqrt{\frac{\left(U_{+}^{2} - U_{-}^{2}\right) - \frac{\nu B_{1}}{H} \left(U_{+} + U_{-}\right)^{2}}{\frac{\nu B_{1}}{H} \left[\left(U_{+} - U_{-}\right)^{2} - \left(U_{+}^{2} - U_{-}^{2}\right) \frac{\nu B_{1}}{H}\right]}}$$

$$= \sqrt{\frac{\left(U_{+} + U_{-}\right)H}{\left(U_{+} - U_{-}\right)\nu B_{1}}} = \sqrt{\frac{U_{\text{m,max}}H}{U_{\text{m,min}}\nu B_{1}}}$$
(3.135)

Thus the instantaneous time corresponding to the peak value of the phase difference of the carrier wave is

$$t_{\text{max}} = \frac{\arctan\left\{\sqrt{\frac{(\mu^2+1)[\lambda_+(\mu^2+1+m)+\lambda_-(\mu^2+1-m)]}{m[\lambda_-(\mu^2+1-m)-\lambda_+(\mu^2+1+m)]}}\right\}}{\dot{m}\dot{\varphi}_0}$$
(3.136)

According to Eq. (3.136), the instantaneous time corresponding to the minimum value of the phase difference of the carrier wave is

$$t_{\min} = \frac{\pi - \arctan\left\{\sqrt{\frac{(\mu^2 + 1)[\lambda_+(\mu^2 + 1 + m) + \lambda_-(\mu^2 + 1 - m)]}{m[\lambda_-(\mu^2 + 1 - m) - \lambda_+(\mu^2 + 1 + m)]}}\right\}}{\frac{\pi}{m\dot{\varphi}_0}} = \frac{\pi}{m\dot{\varphi}_0} - t_{\max}$$

Considering the situation in Eq. (3.136), the form of Eq. (3.125) is

$$\begin{split} \chi_{\text{carrier wave peak}} &= \arctan \Biggl\{ \sqrt{\frac{\left[(\mu^2+1) + m \right]^2 \lambda_+^2 + \left[(\mu^2+1) - m \right]^2 \lambda_-^2 - 2 \left[(\mu^2+1)^2 - m^2 \right] \lambda_+ \lambda_- \cos \left(\chi_+ + \chi_- \right)}{\left[(\mu^2+1) + m \right]^2 \lambda_+^2 + \left[(\mu^2+1) - m \right]^2 \lambda_-^2 + 2 \left[(\mu^2+1)^2 - m^2 \right] \lambda_+ \lambda_- \cos \left(\chi_+ + \chi_- \right)} \\ &\times \frac{\sin \left[\arctan \left(\sqrt{\frac{(\mu^2+1)[\lambda_+(\mu^2+1+m) + \lambda_-(\mu^2+1-m)]}{m[\lambda_-(\mu^2+1-m) - \lambda_+(\mu^2+1-m)]}} \right) - \frac{\chi_+ + \chi_-}{2} + \\ &\cos \left[\arctan \left(\sqrt{\frac{(\mu^2+1)[\lambda_+(\mu^2+1+m) + \lambda_-(\mu^2+1-m)]}{m[\lambda_-(\mu^2+1-m) - \lambda_+(\mu^2+1-m)]}} \right) - \frac{\chi_+ - \chi_-}{2} + \\ &\frac{\arctan \left(\frac{\left[(\mu^2+1) + m \right] \lambda_+ \sin \chi_+ + \left[(\mu^2+1) - m \right] \lambda_- \sin \chi_-}{\left[(\mu^2+1) + m \right] \lambda_+ \cos \chi_+ - \left[(\mu^2+1) - m \right] \lambda_- \cos \chi_-} \right] \right]}{\arctan \left(\frac{\left[(\mu^2+1) + m \right] \lambda_+ \sin \chi_+ + \left[(\mu^2+1) - m \right] \lambda_- \cos \chi_-}{\left[(\mu^2+1) + m \right] \lambda_+ \cos \chi_+ + \left[(\mu^2+1) - m \right] \lambda_- \cos \chi_-} \right]} \right\} \\ &- \arctan \left\{ \sqrt{\frac{m \left[\lambda_+ (\mu^2+1 + m) + \lambda_-(\mu^2+1-m) \right]}{(\mu^2+1) \left[\lambda_- (\mu^2+1) - m \right] \lambda_- \cos \chi_-}} \right\}} - \chi_{\text{carrier wave 0}} \right. \end{split}$$

The relationship curve in Eq. (3.137) is shown in Fig. 3.18.

From Fig. 3.18, it can be seen that when m = 0, i.e. v = 0, the maximum value of the phase difference of the carrier wave equals zero. This situation can be explained by the fact that the constant phase shift is compensated in the expression of the phase difference of the carrier wave. However, as long as there is a very small angular oscillation frequency the mutation can occur in the maximum value of the phase difference of the carrier wave and this situation can be explained by the fact that at this moment the angular acceleration of the aircraft has a maximum value. And, with the increase of the angular oscillation frequency the jump amplitude of this mutation will be reduced.

In Fig. 3.18, $\chi_{\text{carrier wave peak}}$ with a negative value can be explained by the following facts: when the angular oscillation frequency changes in a short time, the phase slopes of the carrier waves of the input signal or the output signal change and with the increase of the angular oscillation frequency the two slopes approach each

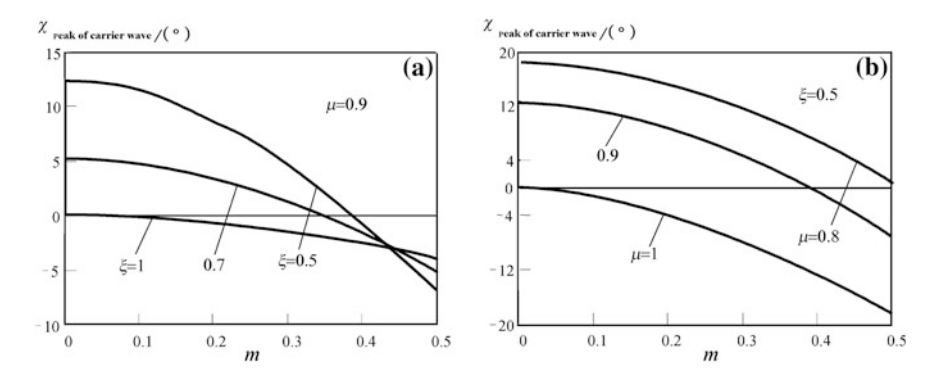


Fig. 3.18 Relationship curve between $\chi_{\text{carrier wave peak}}$ and m. a Different attenuation coefficients; b Different detuning coefficients

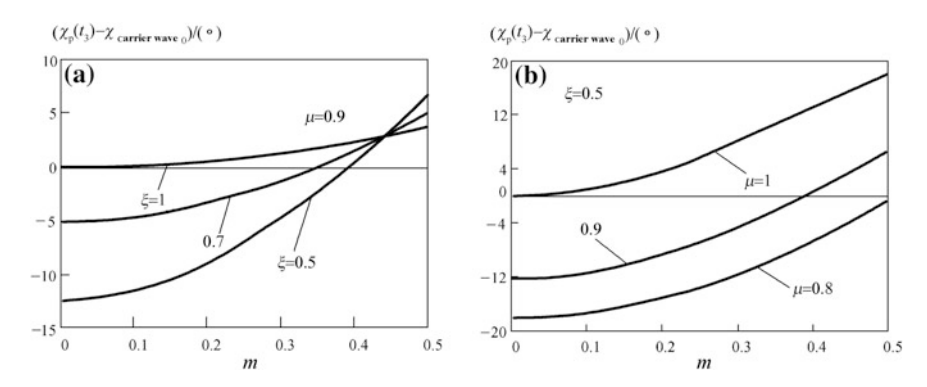


Fig. 3.19 Relationship curve between $\chi_p(t_3) - \chi_{\text{carrier wave 0}}$ and m. a Different attenuation coefficients; **b** Different detuning coefficients

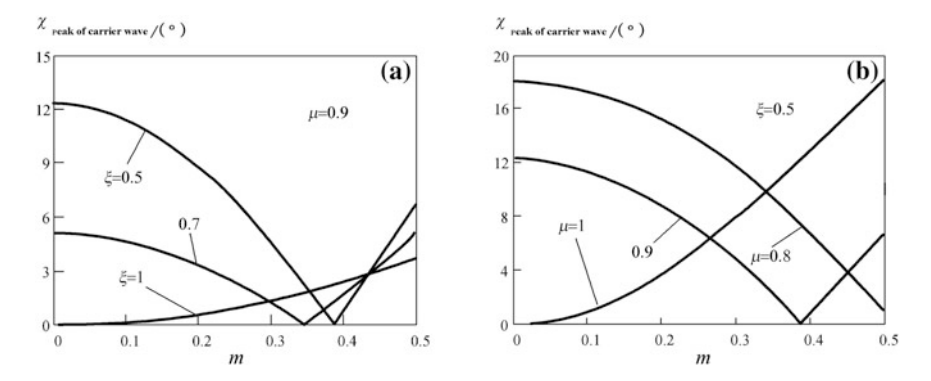


Fig. 3.20 Relationship curve between $\chi_{\text{carrier wave peak}}$ and m. a Different attenuation coefficients; b Different detuning coefficients

other, so that when the angular oscillation frequency takes a certain value the two slopes are equivalent. The peak value and the instantaneous time t of the characteristic curve in Fig. 3.16, and the measured phase differences of the carrier wave are equivalent, but $\chi_{\text{carrier wave peak}} = 0$.

Continue to increase the angular vibration frequency, or in other words continue to change the phase slope of the carrier wave of the two signals and they no longer approach each other but instead keep apart from each other. At the same time, at the moment of t_{peak} , the phase difference has the minimum value and not the maximum value. However, from Fig. 3.16, it can be seen that the maximum value and the minimum value have many changes, or in other words the phase difference of the carrier wave has the maximum value at the instantaneous time t_3 , and according to the modulus this value will be equal to the difference of $\chi_{\text{carrier wave 0}} - \chi_{\text{carrier wave peak}}$ (Fig. 3.19).

The phase difference of the carrier wave in the curves of Figs. 3.19 and 3.18 according to the modulus are the same, but according to the symbol they are opposite. In this case, the frequency characteristic of the component that changes is the peak shape, and this is determined by the modulus of Eq. (3.137), and is also determined by Eq. (3.138) and the relationship curve of this expression is shown in Fig. 3.20.

$$\begin{split} \chi_{\text{carrier wave peak}} &= \left| \arctan \left\{ \sqrt{\frac{\left[(\mu^2+1) + m \right]^2 \lambda_+^2 + \left[(\mu^2+1) - m \right]^2 \lambda_-^2 - 2 \left[(\mu^2+1)^2 - m^2 \right] \lambda_+ \lambda_- \cos \left(\chi_+ + \chi_- \right)}{\left[(\mu^2+1) + m \right]^2 \lambda_+^2 + \left[(\mu^2+1) - m \right]^2 \lambda_-^2 + 2 \left[(\mu^2+1)^2 - m^2 \right] \lambda_+ \lambda_- \cos \left(\chi_+ + \chi_- \right)} \right. \\ &\times \frac{\sin \left[\arctan \left(\sqrt{\frac{(\mu^2+1) \left[\lambda_+ (\mu^2+1 + m) + \lambda_- (\mu^2+1 - m) \right]}{m \left[\lambda_- (\mu^2+1 - m) - \lambda_+ (\mu^2+1 - m) \right]}} \right) - \frac{\chi_+ + \chi_-}{2} + \\ &\times \frac{\cot \left(\sqrt{\frac{(\mu^2+1) \left[\lambda_+ (\mu^2+1 + m) + \lambda_- (\mu^2+1 - m) \right]}{m \left[\lambda_- (\mu^2+1 - m) - \lambda_+ (\mu^2+1 - m) \right]}} \right) - \frac{\chi_+ + \chi_-}{2} + \\ &\frac{\arctan \left(\frac{\left[(\mu^2+1) + m \right] \lambda_+ \sin \chi_+ - \left[(\mu^2+1) - m \right] \lambda_- \sin \chi_-}{\left[(\mu^2+1) + m \right] \lambda_+ \cos \chi_+ - \left[(\mu^2+1) - m \right] \lambda_- \cos \chi_-} \right) \right]}{\arctan \left(\frac{\left[(\mu^2+1) + m \right] \lambda_+ \sin \chi_+ + \left[(\mu^2+1) - m \right] \lambda_- \sin \chi_-}{\left[(\mu^2+1) + m \right] \lambda_+ \cos \chi_+ + \left[(\mu^2+1) - m \right] \lambda_- \cos \chi_-} \right) \right]} \\ &- \arctan \left\{ \sqrt{\frac{m \left[\lambda_+ (m + \mu^2+1) - \lambda_- (m - \mu^2-1) \right]}{(\mu^2+1) \left[\lambda_+ (m + \mu^2+1) + \lambda_- (m - \mu^2-1) \right]}}} \right\} - \chi_{\text{carrier wave 0}} \right| \end{split}$$

Figure 3.20 shows that the angular oscillation frequency increases to a certain frequency, which will lead to a decrease of the maximum value of the phase difference of the carrier wave over this frequency, and the increase of the angular vibration frequency will cause the peak value of the phase difference to increase.

Calculate Eqs. (3.127) and (3.138) and obtain the relationship curves between the maximum value of the phase difference of the carrier wave and the angular oscillation frequency of the output signal and the input signal, as shown in Fig. 3.21.

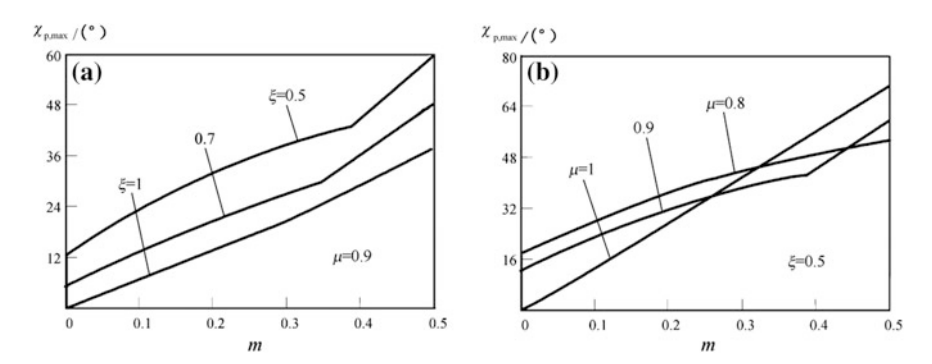


Fig. 3.21 Relationship curve between $\chi_{p,max}$ and m. **a** Different attenuation coefficients; **b** Different detuning coefficients

$$\begin{split} \chi_{\text{p,max}} &= \left| \arctan \left\{ \sqrt{\frac{\left[(\mu^2+1) + m \right]^2 \lambda_+^2 + \left[(\mu^2+1) - m \right]^2 \lambda_-^2 - 2 \left[(\mu^2+1)^2 - m^2 \right] \lambda_+ \lambda_- \cos \left(\chi_+ - \chi_- \right)}{\left[(\mu^2+1) + m \right]^2 \lambda_+^2 + \left[(\mu^2+1) - m \right]^2 \lambda_-^2 + 2 \left[(\mu^2+1)^2 - m^2 \right] \lambda_+ \lambda_- \cos \left(\chi_+ - \chi_- \right)} \right. \\ &\times \frac{\sin \left[\arctan \left(\sqrt{\frac{(\mu^2+1)[\lambda_+ (m+\mu^2+1) - \lambda_- (m-\mu^2-1)]}{m[\lambda_+ (m+\mu^2+1) + \lambda_- (m-\mu^2-1)]}} \right) - \frac{\chi_+ + \chi_-}{2} + \\ &\times \cos \left[\arctan \left(\sqrt{\frac{(\mu^2+1)[\lambda_+ (m+\mu^2+1) - \lambda_- (m-\mu^2-1)]}{m[\lambda_+ (m+\mu^2+1) + \lambda_- (m-\mu^2-1)]}} \right) - \frac{\chi_+ + \chi_-}{2} + \\ & \arctan \left(\frac{\left[(\mu^2+1) + m \right] \lambda_+ \sin \chi_+ - \left[(\mu^2+1) - m \right] \lambda_- \sin \chi_-}{\left[(\mu^2+1) + m \right] \lambda_+ \cos \chi_- - \left[(\mu^2+1) - m \right] \lambda_- \cos \chi_-} \right)}{\arctan \left(\frac{\left[(\mu^2+1) + m \right] \lambda_+ \sin \chi_+ + \left[(\mu^2+1) - m \right] \lambda_- \sin \chi_-}{\left[(\mu^2+1) + m \right] \lambda_+ \cos \chi_+ + \left[(\mu^2+1) - m \right] \lambda_- \cos \chi_-} \right)} \\ & - \arctan \left\{ \sqrt{\frac{m \left[\lambda_+ (m+\mu^2+1) - \lambda_- (m-\mu^2-1) \right]}{\left(\mu^2+1 \right) \left[\lambda_+ (m+\mu^2+1) + \lambda_- (m-\mu^2-1) \right]}} \right\} - \chi_{\text{carrier wave 0}} \right. \\ &+ \chi_{\text{carrier wave 0}} \end{aligned}$$

It should be pointed out that the value determined by Eq. (3.127) can be regarded as the error of the carrier phase of the effective signal.

When the angular vibration problem of the instrument around the axis of the aircraft is analyzed, the following conclusions can be drawn:

- (1) The accuracy of the angular velocity that the instrument deals with in the input according to the change of harmonic mode is slightly lower than the accuracy that the instrument deals with regarding the constant angular velocity.
- (2) In order to describe the accuracy with which the instrument processes the angular oscillation of the aircraft, four frequency relationships should be used, which represents the relationship among the relative changes of the parameters of the output signal, the input signal and the angular vibration frequency.
- (3) Three frequency characteristics of the maximum envelope, the minimum envelope and the phase were described previously, and the phase frequency characteristics of the carrier wave (Fig. 3.17 and Eq. (3.137)) are added, thus the phase shift represented by this frequency characteristics is different from that of the input signal.
- (4) In ideal flight conditions, the angular vibration frequency of the aircraft is limited to 2.5 Hz, so the coefficient *m* can be limited to 0.2. It can be seen from the analysis and calculation of the angular vibration accuracy of the instrument that the accuracy of the angular acceleration of the instrument is very poor. A conclusion can be drawn that in the condition that the angular vibration frequency is very small—in fact in the full cycle of angular oscillation—the amplitude and the phase of the output signal are determined by the curves of Figs. 3.7, 3.8 and 3.17a, and in a short moment that the amplitude of the angular oscillation velocity changes the symbol, the maximum error of the output signal is determined by the curves in Figs. 3.12 and 3.21.

3.4 Performance of Non-driven Mechanical Gyroscope in a Circumferential Vibration

It is assumed that the input signal has a circumferential vibration form and the solution for the general motion Eq. (1.46) of the instrument is analyzed. According to Eq. (3.3), there are

$$\begin{cases} \Omega_{\xi} = \Omega^{\psi} \sin \delta_{\psi} \cos(\psi t + \gamma_{\psi}) \\ \Omega_{\eta} = \Omega^{\psi} \sin \delta_{\psi} \sin(\psi t + \gamma_{\psi}) \end{cases}$$

where

$$\begin{cases} \dot{\rho} = \Omega_{\xi} = \Omega^{\psi} \sin \delta_{\psi} \cos(\psi t + \gamma_{\psi}) \\ \dot{\sigma} = \Omega_{\eta} \cos \rho = \Omega^{\psi} \sin \delta_{\psi} \sin(\psi t + \gamma_{\psi}) \cos \rho \end{cases}$$

In this case, as with the angular vibration of the aircraft, because ρ and σ are very small and can be ignored, when comparing with the velocity of the aircraft around the longitudinal axis it can be considered that the velocity acting on the aircraft is very small and the following equation can be deduced:

$$\begin{cases} \dot{\rho} = \Omega_{\xi} = \Omega^{\psi} \sin \delta_{\psi} \cos(\psi t + \gamma_{\psi}) \\ \dot{\sigma} = \Omega_{\eta} = \Omega^{\psi} \sin \delta_{\psi} \sin(\psi t + \gamma_{\psi}) \end{cases}$$
(3.140)

From Eq. (3.140), there holds

$$\begin{cases} \ddot{\rho} = \dot{\Omega}_{\xi} = -\psi \Omega^{\psi} \sin \delta_{\psi} \sin(\psi t + \gamma_{\psi}) \\ \ddot{\sigma} = \dot{\Omega}_{\eta} = \psi \Omega^{\psi} \sin \delta_{\psi} \cos(\psi t + \gamma_{\psi}) \end{cases}$$
(3.141)

In this case, Eq. (1.46) has the following form:

$$\ddot{\alpha} + 2\xi\omega_0\dot{\alpha} + \omega_0^2\alpha = \frac{H}{B_1}\Omega\sin(\dot{\varphi}_0t - \delta_1) + \dot{\Omega}\sin(\dot{\varphi}_0t + \delta_2)$$
 (3.142)

where

$$\Omega = \sqrt{\Omega_{\xi}^2 + \Omega_{\eta}^2} = \Omega^{\psi} \sin \delta_{\psi} \tag{3.143}$$

$$\dot{\Omega}_1 = \sqrt{\dot{\Omega}_{\xi}^2 + \dot{\Omega}_{\eta}^2} = \dot{\psi}\Omega^{\psi}\sin\delta_{\psi} \tag{3.144}$$

$$\delta_1 = \arctan\left(\frac{\Omega_{\eta}}{\Omega_{\xi}}\right) = \dot{\psi}t + \gamma_{\psi} \tag{3.145}$$

$$\delta_2 = \arctan\left(\frac{\dot{\Omega}_{\xi}}{\dot{\Omega}_{\eta}}\right) = -\dot{\psi}t - \gamma_{\psi}$$

$$\omega_0 = \sqrt{\frac{C_1 - A_1}{B_1}}\dot{\varphi}_0$$
(3.146)

Substitute Eqs. (3.143)–(3.146) into (3.142) and rewrite them as

$$\ddot{\alpha} + 2\xi\omega_0\dot{\alpha} + \omega_0^2\alpha = \frac{H}{B_1}\Omega^{\psi}\sin\left(\dot{\varphi}_0t - \dot{\psi}t - \gamma_v\right) - \dot{\psi}\Omega^{\psi}\sin\left(\dot{\varphi}_0t - \dot{\psi}t - \gamma_v\right)$$

$$= \frac{H}{B_1}\Omega^{\psi}\sin\left[\left(\dot{\varphi}_0 - \dot{\psi}\right)t - \gamma_v\right] - \dot{\psi}\Omega^{\psi}\sin\left[\left(\dot{\varphi}_0 - \dot{\psi}\right)t - \gamma_v\right]$$
(3.147)

$$\ddot{\alpha} + 2\xi\omega_0\dot{\alpha} + \omega_0^2\alpha = \left(\frac{H}{B_1} - \dot{\psi}\right)\Omega^{\psi}\sin\left[\left(\dot{\varphi}_0 - \dot{\psi}\right)t - \gamma_v\right]$$
 (3.148)

Therefore, it can clearly be seen that the effect of the circumferential vibration is similar to that of constant angular velocity, and is similar to that of the velocity instability of the aircraft around the longitudinal axis of the output signal.

In this case, the established output signal looks like:

$$U_{\text{out}}(t) = |\Phi(j\omega)| \Omega^{\psi} \Big(H - \dot{\psi} B_1 \Big) \sin \left\{ \Big(\dot{\varphi}_0 - \dot{\psi} \Big) t - \gamma_{\psi} + \arctan \left[\Phi(j\omega) \right] \right\}$$

$$\omega = \dot{\varphi}_0 - \dot{\psi}$$
(3.149)

or

$$U_{\text{out}}(t) = U_{\psi} \sin\left[\left(\dot{\varphi}_{0} - \dot{\psi}\right)t - \gamma_{v} + \chi_{\psi}\right]$$
 (3.150)

where $\xi_0 = 0$ and T_{damping} is very small, T_1 and T_2 are very large. According to Eqs. (2.53) and (2.60), obtain

$$U_{\psi} = \frac{KK_{\mathrm{integrator}\,2}T_{1}\left[\left(C_{1}-A_{1}+B_{1}\right)\dot{\varphi}_{0}-\dot{\psi}B_{1}\right]\Omega^{\nu}}{\left[X\sqrt{\left[\left(nT_{\mathrm{amplify}}+2\xi T_{0}\right)\left(\dot{\varphi}_{0}-\dot{\psi}\right)-T_{0}^{2}nT_{\mathrm{amplify}}\left(\dot{\varphi}_{0}-\dot{\psi}\right)^{3}\right]^{2}+\left[1-T_{0}^{2}\left(\dot{\varphi}_{0}-\dot{\psi}\right)^{2}\right]^{2}}\right]}$$

$$(3.151)$$

$$\begin{split} \chi_{\psi} &= \frac{\pi}{2} + \arctan \left[T_{\text{damping}} \left(\dot{\varphi}_{0} - \dot{\psi} \right) \right] + \arctan \left[T_{1} \left(\dot{\varphi}_{0} - \dot{\psi} \right) \right] \\ &- \arctan \left[\frac{2 \xi_{\text{integrator}} T_{2} \left(\dot{\varphi}_{0} - \dot{\psi} \right)}{1 - T_{2}^{2} \left(\dot{\varphi}_{0} - \dot{\psi} \right)^{2}} \right] \\ &- \arctan \left[\frac{\left(n T_{\text{amplify}} + 2 \xi T_{0} \right) \left(\dot{\varphi}_{0} - \dot{\psi} \right) - T_{0}^{2} n T_{\text{amplify}} \left(\dot{\varphi}_{0} - \dot{\psi} \right)^{3}}{1 - T_{0}^{2} \left(\dot{\varphi}_{0} - \dot{\psi} \right)^{2}} \right] \end{split}$$
(3.152)

Because nT_{amplify} is very small, from Eqs. (3.151) and (3.152) obtain

$$U_{\psi} = \frac{KK_{\text{integrator}} {}_{2}T_{1} \left[(C_{1} - A_{1} + B_{1})\dot{\varphi}_{0} - \dot{\psi}B_{1} \right] \Omega^{\nu}}{2K_{\text{moment}}K_{\text{electric current}} T_{2}^{2} \sqrt{\left[2\xi T_{0} \left(\dot{\varphi}_{0} - \dot{\psi} \right) \right]^{2} + \left[1 - T_{0}^{2} \left(\dot{\varphi}_{0} - \dot{\psi} \right)^{2} \right]^{2}}$$

$$(3.153)$$

$$\chi_{\psi} = \frac{\pi}{2} + \arctan\left[T_{\text{damping}}\left(\dot{\varphi}_{0} - \dot{\psi}\right)\right] + \arctan\left[T_{1}\left(\dot{\varphi}_{0} - \dot{\psi}\right)\right]$$
$$-\arctan\left[\frac{2\xi_{\text{integrator}}T_{2}\left(\dot{\varphi}_{0} - \dot{\psi}\right)}{1 - T_{2}^{2}\left(\dot{\varphi}_{0} - \dot{\psi}\right)^{2}}\right] - \arctan\left[\frac{2\xi T_{0}\left(\dot{\varphi}_{0} - \dot{\psi}\right)}{1 - T_{0}^{2}\left(\dot{\varphi}_{0} - \dot{\psi}\right)^{2}}\right]$$
(3.154)

Obviously, the relationship curves with U_{ψ} are related not only to the circumferential vibration frequency $\dot{\psi}$, but also to the velocity instability $\Delta \dot{\varphi}_0$ of the aircraft around the longitudinal axis, and this relationship can be represented in the resonant state. At resonance, U_{ψ} and χ_{ψ} can be obtained as

$$U_{\psi} = \frac{KK_{\text{integrator}} {}_{2}T_{1}B_{1}\left(2\dot{\varphi}_{0} - \dot{\psi}\right)\Omega^{\nu}}{2K_{\text{moment}}K_{\text{electric current}}T_{2}^{2}\sqrt{\left[2\xi\left(1 - \frac{\dot{\psi}}{\dot{\varphi}_{0}}\right)\right]^{2} + \left[1 - \left(1 - \frac{\dot{\psi}}{\dot{\varphi}_{0}}\right)^{2}\right]^{2}}}$$
(3.155)

$$\chi_{\psi} = \frac{\pi}{2} + \arctan\left[T_{\text{damping}}\left(\dot{\varphi}_{0} - \dot{\psi}\right)\right] + \arctan\left[T_{1}\left(\dot{\varphi}_{0} - \dot{\psi}\right)\right]$$
$$-\arctan\left[\frac{2\xi_{\text{integrator}}T_{2}\left(\dot{\varphi}_{0} - \dot{\psi}\right)}{1 - T_{2}^{2}\left(\dot{\varphi}_{0} - \dot{\psi}\right)^{2}}\right] - \arctan\left[\frac{2\xi\mu\left(1 - \frac{\dot{\psi}}{\dot{\varphi}_{0}}\right)}{\mu^{2} - \left(1 - \frac{\dot{\psi}}{\dot{\varphi}_{0}}\right)^{2}}\right]$$
(3.156)

When the circumferential vibration frequency $\dot{\psi} = 0$:

$$U_{\psi} = \frac{K_{\text{integrator 2}} T_1 B_1 \Omega^{\psi}}{K_{\text{moment}} K_{\text{electric current}} T_2^2}$$
(3.157)

It is in accord with the constant angular velocity (2.12) acting on the instrument. By using the dynamic coefficients in Eq. (3.153), there is

$$U_{\psi} = \frac{KK_{\text{integrator }2}T_{1}\Big[(C_{1} - A_{1} + B_{1})\dot{\varphi}_{0} - \dot{\psi}B_{1}\Big]\lambda_{\psi}\Omega^{\psi}}{2K_{\text{moment}}K_{\text{electric current}}T_{\text{integrator}}T_{2}^{2}}$$
(3.158)

With the correlation value, how the circumferential vibration frequency affects the output signal can be studied. Thus introduce the coefficient $h=\frac{\dot{\varphi}}{\dot{\varphi}_0}$ and when using the detuning coefficient there holds

$$\frac{U_{\psi}}{U_{\psi}(\dot{\psi}=0)} = \frac{[(\mu^2+1)-h]\lambda_{\psi}}{(\mu^2+1)\lambda} = \frac{\lambda_{\psi}}{\lambda} - \frac{h\lambda_{\psi}}{(\mu^2+1)\lambda} = \frac{\lambda_{\psi}}{\lambda} \left(1 - \frac{h}{\mu^2+1}\right) \quad (3.159)$$

or

$$\frac{U_{\psi}}{U_{\psi}(\dot{\psi}=0)} = \frac{\sqrt{(\mu^2-1)^2 + (2\xi\mu)^2}}{\sqrt{\left[\mu^2 - (1-h)^2\right]^2 + \left[2\xi(1-h)\mu\right]^2}} \left(1 - \frac{h}{\mu^2 + 1}\right)$$
(3.160)

Figure 3.22 gives the relationship curves of Eq. (3.160) with different detuning coefficients and different attenuation coefficients.

According to the curve characteristic given by Fig. 3.22, it can be seen that the scale factor of the instrument is varied and it is strongly dependent on the

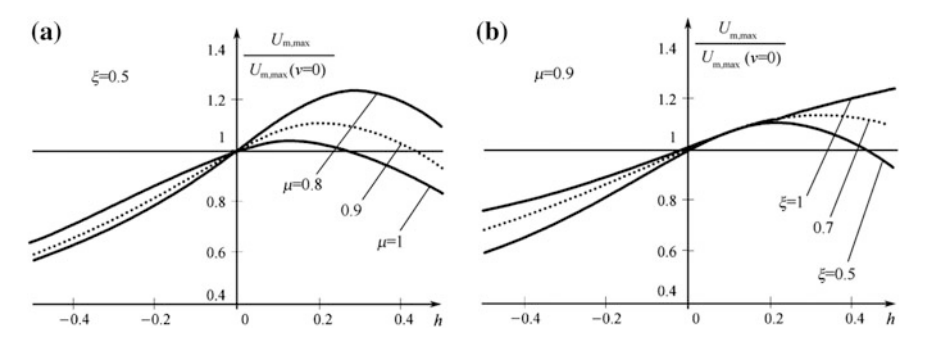


Fig. 3.22 Relationship curve between $\frac{U_{\psi}}{U_{\psi}(\psi=0)}$ and (μ, ξ, h) . **a** When ξ is constant, the Relationship curves between the magnitude ratio, h and μ when ξ is constant; **b** Relationship curves between the magnitude ratio, h and ξ when μ is constant

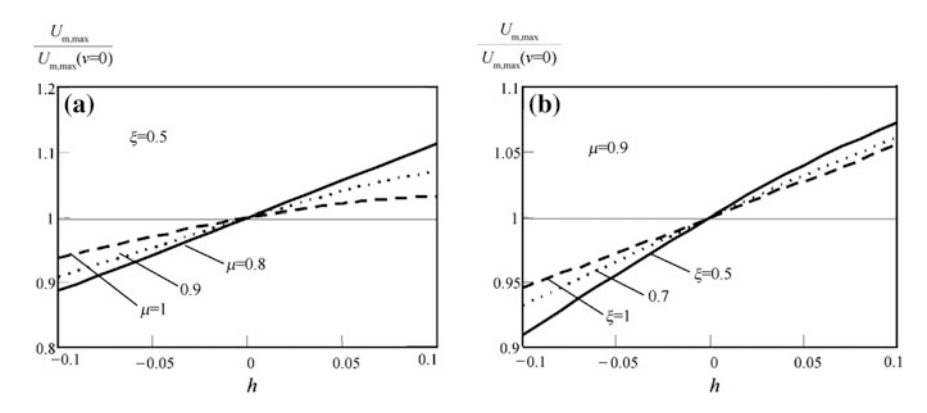


Fig. 3.23 Impact of the circumferential vibration on the amplitude of the output signal of a non-driven mechanical gyroscope. a Different detuning coefficients; b Different attenuation coefficients

circumferential vibration frequency. In fact, the shapes of the curves in Fig. 3.22 can be interpreted in the following way. According to the variation characteristics the curves in Fig. 3.22 are in accord with the straight line of the λ function whose specular reflection is perpendicular to the symmetry axis and h=0. With an increase of the circumferential vibration frequency, the working point in Fig. 1.10 moves leftward and upward until the resonance point. Over the resonance point, it moves leftward and downward, or in other words increases first and then decreases. With the increase of the attenuation coefficient the resonance peak is reduced and the curve is flat. Similarly, with the increase of the detuning coefficient and the decrease of the attenuation coefficient, the resonant peak is close to the value h=0. So the working point moves along the λ curve in Fig. 1.10, and the situation can be explained through the above situation.

In Chap. 1, the circumferential vibration frequency is limited by the possible ideal value. As has been pointed out, according to Eq. (1.15), $\dot{\psi} = 0.05\dot{\varphi}_0$, then considering the reserve margin, the circumferential vibration frequency is limited by h = 0.1.

That is, under the ideal condition of aircraft motion, the amplitude error of the output signal due to the influence of the circumferential vibration is limited by the numbers in Fig. 3.23.

Different from the situation of the angular vibration that the aircraft is rotating around the horizontal axis, the symbol of the circumferential vibration frequency affects the sign and magnitude of the scale factor error.

Like the angular oscillation of the aircraft, it is more reasonable and feasible that the scale factor of the instrument is not analyzed but the relationship between the output signal and the input signal is analyzed, and in the circumferential vibration case from Eq. (3.148) the input signal has the following form

$$M_{\rm intertia} = \left(H - \dot{\psi} \mathbf{B}_1\right) \Omega^{\psi} \sin \left[\left(\dot{\varphi}_0 - \dot{\psi}\right)t - \gamma_v\right] \tag{3.161}$$

The amplitude ratio of the output signal and the input signal is expressed in the following form:

$$\frac{U_{\psi}}{M_{\text{inertia}}} = \frac{KK_{\text{integrator }2}T_{1}\lambda_{\psi}}{2K_{\text{moment}}K_{\text{electric current}}T_{2}^{2}} \\
= \frac{KK_{\text{integrator }2}T_{1}}{2K_{\text{moment}}K_{\text{electric current}}T_{2}^{2}} \frac{\mu}{\sqrt{\left[2\xi\mu(1-h)\right]^{2} + \left[\mu^{2} - (1-h)^{2}\right]^{2}}} \tag{3.162}$$

The obtained expression belongs to the condition that the circumferential vibration frequency is zero:

$$\frac{U_{\psi}/U_{\psi}(\dot{\psi}=0)}{M_{\text{inertia}}/M_{\text{inertia}}(\dot{\psi}=0)} = \frac{\sqrt{(2\xi\mu)^2 + (\mu^2 - 1)^2}}{\sqrt{[2\xi\mu(1-h)]^2 + [\mu^2 - (1-h)^2]^2}}$$
(3.163)

Thus, the amplitude ratio of the output signal and the input signal is determined by the dynamic coefficient. The difference between Eqs. (3.163) and (3.160) is that in Eq. (3.160), there is a cofactor, an added entry which is determined by the circumferential vibration frequency. Comparing these two expressions an important conclusion can be drawn about the circular frequency of the aircraft. This conclusion can be obtained from the comparison of the relationship curves corresponding to Eq. (3.160) in Fig. 3.23 and the relationship curves corresponding to Eq. (3.163) in Fig. 3.24.

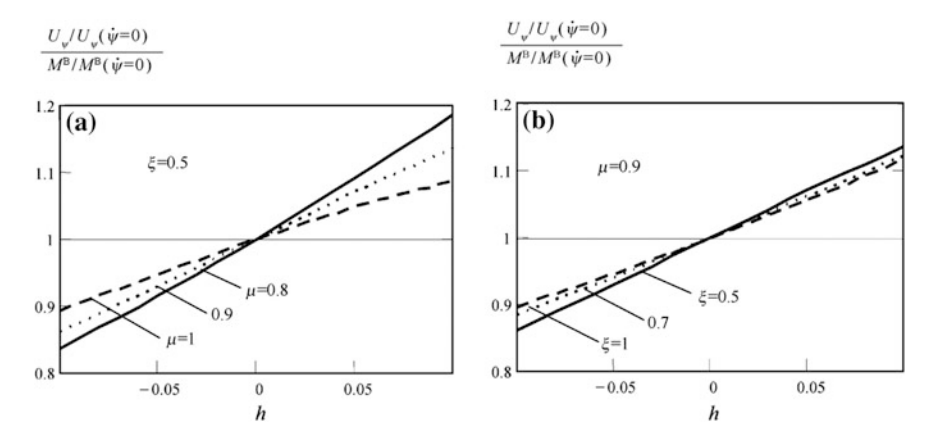


Fig. 3.24 Amplitude ratio of the output signal and the input signal in the case of circular vibration of the aircraft. a Different detuning coefficients; b Different attenuation coefficients

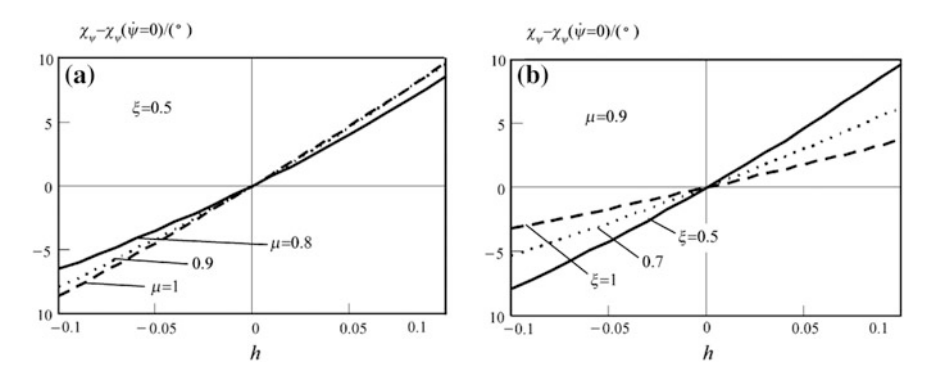


Fig. 3.25 Impact of circumferential vibration on the phase of the output signal of a non-driven mechanical gyroscope. a Different detuning coefficients; b Different attenuation coefficients

The circular vibration brings a large phase shift into the indicator value of the instrument (Fig. 3.25). Figure 3.25 shows that the phase characteristic curves corresponding to Eq. (3.164), compensate the constant phase shift caused by turning the instrument shell and eliminate $\chi_{\psi}(\dot{\psi}=0)$, namely,

$$\chi_{\psi} = \frac{\pi}{2} + \arctan\left[T_{\text{damping}}\dot{\varphi}_{0}(1-h)\right] + \arctan\left[T_{1}\dot{\varphi}_{0}(1-h)\right] - \arctan\left[\frac{2\xi_{\text{integrator}}T_{2}\dot{\varphi}_{0}(1-h)}{1 - T_{2}^{2}\dot{\varphi}_{0}^{2}(1-h)^{2}}\right] - \arctan\left[\frac{2\xi\mu(1-h)}{\mu^{2} - (1-h)^{2}}\right]$$
(3.164)

Obviously, similar to the impact of $\Delta \dot{\varphi}_0$, determining the correct $T_{\rm damping}$ will greatly reduce the impact of $\dot{\psi}$ on the phase of the output signal.

In the range of the circumferential vibration frequency, the impact of the detuning coefficients on the phase of the output signal is much smaller than that of the vibration attenuation coefficients on the phase of the output signal. In Fig. 3.25b, with the decrease of the attenuation coefficient, the slope of the phase characteristics increases. This phenomenon can be explained by the fact that across the point of the natural non-damped vibration frequency, the phase change of the oscillation element is very sharp and the natural non-damping vibration frequency, in this case, with $\mu=0.9$ approaches the point with h=0.

The above data show that in the case of the circumferential vibration of the aircraft, increasing the damping in the instrument and improving the accuracy of tuning can reduce the error of the instrument.

Chapter 4 The Operating Errors of a Non-driven Mechanical Gyroscope

The operating error of a rotating aircraft with a rotor vibrating gyroscope can be divided into two categories.

The first category includes three errors, the error in a non-driven mechanical gyroscope; the error due to the residual imbalance of the sensitive element; in the condition of the aircraft with the angular oscillation and circumferential vibration, the double frequency error with the self-rotating of the aircraft.

The second category includes the error due to the installation accuracy of the instrument installed on the aircraft and the error due to the temperature instability, which is limited by the application characteristics of a non-driven mechanical gyroscope on a rotating aircraft and the structural characteristics of the instrument.

4.1 Error Caused by Static Unbalance of the Framework

As shown in Fig. 4.1, the mass center of the sensitive element is not coincident with the axis OY while the axis is oscillating around the axis OY and in the condition of the constant and vibration overload, a harmful moment can be caused, which is called the unbalanced torque. The center of mass of the sensitive element has some deviation, $x_0 \neq 0$; $z_0 \neq 0$ makes the center of mass of the sensitive element deviate relative to the crossing point of the rotation axis. Assume that n_{ζ} is an overload along the flying direction of the aircraft and $n_{\xi\eta}$ is a lateral overload of the aircraft. The research work is limited to the constant overload and the vibration overload, whose overload frequencies are equal to the twice frequency and the one times the frequency around the longitudinal axis of the aircraft respectively.

$$n_{\xi\eta} = n_{\xi\eta_0} + n_{\xi\eta_1} \sin(\dot{\varphi}_0 t + \delta_{\xi\eta_1}) + n_{\xi\eta_2} \sin(2\dot{\varphi}_0 t + \delta_{\xi\eta_2}) n_{\xi} = n_{\xi_0} + n_{\xi_1} \sin(\dot{\varphi}_0 t + \delta_{\xi_1}) + n_{\xi_2} \sin(2\dot{\varphi}_0 t + \delta_{\xi_2})$$
(4.1)

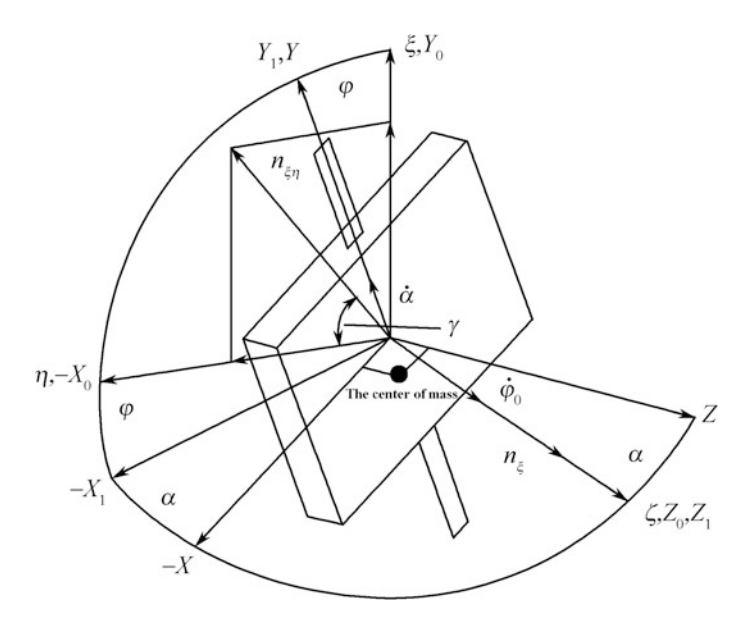


Fig. 4.1 Error from an unbalanced force

The unbalance torque is

$$M_{\text{unbalance}} = m_{\text{sensitive mass}}(z_0 n_x - x_0 n_z)$$

where $m_{\text{sensitive mass}}$ is the mass of the sensitive element; n_x and n_z are the projections of the longitudinal overload and the transverse overload on the axes OX and OZ which are connected with the sensitive element respectively, or in other words

$$n_Z = n_{\zeta} \cos \alpha - n_{\xi\eta} \cos(\dot{\varphi}_0 t + \gamma) \sin \alpha$$

$$n_X = -n_{\zeta} \sin \alpha - n_{\xi\eta} \cos(\dot{\varphi}_0 t + \gamma) \cos \alpha$$

Each component of the overload is determined by γ . It is necessary to consider Eq. (4.1), and assume that α is very small:

$$\begin{split} n_{Z} &= n_{\zeta} = n_{\zeta_{0}} + n_{\zeta_{1}} \sin(\dot{\varphi}_{0}t + \delta_{\zeta_{1}}) + n_{\zeta_{2}} \sin(2\dot{\varphi}_{0}t + \delta_{\zeta_{2}}) \\ n_{X} &= -n_{\xi\eta} \cos(\dot{\varphi}_{0}t + \gamma) = -n_{\xi\eta_{0}} \cos(\dot{\varphi}_{0}t + \gamma_{0}) - n_{\xi\eta_{1}} \sin(\dot{\varphi}_{0}t + \delta_{\xi\eta_{1}}) \\ \cos(\dot{\varphi}_{0}t + \gamma_{1}) - n_{\xi\eta_{2}} \sin(2\dot{\varphi}_{0}t + \delta_{\xi\eta_{2}}) \cos(\dot{\varphi}_{0}t + \gamma_{2}) \end{split}$$

The unbalanced torque is

$$\begin{split} M_{\text{unbalance}} &= m_{\text{sensitive mass}} \mathsf{Z}_0 n_{\xi\eta0} \cos(\dot{\varphi}_0 \mathsf{t} \ + \ \gamma_0) \\ &+ m_{\text{sensitive mass}} \mathsf{Z}_0 n_{\xi\eta1} \sin(\dot{\varphi}_0 \mathsf{t} \ + \ \delta_{\xi\eta1}) \cos(\dot{\varphi}_0 t + \gamma_1) \\ &+ m_{\text{sensitive mass}} \mathsf{Z}_0 n_{\xi\eta2} \sin(2\dot{\varphi}_0 t + \delta_{\xi\eta2}) \cos(\dot{\varphi}_0 t + \gamma_2) + m_{\text{sensitive mass}} \mathsf{X}_0 n_{\zeta0} \\ &+ m_{\text{sensitive mass}} \mathsf{X}_0 n_{\zeta1} \sin(\dot{\varphi}_0 t + \delta_{\zeta1}) + m_{\text{sensitive mass}} \mathsf{X}_0 n_{\zeta2} \sin(2\dot{\varphi}_0 t + \delta_{\zeta2}) \end{split}$$

The unbalanced torque component of the effective signal frequency is isolated and other frequency signals can be filtered in the narrow band circuit such that the accuracy of the instrument is not affected. The unbalanced torque can also be written as

$$\begin{split} M_{\text{unbalance}} &= m_{\text{sensitive mass}} \left[z_0 n_{\xi\eta 0} \cos(\dot{\varphi}_0 t + \gamma_0) + x_0 n_{\zeta 1} \sin(\dot{\varphi}_0 t + \delta_{\zeta 1}) \right. \\ &\left. + \frac{1}{2} z_0 n_{\xi\eta 2} \sin(\dot{\varphi}_0 t + \delta_{\xi\eta 2} - \gamma_2) \right] \end{split}$$

That is to say, the unbalanced force of the sensitive element along the rotating axis, under the action of constant acceleration and acceleration with the frequency $2\dot{\phi}_0$ will generate harmful torque, and under the action of the acceleration of the effective signal frequency, the unbalanced force along the vertical direction will also generate harmful torque.

According to Eq. (2.4), the unbalanced force is substituted into the motion equation of the sensitive element in Eq. (1.46) and the following equation is obtained

$$\Delta U_{\text{out}} = \left| \frac{\Phi(j\omega)}{\omega = \dot{\varphi}_{0}} \right| m_{\text{sensitive mass}} z_{0} n_{\xi \eta_{0}} \cos \left\{ \dot{\varphi}_{0} t + \gamma_{0} + \arctan[\Phi(j\omega)] \right\} \\
+ \left| \frac{\Phi(j\omega)}{\omega = \dot{\varphi}_{0}} \right| m_{\text{sensitive mass}} x_{0} n_{\xi_{1}} \sin \left\{ \dot{\varphi}_{0} t + \delta_{\xi_{1}} + \arctan[\Phi(j\omega)] \right\} \\
+ \frac{1}{2} \left| \frac{\Phi(j\omega)}{\omega = \dot{\varphi}_{0}} \right| m_{\text{sensitive mass}} z_{0} n_{\xi \eta_{2}} \sin \left\{ \dot{\varphi}_{0} t + \delta_{\xi \eta_{2}} - \gamma_{2} + \arctan[\Phi(j\omega)] \right\} \\
+ \frac{1}{2} \left| \frac{\Phi(j\omega)}{\omega = \dot{\varphi}_{0}} \right| m_{\text{sensitive mass}} z_{0} n_{\xi \eta_{2}} \sin \left\{ \dot{\varphi}_{0} t + \delta_{\xi \eta_{2}} - \gamma_{2} + \arctan[\Phi(j\omega)] \right\} \\
(4.2)$$

The maximum value of the error occurs when the phase shifts of three components coincide.

Without considering the phase shift in Eq. (4.2), the form is

$$\Delta U_{\text{out}} = \left| \frac{\Phi(j\omega)}{\omega = \dot{\varphi}_{0}} \right| \left(m_{\text{sensitive mass}} z_{0} n_{\xi \eta_{0}} + m_{\text{sensitive mass}} x_{0} n_{\zeta_{1}} + \frac{1}{2} m_{\text{sensitive mass}} z_{0} n_{\xi \eta_{2}} \right)$$

$$\sin \left\{ \dot{\varphi}_{0} t + \arctan[\Phi(j\omega)] \right\}$$

$$\omega = \dot{\varphi}_{0}$$

$$(4.3)$$

The impact of the unbalanced force only affects the amplitude of the output signal because the unbalanced torque has nothing to do with the measured angular velocity, so with the increase of the measured angular velocity the impact of the unbalanced force on the amplitude of the output signal is reduced by the form of the relative value.

It should be pointed out that the torque caused by the unbalanced force of the sensitive element is generated not only under the action of the various accelerations outside but also under the action of the centrifugal acceleration which act on the center of mass and when the center of mass moves along the axis OZ and the axis OX, the torque is

$$M_{\text{unbalance}} = a_{\text{centrifugal}} m z_0 = m \dot{\varphi}_0^2 x_0 z_0 \tag{4.4}$$

The torque at this moment is constant so when the aircraft rotates around the longitudinal axis the frequency does not produce an alternating and false signal. The sensitive element acts on this torque and will be slightly deflected by the constant angle α :

$$\alpha = \frac{M_{\text{unbalance}}}{B_0} = \frac{mx_0z_0}{\mu^2 B_1} \tag{4.5}$$

It should be noted that unlike with the unbalanced torque, the angle has nothing to do with the instability of the rotating velocity around the longitudinal axis of the aircraft. In the design of the structure of the instrument, the problem of Eq. (4.5) should be noted to ensure the design margin of the deflection angle of the sensitive element. However, the angle α described by Eq. (4.5) is very small under the condition of good balance. In order to eliminate it, some measures are required to be taken in advance.

In a similar way that the amplitude of the output signal is affected, the dynamic unbalance of the sensitive element is also affected. That is to say, the inertia centrifugal torque of the sensitive element is not zero when the three axes of the coordinate system connected to the sensitive element are selected as a reference. At this time, the constant unbalanced torque $M_{\rm unbalance} = J_{xz} \dot{\varphi}_0^2$ can make the sensitive element deflect by a fixed angle.

4.2 Error Caused by Angular Vibration and Circumferential Vibration

Chapter 3 shows that the instrument is capable of measuring the angular velocity of the aircraft when the aircraft has angular oscillation and circumferential vibration, even if the frequencies of the angular oscillation and the circumferential vibration are less than 1/2 of the rotation frequency of the aircraft.

Obviously, continually increasing the angular oscillation frequency and the circumferential vibration frequency of the aircraft will lead to the result that the component of the self-rotation frequency of the aircraft is not in the input signal and the output signal of the instrument and the error of the instrument will rise.

The input signal of the aircraft rudder can correctly process the angular velocity and must modulate the angular oscillation frequency and the circumferential vibration frequency by the self-rotating frequency of the aircraft. These frequencies produce the harmonic signal of the self-rotating frequency of the aircraft at the end of the output signal.

The instrument's harmonic signal of the self-rotating frequency of the aircraft will be explained and occurs in the case that the angular vibration frequency and the circumferential vibration frequency are twice the self-rotating frequency of the aircraft.

For any rotating object in fact, there is such a vibration and the rotating element of a non-driven mechanical gyroscope is no different.

The impact of the angular vibration of the aircraft on the instrument's output signal has been analyzed previously and this angular vibration rotates around a horizontal axis when this frequency is equal to twice the self-rotating frequency of the aircraft around a longitudinal axis. In this case, the angular velocity of the aircraft in Eq. (3.2) can be described by the following expression:

$$\Omega_{\xi} = \Omega^{\nu} \sin \delta_{\nu} \cos \gamma_{\nu} \cos 2\dot{\varphi}_{0} t
\Omega_{n} = \Omega^{\nu} \sin \delta_{\nu} \sin \gamma_{\nu} \cos 2\dot{\varphi}_{0} t$$
(4.6)

Select $\delta_v = \frac{\pi}{2}$, and the output signal component of the effective frequency in the form of (3.41) is:

$$U_{\text{out}}(t) = -U_{-}\sin(\dot{\varphi}_{0}t + \gamma_{v} - \chi_{-})$$
 (4.7)

where $\xi_0 = 0$, the constant T_{damping} is very small, and the constants T_1 and T_2 are very large.

$$U_{-} = \frac{KK_{\mathrm{integrator2}}T_{1}(C_{1} - A_{1} - B_{1})\dot{\varphi}_{0}\Omega^{\nu}}{2K_{\mathrm{moment}}K_{\mathrm{electric\,current}}T_{2}^{2}\sqrt{\left[T_{0}^{2}nT_{\mathrm{amplify}}\dot{\varphi}_{0}^{3} - (nT_{\mathrm{amplify}} + 2\xi T_{0})\dot{\varphi}_{0}\right]^{2} + (1 - T_{0}^{2}\dot{\varphi}_{0}^{2})^{2}}} \tag{4.8}$$

$$\begin{split} \chi_{-} &= \frac{\pi}{2} - \arctan(T_{\text{damping}} \dot{\varphi}_{0}) - \arctan(T_{1} \dot{\varphi}_{0}) + \arctan\left(\frac{2\xi_{\text{integrator}} T_{2} \dot{\varphi}_{0}}{1 - T_{2}^{2} \dot{\varphi}_{0}^{2}}\right) \\ &- \arctan\left\{\frac{\left[nT_{\text{amplify}} - 2T_{0}(\xi_{0} + \xi)\right] \dot{\varphi}_{0} + T_{0}^{2} nT_{\text{amplify}} \dot{\varphi}_{0}^{3}}{1 - \left(T_{0}^{2} + 2\xi_{0} T_{0} nT_{\text{amplify}}\right) \dot{\varphi}_{0}^{2}}\right\} \end{split} \tag{4.9}$$

The phase relation of the error indicates that the change of the error occurs in the case of the opposite of the effective signal phase. The maximum value of the error is analyzed, namely the amplitude value. Assume that $nT_{\rm amplify}$ is very small, then

$$U_{-} = \frac{KK_{\rm integrator2}T_{1}(C_{1} - A_{1} - B_{1})\dot{\varphi}_{0}\Omega^{\nu}}{2K_{\rm moment}K_{\rm electric \, current}T_{2}^{2}\sqrt{(2\xi T_{0}\dot{\varphi}_{0})^{2} + (1 - T_{0}^{2}\dot{\varphi}_{0}^{2})^{2}}}$$
(4.10)

It is obvious that Eq. (4.10) is zero in the resonance condition, that is, in the condition of the angular vibration with twice the self-rotating frequency of the aircraft the instrument has no error.

Because

$$\lambda_{2\dot{\varphi}_0} = \frac{1}{\sqrt{(2\xi T_0 \dot{\varphi}_0)^2 + (1 - T_0^2 \dot{\varphi}_0^2)^2}} = \frac{\mu^2}{\sqrt{(2\xi \mu)^2 + (\mu^2 - 1)^2}} = \lambda \tag{4.11}$$

Then, by using the detuning coefficient, Eq. (4.10) can be simplified as

$$U_{-} = \frac{\lambda B_1 K K_{\text{integrator}} T_1(\mu^2 - 1) \dot{\varphi}_0 \Omega^{\nu}}{2 K_{\text{moment}} K_{\text{electric current}} T_2^2}$$
(4.12)

The maximum error is

$$U_{\text{max}} = -U_{-} = -\frac{\lambda K K_{\text{integrator2}} T_{1}(\mu^{2} - 1) \dot{\varphi}_{0} \Omega^{\nu}}{2 B_{1} K_{\text{moment}} K_{\text{electric current}} T_{2}^{2}} = \frac{\lambda B_{1} K K_{\text{integrator2}} T_{1}(1 - \mu^{2}) \dot{\varphi}_{0} \Omega^{\nu}}{2 K_{\text{moment}} K_{\text{electric current}} T_{2}^{2}}$$

Assume that $\mu^2 < 1$, and the amplitude $U_{\text{out}} > 0$. Because there is the angular vibration of the aircraft whose frequency is twice the self-rotating frequency the amplitude of the effective output signal of the instrument is reduced. The vibration frequency of the circumferential vibration is equal to the self-rotating frequency of the aircraft but the signs are opposite.

In this case, the angular velocity of the aircraft in Eq. (3.3) can be described by the following expressions:

$$\Omega_{\xi} = \Omega^{\psi} \sin \delta_{\psi} \cos(\psi t - \gamma_{\psi})
\Omega_{\eta} = -\Omega^{\psi} \sin \delta_{\psi} \sin(\psi t + \gamma_{\psi})$$
(4.13)

Select $\delta_{\nu} = \frac{\pi}{2}$, and the output signal component of the effective frequency in the form of (3.150) is:

$$U_{\text{out}}(t) = -U_{\psi} \sin(\dot{\varphi}_0 t + \gamma_{\nu} - \chi_{\psi}) \tag{4.14}$$

Because Eqs. (4.7) and (4.14) are the same, it is certain that in the condition that the frequency of the circumferential vibration is twice the self-rotating frequency, the effective frequency of the output signal is generated and the phase and the amplitude are equal to twice the self-rotating frequency.

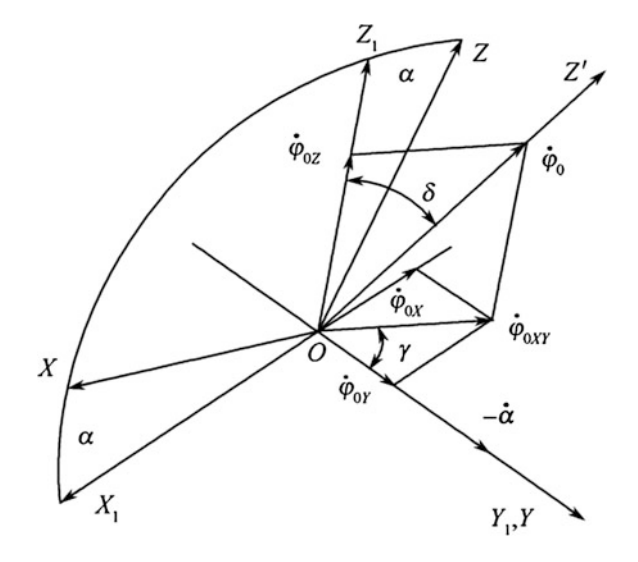
It is obvious that when the resonant point is more precisely tuned, the error with the vibration whose frequency is twice the self-rotating frequency of the aircraft will be greatly reduced.

4.3 Error Caused by Imprecise Installation

The deflection angles of the self-rotating axis of the aircraft and the vertical axis of the sensitive surface of the instrument's sensitive element are investigated in this book. When the circumferential vibration frequency is equal to the self-rotating frequency of the aircraft, it can be regarded as the partial circumferential vibration.

In this case, apart from rotating around the longitudinal structure axis OZ_1 , the aircraft rotates around the horizontal axes OX_1 and OY_1 as shown in Fig. 4.2. At the same time the rotating velocity around the horizontal axes OX_1 and OY_1 of the aircraft is constant in the coordinate system connected to the aircraft. Because the angle δ is very small, the rotating velocity around the longitudinal axis OZ_1 of

Fig. 4.2 Determination of the angle by which the rotation axis of the aircraft deviates from the longitudinal axis



the aircraft, is in fact equal to the rotating velocity around the axis OZ' of the aircraft and is equal to $\dot{\varphi}_0 \cos \gamma$.

The projections of the angular velocity of the aircraft on the three axes of the coordinate system *OXYZ*:

$$\Omega_X = \Omega_{X_1} \cos \alpha + \Omega_{Z_1} \sin \alpha = \Omega_{X_1} - \Omega_{Z_1} \alpha = -\dot{\varphi}_{0X} - \dot{\varphi}_{0Z} \alpha
\Omega_Y = -\dot{\alpha} + \Omega_{Y_1} = -\dot{\alpha} + \dot{\varphi}_{0Y}
\Omega_Z = \Omega_{X_1} \sin \alpha + \Omega_{Z_1} \cos \alpha = \Omega_{X_1} \alpha + \Omega_{Z_1} = -\dot{\varphi}_{0X} a + \dot{\varphi}_{0Z}$$
(4.15)

Substitute Eq. (4.15) into Eq. (1.30) and obtain

$$-B_1\ddot{\alpha} - (C_1 - A_1)(-\dot{\varphi}_{0X}\alpha + \dot{\varphi}_{0Z})(-\dot{\varphi}_{0Z}\alpha - \dot{\varphi}_{0X}) - D_{\alpha}\dot{\alpha} = 0$$

$$-B_1\ddot{\alpha} - D_{\alpha}\dot{\alpha} + (C_1 - A_1)(\dot{\varphi}_{0Z}^2 - \dot{\varphi}_{0X}^2)\alpha = (C_1 - A_1)(\alpha^2 - 1)\dot{\varphi}_{0X}\dot{\varphi}_{0Z}$$

$$(4.16)$$

When the angle α is very small and α^2 is compared with 1, α^2 can be ignored. Then

$$-B_1\ddot{\alpha} - D_{\alpha}\dot{\alpha} + (C_1 - A_1)(\dot{\varphi}_{0Z}^2 - \dot{\varphi}_{0X}^2)\alpha = -(C_1 - A_1)\dot{\varphi}_{0X}\dot{\varphi}_{0Z}$$

Because

$$\dot{\varphi}_{0X} = \dot{\varphi}_0 \sin \delta \sin \gamma
\dot{\varphi}_{0Y} = \dot{\varphi}_0 \sin \delta \cos \gamma
\dot{\varphi}_{0Z} = \dot{\varphi}_0 \cos \delta$$
(4.17)

After some replacement:

$$B_1\ddot{\alpha} + D_\alpha\dot{\alpha} - (C_1 - A_1)\dot{\varphi}_0^2(\cos^2\delta - \sin^2\delta\sin^2\gamma)\alpha = (C_1 - A_1)\dot{\varphi}_0^2\sin\delta\sin\gamma\cos\delta$$
(4.18)

Because the angle δ is very small, the sine squared of this angle can be ignored. The solution for the motion Eq. (4.18) of the sensitive element has the following form:

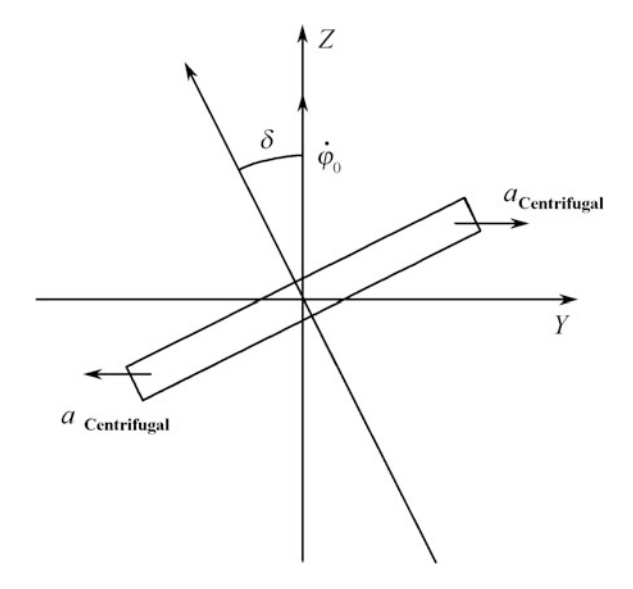
$$\alpha = -\frac{(C_1 - A_1)\dot{\varphi}_0^2 \sin\delta \sin\gamma \cos\delta}{(C_1 - A_1)\dot{\varphi}_0^2 \cos^2\delta} = -\tan\delta \sin\gamma \tag{4.19}$$

While δ is very small, there holds

$$\alpha = -\delta \sin \gamma \tag{4.20}$$

Equation (4.20) shows that in this case the deflection of the sensitive element is a constant angle α and this angle is determined by the ratio of the projection of the rotation velocity $\dot{\varphi}_0$ on the axis OX_1 and $\dot{\varphi}_0$.

Fig. 4.3 Illustration diagram of physical meaning



It should be noted that when $\gamma = 90^\circ$, the angle α will have a maximum value $(\alpha = \delta)$. Because, in the ideal movement condition of the aircraft, δ may be quite large, it should be guaranteed that the swing angle of the sensitive element of the instrument is more than a few times δ . δ can reach 5° , therefore, a margin of a reasonable multiple such as 10° should be added to the swing angle of the sensitive element.

Equation (4.20) can be physically explained in the following way.

As shown in Fig. 4.3, when there is the angle δ , the centrifugal acceleration acting on the sensitive element should make its plane perpendicular to the rotation vector.

The above description is related to the component $\dot{\varphi}_{0X}$. The impact of the component $\dot{\varphi}_{0Y}$ on the instrument is determined by making the angle $\alpha = 0$.

According to Eq. (4.20), the angle $\alpha=0$, because the component $\dot{\varphi}_{0Y}$ is directed along the vibration axis of the sensitive element, but due to $\dot{\varphi}_{0Y}$, the resulting gyroscope torque is balanced on the base of the sensitive element. When the aircraft or the base of the instrument has the velocity $\dot{\varphi}_{0Y}$, the relative velocity of the sensitive element with respect to the base of the instrument occurs. At this time, the constant output signal of the instrument is generated and together with this signal the damping torque is also generated. This torque is proportional to the relative velocity of the sensitive element with respect to the base of the instrument and this torque enables the sensitive element to rotate along with the base.

4.4 Error Caused by Change of Environmental Temperature

The normal working temperature range of the instrument is -40 to +75 °C. The effect of the temperature on the output value of the instrument is related to the temperature characteristics of the magnetic induction of the magnet. The magnetic induction of different magnetic materials in different temperature ranges can reduce or increase with an increase of temperature. Thus, the magnetic induction of the magnet in a general form is as follows:

$$B = B^0 (1 + \beta \Delta t) \tag{4.21}$$

where B^0 is the magnetic induction, which does not change with the change of the temperature; β is the temperature coefficient (1/°C) (β can be positive or negative); and Δt is a change of the temperature (°C).

The temperature on the magnetic induction in the working gap of the magnetic system affects the output value of the instrument twice: the first time is to measure the coefficient of the winding and the second time is to measure the coefficient of the torque winding. If the measurement of the change of the winding coefficient leads to a change of the damping effect [Eq. (1.179), then the winding coefficient change of the torque affects not only the damping coefficient expression (1.179), but also the amplitude of the instrument output signal (Eq. 2.12)]. Firstly, the impact of the temperature on the damping of the instrument is analyzed and then the impact of the temperature on the amplitude and the phase of the output signal is analyzed:

$$D_{\text{feedback}} = \left(B^0\right)^2 w_{\text{measure}} w_{\text{moment}} a^2 c^2 \frac{R_2}{R_1 R_7} (1 + \beta \Delta t)^2 = D_{\text{feedback}}^0 (1 + \beta \Delta t)^2$$

$$(4.22)$$

where $D^0_{
m feedback}$ is the damping effect that does not change with temperature. The attenuation coefficient of vibration is

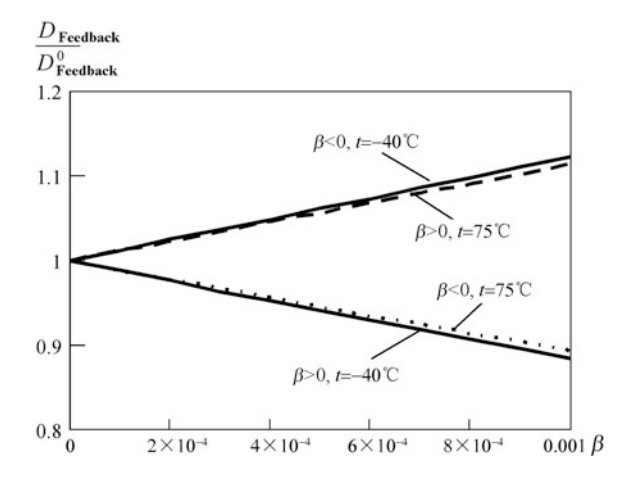
$$\xi = \frac{D_{\text{feedback}}}{2\omega_0 B_1} = \frac{D_{\text{feedback}}^0}{2\omega_0 B_1} (1 + \beta \Delta t)^2 = \xi^0 (1 + \beta \Delta t)^2$$
 (4.23)

where ξ^0 is the attenuation coefficient that is not related to temperature.

Because β is very small (the temperature coefficient of a good magnetic material does not exceed 10%/°C), the temperature characteristics in Eqs. (4.22) and (4.23) can be regarded as linear and as reaching the maximum value at the edge of the temperature range. The relation curves between the ratio of the maximum error and D_{feedback}^0 , and the temperature coefficient β are shown in Fig. 4.4.

Therefore, the temperature change causes the damping change, which leads to the change of amplitude and phase of the output signal.

Fig. 4.4 Impact of temperature on the damping coefficient



In order to reduce the influence of temperature, small temperature coefficients of the magnetic material must be selected as shown in Fig. 4.4. For example, the temperature coefficient of $(Nd_{15}Fe_{77}B_8)\beta=-0.000151/^{\circ}C$, and in this case the change of the variation of the damping coefficient and the attenuation coefficient within the range of the whole operating temperature is 3.5% (or a relative value $D_{\text{feedback}}^0=\pm 1.75\%$).

The impacts of temperature on the amplitude and phase of the output signal are analyzed. According to Eq. (2.11) and the impact of the tuning coefficient, the amplitude of the output signal has the following form:

$$U_{\text{amplitude}} = (\mu^2 + 1)B_1 \Omega \frac{2\xi K_{\text{integrator2}}}{K_{\text{moment}} K_{\text{electric current}}} \frac{T_1 \mu}{T_2^2 \sqrt{(\mu^2 - 1)^2 + (2\xi\mu)^2}}$$
(4.24)

Using the expressions of the torque winding coefficient and the current amplifier coefficient (Eqs. 1.176 and 1.178), and the expressions of the integrator parameters (Eqs. 2.74 and 2.76) obtains

$$U_{\text{amplitude}} = \frac{2\zeta R_7}{B\omega_{\text{moment}} ac R_4 C_1} \frac{\mu(\mu^2 + 1)B_1 \Omega}{\sqrt{(\mu^2 - 1)^2 + (2\zeta\mu)^2}}$$
(4.25)

Substitute Eqs. (4.21), (4.22) and (4.23) and obtain

$$U_{\rm amplitude} = \frac{B^0 \omega_{\rm measure} ac R_2 R_7 B_1 (\mu^2 + 1) \Omega (1 + \beta \Delta t)}{R_4 C_1 \sqrt{\left[\dot{\varphi}_0 B_1 R_1 R_7 (\mu^2 - 1)\right]^2 + \left[(B^0)^2 \omega_{\rm measure} \omega_{\rm moment} a^2 c^2 R_2 (1 + \beta \Delta t)^2 \right]^2}}$$
 (4.26)

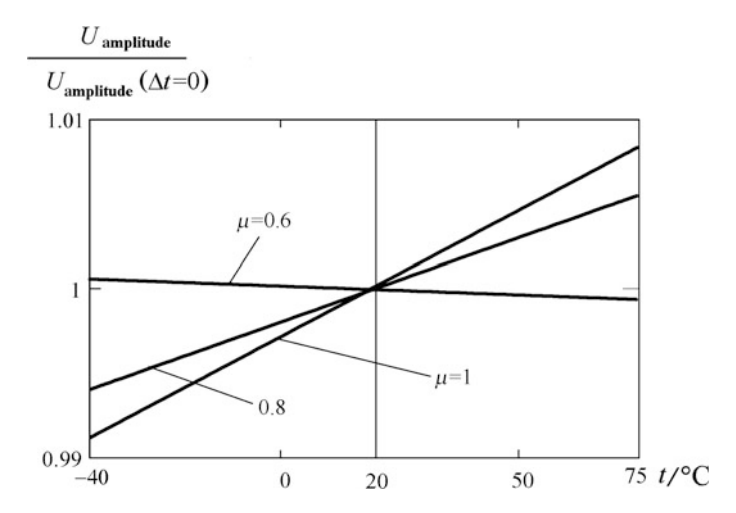


Fig. 4.5 Impact of temperature on the amplitude of the output signal

In the case of resonance ($\mu = 1$), Eq. (4.26) can be simplified as

$$U_{\text{amplitude}} = \frac{R_7 2 B_1 \Omega}{(B^0) \omega_{\text{moment}} a c R_4 C_1 (1 + \beta \Delta t)}$$
(4.27)

From Eq. (4.27) it can be seen that for the stability of the amplitude of the output signal the parameters of the mechanical and electronic elements of the instrument must be stable.

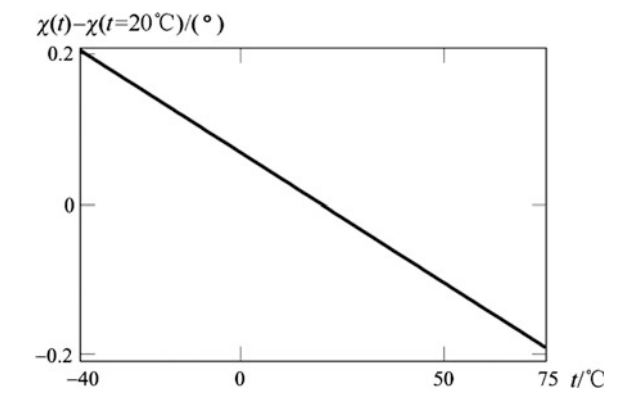
When the temperature changes, the ratio of the amplitude of the output signal to the amplitude at room temperature is analyzed. Therefore, using Eq. (4.26) and ξ^0 obtains

$$\frac{U_{\text{amplitude}}}{U_{\text{amplitude}}(\Delta t = 0)} = \frac{(1 + \beta \Delta t)\sqrt{(\mu^2 - 1)^2 + (2\xi^0 \mu)^2}}{\sqrt{(\mu^2 - 1)^2 + \left[2\xi^0 \mu (1 + \beta \Delta t)^2\right]^2}}$$
(4.28)

The relationship between Eq. (4.28) and the temperature t is shown in Fig. 4.5. In order to establish Fig. 4.5, the temperature coefficient and the vibration attenuation coefficient $\xi^0 = 0$ of $(Nd_{15}Fe_{77}B_8)$ are used. Because the amplitude error is small and the impact of the attenuation coefficient is very small, it is not necessary to analyze the errors with different ξ^0 . When the tuning coefficient is 0.9, the error in the range of the whole operating temperature is 1.6%.

It should be noted that due to the error caused by the environmental temperature, the electronic part of the instrument must be chosen from circuit elements with good temperature stability.

Fig. 4.6 Impact of temperature on the phase of the output signal



The impact of temperature on the phase of the output signal is demonstrated by the damping. As a result, the temperature only affects the phase component of the output signal of the oscillating element. According to Eq. (2.23) and the tuning coefficient

$$\chi = -\arctan\left(\frac{2\xi\mu}{\mu^2 - 1}\right) \tag{4.29}$$

Substitute Eq. (4.23) into Eq. (4.29) and obtain

$$\chi = -\arctan\left(\frac{2\xi^{0}(1+\beta\Delta t)^{2}\mu}{\mu^{2}-1}\right)$$
(4.30)

The phase of the output signal in Eq. (4.30) is described graphically and the phase of the output signal at room temperature is deducted as shown in Fig. 4.6. The precondition of establishing this figure is to use $(Nd_{15}Fe_{77}B_8)$ and assume that $\mu = 0.9$ and $\xi^0 = 0.5$ in Eq. (4.30). In this way, in the range of the whole operating frequency, the maximum error of the phase is 0.4° .

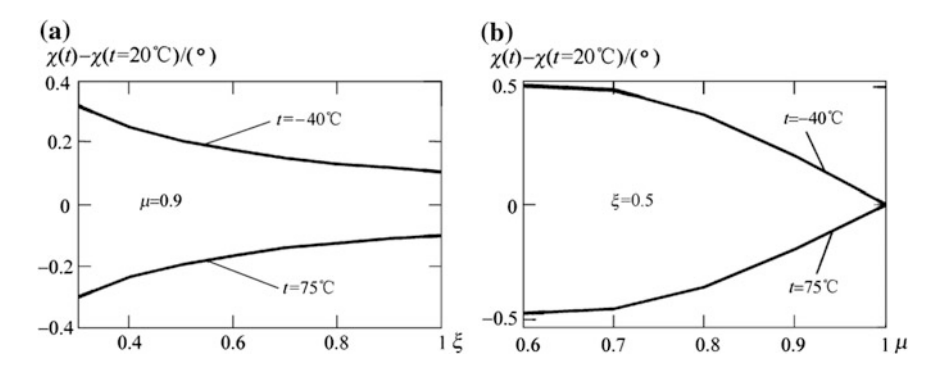


Fig. 4.7 Relationship curve between $\chi(t) - \chi(t = 20 \, ^{\circ}\text{C})$ and ξ and μ **a** Relationship curve between the maximum error and the attenuation coefficient. **b** Relationship curve between the maximum error and the detuning coefficient

The shape of Fig. 4.6 is actually linear and at the end of the operating temperature range the maximum phase error is obtained, and the relationship between the maximum error, the attenuation coefficient and the tuning factor can be found (Fig. 4.7).

Figure 4.7a shows that with an increase of the attenuation coefficient, the phase of the output signal is reduced. When the tuning coefficient increases, the phase of the output signal decreases (Fig. 4.7b), and in the case of an accurate tuning the relation curve between the phase of the output signal and temperature does not exist.

Therefore, the scheme that is independent of temperature can guarantee stability of damping and reduce the temperature error to an insignificant level.

Part II Non-driven Micromechanical Gyroscopes

Chapter 5 The Micromechanical Accelerometer and the Micromechanical Gyroscope

The micromechanical inertial sensors in the fabrication of micromechanical technology mainly include the micromechanical accelerometer and the micromechanical gyroscope.

5.1 The Micromechanical Accelerometer

5.1.1 Basic Principle, Technology Type and Applications of a Micromechanical Accelerometer

The micromechanical accelerometer is usually composed of the masses that meet the standards and hang in the benchmark framework with the aid of elastic elements (such as cantilever beams, etc.). Due to the action of acceleration, displacement of the standard mass occurs and is proportional to the acceleration. The movement of the mass can be measured by many methods, for example by measuring the capacitance change between the mass and the auxiliary electrode, or by measuring the change of the pressure-sensitive resistance through the strain gauge that is integrated with the elastic element. The basic principles of these two kinds of measurement methods are shown in Fig. 5.1.

In order to achieve a high sensitivity and low noise it is necessary to use a large mass, which is suitable for the bulk micromachining process. It is easy to integrate the surface micromachining process together with electronic circuit, which can avoid a wafer bonding process in the bulk micromachining process. Now consider the combination of a bulk micromachining process with a surface micromachining process, and only one process is needed to achieve a micromechanical accelerometer with a large mass on a wafer. Micromechanical accelerometers with a protection function for damping and overload, and the property of self-detection are produced by surface micromachining technology in large quantities.

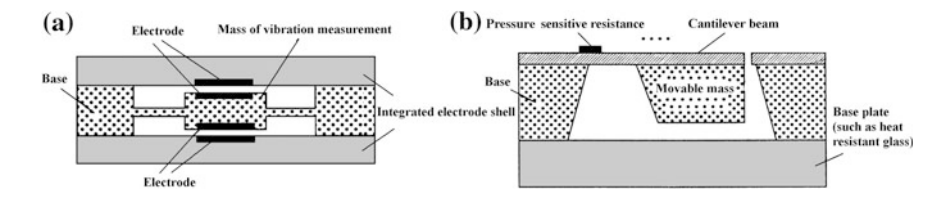


Fig. 5.1 Basic types and basic principles of a micromechanical accelerometer, a Capacitor; b Pressure-sensitive resistance

Table 5.1 Micromechanical accelerometers in the United States automotive market (unit: millions Euros)

Years/Year	1991	1992	1993	1994	1995	1996	1997	1998	1999	2000
Airbag system	21	55	89	88	151	127	129	131	133	135
ABS	0	8	8	16	24	31	50	52	54	56
Suspension system	0	6	13	18	26	19	19	20	21	22
Total	21	69	110	122	201	177	198	203	208	213

The main application market for micromechanical accelerometers is the automobile industry, for use in anti-lock braking systems (ABS), suspension systems (0–2 g) and airbag systems (up to 50 g). Table 5.1 details the automotive applications of the micromechanical accelerometer in the United States over the ten years between 1991 and 2000. Only in the United States has the market sales of a micromechanical accelerometer exceeded two billion Euros. It must be noted that in this period the price of each micromechanical accelerometer reduced from 100 Euros to 9 Euros, but the sales volume has continued to grow.

In addition to the automotive industry, the micromechanical accelerometer is widely used in other fields especially in those application fields with a lower fitting cost or a need for miniaturization such as the active monitoring devices in the fields of biological medicine and medical equipment. In addition, it also has a wide range of applications in consumer electronics such as the active anti-shake system in video cameras. The parameter comparisons of some commercially available micromechanical accelerometers are brought together in Table 5.2.

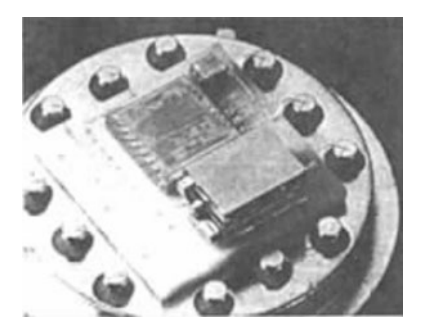
The ADXL 250 micromechanical accelerometer is a flexible folding structure with good linearity and can perform a biaxial measurement. Figure 5.2 shows a product photo of the CSEM MS 6100, which is a precise low-power capacitive micromechanical accelerometer (170 μ A, 3 V) with a high dynamic stability (at 2 g, the stability is 2 mg), but poor low temperature stability (the typical error is 200 μ g/°C).

The variable stress of the mechanical structure is used to change the resonant frequency of the structure and can produce a resonant micromechanical accelerometer with high resolution and high stability (Sect. 5.1.6). By enhancing

Model (Manufacturer) Parameter	XMMAS 401GID (Motorola)	SMB050 (Bosch)	SMB060 (Bosch)	ADXL50JH (Analog Devices)	ADXL250JQC (Analog Devices)
Axis number	1	1	2	1	2
Full scale range	±40 g	±35 g	±35 g	±50 g	±1 g
Drift error as $g = 0$	_	-	-	1.5 g	0.3 g
Temperature range/°C	-40-105	-	-	_	-40-85
Direct current/ mA	5	7	12	10	3.5
3dB bandwidth/Hz	400	400	400	1 300	1 000
Nonlinearity/ %FS	0.5	0.5	0.5	0.2	0.2
Axis alignment/(°)	N/A	N/A	1	N/A	0.1
Noise density/ (mg/Hz)	7.8	-	-	6.6	2
Encapsulation	16 foot, DIP, SIP	28 foot, PLCC	28 foot, PLCC	10 foot, TO-100	14 foot, Cerpak

Table 5.2 Parameter comparison of commercial micromechanical accelerometers

Fig. 5.2 CSEM MS 6100 capacitive micromechanical accelerometer (assembled with the corresponding circuit on the mixed circuit board)



the damping capacity and the rigidity of the micro-resonator, their dynamic ranges can be further expanded. In the military industry, the micromechanical accelerometer has also been used in a many ways such as in the rotating flight control system and so on.

5.1.2 The Working Principle of a Micromechanical Accelerometer

There is a standard mass in the basic structure of a silicon micromechanical accelerometer, which is connected to a relatively fixed frame by one or several elastic elements. Assuming that the effective elastic coefficient of the elastic component is K and the damping coefficient is D, then according to the Newton's second law of motion

$$F_{\text{ext}} = \frac{\mathrm{d}p}{\mathrm{d}t} = ma \tag{5.1}$$

where F_{ext} is the force acting on the mass; p is the momentum; and a is the acceleration of the mass m.

The deformation of the elastic element is caused by the force acting on the elastic element, which leads to the displacement of the mass, that is,

$$d_{\rm st} = \frac{F_{\rm ext}}{K} = \frac{ma}{K} \tag{5.2}$$

The subscript st of the displacement d represents static, that is, Eq. (5.2) is only applicable to acceleration with a slow change.

Figure 5.3 shows the simplified structure and integrated component composition model. The dynamic behavior of the system can be analyzed by the following differential equation:

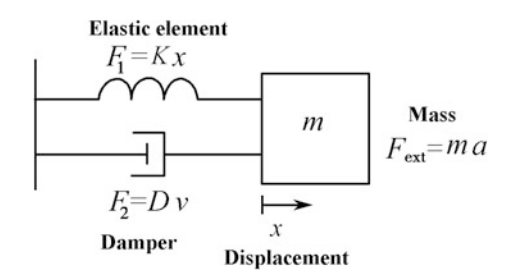
$$F_{1} = Kx$$

$$F_{2} = Dv$$

$$m\frac{d^{2}x}{dt^{2}} + D\frac{dx}{dt} + Kx = F_{\text{ext}} = ma$$
(5.3)

where F_{ext} is the external force acting on the reference frame, $Kx = F_1$, $D\frac{dx}{dt} = F_2$ and a mass is fixed on the frame.

Fig. 5.3 Integrated component structure model of a micromechanical accelerometer



By using a Laplace transform, the second order transfer function can be obtained from the mass displacement due to acceleration:

$$H(s) = \frac{X(s)}{A(s)} = \frac{1}{s^2 + \frac{D}{m}s + \frac{K}{m}} = \frac{1}{s^2 + \frac{\omega_r}{O}s + \omega_r^2}$$
(5.4)

where ω_r is the resonant frequency, $\omega_r = \sqrt{K/m}$; Q is the quality factor and $Q = \omega_r m/D$.

According to these relationships, Eq. (5.2) can be rewritten as

$$d_{\rm st} = a/\omega_{\rm r}^2 \tag{5.5}$$

The above equation marks the break point between the resonant bandwidth (the resonant frequency range) and sensitivity. In order to achieve a higher DC sensitivity, the resonant frequency of the system should be lower. The impact of feedback on this equation will be discussed later.

The thermal motion of the standard mass is one of the main factors limiting the performance of the micromechanical accelerometer. According to the theory of thermal dynamics, for any form of energy storage the thermal energy of a system with an equilibrium state is equal to $k_BT/2$, where k_B is the Boltzmann constant and T is the temperature. Therefore, for a smaller mass, its thermal motion is also larger and is called "the acceleration which is equivalent to the total noise (TNEA)". It can be calculated by

TNEA =
$$\sqrt{\frac{a_n^2}{\Delta f}} = \frac{\sqrt{4k_B TD}}{m} = \sqrt{\frac{\sqrt{4k_B T\omega_r}}{Qm}}$$
 (5.6)

From Eq. (5.6) it can be seen that in order to measure smaller acceleration a larger mass and a higher quality factor are needed.

5.1.3 The Micromechanical Accelerometer Manufactured by a Bulk Micromachining Process

The micromechanical accelerometer manufactured by bulk micromachining can produce a mass block with a wafer thickness, which is especially suitable for a micromechanical accelerometer with high sensitivity and low noise. Figure 5.4 gives the section structure of a micromechanical accelerometer manufactured by bulk micromachining, whose middle part is made up of a mass and a cantilever beam, and whose upper and lower sides are glued with a piece of glass that protects the structure and offers a limiting shock amplitude and a damping for the mass vibration. The voltage sensitive resistor is integrated in the cantilever beam. When the mass moves, the resistance of voltage sensitive resistor will produce a corresponding change.

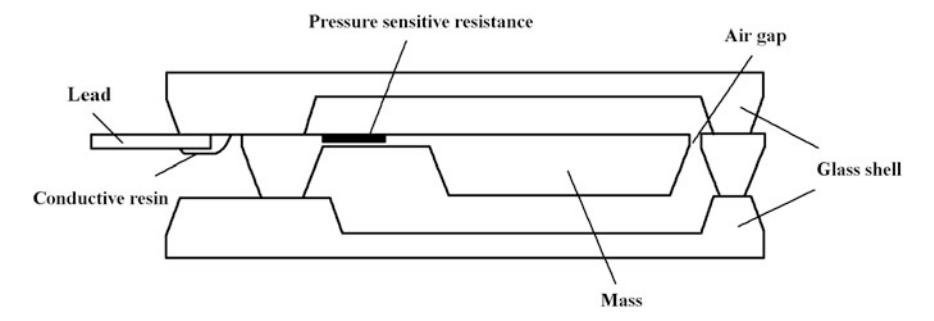
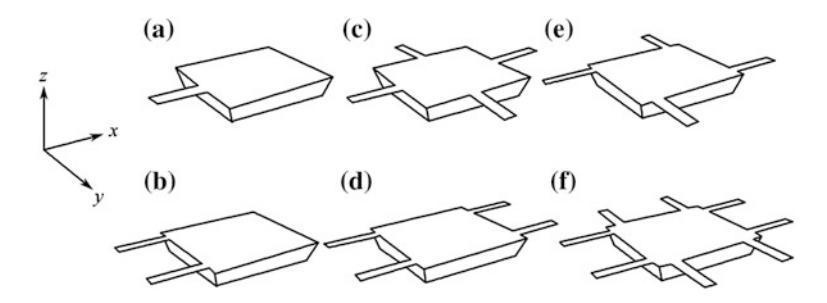


Fig. 5.4 Structure of a pressure-sensitive resistance micromechanical accelerometer

One of the most important characteristics that a micromechanical accelerometer must possess is off-axis sensitivity. This requires that the device is only sensitive to the acceleration in a certain direction and is insensitive to other directions. From Fig. 5.5a it is easy to understand that in the case of a simple cantilever support, the width of the arm beam is key. A y axial acceleration can cause the mass to rotate around the x axis so that the cantilever beam is twisted. Figure 5.5 also shows a variety of beam connection structures for a micromechanical accelerometer which can be used for bulk micromachining. The double arm structure shown in Fig. 5.5b has very low sensitivity to the y axial acceleration. However, the x axial acceleration will make two cantilever beams bend because the gravity center of the mass is lower than the position of the cantilever plane, and this bending displacement cannot be distinguished from the amount of the bending caused by the z axial acceleration. This problem can only be solved by use of a multi-beam structure as shown in Fig. 5.5c–f. In the structures shown in Fig. 5.5c–f, the z axial acceleration causes the mass to rotate. The effect of these structures can be detected separately, so their off-axis sensitivities can be reduced to a very low level. The main problem of a multi-beam structure is the influence of the residual stress in every cantilever beam. In addition, when the displacement is large, the tension force in the cantilever will change the linear characteristic between the acceleration and the displacement.



 $\textbf{Fig. 5.5} \quad \text{A variety of beam connection structures for a micromechanical accelerometer which can be used for bulk micromachining}$

The symmetrical structure shown in Fig. 5.5e does not have the above effect. If a certain stress occurs in the cantilever, the mass will make a small rotation around the shaft to make the stress effect disappear.

It is easy to make the pressure-sensitive resistance type of micromechanical accelerometer and electronic circuit for measuring the change of resistance. However, compared with the capacitance, it is affected by the temperature change and the sensitivity is low. The advantages of a capacitance type of micromechanical accelerometer include high sensitivity, good performance in terms of low frequency response, low noise, little drift, less sensitivity to temperature changes and a low energy consumption.

Furthermore, the capacitor structure of the capacitive micromechanical accelerometer can be integrated in production and a closed-loop feedback circuit with an electrostatic force rebalance can be formed for the automatic detection system. The automatic detection system is especially important for safety equipment in the monitoring field such as automobile safety air bag systems. The main drawbacks of a capacitive micromechanical accelerometer include: higher requirement for the detection circuit; and the fact that in order to reduce the parasitic capacitance, the interface of the electronic circuit should be as close to the sensor as possible and in order to prevent the interference of the electromagnetic field, it is necessary to have good shielding.

The structure of a capacitive micromechanical accelerometer for bulk micromachining is shown in Fig. 5.6. The mass can be connected to one or two cantilevers (or more cantilevers) and its aim is to improve the suspension symmetry of the sensor and reduce the off-axis sensitivity of the system. On the other hand, the asymmetry suspension structure can be achieved by measuring three axial accelerations with a mass. One example is shown in Fig. 5.7, where the mass has four electrodes with a shape similar to a four-leaf clover and is suspended on four cantilever beams. The structure and the shape of the mass block allows for a longer arm beam and a larger capacitance area in a smaller space. In the z axial acceleration, the mass also moves along the z axis such that all the capacitive reactance of the four capacitances will be changed (Fig. 5.7b). If the acceleration is on the x axis or the y axis, then they will make the mass tilt (Fig. 5.7c) and the capacitive reactance of two capacitances will increase, while the two other capacitances will

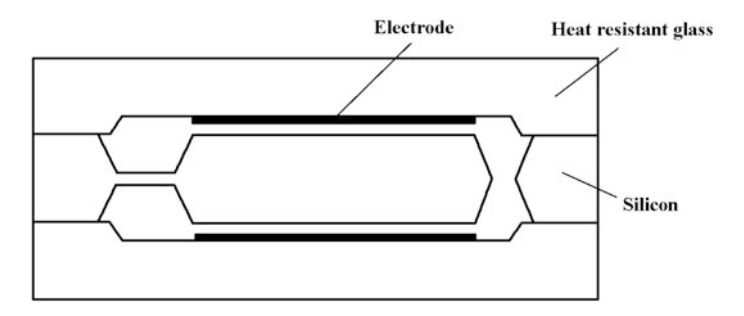


Fig. 5.6 Structure of a capacitive micromechanical accelerometer for bulk micromachining

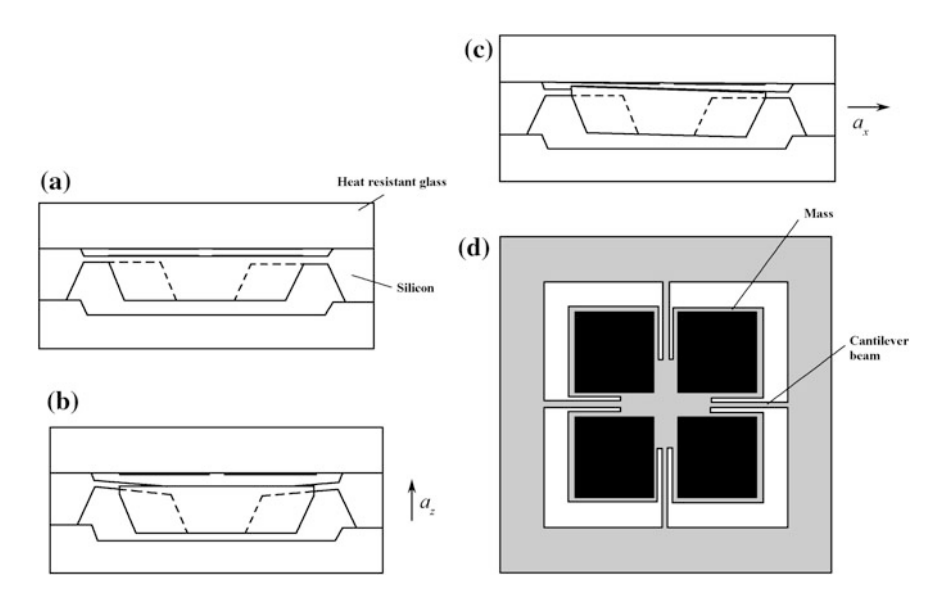


Fig. 5.7 Three axis capacitive micromechanical accelerometers for bulk micromachining, $\bf a$ Rest position; $\bf b$ Vertical displacement due to z axial acceleration; $\bf c$ Tilt due to x axial acceleration; $\bf d$ Top view of the mass and suspension structure

decrease. Under the condition of a first order approximation, by changing the magnitude of four capacitances the three axial components of an arbitrary input acceleration vector can be measured independently.

The sensitive axes of most single axis micromechanical accelerometers with bulk machining are perpendicular to the surface of the wafer and hence the accelerometers are called z axis micromechanical accelerometers. One of the reasons for this design is that it is easier to make this structure by wet etching. The structure of a micromechanical accelerometer whose sensitive axis is perpendicular to the crystal sphere surface is shown in Fig. 5.8a. This requires that the elastic element has a high rigidity in the vertical direction, or in other words the thickness of the cantilever should be much larger than its width. The main advantage of this structure is that the off-axis sensitivity is very low since it is highly symmetrical. The usual method of making a cantilever beam with a large aspect ratio was to use reaction ion deep dry etching, but in 1997 a lower cost method was developed where a standard KOH wet etching process is used to vertically etch the (100) plane on the wafer (100). The etching process is shown in Fig. 5.8b. It should be noted that the amount of wet etching under the oxide mask layer should not be less than 1/ 2 the thickness of the wafer so the wet etching time must be carefully designed and strictly controlled.

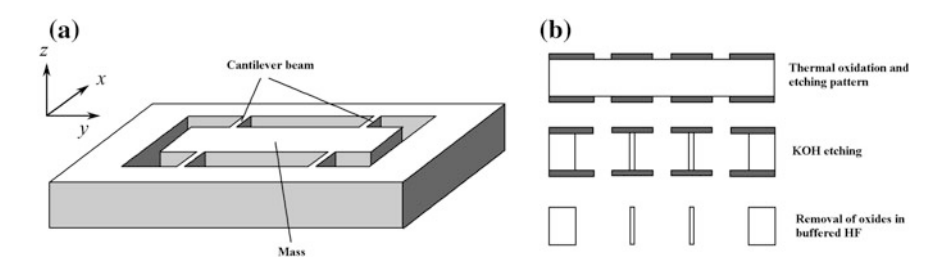


Fig. 5.8 Fabrication process of the z axial micromechanical accelerometer and cantilever beam, a Micromechanical accelerometers with bulk machining whose sensitive axis is parallel to the crystal sphere surface; **b** A large aspect ratio cantilever beam manufactured by a standard wet etching process

5.1.4 The Micromechanical Accelerometer Manufactured by a Surface Micromachining Process

A bulk micromachining process for manufacturing a micromechanical accelerometer also has many disadvantages and one of the most important disadvantages is that there must be a process where the glass is bonded to both sides of the silicon wafer with the aim of creating a suitable and mobile air gap for the mass, and to control its damping capacity and provide a capacitive interface. Because the thermal compatibility between the silicon and the glass is very poor, their adhesion may exacerbate the impact of the external temperature on the device and the long-term stability of the device becomes worse due to the slow self-release of the residual mechanical force. Therefore, high precision devices can only be manufactured with a silicon wafer. When a capacitive micromechanical accelerometer is manufactured, there is a compromise method with a large capacity and a low damping. This reducing of the air gap can effectively increase the capacitance, and can increase the damping so the micromechanical accelerometer for bulk micromachining is packaged in the condition of the designed pressure, which can control the damping performance of the product. The surface micromachining process can integrate the product in a wafer and it is very easy to integrate with the interface of the electronic circuit. Also, because it is a thin film structure, the method for making a through-hole array can be used to control the damping.

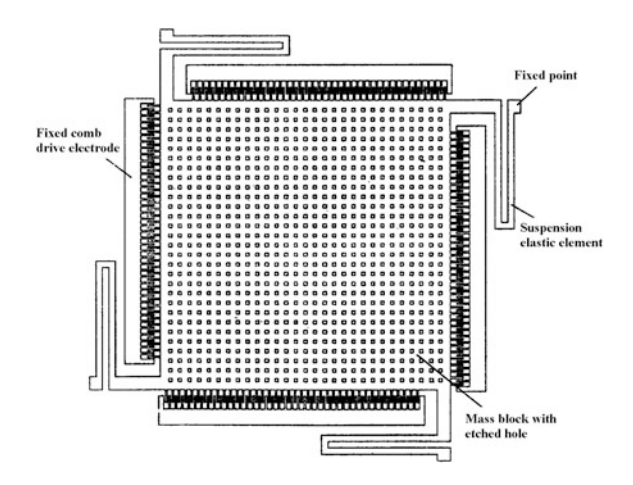
Micromechanical accelerometers manufactured by a bulk micromachining process and micromechanical accelerometers manufactured by a surface micromachining process can also be distinguished by their sensitive axes. In the vertical structure, the mass is perpendicular to the movement of the wafer surface axial, and the mass itself constitutes one of the electrodes of the flat capacitor. In the planar structure, the sensitive axis is parallel to the surface of a wafer, the mass is attached to a comb structure, and the other group of the fixed comb structure is deposited on

the base. These two groups of the comb finger structure are crossed and overlapped to constitute a comb capacitor. When the mass senses the acceleration and moves, the comb electrode on the mass will move, that is, the acceleration can be measured by the change of the capacitances between the two groups of comb electrodes. The advantage of the vertical structure is that it has a much larger capacity than the parallel structure, and this can be as high as 1 pF, while the capacity of the plane structure is less than 200 pF. However, the electrostatic force generated by the asymmetry of the vertical structure and the capacitance between the capacitor electrodes will push the mass to the surface of the wafer.

Figure 5.9 shows an example of a micromechanical accelerometer with a vertical structure, where the area of the mass is $400 \mu m \times 400 \mu m$ and the mass is suspended on the base by four supporting beams. The mass is one of the electrodes of the capacitor and the other electrode is made on the surface of the substrate. Firstly, the through-hole array on the mass completely etches the oxide sacrificial layer between the mass and the surface of the substrate. Because there is some air between the mass and the substrate these holes will reduce the damping effect caused by air compression. In order to optimize the sensitivity of a micromechanical accelerometer, the inertial mass must be as large as possible while the elasticity coefficient in the z axial of the suspension system should be as small as possible. The upper limit of the dimension of a mechanical structure is dependent on the smoothness of the polysilicon layer, and also affects the size of the mass. For micromechanical accelerometers with a micromachined silicon surface, the typical weight of the mass is about 0.5 μ g.

Because the mass is very small, in order to achieve certain sensitivity a soft elastic element must be selected. However, this must not be too soft otherwise the mass will droop due to gravity or self-vibrate and even adhere with the substrate. In Fig. 5.9, the vertical elastic coefficient of the supporting cantilever beam is designed as 1.1 N/m, thus the 10 mg acceleration can only cause 0.05 nm displacement and also requires a sensor circuit that is very sensitive to position.

Fig. 5.9 *Z* axial micromechanical accelerometer fabricated by a surface micromachining process



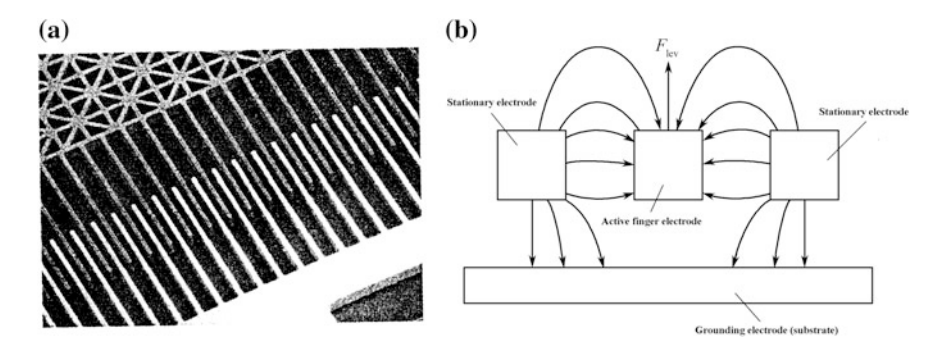


Fig. 5.10 Microphoto of a comb electrostatic drive actuator and the schematic diagram of the floating effect caused by an asymmetric electrostatic field force, a Comb electrostatic drive actuator; b Schematic diagram of a floating effect

As has been mentioned previously, there is a critical defect in the vertical structure such that the voltage of measuring the change of capacitance can generate an electrostatic force that pulls downward. In order to solve this problem, in the design of Fig. 5.9, a circle of a comb structure is added to the periphery of the mass. A force that is opposite to the electrostatic force is generated by the comb structure enabling the mass to stay in the normal position as shown in Fig. 5.10. The silicon substrate surface plays the role of a grounding electrode and can cause an asymmetric electric field, that is, an asymmetrical electric field distribution around the active finger electrode is formed and generates a pure pulling force, and if the displacement is small this force is approximately proportional to the square of the bias voltage. There is another solution where an auxiliary electrode is added to the mass but the whole manufacturing process becomes more complex.

Figure 5.11 shows a micromechanical accelerometer with a plane structure—a product developed by Devices Analog Inc. in 1995. The mass of this micromechanical accelerometer is suspended on the substrate through a U-shaped spring piece and two fixed points, and the mass also has a large number of through holes. These through holes are also used for etching the oxide sacrificial layer under the mass as it is difficult to completely remove the sacrificial layer without these through holes. However, unlike the vertical structure, for the planar structure these through holes are no longer needed to control the damping properties of the *z* axial movement of the mass. A comb structure is assembled onto the sensitive position of both sides of the mass and the electrostatic field force is applied onto the mass. The electrostatic field force can also be used for force feedback (Sect. 5.1.5) and self-detection.

Obviously, as long as one micromechanical accelerometer with a vertical structure and two micromechanical accelerometers with a plane structure are made simultaneously on a chip, a three axis micromechanical accelerometer can be achieved. Figure 5.12 gives the chip photo of this device—a micromechanical accelerometer with a surface micromachining with three axial accelerations

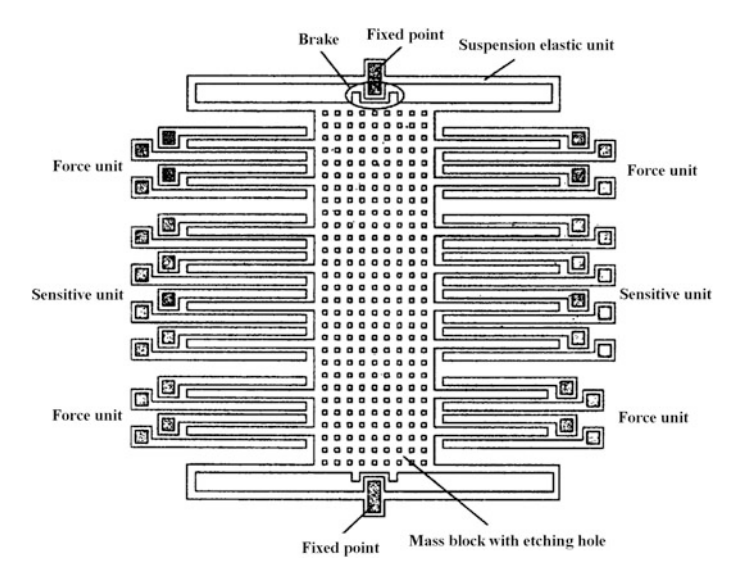
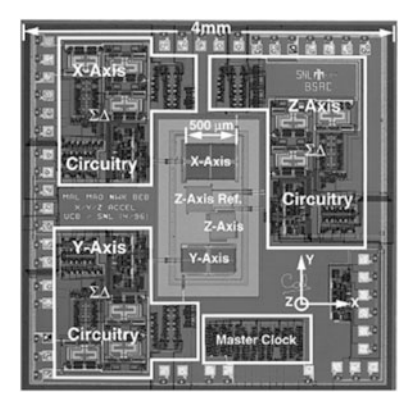


Fig. 5.11 Top view of a micromechanical accelerometer made by a surface micromachining process and with a sensitive axis parallel to the wafer plane

Fig. 5.12 A micromechanical accelerometer made by a three axial polysilicon surface micromachining process (middle part), the Σ - Δ readout circuit and control circuit (a peripheral part of the chip), and a master clock in the lower right part integrated in the chip



completely integrated in the middle part of the chip. The control circuit (labeled as Circuitry) and the readout circuit Σ – Δ (labeled as $\Sigma\Delta$) of every axial accelerometer are simultaneously integrated in the chip by the process of 2 μ m CMOS.

Compared with a bulk micromachined device, a micromechanical accelerometer with surface micromachining has many advantages, but its mass is too small and the noise is too large and these are critical defects. Because the bulk micromachined accelerometer is very large, the whole bandwidth from DC to 100 Hz can achieve an equivalent noise level that is less than $1 \,\mu\text{g}/\sqrt{\text{Hz}}$ Eq. (5.6) of a high sensitivity device, the noise level of a micromechanical accelerometer with surface micromachining is 100 times higher than that of a bulk micromachined accelerometer.

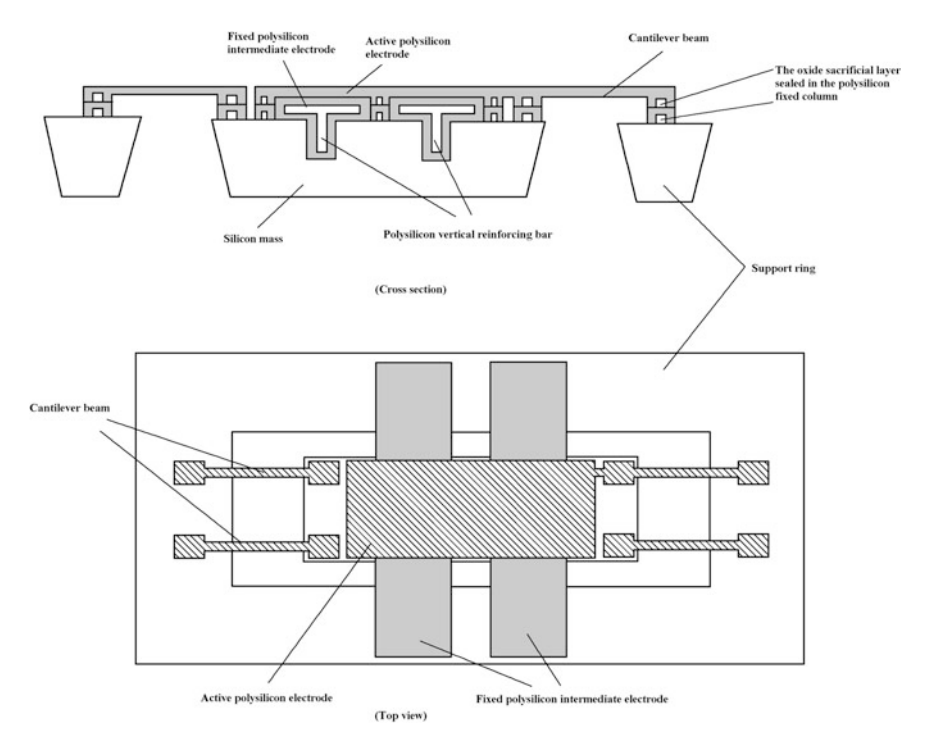


Fig. 5.13 Structure of a micromechanical accelerometer made by the combination of a bulk micromachining process and a surface micromachining process (simplified)

For many commercial applications (such as in the automotive industry), the micromechanical accelerometer with surface micromachining is not suitable and is unable to satisfy many systems that require precision measurement such as an inertial navigation and head mounted display tracking system. One of the solutions is that as shown in Fig. 5.13, the bulk micromachining process and the surface micromachining process are combined to create a micromechanical accelerometer. In this device, when the polysilicon of the two layers is used to make the large mass and the top cantilever beam, a process of adhering the wafer is not required. The first layer (bottom) of a polysilicon structure layer is used to fabricate the fixed electrode between the mass and the top (the electrode on top of the polysilicon is movable), the fixed polysilicon middle electrode is reinforced by the polysilicon vertical reinforcing bar which is made by using the method of a thin film deposition and a backfill aspect ratio trench on the mass. The reinforcement of the upper electrode is designed to be wider and shorter and some pillars of the electrical insulation are made on the mass to support the upper electrode. These pillars are made on the first layer of a polysilicon layer and an insulating layer is formed on the bottom and the top surface of these pillars. The oxide sacrificial layers between the mass and the first layer of polysilicon, and between the two electrodes is sealed in the polysilicon layer, and fixed to enable them to achieve and maintain a necessary height.

5.1.5 Force Feedback

From Eq. (5.5) it can be seen that the sensitivity of the micromechanical accelerometer can be improved effectively by reducing the resonant frequency of the mass. As long as an appropriate force gives a feedback to the device, the sensitivity of the micromechanical accelerometer and the mutual restriction relation between the vibration frequencies can be significantly changed. The feedback makes the useful bandwidth of the micromechanical accelerometer increase, the gain in the feedback loop becomes much larger and the bandwidth is increased. In fact, because the auxiliary circuit can be added, a larger gain can be obtained. Thus the bandwidth of the integrated micromechanical accelerometer cannot be considered and the mechanical bandwidth of the micromechanical accelerometer structure can be used to optimize the sensitivity. In addition, a force feedback cannot improve the dynamic range, linearity and drift of the device. For a micromechanical accelerometer with a low resistance and a high Q value, a force feedback is one of the main measures that prevents the mass from moving resonantly. This large movement will deteriorate the linearity of this device and the vibration amplitude also very easily exceeds the electrode spacing of a capacitive micromechanical accelerometer.

Figure 5.14 gives the block diagram of a micromechanical accelerometer with a feedback loop. The sensor part of the circuit is composed of a mass and a position measuring circuit, and a compensator and a force feedback transmitter are added. The feedback force is exactly opposite to the normal displacement of the mass so it is necessary to maintain the stability of the system. No compensator system is unstable because the micromechanical accelerometer is introduced beyond a force whose phase shift, is 180° and whose frequency is beyond the resonance point.

An electrostatic excitation is generally used to generate the feedback force. As is well known, there is an electrostatic attraction between the electrodes of the parallel plate capacitors, i.e.,

$$F_{\rm el} = \frac{1}{2} \frac{\varepsilon bl}{x^2} v^2 \tag{5.7}$$

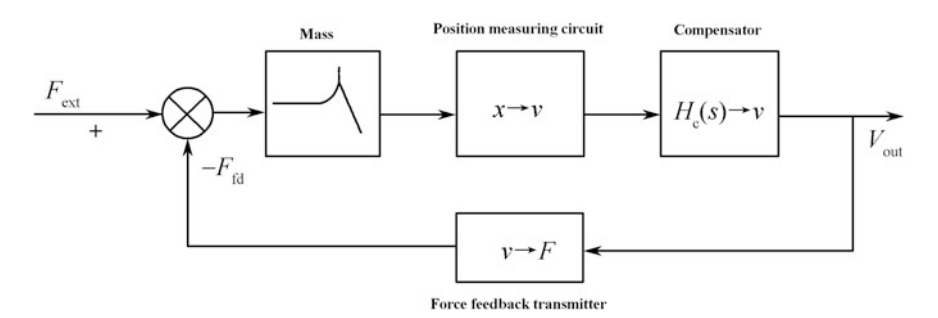


Fig. 5.14 Block diagram of a micromechanical accelerometer with a feedback loop

where b and l are the sizes of the capacitor plates; x is the distance between the electrodes; and v is the voltage between the electrodes.

It is can be seen that there is a quadratic relationship between the force and x and v. If the plate distance is less than a critical value, the system is unstable and the capacitor may fail. Thus it is necessary to anticipate and prevent the occurrence of this process.

Because there is a quadratic relationship between the electrostatic attraction and the voltage, the electrostatic actuator cannot be directly used. It is necessary to linearize the electrostatic actuator as shown in Fig. 5.11. It is very easy to linearize the symmetric micromechanical accelerometer. Each finger electrode of the mass is configured with two fixed finger-shape electrodes to form a capacitance unit and the voltages $v_0 + \Delta v$ and $v_0 - \Delta v$ are loaded. So, if the active finger-shaped electrode is in the middle position of two fixed electrodes, there is a linear relationship between the effective force $F_{\rm eff}$ and Δv , i.e.,

$$F_{\text{eff}} = \frac{1}{2} \frac{\varepsilon bl}{x^2} (v_0 + \Delta v)^2 - \frac{1}{2} \frac{\varepsilon bl}{x^2} (v_0 - \Delta v)^2 = \frac{2\varepsilon bl}{x^2} v_0 \Delta v \tag{5.8}$$

This is of course, not possible, so there will be some nonlinear relationships. This technique cannot be used for an asymmetrical structure such as the micromechanical accelerometer with a vertical structure in Fig. 5.9.

The common method and technology used to improve the linearity is to use a pulse modulated feedback signal, which quantifies the feedback signal into two electrical levels, and to use a comparator to select the feedback force signal. Figure 5.15 gives a block diagram of a micromechanical accelerometer with a digital force feedback loop where the comparator is only opened within a prescribed time period specified by the sample frequency f_s . In this method, the widths of all feedback pulses are the same so when the unbalance occurs it will only cause unbalance or increase the error but will not cause a distortion. This system is equivalent to a modulator that converts A/D into Σ - Δ , and the mechanical sensor is replaced by the noise wave filter. Through a low pass filter, the 1bit digital output pulse-density tracking input acceleration is selected from 10 pulse-density codes and outputs.

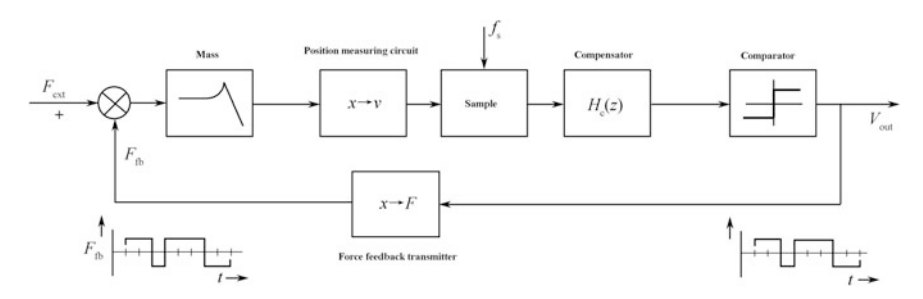


Fig. 5.15 Block diagram of a micromechanical accelerometer with digital force feedback loop

5.1.6 The Resonant Micromechanical Accelerometer

Since the emergence of silicon sensors, one of the key research directions has been to develop a sensor with a high resolution and a high stability, one of which is the resonant micromechanical accelerometer. The basic working principle of the resonant micromechanical accelerometer is that the variable stress of the mechanical structure can be used to change the resonant frequency of the structure and its outstanding advantages include high stability, high resolution and quasi-digital output.

Now, there are many varieties of resonant micromechanical accelerometers and many successful commercial products have been developed since the 1990s. However, it is not fast enough to be commercialized and there are not a lot of the large scale mass products. The reason may be higher manufacturing costs, the fact that its corresponding electronic circuit is more complex or the fact that its vacuum packaging technology is more complex and has some specialized requirements.

The development of the resonant micromechanical accelerometer is based on the resonant pressure transmitter and the difference is that the sensitive element of the resonant micromechanical accelerometer is installed at a suitable position of the cantilever beam in the cantilever-mass structure. Generally speaking, the design and manufacture of a resonant micromechanical accelerometer is much more difficult than that of the pressure transmitter. The main reason is that the cantilever-mass structure of the resonant micromechanical accelerometer must have the appropriate damping characteristics, i.e., characteristics that come close to the critical damping state, while the damping of the cantilever resonator should be as small as possible so the sensitive element must be mounted in a sealed vacuum chamber.

For a resonant micromechanical accelerometer, most common structures of the sensitive elements is that the strain change of a dual retention cantilever and other programs are used such as the stiffness change. The structure of a resonant micromechanical accelerometer based on the stiffness change is shown in Fig. 5.16. The structure of this sensor is made with a single crystal silicon layer on SOI

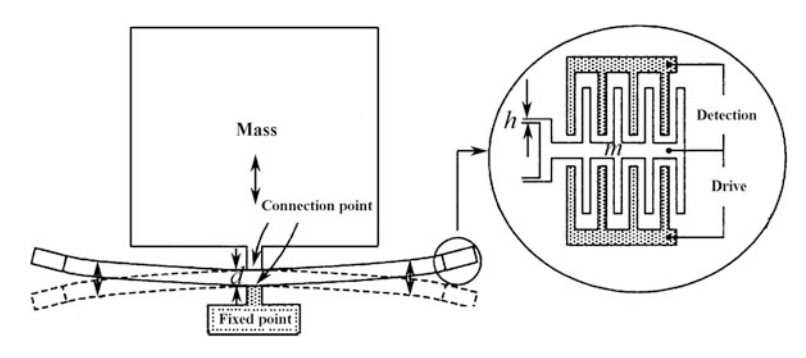


Fig. 5.16 Structure of a resonant micromechanical accelerometer based on the stiffness change

(Silicon on Insulator) wafer. Its thickness is about $10 \mu m$ and includes the mass, the resonator and the retainer connected by both ends of two parallel beams, two nodes connected to the beam and the mass, and the retainer. There is a comb-shaped electrode at both ends of the beam resonator, and these are used for capacitance detection of the resonant state and beam vibration of the electrostatic drive resonator.

As described in Sect. 5.1.2, the resonant frequency of the cantilever mass is $\omega_r = \sqrt{K/m}$, where the elastic coefficient *K* is

$$K = Ebh^3/l^3 (5.9)$$

where b is the width of the beam (i.e., the width of SOI); h is the thickness of the beam; and l is the length of the beam.

For the prototype shown in Fig. 5.16, $b = 10 \, \mu \text{m}$, $h = 1 \, \mu \text{m}$, $l = 500 \, \mu \text{m}$, thus $K = 1.36 \times 10^{-2} \, \text{N/m}$. In this example m is $6 \times 10^{-9} \, \text{kg}$, thus $\omega_{\text{r}} = 1\,505$ rad/s or $f_{\text{r}} = 240 \, \text{Hz}$ can be obtained with this device.

In the mode of a fundamental frequency vibration, the resonant frequency of the beam resonator can be expressed as

$$\omega_b = \sqrt{\frac{3EI_b}{m'l_{\text{eff}}^3}} \tag{5.10}$$

where I_b is the inertia moment of the parallel beam structure; m' is the mass of the beam; and $l_{\rm eff}$ is the effective length of the beam, which is different from the length l of the realistic beam because the driving mechanism is at the end of the parallel beam.

For the bending motion of the parallel beam structure, the inertia moment will be

$$I_b = \int_{-\frac{d}{2}}^{-\frac{d}{2}+h} by^2 dy + \int_{\frac{d}{2}-h}^{\frac{d}{2}} by^2 dy$$

where d is the width of the beam (Fig. 5.16). After integration

$$I_b = \frac{2}{3}b \left[\left(\frac{d}{2} \right)^3 - \left(\frac{d}{2} - h \right)^3 \right]$$
 (5.11)

If the above-mentioned structural parameters are still selected, and for the beam structure, $d=20~\mu m$, the initial inertia moment of the beam structure can be calculated.

$$I_{\text{bo}} = 1.81 \times 10^{-21} \text{ m}^4$$

Assume the mass of the end of the parallel beam structure $m'=2\times 10^{-9}$ kg, the effective length of one side of the beam structure $l_{\rm eff}=650~\mu m$, and by using the above equation the initial vibration frequency of a beam structure can be obtained: $\omega_{\rm bo}=41\,000~{\rm rad/s}$ or $f_{\rm bo}=6.52~{\rm kHz}$.

Equations (5.10) and (5.11) show that the resonant frequency is a function of the parameter d. According to Eq. (5.2), d can be changed by the displacement of the mass and the vibration frequency of the beam is changed due to the acceleration.

The average width of the beam structure is

$$\bar{d} = d_0 - \frac{ma}{2K} \tag{5.12}$$

After taking the first order approximation

$$I_b \approx \frac{1}{2} b h \bar{d}^2 \tag{5.13}$$

Substitute Eqs. (5.12) and (5.13) into (5.10) and obtain

$$\omega_b = \sqrt{\frac{3Ebh}{2ml_{\text{eff}}^3}} \left(d_0 - \frac{ma}{2K} \right) \tag{5.14}$$

Thus

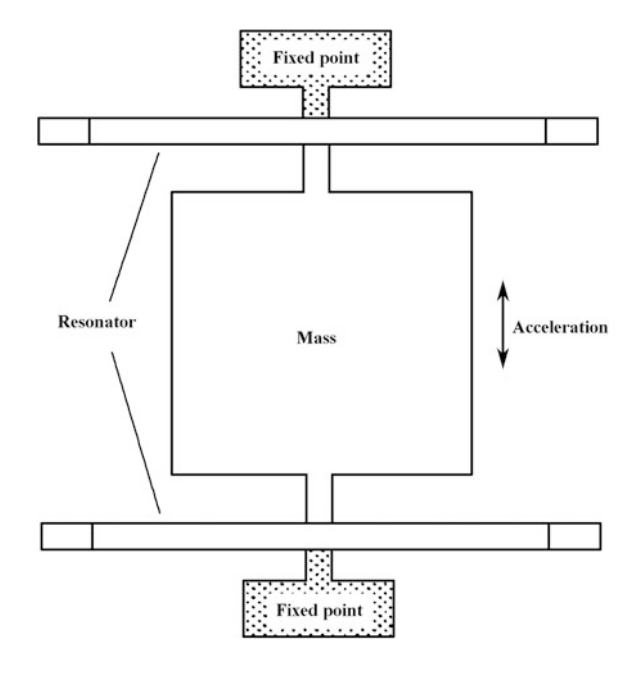
$$\frac{\Delta\omega_b}{\omega_{\text{bo}}} = \frac{ma}{2Kd_0} \tag{5.15}$$

If the acceleration is 1 g, for this example, there is

$$\frac{\Delta\omega_b}{\omega_{bo}} \approx \frac{6 \times 10^{-9} \times 9.8}{2 \times 1.36 \times 10^{-2} \times 2 \times 10^{-5}} = 10.8\%$$

The basic design scheme of Fig. 5.16 can also be modified into the design scheme of Fig. 5.17. In this structure, a pair of resonators is hung at two ends of the mass respectively. The obvious advantage is that the orthogonal axial sensitivity can be reduced and the temperature coefficient of the temperature effect is also small.

Fig. 5.17 Schematic diagram of a differential design for the resonant accelerometer



5.2 The Micromechanical Gyroscope

5.2.1 The Structural Basis of a Micromechanical Gyroscope

The structure of a gyroscope made by the process of silicon micromachining is based on the mutual coupling resonator with two vibration modes. The first vibration mode is used to drive the structure and the second vibration mode is induced by the structure input angular velocity under the action of Coriolis force and its frequency is the same as that of the first vibration mode. The amplitude of the secondary vibration is proportional to the angular velocity. Because the amplitude of the second vibration mode is much smaller than that of the first vibration mode, it is important to match the induced oscillation frequency with each other and increase the induced amplitude. The electronic regulator with an adjustable elastic constant or the design of a high symmetry structure can be used.

The first silicon coupled resonator gyroscope appeared in the early 1990s and its structural layout is shown in Fig. 5.18. The device is made by the micromachining process and is supported on the torsion beam. It has a micro mass made by doped (p⁺⁺) single crystal silicon. Its peripheral universal support is driven by the static electricity with a uniform amplitude, and the inner universal support moves due to the induction. The rate resolution of this gyroscope is very low at only 4 (°)/s, and the bandwidth is only 1 Hz.

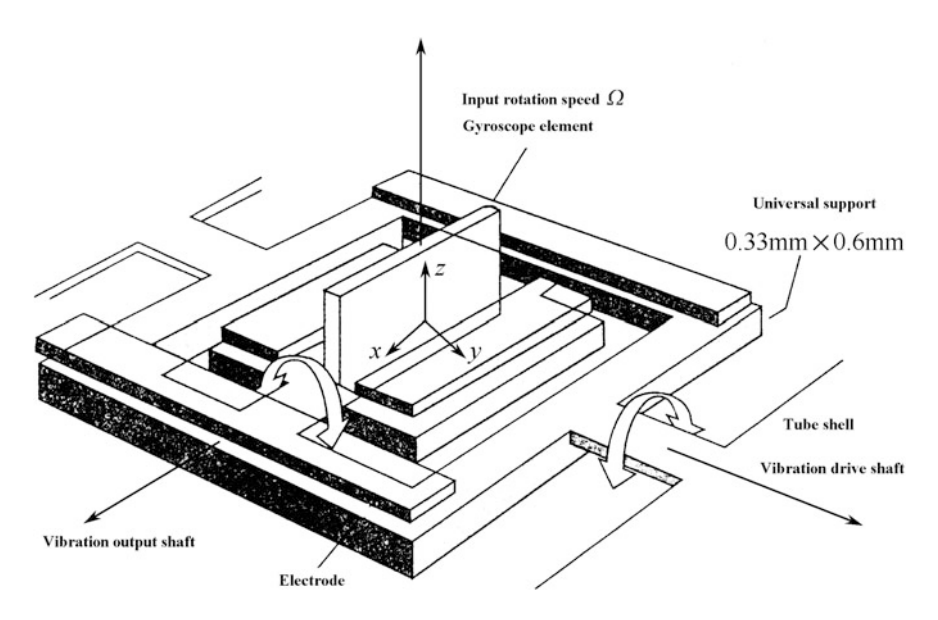


Fig. 5.18 Coupled resonator gyroscope made with early silicon material

Table 5.3 Properties of the MARS-RR1 coupled resonator gyroscope

Parameters	Values
Tilt stability	0.018 (°)/s
Noise	0.27 (°)/h
Sensitivity	10 mV/((°)/s)
Nonlinearity	<0.2%
Source voltage	15 V
Current (Separation Device circuit)	20 mA
Impact resistance	1000 g

By the end of the 1990s, micro gyroscopes made by the polysilicon surface micromachining process were much more advanced numerous models were available. The properties of the MARS-RR1 coupled resonator gyroscope are shown in Table 5.3.

There are a number of other types of gyroscope that can measure the precise rate such as IDT MEMS (Ion Doping Technology), and ring gyroscopes, etc. The ring gyroscope also uses Coriolis force to transfer the energy from one mode to another mode with 45°. In particular, the basic manufacturing process does not require the use of deep etching technology for the manufacture of the vibrating parts. Figure 5.19 shows prototype photos of two ring gyroscopes.

The national defense industry is very interested in silicon micromechanical gyroscopes for applications such as the control of the rotating flight carrier, but with the decrease in price of commercially available products there are rapidly expanding civilian industries such as the automobile industry and mobile robot technology.

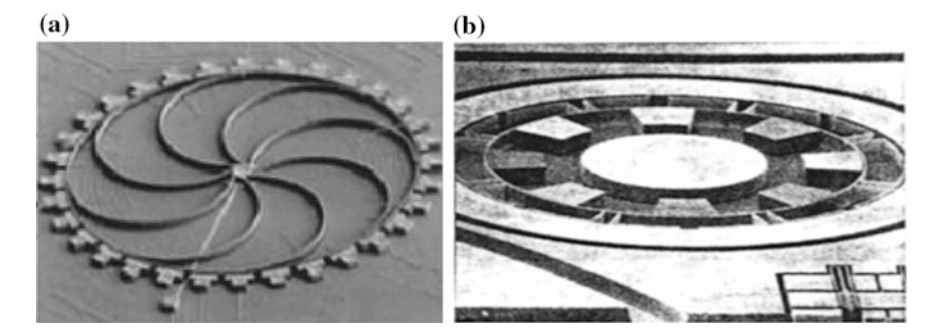


Fig. 5.19 Ring gyroscopes, a University of Michigan, USA; b British DERA

5.2.2 The Basic Principle of a Micromechanical Gyroscope

Almost all the micromechanical angular velocity sensors are used to sense the rotational motion of the vibrational element. The speed and rotational motion of the vibrational element are combined together to generate a Coriolis acceleration that is perpendicular to the vibrational direction and forces the vibrational element vibrate according to the second mode. This mode is perpendicular to the first mode and its amplitude is proportional to its rotational speed.

The Coriolis effect can be easily explained using Fig. 5.20a. Assume that there is a ball that linearly moves on the rotating disk. Although the ball moves linearly from the disk center to the disk side, the ball follows an arc trajectory on the disk and the size of the arc is proportional to the rotating speed of the disk. The Coriolis force is generated under the action of the acceleration. This Coriolis acceleration is generated by the combination of the disk's angular velocity vector $\boldsymbol{\nu}$ and the velocity vector $\boldsymbol{\nu}$ of the ball motion, i.e.,

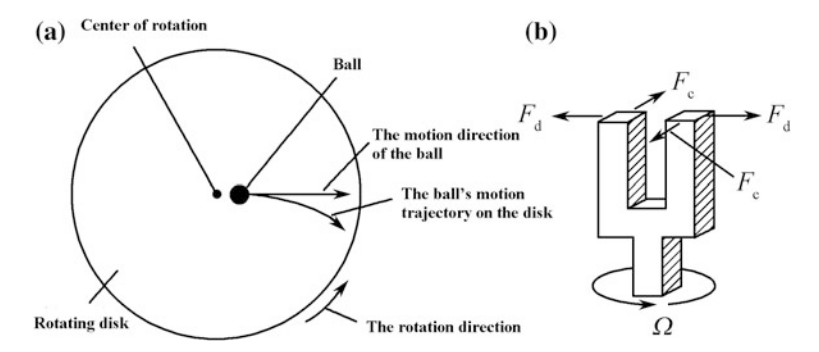
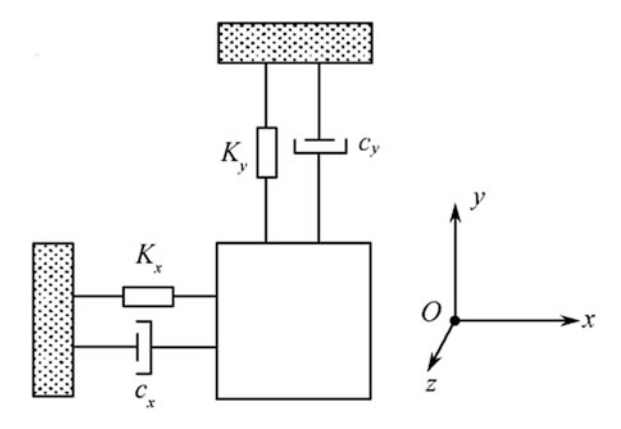


Fig. 5.20 Coriolis effect, a Motion trajectory of the small ball shows the Coriolis effect on the rotating disk; b Tuning fork angular velocity sensor with the principle of the Coriolis effect

Fig. 5.21 Simplified equivalent model of a vibrating gyroscope



$$a_C = 2v \times \Omega \tag{5.16}$$

A good example of Coriolis acceleration is the tuning fork angular velocity sensor in Fig. 5.20b. The fork finger of the tuning fork is the differential drive but its amplitude remains unchanged. The rotational movement with the fork handle as the axis produces a Coriolis acceleration that is vertical to the driving force. This Coriolis force can be detected by the fork finger bending or the torsional vibration of the fork handle.

So far, almost all vibration gyroscopes are micromechanical gyroscopes. The simplified equivalent model of the vibration gyroscope is shown in Fig. 5.21. This equivalent model is a vibrational system with two orthogonal modes: the mass along the x axis of driving vibration mode, the vibration frequency is ω_x , the mass along the y axis of the induced vibrational mode, the vibrational frequency is ω_y . When working, the mass is excited to vibrate along the axis x. The driving vibrational frequency of the excitation is ω_d , and the amplitude is A_d , thus

$$x = A_d \sin \omega_d t \tag{5.17}$$

If the system rotates around the z axis (a vertical paper) and its angular velocity is Ω , there will be a Coriolis force that acts on the mass along the direction of the y axis:

$$F_c = 2m\dot{x}\Omega \tag{5.18}$$

Substitute Eq. (5.7) into Eq. (5.18) and obtain

$$F_c = 2mA_d\omega_d\Omega\cos\omega_dt \tag{5.19}$$

The differential equation for the y axis motion of the mass is

$$m\ddot{y} + c_y \dot{y} + K_y y = 2mA_d \Omega \omega_d \sin\left(\omega_d t + \frac{\pi}{2}\right)$$
 (5.20)

where c is the damping coefficient, K is the elastic coefficient, and their subscripts indicate the motion direction.

The displacement in the y axis direction is

$$y = A_y \sin\left(\omega_d t + \frac{\pi}{2} - \varphi\right) = A_y \cos(\omega_d t - \varphi)$$
 (5.21)

where A_{y} is the amplitude of the induced vibration (the y axis vibration).

Assume that $\zeta_{\rm v} = c_{\rm v}/(2m\omega_{\rm v})$, thus

$$A_{y} = \frac{2A_{d}\omega_{d}\Omega}{\omega_{y}^{2}\sqrt{\left(1 - \frac{\omega_{d}^{2}}{\omega_{y}^{2}}\right) + 4\zeta_{y}^{2}\frac{\omega_{d}^{2}}{\omega_{y}^{2}}}}$$
(5.22)

$$\varphi = \arctan \frac{2\zeta_y \omega_d \omega_y}{\omega_y^2 - \omega_d^2} \tag{5.23}$$

From Eq. (5.22), the amplitude of the induced vibration A_y is proportional to the angular velocity Ω . A_y can be measured by a variety of methods and the angular velocity can be calculated. If the damping ratio ζ_y is smaller, Eq. (5.22) can be rewritten as

$$A_{y} = \frac{2A_{d}\omega_{d}\Omega}{\omega_{y}^{2}\sqrt{\left(1 - \frac{\omega_{d}^{2}}{\omega_{y}^{2}}\right) + \frac{1}{Q_{y}^{2}}\frac{\omega_{d}^{2}}{\omega_{y}^{2}}}}$$
(5.24)

where Q_y is the quality factor of the induced vibration mode, $Q_y = \frac{1}{2\zeta_y}$.

If the vibration frequency induction ω_y is equal to the driving frequency ω_d , Eq. (5.24) can be changed into

$$A_{y} = \frac{2A_{d}\Omega Q_{y}}{\omega_{y}} \tag{5.25}$$

Since Ω is much smaller than ω_y , and in order to obtain a larger output signal, the drive amplitude A_d and the sensing pattern Q should be as large as possible, while ω_y should be small.

For the gyroscope, the driver can use the electrostatic method, the piezoelectric method, the electromagnetic method and the electric heating method and the sensing mode can use the capacitance method, the pressure sensitive resistance method or the piezoelectric effect method.

5.2.3 Frequency Bandwidth

Equation (5.25) gives the gyroscope's sensitivity, but it only has maximum sensitivity in the condition of resonance with $\omega_d = \omega_y$. Therefore, it is only applicable to the condition when the angular velocity is constant and the bandwidth is equal to zero. Generally speaking, the rate signal is dependent on time so it contains a series of frequency components. Therefore, when the frequency component is non-zero, the above discussion is insufficient. Two methods are often used to establish a clear frequency range (bandwidth), which is then used to regulate the frequency component of the signal that cannot be avoided:

- (1) ω_d is separated from ω_y . This method can make the system's bandwidth large, but the sensitivity is decreased.
- (2) To broaden the bandwidth of the system by using electromechanical feedback technology, which includes the maximum sensitivity with $\omega_d = \omega_y$, but it must be equipped with sophisticated electronic circuits.

Only the first method is discussed here. Assuming that the angular velocity signal of the radial frequency ω_s is

$$\Omega(t) = \Omega_0 \cos \omega_s t \tag{5.26}$$

According to Eq. (5.20), the differential equation of the mass along the y axis motion should be

$$m\ddot{y} + c_y\dot{y} + K_yy = 2mA_d\Omega_0\omega_d\cos\omega_dt\cos\omega_st$$

where the right part of the Coriolis force can be divided into two parts (one part being the high end and the other part being the low end), the equation can be written as

$$\ddot{y} + \frac{\omega_y}{Q_y} \dot{y} + \omega_y^2 y = A_d \Omega_0 \omega_d [\cos(\omega_d + \omega_s)t + \cos(\omega_d - \omega_s)t]$$
 (5.27)

The solution of this equation is

$$y(t) = B_u \cos[(\omega_d + \omega_s)t + \phi_u] + B_l[\cos(\omega_d - \omega_s)t + \phi_l]$$
 (5.28)

where the parameters of the subscript u and 1 represent the high-end frequency $(\omega_d + \omega_s)$ and the low-end frequency $(\omega_d - \omega_s)$ respectively. The parameters in this equation are

$$B_{u} = \frac{A_{d}\Omega_{0}\omega_{d}}{\sqrt{\left[\omega_{y}^{2} - (\omega_{d} + \omega_{s})^{2}\right]^{2} + \left[\frac{(\omega_{d} + \omega_{s})\omega_{y}}{Q_{y}}\right]^{2}}}$$
(5.29)

$$\phi_u = \arctan \frac{\omega_d(\omega_d + \omega_s)}{\left[\omega_y^2 - (\omega_d + \omega_s)^2\right] Q_y}$$
 (5.30)

$$B_1 = \frac{A_d \Omega_0 \omega_d}{\sqrt{\left[\omega_y^2 - (\omega_d - \omega_s)^2\right]^2 + \left[\frac{(\omega_d - \omega_s)\omega_y}{Q_y}\right]^2}}$$
(5.31)

$$\phi_1 = \arctan \frac{\omega_d(\omega_d - \omega_s)}{\left[\omega_y^2 - (\omega_d - \omega_s)^2\right]Q_y}$$
(5.32)

According to Eq. (5.23), the frequency differences between φ , and ω_y and ω_d (i.e., $\Delta \omega = \omega_y - \omega_d$) are dependent, and if the difference between ω_d and ω_y is not much, then

$$\varphi pprox \arctan rac{\omega_y}{2Q_y\Delta\omega}$$

For example, if $\omega_y=1$ kHz, Q=1000, $\Delta\omega=180$ rad/s (29 Hz), then $\varphi\approx1^\circ$. In general, ω_d is usually smaller than ω_y by a few percent and when ω_s is a fixed value, ϕ_1 is also very small, and it can be approximately taken that with $\phi_1=0$, the amplitude of the sensing mode is expanded as

$$y(t) = B_u \cos \Phi_u \cos \omega_d t \cos \omega_s t - B_u \cos \phi_u \sin \omega_d t \sin \omega_s t - B_u \sin \phi_u \sin \omega_d t \cos \omega_s t - B_u \sin \phi_u \cos \omega_d t \sin \omega_s t + B_1 \cos \omega_d t \cos \omega_s t + B_1 \sin \omega_d t \sin \omega_s t$$

$$(5.33)$$

The signal is synchronously demodulated with $\cos\omega_{\rm d}t$, and the output will be

$$y_0(t) = (B_u \cos \phi_u + B_1)\cos \omega_s t - B_u \sin \phi_u \sin \omega_s t \qquad (5.34)$$

This equation can also be rewritten as

$$y_0(t) = A(\omega_s)\cos[\omega_s t - \theta(\omega_s)]$$
 (5.35)

where

$$A(\omega_s) = \sqrt{(B_u \cos \phi_u + B_1)^2 + (B_u \sin \phi_u)^2}$$
 (5.36)

$$\theta(\omega_s) = \arctan\left(-\frac{B_u \sin \phi_u}{B_u \cos \phi_u + B_1}\right) \tag{5.37}$$

Substitute Eqs. (5.29), (5.30) and (5.31) into Eq. (5.36) and obtain

$$A(\omega_s) = \frac{A_d \Omega_0 \omega_d}{\omega_y \Delta \omega \sqrt{4 \left(1 - \frac{\omega_s}{\Delta \omega}\right)^2 + \frac{1}{Q_i^2}}} \sqrt{1 + \frac{\left(1 - \frac{\omega_s}{\Delta \omega}\right)^2 + \frac{1}{4Q_i^2}}{\left(1 + \frac{\omega_s}{\Delta \omega}\right)^2 + \frac{1}{4Q_i^2}} + \frac{4 \left(1 - \frac{\omega_s}{\Delta \omega}\right)}{\sqrt{4 \left(1 + \frac{\omega_s}{\Delta \omega}\right)^2 + \frac{1}{Q_i^2}}}}$$

$$(5.38)$$

where Q_i is defined as

$$Q_i \equiv \frac{\Delta\omega}{\omega_y} Q_y \tag{5.39}$$

Equation (5.38) shows that the function $A(\omega_s)$ is equivalent to the amplitude of the resonant vibrational system with the effective quality factor Q_i . From Eq. (5.39) it can be seen that Q_i is dependent on $\Delta\omega$ and is usually much smaller than Q_y . For example, if $Q_y = 1000$, $f_d = 900$ Hz and $f_y = 1000$ Hz, then $Q_i = 100$.

The relationship curve between $A(\omega_s)$ and ω_s is shown in Fig. 5.22. From Eq. (5.38), in the case that $\omega_s = 0$, $A(0) \approx A_d \Omega_0 / \Delta \omega$, i.e., the amplitude is inversely proportional to $\Delta \omega$. When $\omega_s = \Delta \omega$, its peak value can be Q_i times higher than A(0), i.e., $A(0):A(\Delta \omega) \approx Q_i A(0)$.

The bandwidth of the gyroscope can be calculated using Eq. (5.38). If the signal frequency is smaller than $\Delta\omega$ and their difference is very large, $1/Q_i^2$ in Eq. (5.38) can be ignored and Eq. (5.38) can be approximated by

$$A(\omega_s) = \frac{A_d \Omega_0 \omega_d}{\omega_y \Delta \omega \left(1 - \frac{\omega_s^2}{\Delta \omega^2}\right)}$$
 (5.40)

The gain bandwidth $\Delta\omega_s$ whose gain is 3 dB can be determined by:

$$1 - \frac{\Delta\omega_s^2}{\Delta\omega^2} = \frac{1}{\sqrt{2}} \tag{5.41}$$

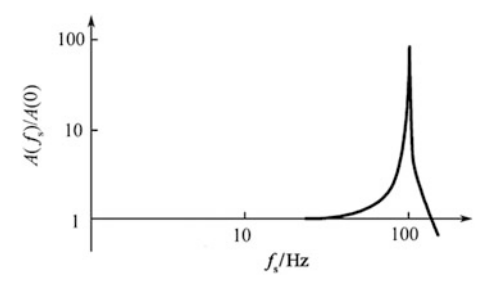


Fig. 5.22 Relationship curve between $A\omega_s$ and ω_s , $(Q_y = 1000, f_d = 900 \text{ Hz}, f_y = 1000 \text{ Hz})$

Thus $\Delta\omega_s = 0.54\Delta\omega$. This means that if the increase of the 1 Hz bandwidth is needed $(\Delta\omega_s)$, $\Delta\omega$ must be increased by at least 1.85 Hz.

5.2.4 Thermal Mechanical Noise

The intrinsic thermal mechanical noise of the mechanical structure, in the process of a small signal detection, often plays a key role in the restrictive function. The noise level and the inertial force of a micromechanical accelerometer may be very small, but for the gyroscope the Coriolis force is even smaller than the inertial force so the influence of the thermal mechanical noise may be very serious.

For the induced vibration, as in Eqs. (5.18) and (5.19), $m\ddot{y} + c_y\dot{y} + K_yy = F_c = 2m\Omega\omega_dA_d$. If the bandwidth of the system is Δf , the fluctuating force which is caused by the thermal mechanical noise and is dependent on the system is determined by

$$F_N = \sqrt{4k_BTc\Delta f}$$

where c is the damping coefficient; and k_B is the Boltzmann constant.

Therefore, the angular velocity signal Ω_n , which is determined by the thermal mechanical noise and is equivalent to the thermal mechanical noise can be calculated by the following conditions:

$$2m\Omega_n\omega_d A_d = \sqrt{4k_BT_C\Delta f}$$

Then

$$\Omega_n = \sqrt{\frac{k_B T \omega_y \Delta f}{m \omega_d^2 A_d^2 Q_y}}$$
 (5.42)

where Q_y is the quality factor for the y axis; and ω_d is usually very close to ω_y .

According to Eq. (5.42), in order to decrease the angular velocity signal which is equivalent to the mechanical thermal noise, some measures must be taken to make the mass of the vibratory gyroscope, the working frequency ω_d , and the driving amplitude A_d as large as possible, and the system bandwidth Δf limited to a small value. One of the most effective ways is to seal the device in a vacuum such that the value Q of the system can be significantly improved.

For example, the parameters of the gyroscope working at room temperature (T=300 K) are as follows: $A_d=10 \text{ \mu m}$, $m=1.2 \times 10^{-9} \text{ kg}$; $f_d=1000 \text{ Hz}$, $\Delta f=100 \text{ Hz}$, Q=1000. $\Omega_n=7.4 \times 10^{-4} \text{ rad/s}$ is calculated, or 153° per hour. Obviously, this is not a small amount and cannot be ignored in many applications.

If you want to extend the bandwidth but do not want to increase the impact of the thermal mechanical noise on the equivalent angular velocity signal, then advanced mechanical and electrical technology can be used but the signal processing circuit must be applied.

5.2.5 Types of Micromechanical Gyroscope

The realization of a vibration gyroscope has many methods but the most commonly used design method is still the tuning fork gyroscope. However, its structure is completely unlike the traditional tuning fork shape and only their principles are similar. The tuning fork gyroscope in Fig. 5.23 has a movable mass plate which is similar to a tuning fork finger, but is driven by the comb potential driver. These two movable mass plates can axially vibrate along two mutually perpendicular axes, and in the structure shown in this figure the x axis has the same plane as the movable mass plate and the y axis is perpendicular to the movable mass plate. The two axial intrinsic vibration frequencies are ω_x and ω_y , respectively.

When working, two movable mass plates are driven into the different phases of the vibration mode. When the device rotates around the axis z, the Coriolis force begins to work on the two movable mass plates. The two forces are perpendicular to the movable mass plate, but their directions are opposite. As a result, the oscillations of the two movable mass plates caused by the Coriolis force are in a different phase. At the same time, such oscillations can be detected by the capacitance change of the movable mass plate.

It is assumed that the structure in Fig. 5.23 is made of the polysilicon and the movable mass plate is hung on the substrate and the space is 2 μ m. The geometric parameters of this structure are also assumed as follows: the area of the movable mass plate is 500 μ m \times 500 μ m, the length of the cantilever beam is 500 μ m, and the width of the cantilever beam is 2.5 μ m. From these parameters, the following results can be calculated: $m = 1.165 \times 10^{-9}$ kg, $K_x = 0.17$ N/m,

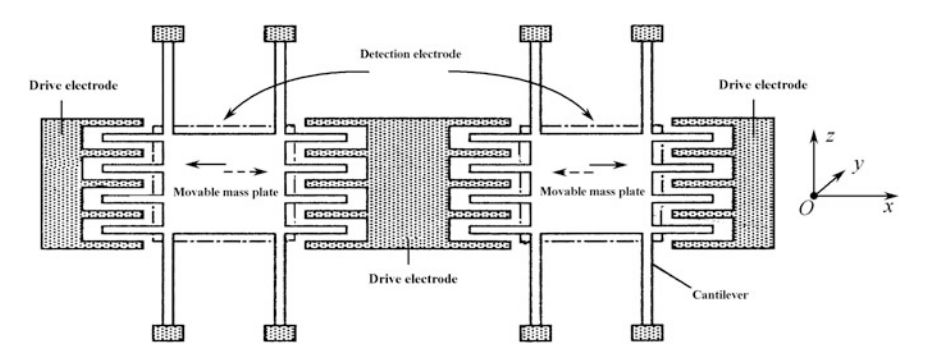


Fig. 5.23 Schematic structure of a tuning fork gyroscope

 $\omega_x = 12080$ rad/s, $K_y = 0.109$ N/m, $\omega_y = 9664$ rad/s, and the initial capacitance $C_0 = 1.11$ pF between the mass plate and the substrate.

If the amplitude of the driving vibration is 1 μ m, the value of Q is 1000, and for an angular velocity signal of 1 (°)/s, the amplitude of the induced vibration is $A_v = 3.61 \times 10^{-9}$ m.

As a result, the relative change of the capacitance is

$$\frac{\Delta C}{C_0} \approx \frac{A_y}{d_0} = 1.81 \times 10^{-3}$$
 (5.43)

that is, if the change of the capacitance range reaches about 20% of the capacitance of the sensor, the operating range of the device will be about 100 (°)/s.

The biggest problem with an angular velocity sensor based on the Coriolis effect is that the amplitude of the induced vibration is too small. For example, if the vibration driving structure of the sine wave $x(t) = A_d \sin(\omega_d t)$, the Coriolis acceleration in Eq. (5.19) is

$$a_c = 2\Omega A_d \omega_d \cos(\omega_d t) \tag{5.44}$$

Therefore, when the driving amplitude $A_{\rm d}$ is 1 μ m, the driving frequency ω_d is 20 kHz, and the angular velocity Ω is 1 (°)/s, then the amplitude of the Coriolis acceleration is only 4.4 mm/s². If it is assumed that the value Q of the induced mass system is 1 and the resonant frequency is similar to the driving frequency, then from Eq. (5.5) the displacement is only 0.0003 nm.

In order to increase the amplitude of the induced vibration, two kinds of technique are usually adopted.

- (1) Increase the amplitude of the driving vibration. From Eq. (5.44), the system sensitivity can be improved by increasing the amplitude of the driving vibration. The electromagnetic excitation technique can be used to raise the vibration amplitude to 50 μ m, but although this method can greatly improve the output signal level, it increases the total energy consumption of the system and in the long-term working process the problem of fatigue damage may occur.
- (2) Match the high quality factor, the driving frequency, and the resonant frequency of the induction mode. From Eq. (5.44) it is known that the Coriolis acceleration is essentially a signal of an amplitude modulation with a carrier frequency ω_d . In order to match the resonant frequency of the induction mode with ω_d , the gain of the structure can be increased by Q times, but at the same time the bandwidth will be limited to the level of ω_d/Q . Therefore, the typical value of Q in a vacuum is 10,000 and the bandwidth will be reduced to only a few Hz. As has been mentioned before, in order to achieve an acceptable bandwidth and improve sensitivity, it should disturb the resonant frequency and the driving frequency moderately (mildly).

In order to obtain a larger driving amplitude the logical choice is to use electromagnetic excitation technology. Figure 5.24 shows a diagram of two kinds of

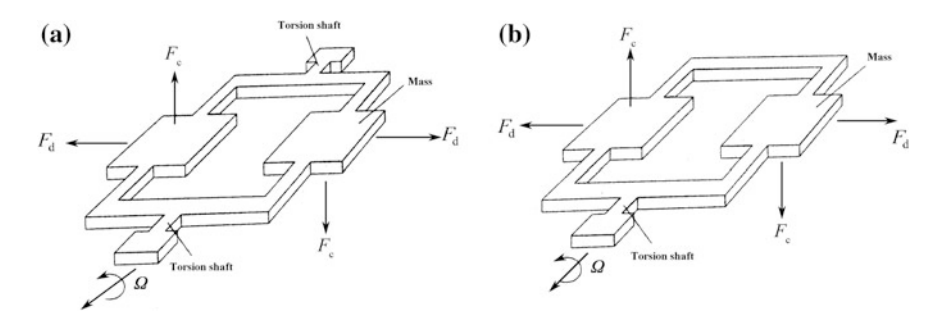


Fig. 5.24 Tuning fork gyroscope a Double torsion shaft suspension structure; b Single torsion shaft suspension structure

tuning fork gyroscope manufactured with a micromachining process using an electromagnetic drive. A permanent magnet is assembled in the package tube to form a static magnetic field which is necessary and is perpendicular to the surface of the wafer. The alternating current is input through the finger of a tuning fork and interacts with the magnetic field to produce a driving Lorenz force. The silicon structure is bonded between two pieces of glass sheet and the vibration caused by the Coriolis acceleration is sent through the capacitance, and the capacitance of the electrode is made on the glass sheet. With the aid of finite element method (FEM) analysis, the match of the driving and the resonant frequency of the induction mode is very good. If the single torsion shaft suspension structure is used as shown in Fig. 5.24b, then the metallization pattern should be deposited on the tuning fork to conduct the excitation current. The production process of a single torsion shaft is slightly more complex, but compared with a double torsion shaft it has many advantages. Firstly, the loss caused by the suspension point is reduced and the value Q of the single torsion shaft is much higher than that of the double torsion shaft. In addition, the influence of the package stress and the temperature fluctuation on the single torsion shaft is small for similar reasons.

In the tuning fork structure shown in Fig. 5.24, two masses undergo linear acceleration. The effects of linear acceleration on the two masses are the same so the position difference of the sensor can be used to eliminate the effect of a linear acceleration. This is also the reason that two blocks of masses are used.

Figure 5.25 Top view of a double shaft angular velocity sensor with four masses Four masses of a similar motor rotor structure can be chosen (Fig. 5.25) to replace the above double mass structure. By using this method, the double axis angular velocity sensor can be realized and the rotation around any input shaft will force the structure to tilt, whose inclination can be detected by the electrode capacitance of the structure and the substrate under the structure. Like the structure in Fig. 5.24b, there is only one fixed point between the double axis angular velocity sensor and the substrate. Thus the sensitivities of the structure to the mechanical stress and the thermal stress of the substrate and the packaging can obviously be reduced.

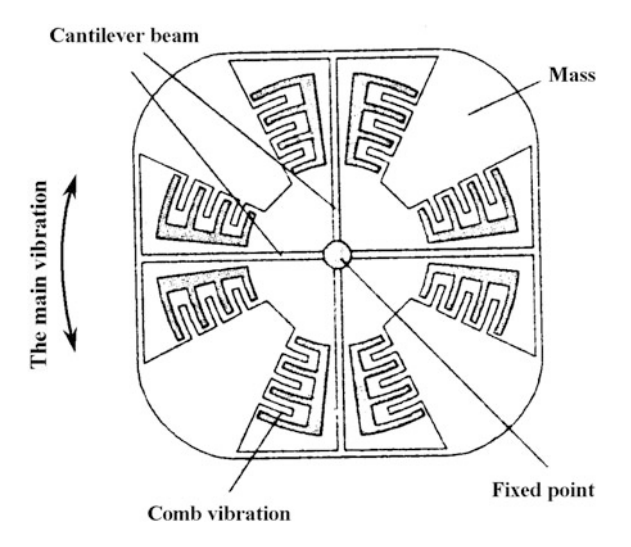


Fig. 5.25 Top view of a double shaft angular velocity sensor with four masses

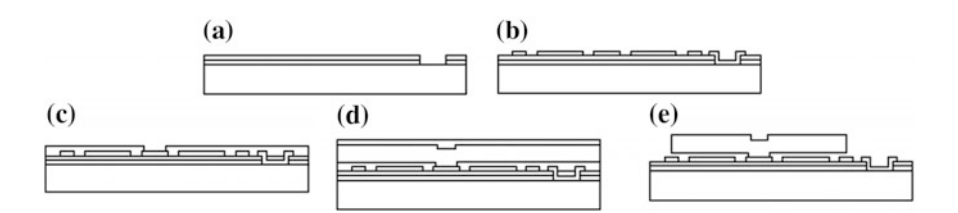


Fig. 5.26 Main manufacturing processes of a double axis angular velocity sensor, **a** Constituting an insulating layer; **b** Forming a grounding solder joint; **c** Making a capacitor electrode; **d** Depositing a buffering layer; **e** Etching a pattern

Figure 5.26 shows the main manufacturing process of a double axis angular velocity sensor. Firstly, an oxide layer is generated by thermal oxidation, a silicon nitride layer is deposited and they constitute the insulation layer on the silicon substrate. The pattern and the window should be made on the insulation layer to form a grounding solder joint with the substrate. The polysilicon layer of 300 nm is deposited and the pattern is etched as the capacitor electrode before a layer of 10% PSG (phosphor silicate glass) is deposited as a sacrificial layer. Next, a polysilicon layer of 7 µm thickness is deposited and the second layer of PSG is deposited on the structure layer. When there is PSG on the structure layer and under the structure layer, the relatively balanced low impedance layer can be guaranteed to be formed by the polysilicon during the annealing process. The polysilicon layer is then etched to form the structure pattern by a rapid ion etching (RIE) process. The comb

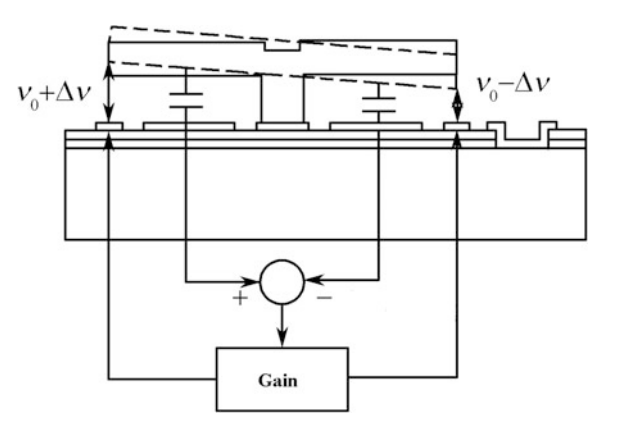
structure part needs doping by the POCl₃ diffusion process to further improve electrical conductivity and finally the sacrificial layer (PSG) is completely removed in the buffer solution of HF.

The main problem of a double axis angular velocity sensor is the mutual crosstalk between two induction modes. As has been mentioned previously, in order to enhance the amplitude of the sensor signal the resonant frequency of the induced vibration should be close to the driving frequency. But it is clear that if the resonant frequencies of two induction modes are selected as the driving frequency, coupling between them is inevitable. The developers of the double axis angular velocity sensor proposed a solution in which one resonant frequency of the induction mode is tuned at the upper end of the driving frequency and the other is tuned at the lower end of the driving frequency. In this way, the resonant frequencies of two modes are very close to the driving frequency, but there is an optimized isolation between them. The tuning of the induction mode is implemented by controlling the bias voltage of the capacitor electrode.

This scheme also uses force feedback technology in order to better detect the induction mode vibration as shown in Fig. 5.27. The feedback scheme imitates the feedback system for an acceleration sensor in Sect. 5.1.5, with the difference being that this scheme cannot increase the bandwidth because the resonance peak of the induction mode is usually used to increase the sensitivity with the cost of reducing bandwidth. The main advantage of this closed-loop system is to enlarge the dynamic working range and improve linearity. Figure 5.27 shows that differential induction and the driving process are applied to this structure and like Eq. (5.8) there is a linear function relationship between the feedback force and the voltage ΔV .

Figure 5.28 shows another angular velocity sensor based on rotational vibration. A good performance is obtained through the coupling between the drive and the mode. There is a ring component in the center of this structure and a square component around the ring component. These two components are connected to each other through two torsion springs and the comb driver is made into the spoke of the inner turntable. The whole structure rotates with an oscillation around the *z*-axial rotating oscillation under the electrostatic driving of the comb electrode. Four

Fig. 5.27 Feedback system of a double axis angular velocity sensor



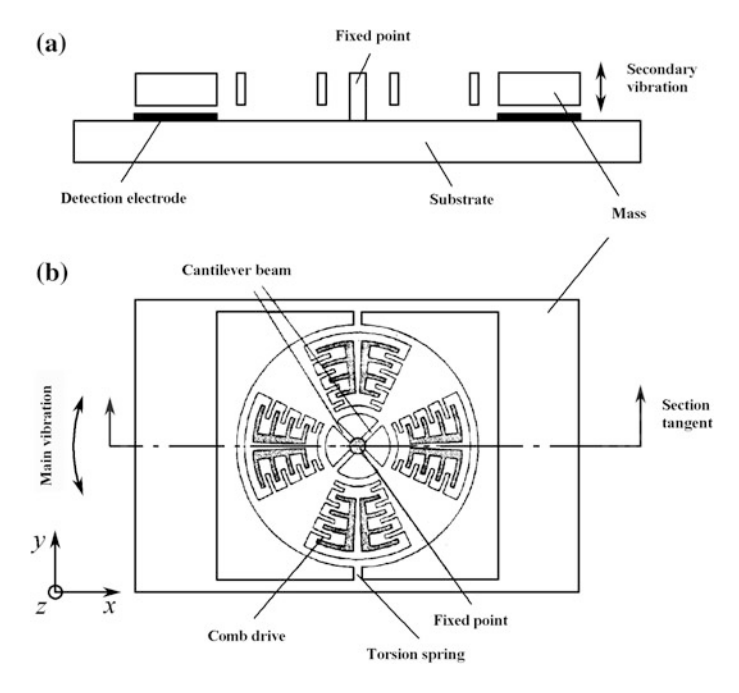
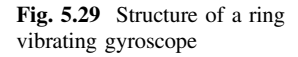
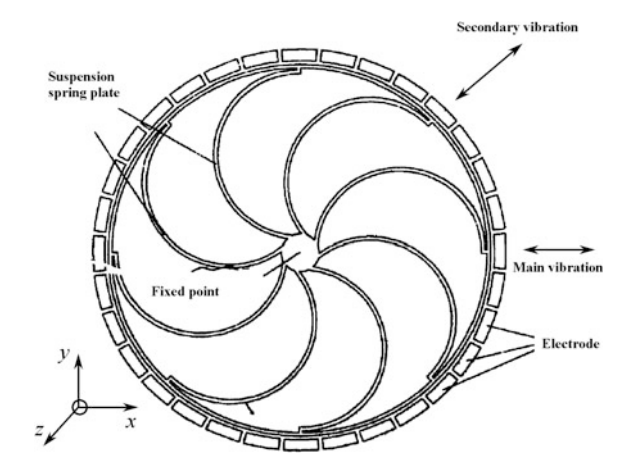


Fig. 5.28 MARS-RR angular velocity sensor, a Sectional drawing; b Top view

comb drivers are used as the actuators of an initial vibration, while another four comb drivers are used as a vibration detector. When the device is adjusted to its sensitive axis (here the x axis), the Coriolis force will cause a rotation with oscillation along the y axis. In this direction, the cantilever beam is very rigid and completely curbs the vibration of the inner disk. Only the square structure can respond to the motion of the Coriolis force because it connects the inner disk with a torsion spring. As mentioned above, the secondary vibration (an induced vibration) can be detected by the capacitance change of the electrode on the substrate.

There is an angular velocity sensor which is a kind of ring vibrational gyroscope and its structure is shown in Fig. 5.29. The gyroscope loop is supported at the center of the circle through eight semicircular leaf springs and a large number of the driving and detecting electrodes are placed at the surrounding of the structure. The ring is driven by the electrostatic force and vibrates with an elliptic curve (from the circle to the ellipse) of the constant amplitude on the plane. When the structure rotates around the z axis, the Coriolis force will result in the transfer of energy from the first drive mode to the secondary flexural vibration mode with an angle of 45° . The variation of the orientation of the long axis of the ellipse and the amplitude of the secondary vibration are proportional to the angular velocity and can be detected by the capacitance. The ring vibrating structure has some important characteristics: due to the inherent symmetry of the structure, the system is less sensitive to parasitic and noise vibration and secondly, because the driver and the induction mode





are the same, the matching degree of their resonant frequencies is very good and a very high sensitivity can be achieved. Because of the asymmetry of the quality of the mass or the elasticity of the spring sheet caused by the production process, appropriate bias can be applied to the electrode and the electronic circuit is used to compensate.

Chapter 6 The Working Principle of a Non-Driven Micromechanical Gyroscope

In 1990s, with the development of microelectronic technology there was a variety of silicon micromechanical gyroscopes available and they used the Coriolis force generated by the vibration mass that is driven to rotate by the base, to be sensitive to the rotating angular velocity of the carrier. Because the micromechanical gyroscope must be driven and the established initial vibration can be sensitive to the rotating angular velocity of the carrier, the design and the production of this gyroscope is problematic.

In order to avoid the difficulties that are brought to the design and the production of a silicon micromechanical gyroscope by the driving component, this chapter uses the rotation of the rotating carrier as a driver and uses the Coriolis force generated through the transverse angular velocity that is perpendicular to the self-rotation angular velocity of the carrier (the pitch or yaw angular velocity) to be sensitive to the transverse angular velocity of the carrier (the pitch or yaw angular velocity). This gyroscope has no drive component so its structure is simple and easy to process.

6.1 The Structure Principle

Figure 6.1 shows the structure principle of a silicon micromechanical gyroscope which is sensitive to the transverse angular velocity of the rotating carrier (the pitch or yaw angular velocity) and is driven by the self-angular velocity of the rotating carrier. Four capacitors are formed between four electrodes and the silicon mass. The coordinate system oxyz is fixed on the silicon mass of the gyroscope, $\dot{\alpha}$ is the angular velocity that swings around the oy axis of the silicon mass, $\dot{\phi}$ is the rotating angular velocity of the carrier, and Ω is the pitch or yaw angular velocity of the carrier. The gyroscope is fixed on the rotating carrier and with the rotation of the carrier, so when the gyroscope rotates with the angular velocity $\dot{\phi}$ and pitches or yaws with the angular velocity Ω , the silicon mass is subjected to a Coriolis force

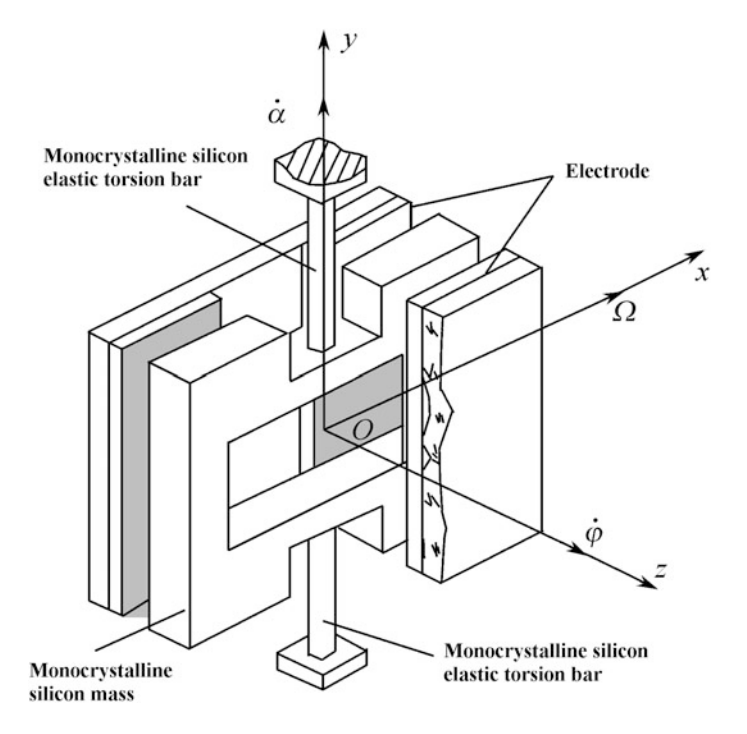


Fig. 6.1 Structure principle of a silicon micromechanical gyroscope

with a periodic change (the frequency of the Coriolis force is the rotating frequency of the carrier), and the swing along the axis oy is generated, which causes the capacitance change of four capacitors (C_1, C_2, C_3, C_4) consisting of the silicon mass and four electrodes. As shown in Fig. 6.2, the capacitance change signal is converted into a voltage change signal and amplified. The voltage signal which is proportional to the measured angular velocity Ω is obtained.

Figure 6.3 shows the structure of the silicon mass for the sensitive element of the gyroscope, where a_0, a_1, a_2, a_3 are the sizes of the x axis, b_1, b_2, b_3 are the sizes of the y axis and h is the thickness of the silicon mass.

6.2 The Dynamic Model

6.2.1 The Mass Vibrational Model

The angular velocity of the rotating carrier is used to drive the mass vibration of the silicon micromechanical gyroscope, which can be described through the coordinate transformation in Fig. 6.4. In this figure, $o\xi\eta\zeta$ is an inertial coordinate system (a fixed coordinate system); $ox_1y_1z_1$ is the pitch or yaw coordinate system; $ox_2y_2z_2$ is

Fig. 6.2 Principle of a signal detection circuit

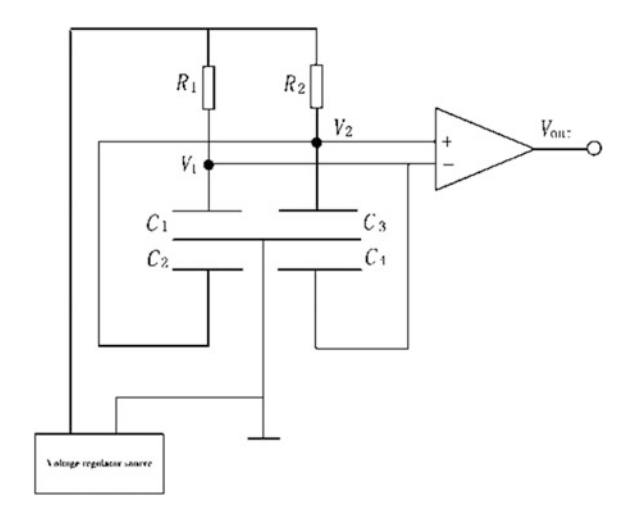
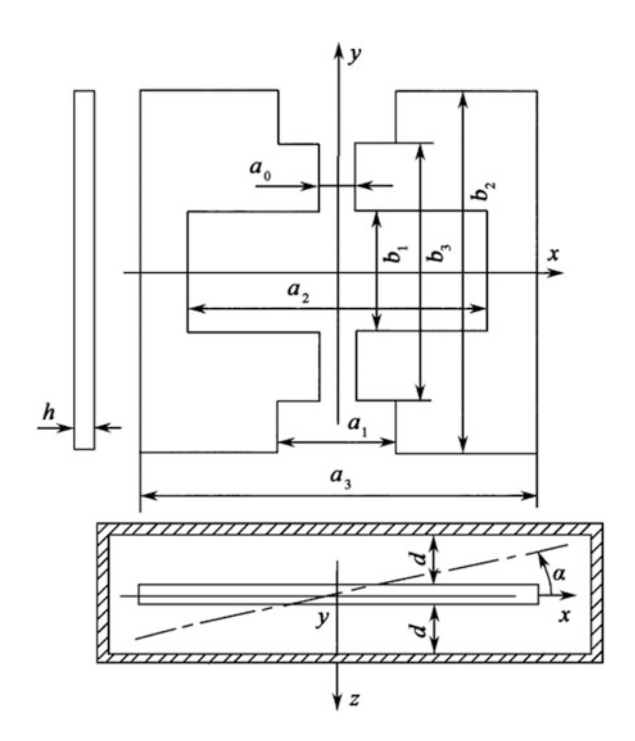


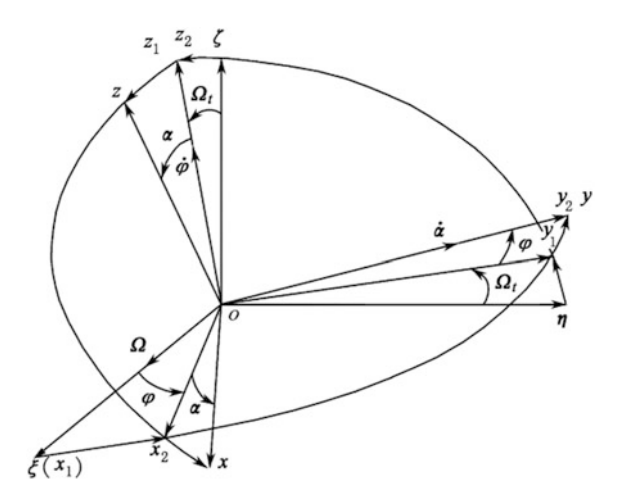
Fig. 6.3 Structure of the silicon mass for the sensitive element of the gyroscope



the spin coordinate system of the carrier; and oxyz is the coordinate system connected to the silicon mass.

In the inertial coordinate system $o\xi\eta\zeta$, from the momentum moment theorem of the fixed point rotation of a rigid body, the following result can be obtained:

Fig. 6.4 Coordinate system



$$\frac{\mathrm{d}}{\mathrm{d}t} \begin{pmatrix} G_{\xi} \\ G_{\eta} \\ G_{\zeta} \end{pmatrix} = \begin{pmatrix} M_{\xi} \\ M_{\eta} \\ M_{\zeta} \end{pmatrix} \tag{6.1}$$

where $\begin{pmatrix} G_{\xi} \\ G_{\eta} \\ G_{\zeta} \end{pmatrix}$ is the momentum moment of the silicon mass of the gyroscope in

the coordinate system $o\xi\eta\zeta$, i.e., $\begin{pmatrix} G_\xi\\G_\eta\\G_\zeta \end{pmatrix} = J\begin{pmatrix} \omega_\xi\\\omega_\eta\\\omega_\zeta \end{pmatrix}; \begin{pmatrix} M_\xi\\M_\eta\\M_\zeta \end{pmatrix}$ is the moment of

the silicon mass of the gyroscope in the coordinate system $o\xi\eta\zeta$.

When the coordinate system oxyz is selected as the inertial principal coordinate system of the silicon gyroscope mass, the inertial moment matrix J is constant.

(1) In the inertial principal coordinate system $o\xi\eta\zeta$, the coordinate system $ox_1y_1z_1$ can be reached by rotating around the $o\xi$ axis with the angular velocity Ω and the included angle Ω_t , then

$$\begin{pmatrix} G_{\xi} \\ G_{\eta} \\ G_{\zeta} \end{pmatrix} = A^{-1} \begin{pmatrix} G_{x1} \\ G_{y1} \\ G_{z1} \end{pmatrix} \cdot \begin{pmatrix} M_{\xi} \\ M_{\eta} \\ M_{\zeta} \end{pmatrix} = A^{-1} \begin{pmatrix} M_{x1} \\ M_{y1} \\ M_{z1} \end{pmatrix}$$
(6.2)

where A is the transformation matrix, $A = \begin{pmatrix} 1 & 0 & 0 \\ 0 & \cos \Omega t & \sin \Omega t \\ 0 & -\sin \Omega t & \cos \Omega t \end{pmatrix}$, which is a

function of the time.

Substitute Eq. (6.2) into Eq. (6.1) and obtain

$$\frac{\mathrm{d}}{\mathrm{d}t} \begin{pmatrix} G_{x1} \\ G_{y1} \\ G_{z1} \end{pmatrix} + \begin{pmatrix} 0 & 0 & 0 \\ 0 & 0 & -\Omega \\ 0 & \Omega & 0 \end{pmatrix} \begin{pmatrix} G_{x1} \\ G_{y1} \\ G_{z1} \end{pmatrix} = \begin{pmatrix} M_{x1} \\ M_{y1} \\ M_{z1} \end{pmatrix} \tag{6.3}$$

(2) In the coordinate system $ox_1y_1z_1$, the coordinate system $ox_2y_2z_2$ can be reached by rotating around the oz_1 axis with the angular velocity $\dot{\varphi}$ and the included angle φ , then

$$\begin{pmatrix} G_{x1} \\ G_{y1} \\ G_{z1} \end{pmatrix} = B^{-1} \begin{pmatrix} G_{x2} \\ G_{y2} \\ G_{z2} \end{pmatrix} \cdot \begin{pmatrix} M_{x1} \\ M_{y1} \\ M_{z1} \end{pmatrix} = B^{-1} \begin{pmatrix} M_{x2} \\ M_{y2} \\ M_{z2} \end{pmatrix}$$
(6.4)

where *B* is the transformation matrix, $B = \begin{pmatrix} \cos \varphi & \sin \varphi & 0 \\ -\sin \varphi & \cos \varphi & 0 \\ 0 & 0 & 1 \end{pmatrix}$, which is a function of the time.

Substitute Eq. (6.4) into Eq. (6.3) and obtain

$$\begin{pmatrix} 0 & -\dot{\varphi} & 0 \\ \dot{\varphi} & 0 & 0 \\ 0 & 0 & 0 \end{pmatrix} \begin{pmatrix} G_{x2} \\ G_{y2} \\ G_{z2} \end{pmatrix} + \frac{d}{dt} \begin{pmatrix} G_{x2} \\ G_{y2} \\ G_{z2} \end{pmatrix} + B \begin{pmatrix} 0 & 0 & 0 \\ 0 & 0 & -\Omega \\ 0 & \Omega & 0 \end{pmatrix}$$

$$B^{-1} \begin{pmatrix} G_{x2} \\ G_{y2} \\ G_{z2} \end{pmatrix} = \begin{pmatrix} M_{x2} \\ M_{y2} \\ M_{z2} \end{pmatrix}$$
(6.5)

(3) In the coordinate system $ox_2y_2z_2$, the coordinate system oxyz can be reached by rotating around the oy_2 axis with the angular velocity $\dot{\alpha}$ and the included angle α , then

$$\begin{pmatrix} G_{x2} \\ G_{y2} \\ G_{z2} \end{pmatrix} = C^{-1} \begin{pmatrix} G_x \\ G_y \\ G_z \end{pmatrix}, \begin{pmatrix} M_{x2} \\ M_{y2} \\ M_{z2} \end{pmatrix} = C^{-1} \begin{pmatrix} M_x \\ M_y \\ M_z \end{pmatrix}$$
(6.6)

where C is the transformation matrix, $C = \begin{pmatrix} \cos \alpha & 0 & -\sin \alpha \\ 0 & 1 & 0 \\ \sin \alpha & 0 & \cos \alpha \end{pmatrix}$, which is a function of the time.

Substitute Eq. (6.6) into Eq. (6.5) and obtain

$$\begin{pmatrix}
0 & -\dot{\varphi} & 0 \\
\dot{\varphi} & 0 & 0 \\
0 & 0 & 0
\end{pmatrix} C^{-1} \begin{pmatrix} G_x \\ G_y \\ G_z \end{pmatrix} + \frac{d}{dt} \begin{bmatrix} C^{-1} \begin{pmatrix} G_x \\ G_y \\ G_z \end{bmatrix} \end{bmatrix} + B \begin{pmatrix} 0 & 0 & 0 \\ 0 & 0 & -\Omega \\ 0 & \Omega & 0 \end{pmatrix} B^{-1} C^{-1} \begin{pmatrix} G_x \\ G_y \\ G_z \end{pmatrix} = C^{-1} \begin{pmatrix} M_x \\ M_y \\ M_z \end{pmatrix} \tag{6.7}$$

Simplify Eq. (6.7) and obtain

$$\begin{pmatrix} 0 & -\Omega\cos\varphi\sin\alpha - \dot{\varphi}\cos\alpha & -\Omega\sin\varphi + \dot{\alpha} \\ \Omega\sin\alpha\cos\varphi + \dot{\varphi}\cos\alpha & 0 & \dot{\varphi}\sin\alpha - \Omega\cos\varphi\cos\alpha \end{pmatrix} \times \begin{pmatrix} G_x \\ G_y \\ \Omega\sin\varphi - \dot{\alpha} & \Omega\cos\varphi\cos\alpha - \dot{\varphi}\sin\alpha & 0 \end{pmatrix} + \frac{d}{dt}\begin{pmatrix} G_x \\ G_y \\ G_z \end{pmatrix} = \begin{pmatrix} M_x \\ M_y \\ M_z \end{pmatrix}$$

$$(6.8)$$

In the coordinate system *oxyz*, the momentum moment of the silicon block of the gyroscope is

$$\begin{pmatrix} G_x \\ G_y \\ G_z \end{pmatrix} = J \begin{pmatrix} \psi_x \\ \psi_y \\ \psi_z \end{pmatrix} = \begin{pmatrix} J_x \ \psi_x \\ J_y \ \psi_y \\ J_z \ \psi_z \end{pmatrix}$$
(6.9)

where J_x , J_y and J_z are the inertia moment of the silicon block of the gyroscope on the axes x, y and z respectively; and ψ_x , ψ_y and ψ_z are the components that are the projections of the angular velocity vector of the gyroscope silicon block on the coordinate system oxyz, i.e.,

$$\begin{pmatrix} \psi_x \\ \psi_y \\ \psi_z \end{pmatrix} = \begin{pmatrix} \Omega \cos \varphi \cos \alpha - \dot{\varphi} \sin \alpha \\ -\Omega \sin \varphi + \dot{\alpha} \\ -\Omega \cos \varphi \sin \alpha + \dot{\varphi} \cos \alpha \end{pmatrix}$$
(6.10)

Thus

$$\begin{pmatrix} G_{x} \\ G_{y} \\ G_{z} \end{pmatrix} = J \begin{pmatrix} \psi_{x} \\ \psi_{y} \\ \psi_{z} \end{pmatrix} = \begin{pmatrix} J_{x} & \psi_{x} \\ J_{y} & \psi_{y} \\ J_{z} & \psi_{z} \end{pmatrix} = \begin{pmatrix} J_{x}(\Omega \cos \varphi \cos \alpha - \dot{\varphi} \sin \alpha) \\ J_{y}(-\Omega \sin \varphi + \dot{\alpha}) \\ J_{z}(-\Omega \cos \varphi \sin \alpha + \dot{\varphi} \cos \alpha) \end{pmatrix}$$
(6.11)

Substitute Eq. (6.11) into Eq. (6.8) and obtain three dynamic equations, where the dynamic equation on the oy axis is

$$\begin{split} (J_x + J_z) \Omega^2 \cos^2 \varphi \sin \alpha \cos \alpha + (J_z - J_x) \dot{\varphi}^2 \sin \alpha \cos \alpha + J_y \Omega \, \dot{\varphi} \cos \varphi \cos 2\alpha \\ - J_z \Omega \, \dot{\varphi} \cos \varphi + J_y \ddot{\alpha} - J_y \Omega \, \dot{\varphi} \cos \varphi - J_y \frac{\mathrm{d}\Omega}{\mathrm{d}t} \sin \varphi = M_y \end{split} \tag{6.12}$$

The external moment on the oy axis is

$$M_{\rm v} = -K_T \alpha - D\dot{\alpha}$$

Because $\Omega \ll \dot{\phi}$, Ω^2 is ignored. Because $\alpha \approx 0$, there holds $\sin \alpha \approx \alpha$ and $\cos \alpha = \cos 2\alpha \approx 1$. Set $d\Omega/dt = 0$, then

$$J_{y}\ddot{\alpha} + D\dot{\alpha} + \left[(J_{z} - J_{x})\dot{\varphi}^{2} + K_{T} \right] \alpha = (J_{z} + J_{y} - J_{x})\Omega \dot{\varphi} \cos(\dot{\varphi}t)$$
 (6.13)

where J_x , J_y and J_z are the inertia moments of the silicon mass on the axes ox, oy and oz; K_T is the torsion stiffness coefficient; and D is the damping coefficient.

$$\begin{cases}
J_{x} = \frac{\rho}{12} \left\{ a_{3}b_{3}h(b_{3}^{2} + h^{2}) - a_{2}b_{2}h(b_{2}^{2} + h^{2}) - a_{1}(b_{3} - b_{1}) \cdot \\
\times h \left[\frac{1}{4}(b_{3} - b_{1}) + h^{2} + \frac{3}{4}(b_{3} + b_{1})^{2} \right] \right\} \\
J_{y} = \frac{\rho}{12} \left[a_{3}b_{3}h(a_{3}^{2} + h^{2}) - a_{2}b_{2}h(a_{2}^{2} + h^{2}) \\
-a_{1}(b_{3} - b_{1})h(a_{1}^{2} + h^{2}) \right] \\
J_{z} = \frac{\rho}{12} \left\{ a_{3}b_{3}h(b_{3}^{2} + a_{3}^{2}) - a_{2}b_{2}h(b_{2}^{2} + a_{2}^{2}) \cdot \\
-a_{1}(b_{3} - b_{1}) \times h \left[\frac{1}{4}(b_{3} - b_{1})^{2} + a_{1}^{2} + \frac{3}{4}(b_{3} + b_{1})^{2} \right] \right\}
\end{cases} (6.14)$$

Assume $a_0 = 1.0$ mm, $a_1 = 3.2$ mm, $a_2 = 8.0$ mm, $a_3 = 10.6$ mm; $b_1 = 6.8$ mm, $b_2 = 3.2$ mm, $b_3 = 9.6$ mm; h = 0.335 mm; $\rho = 2.33 \times 10^{-3} \text{g/mm}^3$. Substitute these values into Eq. (6.14) and obtain $J_x = 0.475$ g mm²; $J_y = 0.632$ g·mm²; $J_z = 1.105$ g·mm².

6.2.2 The Solution of the Angular Vibrational Equation

Simplify Eq. (6.13) and obtain

$$\ddot{\alpha} + 2\xi\omega_0\dot{\alpha} + \omega_0^2 a = f_0\cos(\dot{\varphi}t) \tag{6.15}$$

where

$$\omega_0^2 = \frac{1}{J_y} \left[(J_z - J_x) \dot{\varphi}^2 + K_T \right]$$
 (6.16)

$$\xi = \frac{D}{2\omega_0 J_y} = \frac{D}{2\sqrt{[(J_z - J_x)\dot{\varphi}^2 + K_T]J_y}}$$
(6.17)

$$f_0 = \frac{1}{J_y} (J_z + J_y - J_x) \Omega \dot{\varphi}$$
 (6.18)

Its solution is

$$\alpha = Ae^{-nt}\cos\left(\sqrt{\omega_0^2 - n^2t} + \delta\right) + B\cos(\dot{\phi}t - \beta)$$

$$\tan\beta = \frac{2n\,\dot{\phi}}{\omega_0^2 - \dot{\phi}^2}$$

where A and δ are the integral constants and are determined by the initial motion conditions; B is the amplitude of the stable vibration; β is the phase difference, i.e., the angular vibration phase lag behind the exciting force with a phase angle β ; and n is the damping factor, $n = \xi \omega_0$.

With the increase of the vibrational time, the first part of this equation is failing fast. The second part is determined by the forcing force and its frequency is the exciting frequency of the forced force (i.e. the spin angular velocity of the carrier), whose vibration amplitude is determined not only by the exciting force but also by the exciting frequency and the parameters of the vibrational system J_x , J_y , J_z , K_T and D. The steady state solution of this equation is

$$\alpha = B \cos(\dot{\phi}t - \beta) = \frac{f_0 \cos(\dot{\phi}t - \beta)}{\sqrt{(\omega_0^2 - \dot{\phi}^2)^2 + 4n^2\dot{\phi}^2}}$$
(6.19)

Substituting the parameters and simplifying the result, obtains

$$\alpha = \frac{(J_z + J_y - J_x)\Omega\dot{\phi}\cos(\dot{\phi}t - \beta)}{\sqrt{\left[(J_z - J_x - J_y)\dot{\phi}^2 + K_T\right]^2 + (D\dot{\phi})^2}}$$
(6.20)

The amplitude of the angular vibration is

$$\alpha_{m} = \frac{(J_{z} + J_{y} - J_{x})\dot{\varphi}}{\sqrt{\left[(J_{z} - J_{x} - J_{y})\dot{\varphi}^{2} + K_{T}\right]^{2} + (D\dot{\varphi})^{2}}}\Omega$$
(6.21)

In the denominator of this expression there is an elastic torsion coefficient K_T . Therefore, the impact of the unstable parameters (the spin angular velocity $\dot{\varphi}$ of the aircraft) on the output signal cannot be excluded even if it is in the resonant mode. At the same time, the dynamic viscosity is

$$\mu = \frac{J_z}{J_x + J_y} = 1$$

According to the proposed measurement precision, the silicon micromechanical gyroscope uses other strategies to choose the parameters. Firstly, the physical properties and the existing processing technology of the silicon should be noted. In the design, the relationship between the inertia moment and the elastic torsion interaction coefficient is

$$(J_z - J_x - J_y)\dot{\varphi}^2 \ll K_T \tag{6.22}$$

It should be noted that when the parameters in Eq. (6.21) are selected such that the parameters in the denominator do not satisfy the following relationship:

$$K_T < D\dot{\varphi}$$
 (6.23)

the stability of the damping coefficient D is lower than the elastic torsion coefficient K_T . In addition, it is difficult to achieve the parameter relationship because increasing the damping coefficient D needs a reducing of the space between the sensitive components (the silicon mass) and the plate, thereby the maximum deflection angle of the silicon and the tangent of the corresponding output curve will be reduced. Therefore, in the parameter design there holds

$$K_T > D\dot{\varphi} \tag{6.24}$$

Thus the value of the denominator in Eq. (6.21) is determined by the stable elastic coefficients of the gyroscope's sensitive element (the silicon block).

However, in this case, the output signal of the silicon micromechanical gyroscope is directly proportional to the rotating angular velocity of the aircraft, and the output signal is very unstable. In the actual research, in order to eliminate this drawback the output signal is obtained by measuring the differential angular velocity in order to calculate the constant $\dot{\varphi}$, which can be obtained by adding a microprocessor to the gyroscope (or by using the aircraft's computer). Therefore, in the silicon micromechanical gyroscope the resonant mode may not be used but in order to avoid the dynamic error, the lead non-resonant mode should be selected.

6.3 Analysis and Calculation of Kinetic Parameters

6.3.1 Torsion Stiffness of the Elastic Supporting Beam

The structure of the elastic supporting beam of the gyroscope is shown in Fig. 6.5. The length, width and thickness of the beam are, respectively, L, w and t. In order to obtain the torsion stiffness of the supporting beam, the following assumptions are satisfied:

- (1) The torsion angle is proportional to the length of the supporting beam.
- (2) The distortions of all the cross–sections for the supporting beam are the same.
- (3) The torsion moments for two sides of the supporting beam torque are the same and their directions are opposite.

In the above conditions, from elastic mechanics the torsion stiffness of the supporting beam with a rectangular cross–section can be obtained

$$K = \frac{512Ga^3b}{\pi^4 L} \sum_{n=1,3,5}^{\infty} \frac{1}{n^4} \left(1 - \frac{2a}{n\pi b} \tan h \frac{n\pi b}{2a} \right)$$
 (6.25)

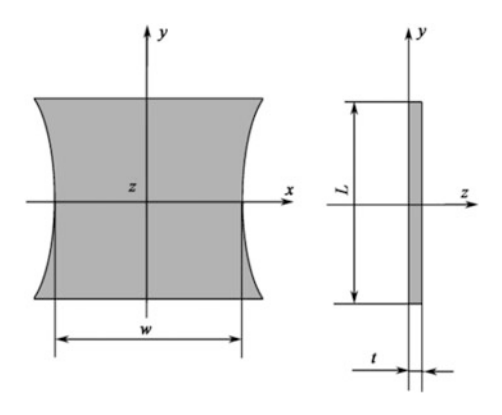
where a and b are the width and length of the rectangular cross–section; and G is the shear modulus for the material of the supporting beam.

From Eq. (6.25), the total stiffness for the supporting beam is obtained by

$$K_T = \frac{0.657Gt^3\omega}{L} \sum_{n=1,3,5}^{\infty} \frac{1}{n^4} \left(1 - \frac{2t}{n\pi\omega} \tan h \frac{n\pi\omega}{2t} \right) \approx \frac{2}{3} \frac{Gt^3\omega}{L}$$
 (6.26)

Substitute $w = 0.8 \, mm$, $L = 0.8 \, mm$, $t = 0.025 \, mm$ and $G = 5.1 \times 10^{10} N/m^2$ into Eq. (6.26), there holds $K_T = 5.313 \times 10^{-4} N \cdot m$.

Fig. 6.5 Structure of the supporting beam



6.3.2 Parameter Calculation of the Flexible Joints

The size calculation of the elastic joint section is shown in Fig. 6.6.

The function for the torsion rigidity of the section has the following form:

$$\begin{split} \Phi(x,z) &= AG\alpha \left(z^2 - \frac{1}{4}h^2\right) \left[(z\cot\alpha + x)^2 - \frac{1}{4}(a + h\cot\alpha)^2 \right] \left[(z\cot\alpha - x)^2 - \frac{1}{4}(a + h\cot\alpha)^2 \right] \\ &= AG\alpha \left(z^2 - \frac{1}{4}h^2\right) \left[(z\cot\alpha + x)^2 (z\cot\alpha - x)^2 - (z\cot\alpha + x)^2 \frac{1}{4}(a + h\cot\alpha)^2 \right] \\ &- \frac{1}{4}(a + h\cot\alpha)^2 (z\cot\alpha - x)^2 + \frac{1}{16}(a + h\cot\alpha)^4 \right] \\ &= AG\alpha \left(z^2 - \frac{1}{4}h^2\right) \left\{ (z\cot\alpha + x)^2 (z\cot\alpha - x)^2 \\ &- \frac{1}{2}(a + h\cot\alpha)^2 \left[(z\cot\alpha)^2 + x^2 \right] + \frac{1}{16}(a + h\cot\alpha)^4 \right\} \\ &= AG\alpha \left(z^2 - \frac{1}{4}h^2\right) \left\{ \left[(z\cot\alpha)^2 - x^2 \right]^2 \\ &- \frac{1}{2}(a + h\cot\alpha)^2 \left[(z\cot\alpha)^2 + x^2 \right] + \frac{1}{16}(a + h\cot\alpha)^4 \right\} \\ &= AG\alpha \left(z^2 - \frac{1}{4}h^2\right) \left[z^4\cot^2\alpha - 2z^2x^2\cot^2\alpha + x^4 \right. \\ &- \frac{1}{2}(a + h\cot\alpha)^2 (z^2\cot^2\alpha + x^2) + \frac{1}{16}(a + h\cot\alpha)^4 \right] \end{split}$$

$$(6.27)$$

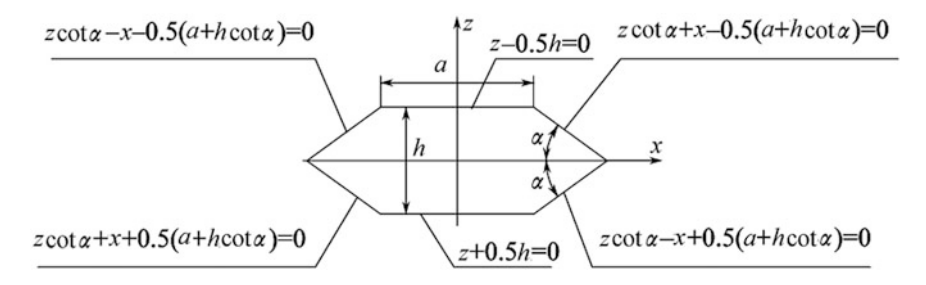


Fig. 6.6 Size of the elastic joint section

$$\begin{split} \frac{\partial \Phi(x,z)}{\partial x} &= AG\alpha \left(z^2 - \frac{1}{4}h^2\right) \left[-4z^2x \cot^2\alpha + 4x^3 - x(a+h\cot\alpha)^2 \right] \\ \frac{\partial \Phi(x,z)}{\partial z} &= AG\alpha \left\{ 6z^5 \cot^4\alpha - 8z^3x^2 \cot^2\alpha + 2zx^4 - z^3 \left[h^2 \cot^2\alpha + 2(a+h\cot\alpha)^2 \right] \cot^2\alpha \right. \\ &\quad \left. + zx^2 \left[h^2 \cot^2\alpha - (a+h\cot\alpha)^2 \right] + \frac{1}{8}z \left[2h^2 \cot^2\alpha + (a+h\cot\alpha)^2 \right] (a+h\cot\alpha)^2 \right\} \end{split}$$

According to the minimum integral condition of the section, the coefficient A is determined as

$$\sigma = \iint_{S} \left\{ \frac{1}{2} \left[\left(\frac{\partial \Phi(x, z)}{\partial x} \right)^{2} + \left(\frac{\partial \Phi(x, z)}{\partial z} \right)^{2} \right] - 2Ga \, \Phi(x, z) \right\} dxdz \qquad (6.29)$$

Substitute Eqs. (6.27) and (6.28) into Eq. (6.29) and obtain

$$\begin{split} \sigma &= G^2\alpha^2 \iiint_S \left\{ \frac{1}{2} A^2 \left[\left(z^2 - \frac{1}{4} h^2 \right)^2 \left[-4 z^2 x \cot^2 \alpha + 4 x^3 - x (a + h \cot \alpha)^2 \right]^2 \right. \\ &\quad + \left\{ 6 z^5 \cot^4 \alpha - 8 z^3 x^2 \cot^2 \alpha + 2 z x^4 - z^3 \left[h^2 \cot^2 \alpha + (a + h \cot \alpha)^2 \right] \cot^2 \alpha \right. \\ &\quad + z x^2 \left[h^2 \cot^2 \alpha - (a + h \cot \alpha)^2 \right] + \frac{1}{8} z \left[2 h^2 \cot^2 \alpha + (a + h \cot \alpha)^2 \right] (a + h \cot \alpha)^2 \right\}^2 \right] \\ &\quad - 2 A \left(z^2 - \frac{1}{4} h^2 \right) \left[z^4 \cot^4 \alpha - 2 z^2 x^2 \cot^2 \alpha \right. \\ &\quad + x^4 - \frac{1}{2} (a + h \cot \alpha)^2 (z^2 \cot^2 \alpha + x^2) + \frac{1}{16} (a + h \cot \alpha)^4 \right] \right\} \mathrm{d}x \mathrm{d}z \\ &= G^2\alpha^2 \iint_S \left\{ Q(x, z) \right\} \mathrm{d}x \mathrm{d}z \\ &= G^2\alpha^2 \left\{ \int_{-\frac{1}{2}(a + h \cot \alpha)}^{\left(z + \frac{1}{2}(a + h \cot \alpha) \right) \tan \alpha} \left\{ Q(x, z) \right\} \mathrm{d}z + \int_{-\frac{1}{2}a}^{\frac{1}{2}a} \int_{-\frac{1}{2}h}^{\frac{1}{2}h} \left\{ Q(x, z) \right\} \mathrm{d}z \right. \\ &\quad + \int_{\frac{1}{2}a}^{\left(z + \frac{1}{2}(a + h \cot \alpha) \right) \tan \alpha} \left\{ Q(x, z) \right\} \mathrm{d}z \right\} \\ &\quad + \int_{\frac{1}{2}a}^{\left(z + \frac{1}{2}(a + h \cot \alpha) \right) \tan \alpha} \left\{ Q(x, z) \right\} \mathrm{d}z \right\} \end{split}$$

$$\begin{split} Q(x,z) &= \frac{1}{2}A^2 \left[\left(z^2 - \frac{1}{4}h^2\right)^2 \left[-4z^2x\cot^2\alpha + 4x^3 - x(a+h\cot\alpha)^2 \right]^2 \right. \\ &\quad + \left. \left\{ 6z^5\cot^4a - 8z^3x^2\cot^2\alpha + 2zx^4 - z^3 \left[h^2\cot^2\alpha + (a+h\cot\alpha)^2 \right] \cdot \cot^2\alpha \right. \\ &\quad + zx^2 \left[h^2\cot^2\alpha - (a+h\cot\alpha)^2 \right] \\ &\quad + \frac{1}{8}z \left[2h^2\cot^2\alpha + (a+h\cot\alpha)^2 \right] (a+h\cot\alpha)^2 \right\}^2 \right] \\ &\quad - 2A \left(z^2 - \frac{1}{4}h^2 \right) \left[z^4\cot^4\alpha - 2z^2x^2\cot^2\alpha + x^4 \right. \\ &\quad - \frac{1}{2} \left(a+h\cot\alpha \right)^2 \left(z^2\cot^2\alpha + x^2 \right) + \frac{1}{16} \left(a+h\cot\alpha \right)^4 \right] \right\} \\ &\sigma = \iint_S \left\{ \frac{1}{2} \left[\left(\frac{\partial \Phi(x,z)}{\partial x} \right)^2 + \left(\frac{\partial \Phi(x,z)}{\partial z} \right)^2 \right] - 2G\alpha\Phi(x,z) \right\} dxdz \\ &\quad \frac{1}{2} \iint_S \left[\left(\frac{\partial \Phi(x,z)}{\partial x} \right)^2 + \left(\frac{\partial \Phi(x,z)}{\partial z} \right)^2 \right] dxdz - 2G\alpha \iint_S \Phi(x,z) dxdz \right. \\ &\quad = \left. \left(G\alpha \right)^2 \left\{ \frac{1}{2}A^2 \iint_S \left[\left(\frac{\partial \Phi_0(x,z)}{\partial x} \right)^2 + \left(\frac{\partial \Phi_0(x,z)}{\partial z} \right)^2 \right] dxdz - 2A \iint_S \Phi_0(x,z) dxdz \right\} = 0 \\ &A = 2 \underbrace{\int_S \Phi_0(x,z) dxdz}_{\int_S \left[\left(\frac{\partial \Phi_0(x,z)}{\partial x} \right)^2 + \left(\frac{\partial \Phi_0(x,z)}{\partial z} \right)^2 \right] dxdz}_{\int_S \left[\left(\frac{\partial \Phi_0(x,z)}{\partial x} \right)^2 + \left(\frac{\partial \Phi_0(x,z)}{\partial z} \right)^2 \right] dxdz} \end{split}$$

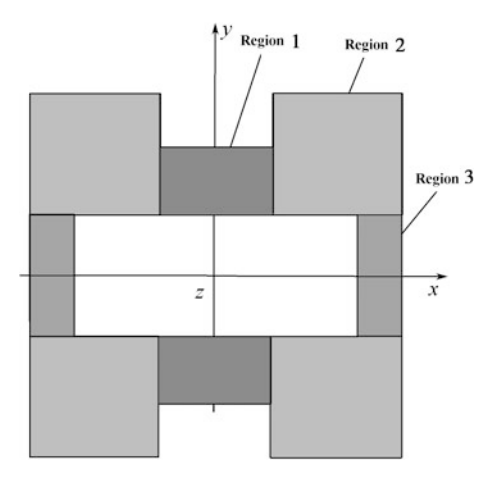
6.3.3 The Damping Coefficient of Angular Vibration for the Vibrating Element

A rectangular plane whose length is A and whose width is B moves with respect to the bottom surface with the gap h, and the damping coefficient of the film resistance is produced as

$$D = \frac{F_{\text{dam}p}}{dh/dt} = \frac{AB^3 \mu}{h^3} \left[1 - \frac{192B}{A\pi^5} \sum_{n=1,3,5,\dots} \frac{1}{n^5} \tan h \frac{n \pi A}{2B} \right]$$
(6.30)

where μ is the viscosity coefficient of gas.

Fig. 6.7 Sketch map of the damping regions



Because the infinite series converges quickly, only the first item is selected, i.e.,

$$D \approx \frac{AB^3 \mu}{h^3} \left[1 - \frac{192B}{A\pi^5} \tan h \frac{\pi A}{2B} \right] \approx \frac{96 \times \mu}{h^3 \pi^4} B^3 A \left[1 - \frac{2B}{\pi A} \tan h \left(\frac{\pi A}{2B} \right) \right]$$
 (6.31)

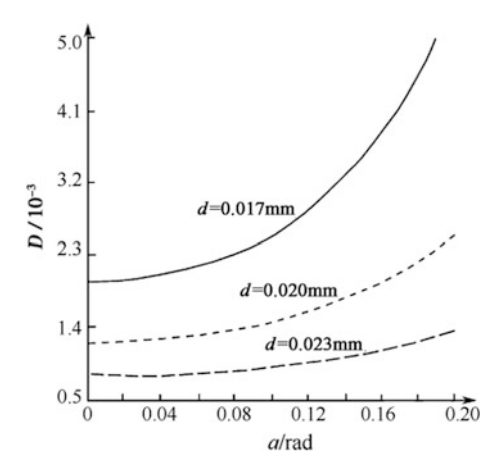
Due to the structural complexity for the silicon mass of the gyroscope vibration, it is difficult to calculate the damping coefficient. In order to simplify the calculation, the silicon mass of the gyroscope vibration is divided into three regions with different colors, as shown in Fig. 6.7. Then the overall damping of the gyroscope vibration can be approximated to the accumulation of three regional dampings (Fig. 6.3), from Eq. (6.31). The damping coefficients of the angular vibration for the three regions can be obtained respectively, where $r_1 = (a_3 + a_1)/4$; $r_2 = (a_3 + a_2)/4$; $r_3 = (a_1)/4$.

$$\begin{cases} D_{1}(d,\alpha) = \frac{4\times96\mu}{\pi^{4}} \left[\frac{1}{(d+r_{1}\alpha)^{3}} + \frac{1}{(d-r_{1}\alpha)^{3}} \right] \left(\frac{b_{3}-b_{2}}{2} \right)^{3} \times \frac{a_{3}-a_{1}}{2} \left[1 - \frac{2(b_{3}-b_{2})}{\pi(\alpha_{3}-\alpha_{1})} \tanh \frac{\pi(\alpha_{3}-a_{1})}{2(b_{3}-b_{2})} \right] r_{1}^{2} \\ D_{2}(d,\alpha) = \frac{2\times96\mu}{\pi^{4}} \left[\frac{1}{(d+r_{2}\alpha)^{3}} + \frac{1}{(d-r_{2}\alpha)^{3}} \right] \left(\frac{a_{3}-a_{2}}{2} \right)^{3} \times b_{2} \left[1 - \frac{1}{\pi} \frac{(a_{3}-a_{2})}{b_{2}} \tanh \frac{\pi b_{2}}{a_{3}-a_{2}} \right] r_{2}^{2} \\ D_{3}(d,\alpha) = \frac{4\times96\mu}{\pi^{4}} \left[\frac{1}{(d+r_{3}\alpha)^{3}} + \frac{1}{(d-r_{3}\alpha)^{3}} \right] \left(\frac{a_{1}}{2} \right)^{3} \times \frac{b_{1}-b_{2}}{2} \left[1 - \frac{2}{\pi} \frac{a_{1}}{b_{1}-b_{2}} \tanh \frac{\pi(b_{1}-b_{2})}{2a_{1}} \right] r_{3} \end{cases}$$

$$(6.32)$$

The overall damping coefficient of the angular vibration $D(d,\alpha) = D_1(d,\alpha) + D_2(d,\alpha) + D_3(d,\alpha)$. When the gaps are $d = 0.017 \, mm$, 0.020 mm and 0.023 mm respectively, and the three relation curves between the damping coefficients D and the vibration a_1 swing angles α are shown in Fig. 6.8. Fig. 6.8, when $d = 0.020 \, mm$ and a = 0, $D(2 \times 10^{-5}, 0) =$ From $1.231 \times 10^{-5} N \cdot m \cdot s.$

Fig. 6.8 Relationship between the damping coefficients D and vibrational swing angles αl



6.3.4 Relationship Between the Angular Vibration Natural Frequency, the Angular Vibration Amplitude and the Measured Angular Velocity

From the calculation of the dynamics parameters, the angular vibration natural frequency of the gyroscope can be obtained as

$$\omega_s = \sqrt{\frac{K_T}{J_y}} = 917 \text{rad/} s = 146 \text{Hz}$$
 (6.33)

Substitute the dynamics parameters into Eq. (6.21), the relationship between a_m and the measured angular velocity Ω (Fig. 6.9) and the relationship between $k(\dot{\varphi})$ and $\dot{\varphi}$ (Fig. 6.10).

Fig. 6.9 Relationship between a_m and the measured angular velocity Ω

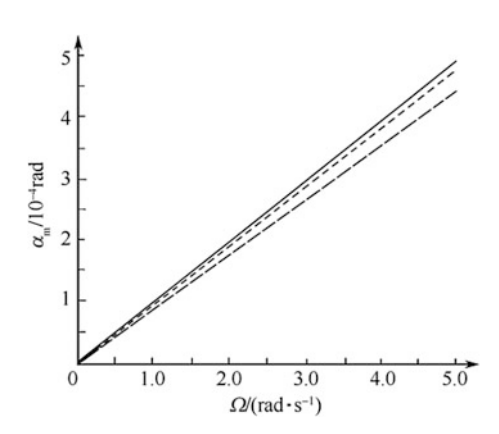
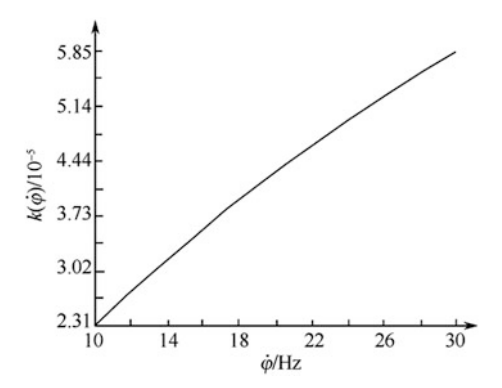


Fig. 6.10 Relationship between the scale factor $k(\dot{\varphi})$ and the rotating angular velocity $\dot{\varphi}$ of the carrier



When $\dot{\varphi} = 17$ Hz, $\Omega = 0.01$ rad/s and $a_m = 9.505 \times 10^{-7}$ rad, the vibration amplitude of the outer edge of the silicon vibrating mass of the gyroscope is

$$A_m = \alpha_m \frac{a_3}{2} = 5.03756 \times 10^{-9} m$$

6.4 Signal Detection

The signal detection circuit of the silicon micromechanical gyroscope is shown in Fig. 6.2. The pendulous reed of the monocrystalline silicon mass rotates with an angular velocity $\dot{\varphi}$, and the change of the deflection angle α will lead to changes in the four capacitors C_1 , C_2 , C_3 and C_4 which are composed of the pendulous reed of the monocrystalline silicon mass and a ceramic electrode plate. The varying signal of the capacitance is changed into that of the voltage and is amplified, or in other words the voltage signal change corresponding to the amplitude and the measured angular velocity Ω can be obtained. The capacitance change rate of a rotating carrier with a silicon micromechanical gyroscope is low and is susceptible to influence by the distributed capacitor. As a result the signal is processed by the transform circuit which uses the AC capacitance bridge as the interface and the capacitive sensitive element as the working arm of the bridge. The bridge power supply is an AC voltage with uniform amplitude, high frequency and stability. When the working capacitance changes, the signal output of the amplitude modulated wave which is modulated by the working capacitance change at the output end of the bridge can be obtained. After the signal of the amplitude modulated wave is amplified and demodulated, the low frequency signal output can be obtained.

6.4.1 The Relationship Between the Output Voltage and The Swing Angle

From Fig. 6.2, when the monocrystalline silicon pendulum has no deflection $(\alpha = 0)$, there holds $C_1 = C_2 = C_3 = C_4 = C_0$, but

$$C_0 = \varepsilon \left[(b_1 - b_2) \left(\frac{a_1 - a_0}{2d} \right) + (b_3 - b_2) \left(\frac{a_2 - a_1}{2d} \right) + b_3 \left(\frac{a_3 - a_2}{2d} \right) \right]$$
(6.34)

When the monocrystalline silicon pendulum has a deflection ($\alpha \neq 0$), there holds $C_1 = C_4$ and $C_2 = C_3$, and the capacitance change is

$$dC = \frac{\varepsilon}{d + \alpha r} dS = \frac{\varepsilon \Delta b}{d + \alpha r} dr \tag{6.35}$$

where d is the gap between the silicon mass and the ceramic electrode; α is the deflection angle of a silicon mass angular vibration; and ε is a dielectric constant.

By integrating Eq. (6.35), the following result can be obtained

$$C = \int_{r_1}^{r_2} \frac{\varepsilon \Delta b}{d + \alpha r} dr = \frac{\varepsilon \Delta b}{\alpha} \ln \left(1 + \frac{\frac{r_2 - r_1}{d}}{1 + \frac{r_1}{d} \alpha} \alpha \right)$$
 (6.36)

$$C(d,\alpha) = \frac{\varepsilon}{\alpha} \left[(b_1 - b_2) \ln \left(1 + \frac{\frac{a_1 - a_0}{2d}}{1 + \frac{a_0}{2d}} \alpha \right) + (b_3 - b_2) \times \ln \left(1 + \frac{\frac{a_2 - a_1}{2d}}{1 + \frac{a_1}{2d}} \alpha \right) + b_3 \ln \left(1 + \frac{\frac{a_3 - a_2}{2d}}{1 + \frac{a_2}{2d}} \alpha \right) \right]$$
(6.37)

 $C_{1} = \frac{\varepsilon}{\alpha} \left[(b_{1} - b_{2}) \ln \left(1 + \frac{\frac{a_{1} - a_{0}}{2d}}{1 + \frac{a_{0}}{2d}} \alpha \right) + (b_{3} - b_{2}) \times \ln \left(1 + \frac{\frac{a_{2} - a_{1}}{2d}}{1 + \frac{a_{1}}{2d}} \alpha \right) + (b_{3} - b_{2}) \times \ln \left(1 + \frac{\frac{a_{3} - a_{1}}{2d}}{1 + \frac{a_{1}}{2d}} \alpha \right) \right]$ (6.38)

$$C_{2} = \frac{\varepsilon}{\alpha} \left[(b_{1} - b_{2}) \ln \left(1 - \frac{\frac{a_{1} - a_{0}}{2d}}{1 - \frac{a_{0}}{2d}} \alpha \right) + (b_{3} - b_{2}) \times \ln \left(1 - \frac{\frac{a_{2} - a_{1}}{2d}}{1 - \frac{a_{1}}{2d}} \alpha \right) + (b_{3} - b_{2}) \times \ln \left(1 - \frac{\frac{a_{2} - a_{1}}{2d}}{1 - \frac{a_{2}}{2d}} \alpha \right) \right]$$

$$(6.39)$$

From Fig. 6.2, the AC resistance is

$$R_{C_1} = \frac{1}{2j\omega_e C_1}$$

$$R_{C_2} = \frac{1}{2j\omega_e C_2}$$

where ω_e is the AC angular frequency.

Thus

$$V_{1} = \frac{1}{1 + 2j\omega_{e}C_{1}R_{1}}V_{S}$$

$$V_{2} = \frac{1}{1 + 2j\omega_{e}C_{2}R_{2}}V_{S}$$

where V_S is the AC voltage on the bridge. Because C_1 and C_2 are very small, there holds

$$V_1 - V_2 \approx 2j\omega_e (C_2 R_2 - C_1 R_1) V_S \tag{6.40}$$

Assume that $R_1 = R_2 = R$, there holds

$$V_1 - V_2 = 2\omega_e R(C_2 - C_1)V_S \tag{6.41}$$

$$C_{1} - C_{2} = \frac{2\varepsilon_{0}}{\alpha} \left\{ (b_{1} - b_{2}) \ln \left[\frac{1 + \frac{(a_{1} - a_{0})\alpha}{2d + a_{0}\alpha}}{1 - \frac{(a_{1} - a_{0})\alpha}{2d - a_{0}\alpha}} \right] + (b_{3} - b_{2}) \ln \left[\frac{1 + \frac{(a_{2} - a_{1})\alpha}{2d + a_{1}\alpha}}{1 - \frac{(a_{2} - a_{1})\alpha}{2d - a_{1}\alpha}} \right] + b_{3} \ln \left[\frac{1 + \frac{(a_{3} - a_{2})\alpha}{2d + a_{2}\alpha}}{1 - \frac{(a_{3} - a_{2})\alpha}{2d - a_{2}\alpha}} \right] \right\}$$

$$(6.42)$$

$$|V_{1} - V_{2}| = \frac{4\varepsilon_{0}\omega_{e}RV_{s}}{\alpha} \left\{ (b_{1} - b_{2}) \ln \left[\frac{1 + \frac{(a_{1} - a_{0})\alpha}{2d + a_{0}\alpha}}{1 - \frac{(a_{1} - a_{0})\alpha}{2d - a_{0}\alpha}} \right] + (b_{3} - b_{2}) \ln \left[\frac{1 + \frac{(a_{2} - a_{1})\alpha}{2d + a_{1}\alpha}}{1 - \frac{(a_{2} - a_{1})\alpha}{2d - a_{1}\alpha}} \right] + b_{3} \ln \left[\frac{1 + \frac{(a_{3} - a_{2})\alpha}{2d + a_{2}\alpha}}{1 - \frac{(a_{3} - a_{2})\alpha}{2d - a_{2}\alpha}} \right] \right\}$$

$$(6.43)$$

where V_S is the AC voltage on the bridge; ω_e is the AC angular frequency; and R is the bridge resistance.

Substitute $\varepsilon_0 = 8.85 \times 10^{-12} \text{F/m}$, $\omega_e = 3.7 \times 10^5 \text{rad/s}$, $R = 75 \text{k}\Omega$, $V_S = 5 \text{V}$ and the size of the mass (mm) into Eq. (6.43), and the relationship between the voltage and the swing angle can be obtained (Fig. 6.11).

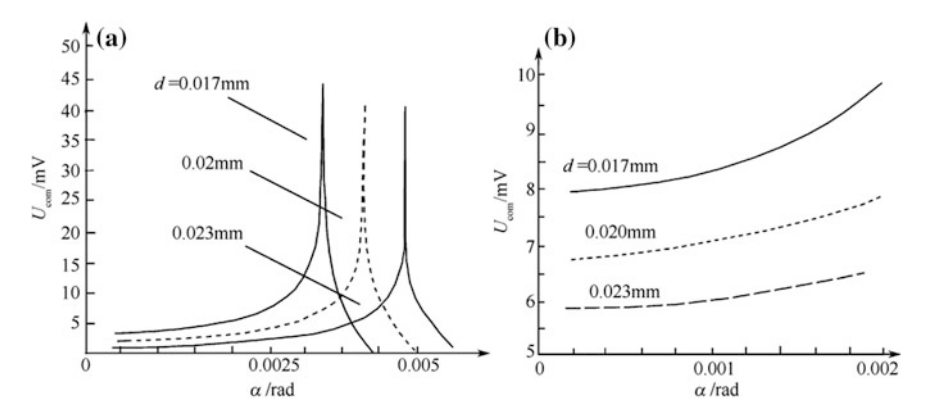


Fig. 6.11 Relationship between voltage and swing angle $\mathbf{a} \propto (0, 0.005)$; $\mathbf{b} \propto (0, 0.002)$

From Fig. 6.11a, it can be seen that when the values of d are 0.017, 0.020 and 0.023 mm respectively, three curves appear at infinity when α equals 0.00325, 0.00327 and 0.00437 rad. This means that the vibrating silicon mass contacts with the upper and lower electrode plates. In order to maintain that when the silicon mass vibrates it does not contact the upper and lower electrode plates, the structure size of the sensitive element should make the vibration angle $\alpha \propto (0, 0.002)$. From Fig. 6.11b it can be seen that with the decrease of d, the changing rate of the output voltage with respect to the swing angle becomes larger, therefore the value of d should be reduced. But due to the decrease of d the processing difficulty is also increased, thus d = 0.020mm. In Fig. 6.11b, when d = 0.020mm, and α lies in the range of $0 \sim 0.002$ rad, the amplitude change of the output voltage is

$$U_{\text{out}} = (7.875 - 6.75) \text{mV} = 1.125 \text{mV}$$

6.4.2 Signal Processing Circuit

1. Circuit Composition

The signal processing circuit is shown in Fig. 6.12. The power regulator provides a stable voltage for the pulse generator such that the pulse generator generates a stable pulse signal.

The principle of the pulse generator is that when the input voltage reaches a certain value, the Schmitt trigger changes from the static state to the working state, but when the input voltage is dropped to a certain value, it changes from the working state to the static state and a feedback resistor and a capacitor with a charge and a discharge are added, and the final output is a periodic rectangular wave $U_{\rm gen}$ as shown in Fig. 6.13. In this figure, $U_{\rm sens}$ is the voltage of the signal pick-up capacitor.

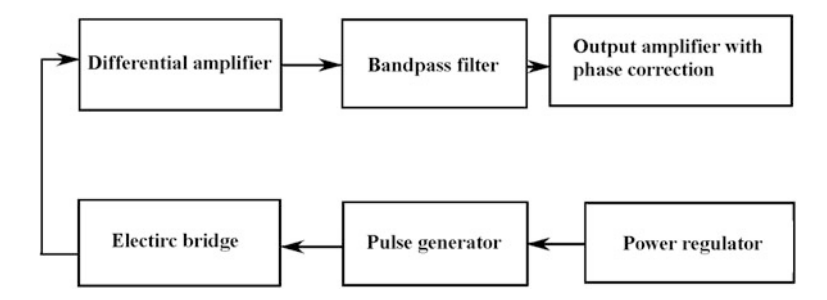
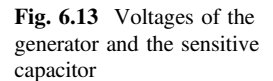


Fig. 6.12 Diagram of a signal processing circuit



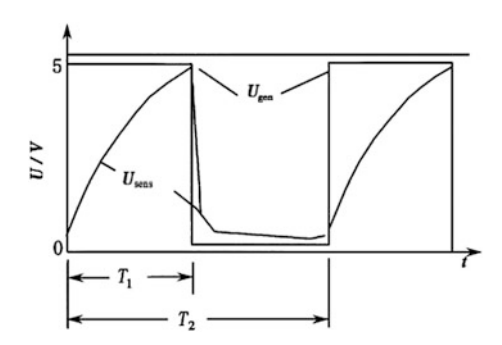


Figure 6.14a gives a capacitance–voltage conversion circuit, i.e., a capacitance–voltage conversion bridge, which obtains the capacitors C_{s1} and C_{s2} by a variable spacing signal and is charged and discharged by diodes VD_1 , VD_2 and R_1 , R_2 . The voltage U_{gen} which is generated by the pulse generator is added to the voltage input end of the bridge and the charging and the discharging of the diode adjusts the performance of the bridge. Inside the differential amplifier, there is an instrument amplifier composed of three operational amplifiers whose amplification factor is determined by R_5 , as shown in Fig. 6.14b. The first part of the dual operational amplifier is the band–pass filtering and the second part is used to correct the phase and the output amplification as shown in Fig. 6.14c, d.

2. Circuit Analysis

(1) A capacitance–voltage converter

A pulse generator generates a rectangular pulse voltage U_{gen} , whose high voltage is +5 V and whose low voltage is 0 V. This voltage is added to the bridge. The electric current charges the capacitors C_{s1} and C_{s2} through R_1 and R_2 , and also charges C_{s1} and C_{s2} through the reverse diode. But the current through the diode is small and can be ignored in the actual situation.

When $t = 0 \sim T_1(U_{gen} = 5 V)$, the value of the voltage U_{sens} which is picked up by the capacitor pickup depends on the value of the capacitors when

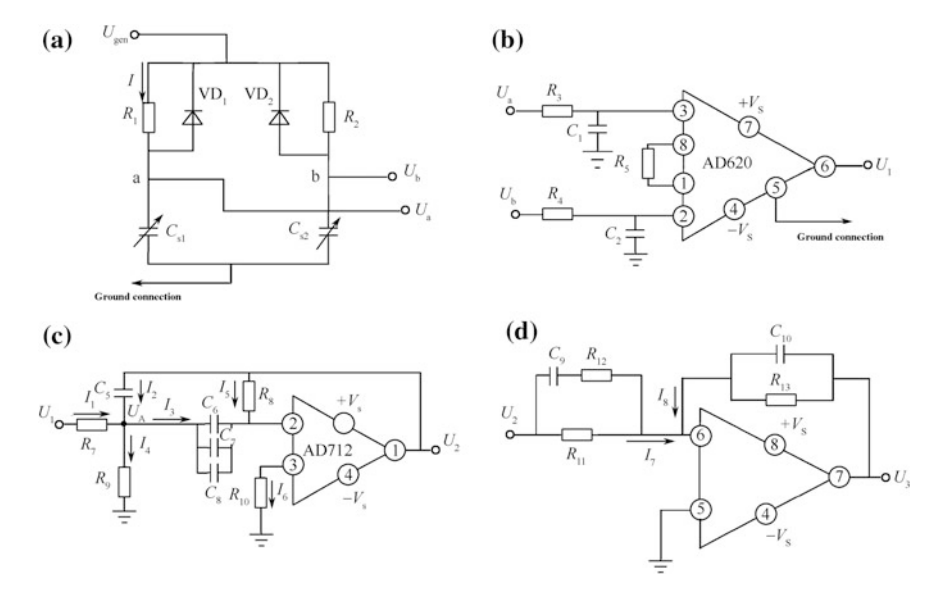


Fig. 6.14 Diagram of a signal processing principle a Bridge; b Amplifier circuit; c Band pass filter; d Phase correction and output circuit

 $t = T_1 \sim T(U_{gen} = 0)$. The voltage is determined by the characteristic of the diode and can be regarded as 0.

(1) In the process of charging, i.e.,

$$kT \le t \le kT + T_1$$
 $k = 0, \pm 1, \pm 2, \dots$

there holds

$$U_{\rm a} = U_{\rm m} \left(1 - e^{-\frac{t}{R_1 C_{\rm s1}}} \right) \tag{6.44}$$

$$U_{\rm b} = U_{\rm m} \left(1 - e^{-\frac{t}{R_2 C_{s2}}} \right) \tag{6.45}$$

where $U_{\rm m}$ is the amplitude of the exciting signal $U_{\rm gen}$.

(2) In the process of discharging, i.e.,

$$kT + T_1 \le t \le (k+1)T$$
 $k = 0, \pm 1, \pm 2, \dots$

Because the positive conductive resistance of the diode is very small, the charge of the capacitor C_{s1} is abruptly released to zero through the diode VD_1 , thus $U_a=0$. In the process of charging and discharging $(t=0\sim T)$, the DC component at the a end of the output voltage is

$$U_a = \frac{1}{T} \int_{0}^{T_1} U_a dt = \frac{U_m}{T} \left[T_1 - R_1 C_{s1} \left(1 - e^{\frac{-T_1}{R_1 C_{s1}}} \right) \right]$$
 (6.46)

Consider the actual structure of the sensitive element and assume that $C_{s1} = C_0 - \Delta C$ and $C_{s2} = C_0 + \Delta C$ where C_0 is the intrinsic capacitance between the electrode plates when the sensitive element is not subject to the Coriolis force, and ΔC is the capacitance variation after the sensitive element is subject to the force. Because $\Delta C \ll C_0$, there exists $C_{s1} = C_0 - \Delta C \approx C_0$, and

$$U_{\rm a} \approx \frac{U_{\rm m}}{T} \left[T_1 - R_1 (C_0 - \Delta C) \left(1 - e^{\frac{-T_1}{R_1 C_0}} \right) \right]$$
 (6.47)

Similarly

$$U_{\rm b} \approx \frac{U_{\rm m}}{T} \left[T_1 - R_2 (C_0 + \Delta C) \left(1 - e^{\frac{-T_1}{R_2 C_0}} \right) \right]$$
 (6.48)

Assume that $R_1 = R_2$, there holds

$$U_{\rm ab} \approx U_{\rm a} - U_{\rm b} = \frac{2U_{\rm m}R_{\rm l}}{T} \left(1 - e^{\frac{-T_{\rm l}}{R_{\rm l}C_{\rm 0}}}\right) \Delta C$$
 (6.49)

The voltage of the bridge output is simplified as

$$U_{\text{out}} = G\bar{U}_{\text{ab}} \tag{6.50}$$

where G is a magnification factor and $G = 49.4 \text{k}\Omega/R_5 + 1$.

Equation (6.50) can be expressed as

$$U_{\text{out}} = K\Delta C \tag{6.51}$$

where

$$K = \frac{2U_{\rm m}R_1}{T}G\left(1 - e^{\frac{-T_1}{R_1C_0}}\right) \tag{6.52}$$

Because R_1 , R_2 and R_5 are selected, G is not changed, T and T_1 are two fixed values which are determined by the pulse generator and the connected resistor and capacitance, and the amplitude of the exciting signal $U_{\rm gen}$ is $U_{\rm m}$, and thus K is a constant. The output signal is proportional to the size of the capacitance change.

(2) The transfer function of the circuit

In Fig. 6.14b, the low pass filter is composed of R_3 , C_1 and R_4 , C_2 respectively. After the signal is amplified the transfer function of the circuit is

$$H_1(s) = \frac{G}{R_3 C_1 s + 1} = \frac{4.94 \times 10^4 + R_5}{R_5 R_3 C_1 s + R_5}$$
(6.53)

where $R_3 = R_4$; $C_1 = C_2$; and $s = j\omega$ (ω is the angular frequency of the voltage signal).

In Fig. 6.14c, the amplifier can be regarded as an ideal operational amplifier so the input current of the operational amplifier is zero, $I_3 = -I_5$ and $I_6 = 0$. From Kirchhoff's law, there holds

$$I_1 + I_2 = I_3 + I_4$$

$$I_1 = \frac{U_1 - U_A}{R_7}, I_2 = \frac{U_2 - U_A}{Z_1}, I_3 = \frac{U_A}{Z_2}, I_4 = \frac{U_A}{R_9}, I_5 = \frac{U_2}{R_8}$$

where

$$Z_1 = \frac{1}{sC_5}, \ Z_2 = \frac{1}{s(C_6 + C_7 + C_8)}$$

Thus the transfer function of the circuit in Fig. 6.14c is

$$H_2(s) = \frac{U_2(s)}{U_1(s)} = \frac{\frac{1}{R_7 C} s}{s^2 + \frac{(C + C_5)}{R_8 C C_5} s + \frac{1}{R_8 C C_5} \left(\frac{1}{R_7} + \frac{1}{R_9}\right)}$$
(6.54)

where $C = C_6 + C_7 + C_8$.

By adjusting the values of C, C_5 , R_7 , R_8 and R_9 in Eq. (6.54), improved frequency characteristics can be obtained in the range of the spin cycle of the measured carrier.

In Fig. 6.14d, the amplifier can be regarded as an ideal operational amplifier, the input current of the operational amplifier is 0, $I_7 = -I_8$, so from Kirchhoff's law, there holds

$$I_7 = \frac{U_2}{Z_2}, \quad I_8 = \frac{U_3}{Z_4}$$

where Z_3 is the impedance after C_9 , R_{12} and R_{11} are mix-connected, $Z_3 = R_{11} + R_{11}R_{12}C_9s/[1 + (R_{11} + R_{12})C_9s]$; and Z_4 is the impedance after C_{10} and R_{13} are parallel-connected, $Z_4 = R_{13}/(1 + R_{13}C_{10}s)$.

Thus the transfer function of the circuit in Fig. 6.14d is

$$H_3(s) = \frac{U_3(s)}{U_2(s)} = \frac{R_{13}}{R_{11}} \frac{1 + (R_{11} + R_{12})C_9s}{(1 + R_{13}C_{10}s)(1 + R_{12}C_9s)}$$
(6.55)

By adjusting the values of C_9 , C_{10} , R_{11} , R_{12} and R_{13} in Eq. (6.55), the phases lag. This is generated by the pre-amplifier and can be corrected, and the pre-signal is amplified again.

The transfer function of the whole circuit is

$$H(s) = H_1(s)H_2(s)H_3(s) = \frac{4.94 \times 10^4 + R_5}{R_5R_3C_1s + R_5} \frac{\frac{1}{R_7C}s}{s^2 + \frac{C + C_5}{R_8CC_5}s + \frac{1}{R_8CC_5}\left(\frac{1}{R_7} + \frac{1}{R_9}\right)}$$

$$\frac{R_{13}}{R_{11}} \times \frac{1 + (R_{11} + R_{12})C_9s}{(1 + R_{13}C_{10}s)(1 + R_{12}C_9 \cdot s)}$$
(6.56)

By adjusting all the parameters in Eq. (6.56), the performance of the whole circuit can be adjusted.

6.5 ANSYS Simulation and Analogy

6.5.1 Modal Analysis

The size of the structure and the corresponding material constants of the silicon mass are imported and by solving and post-processing three modes can be obtained:

Fig. 6.15 Finite element modal analysis

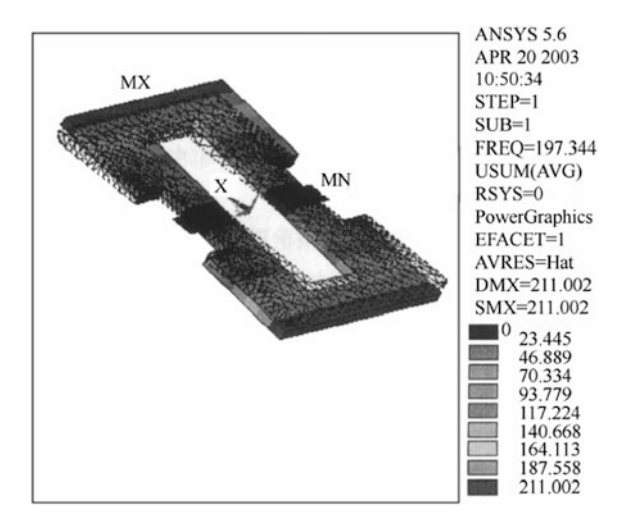
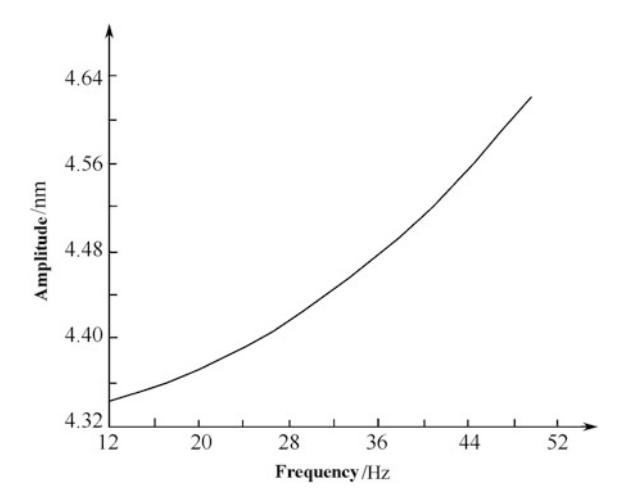


Fig. 6.16 Frequency response curve



the resonant frequency of the first mode is 197.34 Hz as shown in Fig. 6.15. The frequencies of the second mode and the third mode are 1806 and 2292 Hz respectively and can be ignored.

6.5.2 Frequency Response Analysis

From the dynamic parameters, the following result can be obtained

$$K_{\rm T} \gg (J_z - J_x)\dot{\varphi}^2 \tag{6.57}$$

Thus Eq. (6.13) is simplified as

$$J_{\mathbf{v}}\ddot{\alpha} + D\dot{\alpha} + K_{\mathbf{T}}\alpha = (J_{\mathbf{v}} + J_{\mathbf{v}} - J_{\mathbf{x}})\Omega\,\dot{\varphi}\,\cos(\dot{\varphi}t) \tag{6.58}$$

Equation (6.58) is a standard forced vibration equation with damping.

After the above modal analysis, the analysis type is selected as frequency response analysis, the range of the load forced frequency is $10 \sim 50$ Hz, the load amplitude is changed by the mean of Ramped, the load acts at two edges of the vibrating silicon mass and forms the couple moment, the damping type is the constant damping ratio, and finally the frequency analysis result can be solved when the measured angular velocity rate is $\Omega = 0.01$ rad/s, as shown in Fig. 6.16. This frequency response analysis curve is the response of the silicon vibrational mass—

displacement of the edge node–frequency (the rotating frequency of the carrier). From this figure, it can be seen that when $\dot{\varphi}=17Hz$, the vibrational amplitude of the outer edges of the silicon vibrating mass is

$$A'_{\rm m} = 4.36 \times 10^{-9} {\rm m}$$

Chapter 7 Error of a Non-driven Micromechanical Gyroscope

7.1 Motion Equations of a Vibratory Gyroscope

The vibratory gyroscope is a sensor which is designed to measure the absolute angular velocity of a non-rotating aircraft, and comprises a platform which is suspended in a frame by two elastic axes (internal and external), an electrostatic actuator and an angular pickup capacitor with two axes. Figure 7.1a gives the principle diagram of the gyroscope. Introduce the following coordinates: x, y and z is a coordinate system which is fixed with a silicon pendulum; x_0 , y_0 and z_0 is a coordinate system which is fixed with the frame; x_1 , y_1 and z_1 is a coordinate system which is fixed with the aircraft rotates with an absolute angular velocity $\omega\{\omega_{x1}, \omega_{y1}, \omega_{z1}\}$ in absolute space, and ω_{z1} is the angular velocity to be measured.

The position of the platform relative to the aircraft is determined by the angles α and β . A, B and C are the inertia moments of the platform relative to the axes x, y, and z; A_0 , B_0 and C_0 are the inertia moments of the frame relative to the axes x_0 , y_0 and z_0 ; and the gravity centers for the silicon pendulum and the frame lie at the midpoint O of the suspension support. On the basis of Fig. 7.1b, the projections of the frame angular velocities ω_{x0} , ω_{y0} and ω_{z0} on the axis and the projections of the platform angular velocities ω_x , ω_y and ω_z on the axes x, y and z which is fixed to the silicon pendulum can be obtained:

$$\begin{cases}
\omega_{x0} = -\omega_{z1} \sin \alpha + \omega_{x1} \cos \alpha \\
\omega_{y0} = \dot{\alpha} + \omega_{y1} \\
\omega_{z0} = \omega_{z1} \cos \alpha + \omega_{x1} \sin \alpha
\end{cases}$$
(7.1)

$$\begin{cases} \omega_{x} = \dot{\beta} - \omega_{z1} \sin \alpha + \omega_{x1} \cos \alpha \\ \omega_{y} = (\dot{\alpha} + \omega_{y1}) \cos \beta + (\omega_{z1} \cos \alpha + \omega_{x1} \sin \alpha) \sin \beta \\ \omega_{z} = (\omega_{z1} \cos \alpha + \omega_{x1} \sin \alpha) \cos \beta - (\dot{\alpha} + \omega_{y1}) \sin \beta \end{cases}$$
(7.2)

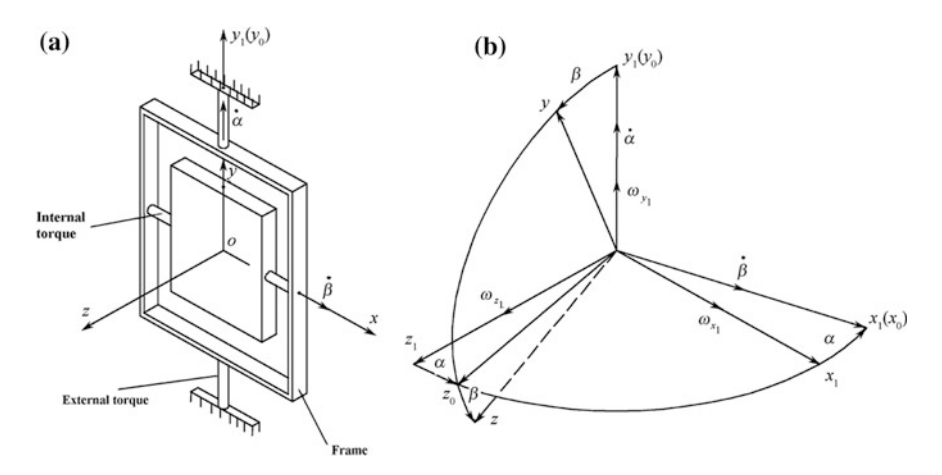


Fig. 7.1 Principle diagram of a vibratory gyroscope a Principle diagram. b Coordinate transformation diagram

From the small angles α and β , there holds

$$\begin{cases}
\omega_{x0} = -\omega_{z1}\alpha + \omega_{x1} \\
\omega_{y0} = \dot{\alpha} + \omega_{y1} \\
\omega_{z0} = \omega_{z1} + \omega_{x1}\alpha
\end{cases}$$
(7.3)

$$\begin{cases}
\omega_{x} = \dot{\beta} - \omega_{z1}\alpha + \omega_{x1} \\
\omega_{y} = \dot{\alpha} + \omega_{y1} + \omega_{z1}\beta + \omega_{x1}\alpha\beta \\
\omega_{z} = \omega_{z1} + \omega_{x1}\alpha - \dot{\alpha}\beta - \omega_{y1}\beta
\end{cases} (7.4)$$

The projections of the protagonist momentum $\overline{\Theta^{II}}$ of the silicon pendulum on the axes x, y, and z, and the projections of the protagonist momentum $\overline{\Theta^P}$ of the external frame on the axes x_0 , y_0 and z_0 are

$$\begin{cases}
\Theta_{x}^{II} = A\omega_{x} = A(\dot{\beta} - \omega_{z1}\alpha + \omega_{x1}) \\
\Theta_{y}^{II} = B\omega_{y} = B(\dot{\alpha} + \omega_{y1} + \omega_{z1}\beta + \omega_{x1}\alpha\beta) \\
\Theta_{z}^{II} = C\omega_{z} = C(\omega_{z1} + \omega_{x1}\alpha - \omega_{y1}\beta - \dot{\alpha}\beta)
\end{cases}$$
(7.5)

$$\begin{cases} \Theta_{x0}^{P} = A_{0}\omega_{x0} = A_{0}(-\omega_{z1}\alpha + \omega_{x1}) \\ \Theta_{y0}^{P} = B_{0}\omega_{y0} = B_{0}(\dot{\alpha} + \omega_{y1}) \\ \Theta_{z0}^{P} = C_{0}\omega_{z0} = C_{0}(\omega_{z1} + \omega_{x1}\alpha) \end{cases}$$
(7.6)

Because the deflection angle of the silicon pendulum in the actual design is less than 0.1′–0.2′, the terms including the angle product in Eqs. (7.3)–(7.6) are eliminated and the following result can be obtained as

$$\begin{cases}
\omega_{x0} = \omega_{x1} - \omega_{z1}\alpha \\
\omega_{y0} = \dot{\alpha} + \omega_{y1} \\
\omega_{z0} = \omega_{z1}
\end{cases}$$
(7.7)

$$\begin{cases}
\omega_{x} = \dot{\beta} + \omega_{x1} - \omega_{z1}\alpha \\
\omega_{y} = \dot{\alpha} + \omega_{y1} + \omega_{z1}\beta \\
\omega_{z} = \omega_{z1}
\end{cases}$$
(7.8)

Due to the higher change frequency of α and β , the small variables $\omega_{z1}\alpha$ and $\omega_{z1}\beta$ in this expression are retained and in the following Euler equation the derivatives of two time variables can be obtained as

$$\begin{cases}
\Theta_x^{\text{II}} = A(\dot{\beta} + \omega_{x1} - \omega_{z1}\alpha) \\
\Theta_y^{\text{II}} = B(\dot{\alpha} + \omega_{y1} + \omega_{z1}\beta) \\
\Theta_z^{\text{II}} = C\omega_{z1}
\end{cases}$$
(7.9)

$$\begin{cases} \Theta_{x0}^{P} = A_0(\omega_{x1} - \omega_{z1}\alpha) \\ \Theta_{y0}^{P} = B_0(\dot{\alpha} + \omega_{y1}) \\ \Theta_{z0}^{P} = C_0\omega_{z1} \end{cases}$$
 (7.10)

By using the Euler dynamic equations, the dynamic equation of the platform relative to the internal elastic torsion axis in the coordinate system xyz can be obtained as

$$\frac{d\Theta_x^{II}}{dt} - \Theta_y^{II}\omega_z + \Theta_z^{II}\omega_y = M_x \tag{7.11}$$

Replace Eqs. (7.8) and (7.9) and obtain

$$A(\ddot{\beta} + \dot{\omega}_{x1} - \dot{\alpha}\omega_{z1} - \alpha\dot{\omega}_{z1}) - B(\dot{\alpha} + \omega_{y1} + \omega_{z1}\beta)\omega_{z1} + C\omega_{z1}(\dot{\alpha} + \omega_{y1} + \omega_{z1}\beta)$$

$$= M_x$$
(7.12)

Replace the x axis by

$$M_x = M_x^{\mathrm{B}} + M_x^{\mathrm{M}} - D_{\beta}\dot{\beta} - K_{\beta}\beta \tag{7.13}$$

where $M_x^{\rm B}$ is the external moment acting on the platform; M_x^{M} is the torsion moment; $D_{\beta}\dot{\beta}$ is the damping torque; D_{β} is the damping coefficient of the x axis; $K_{\beta}\beta$ is the elastic torque of the internal elastic supporting bar; and K_{β} is the stiffness of the internal torsion supporting bar.

From Eq. (7.12) obtain

$$A\ddot{\beta} + D_{\beta}\dot{\beta} + K_{\beta}\beta - (A + B - C)\dot{\alpha}\omega_{z1} = M_{x}^{B} + M_{x}^{M} + (B - C)\omega_{y1}\omega_{z1} - A\dot{\omega}_{x1} + A\dot{\omega}_{z1}\alpha$$

$$(7.14)$$

On the basis of the Euler dynamic equation, the motion equation of the platform relative to the y axis in the coordinate system xyz can be obtained as

$$\frac{\mathrm{d}\Theta_{y}^{\mathrm{II}}}{\mathrm{d}t} - \Theta_{z}^{\mathrm{II}}\omega_{x} + \Theta_{x}^{\mathrm{II}}\omega_{z} = M_{y}$$

Substitute Eqs. (7.8) and (7.9) and obtain

$$B(\ddot{\alpha} + \dot{\omega}_{y1} + \dot{\beta}\omega_{z1} + \beta\dot{\omega}_{z1}) - C(\dot{\beta} + \omega_{x1} - \omega_{z1}\alpha)\omega_{z1} + A(\dot{\beta} + \omega_{x1} - \omega_{z1}\alpha)\omega_{z1} = M_y$$
(7.15)

The torque relative to the y axis is written as

$$M_{y} = M_{y}^{\mathrm{B}} - D_{\alpha}\dot{\alpha} + M_{y}^{\mathrm{R}} \tag{7.16}$$

where $M_y^{\rm B}$ is the external moment; $D_\alpha \dot{\alpha}$ is the damping torque acting on the platform; D_α is the damping coefficient of the axis y; and $M_y^{\rm R}$ is the restriction moment (the bending stiffness of the internal torsion bar is infinite).

The dynamic equation of the framework around the $y_1(y_0)$ axis in the coordinate system of x_0 , y_0 and z_0 can be obtained as

$$\frac{d\Theta_{y1}^{P}}{dt} - \Theta_{z0}^{P}\omega_{x0} + \Theta_{x0}^{P}\omega_{z0} = M_{y1}$$
 (7.17)

Substitute Eqs. (7.7) and (7.10) and obtain

$$B_0(\ddot{\alpha} + \dot{\omega}_{v1}) - C_0\omega_{z1}(\omega_{x1} - \omega_{z1}\alpha) + A_0(\omega_{x1} - \omega_{z1}\alpha)\omega_{z1} = M_v$$
 (7.18)

The external torque M_{y1} acting on the external torsion is

$$M_{y1} = -K_{\alpha}\alpha + M_{y}^{M} - M_{y}^{R} \tag{7.19}$$

Because β is small it can be thought that the restriction moments of the y axis and the $y_1(y_0)$ axis are equivalent on the basis of Eqs. (7.15), (7.16), (7.18) and (7.19) the following result can be obtained:

$$(B+B_0)\ddot{\alpha} + D_{\alpha}\dot{\alpha} + K_{\alpha}\alpha - (C-B-A)\dot{\beta}\omega_{z1}$$

$$= M_y^B + M_y^M + (C+C_0 - A - A_0)\omega_{x1}\omega_{z1} - (B+B_0)\dot{\omega}_{y1}$$

$$-B\dot{\omega}_{z1}\beta - (C+C_0 - A - A_0)\omega_{z1}^2\alpha$$
(7.20)

Equations (7.14) and (7.20) are the dynamics equations of the vibratory gyroscope.

Assume that the gyroscope only measures a constant angular velocity $\omega_{z1} = \Omega$ of the aircraft, and there holds

$$\omega_{x1} = \omega_{y1} = \dot{\omega}_{x1} = \dot{\omega}_{y1} = \dot{\omega}_{z1} = 0$$

From Eqs. (7.14) and (7.20), there holds

$$\ddot{A}\ddot{\beta} + D_{\beta}\dot{\beta} + K_{\beta}\beta - (A + B - C)\dot{\alpha}\Omega
= M_{x}^{B} + M_{x}^{M}(B + B_{0})\ddot{\alpha} + D_{\alpha}\dot{\alpha} + K_{\alpha}\alpha + (A + B - C)\dot{\beta}\Omega + (C + C_{0} - A - A_{0})\alpha\Omega^{2}
= M_{y}^{B} + M_{y}^{M}$$
(7.21)

It can be thought that the excitation of the main vibration is applied on the y_1 axis and the output x axis. At this time, like the result of the preliminary calculation, the vibration angular velocity $\dot{\alpha}$ of the y_1 axis is greater than the angular velocity $\dot{\beta}$ of the output axis. Therefore, compared with the inertia moment $(A+B-C)\dot{\alpha}\Omega$ of the y_1 axis, the output axis of the inertia moment $(A+B-C)\dot{\beta}\Omega$ can be ignored.

From Eq. (7.21) there holds

$$A\ddot{\beta} + D_{\beta}\dot{\beta} + K_{\beta}\beta - (A + B - C)\dot{\alpha}\Omega = M_x^{\rm B} + M_x^{\rm M}$$

$$(B + B_0)\ddot{\alpha} + D_{\alpha}\dot{\alpha} + K_{\alpha}\alpha = M_y^{\rm B} + M_y^{\rm M}$$
(7.22)

The working mode of the gyroscope can be divided into two types: one is the ahead non-resonant phase output and the other is the resonant amplitude output. The two modes work perfectly well but each mode has its advantages and disadvantages.

Assume that $M_y^{\rm M} = M_y^0 \sin(\omega t)$, then this harmonic torque can produce a steady vibration on the y_1 axis, i.e.,

$$\alpha = \frac{M_y^0}{\sqrt{\left[(K_\alpha - K_\alpha') - (B + B_0)\omega^2 \right]^2 + (D_\alpha \omega)^2}} \sin(\omega t - \varphi(\omega))$$
 (7.23)

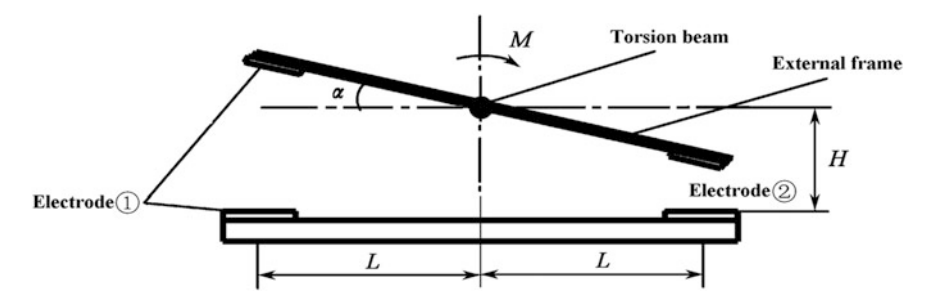


Fig. 7.2 Working principle of a vibratory gyroscope

where

$$\varphi(\omega) = \arctan\left(\frac{D_{\alpha}\omega}{(K_{\alpha} - K_{\alpha}') - (B + B_0)\omega^2}\right)$$
(7.24)

where K'_{α} is the additional negative stiffness of the elastic suspension bar on the y_1 axis, the negative stiffness is produced by the electrostatic torque generator on the y_1 axis and the constant voltage U_0 is applied to the torque generator, whose principle is shown in Fig. 7.2.

In Fig. 7.2, when the same constant voltage U_0 is applied to the electrodes ① and ②, there is an electrostatic torque in the torsion bar, i.e.,

$$M = \frac{\varepsilon S L U_0^2}{\left(H - \alpha L\right)^2} - \frac{\varepsilon S L U_0^2}{\left(H + \alpha L\right)^2}$$
(7.25)

where ε is the dielectric constant; and S is the surface area of the capacitor plate.

If the spacing of the capacitor plate is much larger than the vibration amplitude αL of the frame, the following result can be approximately obtained as

$$M = \frac{4\varepsilon SL^2 U_0^2}{H^3} \alpha \tag{7.26}$$

The additional negative stiffness K'_{α} of the output y_1 axis is

$$K_{\alpha}' = \frac{4\varepsilon SL^2 U_0^2}{H^3} \tag{7.27}$$

The torque generator is used to produce consistent resonance on the inner and outer frame axes. Therefore, according to the working principle the vibration of the y_1 axis is

$$\alpha = \alpha_{\rm m} \sin(\omega_{\rm p} t - \varphi(\omega)) \tag{7.28}$$

The resonant frequency at this time is

$$\omega_{\rm P} = \sqrt{\frac{K_{\alpha} - K_{\alpha}'}{B + B_0}} \varphi(\omega) = \frac{\pi}{2}$$
 (7.29)

The torque of the torque generator is M_y^H . The system can automatically adjust the vibration frequency and the vibration amplitude α_m of the system is detected by the capacitance extraction circuit and can automatically remain constant.

The input angular velocity Ω on the z_1 axis, the Coriolis force acting on the framework generates the torque of the internal frame axis, and under the action of the torque the internal framework begins moving with frequency ω_P .

The steady solution of Eq. (7.22) (for $M_x^B = 0$ and $M_x^M = 0$) is

$$\beta = -\frac{(A+B-C)\Omega\alpha_{\rm m}\omega_{\rm p}}{\sqrt{(K_{\beta}-A\omega^2)^2 + (D_{\beta}\omega_{\rm p})^2}}\sin[\omega t - \chi(\omega)]$$
 (7.30)

or

$$\beta = -\beta_{\rm m} \sin(\omega_{\rm p} t - \chi(\omega)) \tag{7.31}$$

The negative stiffness coefficient K'_{α} is selected such that the resonant frequencies on the vibration axes of the internal and external frames are the same and $\beta_{\rm m}$ is maximized. There holds

$$\omega_{\rm P} = \sqrt{\frac{K_{\beta}}{A}} \chi(\omega_{\rm p}) = \frac{\pi}{2} \tag{7.32}$$

$$\beta_{\rm m} = \frac{(A+B-C)\Omega\alpha_{\rm m}}{D_{\beta}} \tag{7.33}$$

Therefore, the amplitude of the framework is proportional to the input angular velocity Ω . The accuracy of this method of measuring the angular velocity Ω depends on the total resonant precision, the stability of α_m and the damping coefficient D_β . To obtain the larger amplitudes of α_m and β_m , there must be a high vacuum in the device. At this time, the damping of this device is no longer affected by the gas dynamics, but is affected by the internal friction of the elastic torsion bar material such that the damping coefficient D_β is relatively stable.

However, for the signal extraction circuit of the angle β , capacitance signal detection electrodes need to be installed on the inner frame, which will result in an additional error.

This defect can be solved using the method of adding the feedback system to the vibratory angle β in the axis of the internal frame. The capacitance pickup and the electrostatic torque generator are arranged on the axis of the internal framework. If the torque M_x^M is generated holds $M_x^M = -K_M\beta$.

From Eq. (7.22) (for $M_x^{\rm B}=0$), the following equation can be obtained

$$A\ddot{\beta} + D_{\beta}\dot{\beta} + K_{\beta}\beta + K_{M}\beta = (A + B - C)\dot{\alpha}\Omega$$

Substitute Eqs. (7.28) and (7.29) and obtain

$$A\ddot{\beta} + D_{\beta}\dot{\beta} + K_{\beta}\beta + K_{M}\beta = -(A + B - C)\Omega\omega_{p}\alpha_{m}\sin(\omega_{p}t)$$
 (7.34)

Set

$$M_0 = (A + B - C)\omega_{\rm p}\alpha_{\rm m}\Omega \tag{7.35}$$

For the steady vibration, from Eq. (7.34) obtain

$$\beta = \frac{M_0}{\sqrt{(K_\beta + K_M - A\omega_P^2)^2 + (D_\beta \omega_P)^2}} \sin[\omega_p t - \omega(\omega_P)]$$
 (7.36)

where

$$æ(\omega_{\rm P}) = \arctan\left(\frac{D_{\beta}\omega_{\rm P}}{K_{\beta} + K_{\rm M} - A\omega_{\rm P}^2}\right) \tag{7.37}$$

If the resonant frequencies on the input axis and the output axis are the same (without additional negative feedback), there holds

$$\omega_{\mathrm{P}} = \sqrt{\frac{K_{\beta}}{A}}$$

then

$$\beta = \frac{M_0}{\sqrt{K_{\rm M}^2 + (D_\beta \omega_{\rm P})^2}} \sin[\omega_{\rm p} t - \varpi(\omega_{\rm P})]$$
 (7.38)

$$æ(\omega_{\rm P}) = \arctan\left(\frac{D_{\beta}\omega_{\rm P}}{K_{\rm M}}\right) \tag{7.39}$$

 $K_{\rm M}$ is selected to reduce the impact of D_{β} on the precision of the device and then there holds

$$K_{\rm M} \gg D_{\beta}\omega_{\rm P}$$

Therefore, it is necessary to pump a vacuum and increase the spacing between the torque generators of the output axes in order to greatly reduce the damping coefficient. If these conditions are fully satisfied, $K_{\rm m}$, $D_{\beta}\omega_{\rm p}$ in Eqs. (7.38) and (7.39) can be ignored, i.e.,

$$\beta = \frac{M_0}{K_M} \sin(\omega_p t), \alpha(\omega_p) \to 0 \tag{7.40}$$

or

$$M_{x}^{\mathrm{M}} = K_{\mathrm{M}}\beta = M_{0}\sin(\omega_{\mathrm{p}}t) \tag{7.41}$$

 $M_{\scriptscriptstyle \rm r}^{\rm M}$ is the torque of the output axis generated by the electrostatic torque generator, which is formed by negative feedback of the angle β : $M_x^M = -K_{\text{torquegenerator}} U_1$

$$M_x^M = -K_{\text{torquegenerator}} U_1 \tag{7.42}$$

where U_1 is the voltage applied to the torque generator; and $K_{\text{torquegenerator}}$ is the transmission coefficient of the torque generator.

If the voltage U_1 is regarded as the output parameter of the gyroscope, the measurement accuracy of the torque M_0 will be increased because there is no transmission coefficient of the capacitance signal extraction circuit on the x axis in the expression of the voltage U_1 . In order to linearize the torque M_x^M which is directly related to the voltage U_1 , the expression of this torque can be written as

$$M_x^{\mathbf{M}} = -\frac{\varepsilon SL}{H^2} \left[(U_0 + U_1)^2 - (U_0 - U_1)^2 \right]$$
 (7.43)

where U_0 is the constant feedback voltage, which is applied to the electrode plate on both sides of the torque generator that is related to the x axis; ε is the dielectric constant; and S, L and H are the structural parameters determined by Fig. 7.2 and Eq. (7.26).

Transform Eq. (7.43) into the following form:

$$M_x^{\rm M} = -\frac{4\varepsilon S L U_0}{H^2} U_1 \tag{7.44}$$

Compare Eqs. (7.44) and (7.42) and obtain the transmission coefficient $K_{\text{torquegenerator}}$ of the torque generator:

$$K_{\text{torquegenerator}} = \frac{4\varepsilon SLU_0}{H^2} \tag{7.45}$$

Substitute Eqs. (7.41) and (7.42) and obtain

$$U_1 = -\frac{M_0}{4\frac{\varepsilon SLU_0}{H^2}}\sin(\omega_P t) \tag{7.46}$$

Substitute Eq. (7.35) and obtain the pickup voltage of the torque generator:

$$U_{1a} = \frac{(A+B-C)\omega_{\rm p}\alpha_{\rm m}\Omega}{4\frac{\varepsilon SLU_0}{H^2}}$$

$$(7.47)$$

The amplitude α_m of the input axis is expressed as

$$\alpha_{\rm m} = \frac{U_{\rm m}}{K_{\rm TS}} \tag{7.48}$$

where $U_{\rm m}$ is the steady voltage amplitude of the angle pick-up circuit on the input axis; and $K_{\rm TS}$ is the transmission coefficient of the angle pick-up circuit on the input axis.

Substitute Eq. (7.48) into Eq. (7.47) and obtain

$$U_{1a} = \frac{(A + B - C)\omega_{\rm p}U_{\rm m}}{4\frac{\&SL}{H^2}U_0K_{\rm TS}}\Omega$$
 (7.49)

Equation (7.49) determines the output characteristics of the device. From Eq. (7.49), it can be seen that the stability of the output signal is determined by a series of parameters and their influences are different.

It is noted that compared with the device the processing algorithm of the output signal of the vibratory gyroscope has many advantages because in the expression of the output characteristic, there are no unstable parameters such as the damping coefficient and the transmission coefficient of the angle pick-up circuit on the output axis.

In Eq. (7.49) the inertia moments A, B and C for the silicon pendulum are unchanged and can be considered as constant. Similarly, it can also be considered that the other constant structural parameters are as follows: S is the surface area of the electrostatic torque generator; L is the space between the rotating axis and the surface of the torque generator; H is the size of the gap between the electrostatic oscillators; and ε is the dielectric constant.

The parameters are: ω_P is the resonant frequency, U_m is the steady-state amplitude of the angle pick-up capacitor on the input axis; K_{TS} is the transmission coefficient of the angle pickup on the input axis; and U_0 is the feedback voltage of the electrostatic torque generator on the output axis.

The approximate expression for the error of the output signal U_{1a} is composed of these parameters and is expanded by a Taylor series as

$$\Delta U_{1a} = \frac{\partial U_{1a}}{\partial \omega_{p}} \Delta \omega_{p} + \frac{\partial U_{1a}}{\partial U_{m}} \Delta U_{m} + \frac{\partial U_{1a}}{\partial K_{TS}} \Delta K_{TS} + \frac{\partial U_{1a}}{\partial U_{0}} \Delta U_{0}$$
 (7.50)

Its partial derivative can be obtained as

$$\frac{\partial U_{1a}}{\partial \omega_{p}} = \frac{(A+B-C)U_{m}}{\frac{4eSL}{H^{2}}U_{0}K_{TS}}\Omega$$

$$\frac{\partial U_{1a}}{\partial U_{m}} = \frac{(A+B-C)\omega_{P}}{\frac{4eSL}{H^{2}}U_{0}K_{TS}}\Omega$$

$$\frac{\partial U_{1a}}{\partial K_{TS}} = -\frac{(A+B-C)\omega_{P}U_{m}}{\frac{4eSL}{H^{2}}U_{0}K_{TS}^{2}}\Omega$$

$$\frac{\partial U_{1a}}{\partial U_{0}} = -\frac{(A+B-C)\omega_{P}U_{m}}{\frac{4eSL}{H^{2}}U_{0}K_{TS}^{2}}\Omega$$
(7.51)

The expression of the relative error is

$$\frac{\Delta U_{1a}}{U_{1a}} = \frac{\Delta \omega_{P}}{\omega_{P}} + \frac{\Delta U_{m}}{U_{m}} + \frac{\Delta K_{TS}}{K_{TS}} + \frac{\Delta U_{0}}{U_{0}}$$

$$(7.52)$$

Through the expression for the relative error, when the vibratory gyroscope measures the angular velocity Ω under the setting state, the stability of the output signal can be predicted and the feedback voltage of the auxiliary torque generator is applied to the output axis.

The resonant frequencies ω_P on the input axis and the output axis are the same and are determined by the inertia moment of the silicon pendulum and the stiffness of the silicon elastic torsion bar, and these parameters can be considered as sufficiently stable. The constant voltage U_0 is applied to the torque generator of the input axis to ensure that the resonant frequencies on the two axes are the same and the voltage provides an additional negative stiffness. A similar but different voltage is applied to the output axis of the torque generator. These two voltages provide the auxiliary stiffness defined by Eq. (7.27) and this stiffness is determined by the structural parameters and depends mainly on the voltage U_0 . The stability of U_0 is determined by the electronic circuit but the stability of modern electronic circuits is very high so the relative error due to the instability of U_0 can be predicted to be 0.1% (without considering the specific principle of the voltage regulator). The error caused by the instability of frequency ω_P which is caused by the instability of voltage U_0 can be predicted by the same method.

The stability of the angle readout voltage $U_{\rm m}$ on the input axis depends on the stability of the reference voltage source and the slope of the input vibration exciting system. The voltage provided by the system at the output end of the angle pick-up voltage is equal to the voltage of the reference voltage source. The relative instability of the system lies within 1% (taking into account the level of modern electronic technology).

The most unstable parameter is the transmission coefficient of the capacitance angle readout circuit. In Eq. (7.52) the coefficient K_{TS} is determined only by the stable amplitude α_m of the input axis. According to the experimental work of the

capacitance angle pick-up circuit, the relative error caused by the K_{TS} instability is expected to be not more than 1% (very close to the error caused by the electronic circuit).

The calculation of the relative error of the vibratory gyroscope has been carried out, but has not been fully confirmed experimentally so there some features are only estimated as there are no experimental conditions for their validation. However, the components of this device (the angle pickup, the torque generator and other parts) have been tested in other devices. So, it can be deemed that the relative error of the vibratory gyroscope manufactured on the basis of the previous principle can achieve a level of 1%.

7.2 Error Principle of a Vibratory Gyroscope

The error of a vibratory gyroscope on a fixed platform will be analyzed. Assume that in Eqs. (7.14) and (7.20) $\omega_{x1}=0$, $\omega_{y1}=0$, $\dot{\omega}_{x1}=0$ and $\dot{\omega}_{y1}=0$. In addition, from the suspension of the internal framework, it can be seen that $B\gg B_0$, thus the latter part of Eq. (7.20) can be ignored. Generally speaking, the main vibration is excited on the x axis, and its output lies on the y axis. The angular velocity on the input x axis is far greater than the angular velocity $\dot{\alpha}$ on the output y axis, and compared with $(B-C)\dot{\alpha}\omega_{z1}$ in Eq. (7.20), the acceleration torque $(C-A)\dot{\beta}\omega_{z1}$ can be ignored. From Eqs. (7.14) and (7.20) the following result can be obtained

$$\begin{split} & A\ddot{\beta} + D_{\beta}\dot{\beta} + K_{\beta}\beta = M_{x}^{\mathrm{B}} + M_{x}^{\mathrm{M}} \\ & B\ddot{\alpha} + D_{\alpha}\dot{\alpha} + K_{\alpha}\alpha - (C - A)\dot{\beta}\omega_{z1} = M_{y}^{\mathrm{B}} + M_{y}^{\mathrm{M}} \end{split} \tag{7.53}$$

When the input generates the vibration on coordinate β , the output generates the reversed-phase vibration with the same frequency on coordinate α . The output vibration around the y axis (phase shift $\pi/2$) will change the total oscillation phase of the output axis, which is proportional to the measured angular velocity ω_{z1} . This data detection method does not rely on the amplitude of the input x axis, and is beneficial to the stability of the gyroscope. The drawback of this method is that for the detection interface circuit of the angle α , it is difficult to detect the angular velocity ω_{z1} , and the sensitivity of the device is reduced.

By using the method for studying the error of the vibratory gyroscope, the vibration amplitude of the output axis ω_{z1} can be obtained. In Eq. (7.53), assume that

$$M_x^{\rm M} = M_x^0 \sin \omega t, \quad M_x^{\rm B} = M_y^{\rm B} = 0$$
 (7.54)

For the stable mode and from Eq. (7.53) obtain

$$\beta = \frac{M_x^0}{\sqrt{(K_\beta - A\omega^2)^2 + (D_\beta\omega)^2}} \sin[\omega t - \varphi(\omega)]$$
 (7.55)

where

$$\varphi(\omega) = \arctan \frac{D_{\beta}\omega}{K_{\beta} - A\omega^2} \tag{7.56}$$

Select the frequency of the input torque as the resonant frequency, i.e.,

$$\omega = \omega_{\rm P} = \sqrt{\frac{K_{\beta}}{A}}, \quad \varphi(\omega) = \frac{\pi}{2}$$
 (7.57)

From Eq. (7.55) obtain

$$\beta = \frac{M_x^0}{D_\beta} \sqrt{\frac{A}{K_\beta}} \cos \omega_P t = \beta_m \cos \omega_P t \tag{7.58}$$

where

$$\beta_{\rm m} = \frac{M_{\rm x}^0}{D_{\beta}} \sqrt{\frac{A}{K_{\beta}}} \tag{7.59}$$

Substitute Eq. (7.58) into Eq. (7.53) and obtain

$$M_{y}^{M} = C_{\alpha}\alpha \tag{7.60}$$

$$B\ddot{\alpha} + D_{\alpha}\dot{\alpha} + (K_{\alpha} - C_{\alpha})\alpha = -(C - A)\beta_{\rm m}\omega_{z1}\omega_{\rm p}\sin\omega_{\rm p}t \qquad (7.61)$$

or

$$B\ddot{\alpha} + D_{\alpha}\dot{\alpha} + (K_{\alpha} - C_{\alpha})\alpha = \frac{(A - C)M_{x}^{0}}{D_{\beta}}\omega_{z1}\sin\omega_{p}t$$
 (7.62)

Select the stable value and obtain the amplitude of the output axis:

$$\alpha = \frac{(A - C)M_{\chi}^{0}\omega_{z1}}{\sqrt{(K_{\alpha} - C_{\alpha} - B\omega_{P}^{2})^{2} + (D_{\alpha}\omega_{P})^{2}}} \frac{1}{D_{\beta}} \sin[\omega_{P}t - \chi(\omega_{P})]$$
 (7.63)

where

$$\chi(\omega_{\rm P}) = \arctan \frac{D_{\alpha}\omega_{\rm P}}{(K_{\alpha} - C_{\alpha}) - B\omega_{\rm P}^2}$$
 (7.64)

Based on the aim that the output axis generates the resonance, in the design K_{α} and B are selected and tuned and C_{α} is selected to satisfy the resonance condition:

$$K_{\alpha} - C_{\alpha} - B\omega_{\rm P}^2 = 0, \quad \chi(\omega_{\rm P}) = \frac{\pi}{2}$$
 (7.65)

However, due to the instability of the parameters, the condition in Eq. (7.65) cannot be satisfied. Therefore, to define the output data of the device, Eq. (7.63) can be rewritten as

$$\alpha = \frac{(A - C)\beta_{\rm m}\omega_{\rm P}\omega_{\rm z1}}{\sqrt{(K_{\alpha} - C_{\alpha} - B\omega_{\rm P}^2)^2 + (D_{\alpha}\omega_{\rm P})^2}}\cos[\omega_{\rm P}t - \lambda(\omega_{\rm P})]$$
(7.66)

where $\lambda(\omega_P) = \frac{\pi}{2} - x(\omega_P)$ and its value is very small.

The measured angular velocity $\omega_{z1} = \Omega$ which is defined in a non-driven micromechanical gyroscope and the output voltage which corresponds to the angles α and β described by U_{α} and U_{β} , are introduced. Then there holds

$$U_{\alpha} = K_{\alpha}^{\mathrm{T}} \alpha, \quad U_{\beta} = K_{\beta}^{\mathrm{T}} \beta \tag{7.67}$$

where $K_{\alpha}^{\rm T}$ and $K_{\beta}^{\rm T}$ are the transmission coefficient of the associated angles. The voltage amplitudes $U_{\alpha}^{\rm m}$ and $U_{\beta}^{\rm m}$ can be expressed as

$$U_{\alpha}^{\mathrm{m}} = K_{\alpha}^{\mathrm{T}} \alpha_{\mathrm{m}}, \quad U_{\beta}^{\mathrm{m}} = K_{\beta}^{\mathrm{T}} \beta_{\mathrm{m}}$$
 (7.68)

Therefore, the amplitude of the harmonic voltage on the output axis α is

$$U_{\alpha}^{\mathrm{m}} = \frac{(A - C)U_{\beta}^{\mathrm{m}}\omega_{\mathrm{p}}}{\sqrt{(K_{\alpha} - C_{\alpha} - B\omega_{\mathrm{p}}^{2})^{2} + (D_{\alpha}\omega_{\mathrm{p}})^{2}}} \frac{K_{\alpha}^{\mathrm{T}}}{K_{\beta}^{\mathrm{T}}} \Omega$$
 (7.69)

Equation (7.69) can be used to define the principle error of the gyroscope.

From Eq. (7.69) it can be seen that the stability of the output voltage depends on a series of parameters and the influence of each parameter is different. The inertia moments A, B and C of the platform actually do not change and can be considered as constant. The resonant tuning on the coordinate β can be accurately achieved by changing the frequency of the driver. In addition, the resonant frequency ω_p can keep stable accurately, because it is determined only by the inertia moment A and the stiffness K_β of the internal torsion beam, while the latter only changes with the

change of load g and temperature. For the silicon beam, these changes can be neglected (see the parameter calculation of a non-driven micromechanical gyroscope).

The amplitude $\beta_{\rm m}$ of the input axis changes with the change of the damping coefficient D_{β} , so these parameters of the vibratory gyroscope can be stabilized by adding the feedback to the voltage U_{β} at the end of the voltage pickup output. The feedback is provided by the electrostatic torsion force. Thus the value U_{β} can be obtained in the range of acceptable error, being less than $3 \sim 5\%$, and is subject to the disturbance interference with less impact.

In addition, the transmission coefficients K_{α}^{T} and K_{β}^{T} are also affected by the amplification coefficient of the electronic amplifier, the detection structure design and the temperature. But if a detection signal which is produced by the same AC voltage generator and added to these two detection structures, these two detection structures can be similarly designed and use the same electronic structure such that the transmission coefficient ratio $K_{\alpha}^{T}/K_{\beta}^{T}$ in the two coordinates is stable.

Because the coefficients K_{α} and K_{β} which are determined by the torsion stiffness are stable, for the resonant regulation of the output coordinate the stiffness of the output axis needs to change and this can be achieved by applying the feedback to the output axis angle α through the torsion torque generator. This additional stiffness is determined by the coefficient C_{α} , whose stability is secondary to the stability of the coefficient K_{α} .

In the analysis of the preliminary theory, define D_{α} as the damping coefficient of the output axis, $U_{\beta}^{\rm m}$ as the detection voltage amplitude of the angle β , and C_{α} as the electric elastic stiffness of the output axis. By using these parameter variables, the amplitude $U_{\alpha}^{\rm m}$ of the output signal can be written in the form of a Taylor series:

$$\Delta U_{\alpha}^{\rm m} = \frac{\partial U_{\alpha}^{\rm m}}{\partial D_{\alpha}} \Delta D_{\alpha} + \frac{\partial U_{\alpha}^{\rm m}}{\partial U_{\beta}^{\rm m}} \Delta U_{\beta}^{\rm m} + \frac{\partial U_{\alpha}^{\rm m}}{\partial C_{\alpha}} \Delta C_{\alpha} + \frac{1}{2} \frac{\partial^{2} U_{\alpha}^{\rm m}}{\partial^{2} C_{\alpha}^{2}} \Delta C_{\alpha}^{2} + \cdots$$
 (7.70)

From Eq. (7.69) obtain

$$f(C_{\alpha}, D_{\alpha}) = (K_{\alpha} - C_{\alpha} - B\omega_{P}^{2})^{2} + (D_{\alpha}\omega_{P})^{2}$$
 (7.71)

$$\begin{cases}
\frac{\partial U_{z}^{m}}{\partial D_{z}} = -\frac{(A-C)U_{\beta}^{m}\omega_{p}K_{z}^{T}}{K_{\beta}^{T}}\frac{\omega_{p}^{2}D_{z}}{f^{3/2}}\Omega \\
\frac{\partial U_{z}^{m}}{\partial U_{\beta}^{m}} = \frac{(A-C)\omega_{p}K_{z}^{T}}{f^{1/2}K_{\beta}^{T}}\Omega \\
\frac{\partial U_{z}^{m}}{\partial C_{z}} = +\frac{(A-C)U_{\beta}^{m}\omega_{p}K_{z}^{T}}{K_{\beta}^{T}}\frac{(K_{z}-C_{z}-B\omega_{p}^{2})}{f^{3/2}}\Omega \\
\frac{\partial^{2}U_{z}^{m}}{\partial^{2}C_{z}} = -\frac{(A-C)U_{\beta}^{m}\omega_{p}K_{z}^{T}}{K_{\beta}^{T}f^{3}}\Omega\left[f^{3/2} - 3(K_{\alpha} - C_{\alpha} - B\omega_{p}^{2})^{2}f^{1/2}\right]
\end{cases} (7.72)$$

The relative error is

$$\frac{\partial U_{\alpha}^{\rm m}}{U_{\alpha}^{\rm m}} = -\frac{\omega_{\rm P}^2 D_{\alpha}}{f} \Delta D_{\alpha} + \frac{\Delta U_{\beta}^{\rm m}}{U_{\beta}^{\rm m}} + \frac{(K_{\alpha} - C_{\alpha} - B\omega_{\rm P}^2)}{f} \Delta C_{\alpha}
- \frac{1}{2f^3} \left[f^2 - 3(K_{\alpha} - C_{\alpha} - B\omega_{\rm P}^2)^2 f \right] \Delta C_{\alpha}^2$$
(7.73)

By selecting the electric elastic coefficient C_{α} , the condition for realizing the resonant tuning is

$$K_{\alpha} - C_{\alpha} - B\omega_{\mathbf{P}}^2 = 0 \tag{7.74}$$

The relative error is approximately expanded as

$$\frac{\Delta U_{\alpha}^{\rm m}}{U_{\alpha}^{\rm m}} = -\frac{\Delta D_{\alpha}}{D_{\alpha}} + \frac{\Delta U_{\beta}^{\rm m}}{U_{\beta}^{\rm m}} - \frac{1}{2} \frac{\Delta C_{\alpha}^2}{(D_{\alpha} \omega_{\rm P})^2}$$
(7.75)

In order to estimate the error, the following method can be adopted to select the parameters. The resonant frequency of the gyroscope needs to exceed the measured maximum angular velocity frequency by one order of the magnitude. Select $\omega_P=1000~{\rm Hz}$, consider

$$\omega_{\mathrm{P}} = \sqrt{\frac{K_{\beta}}{A}}$$

and select

$$K_{\beta} = K_{\alpha} = 100 \text{ g cm}, \quad A = 100 \times 10^{-6} \text{ g cm s}^2$$

Such torque can be achieved by installing a specific mass along the z axis. In this case, there holds

$$C = 0$$
, $2A = 20 \times 10^{-6} \text{ g cm s}^2$,

By using Eq. (7.66) to select the damping coefficient D_{α} and substituting it into Eq. (7.74), the amplitude of the output axis can be obtained as

$$\alpha_{\rm m} = \frac{(A-C)\beta_{\rm m}}{D_{\alpha}}\Omega\tag{7.76}$$

where

$$D_{\alpha} = \frac{(A - C)\beta_{\rm m}}{\alpha_{\rm m}}\Omega\tag{7.77}$$

According to the device design and the research experience, select

$$\beta_{\rm m} = 20 \text{ rad min}$$

By considering the angle pickup structure and the interference of the electronic circuit, the resolution of the output axis is

$$\alpha_{_{m}}^{min} = 0.01 \text{ rad min}$$

If the resolution of the vibratory gyroscope is equal to that of a non-driven micromechanical gyroscope, there holds

$$\Omega^{\min} = 1.5 \, (^{\circ})/s$$

Substitute the parameter into Eq. (7.77) and obtain the damping coefficient D_{α} :

$$D_{\alpha} = \frac{20' \times (100 - 20) \times 10^{-6} \text{ g cm s}^2}{0.01'} \times 1.5 \,(^{\circ})/\text{s}$$

 $D_{\alpha} = 4.2 \times 10^{-3} \text{ g cm s}$

If $\Omega=300\,(^\circ)/s$, the maximum amplitude of the output amplitude on the output axis is

$$\alpha_{_{m}}^{max}=0.01~\text{rad min}\times300/1.5=2~\text{rad min}$$

By using the obtained data, on the basis of Eq. (7.75) the error of the vibratory gyroscope can be pre-estimated.

The change of the damping coefficient D_{α} of the output axis is determined by the change of the dynamic viscosity coefficient μ of the gas in the device box with the temperature. For nitrogen, there holds

$$\Delta \mu = 29.3\%/(100 \,^{\circ}\text{C})$$

In the given temperature range of -40 to +75 °C, the error caused by the change of the damping coefficient is

$$\Delta D_{\alpha}/D_{\alpha} = \pm 17\%$$

The error caused by the inaccurate operation of the exciting axis amplitude stable system is determined by the repeat accuracy of the standard voltage and the slope of

the feedback voltage U_{β} , with the latter determined by the angle pickup output signal. As mentioned above, the predictive error is

$$\frac{\Delta U_{\beta}^{\rm m}}{U_{\beta}^{\rm m}} = 3\% \tilde{5}\%$$

The change of the electrical elastic stiffness C_{α} is caused by the angle pickup component and the torque tester of the output axis along with the instability of the electronic circuit. But the effect of C_{α} on the whole gyroscope error is very small because the emergence of the electrical elasticity is related to the accurate selection and the manufacture of a gyroscope which has the same natural resonant frequency on the input axis and the output axis. The resonant frequency can be adjusted by introducing an electrical elastic $C_{\alpha}(C_{\alpha}, O)$ (the relative elastic torsion stiffness K_{α}). By using a sufficient margin (on the basis of the possible calculation and manufacture), $C_{\alpha} = 0.1K_{\alpha}$ and $\Delta C_{\alpha} = 0.1C_{\alpha}$, there holds $\Delta C_{\alpha} = 0.1K_{\alpha}$.

Thus, by using the selected parameters D_{α} and $\omega_{\rm p}$, the impact of C_{α} on the whole gyroscope error is calculated as

$$\frac{1}{2} \frac{\Delta C_{\alpha}^2}{\left(D_{\alpha} \omega_{\rm P}\right)^2} = 3\%$$

Therefore, it is concluded that the accuracy of the existing vibratory gyroscope can be comparable to that of a non-driven micromechanical gyroscope. Both kinds of gyroscope need error compensation and this is greatly affected by a change of temperature. A temperature sensor is used in both kinds of the gyroscope and the temperature is compensated in advance. The error compensation can be carried out on the ALU of the aircraft.

7.3 Error Calculation of a Non-driven Micromechanical Gyroscope

From Eq. (7.21) and when the measured angular velocity is Ω , the oscillation amplitude of a non-driven micromechanical sensitive element (the silicon wafer) is

$$\alpha_{\rm m} = \frac{(C+B-A)\dot{\varphi}}{\sqrt{\left[(C-A-B)\dot{\varphi}^2 + K\right]^2 + \left(D\dot{\varphi}\right)^2}}\Omega$$

Assume that the inertia moment of the gyroscope's sensitive element (chip) is a constant in the process of calculation, the rotating velocity of the aircraft is $\dot{\varphi}$, the

torsion rigidity is K, and the damping coefficient is D, then the error $\Delta \alpha_m$ of the angle α_m caused by the above unstable parameters is

$$\Delta \alpha_{\rm m} = \frac{\partial \alpha_{\rm m}}{\partial \dot{\varphi}} \Delta \dot{\varphi} + \frac{\partial \alpha_{\rm m}}{\partial K} \Delta K + \frac{\partial \alpha_{\rm m}}{\partial D} \Delta D \tag{7.78}$$

Substitute the expression of α_m and the specific derived expressions, and consider the relationship between the parameters of the silicon micromechanical gyroscope:

$$K \gg (C - A - B)\dot{\varphi}^2 \tag{7.79}$$

There holds

$$\frac{\Delta \alpha_{\rm m}}{(C+B-A)\Omega} \approx \left[\frac{1}{\sqrt{K^2 + D^2 \dot{\varphi}^2}} - \frac{\dot{\varphi}^2 D^2}{(K^2 + D^2 \dot{\varphi}^2)^{3/2}} \right] \Delta \dot{\varphi} - \frac{\dot{\varphi} K}{(K^2 + D^2 \dot{\varphi}^2)^{3/2}} \Delta K - \frac{D \dot{\varphi}^3}{(K^2 + D^2 \dot{\varphi}^2)^{3/2}} \Delta D$$
(7.80)

The expression of the relative error can be written as

$$\frac{\Delta \alpha_{\rm m}}{\alpha_{\rm m}} = \frac{(C+B-A)\Omega}{(K^2+D^2\dot{\varphi}^2)^{3/2}} \left[(K^2)\Delta\dot{\varphi} - \dot{\varphi}K\Delta K - D\dot{\varphi}^3\Delta D \right] \frac{\sqrt{K^2+(D\dot{\varphi})^2}}{(C+B-A)\dot{\varphi}\Omega}$$
(7.81)

or

$$\frac{\Delta \alpha_{\rm m}}{\alpha_{\rm m}} = \frac{1}{\dot{\varphi}(K^2 + D^2 \dot{\varphi}^2)} \left[\left(K^2 \right) \Delta \dot{\varphi} - \dot{\varphi} K \Delta K - D \dot{\varphi}^3 \Delta D \right] \tag{7.82}$$

Then, according to the acceptable technical index the damping coefficient D is selected.

The error of the inertia moment of the gyroscope's sensitive element (chip) is small and the characteristic equation of Eq. (7.13) is

$$BS^{2} + DS + K\alpha = 0$$

$$S^{2} + 2\xi\omega_{0}S + \omega_{0}^{2} = 0$$

where ω_0 is the undamped natural oscillation frequency of the gyroscope's sensitive element (chip); $\omega_0 = \sqrt{K/B}$; and ξ is the relative damping coefficient; $\xi = \frac{D}{2B\omega_0} = \frac{D}{2\sqrt{KB}}$.

Compare with a non-driven micromechanical gyroscope and assume

$$\xi = 0.5 \tag{7.83}$$

Then select

$$D = \sqrt{KB} \tag{7.84}$$

By simplifying Eq. (7.82) there holds

$$K^2 \pm \dot{\varphi}^2 D^2 = K^2 \pm \dot{\varphi}^2 KB = K(K \pm B\dot{\varphi}^2)$$
 (7.85)

For the choice of the lead non-resonant mode, there is

$$\dot{\varphi} < \omega_0 \tag{7.86}$$

Then

$$B\dot{\varphi}^2 \ll B\omega_0^2 = K$$

i.e.,

$$K \gg B\dot{\varphi}^2$$

Compared with K^2 , $\dot{\varphi}^2D^2$ in Eq. (7.85) can be ignored. Therefore, Eq. (7.82) can be written as

$$\frac{\Delta \alpha_{\rm m}}{\alpha_{\rm m}} \approx \frac{\Delta \dot{\phi}}{\dot{\phi}} - \frac{\Delta K}{K} - \frac{D^2 \dot{\phi}^2}{K^2} \frac{\Delta D}{D}$$
 (7.87)

As mentioned above, there holds

$$K \gg D\dot{\varphi}$$

Thus

$$\frac{D^2\dot{\varphi}^2}{K^2} \ll 1\tag{7.88}$$

Therefore, it can be considered that for the given parameters the influence of the damping coefficients on the instability has been greatly reduced. Then in the experimental mode the parameters of the gyroscope are

$$K = 5.33 \text{ g cm}$$

 $B = 6.3 \times 10^{-6} \text{ g cm s}^2$
 $\dot{\varphi} = 100 \text{ s}^{-1}$

$$\frac{D^2\dot{\varphi}^2}{K^2} = \frac{KB\dot{\varphi}^2}{K^2} = \frac{B\dot{\varphi}^2}{K} = \frac{6.3\times10^{-6}\ \text{g cm s}^2\times10^{-4}\ \text{s}^{-2}}{5.33\ \text{g cm}} = 1.18\times10^{-2}$$

At the same time the influence of the damping on the error can be ignored in the pre-computation.

It is considered that the elastic torsion coefficient is the most stable parameter in the gyroscope. In all the experiments, the change of the elastic torsion coefficient $(\Delta K/K)$ is not more than 3.5%. The relative error $\Delta \alpha_m/\alpha_m$ depends on the measurement accuracy of the rotating frequency of the aircraft and the measurement accuracy of the angle α_m , but it does not contain in Eq. (7.87). The relative error $\Delta \alpha_m/\alpha_m$ of the preliminary device will be estimated.

The measurement accuracy of the rotation velocity of the aircraft is determined by the output signal of the gyroscope, in other words it is determined by the measurement precision of the time interval between the zeros of the output signal, which is mainly affected by the noise of the output signal. The experiment of the silicon sensitive element shows that the error is 10-20%.

In addition, the measured angle error α_m is affected by the nonlinear influence of the angle pickup signal, and the influence of the longitudinal acceleration on the output signal curve. The latter influence needs the improved design to increase the linear stiffness of the torsion beam. The nonlinearity of the angle pickup signal can be improved by the method of compensating and optimizing the angle pickup structure design. By adopting the above method, the relative error of the angle pickup is not more than 10--20%.

The expected error of the prototype is estimated to be less than 20–40%, but the error can be quite small by compensating the algorithm of the parameter value and optimizing the parameters of the prototype. If the size of the device is smaller and the silicon etching technology is improved, then under the same condition the non-driven micromechanical gyroscope has more advantages.

The final parameter accuracy of this device is obtained only from the experimental model of a non-driven micromechanical gyroscope and experiments with the prototype. The experimental model of a non-driven micromechanical gyroscope is tested under the laboratory conditions and the measurement range is ± 300 °/s and the resolution is 1.5 °/s.

7.4 Error of a Non-driven Micromechanical Gyroscope

The balance of the gyroscopic torque can be measured by the stable elastic torque of the silicon elastic torsion beam and its advantage is that the rotating velocity $\dot{\varphi}$ of the aircraft can be obtained by measuring the frequency of the output signal of the aircraft. But the damping torque of manufacturing and packaging the gyroscope prototype caused by the attenuation is also needed because the impact of the filling gas pressure on the damping coefficient should be small, and a high vacuum (0.133 Pa or lower) is needed. In such a thin state, the electronic elements will release gas molecules and affect the vacuum degree. It is not feasible to place the electronic device in another package because it will then be greater than the size of the device.

Therefore, in order to make the gyroscope the nitrogen is pumped into the gyroscope under standard atmospheric pressure to reduce the manufacturing cost and reduce the size of the device.

By using the previous data, the amplitude of the output oscillation voltage of the angle α is

$$U_{\rm m} = \frac{K_{TS}(C + B - A)\dot{\varphi}}{\sqrt{\left[(C - A - B)\dot{\varphi}^2 + K\right]^2 + (D\dot{\varphi})^2}}\Omega\tag{7.89}$$

where K_{TS} is the angle pickup transmission coefficient; $\dot{\varphi}$ is the rotation velocity of the aircraft; K is the torsion stiffness coefficient; and D is the damping coefficient.

When these parameters change the error can be expressed by the following approximate form:

$$\Delta U_{\rm m} = \frac{\partial U_{\rm m}}{\partial \dot{\varphi}} \Delta \dot{\varphi} + \frac{\partial U_{\rm m}}{\partial K} \Delta K + \frac{\partial U_{\rm m}}{\partial D} \Delta D + \frac{\partial U_{\rm m}}{\partial K_{\rm TS}} \Delta K_{\rm TS} + \cdots$$
 (7.90)

In this expression, for the silicon micromechanical gyroscope there is

$$K \gg (C - A - B)\dot{\phi}^2$$

For high damping devices there is

$$K \ll D\dot{\varphi}^2 \tag{7.91}$$

In this case, by using Eqs. (7.78)–(7.87) the relative error of the output signal can be obtained as

$$\frac{\Delta U_{\rm m}}{U_{\rm m}} = \frac{K^2}{D^2 \dot{\varphi}^2} \frac{\Delta \dot{\varphi}}{\dot{\varphi}} - \frac{K^2}{D^2 \dot{\varphi}^2} \frac{\Delta K}{K} - \frac{\Delta D}{D} + \frac{\Delta K_{\rm TS}}{K_{\rm TS}}$$
(7.92)

Compared with (7.87) the coefficients are changed, and this determines the damping and rotation velocity of the aircraft. These changes are very important and from Eq. (7.91) the impact of the instability of $\dot{\varphi}$ and K on the gyroscope can be ignored.

From Eqs. (7.91) and (7.92) the error of the output signal of a non-driven micromechanical gyroscope is mainly affected by the instability of the damping coefficient and the angle pickup. As mentioned before, the change of the damping coefficient caused by a change of temperature can be up to $\pm 17\%$.

The measurement error of the angle α is determined by the parameters of the electronic circuit (in fact the frequency characteristic of the electronic circuit) as mentioned earlier, and can be up to 10–20%. The error of the output signal caused by the design concept change of a non-driven micromechanical gyroscope does not exceed the error caused by the instability of the parameter.

Chapter 8 Phase Shift of a Non-driven Micromechanical Gyroscope

8.1 Phase Shift Calculation of a Non-driven Micromechanical Gyroscope

Set the following coordinate systems: x_a , y_a and z_a is the inertial coordinate system; x_0 , y_0 and z_0 is the coordinate system of a silicon pendulum; and x, y and z is the frame coordinate system.

The absolute angular velocity of a silicon pendulum in its coordinate system is

$$\bar{\omega}_a = \begin{pmatrix} \omega_{xa} \\ \omega_{ya} \\ \Omega \end{pmatrix} \tag{8.1}$$

where ω_{xa} and ω_{ya} are the projection of measuring the angular velocity of the aircraft; and Ω is the rotating angular velocity of the aircraft around its symmetry axis.

In the coordinate system x_0 , y_0 and z_0 , which is connected to the silicon pendulum, there holds

$$\bar{\omega}_{0} = \begin{pmatrix} \cos \varphi & \sin \varphi & 0 \\ -\sin \varphi & \cos \varphi & 0 \\ 0 & 0 & 1 \end{pmatrix} \begin{pmatrix} \omega_{xa} \\ \omega_{ya} \\ \Omega \end{pmatrix} = \begin{pmatrix} \omega_{xa} \cos \varphi + \omega_{ya} \sin \varphi \\ -\omega_{xa} \sin \varphi + \omega_{ya} \cos \varphi \\ \Omega \end{pmatrix}$$
(8.2)

The absolute angular velocity of the framework is the sum of the relative angular velocity of the silicon pendulum and the implicated angular velocity $\dot{\theta}_x$ of the aircraft around the axis x_0 :

$$\overline{\omega} = \begin{pmatrix} 1 & 0 & 0 \\ 0 & \cos \theta_x & \sin \theta_x \\ 0 & -\sin \theta_x & \cos \theta_x \end{pmatrix} \begin{pmatrix} \omega_{x0} + \dot{\theta}_x \\ \omega_{y0} \\ \Omega \end{pmatrix} = \begin{pmatrix} \omega_{x0} + \dot{\theta}_x \\ \omega_{y0} \cos \theta_x + \Omega \sin \theta_x \\ -\omega_{y0} \sin \theta_x + \Omega \cos \theta_x \end{pmatrix}$$
(8.3)

Because the deflection angular velocity of the framework is very small, the matrix can be changed into

$$A = \begin{pmatrix} 1 & 0 & 0 \\ 0 & 1 & \theta_x \\ 0 & -\theta_x & 1 \end{pmatrix} \begin{pmatrix} \omega_{x0} + \dot{\theta}_x \\ \omega_{y0} \\ \Omega \end{pmatrix}$$
(8.4)

The absolute angular velocity of the framework is

$$\overline{\omega} = \begin{pmatrix} \omega_{x0} + \dot{\theta}_x \\ \omega_{y0} + \Omega\theta_x \\ -\omega_{y0}\theta_x + \Omega \end{pmatrix}$$
(8.5)

Therefore, each part of the absolute angular velocity can be written as

$$\omega_{x0} = \omega_{xa} \cos(\Omega t) + \omega_{ya} \sin(\Omega t)$$

$$\omega_{y0} = -\omega_{xa} \sin(\Omega t) + \omega_{ya} \cos(\Omega t)$$
(8.6)

From Eq. (8.6) obtain

$$\dot{\omega}_{x0} = \Omega \omega_{y0} + \dot{\omega}_{xa} \cos(\Omega t) + \dot{\omega}_{ya} \sin(\Omega t) \tag{8.7}$$

$$\begin{aligned}
\omega_{x} &= \omega_{x0} + \dot{\theta}_{x} \\
\omega_{y} &= \omega_{y0} + \Omega\theta_{x}
\end{aligned} (8.8)$$

The equation of the framework is

$$A\dot{\omega}_x + (C - B)\Omega\omega_v = M_x \tag{8.9}$$

The torque of the framework is

$$M_x = -C_x \theta_x - D_x \dot{\theta}_x \tag{8.10}$$

where C_x is the torsion angle stiffness; and D_x is the damping coefficient.

Eliminate M_x from Eq. (8.10) and eliminate ω_x and ω_y from Eqs. (8.8) and (8.9), thus there holds

$$A(\dot{\omega}_{x0} + \ddot{\theta}_x) + (C - B)\Omega(\omega_{y0} + \Omega\theta_x) + C_x\theta_x + D_x\dot{\theta}_x = 0$$
 (8.11)

Equation (8.11) can be changed into

$$[Ap^{2} + D_{x}p + (C - B)\Omega^{2} + C_{x}]\theta_{x} = -(A + C - B)\Omega\omega_{y0} - A[\dot{\omega}_{xa}\cos(\Omega t) + \dot{\omega}_{ya}\sin(\Omega t)]$$
(8.12)

where $\omega_{y0} = \omega_{ya} \cos(\Omega t) - \omega_{xa} \sin(\Omega t)$; and p is the differential operation. Assume that

$$\omega_a^2 = \frac{(C-B)\Omega^2 + C_x}{A}, \quad \xi = \frac{D_x}{2A\omega_a}, \quad q = \frac{A+C-B}{A}$$

then Eq. (8.12) can be changed into

$$(p^2 + 2\xi\omega_a p + \omega_a^2)\theta_x = -q\Omega\omega_{y0} - \dot{\omega}_{xa}\cos(\Omega t) - \dot{\omega}_{ya}\sin(\Omega t)$$
(8.13)

Assume that the aircraft vibrates along a vertical axis (e.g. the axis x_a) and its torque is

$$\begin{cases}
\omega_{xa} = \omega_0 \cos(vt + \varphi) \\
\omega_{ya} = 0
\end{cases}$$
(8.14)

then

$$\omega_{y0} = \omega_{ya} \cos(\Omega t) - \omega_{xa} \sin(\Omega t)$$
$$= -\omega_0 \cos(\nu t + \varphi) \sin(\Omega t)$$
$$\dot{\omega}_{xa} = -\omega_0 \nu \sin(\nu t + \varphi)$$

Substitute Eq. (8.14) into (8.13) and obtain

$$\begin{split} \left(p^2 + 2\xi\omega_a p + \omega_a^2\right)\theta_x &= q\Omega\omega_0\cos(vt + \varphi)\sin(\Omega t) + \omega_0 v\,\sin(vt + \varphi)\cos(\Omega t) \\ &= \frac{1}{2}q\Omega\omega_0\left\{\sin[(\Omega + v)t + \varphi] + \sin[(\Omega - v)t - \varphi]\right\} \\ &+ \frac{1}{2}\omega_0 v\left\{\sin[(\Omega + v)t + \varphi] - \sin[(\Omega - v)t - \varphi]\right\} \\ &= \frac{1}{2}\Omega\omega_0\left\{\left(q + \frac{v}{\Omega}\right)\sin[(\Omega + v)t + \varphi] + \left(q - \frac{v}{\Omega}\right)\sin[(\Omega - v)t - \varphi]\right\} \end{split}$$

$$(8.15)$$

From Eq. (8.15) the steady state torque can be obtained as

$$\theta_x = \Delta_{\omega} \{ \theta_1 \sin[(1 + \Delta_{\nu})\Omega t + \varphi - \varphi_1] + \theta_2 \sin[(1 - \Delta_{\nu})\Omega t - \varphi - \varphi_2] \}$$
 (8.16)
where $\Delta_{\omega} = \frac{\omega_0}{O}$, $\Delta_{\nu} = \frac{\nu}{O}$, $\Delta_c = \frac{\omega_c}{O}$.

For $\xi < 1$, there holds

$$\begin{cases} \varphi_{1} = \arctan \frac{2\xi \Delta_{c}(1 + \Delta_{v})}{\Delta_{c}^{2} - (1 + \Delta_{v})^{2}} \\ \varphi_{2} = \arctan \frac{2\xi \Delta_{c}(1 - \Delta_{v})}{\Delta_{c}^{2} - (1 - \Delta_{v})^{2}} \\ \theta_{1} = \frac{(q + \Delta_{v})}{2\sqrt{\left[\Delta_{c}^{2} - (1 + \Delta_{v})^{2}\right]^{2} + \left[2\xi \Delta_{c}(1 + \Delta_{v})\right]^{2}}} \\ \theta_{2} = \frac{(q - \Delta_{v})}{2\sqrt{\left[\Delta_{c}^{2} - (1 - \Delta_{v})^{2}\right]^{2} + \left[2\xi \Delta_{c}(1 - \Delta_{v})\right]^{2}}} \end{cases}$$
(8.17)

From $\xi > 1$, there holds

$$\begin{cases} \varphi_{1} = \arctan \frac{1 + \Delta_{\nu}}{\left(\xi - \sqrt{\xi^{2} - 1}\right)\Delta_{c}} + \arctan \frac{1 + \Delta_{\nu}}{\left(\xi + \sqrt{\xi^{2} - 1}\right)\Delta_{c}} \\ \varphi_{2} = \arctan \frac{1 - \Delta_{\nu}}{\left(\xi - \sqrt{\xi^{2} - 1}\right)\Delta_{c}} + \arctan \frac{1 - \Delta_{\nu}}{\left(\xi + \sqrt{\xi^{2} - 1}\right)\Delta_{c}} \\ \theta_{1} = \frac{q + \Delta_{\nu}}{2\sqrt{\left(\xi - \sqrt{\xi^{2} - 1}\right)^{2}\Delta_{c}^{2} + (1 + \Delta_{\nu})^{2}}\sqrt{\left(\xi + \sqrt{\xi^{2} - 1}\right)^{2}\Delta_{c}^{2} + (1 + \Delta_{\nu})^{2}}} \\ \theta_{2} = \frac{q - \Delta_{\nu}}{2\sqrt{\left(\xi - \sqrt{\xi^{2} - 1}\right)^{2}\Delta_{c}^{2} + (1 - \Delta_{\nu})^{2}}\sqrt{\left(\xi + \sqrt{\xi^{2} - 1}\right)^{2}\Delta_{c}^{2} + (1 - \Delta_{\nu})^{2}}} \end{cases}$$
(8.18)

Equation (8.16) can be changed into

$$\theta_x = A \sin(\psi + \varphi_0) \tag{8.19}$$

where $\psi = \Omega t$; φ_0 is the phase shift; and A is the fluctuation range of the framework, which is equivalent to

$$A = \Delta_{\omega} \sqrt{\theta_1^2 + \theta_2^2 + 2\theta_1\theta_2 \cos(2\Delta_{\nu}\Omega t + 2\varphi + \varphi_1 - \varphi_2)}$$

$$\varphi_{0} = \arctan$$

$$= \frac{\cos(\Delta_{\nu}\psi + \varphi)(\theta_{1}\sin\varphi_{1} + \theta_{2}\sin\varphi_{2}) + \sin(\Delta_{\nu}\psi + \varphi)(\theta_{1}\cos\varphi_{1} - \theta_{2}\cos\varphi_{2})}{\cos(\Delta_{\nu}\psi + \varphi)(\theta_{1}\cos\varphi_{1} + \theta_{2}\cos\varphi_{2}) - \sin(\Delta_{\nu}\psi + \varphi)(\theta_{1}\sin\varphi_{1} - \theta_{2}\sin\varphi_{2})}$$
(8.20)

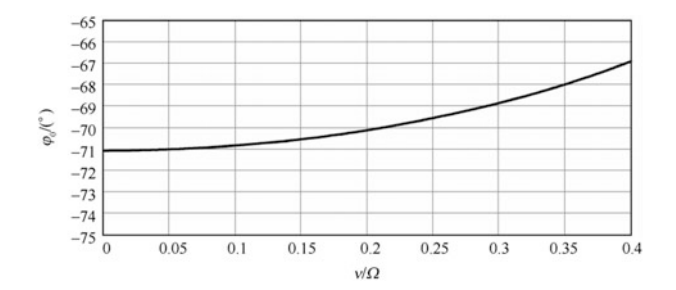


Fig. 8.1 Phase shift curve caused by fluctuation of the frequency v of the aircraft when $\varphi = 0^{\circ}$

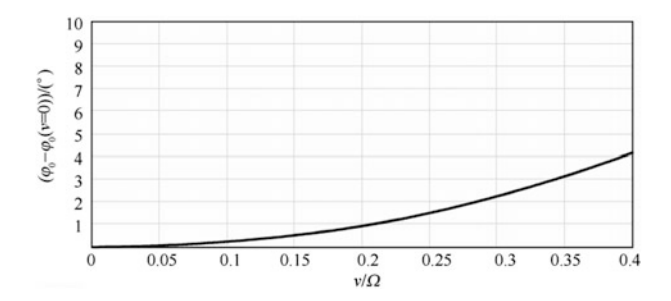


Fig. 8.2 Instability of the phase shift when $\varphi = 0^{\circ}$

When $\varphi = 0^{\circ}$, the curve of the phase shift caused by the fluctuation with the frequency v of the aircraft (Eq. 8.20) is shown in Fig. 8.1.

When $\phi=0^\circ$, the instability of the phase shift is shown in Fig. 8.2. From this figure it can be seen that the phase shift is no more than 5° . In the range of large frequencies, the phase shift has high stability and can be compensated by adjusting the angle of the non-driven micromechanical gyroscope on the aircraft.

8.2 Phase Shift of a Non-driven Micromechanical Gyroscope

Assume that φ_c is the rotation angle of a non-driven micromechanical gyroscope in the direction of the rotation axis of the aircraft; Ω is the rotation angular velocity of the aircraft; v is the vibration frequency of the input axis; $\psi = \Omega t$ is the rotation angle of the framework around the axis x; φ is the vibration phase of the framework with the frequency Ω ; φ_1 is the vibration phase of the framework with the frequency $\Omega + v$; φ_2 is the vibration phase of the framework with the frequency $\Omega + v$; φ_2 is the

vibration amplitude of the framework with the frequency $\Omega - v$; D is the damping coefficient; ξ is the relative damping coefficient; A is the angular momentum of the framework on the y axis; B is the moment of inertia of the framework on the x axis (the vibration axis of the framework); C is the moment of inertia of the framework on the x axis; x is the elastic torsion stiffness on the axis y; x is the magnitude of the input velocity, x is the elastic torsion stiffness on the axis y; x is the magnitude of the input velocity, x is the aircraft rotates. The phase shift x of the framework vibration is determined by

$$\begin{split} \varphi_0 &= \arctan \\ &= \left[\frac{\cos(vt + \varphi)(\theta_1 \sin \varphi_1 + \theta_2 \sin \varphi_2) + \sin(vt + \varphi)(\theta_1 \cos \varphi_1 - \theta_2 \cos \varphi_2)}{\cos(vt + \varphi)(\theta_1 \cos \varphi_1 + \theta_2 \cos \varphi_2) - \sin(vt + \varphi)(\theta_1 \sin \varphi_1 - \theta_2 \sin \varphi_2)} \right] \\ &- \varphi_c \end{split}$$

When t = 0 and $\varphi = 0^{\circ}$, there holds

$$\varphi_0 = \arctan\left(\frac{\theta_1 \sin \varphi_1 + \theta_2 \sin \varphi_2}{\theta_1 \cos \varphi_1 + \theta_2 \cos \varphi_2}\right) - \varphi_c$$

where

$$\begin{split} \varphi_1 &= \arctan \left[\frac{2\xi \Delta_{\omega c} (1 + \Delta_v)}{\Delta_{\omega c}^2 - (1 + \Delta_v)^2} \right] \\ \varphi_2 &= \arctan \left[\frac{2\xi \Delta_{\omega c} (1 - \Delta_v)}{\Delta_{\omega c}^2 - (1 - \Delta_v)^2} \right] \\ \theta_1 &= \left\{ \frac{0.5\Delta_{\omega c} (q + \Delta_v)}{\sqrt{\left[\Delta_{\omega c}^2 - (1 + \Delta_v)^2\right]^2 + \left[2\xi \Delta_{\omega c} (1 + \Delta_v)\right]^2}} \right\} \\ \theta_2 &= \left\{ \frac{0.5\Delta_{\omega c} (q - \Delta_v)}{\sqrt{\left[\Delta_{\omega c}^2 - (1 - \Delta_v)^2\right]^2 + \left[2\xi \Delta_{\omega c} (1 - \Delta_v)\right]^2}} \right\} \\ q &= 1 + \frac{C - A}{B}, \xi = \frac{D}{2B\omega_c}, \omega_c = \sqrt{\frac{(C - A)\Omega^2 + K}{B}}, \Delta_v = \frac{v}{\Omega}, \Delta_{\omega c} = \frac{\omega_c}{\Omega}, \Delta_{\omega 0} = \frac{\omega_{\omega 0}}{\Omega}. \end{split}$$

8.3 Feasibility of Adjusting the Position to Compensate the Phase Shift of the Output Signal

In order to explain the feasibility we compare the following two kinds of output signal—without a phase shift and with a phase shift—but the non-driven micromechanical gyroscope has been adjusted on the aircraft.

(1) Output signal without a phase shift. Compared with the elastic torque of the elastic bar, the damping torque of a non-driven micromechanical gyroscope is very small. When the harmonic angular velocity is measured the dynamic equation of this device is

$$B\ddot{\alpha} + D\dot{\alpha} + K\alpha = (C - A + B)v\Omega \cos(\omega t)\sin(\Omega t) + Bv\omega \sin(\omega t)\cos(\Omega t)$$

The parameters of this device are $k=5.3\times 10^{-4}~{\rm N}~{\rm m};~D=0.001\times 10^{-4}~{\rm N}~{\rm m}$ s and $\Omega=16~{\rm Hz}.$

When the rotation velocity of the aircraft is constant the phase of the output signal is

$$\phi = -\arctan\bigg(\frac{D\Omega}{K}\bigg) = -\arctan\bigg(\frac{0.001\times16\times2\pi}{5.3}\bigg) = -1.08^\circ$$

The output signal of this device on a computer is shown in Fig. 8.3.

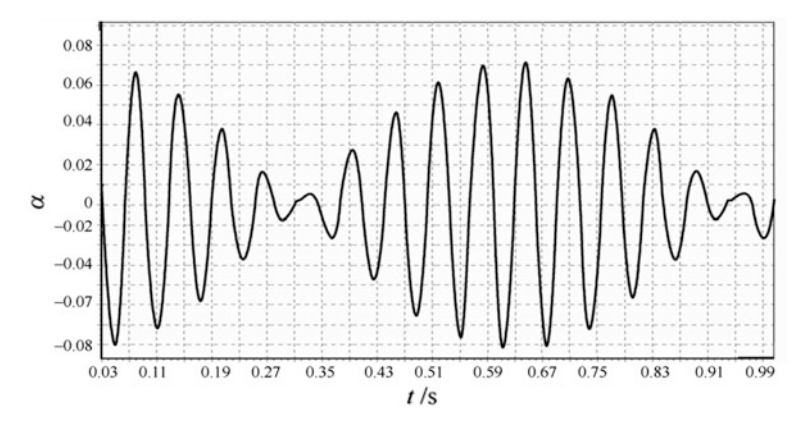


Fig. 8.3 Phase of the output signal when the rotation velocity of the aircraft is constant

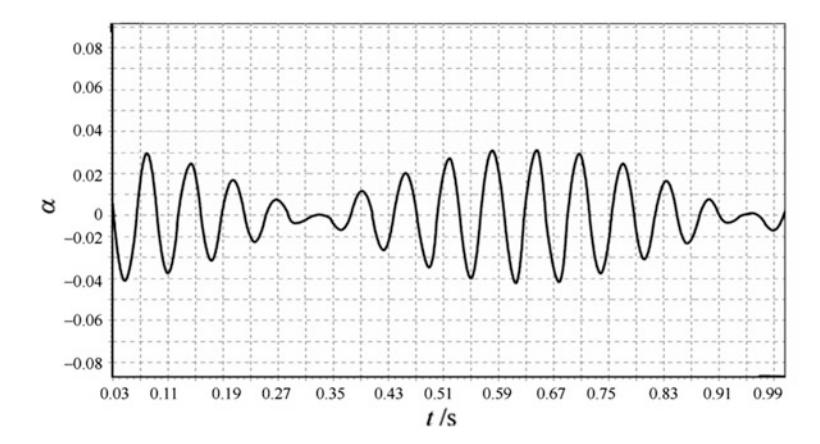


Fig. 8.4 Phase of the output signal when the rotation velocity of the aircraft is constant

(2) The installation on an aircraft with angle φ_0 is equivalent to the phase shift of the output signal when the angular velocity is constant and the motion equation of a non-driven micromechanical gyroscope is

$$B\ddot{\alpha} + D\dot{\alpha} + K\alpha = (C - A + B)v\Omega\cos(\omega t)\sin(\Omega t + \varphi_0) + Bv\omega\sin(\omega t)\cos(\Omega t + \varphi_0)$$

Thus the damping of the device is very large.

When the angular rotation velocity of the aircraft is constant the phase of the output signal is

$$\varphi = -\arctan\left(\frac{D\Omega}{K}\right) = -\arctan\left(\frac{0.1 \times 16 \times 2\pi}{5.3}\right) = -62.2^{\circ}$$

The output signal of this device on a computer is shown in Fig. 8.4.

Comparing the curves in Figs. 8.3 and 8.4, the phase shifts of these two output signals are less than 10° .

(3) The experiment with a non-driven micromechanical gyroscope with a phase shift φ_0 is analyzed. At the time of installation, when the rotation angle of a non-driven micromechanical gyroscope is φ_0 and the constant angular velocity

Fig. 8.5 Phase shift experiments of a non-driven micromechanical gyroscope which rotates at \triangleright angle φ_0 a The output waveform when the initial position rotates with an angle for the first time. b The output waveform when the initial position rotates with an angle for the second time. c The output waveform when the initial position rotates with an angle for the third time. d The output waveform when the initial position rotates with an angle for the fourth time. e The output waveform when the initial position rotates with an angle for the fifth time. f The output waveform when the initial position rotates with an angle for the sixth time. g The output waveform when the initial position rotates with an angle for the seventh time

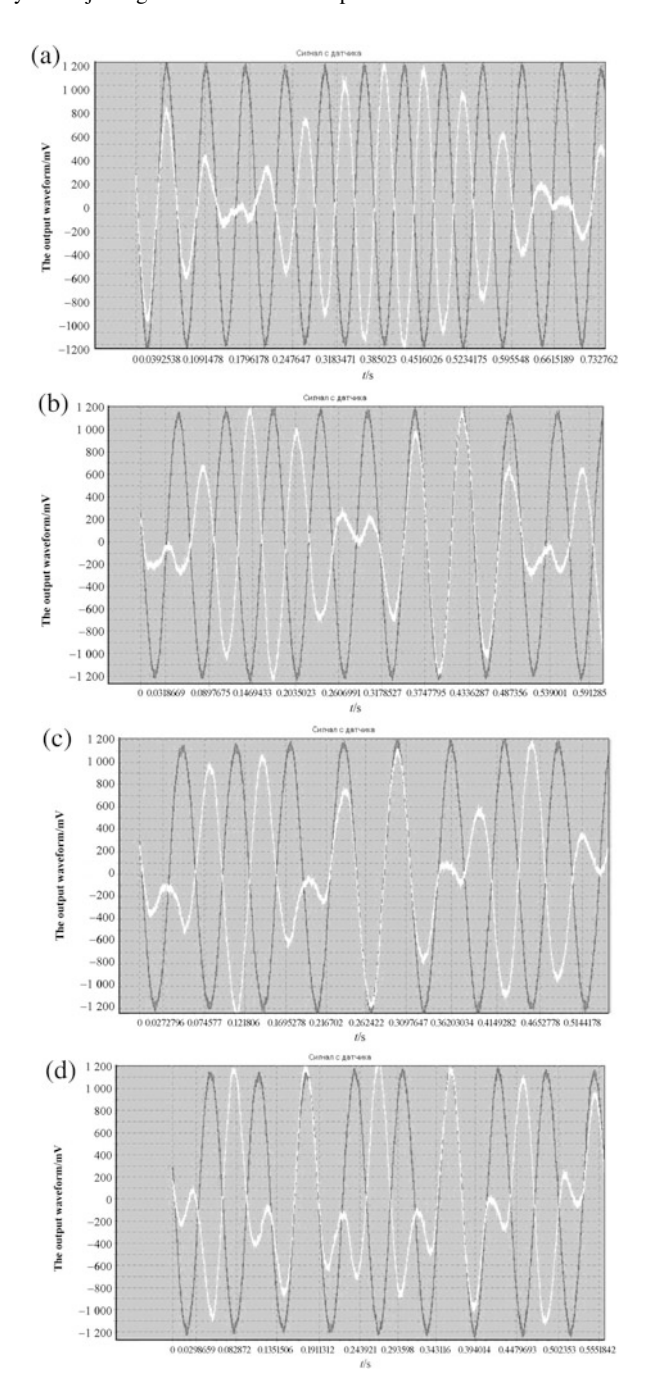
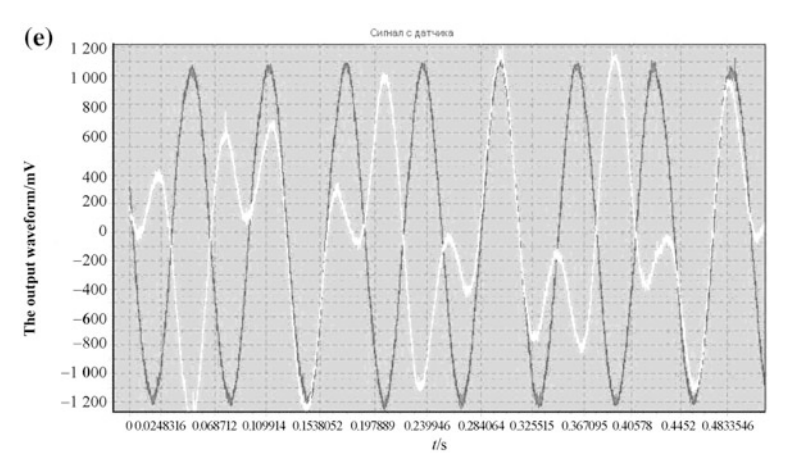
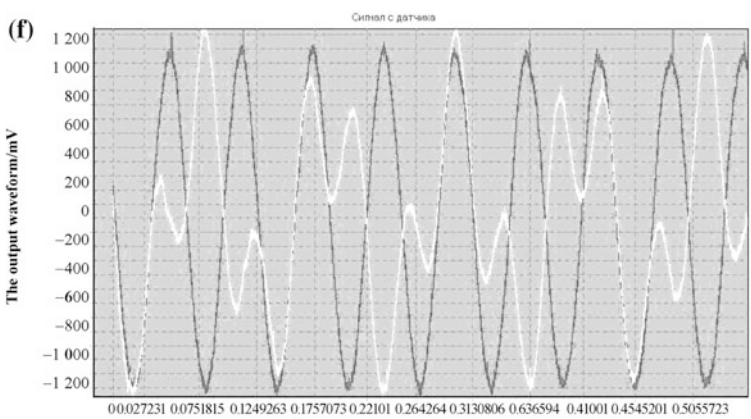
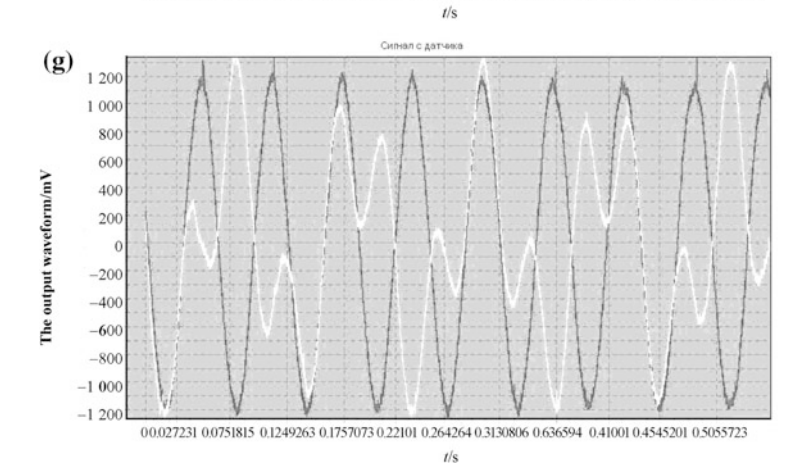


Fig. 8.5 (continued)







is measured, the phase shift can be eliminated. When the installed device rotates at angle φ_0 and the constant angular velocity is measured, the output signals are shown in Fig. 8.5a–g.

When the harmonic angular velocity is measured and the installed device rotates at the angle φ_0 , the signals are also shown in the same figures. Comparing the curves in Fig. 8.5a–g, it can be seen that the phase shift is not more than 10° . The phase is determined by the zeros of the output signal in the region that the amplitude of the input angular velocity is close to the peak value.

8.4 Characteristic Calculation of a Non-driven Micromechanical Gyroscope in the Angular Vibration Table

Define

$$\theta = \theta_1 \sin((\Omega + v)t + \phi + \phi_1) + \theta_2 \sin((\Omega - v)t - \phi + \phi_2)$$

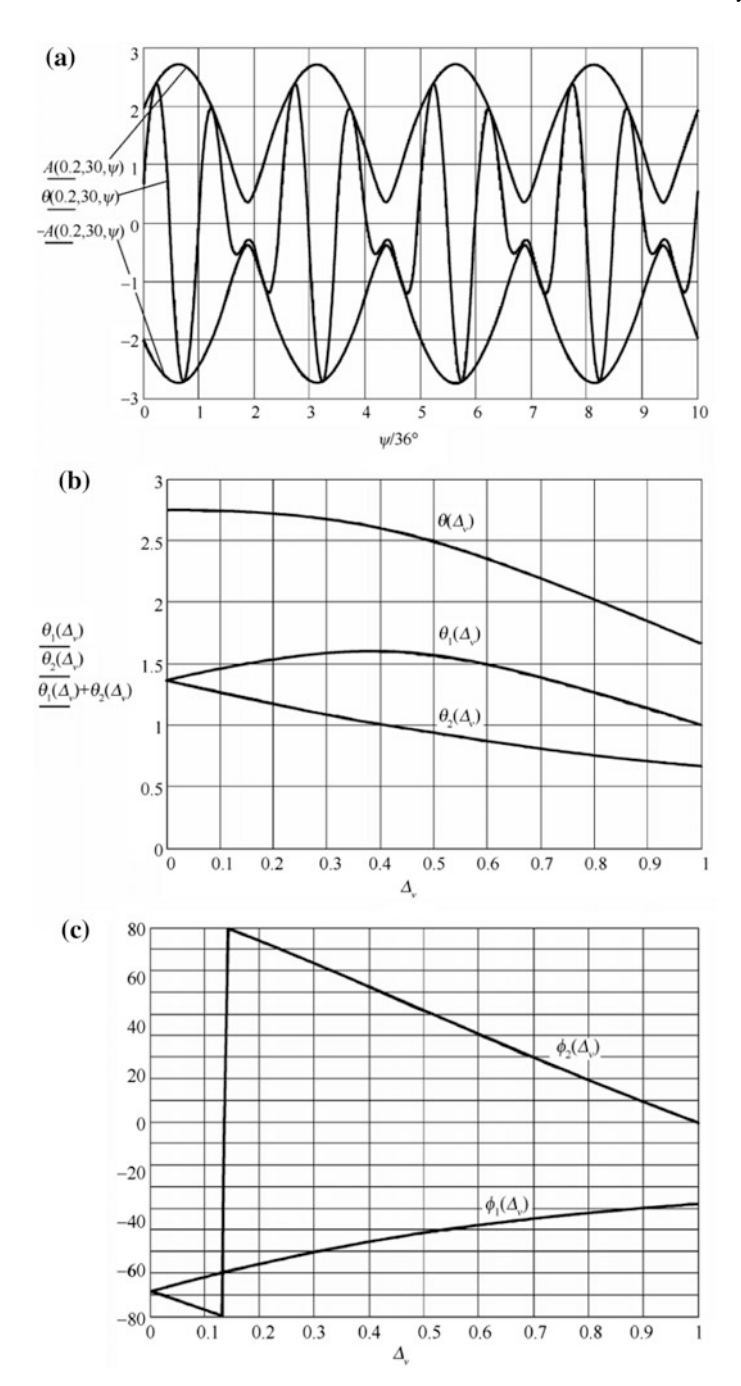
$$A = \sqrt{v\theta_1^2 + \theta_2^2 + 2\theta_1\theta_2 \cos(2vt + 2\phi + \phi_1 - \phi_2)}$$

Assume that n is the number of the vibration period of the framework; N is the number of vibration periods starting from 0; ψ is the phase angle of the framework; v is the vibration frequency of the framework; t is the time; $\Delta_v = v/\Omega$; Ω is the angular velocity of the angular vibration table; ϕ is the vibration phase of the framework corresponding to the frequency Ω ; ϕ_1 is the vibration phase of the framework corresponding to the frequency $\Omega + v$; ϕ_2 is the vibration amplitude corresponding to the frequency $\Omega - v$; θ_1 is the vibration amplitude corresponding to the frequency $\Omega + v$; θ_2 is the vibration amplitude corresponding to the frequency $\Omega - v$; and A is the vibration amplitude of the framework. The relationships between the amplitude, phase, and frequency are shown in Fig. 8.6a, b, and the relationship between the phase and the frequency is shown in Fig. 8.7.

$$n = 10; \quad \varphi = N - 360^{\circ} (N = 0, 1, ..., n); \quad \Delta_{\nu} = 0, 0.1, ..., 1$$

$$\phi_{1}(\Delta_{\nu}) = -\arctan\left(1.248 \frac{1 + \Delta_{\nu}}{0.253 + 2\Delta_{\nu} + \Delta_{\nu}^{2}}\right) \frac{180}{\pi}$$

$$\phi_{2}(\Delta_{\nu}) = -\arctan\left(1.248 \frac{1 - \Delta_{\nu}}{0.253 - 2\Delta_{\nu} + \Delta_{\nu}^{2}}\right) \frac{180}{\pi}$$



◄Fig. 8.6 Frequency characteristics of a non-driven micromechanical gyroscope a Relationship between amplitude and phase. b Relationship between amplitude and frequency. c Relationship between phase and frequency

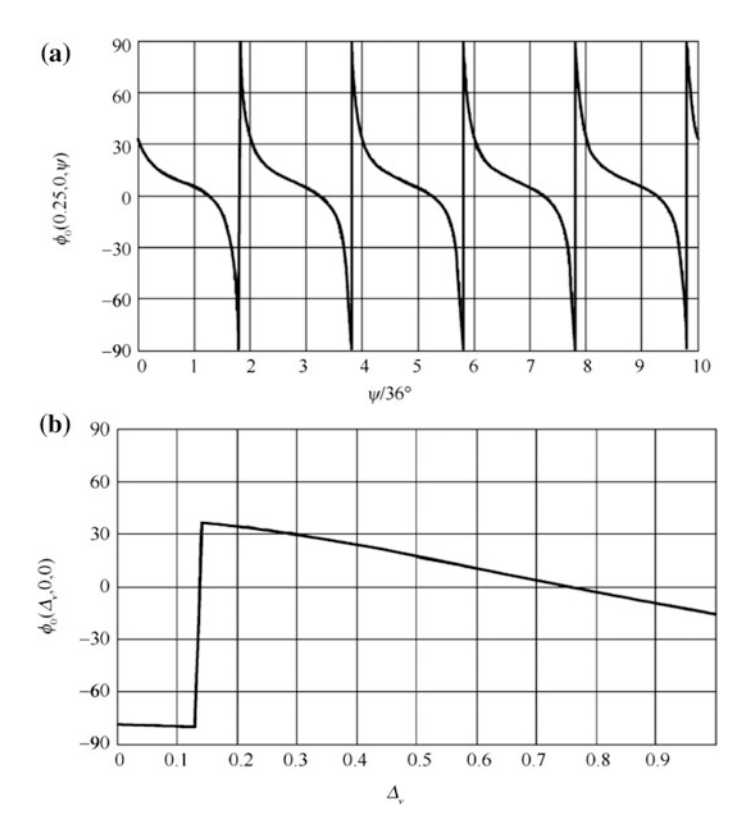


Fig. 8.7 Relationship between the phase and the angular vibration of a non-driven micromechanical gyroscope **a** Relationship between phase ϕ_0 and Ω_t . **b** Relationship between ϕ_0 and change of angular vibration frequency

$$\begin{split} \theta_1(\Delta_{\nu}) &= \frac{1.747 + \Delta_{\nu}}{\sqrt{(0.253 + 2\Delta_{\nu} + \Delta_{\nu}^2)^2 + 1.557(1 + \Delta_{\nu})^2}} \\ \theta_2(\Delta_{\nu}) &= \frac{1.747 - \Delta_{\nu}}{\sqrt{(0.253 - 2\Delta_{\nu} + \Delta_{\nu}^2)^2 + 1.557(1 - \Delta_{\nu})^2}} \\ \theta(\Delta_{\nu}, \phi, \psi) &= \theta_1(\Delta_{\nu}) \sin\Bigl\{ [(1 + \Delta_{\nu})\psi + \phi + \phi_1(\Delta_{\nu})] \frac{\pi}{180} \Bigr\} \\ &+ \theta_2(\Delta_{\nu}) \sin\Bigl\{ [(1 - \Delta_{\nu})\psi - \phi + \phi_2(\Delta_{\nu})] \frac{\pi}{180} \Bigr\} \end{split}$$

$$\begin{split} A(\Delta_{\nu},\phi,\psi) &= \sqrt{\theta_{1}^{2}(\Delta_{\nu}) + \theta_{2}^{2}(\Delta_{\nu}) + 2\theta_{1}(\Delta_{\nu})\theta_{2}(\Delta_{\nu})\cos\left\{\left[2\Delta_{\nu}\psi + 2\phi + \phi_{1}(\Delta_{\nu}) - \phi_{2}(\Delta_{\nu})\right]\frac{\pi}{180}\right\}} \\ A_{11}(\Delta_{\nu},\phi,\psi) &= \cos\left[\left(\Delta_{\nu}\psi + \phi\right)\frac{\pi}{180}\right]\left[\theta_{1}(\Delta_{\nu})\sin\left(\phi_{1}(\Delta_{\nu})\frac{\pi}{180}\right) + \theta_{2}(\Delta_{\nu})\sin\left(\phi_{2}(\Delta_{\nu})\frac{\pi}{180}\right)\right] \\ A_{12}(\Delta_{\nu},\phi,\psi) &= \sin\left[\left(\Delta_{\nu}\psi + \phi\right)\frac{\pi}{180}\right]\left[\theta_{1}(\Delta_{\nu})\cos\left(\phi_{1}(\Delta_{\nu})\frac{\pi}{180}\right) - \theta_{2}(\Delta_{\nu})\cos\left(\phi_{2}(\Delta_{\nu})\frac{\pi}{180}\right)\right] \\ A_{21}(\Delta_{\nu},\phi,\psi) &= \cos\left[\left(\Delta_{\nu}\psi + \phi\right)\frac{\pi}{180}\right]\left[\theta_{1}(\Delta_{\nu})\cos\left(\phi_{1}(\Delta_{\nu})\frac{\pi}{180}\right) + \theta_{2}(\Delta_{\nu})\cos\left(\phi_{2}(\Delta_{\nu})\frac{\pi}{180}\right)\right] \\ A_{22}(\Delta_{\nu},\phi,\psi) &= \sin\left[\left(\Delta_{\nu}\psi + \phi\right)\frac{\pi}{180}\right]\left[\theta_{1}(\Delta_{\nu})\sin\left(\phi_{1}(\Delta_{\nu})\frac{\pi}{180}\right) - \theta_{2}(\Delta_{\nu})\sin\left(\phi_{2}(\Delta_{\nu})\frac{\pi}{180}\right)\right] \\ \phi_{0}(\Delta_{\nu},\phi,\psi) &= a \tan\left(\frac{A_{11}(\Delta_{\nu},\phi,\psi) + A_{12}(\Delta_{\nu},\phi,\psi)}{A_{21}(\Delta_{\nu},\phi,\psi)}\right)\frac{180}{\pi} \end{split}$$

Chapter 9 Static Performance Test of a Non-driven Micromechanical Gyroscope

9.1 Performance of the Prototype of a Non-driven Micromechanical Gyroscope

9.1.1 Temperature Performance of the Prototype

The prototype of non-driven micromechanical gyroscope with a circuit is tested. The test is performed on a dynamic turntable controlled by a computer. The rotational velocity of the gyroscope is set to be $12 \sim 22$ Hz through the simulator and the environment temperature is provided by a special incubator.

During the test, the following parameters are adjusted: the gyroscope's resolution, zero bias signal and its dependence on the temperature, the scale factor and the nonlinearity of the output signal and its dependence on the temperature and rotation frequency of the simulator. The test results are shown in Tables 9.1, 9.2, 9.3, 9.4, 9.5, and 9.6.

- (1) Resolution. The prototype of the micromechanical gyroscope is mounted on the turntable, and the measured angular velocity is smoothly increased by the turntable until the measured signal appears. The results are shown in Table 9.1.
- (2) Zero bias. The micromechanical gyroscope is mounted on the turntable and the output signal is measured in the absence of an angular velocity. The results are shown in Table 9.2.
- (3) The temperature performance test of the sensor. The relationships between the output signal (V) of the prototype of the micromechanical gyroscope and the temperature t, and between the rotating angular velocity $\dot{\varphi}$ of the simulator and the measured angular velocity Ω are shown in Table 9.3.
- (4) The scale factor and its stability. The scale factor for the prototype of the micromechanical gyroscope is 27.7, and the stability of the scale factor with respect to its average value is shown in Tables 9.4, 9.5 and 9.6.
- (5) The relationships between the output signal and the temperature, and between the measured angular velocity and the rotating velocity of the simulator.

t/°C	Resolution ((°)/s)			
	CW	CCW		
+25	1.00	1.00		
+50	1.09	1.12		
+75	1.26	1.30		

Table 9.1 Resolution of the prototype of a micromechanical gyroscope

Table 9.2 Zero bias signal of the prototype of a micromechanical gyroscope

t/°C	Zero bias (mV/(°)/s)			
	DC	AC		
+25	7.3	4.1		
+50	7.5	4.5		
+75	7.8	5.0		

Table 9.3 Relationships between the output signal (V) of the prototype of the micromechanical gyroscope and the temperature, and between the rotating angular velocity and the measured angular velocity

Ω (°/s)		50		100		150		200	
t (°C)	φ/Hz	CW	CCW	CW	CCW	CW	CCW	CW	CCW
+25	12	1.247	1.254	2.461	2.468	3.808	3.815	5.032	5.042
	16	1.409	1.416	2.795	2.798	4.230	4.290	5.700	5.709
	22	1.475	1.478	2.926	2.930	4.494	4.500	5.985	5.993
+50	12	1.304	1.31	2.573	2.577	3.979	3.983	5.258	5.264
	16	1.463	1.468	2.914	2.921	4.471	4.479	5.953	5.961
	22	1.598	1.606	3.055	3.059	4.692	4.698	6.253	6.257
+75	12	1.368	1.376	2.700	2.708	4.177	4.185	6.522	6.531
	16	1.546	1.553	3.030	3.070	4.700	4.706	6.255	6.263
	22	1.618	1.621	3.209	3.214	4.932	4.937	6.568	6.575

Table 9.4 The scale factor for the gyroscope (in the ranges of the rotating angular velocity of the simulator $\dot{\varphi}$ and the measured angular velocity Ω) under the condition of the room temperature (+25 °C) (Unit: mV/°/s)

Ω (°/s)									
	50		100	100		150			Stability of
<i>φ</i> (Hz)	CW	CCW	CW	CCW	CW	CCW	CW	CCW	scale factor (%)
12	24.94	25.08	24.61	24.68	25.39	25.43	25.16	25.21	±1.64
16	28.18	28.32	27.95	27.98	28.20	28.60	28.50	28.55	±1.15
22	29.50	29.56	29.26	29.30	29.96	30.00	29.93	29.97	±1.25
Stability of scale factor (%)	±8.34		±8.47		±8.32		±8.68		

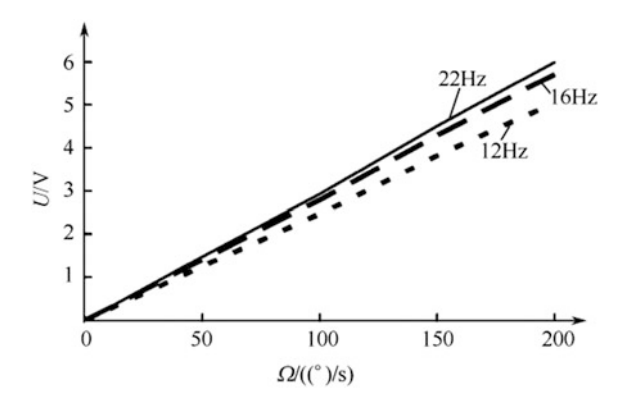
Ω (°/s)										
t (°C)	50	50		100		150			Stability of	
	CW	CCW	CW	CCW	CW	CCW	CW	CCW	scale factor (%)	
+25	28.18	28.32	27.95	27.98	28.20	28.60	28.50	28.55	±1.20	
+50	29.26	29.36	29.14	29.21	29.81	29.86	29.77	29.81	±1.22	
+75	30.92	31.06	30.30	30.70	31.33	31.37	31.28	31.32	±1.10	
Stability of scale factor	10.21		9.82		11.24		9.89			

Table 9.5 The scale factor of the gyroscope when the rotating frequency of the simulator is 16 Hz (in the ranges of the measured temperature t and the measured angular velocity Ω) (Unit: $\text{mV}/^{\circ}/\text{s}$)

Table 9.6 The scale factor of the gyroscope (in the ranges of the change of the temperature t and the rotating frequency $\dot{\varphi}$ of the simulator) when the measured angular velocity is 100°/s (Unit: mV/°/s)

φ (Hz)	10		16		20		0.122. 6.1
<i>t</i> (°C)	12		16		22		Stability of scale
	CW	CCW	CW	CCW	CW	CCW	factor (%)
+25	24.61	24.68	27.95	27.98	29.26	29.30	±8.47
+50	25.73	25.77	29.14	29.21	30.55	30.59	±9.71
+75	27.00	27.08	30.30	30.70	32.09	32.14	±9.65
Stability of scale factor (%)	10.00		9.82		9.83		

Fig. 9.1 Relationship between output signal and measured angular velocity at room temperature (when the rotating frequencies of the simulator are different)



The output signals of the prototype of the micromechanical gyroscope with different angular velocities and rotating frequencies of different simulators and different temperatures are shown in Figs. 9.1, 9.2 and 9.3.

Fig. 9.2 Influence of temperature on output signal when the measured angular velocity is 100°/s (the rotating frequencies of the simulator are different)

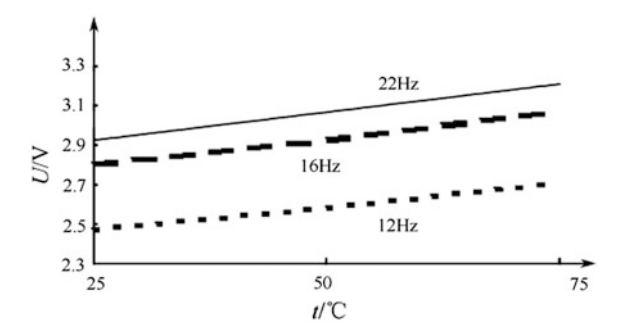
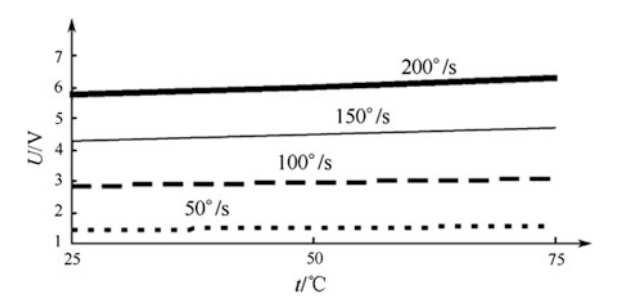


Fig. 9.3 Influence of temperature on output signal when rotating frequency of the simulator is 16 Hz (when the measured angular velocities are different)



9.1.2 Performance of the Prototype

Tests of five prototypes are carried out on the dynamic turntable controlled by the computer. The rotating velocity of the device is set at 12–22 Hz through the simulator and a special temperature box is used to provide the temperature environment. The performances of the prototype are as follows:

- (1) The resolution is 1°/s.
- (2) Zero bias: DC 6 mV and AC 5 mV (The simulator rotates at a certain frequency).
- (3) When the simulator rotates at different frequencies the relationship between the output signal and the input angular velocity of the prototype is shown in Table 9.7.

Table 9.7 The relationship between the output signal and the input angular velocity of the prototype

Ω (°/s)							
<i>φ</i> (Hz)	50		100		150	150	
	CW	CCW	CW	CCW	CW	CCW	
12	1.942	1.960	3.920	3.905	6.000	6.000	
17	2.140	2.138	4.315	4.315	6.600	6.600	
22	2.258	2.260	4.556	4.560	6.900	6.900	
Stability (%)	±7.38	±7.00	±7.37	±7.60	±6.82	±6.82	

$\dot{\varphi}$ (Hz)	50		100	100			Stability (%)
	CW	CCW	CW	CCW	CW	CCW	
12	38.84	39.20	39.20	39.05	40.00	40.00	2.94
17	42.80	42.76	43.15	43.15	44.00	44.00	2.86
22	45.16	45.20	45.56	45.60	46.00	46.00	1.84

Table 9.8 Relationship between the input angular velocity and the scale factor of the prototype

Fig. 9.4 Relationship between output signal and input angular velocity of the prototype

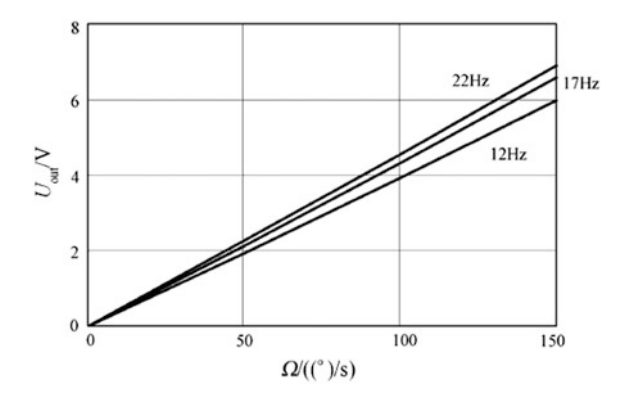
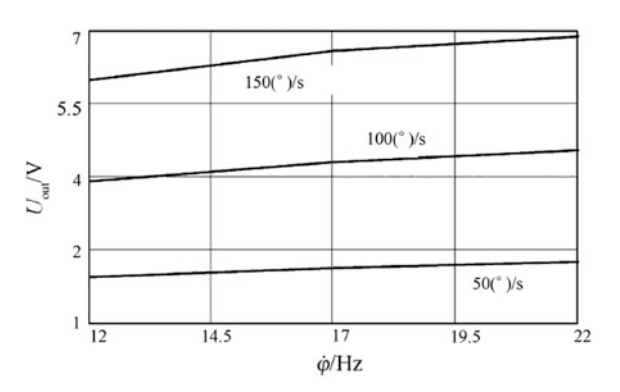


Fig. 9.5 Relationship between output signal of the prototype and frequency of the simulator



- (4) The scale factor is 42.76 mV/°/s.
- (5) The relationship between the input angular velocity and the scale factor of the prototype is shown in Table 9.8.
- (6) The relationship between the output signal and the input angular velocity of the prototype is shown in Fig. 9.4.
- (7) The relationship between the output signal of the prototype and the frequency of the simulator is shown in Fig. 9.5.

9.1.3 Temperature Stability of the Prototype

- (1) When the ambient temperatures are +25 and +75 °C, the stability of the zero position signal temperature is shown in Table 9.9.
- (2) When the ambient temperatures are +25 and +75 °C, the stability of the resolution and the temperature is shown in Table 9.10.
- (3) When the ambient temperatures are +25 and +75 °C, the relationships between the amplitude of the output signal (mV) and the phase (°), and between the input angular velocity and the rotating frequency of the simulator are shown in Table 9.11.
- (4) When the ambient temperatures are +25 and +75 °C, and the rotating frequency of the simulator is 17 Hz, the relationships between the relative mean value (%) of the scale factor stability of the output signal and the phase shift of the output signal, and the measured input angular velocity are shown in Table 9.12.
- (5) When the ambient temperatures are +25 and +75 °C, and the input angular velocity is 100°/s, the relationships between the relative mean value (%) of the scale factor stability of the output signal and the phase shift of the output signal, and the rotating frequency of the simulator are shown in Table 9.13.

Table 9.9 Stability of the zero signal temperature

Temperature(°C)	25	75
DC zero position signal(mV)	-4	-5
AC zero position signal (in the range of the rotating frequency of the simulator)(mV)	2	5

Table 9.10 Stability of the resolution and the temperature

Temperature (°C)	25	75
Resolution (°/s)	1	1

Table 9.11 Relationships between the amplitude of the output signal (mV) and the phase (°), and between the input angular velocity and the rotating frequency of the simulator

t (°C)						
	Ω	50		100		150	
	(°/s)						
	φ Hz	Amplitude	Phase	Amplitude	Phase	Amplitude	Phase
		(mV)	(°)	(mV <u>)</u>	(°)	(mV)	(°)
+25	12	1.820	-6.10	3.680	-6.120	5.64	-6.48
	17	2.015	-13.75	4.100	-13.720	6.26	-13.90
	22	2.150	-18.15	4.340	-18.100	6.65	-18.00
+75	12	1.730	-7.70	3.490	-7.700	5.36	-7.70
	17	1.900	-15.50	3.810	-15.600	5.87	-5.60
	22	2.000	-20.00	4.015	-20.000	6.20	-19.90

t (°C)	Parameter	Ω (°/s)	Ω (°/s)				
		50	100	150			
+25	Scale factor	40.30	41.00	41.73	3.5%		
	Phase shift	-13.75	-13.72	-13.90	0.15°		
+75	Scale factor	38.0	38.1	39.1	2.9%		
	Phase shift	-7.7	-15.6	-5.6	0.1°		

Table 9.12 Relationships between the scale factor and the phase shift, and the input angular velocity

Table 9.13 Relationships between the relative mean value (%) of the scale factor stability and the phase shift, and the rotating frequency of the simulator

t (°C)	Parameter	<i>φ</i> (Hz)			Stability (%)
		12	17	22	
+25	Amplitude	3.68	4.10	4.34	±8
	Phase shift	-6.12	-13.72	-18.10	±6
+75	Amplitude	3.490	3.810	4.015	±6.900
	Phase shift	-7.70	-15.60	-20.00	±6.15

Table 9.14 Relationships between the amplitude (%) of the output signal and the relative phase shift, and the input angular velocity and the rotating frequency of the simulator

<i>t</i> (° C)	Ω (°/s)	50		100		150	
	<i>φ</i> (Hz)	Amplitude	Phase shift	Amplitude	Phase shift	Amplitude	Phase shift
+75	12	-5.0	-1.60	-5.16	-1.58	-5.0	-7.7
	17	-5.7	-1.75	-7.00	-1.88	-6.2	-5.6
	22	-7.0	-1.85	-7.50	_	-6.7	-19.9

(6) When the ambient temperatures is +75 °C, the relationships between the relative amplitude (%) of the output signal and the relative phase shift, and the different input angular velocity and the rotating frequency of the simulator are shown in Table 9.14.

9.2 Performance of a CJS-DR-WB01 Type Silicon Micromechanical Gyroscope

Tests of five CJS-DR-WB01 type silicon micromechanical gyroscopes are carried out on the dynamic turntable controlled by the computer. The velocity of the gyroscope is set at 5–25 Hz through the simulator. The performance of the CJS-DR-WB01-0639 type prototype is as follows

- (1) The resolution is $0.1^{\circ}/s$.
- (2) The zero bias is DC 1.8 mV.
- (3) When the simulator rotates at different frequencies the relationship between the output signal of the gyroscope and the input angular velocity is shown in Table 9.15.
- (4) The scale factor is 14.27 mV/°/s.
- (5) The relationship between the input angular velocity and the scale factor is shown in Table 9.16.
- (6) The relationship between the output signal of the CJS-DR-WB01-0639 and the input angular velocity is shown in Fig. 9.6.
- (7) The relationship between the output signal of the CJS-DR-WB01-0639 and the frequency of the simulator is shown in Fig. 9.7.

9.3 Performance of a CJS-DR-WB02 Type Silicon Micromechanical Gyroscope

The performance tests of ten CJS-DR-WB02 type micromechanical gyroscopes are carried out and the performance of the CJS-DR-WB02 0701 prototype is as follows:

- (1) The resolution is 0.05 °/s.
- (2) The zero bias is AC 21.61 mV (the simulator rotates at 11 Hz).
- (3) When the simulator rotates at different frequencies the relationship between output signal of the gyroscope and the input angular velocity is shown in Table 9.17.
- (4) The scale factor is 16.79 mV/°/s.
- (5) The relationship between the input angular velocity and the scale factor is shown in Table 9.18.
- (6) The relationship between the output signal of the CJS-DR-WB01-0701-0506 and the input angular velocity is shown in Fig. 9.8.
- (7) The relationship between the output signal of the CJS-DR-WB01-0701-0506 and the frequency of the simulator is shown in Fig. 9.9.

9.4 Performance Test of CJS-DR-WB03 Type Silicon Micromechanical Gyroscope

The performance test of the CJS-DR-WB03 type silicon micromechanical gyroscope includes two parts: the performance parameter test and the environmental adaptability test. The performance parameter test includes the scale factor of the gyroscope, the nonlinearity of the scale factor, the repeatability of the scale factor, the symmetry of the scale factor, the temperature coefficient of the scale factor, the

Table 9.15	Relationship be	(able 9.15) Relationship between the output signal of the CJS-DR-WB01-0639 type gyroscope and the input angular velocity	t signal of the C	JS-DR-WB0	1-0639 type g	syroscope and	the input angu	ılar velocity		
Ω (°/s)										
φ (Hz)	100		200		300		400		500	
	CW	CCW	CW	CCW	CW	CCW	CW	CCW	CW	CCW
5	703.4	9.769	1405	1499	2107.2	2101.6	2808.4	2800.4	3511.2	3503
11	1426.8	1428.4	2845.4	2853.6	4263.6	4279.8	5697.4	5716.4	7145.6	7159.2
17	1802.8	1809	3567.6	3598.6	5360.4	5385.8	7094.6	7172.2	9119.4	9048.2
25	1922.4	1896.4	3760	3751.2	5621	5632.2	7641.6	7645.8	9590.2	9947.6
Stability(%) ±32.49		±31.96	±30.4	±31.9	$ \pm 32.1$	±32.2	±32.4	±32.6	± 33.3

Table 9.16 Relationship between the input angular velocity of the CJS-DR-WB01-0639 type gyroscope and the scale factor

Ω (°/s)											
φ (Hz)	100		200		300		400		500		Stability (%)
	CW	CCW									
5	7.034	926.9	7.025		7.024		7.021	7.001	7.022	7.006	2.4
11	14.268	14.284	14.227	14.268	14.212	14.266	14.243	14.291		14.318	2.3
17	18.028	18.09	17.838		17.868		17.986	17.936	18.239		2.5
25	19.224	18.964	18.8	18.765	18.737		19.104	19.114	19.18		2.6

Fig. 9.6 Relationship between output signal of the CJS-DR-WB01-0639 and input angular velocity

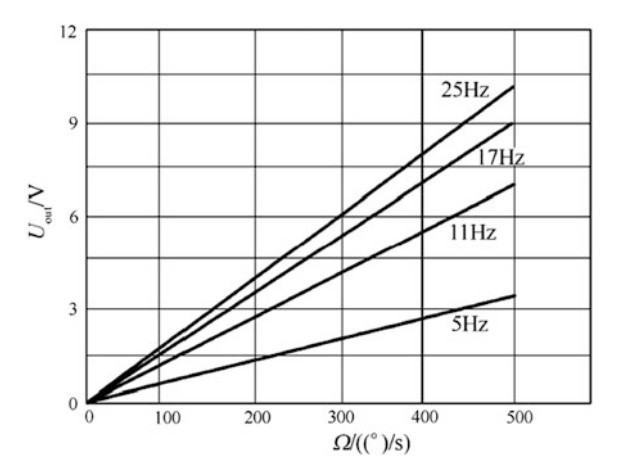
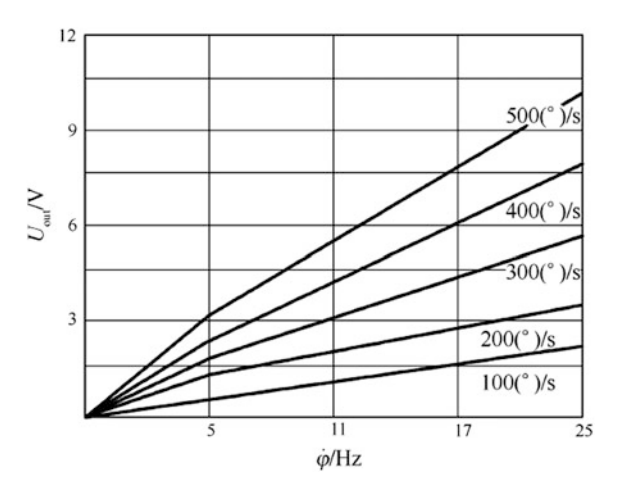


Fig. 9.7 Relationship between output signal of CJS-DR-WB01-0639 and frequency of the simulator



threshold, the resolution, the range, the zero bias, the stability of the zero bias, the repeatability of the zero bias, the acceleration sensitivity of the zero bias, the static state noise, the temperature sensitivity of the zero bias, the start time and the bandwidth. The environmental adaptability test includes the vibration function test and the impact test. The rules of this test are as follows:

- (1) The detailed specification of the CJS-DR-WB03 type silicon micromechanical gyroscope.
- (2) IEEE Standard Specification Format Guide and Test Procedure for the Coriolis Vibratory Gyroscope (IEEE Std 1431TM—2004).

The test results of the CJS-DR-WB03 type silicon micromechanical gyroscope CJS-DR-WB03 are shown in Table 9.19.

Table 9.17 Relationship between the output signal of the CJS-DR-WB02-0701-0506 type gyroscope and the input angular velocity

(°/s)												
$\dot{\phi}$ (Hz)	50		100		150		200		250		300	
	CW	CCW	CW	CCW								
9	332	298.8	634.8	595.4	873.2	795.6	1155.6	1155.2	1579.2	1666.2	2786.81	2117.2
11	828	785.6	1637	1613.4	2487.6	2415	3343	3287.4	4209	4179.8	9909	5006
17	1354.6	1330.6	2721.6	2681	4035	3995.2	5343.8	5331.2	6719	6645.2	8044.2	7962.4
25	1676.6	1643.4	3311	3278.8	4949.6	4912.4	6596.4	6561.6	8301.2	8260.2	10051.4	10038.4
Stability (%)	±68.31	±70.55	±69.42	±70.84	±71.71	±73.74	±71.88	±71.71	±69.64	±67.88	±57.04	±66.29

Table 9.18 Relationship between the input angular velocity and the scale factor of the CJS-DR-WB01-0701-0506 type micromechanical gyroscope

		- dumin		and and	caracter mine					1010	adversaria marmania mala margania de la companya de		adagare
Ω (°/s)													
φ (Hz)	50		100		150		200		250		300		Stability (%)
	CW	CCW	CW	CCW	CW	CCW	CW	CCW	CW	CCW	CW	CCW	
9	6.64	5.976	6.348	5.954	5.976 6.348 5.954 5.821333 5.304	5.304	5.778	5.776	6.3168	6.6648	5.778 5.776 6.3168 6.6648 9.289367 7.057333	7.057333	44.9093
11	16.56	15.712	16.37	16.134	.712 16.37 16.134 16.584	16.1	16.715	16.437	16.836	16.7192	16.715 16.437 16.836 16.7192 16.88667	16.68667	4.650808
13	27.092	26.612	26.612 27.216 26.81	26.81	26.9	26.63467 26.719 26.656 26.876 26.5808 26.814	26.719	26.656	26.876	26.5808	26.814	26.54133	1.599058
20	33.532	32.868	33.11	32.788	33.532 32.868 33.11 32.788 32.99733 32.74933 32.982 32.808 33.2048 33.0408 33.50467 33.46133	32.74933	32.982	32.808	33.2048	33.0408	33.50467	33.46133	1.344361

Fig. 9.8 Relationship between output signal of CJS-DR-WB01-0701-0506 and input angular velocity

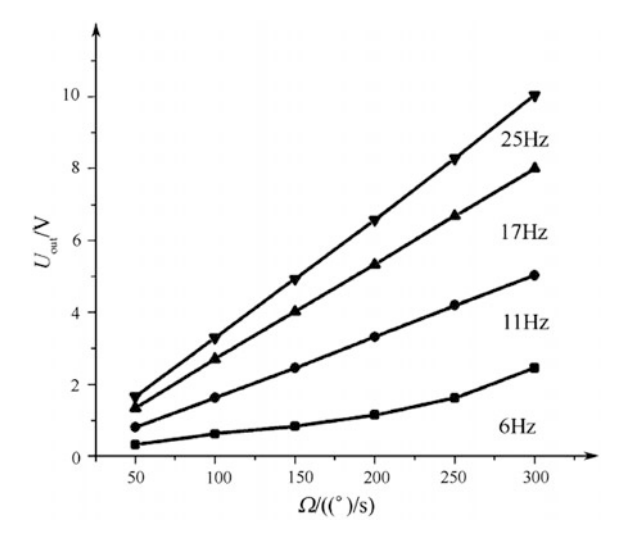
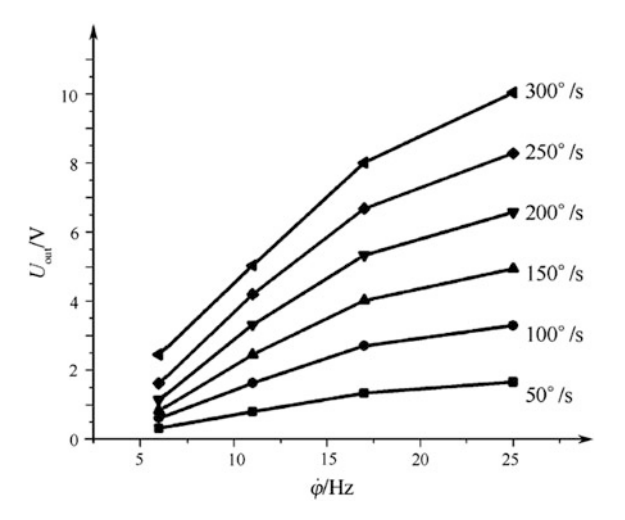


Fig. 9.9 Relationship between output signal of CJS-DR-WB01-0701-0506 and frequency of the simulator



1. Scale factor

(1) Test equipment.

- ① Three-axis angular rate turntable.
- ② DC regulated power supply.
- 3 Number table (or data acquisition card).
- ① Computer.
- S Assembly test.

Number	Entry name	Coded num	ber	
		0801-4003	0801-4005	0801-4031
01	Range (°/s)	±500	±500	±500
02	Scale factor (mV/°/s)	15.7	19.0	19.0
03	Nonlinearity of the scale factor (%)	2.34	1.22	0.62
04	Symmetry of the scale factor (%)	0.039	0.022	0.048
05	Repeatability of the scale factor ($\times 10^{-6}$)	14.36	15.86	105.08
06	Threshold (°/s)	<0.001	< 0.001	< 0.001
07	Resolution (°/s)	0.007	0.003	0.007
08	Temperature coefficient of the scale factor $(10^{-6})^{\circ}$ C)	1086.01	760.01	520.32
09	Zero bias (°/s)	-0.011	-0.019	-0.0002
10	Stability of the zero bias (°/h)	12.07	13.88	1.188
11	Repeatability of the zero bias (°/h)	102.35	44.28	0.054
12	Start time/min	30	5	20
13	Acceleration sensitivity of the zero bias ($^{\circ}$ /s g^{-1})	0.00052	0.00063	0.00024
14	Noise (°/h·Hz-½)	13.72	11.58	6.46
15	Temperature coefficient of the zero bias (°/h·°C ⁻¹)	3.77	0.58	55.48
16	Bandwidth (Hz)			
17	Vibration/sine sweep 20-2000 Hz, 2 g			
18	Impact (100 g, 6 ms)			
19	Working temperature (°C)	-40 to +85		
20	Dimension (mm) (with circuit)	60 × 55 × 22 × 22 ×	30 (Without 5)	circuit
21	Weight (g) (with circuit)	<85 (Without	ut circuit 8)	

Table 9.19 Main specifications of the CJS-DR-WB03 type silicon micromechanical gyroscope

(2) Test method.

- ① The gyroscope is fixed on the rate table and its input reference axis is oriented to the sky.
- ② Check the cable connection, start the turntable and set the sampling period of the computer to 1 s (if the sampling period of the tested data acquisition instrument is not 1 s, the collected data are averaged to be 1 s).

When the gyroscope's power supply is connected and the longest preheating time is 30 min, the turntable is rotated at rates of ± 0.1 , ± 0.2 , ± 0.5 , ± 1 , ± 2 , ± 5 , ± 10 , ± 20 , ± 50 , ± 100 , ± 200 , ± 300 , ± 400 , ± 500 and 200° /s. When the turntable is in the forward, stop and reverse steady states respectively, start the sampling procedure of the computer and record the output voltage of the gyroscope. If the sampling data of the rate points which are less than $\pm 100^{\circ}$ /s is not less than

30, the sampling data of ± 100 and $\pm 200^{\circ}$ /s are not less than 10, and the sampling data of ± 300 , ± 400 and $\pm 500^{\circ}$ /s are not less than 5, the test is completed and the gyroscope's power supply is shut down.

- 3 The zero position data of 30 s are sampled before and after the angular rates are tested.
- 4 After 30 min, repeat the above steps and repeat the test three times.
- (3) The computing method. The formula of the scale factor is

$$\overline{F_j} = \left(\sum_{m=1}^N F_{jm}\right) / N \tag{9.1}$$

$$\overline{F_r} = (\overline{F_s} + \overline{F_e})/2 \tag{9.2}$$

$$F_i = \overline{F_i} - \overline{F_r} \tag{9.3}$$

where $\overline{F_{jm}}$ is the *m*th output value of the gyroscope; N is the sampling number; $\overline{F_r}$ is the average value of the gyroscope's output when the turntable is static; $\overline{F_s}$ and $\overline{F_e}$ are the average values of the gyroscope's output before and after the test of the angular rate; and F_j is the gyroscope's output corresponding to the *j*th input angular rate Ω_{ii} .

The relationship between the input and output of the gyroscope can be established as the following linear model:

$$F_i = K\Omega_{ii} + F_0 + \nu_i \tag{9.4}$$

where K is a scale factor (mV s⁻¹/(°)); and F_0 and v_j are the fitting zero position and the fitting error respectively.

2. Nonlinearity of the scale factor

Based on the test data of (1), the nonlinearity of the scale factor is calculated as follows:

$$K'_{m} = \frac{\hat{F}_{j} - F_{j}}{K|\Omega_{\text{max}} + \Omega_{\text{max}}|}\Big|_{\text{max}}$$

$$(9.5)$$

$$K' = \frac{1}{Q} \sum_{m=1}^{Q} K'_m \tag{9.6}$$

where \hat{F}_j is the jth input angular velocity corresponding to the calculated values on the fitting line; K'_m is the nonlinearity of the scale factor in the mth test; K' is the nonlinearity of the scale factor; Q is the number of tests; and Ω_{\max} and Ω_{\max} are the maximum input angular velocities corresponding to the forward rotation and the reverse rotation.

3. Symmetry of the scale factor

Based on the test data of (1), the scaling factor is calculated as follows:

$$K_{mu} = \frac{|K_+ - K_-|}{\overline{K}} \tag{9.7}$$

$$K_{u} = \frac{1}{Q} \sum_{m=1}^{Q} K_{mu} \tag{9.8}$$

where K_{mu} is the asymmetry of the scale factor corresponding to the mth test; K_{+} is the scale factor obtained by fitting in the range of the forward input angular velocity; K_{-} is the scale factor obtained by fitting in the range of the reverse input angular rate; K_{u} is the asymmetry of the scale factor; and \overline{K} is the average value of the scale factor.

4. Repeatability of the scale factor

Using the test data in (1), the repeatability of the scale factor can be calculated as follows:

$$K_r = \frac{1}{\overline{K}} \left[\frac{1}{Q - 1} \sum_{m=1}^{Q} \left(K_m - \overline{K} \right)^2 \right]^{1/2}$$

$$(9.9)$$

where K_m is the scale factor measured in the *m*th time; and K_r is the repeatability of the scale factor.

5. Range

The test equipment and the test method are the same as 1.

The ranges in two directions should satisfy the nonlinear index of the nominal scale factor.

6. Threshold

The test equipment is the same as 1.

(1) The test method.

① After test in 1., the gyroscope is not cut off. First the output of the gyroscope is measured when the input angular velocity is zero and then a prescribed angular velocity input is applied to the gyroscope. Assume that the sampling period of the computer is 1 s and the sampling time is 10 s, the output of the gyroscope is recorded and the output change of the gyroscope relative to the zero velocity input should be larger than the output value of 50% relative to the scale factor.

- ② The above steps are repeated in the opposite direction of the angular velocity input and the threshold data from the opposite direction are obtained.
- 3 The tests are implemented three times in succession.
- (2) Calculation method. The minimum angular velocity inputs in two directions are averaged, i.e., the threshold of the gyroscope.

7. The resolution

The test equipment is the same as 1.

- (1) The test method.
 - ① After test in 6., the gyroscope is not cut off. First the input angular velocity which is 30 times as much as the threshold is applied on the gyroscope and when the turntable runs smoothly a specified velocity increment is added. The output increment of the gyroscope should be larger than 50% of the output increment of the corresponding scale factor, return to the original constant input velocity and then decrease by a specified velocity again. The measured output change of the gyroscope should be greater than 50% of the output change corresponding to the scale factor.
 - ② The above steps are repeated in the opposite input direction and the resolution data from the opposite direction are obtained.
 - 3 The tests are implemented three times.
- (2) Calculation method. The minimum velocity increments in two directions are averaged to give the resolution of the gyroscope.
- 8. The temperature coefficient of the scale factor
- (1) The test equipment.
 - ① Temperature controlled turntable velocity.
 - ② DC regulated power supply.
 - 3 Digital pressure meter (or the data acquisition card).
 - 4 Computer.
 - S Assembly test.

(2) Test method.

- ① The gyroscope is fixed to the turntable and the sampling period of the computer is set to 1 s.
- ② The gyroscope is powered and the maximum allowable temperature rise velocity of the temperature controlled turntable velocity is increased to 60 °C and maintained for 1 h.
- 3 The turntable rotates with angular velocities $\pm 1^{\circ}$ /s for 30 s respectively and the data are recorded. The data of the scale factor at 60 °C are obtained.

- The maximum allowable temperature drop velocity of the temperature control turntable velocity is decreased to −40 °C, and maintained for 1 h.
- ⑤ The turntable rotates with angular velocities $\pm 1^{\circ}$ /s for 30 s respectively and the data are recorded. The data of the scale factor for -40° C are obtained.
- (3) Calculation method. The temperature coefficient of the scale factor is obtained as

$$K_T = \frac{F_{(+1(^{\circ})/s)} - F_{(-1(^{\circ})/s)}}{2}$$
(9.10)

where $F_{(+1(^{\circ})/s)} - F_{(-1(^{\circ})/s)}$ is the output mean of the gyroscope with angular velocities $\pm 1^{\circ}$ /s. The temperature coefficient is obtained as

$$K_{\text{TE}} = \left| \frac{K_T - K_n}{100 \cdot K_n} \right|_{\text{max}} \times 10^6 (10^{-6} / ^{\circ}\text{C})$$
 (9.11)

where K_n is the scale factor of the gyroscope at room temperature.

- 9. Zero Bias
- (1) Test equipment.
 - ① DC regulated power supply.
 - ② Number table (or data acquisition card).
 - 3 Computer.
 - (5) Assembly test.
- (2) Test method.
 - ① The gyroscope is fixed to the test ground and the sampling period of the computer is set to 1 s.
 - ② Check whether the cable connection is correct and the power supply of the gyroscope is connected. And at the same time the sampling program is started to count for 90 min and the effective data for 60 min are obtained.
 - 3 The above steps are repeated seven times, and the interval of each test is 1 h.
- (3) Calculation method. The zero bias is obtained as

$$\overline{F} = \frac{1}{N} \sum F_i \tag{9.12}$$

$$B_{0m} = \frac{1}{K} \cdot \overline{F} \tag{9.13}$$

$$B_0 = \frac{1}{Q} \sum_{m=1}^{Q} B_{0m} \tag{9.14}$$

where F_i is the voltage output of each sampling; \overline{F} is the output average of N tests; B_{0m} is the zero bias of the gyroscope for the mth test; and B_0 is the zero bias of the gyroscope.

10. Zero bias stability

By using the test data of (9), the zero bias stability is calculated as

$$B_{sm} = \frac{1}{K} \cdot \left[\frac{1}{(N/P - 1)} \sum_{j=1}^{N/P} (F_j - \overline{F})^2 \right]^{1/2}$$
 (9.15)

$$B_s = \frac{1}{Q} \sum_{m=1}^{Q} B_{sm} \tag{9.16}$$

where F_j is the new data sample obtained by computing the average according to the period P; P is the data average period, P = 10; B_{sm} is the zero bias stability of the gyroscope obtained in the mth test; and B_s is the zero bias stability of the gyroscope.

11. Zero bias repeatability

By using the test data of (10), the zero bias repeatability is calculated as

$$B_r = \left[\frac{1}{Q - 1} \sum_{m=1}^{Q} \left(B_{0m} - \overline{B_0} \right)^2 \right]^{1/2} \tag{9.17}$$

where B_r is zero bias repeatability; $\overline{B_0}$ is the zero bias average; and Q is the number of tests.

12. Startup time

On the basis of the test data in (9) and the data from each measurement, the time interval is recorded from the time that the micromechanical gyroscope is powered to the time that the zero bias stability satisfies the nominal value and the average value of the seven recorded time intervals is the startup time of the gyroscope.

13. Zero bias acceleration sensitivity

The test equipment is the same as 9.

(1) Test methods

① The gyroscope is fixed to the test ground surface.

- ② The gyroscope is preheated for 30 min.
- ③ The gyroscope tool is turned over such that the positive directions of the *x*, *y* and *z* axes are oriented to the sky. After the sampling procedure is started zero bias sampling is performed and the sampling number of each state is not less than 30.
- (2) Calculation method. When the positive directions of the x, y and z axes are oriented to the sky, the difference of the output averaged value is regarded as the output difference of the positive and opposite 1 g of the corresponding axes. This difference divided by 2 g is regarded as the zero bias acceleration sensitivity of the axis. The maximum value of the zero bias acceleration sensitivity of the x, y and z axes is regarded as the zero bias acceleration sensitivity of the gyroscope.

14. Noise

The data from the test in 9 are processed using the Allan variance method:

(1) Assume that there are *n* output samples of the gyroscope. The corresponding angular velocity is calculated and the initial sample of the angular velocity is obtained as

$$\Omega_i(t_0) = \frac{1}{k} \cdot F_i(t_0) \tag{9.18}$$

where $i = 1 \sim n$.

(2) The k data in the n data are regarded as an array with time length $\tau = kt_0$. Take $\tau = t_0, 2t_0, \ldots, kt_0$ (k < n/2)) and calculate the data average value for each time length τ . There are n - k + 1 values:

$$\overline{\Omega}_p(\tau) = \frac{1}{k} \sum_{i=n}^{p+k} \Omega_i(t_0)$$
(9.19)

where p = 1, 2, ..., n.

(3) Find the average differences of two adjacent arrays:

$$\xi_{p+1,p} \equiv \overline{\Omega}_{p+1}(\tau) - \overline{\Omega}_{p}(\tau) \tag{9.20}$$

and obtain the random variable set $\{\xi_{p+1,p}=1,2,...,n-k+1\}$ having n-k differences.

(4) Obtain the variance of (3):

$$\sigma^{2}(\tau) = \frac{1}{2(n-k-1)} \sum_{p=1}^{n-k-1} \left[\overline{\Omega}_{p+2}(\tau) - 2\overline{\Omega}_{p+1}(\tau) + \overline{\Omega}_{p}(\tau) \right]^{2}$$
(9.21)

(5) Take the different values of τ and repeat the above process. A curve between $\sigma(\tau)$ and τ can be obtained in the double logarithmic coordinate system, namely the Allan variance curve. By using the Allan variance model the least square fitting method is used to obtain the noise:

$$\sigma^2(\tau) = \sum_{m=-2}^2 A_m \tau^m \tag{9.22}$$

where A_m (i.e., $A_{-2}, A_{-1}, A_0, A_1, A_2$) are the coefficients of the associated polynomials such as the gyroscope and the quantization noise, the random walk coefficient, the zero bias stability, the rate random walk and rate slope. The noise is

$$NC = \sqrt{A_{-2}} \tag{9.23}$$

- 15. Zero bias temperature coefficients
- (1) Test equipment.
 - ① Temperature test box.
 - ② Level gauge.
 - 3 DC regulated power supply.
 - 4) Digital pressure gauge (or data acquisition card).
 - (5) Computer.
 - (6) Assembly test.
- (2) Test method.
 - ① The gyroscope is fixed to the working table and is connected to the power line and the data line.
 - ② According to the maximum allowable rate of the instrument, the temperature control box is set to −40 °C and maintains this temperature for 20 min. The measured gyroscope is powered for 30 min and the static testing and sampling are performed (see (9)). The temperature control box is raised to 60 °C at the rate of 1 °C/min and after the temperature of the gyroscope has been maintained for 20 min, the sampling is over and the gyroscope is turned off.

- 3 According to the maximum allowable rate of the instrument, the temperature control test box is set to -40 °C.
- 4 Repeat step 3 and perform three tests continuously.
- (3) Calculation method. Each zero bias temperature sensitivity is

$$B_{ii} = \left| \frac{B_i - B_m}{100} \right|_{\text{max}} \tag{9.24}$$

where B_{ti} is the *i*th measured zero bias temperature sensitivity ((°) s⁻¹ °C⁻¹); B_i is the *i*th measured zero bias data; and B_m is the zero bias at room temperature.

The averaged value of three zero bias temperature sensitivities is regarded as the zero bias temperature sensitivity of the gyroscope.

16. Bandwidth

- (1) Test equipment.
 - Angular vibration table.
 - ② Regulated power supply.
 - 3 Data acquisition device.
 - (4) Computer.
 - (5) Test tool.

(2) Test method.

- ① The gyroscope is fixed to the angular vibration table using the tool so that its IRA (input reference axis) is parallel to the power line and the data line of the connecting device.
- ② The gyroscope is turned on. After 30 min the angular vibration table is started. When the frequency is tuned to the nominal bandwidth, the angular vibration table begins to vibrate and the frequency and amplitude of the angular vibration table are recorded at the same time.
- ③ The output amplitude of the gyroscope is divided by the amplitude of the angular vibration table to obtain the scale factor of the test frequency. Compared with the static scale factor, when the scale factor of the test frequency is decreased to be more than 3 dB, the test frequency is decreased and the test is continued. Otherwise, the test frequency is increased and the test is continued.
- (3) Calculation method. The curve fitting is performed when the frequency is regarded as the horizontal coordinate and the scale factor of the gyroscope is regarded as the vertical coordinate. The curve is reduced from the static scale factor to the frequency point of 3 dB, which is the working bandwidth of the gyroscope.

- 17. Vibration function test
- (1) Test equipment.
 - ① Vibration table.
 - ② DC regulated power supply.
 - 3 Digital pressure gauge (or a data acquisition card).
 - ① Computer.
 - (5) Test tool.
- (2) Test condition. Sine sweep vibration, 2 g, $20 \sim 2000$ Hz.

Each unit can be chosen as the vibration test with a higher amplitude.

- (3) Test method.
 - ① The gyroscope is installed on the vibration table using the tool and is turned on. When the output of the gyroscope is stable the test is started.
 - ② The vibration table is opened and the static test of the gyroscope is performed for 10 min. According to the requirements of the vibration function test the vibration stress is applied to the product. In the process of the vibration the gyroscope is turned on. After the vibration is over, the static test is maintained for 10 min and the gyroscope is powered off.

Note: one test is performed in three directions x, y and z respectively.

- (4) Output comparison. After the vibration is over the appearance of the gyroscope is checked and the structure should have no residual deformation and no cracks or other mechanical damage. In the process of vibration the gyroscope should work normally. The average values of the zero bias for the gyroscope are compared before, during, and after vibration.
- 18. Mechanical impact test
- (1) Test equipment.
 - ① Shocking platform.
 - ② DC regulated power supply.
 - 3 Digital pressure gauge (or data acquisition card).
 - (4) Computer.
 - (5) Test tool.
- (2) Test condition.

Test directions: x, y, z.

- ① Waveform: half sine wave.
- ② Peak acceleration:100 g (100 g is the measured peak value. Every unit can increase the value of peak acceleration).

- 3 Duration: 6 ms.
- 4 Impact times: three times in three directions.
- (3) Test method. The gyroscope is firmly installed on the shocking platform and the gyroscope is turned on and tested for 10 min. The power state of the gyroscope is kept and the shocking platform is started. According to the condition of the mechanical shock test, the shocking stress is applied and after the shocking is over the gyroscope is powered for 10 min and is then turned off.
- (4) Output comparison. After the shocking is over, the appearance of the gyroscope is checked and the structure should have no residual deformation, and no cracks or other mechanical damage. In the process of the test the product should work normally. The average values of the zero bias of the gyroscope before and after shocking are compared.
 - 19. Low temperature test
- 1. Low temperature work
 - (1) Test equipment.
 - ① Constant temperature and humidity test box.
 - ② Simulator.
 - (4) DC regulated power supply.
 - 4 Voltmeter (or data acquisition card).
 - (5) Test tool.
- (2) Test method. The low temperature test is performed according to GJB 150.4—1986 and the following conditions.
 - ① The gyroscope is mounted on the special detection circuit module and is then installed at the central position of the rotating plane (built in the test box) of the simulator motor fixture such that the motor shaft is parallel to the direction of the horizontal plane.
 - ② The motor is powered so that the gyroscope and the test circuit module rotate in the fixture (the rotating velocity is 17 Hz). When the gyroscope and the test circuit module are powered for 3 min, the output voltage of the gyroscope is recorded.
 - ③ The motor is turned off and cooled to -40 °C. After the temperature reaches -40 °C \pm 2 °C the gyroscope is maintained for 1 h and step ② is repeated and the output voltage of the gyroscope is tested.
- (3) Detection method. The test results should be consistent with the requirements of "the detail standard of CJS-DR-WB03 type silicon micromechanical gyroscope" in 3.4.1 and the appearance should be consistent with the regulations in 3.5.2.

- 2. Low temperature storage
- (1) Test equipment.
 - ① Rotating platform.
 - ② Constant temperature and humidity test box.
 - 3 DC regulated power supply.
 - 4 Voltmeter (or data acquisition card).
 - (5) Test tool.
- (2) Test method. The low temperature test is performed according to GJB 150.4—1986 and the following conditions.
 - ① The gyroscope is installed in a special detecting circuit module and fixed on the roll plane of the rate turntable. The roll of the rate turntable rotates with a rotation velocity of 17 Hz; the powers of the gyroscope and the detection circuit module are connected. The voltmeter is connected at the output end of the detection circuit module and powered and after 3 min the output voltage of the gyroscope is recorded.
 - ② The gyroscope is put into the constant temperature and the humidity test box and the temperature is cooled to the low temperature of -55 °C. Under the condition of -55 °C \pm 2 °C, this temperature is maintained for 24 h. The test box then returns to the normal test atmosphere conditions until the temperature of the gyroscope stabilizes.
 - ③ Operation ① is repeated and the output voltage of the gyroscope is recorded again.
- (3) Detection method. The test results should be consistent with the requirements of "the detail standard of CJS-DR-WB03 type silicon micromechanical gyroscope" in 3.4.1 and the appearance should be consistent with the regulations in 3.5.2.
- 20. High temperature test
- 1. High temperature work.
- (1) Test equipment.
 - ① Constant temperature and the humidity test box.
 - ② Simulator.
 - 3 DC regulated power supply.
 - 4 Voltmeter (or a data acquisition card).
 - (5) Test tool.
- (2) Test method. The high temperature test is performed according to GJB 150.3—1986 and the following conditions.
 - ① The gyroscope is installed on the special detection circuit module and then mounted in the center position of the rotating plane of the simulator

- motor fixture (built in the test box) such that the motor shaft is parallel to the horizontal direction.
- ② The motor is connected such that the gyroscope and the detection circuit module rotate in the fixture (the rotation velocity is 17 Hz). The gyroscope and the detection circuit module are connected and powered and after 3 min the output voltage of the gyroscope is recorded.
- ③ The power of the motor is disconnected and the gyroscope is heated up to 85 °C. Under the condition of 85± 2 °C, this temperature is maintained for 1 h. Operation ② is repeated and the output voltage of the gyroscope is tested.
- (3) Detection method. The test results should be consistent with the requirements of "the detail standard of CJS-DR-WB03 type silicon micromechanical gyroscope" in 3.4.2 and the appearance should be consistent with the regulations in 3.5.2.
- 2. High temperature storage
- (1) Test equipment.
 - ① Rotating platform.
 - 2 Constant temperature and humidity test box.
 - 3 DC regulated power supply.
 - 4 Voltmeter (or data acquisition card).
 - (5) Test tool.
- (2) Test method. The high temperature test is performed according to GJB 150.3—1986 and the following conditions.
 - ① The gyroscope is installed in a special detecting circuit module and fixed on the roll plane of the rate turntable. The roll of the rate turntable rotates with the rotating velocity 17 Hz and the powers of the gyroscope and the detection circuit module are connected. The voltmeter is connected at the output end of the detection circuit module and powered and after 3 min the output voltage of the gyroscope is recorded.
 - ② The gyroscope is put into the constant temperature and the humidity test box and the gyroscope is heated to 85 °C. Under the condition of 85 ± 2 °C, this temperature is maintained for 48 h. The test box returns to normal test atmosphere conditions until the temperature of the gyroscope stabilizes.
 - ③ Operation ① is repeated and the output voltage of the gyroscope is recorded again.
- (3) Detection method. The test results should be consistent with the requirements of "the detail standard of CJS-DR-WB03 type silicon micromechanical gyroscope" in 3.4.2 and the appearance should be consistent with the regulations in 3.5.2.

- 21. Temperature impact
- (1) Test equipment.
 - ① Rotating platform.
 - ② One low temperature box and one high temperature box.
 - 3 DC regulated power supply.
 - 4 Voltmeter (or a data acquisition card).
 - (5) Test tool.
- (2) Test method. The experiment is performed according to method 107 in GJB 360A—1996 and the following conditions.
 - ① The gyroscope is installed in a special detecting circuit module and fixed on the roll plane of the rate turntable. The roll of the rate turntable rotates with the rotating velocity 17 Hz and the powers of the gyroscope and the detection circuit module are connected. The voltmeter is connected at the output end of the detection circuit module and powered and after 3 min the output voltage of the gyroscope is recorded.
 - ② The gyroscope is put into the test box. Its high temperature is 85 °C and its low temperature is -55 °C, and these are maintained for 0.5 h. The conversion process from high temperature to low temperature is within 1 min and 10 cycles are completed.
 - ③ The gyroscope in the test box returns to normal test atmosphere conditions until the temperature of the gyroscope stabilizes. Operation ① is repeated and the output voltage of the gyroscope is recorded again.
- (3) Detection method. The test results should be consistent with the requirements of "the detail standard of CJS-DR-WB03 type silicon micromechanical gyroscope" in 3.4.2 and the appearance should be consistent with the regulations in 3.5.2.
- 22. Vibration
- (1) Test equipment.
 - ① Rotating platform.
 - ② Vibration test table.
 - 3 DC regulated power supply.
 - 4 Voltmeter (or a data acquisition card).
 - (5) Test tool.
- (2) Test method. The experiment is performed according to condition D in GJB 360A—1996 and the following conditions.
 - ① The gyroscope is installed in a special detecting circuit module and fixed on the roll plane of the rate turntable. The roll of the rate turntable rotates with a rotation velocity of 17 Hz and the powers of the gyroscope and the detection circuit module are connected. The voltmeter is connected at

- the output end of the detection circuit module and powered and after 3 min the output voltage of the gyroscope is recorded.
- ② Vibration stress is applied to the product according to the requirement of the vibration function test.
- (a) Test condition: frequency range $20 \sim 2000$ Hz, acceleration 20 g.
- (b) Test duration: each direction for 1 h, three directions for 3 h.
- (c) Product installation: the gyroscope is installed in a special fixture.
 - 3 Operation 1 is repeated and the output voltage of the gyroscope is recorded again.
- (3) Detection method. The test results should be consistent with the requirements of "the detail standard of CJS-DR-WB03 type silicon micromechanical gyroscope" in 3.4.4 and the appearance should be consistent with the regulations in 3.5.2.
- 23. Impact
- (1) Test equipment.
 - ① Rotating platform.
 - ② Impact test table.
 - ③ DC regulated power supply.
 - 4 Voltmeter (or a data acquisition card).
 - ⑤ Test tool.
- (2) Test method. The experiment is performed according to condition E in method 213 of GJB 360A—1996 and the following conditions.
 - ① The gyroscope is installed in a special detecting circuit module and fixed on the roll plane of the rate turntable. The roll of the rate turntable rotates with a rotation velocity of 17 Hz and the powers of the gyroscope and the detection circuit module are connected. The voltmeter is connected at the output end of the detection circuit module and powered and after 3 min the output voltage of the gyroscope is recorded.
 - ② According to the requirement of impact function test, the impact force is applied to the gyroscope.
- (a) Test condition: peak 1000 g, duration 0.5 ms, half sine wave.
- (b) Test direction and number of times: six directions, each direction applying three shocks.
- (c) Product installation: the gyroscope is installed in a special fixture.
 - ③ Operation ① is repeated and the output voltage of the gyroscope is recorded again.
- (3) Detection method. The test results should be consistent with the requirements of "the detail standard of CJS-DR-WB03 type silicon micromechanical

gyroscope" in 3.4.5 and the appearance should be consistent with the regulations in 3.5.2.

- 24. Steady damp-heat
- (1) Test equipment.
 - ① Rotating platform.
 - 2 Constant temperature and humidity test box.
 - 3 DC regulated power supply.
 - 4 Voltmeter (or data acquisition card).
 - (5) Test tool.
- (2) Test method. The experiment is performed according to condition B in method 103 of GJB 360A—1996 and the following conditions.
 - ① The gyroscope is installed in a special detecting circuit module and fixed on the roll plane of the rate turntable. The roll of the rate turntable rotates with a rotation velocity of 17 Hz and the powers of the gyroscope and the detection circuit module are connected. The voltmeter is connected at the output end of the detection circuit module and powered and after 3 min the output voltage of the gyroscope is recorded.
 - ② The gyroscope is put into the constant temperature and humidity test box and the gyroscope is heated up to +40 °C at a relative humidity of $90 \sim 95\%$. Under the condition of 40 ± 2 °C, this temperature is maintained for 96 h. The test box returns to normal test atmosphere conditions until the temperature of the gyroscope stabilizes.
 - ③ Operation ① is repeated and the output voltage of the gyroscope is recorded again.
- (3) Detection method. The test results should be consistent with the requirements of "the detail standard of CJS-DR-WB03 type silicon micromechanical gyroscope" in 3.4.6 and the appearance should be consistent with the regulations in 3.5.2.

25. Sealing

The experiment is performed according to the conditions A1 and C1 in method 1014.2 of GJB 360A—1996. The test results should be consistent with requirement 3.4.7 and the appearance should be consistent with the regulations in 3.5.2.

- 26. High temperature life
- (1) Test equipment.
 - ① Constant temperature and humidity test box.
 - ② Speed turntable.
 - 3 DC regulated power supply.
 - 4 Voltmeter (or a data acquisition card).
 - (5) Test tool.

(2) Test method.

The high temperature life test is performed according to the following conditions.

- ① The gyroscope is installed on the special detection circuit module and then mounted in the central position of the rotating plane of the simulator motor fixture (built in the test box) such that the motor shaft is parallel to the horizontal direction.
- ② The power of the motor is connected such that the gyroscope and the detection circuit module rotate in the fixture (the rotating velocity is 17 Hz). The powers of the gyroscope and the detection circuit module are connected and powered and after 3 min the output voltage V_1 of the gyroscope is recorded.
- ③ The power of the motor is disconnected and the temperature is heated to 85 °C. Under the condition of 85 ± 2 °C, the gyroscope and the detection circuit module rotate in the fixture rotation (the rotating velocity is 17 Hz). After 3 min the output voltage of the gyroscope is recorded. After the recording is completed the power of the motor is disconnected again.
- 4 After the high temperature life test has been maintained for 250 h, normal atmospheric conditions are returned until the temperature of the gyroscope stabilizes. The power of the motor is connected such that the gyroscope and the detection circuit module rotate in the fixture (the rotation velocity is 17 Hz). After 3 min the output voltage V_2 of the gyroscope is recorded.
- (3) Detection method. The absolute value of the difference between the zero voltages V_1 and V_2 before and after the test should be consistent with the requirements of "the detail standard of CJS-DR-WB03 type silicon micromechanical gyroscope" in 3.4.8 and the appearance should be consistent with the regulations in 3.5.2.

Part III Applications of Non-driven Micromechanical Gyroscopes

Chapter 10 Signal Processing

10.1 Inhibiting the Influence of a Change in Rolling Angular Velocity of the Rotating Body on the Stability of the Output Signal

10.1.1 Influence of a Change in Rolling Angular Velocity of the Rotating Body on the Output Signal

A non-driven silicon micromechanical gyroscope is different from a conventional gyroscope which uses the rolling of the rotating body as the drive. Therefore the structure of a non-driven silicon micromechanical gyroscope is simple. However, the rolling angular velocity of the rotating flight carrier changes and the angular velocity is not stable such that the output stability of the micromechanical gyroscope is affected.

Figure 10.1 gives the relationship between the output voltage and the input angular velocity of a non-driven silicon micromechanical gyroscope (type CJS–DR–WB02–0606–0767). When the rolling velocity is constant, there is a good linear relation between the input and the output whose nonlinearity is less than 0.1%, but with different rolling angular velocities the scale factor is different. Tests of many micromechanical gyroscopes show that the angular velocity of the rotating body is unstable such that the scaling factor of the output voltage is changed. This can be compensated by modern computer technology.

10.1.2 Method for Inhibiting the Influence of a Change in Rolling Angular Velocity on the Output Signal

The output signal of a micromechanical gyroscope is

286 10 Signal Processing

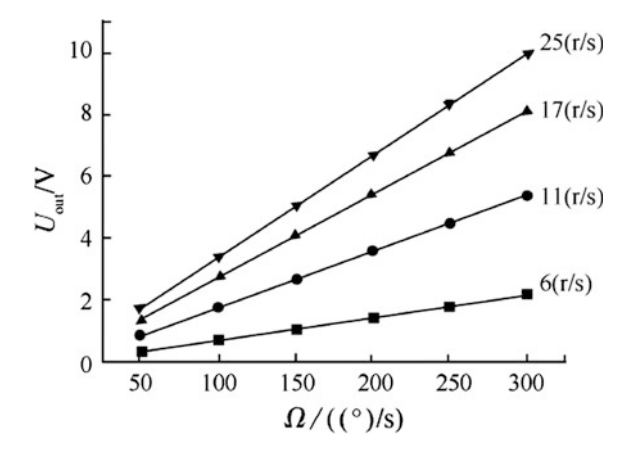


Fig. 10.1 Relationship between output voltage and input angular velocity of a micromechanical gyroscope (type CJS–DR–WB02–0606–0767)

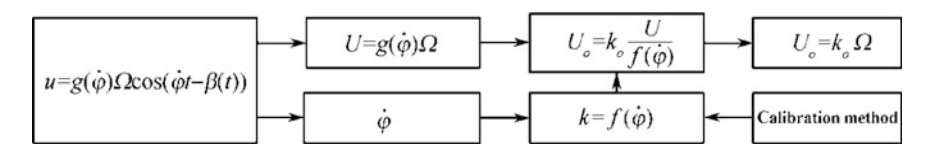


Fig. 10.2 Method for inhibiting rolling angular velocity

$$U = k\Omega \tag{10.1}$$

When the rolling angular velocity is constant, the scaling factor k is constant, but if the rolling angular velocity is changed, the scaling factor k is a variable value.

In order to inhibit the influence of rolling angular velocity on the output signal the method for inhibiting the rolling angular velocity is established, as shown in Fig. 10.2.

The detailed process is as follows:

- (1) Determining the relationship between the rolling angular velocity and the scale factor. The production process causes the performance of each micromechanical gyroscope to be different. First of all, the rolling angular velocity of the gyroscope is a specific value due to the calibration method, and the input angular velocity is changed. The corresponding output is determined according to the records of the experiment and this rolling angular velocity. By applying the method of least squares to the data, the scale factor of the micromechanical gyroscope can be obtained and recorded as $\{k_1, \dot{\varphi}_1\}$.
- (2) Change the rolling angular velocity and obtain $\{k_2, \dot{\varphi}_2\}, \dots, \{k_n, \dot{\varphi}_n\}$.
- (3) According to $\{k_1, \dot{\varphi}_1\}, \{k_2, \dot{\varphi}_2\}, \dots, \{k_n, \dot{\varphi}_n\}$, and by applying the method of least squares to the data in the polynomial form, that is,

$$k = f(\dot{\varphi}) = a_0 + a_1 \dot{\varphi} + a_2 \dot{\varphi}^2 + \dots + a_n \dot{\varphi}^n$$
 (10.2)

Determine the parameters $a_i (i=0,1,...,n)$ such that the mean square error $\sum_{i=1}^{n} \left[k_i - k(\dot{\varphi}_i)\right]^2$ has the minimum value. By using the Lagrangian method, the mean square error can be obtained.

By using the fitting method the mean square error can be obtained and the error decreases with an increase of the fitting order. This shows that the higher the order of the polynomial is, the better the effect of fitting is. However, with the increase of the polynomial's order, the effect of reducing the mean square error is gradually weakened. In addition, the higher the order of the model is, the greater the computational complexity of the system is. When the order reaches five the calculation of the polynomial coefficient is more difficult and it will affect the real-time performance of the system. Thus this book will use the three order polynomial model.

(4) Establish the linear relationship between the input and output of the gyroscope. From (6.20) the output voltage amplitude of a micromechanical gyroscope can be obtained, i.e.

$$U = \frac{(J_z + J_y - J_x)K_s\dot{\phi}}{\sqrt{[(J_z - J_x - J_y)\dot{\phi}^2 + K_T]^2 + (D\dot{\phi})^2}}\Omega = g(\dot{\phi})\Omega$$
(10.3)

Denote

$$U_o = k_o U / f(\dot{\varphi}) \tag{10.4}$$

where k_o is a constant scale factor, because

$$g(\dot{\varphi}) \approx f(\dot{\varphi})$$

Thus Eq. (10.4) can be changed into

$$U_o = k_o \Omega \tag{10.5}$$

From Eq. (10.5) it can be seen that there is a proportional relationship between the output voltage amplitude and the input angular velocity which can:

- ① Inhibit or reduce the influence of the change of the rolling angular velocity on the output signal of a micromechanical gyroscope.
- ② Normalize the scale factor of the gyroscope and improve the consistency of the scale factor of the gyroscope.

10.1.3 Validation of Inhibiting Influence Method

1. The output of the micromechanical gyroscope with different angular velocity and input angular velocity

The three-axis turntable is used to test the micromechanical gyroscope (Type CJS–DR–WB02–0806–0776). When the rolling velocity is 6, 8, 11, 12, 13, 15.5, 17, 19, 20 and 25 r/s respectively, the input angular velocities 30, 70, 125, 150 and 180(°)/s are selected as the test point. From the test the output voltage signal of the micromechanical gyroscope (mV) can be seen in Table 10.1.

2. Calculating the scale factor of the gyroscope with different rolling velocities

The relationship between the output signal and the input angular velocity is shown in Fig. 10.3 and by using the least square method the scale factor of the gyroscope with different rolling velocities can be obtained and is shown in Table 10.2.

3. Determine the relationship between the rolling velocity and the scale factor of the gyroscope

The angular velocities are selected as 6, 8, 11, 13, 15.5, 17, 20 and 25 r/s, and the fitting equation is

$$k = 0.77227 + 2.35383 \,\dot{\varphi} - 0.04256 \,\dot{\varphi}^2 \tag{10.6}$$

The result is shown in Fig. 10.4 and the fitting mean square error is 0.9995. Equation (10.2) is used to calculate the scale factor. The values of the scale factor are compared with the real values as shown in Table 10.2.

	-				-					
φ (r/s)	Ω (°/s)									
	0	30	70	125	150	180				
6	10	405.0	948.0	1671.0	2048.0	2368.5				
8	12	513.0	1198.0	2129.5	2566.5	3078.5				
11	11	651.5	1502.0	2674.5	3217.0	3856.0				
12	9	686.7	1602.2	2861.1	3433.3	4120.0				
13	10	721.0	1664.0	2960.5	3558.0	4292.5				
15.5	11	810.5	1894.0	3406.0	4077.5	4897.0				
17	10	872.5	2020.0	3595.0	4300.0	5154.0				
19	10.2	903.9	2109.1	3766.2	4519.5	5423.4				
20	10	940.0	2184.5	3885.0	4643.5	5564.0				
25	9	1004.5	2327.0	4125.0	4949.5	5938.0				

Table 10.1 Output voltage signal of the micromechanical gyroscope in the test

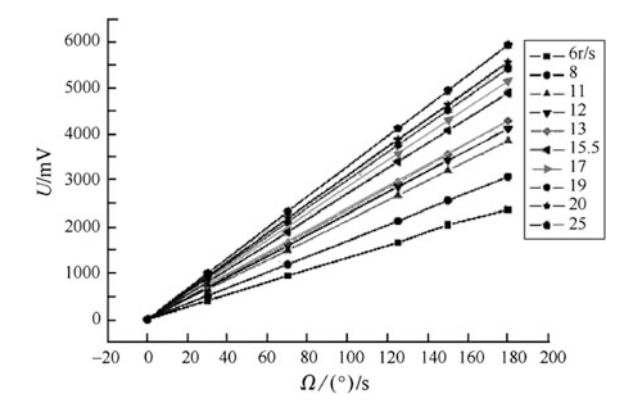
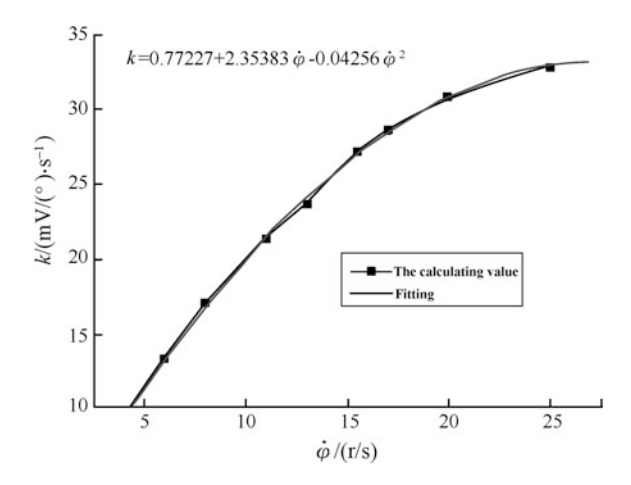


Fig. 10.3 Relationship between input angular velocity and output signal

Table 10.2 Scale factor of the gyroscope with different rolling angular velocities

Rolling angular velocity (r/s)	Scale factor (mV/	° s ⁻¹)	Relative error (%)
	Measured value	Calculated value	
6	13.34	13.36	0.15
8	17.09	16.88	1.24
11	21.40	21.51	0.51
12	22.89	22.89	0.00
13	23.77	24.18	1.70
15.5	27.23	27.03	0.74
17	28.62	28.49	0.46
19	30.13	30.13	0.00
20	30.90	30.82	0.26
25	32.94	33.02	0.24

Fig. 10.4 Relationship between scale factor and rolling velocity

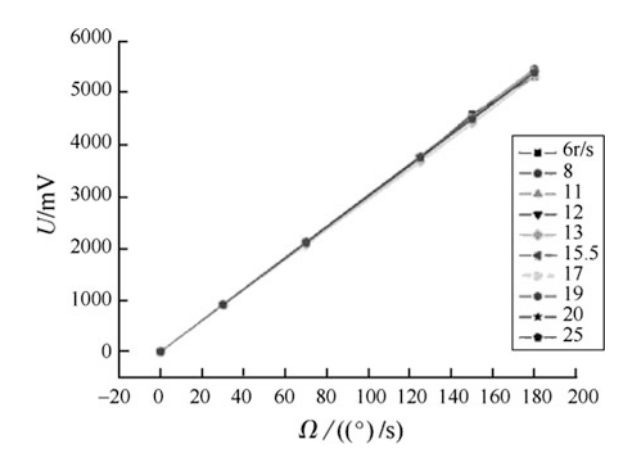


290 10 Signal Processing

$\dot{\varphi}$ (r/s)	Ω (°/s)					
	0	30	70	125	150	180
6	11	909.25	2128.31	3751.49	4597.87	5317.41
8	10	911.81	2129.32	3784.97	4561.69	5471.72
11	11	908.48	2094.45	3729.42	4485.91	5376.95
12	10	896.50	2099.82	3749.35	4500.20	5397.89
13	11	894.59	2064.62	3673.27	4414.62	5325.96
15.5	12	899.53	2102.05	3780.13	4525.39	5434.91
17	11	918.85	2127.31	3785.98	4528.43	5427.79
19	11	899.97	2099.72	3749.90	4501.06	5399.65
20	12	914.87	2126.11	3781.15	4519.38	5415.28
25	10	912.72	2114.37	3748.08	4497.25	5395.42

Table 10.3 Compensated output voltage of the gyroscope with different rolling angular velocities

Fig. 10.5 Relationship between output voltage and input angular velocity after compensation



4. The compensated output voltage

Assume that $k_o = 30.00 \,\text{mV}/^{\circ} \,\text{s}^{-1}$, and according to Eq. (10.4) the amplitude of the compensated output voltage (mV) is shown in Table 10.3 and Fig. 10.5.

According to the output, the scaling factor can be calculated and the calculation results are shown in Table 10.4.

Comparing Figs. 10.3 and 10.5 it can clearly be seen that after compensation the consistency of the scaling factors with different rolling angular velocities can be improved.

According to the above results the micromechanical gyroscope is tested again. For three axis angular velocities of the three-axis turntable, the frame angular velocities are set as 6, 7, 10, 11, 12, 15, 16, 18, 22 and 24 r/s, and the input angular

Rolling velocity (r/s)	Scaling factor (mv/° s ⁻¹)	Rolling velocity (r/s)	Scaling factor (mv/° s ⁻¹)
6	30.18	17	30.33
8	30.38	19	30.00
11	29.96	20	30.27
12	29.97	25	30.11
13	29.54	Average value	30.09
15.5	30.12		

Table 10.4 Scaling factors of a micromechanical gyroscope with different rolling angular velocities

Table 10.5 Comparison of actual output voltage and theoretical output voltage of a micromechanical gyroscope

φ (r/s)	20		80		120		140		170	
	c	t	c	t	c	t	c	t	c	t
6	600	609.3	2400	2428.2	3600	3601.5	4200	4267.8	5100	5117.5
7	600	611.7	2400	2429.4	3600	3635.1	4200	4261.8	5100	5171.7
10	600	608.4	2400	2394.0	3600	3579.3	4200	4185.9	5100	5076.9
11	600	596.4	2400	2400.0	3600	3599.4	4200	4200.3	5100	5097.9
12	600	594.6	2400	2364.6	3600	3613.2	4200	4114.5	5100	5025.9
15	600	599.4	2400	2402.1	3600	3630.0	4200	4225.5	5100	5134.8
16	600	618.9	2400	2427.3	3600	3636.0	4200	4228.5	5100	5127.9
18	600	615.0	2400	2426.1	3600	3631.2	4200	4219.5	5100	5115.3
22	600	615.0	2400	2426.1	3600	3601.2	4200	4219.5	5100	5115.3
24	600	612.6	2400	2414.4	3600	3658.2	4200	4197.3	5100	5095.5
Maximum relative error (%)	3.2		1.5		1.6		2.0		1.5	

velocities under different rolling angular velocities are respectively set as 20, 80, 120, 140 and 170° /s. For different rolling angular velocities and different input angular velocities the output voltage (mV) and the amplitude of the theoretical output voltage (mV) of a micromechanical gyroscope are compared as shown in Table 10.5 where c and t represent the amplitude of the theoretical output voltage and the amplitude of the actual output voltage respectively.

A micromechanical gyroscope (type CJS–DR–WB02–0806–0776) is analyzed. From Table 10.5, it can be observed that the maximum relative error between the theoretical output voltage (the scale factor is $k_o = 30.00 \text{ mV/}^{\circ} \text{ s}^{-1}$ and the actual output voltage is 3.2%. In view of the whole calculation process, the main factor that affects the accuracy of the algorithm is the nonlinearity of the scale factor of a gyroscope with different rolling velocities.

10.2 The Attitude Demodulation Method of a Micromechanical Gyroscope Based on Phase Difference

The frequency of the output signal for a non-driven micromechanical gyroscope is related to the rolling velocity of the rotating flight carrier, while the envelope amplitude of the output signal is proportional to the input angular velocity (the angular velocity combined by the pitch and the yaw). Therefore, according to the usage requirement it is necessary to decompose the pitch angular velocity and the yaw angular velocity, and this decomposition needs a benchmark. If we can determine the deflecting direction of the carrier in the inertial space, the pitch angular velocity and the yaw angular velocity can be decomposed orthogonally. Therefore, the gravity acceleration meter is regarded as the reference signal and the phase difference between the output signal of the micromechanical gyroscope and the reference signal can determine the deflecting direction of the rotating flight carrier in the geographic coordinates, and the pitch angular velocity and the yaw angular velocity can be obtained.

10.2.1 Study of the Phase Difference Between the Output Signal and the Reference Signal of the Gyroscope

The phase difference between the output signal and the reference signal of a micromechanical gyroscope can reflect the deflecting direction of the rotating flight carrier in the geographic coordinates. The principle and demonstration of the method will be discussed in detail.

1. Establishment of the reference coordinate system

In order to get the self-rotating signal of the rotating flight carrier in flight, a MEMS gravity accelerometer is integrated in the circuit. Because the gravity accelerometer is sensitive to the self-rotating of the rotating flight carrier, the spatial position of the rotating flight carrier can be obtained from this self-rotating signal, and the spatial position of the sensitive axis for the gravity accelerometer can be obtained. The position of the sensitive axis can be obtained from the relative position of the silicon micromechanical gyroscope and the accelerometer in the circuit. So in this scheme, the role of the gravity accelerometer is to provide the azimuth reference, which is different from the effect of the accelerometer in the strap down or the platform inertial navigation system combined with the common gyroscope and the accelerometer. The output signal frequency of the accelerometer does not change with the change of the pitch or the yaw of the rotating flight carrier, and is related only to the spatial position of the self-rotating of the rotating flight

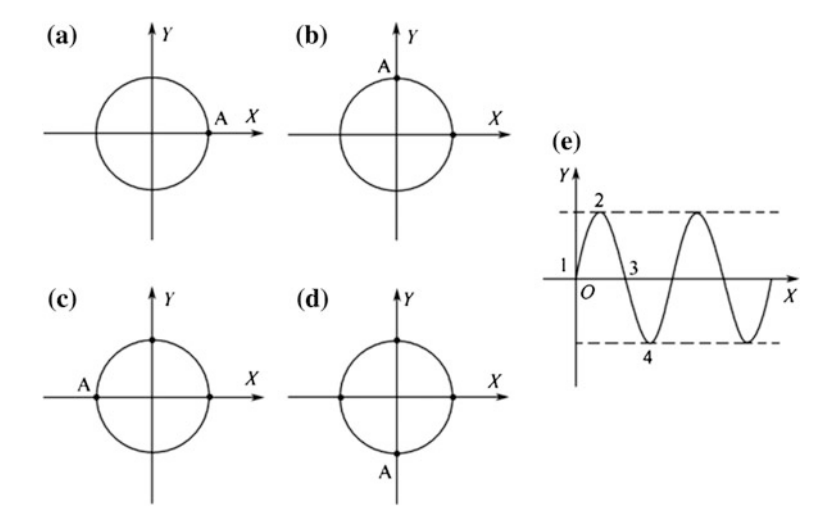


Fig. 10.6 Spatial angular position and its electric angle position of the rotating carrier

carrier. So it can always provide the position signal of the rotating flight carrier in flight.

The establishing process of the specific reference coordinate system is as follows:

As shown in Fig. 10.6, a reference point A is selected on the rotating flight carrier (can be the position of the rudder for the rotating flight carrier) and is regarded as an axis to establish a coordinate system (Fig. 10.6a). The sensitive axis of the accelerometer is installed on the axis line which is vertical to the axis of A. When the point A on the rotating flight carrier rotates in a positive direction of the coordinate X axis (Fig. 10.6a), the output is zero (corresponding to point 1 in Fig. 10.6e); When point A on the rotating flight carrier rotates in the positive direction of the coordinate Y axis (Fig. 10.6b), the output is maximum (corresponding to point 2 in Fig. 10.6e); When point A on the rotating flight carrier rotates in the negative direction of the coordinate X axis (Fig. 10.6c), the output is zero (corresponding to point 3 in Fig. 10.6e); When point A on the rotating flight carrier rotates in the negative direction of the coordinate Y axis (Fig. 10.6d), the output is the peak value in the negative direction (corresponding to the point 4 in Fig. 10.6e). Thus a coordinate system which relies on the rotating flight carrier is established (the coordinate system in Fig. 10.6e), and the waveform in this reference coordinate system is the required reference waveform. The later work for phase comparison is based on this waveform.

2. Phase comparison

In the deflection process of the rotating flight carrier the moment of momentum and the external moment are always in the vertical position, that is, a Coriolis force is always applied on the silicon pendulum of the micromechanical gyroscope. But because there is a sensitive axis in the micromechanical gyroscope, when the direction of the Coriolis force is vertical to that of the sensitive axis, maximum torque is applied to the silicon pendulum such that the deflection of the pendulum around the sensitive axis is maximum. When the direction of the Coriolis force is parallel to that of the sensitive axis the Coriolis force cannot be applied to the silicon pendulum, and only to the sensitive axis such that the silicon pendulum cannot deflect and the output signal is zero. Thus when the output signal of the gyroscope is the peak value of the sine wave, it can be concluded that the sensitive axis of the gyroscope is vertical to the deflection surface of the rotating flight carrier. Thus, if the spatial location of the sensitive axis is known, the rotation plane of the rotating flight carrier can be obtained. In order to obtain the spatial position of the sensitive axis of the gyroscope, the output signal of the gravity accelerometer is needed. When the gyroscope and the accelerometer are combined, the relative positions of these two sensitive axes are determined, while the spatial position of the sensitive axis of the accelerometer can be determined by the output signal. For example, when the sensitive axis of the accelerometer is parallel to the diameter of point A in the coordinate of Fig. 10.6, according to the output signal of the accelerometer, the sensitive axis rotates to the spatial position with the rotation of the rotating flight carrier. According to the above relationships among the deflection direction of the rotating flight carrier, the sensitive axis of the gyroscope and the sensitive axis of the accelerometer and the output signal of the accelerometer, the deflection direction of the rotating flight carrier in the flight can ultimately be determined.

3. Determination of the deflection direction

Compare the output waveforms and if their phase difference is zero (Fig. 10.7a), the datum point output which is relative to the coordinate reference is also zero at this time, thus the rotating plane of the rotating flight carrier is vertical to the sensitive axis of the gyroscope and the deflection direction of the rotating flight carrier in this plane is left. If the phase difference between the output waveform and the reference waveform is 90° (Fig. 10.7b), the datum point output which is relative to the reference coordinate is the peak value, thus the rotating plane of the rotating flight carrier is parallel to the sensitive axis of the gyroscope and the deflection direction of the rotating flight carrier in this plane is upward. If the phase difference between the output waveform and the reference waveform is 180° (Fig. 10.7c), at this time the datum point of the output voltage which is relative to the reference coordinate is zero, thus the rotating plane of the rotating flight carrier is vertical to the sensitive axis of the gyroscope, and the rotating direction of the rotating flight carrier in this plane is right. If the phase difference between the output waveform and the reference waveform is 270° (Fig. 10.7d), at this time the datum point of the output voltage which is relative to the reference coordinate is the maximum negative, thus the rotating plane of the rotating flight carrier is parallel to the sensitive axis of the gyroscope, and the rotating direction of the rotating flight carrier in this plane is downward. In Fig. 10.7, A is the reference signal, B is the output signal of the gyroscope, and Fig. 10.7a–d are the waveforms of two signals when the phase difference is 0°, 90°, 180° and 270° respectively.

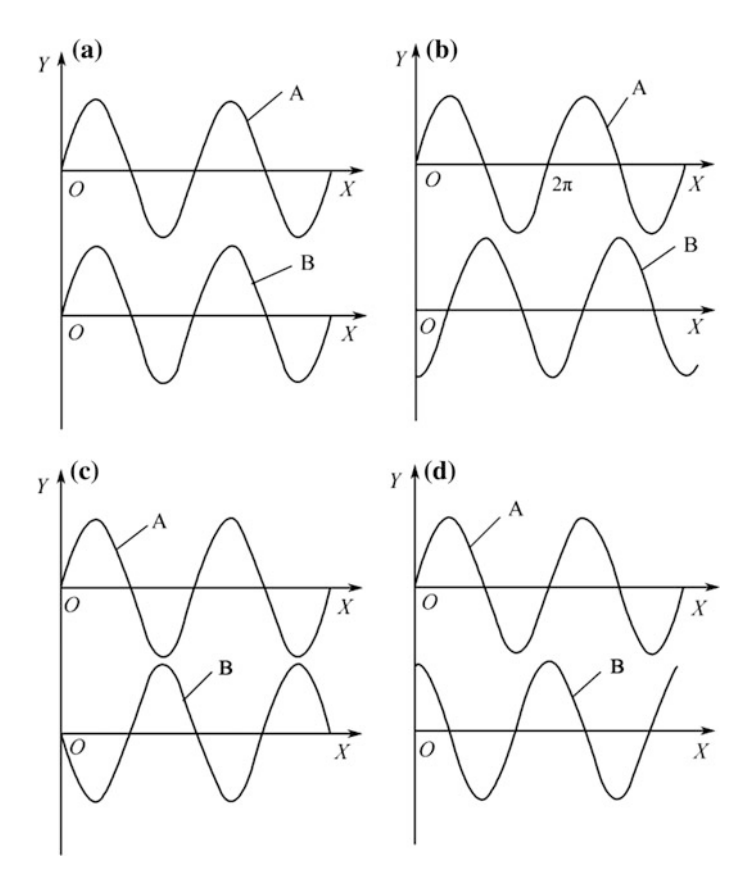


Fig. 10.7 Comparison of output waveforms with different phase differences

Through the above analysis, it can be seen that if the phase difference between the output waveform and the reference waveform are compared, the rotating direction of the rotating flight carrier in flight can be determined. As shown in Fig. 10.8a, when the phase difference between the output waveform and the reference waveform is 60°, the deflection direction of the rotating flight carrier in flight is shown in Fig. 10.8b. As soon as the phase difference between the output signal of the micromechanical gyroscope and the rolling signal (the reference signal) of the rotating flight carrier can be measured, the rotating direction of the rotating flight carrier can be determined.

1. In the case of a constant angular velocity, the relationship between the phase difference and the deflection direction

For the MEMS gravity accelerometer mounted on a rotating flight carrier, the output of the accelerometer is a sinusoidal signal when the rotating flight carrier rotates for one circle, that is,

296 10 Signal Processing

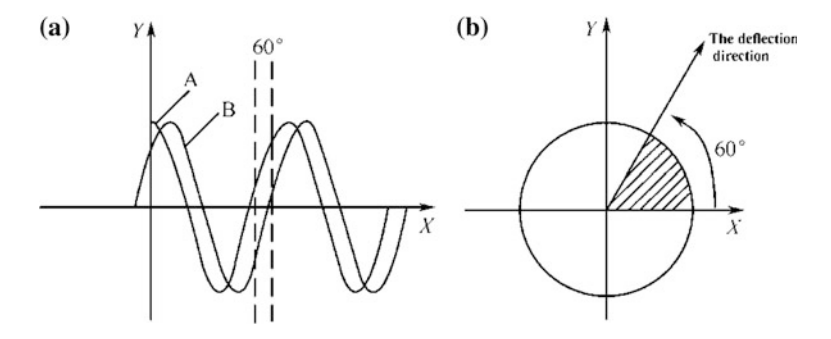


Fig. 10.8 Deflection direction of the corresponding rotating flight carrier in flight when the phase difference is 60°

$$u_{\text{accelerometer}} = K_{\text{accelerometer}} \cos(\dot{\varphi}t - \theta)$$
 (10.7)

where θ is a fixed phase related to the installation location. The output signal of the micromechanical gyroscope is

$$u = K_s f(\dot{\varphi}) \left[\Omega_{\xi} \cos(\dot{\varphi}t) + \Omega_n \sin(\dot{\varphi}t) \right] = K_s f(\dot{\varphi}) \Omega \cos(\dot{\varphi}t - \beta(t))$$
 (10.8)

The difference between the two signals is

$$\Delta \theta = \theta - \beta(t)$$

Assuming that the rotating flight carrier rotates at a constant speed and the deflection direction is right, $\beta(t)$ is a constant phase, and their difference is

$$\Delta \theta = \theta - \beta(t) = \theta_1 \tag{10.9}$$

(1) If at this time the rotating flight carrier rotates at a constant speed upwards, the change of the deflection direction is 90°, that is, the change of the initial phase difference is 90°, then the output is

$$u = K_s f(\dot{\varphi}) \Omega \cos(\dot{\varphi}t - \beta(t) - 90^\circ) \tag{10.10}$$

$$\Delta\theta = \theta - \beta(t) = \theta_1 + 90^{\circ} \tag{10.11}$$

(2) If at this time the rotating flight carrier rotates at a constant speed and the deflection direction is left, the change of the deflection direction is 180°, that is, the change of the initial phase difference is 180°, then the output is

$$u = K_s f(\dot{\varphi}) \Omega \cos(\dot{\varphi}t - \beta(t) - 180^\circ) \tag{10.12}$$

$$\Delta\theta = \theta - \beta(t) = \theta_1 + 180^{\circ} \tag{10.13}$$

(3) If at this time, the rotating flight carrier rotates at a constant speed and the deflection direction is upwards, the change of the deflection direction is 270°, that is, the change of the initial phase difference is 270°, then the output is

$$u = K_s f(\dot{\varphi}) \Omega \cos(\dot{\varphi}t - \beta(t) - 270^\circ)$$
 (10.14)

$$\Delta\theta = \theta - \beta(t) = \theta_1 + 270^{\circ} \tag{10.15}$$

(4) If at this time the rotating flight carrier rotates at a constant speed and the deflection direction is right, the change of the deflection direction is 360°, that is, the change of the initial phase difference is 360°, then the output is

$$u = K_s f(\dot{\varphi}) \Omega \cos(\dot{\varphi}t - \beta(t) - 360^\circ)$$
 (10.16)

$$\Delta\theta = \theta - \beta(t) = \theta_1 + 360^{\circ} \tag{10.17}$$

The micromechanical gyroscope is installed on the precision turntable with three axes and by using the Agilent oscilloscope, the output signal of the gyroscope and the angular velocity output signal of the turntable are simultaneously observed as shown in Fig. 10.9; the rotating velocity of the inner frame of the controlled turntable is 10 Hz, the direction of the external frame (yaw) is left, and the angular velocity is 100°/s, which is shown in Fig. 10.9a, then the phase difference is -22° . If the external frame is stopped, and the middle frame (pitch) rotates upwards, the angular velocity is 100°/s, as shown in Fig. 10.9b, then the phase difference is 68°. If the middle frame is stopped, the direction of the external frame (yaw) is right, and the angular velocity is 100° /s, as shown in Fig. 10.9c, then the phase difference is 158° . If the external frame is stopped, the direction of the middle frame (pitch) is downward, and the angular velocity is 100° /s, as shown in Fig. 10.9d, then the phase difference is 250° .

It is clear that when the deflection direction of the inner frame is changed from left \rightarrow upward \rightarrow right \rightarrow downward, the phase difference between the signal of the micromechanical gyroscope and the signal of the gravity accelerometer is $-22^{\circ} \rightarrow 68^{\circ} \rightarrow 158^{\circ} \rightarrow 250^{\circ}$. When the change of the deflection direction is 90°, the change of the phase difference is 90°. That is, when the rotating flight carrier rotates through a circle in flight, the change of the phase difference is 360°. Thus, the space position of the rotating flight carrier can be determined by the phase difference.

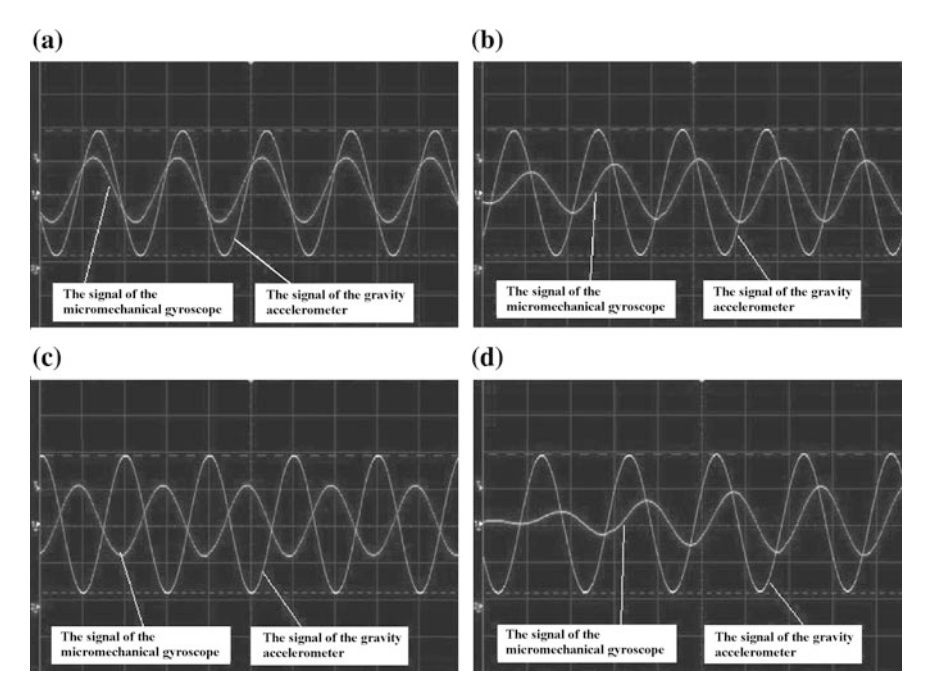


Fig. 10.9 Comparison of output signal and reference signal of the gyroscope with different deflection directions

2. The relationship between the phase difference and the deflection direction when the rotating flight carrier moves circularly and elliptically.

If the pitch and the yaw are synthesized into a circular motion, the yaw angular velocity is $\Omega_{\xi} = A_{\xi}\cos(\omega_1 t + \theta_1)$, the pitch angular velocity is $\Omega_{\eta} = A_{\eta}\cos(\omega_1 t + \theta_2)$, $A_{\xi} = A_{\eta}$, $\theta_1 = \theta_2 \pm \pi/2$, and the output signal of the micromechanical gyroscope is

$$u = \frac{1}{2} K_{s} f(\dot{\varphi}) A_{\xi} \cos((\dot{\varphi} \pm \omega_{1})t \pm \theta_{1})$$
(10.18)

while the output of the gravity accelerometer is

$$u_{\text{accelerometer}} = K_{\text{accelerometer}} \cos(\dot{\varphi}t - \theta)$$
 (10.19)

The phase difference between the signal of the micromechanical gyroscope and the signal of the gravity accelerometer is

$$\Delta\theta = \theta - \beta(t) = \pm(\omega_1 t + \theta_1) + \theta \tag{10.20}$$

Then the phase difference changes by a uniform velocity when the circular motion is a cycle and the phase difference is uniformly changed by 360° .

If the pitch and the yaw are synthesized into an elliptical motion the output signal of the micromechanical gyroscope is

$$u = K_s f(\dot{\varphi}) \Omega \cos(\dot{\varphi}t - \beta(t)) \tag{10.21}$$

where

$$\beta(t) = \arctan\left(\frac{A_{\eta}\cos(\omega_1 t + \theta_2)}{A_{\xi}\cos(\omega_1 t + \theta_1)}\right)$$
(10.22)

The phase difference between the signal of the micromechanical gyroscope and the signal of the gravity accelerometer is

$$\Delta\theta = \theta - \beta(t) = \theta - \arctan\left(\frac{A_{\eta}\cos(\omega_1 t + \theta_2)}{A_{\xi}\cos(\omega_1 t + \theta_1)}\right)$$
(10.23)

When the synthetic motion rotates through one circle, the phase difference changes by 360° in the form of a tangent change only rather than in the form of a linear change.

The micromechanical gyroscope is installed on the precision turntable with three axes. Assume that the rolling angular velocity is 17 r/s, and the frequencies of the pitch and yaw angular vibrations are 1 Hz and their phase difference is adjusted such that the composite motion are the circle and the ellipse respectively. The output signals of the micromechanical gyroscope and the accelerometer are collected by the acquisition system and the sampling frequency is 1 kHz, then the phase difference between two signals is calculated. When the motion trajectories are a circular motion and an elliptical motion, the phase differences are shown in Figs. 10.10 and 10.11 respectively.

It is seen that the phase difference of the two signals varies by 360° when the rotating flight carrier rotates through a circle in flight. According to the phase difference, the flight position of the rotating flight carrier can be judged.

Generally, the deflection direction of the carrier space can be determined by the phase difference of the signals of the micromechanical gyroscope and the accelerometer.

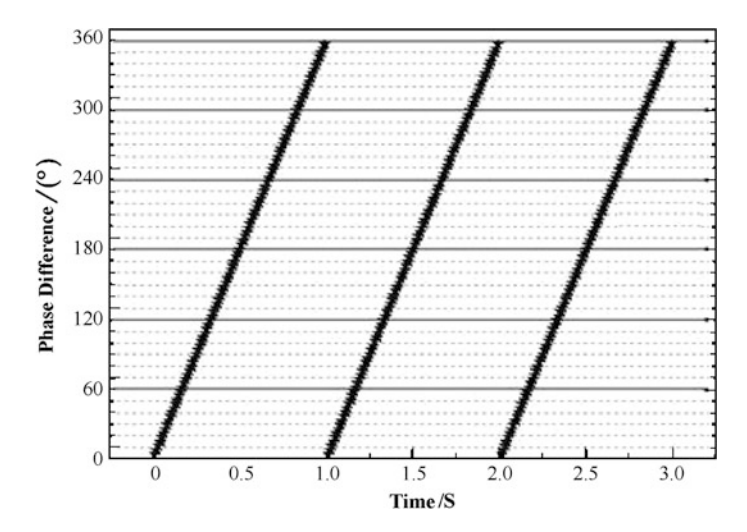


Fig. 10.10 Phase difference between signals of the micromechanical gyroscope and the accelerometer when the motion trajectory is a circular motion

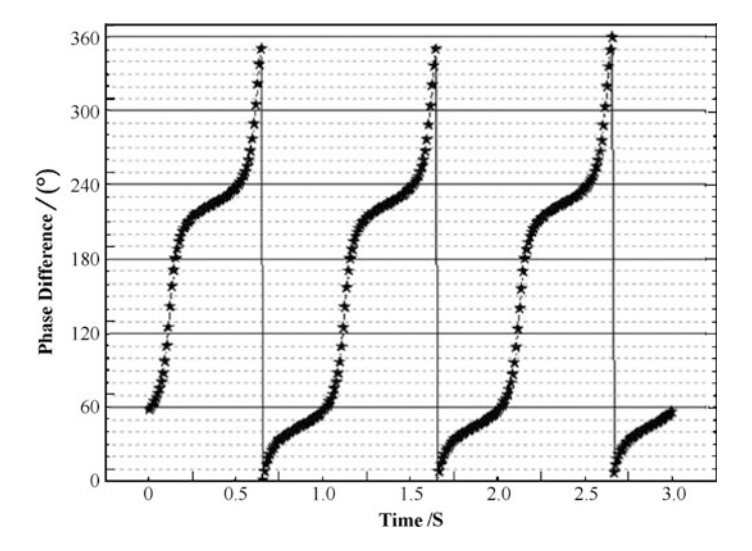


Fig. 10.11 Phase difference between signals of the micromechanical gyroscope and the accelerometer when the motion trajectory is elliptical

10.2.2 Factors Influencing Phase Difference

The phase difference can be used to determine the deflection direction of the rotating flight carrier in flight, and the input angular velocity can be decomposed into the pitch angular velocity and the yaw angular velocity by phase difference.

Phase difference is one of the key parameters in the decomposing process. Therefore, it is necessary to consider the factors that affect the phase difference and compensate for them according to the situation. In the practical application, factors that may affect the phase difference include the rolling angular velocity change, the input angular velocity change, the environmental temperature change and the complex motion modulation problem, etc.

1. The change in rolling angular velocity and input angular velocity

The phase difference between the signals of the micromechanical gyroscope and the accelerometer contains an initial value, that is, the installation angle between the gyroscope and the accelerometer, the lag phase between the gyroscope and the accelerometer, and the lag phase of the detection circuit. This initial value varies with changes of the rolling angular velocity and input angular velocity of the rotating flight carrier. In the practical application, the test calibration method is used to find the initial value of every gyroscope. The detailed test method is as follows:

- (1) Assume that both the rolling direction and the rotating direction of the rotating flight carrier are clockwise. At this time the reference point of the accelerometer is set to zero.
- (2) The composite device of the micromechanical gyroscope and the gravity accelerometer is installed on the test turntable. The yaw (the external frame) velocity of the turntable is set as Ω_1 , and the rolling (the inner frame) velocity is set as $\dot{\varphi}_1, \dot{\varphi}_2, \ldots, \dot{\varphi}_n$, respectively. The output signals of the gyroscope and the accelerometer are connected to the input channel and the reference channel of the phase meter respectively, and the phase difference of the two signals is recorded (the average value of several results).
- (3) Then the yaw velocity of the turntable is set as $\Omega_2, \Omega_3, \dots, \Omega_m$, respectively. According to Step (2), the phase difference between two output signals with every rolling frequency is recorded (the average value of several results).
- (4) According to the recorded data, the rolling velocity of the rotating flight carrier is denoted as the horizontal coordinate, the phase difference between the signals of the micromechanical gyroscope and the accelerometer is denoted as the vertical scale, and the relationship diagram between the phase difference and the rolling velocity of the gyroscope with rotating velocity $(\dot{\varphi}_1 \sim \dot{\varphi}_n)$ is drawn.
- (5) The test points of the micromechanical gyroscope are fitted into a curve. The rolling velocity of the rotating flight carrier is denoted as the independent variable, the phase difference of the micromechanical gyroscope and the accelerometer is denoted as a variable, and the expression for the function is established. According to this expression the corresponding initial difference can be obtained when the rotating flight carrier has any rolling velocity with the pass band.

According to the above test method, one of the gyroscopes (type: CJS-DR-WB01-0702-0614) is selected as an example to perform many of the tests. In the case of different rolling angular velocities and input angular velocities, the phase

Ω (°/s)	φ (r/s)	$\dot{\varphi}$ (r/s)								
	6	8	11	13	17	20	25			
50	92.8	96.0	105.4	111.0	121.2	126.2	137.8			
100	92.2	96.8	105.4	111.6	120.6	127.2	137.0			
150	94.8	98.4	107.4	111.8	122.6	129.4	139.4			
200	95.0	100.0	106.6	114.2	124.4	130.0	140.6			
Mean	93.7	97.8	106.2	112.2	122.2	128.2	138.7			

Table 10.6 Phase difference between signals of the micromechanical gyroscope and the accelerometer with different rolling angular velocities of the rotating flight carrier

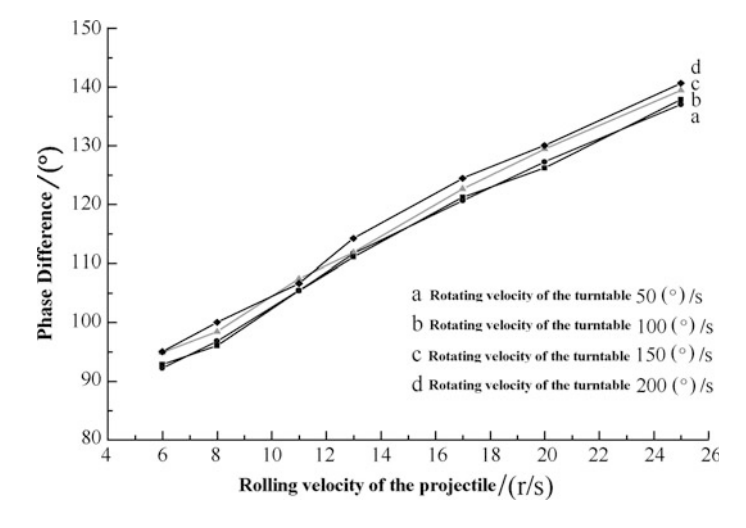
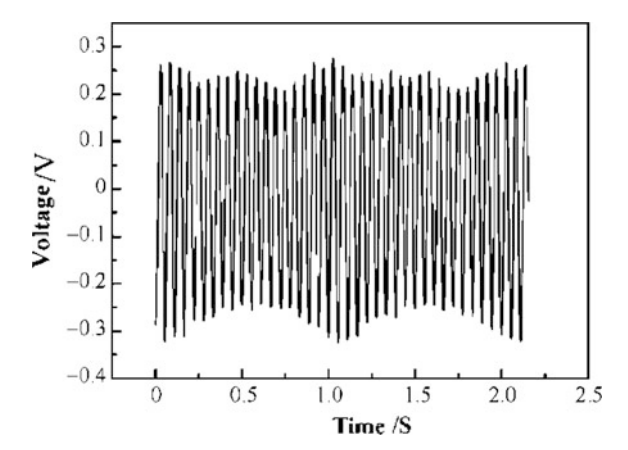


Fig. 10.12 Phase difference between signals of the micromechanical gyroscope and the accelerometer with different rolling angular velocities of the rotating flight carrier when the turntable deflects clockwise

difference between the signals of the micromechanical gyroscope and the accelerometer is obtained and the relationship with changing rolling angular velocities of the rotating flight carrier is shown in Table 10.6.

The positive phase difference presents the lead accelerometer signal of the micro-mechanical gyroscope. From Fig. 10.12 it can be seen that the effect of the rolling angular velocity on the initial phase difference is large, while the effect of the rotating velocity of the turntable is relatively small. In the test range, when the rolling angular velocity of the rotating increases from 6 to 25 r/s, the maximum phase difference between the output signals of the micro-mechanical gyroscope and the accelerometer is 45.6°. When the rotating velocity of the turntable increases from 50 to 200°/s, the maximum phase difference between the output signals of the micromechanical gyroscope and the accelerometer is 4°.

Fig. 10.13 Output signal of the gravity accelerometer



The signal of the accelerometer may be modulated when the rotating flight carrier is accompanied by pitch and yaw motions. The frequency change will lead to a change of the phase difference. In order to verify the experiment, a circuit with the gravity accelerometer is installed on the three-axis turntable and the inner frame of the turntable is set as 10 Hz. The equations of the pitch and yaw angular velocities are respectively,

$$\Omega_{\xi} = 31.4^{\circ} \cos(2\pi t + \pi/3)[(^{\circ})/s]$$
 (10.24)

$$\Omega_n = 31.4^{\circ} \cos(2\pi t + \pi/4)[(^{\circ})/s]$$
 (10.25)

The output signal of the gravity accelerometer is shown in Fig. 10.13. It can be seen that the amplitude of the output signal is modulated and its spectrum analysis is shown in Fig. 10.14. The theoretical value is 10 Hz, the frequency spectrum analysis is 10.0097656 Hz, and the relative error is 0.098%. The frequency of the accelerometer is not modulated and the motion mode has no effect on the frequency of the signal. Therefore, the phase difference between the micromechanical gyroscope and the accelerometer is not affected.

2. Temperature effect

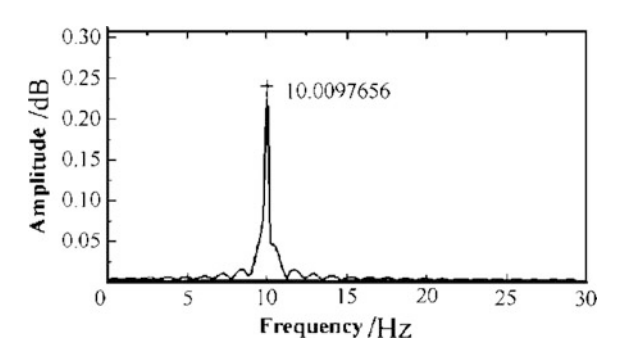
Temperature is an important environmental factor and the effect of temperature on the phase difference should be studied. The computer-controlled single axis turntable with a temperature experiment box is used to study the effect of temperature on the phase.

1. Experimental procedure

(1) The micromechanical gyroscope with the accelerometer is fixed on the turntable. Then according to the environmental indicators of the working temperature, select eight experimental temperatures: -20, -10, 0, 10, 20, 30, 40 and 50 °C. The working environment of the gyroscope is heated or cooled to the corresponding temperature by the temperature experimental box and the temperature

304 10 Signal Processing

Fig. 10.14 Output signal spectrum analysis of the gravity accelerometer



of the experimental box is controlled by the setting on the temperature control device. According to the working range of the gyroscope, select the rolling angular velocities 6 and 17 r/s as two experimental angular velocities, while the experimental yaw angular velocities are selected as 100, 200, 300, -100, -200 and -300° /s).

- (2) The temperature of the temperature box is heated to above 30 °C and any water vapor in the temperature box is removed.
- (3) Set the temperature of the experimental box as $T=-20\,^{\circ}\mathrm{C}$ until the temperature box displays $-20\,^{\circ}\mathrm{C}$, and maintain this temperature for 40 min. Set the rolling angular velocity of the gyroscope as $\dot{\varphi}=6\,\mathrm{r/s}$ and the rotating velocities Ω of the turntable as 100, 200, 300, -100, -200, $-300\,^{\circ}\mathrm{/s}$ in order. Then each group of values of three parameters is measured (the output voltage of the accelerometer, the output voltage of the gyroscope and the phase difference between the output waveforms of the accelerometer and the gyroscope).
- (4) Keep the environment temperature $T=-20\,^{\circ}\mathrm{C}$ unchanged and set the rolling angular velocity of the gyroscope as $\dot{\varphi}=17\,\text{r/s}$ and the rotating velocities Ω of the turntable as 100, 200, 300, -100, -200, $-300^{\circ}/\mathrm{s}$ in order. Then each group of values of three parameters is measured (the output voltage of the accelerometer, the output voltage of the gyroscope and the phase difference between the output waveforms of the accelerometer and the gyroscope).
- (5) Set the temperature T = -10 °C and maintain this temperature for 40 min. Set the rolling angular velocity of the gyroscope as $\dot{\varphi} = 6$ r/s and the rotating velocities Ω of the turntable as 100, 200, 300, -100, -200, -300°/s in order. Then each group of values of three parameters is measured (the output voltage of the accelerometer, the output voltage of the gyroscope and the phase difference between the output waveforms of the accelerometer and the gyroscope).
- (6) Keep the environment temperature $T=-10\,^{\circ}\mathrm{C}$ unchanged and set the rolling angular velocity of the gyroscope as $\dot{\varphi}=17\,\mathrm{r/s}$ and the rotating velocities Ω of the turntable as 100, 200, 300, -100, -200, $-300\,^{\circ}\mathrm{/s}$ in order. Then each group of values with three parameters is measured (the output voltage of the accelerometer, the output voltage of the gyroscope and the phase difference between the output waveforms of the accelerometer and the gyroscope).

Temperature (°C)	Ω (°/s)								
	100	200	300	-100	-200	-300			
-20	110	112	113	-70	-68	-68			
-20 -10	109	112	112	-69	-70	-68			
0	110	111	113	-69	-69	-67			
10	111	112	113	-70	-70	-66			
20	111	112	112	-68	-70	-68			
30	110	113	113	-68	-69	-68			
40	111	112	113	-69	-68	-67			
50	110	113	113	-70	-70	-67			

Table 10.7 Phase differences with different temperatures and different input angular velocities when the rolling angular velocity is 6 r/s

Table 10.8 Phase differences with different temperatures and different input angular velocities when the rolling angular velocity is 17 r/s

Temperature (°C)	Ω (°/s)					
	100	200	300	-100	-200	-300
-20 -10	129	130	132	-50	-49	-48
-10	129	129	132	-51	-50	-49
0	130	131	131	-52	-49	-49
10	129	129	132	-51	-50	-48
20	130	129	130	-50	-50	-49
30	129	130	132	-52	-49	-49
40	129	129	132	-50	-50	-48
50	130	130	132	-52	-49	-50

- (7) And so on, test a set of values every 10 °C, and record them until the temperature is 50 °C.
 - 2. The experimental result. The micromechanical gyroscope is tested according to the above test method and the test results of No. 0702-0619 of type CJS-DR-WB01 type are shown in Tables 10.7 and 10.8.

Figures 10.15 and 10.16 show the phase difference change of the micromechanical gyroscope and the accelerometer when the rolling angular velocities are 6 and 17 r/s at different temperatures and different input angular velocities respectively. The experiments show that the phase difference is small ($<3^{\circ}$) at different temperatures.

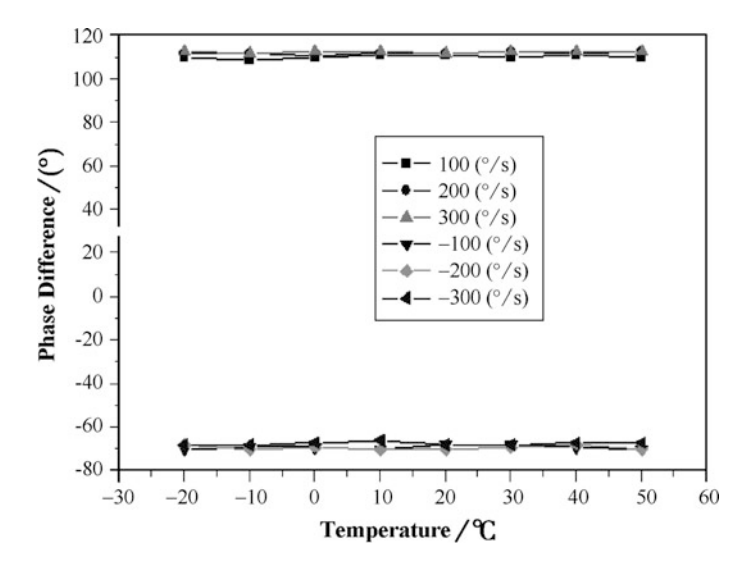


Fig. 10.15 Phase difference change when the rolling angular velocity is 6 r/s at different temperatures and different input angular velocities

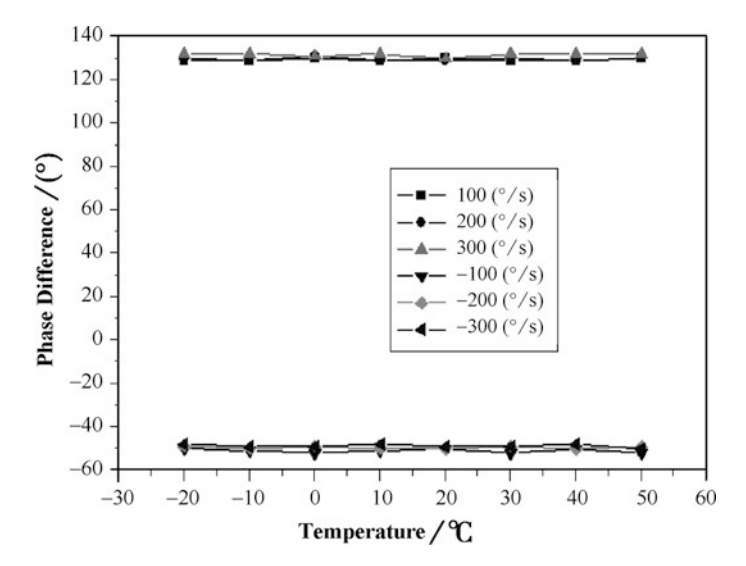


Fig. 10.16 Phase difference change when the rolling angular velocity is 17 r/s at different temperatures and different input angular velocities

10.2.3 Phase Difference Compensating Method

According to the above results, the effect of the rolling angular velocity on the phase is biggest, followed by the effect of the input angular velocity. The phase difference compensating method is as follows:

(1) Determine the rolling angular velocity and the relationship between the change of the measured angular velocity and the phase difference. When the measured data of the phase difference output for the gyroscope and the accelerometer are dealt with, the average value of *m* number of the sampled data of each test point is regarded as the recording data to eliminate the influence of white noise and vibration noise from the turntable.

At every fixed rolling angular velocity, the relationship between the phase difference $\Delta\theta$ and the input angular velocity Ω can be fitted by the following *n*-order polynomial:

$$\Delta\theta(\Omega) = a_0 + a_1\Omega + a_2\Omega^2 + \dots + a_n\Omega^n \tag{10.26}$$

At the constant input angular velocity, the relationship between phase difference $\Delta\theta$ and rolling angular velocity $\dot{\phi}$ can be fitted by the following *m*-order polynomial:

$$\Delta\theta(\dot{\varphi}) = b_0 + b_1 \dot{\varphi} + b_2 \dot{\varphi}^2 + \dots + b_m \dot{\varphi}^m$$
 (10.27)

Because the phase difference is not only a function of the rolling angular velocity but is also related to the input angular velocity, the coefficients a_i and b_i in Eqs. (10.26) and (10.27) are not constant. Rather a_i is a variable that is related to the rolling angular velocity and b_i is a variable that is related to the input angular velocity. Therefore, by considering the influence of the rolling angular velocity and the input angular velocity, the phase difference can be expressed as a two-variable function of the rolling angular velocity and the input angular velocity:

$$\Delta \theta = f(\dot{\varphi}, \Omega) \tag{10.28}$$

(2) A model for the combined effect of the angular velocity and the input angular velocity of the micromechanical gyroscope. The following model with a double input and a single output is taken as the model of the combined influence of the rolling angular velocity and the input angular velocity of the gyroscope (considering the computing complexity and the influence, select n = 2 and m = 3):

$$\Delta\theta = \Omega \cdot C \cdot \dot{\varphi} \tag{10.29}$$

308 10 Signal Processing

where

$$\begin{split} \Delta\theta &= \begin{bmatrix} \Delta\theta_{11} & \Delta\theta_{12} & \Delta\theta_{13} & \Delta\theta_{14} \\ \Delta\theta_{21} & \Delta\theta_{22} & \Delta\theta_{23} & \Delta\theta_{24} \\ \Delta\theta_{31} & \Delta\theta_{32} & \Delta\theta_{33} & \Delta\theta_{34} \\ \Delta\theta_{41} & \Delta\theta_{42} & \Delta\theta_{43} & \Delta\theta_{44} \end{bmatrix} \\ \Omega &= \begin{bmatrix} \Omega_1^2 & \Omega_1^1 & \Omega_1^0 \\ \Omega_2^2 & \Omega_2^1 & \Omega_2^0 \\ \Omega_3^2 & \Omega_3^1 & \Omega_3^0 \end{bmatrix} \\ C &= \begin{bmatrix} C_{11} & C_{12} & C_{13} & C_{14} \\ C_{21} & C_{22} & C_{23} & C_{24} \\ C_{31} & C_{32} & C_{33} & C_{34} \end{bmatrix} \\ \dot{\varphi} &= \begin{bmatrix} \dot{\varphi}_1^3 & \dot{\varphi}_2^3 & \dot{\varphi}_3^3 & \dot{\varphi}_4^3 & \dot{\varphi}_5^3 & \dot{\varphi}_5^3 & \dot{\varphi}_5^3 \\ \dot{\varphi}_1^2 & \dot{\varphi}_2^2 & \dot{\varphi}_3^2 & \dot{\varphi}_4^2 & \dot{\varphi}_5^2 & \dot{\varphi}_5^2 & \dot{\varphi}_5^2 \\ \dot{\varphi}_1^1 & \dot{\varphi}_2^1 & \dot{\varphi}_3^1 & \dot{\varphi}_4^1 & \dot{\varphi}_5^1 & \dot{\varphi}_5^1 & \dot{\varphi}_5^1 \\ \dot{\varphi}_1^0 & \dot{\varphi}_2^0 & \dot{\varphi}_3^0 & \dot{\varphi}_4^0 & \dot{\varphi}_5^0 & \dot{\varphi}_5^0 & \dot{\varphi}_5^0 \end{bmatrix} \end{split}$$

(3) According to the recorded data, C can be obtained by using Eq. (10.29) and the actual initial phase difference is

$$\theta = \theta_{\text{measured}} - \Delta\theta \tag{10.30}$$

According to the above method the phase of the micromechanical gyroscope (CJS–DR–WB type 02–0606–0767) is compensated. According to Eq. (4.20), the matrix C is determined and then the phase difference $\Delta\theta$ is calculated at 40, 80, 120, and 180°/s. The calculated value is compared with the actual measured phase difference in Table 10.9, where t is the measured value and C is the calculated value.

According to Table 10.9, the absolute error of the phase difference can be calculated at different rolling angular velocities and different input angular velocities as shown in Table 10.10. After compensation, the maximum absolute error of the initial phase difference is less than 2°.

Table 10.9 Measured value and theoretical value of the phase difference at different rolling angular velocities and different input angular velocities

)	,					
Ω (°/s)	φ(r/s)													
	9		8		11		13		17		20		25	
	c	t	c	t	c	t	c	t	c	t	C	t	c	t
40	92.4	91.75	96.2		105.3	105.28	109.7	110.45	119.4	120.27	125.9	127.11		137.34
80	92.7	92.58	6.96	97.84	105.9	105.76	110.6	110.98	119.4	120.98	126.3	127.87		137.59
120	94.5	93.70	98.2	98.77	107.6	107.6 106.64 112.8 11	112.8	111.91	122.7	111.91 122.7 122.14 1	128.4	129.16	139.6	138.69
180	95.3	95.09	7.66	100.04	106.8	107.91	113.5	113.27	122.9	123.14	132.0	131.0		140.65

Ω	$\dot{\varphi}(r/s)$						
(°/s)	6	8	11	13	17	20	25
	Absolute error (°)	Absolute error (°)	Absolute error (°)	Absolute error (°)	Absolute error (°)	Absolute error (°)	Absolute error (°)
40	-0.65	1.06	-0.02	0.75	0.87	1.21	0.54
80	-0.12	0.94	-0.14	0.38	1.58	1.57	-0.21
120	-0.8	0.57	-0.96	-0.89	-0.56	0.76	-0.91
180	-0.21	0.34	1.11	-0.23	0.24	-1	-0.55

Table 10.10 Absolute error of the phase difference at different rolling angular velocities and different input angular velocities

10.3 Posture Demodulation of the Rotating Body Based on the Micromechanical Gyroscope

The output signal of the micromechanical gyroscope is a modulated signal which contains three angular velocities of roll, yaw and pitch. If the rotating flying carrier of the rolling and rotating flight carrier only performs the yaw or pitch motion, the output signal frequency of the micromechanical gyroscope is equal to the rolling angular velocity of the rotating flight carrier, and the amplitude of the signal envelope is proportional to the yaw or pitch angular velocity. However, if the rotating flight carrier performs the pitch and yaw motion, the output signal frequency of the micromechanical gyroscope will be modulated, while the amplitude of the signal envelope is proportional to the yaw and pitch angular velocities combined. How to extract three roll, yaw and pitch angular velocities from the complex signal provides the control basis for the multi-channel control system of the rotating flight carrier and becomes the key technology of the micromechanical gyroscope.

10.3.1 Demodulation Method

From signal spectrum analysis of the micromechanical gyroscope, the rolling angular velocity of the rotating flight carrier can be obtained or the rolling angular velocity is obtained by using the signal of the accelerometer since they are equal. The envelope amplitude of the output signal can be used to calculate the pitch and yaw angular velocity, while the pitch and yaw angle is exactly equal to the phase difference between the signals of the micromechanical gyroscope and the accelerometer. Therefore, the micromechanical gyroscope demodulates to the roll, yaw and pitch angular velocity algorithm of the rotating flight carrier. The corresponding algorithm is shown in Fig. 10.17, which includes ① the algorithm for solving the filtering; ② the algorithm for solving the signal peak; ③ the algorithm for solving the envelope; ④ the algorithm for solving the phase difference between

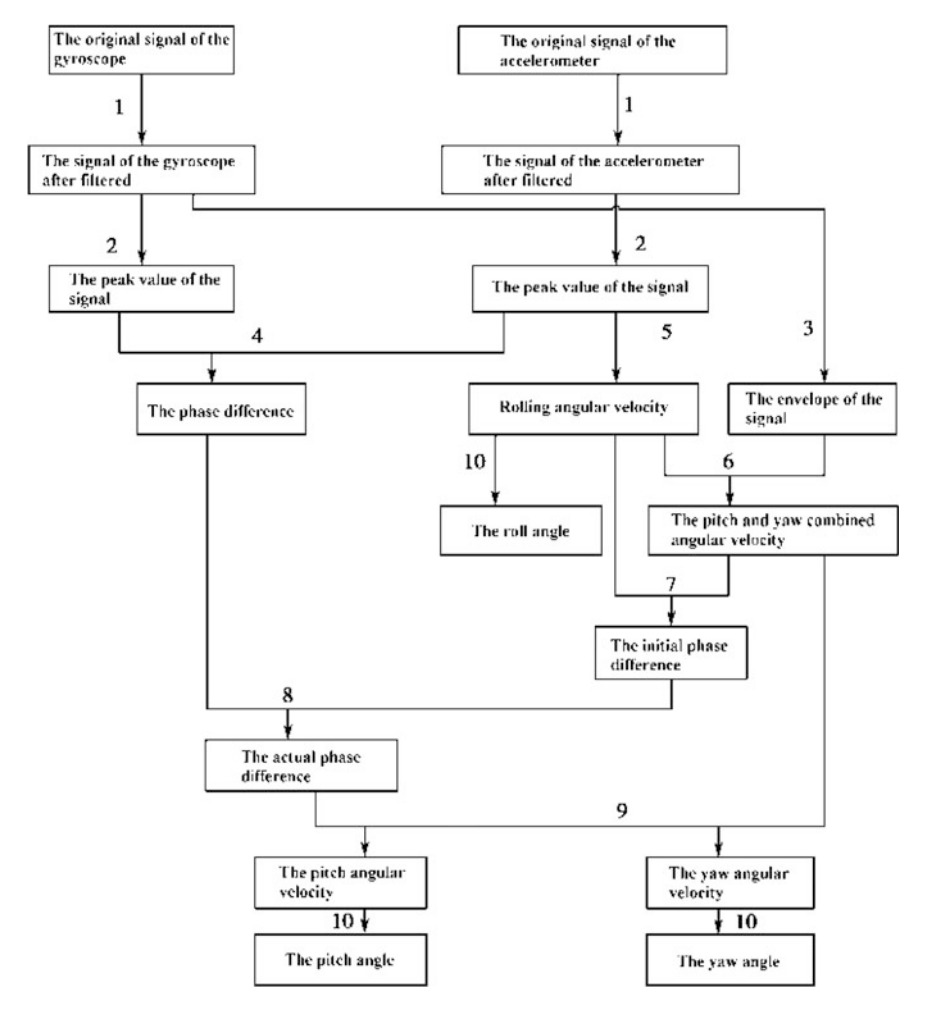


Fig. 10.17 Demodulation process of the micromechanical gyroscope

two signals; ⑤ the algorithm for solving the rolling angular velocity; ⑥ inhibiting the effect of the rolling angular velocity on the output signal, and solving the pitch and yaw combined angular velocities; ⑦ the algorithm for solving the combined molding compensation of the phase difference; ⑧ the algorithm for solving the actual phase difference; ⑨ the algorithm for solving the yaw angular velocity and the pitch angular velocity; ⑩ the algorithm for solving the roll, pitch and yaw angles.

1. Filtering algorithm and simulation

After the signals of the micromechanical gyroscope and the accelerometer have passed through the pre-processing circuit they still contain a lot of noise. Before the

signal is demodulated it needs a smoothing filter. There are many common filtering algorithms such as the adaptive filtering algorithm, the Kalman filtering algorithm, the wavelet filtering algorithm, the IIR filtering algorithm, and the FIR filtering algorithm, etc. Because the phase information of the signal is important, in order not to affect the calculation of the next phase difference the zero phase filtering algorithm is selected to filter the signal. The basic idea of the zero phase digital filtering algorithm is that the input sequence is filtered in order (the forward filter), the obtained result is reversed and passes the filter (the reverse filter) reversely, and the obtained result is reversed and is output (the reverse output), that is, the output sequence of the exact zero phase distortion is obtained and the realizing process of this algorithm is as follows:

(1) Write the difference filter function Diff Filter (*b*, *a*, *x*). For the linear shift invariant (Linear Shift Invariant, LSI) discrete time system, the difference equation can be expressed as

$$y(n) + \sum_{k=1}^{N} a(k)y(n-k) = \sum_{r=0}^{M} b(r)x(n-r)$$
 (10.31)

where a(k) and b(r) are coefficients of this equation.

Write the difference filter function Diff Filter Diff Filter (b, a, x), the parameters are three arrays, b is used to store the coefficients b(r), (r = 0, 1, ..., M) of the filter; a is used to store the coefficients a(k), (k = 0, 1, ..., N), and a(0) = 1; x is used to store the input signal and afterwards to store the filtered output signal.

(2) For the IIR filter, there holds M = N and calculating the initial condition of the filter e(q), q = 0, 1, ..., N - 1, where $E = [e(0), e(1), ..., e(N - 1)]^T$, there holds

$$E = \begin{bmatrix} 1 + a(1) & 1 & -1 & \cdots \\ a(2) & 0 & 1 & \cdots \\ \vdots & \vdots & \vdots & \cdots \\ a(N) & 0 & 0 & \cdots \end{bmatrix} \times \begin{bmatrix} b(1) - b(0)a(0) \\ b(2) - b(0)a(1) \\ \vdots \\ b(N) - b(0)a(N-1) \end{bmatrix}$$
(10.32)

(3) The head and the end of the original input sequence x(n) is expanded and 3 N numbers are added before x(n) and 3 N numbers are added behind. The expanded sequence is denoted by x'(n), n = 0, 1, ..., P + 6N.

$$x'(n) = \begin{cases} 2x(0) - x(3N - n), & n < 3N \\ x(n - 3N), & 3N \le n < P + 3n \\ 2x(P) - x(P - 1 - (n - P - 3N - n)), P + 3N \le n \le P + 6N \end{cases}$$
(10.33)

(4) Forward filtering is performed. The function Diff Filter (b, a, x) is called b, a and x'(n). The output y'(n) of x'(n) is calculated by

$$H(z) = \sum_{m=0}^{M} b(m)z^{-m} / \left(1 + \sum_{m=1}^{M} a(m)z^{-m}\right)$$
 (10.34)

Then a unit pulse signal h(n) with length P+6N+1 is generated and the function Diff Filter (b,a,x) is called by z,a and h(n). The output y''(n) of the h(n) is calculated by

$$H(z) = \sum_{m=0}^{M-1} y'(0)e(m)z^{-m} / \left(1 + \sum_{m=1}^{M} a(m)z^{-m}\right)$$
 (10.35)

where denotes y(n) = y'(n) + y''(n).

- (5) Inverse filtering is performed and the result of the forward filtering is inversed. Denote x'(n) = y(P + 6N n), repeat Step (4) and obtain the result after inverse filtering.
- (6) The results of the inverse filtering are inversed and the extension of the head and the end is removed and the final filtering result can be obtained.

Set the inner frame of the turntable as 10 Hz and the pitch and yaw as the angular vibration at 1 Hz and 5° and record the output signal of the micromechanical gyroscope and the signal of the accelerometer. Figure 10.18 shows a piece of the original data output of the micromechanical gyroscope and Fig. 10.19 shows the zero phase filtering, where A and B represent the original signal of the micromechanical gyroscope and the filtered signal. Figure 10.20 shows the waveforms after IIR and FIR filtering, where C, E and G represent the original signals of the micromechanical gyroscope, the waveform after the IIR filtering and the waveform after the FIR filtering respectively.

Figure 10.21 shows a piece of data of the original signal of the accelerometer and Fig. 10.22 shows the zero phase filtering, where B and H represent the original signal and the filtered signal of the accelerometer. Figure 10.23 shows the waveforms after IIR and FIR filtering, where B, D and F represent the original signal, the IIR filtered waveform and the FIR filtered waveform of the accelerometer respectively.

314 10 Signal Processing

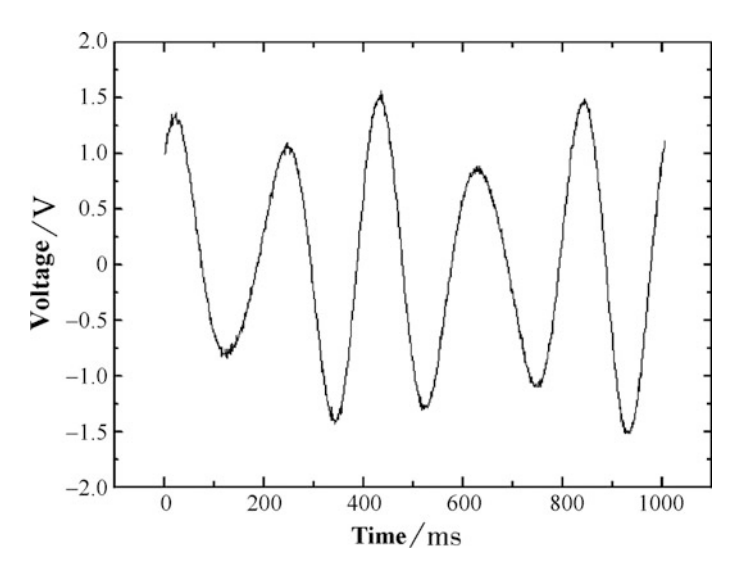


Fig. 10.18 Original signal of the micromechanical gyroscope

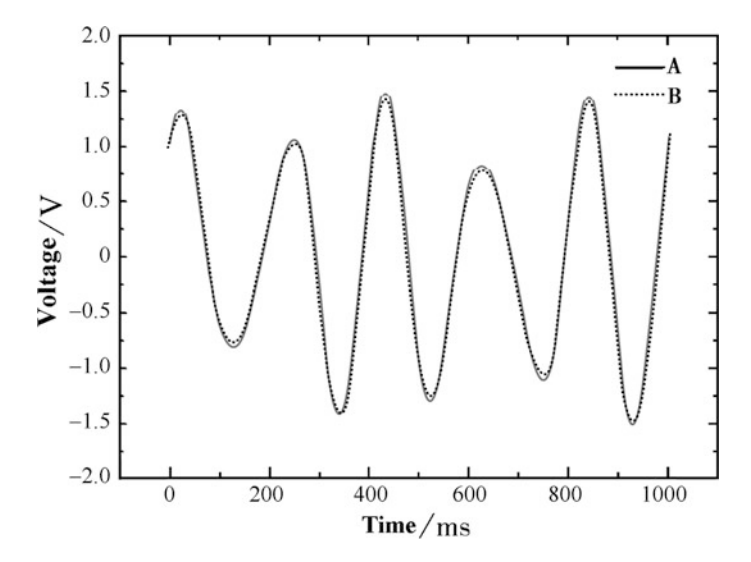


Fig. 10.19 Zero phase filtered result for the signal of the micromechanical gyroscope

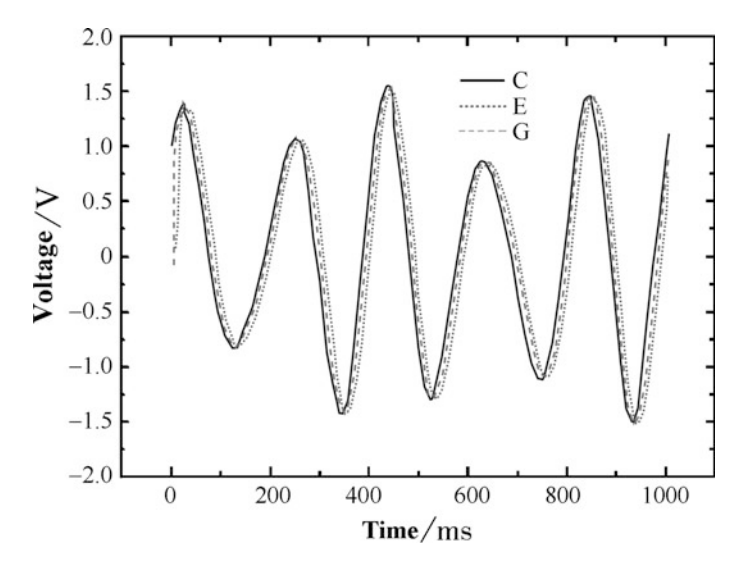


Fig. 10.20 IIR and FIR filtered result for the signal of the micromechanical gyroscope

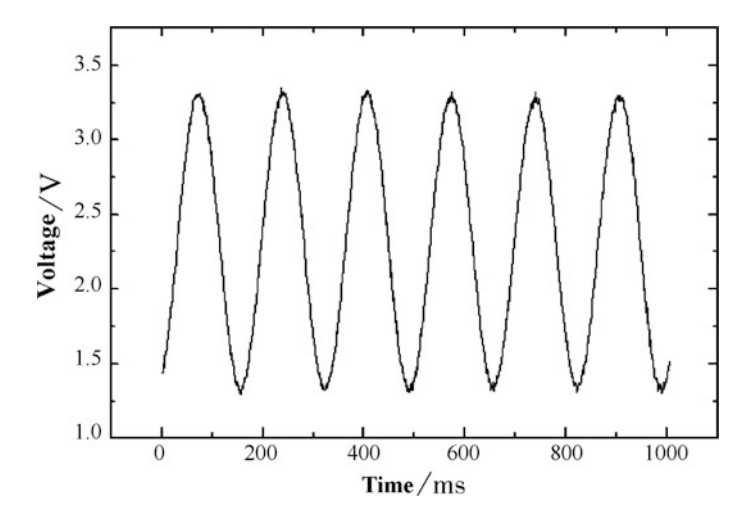


Fig. 10.21 Original signal of the accelerometer

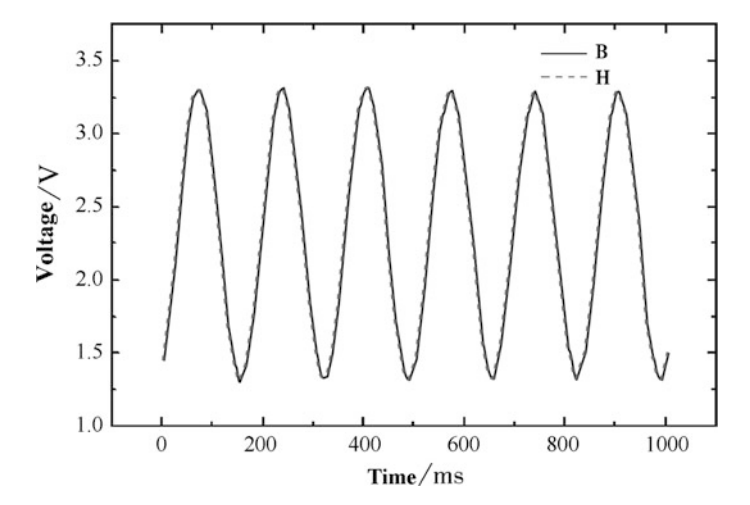


Fig. 10.22 Zero phase filtering result for the signal of the accelerometer

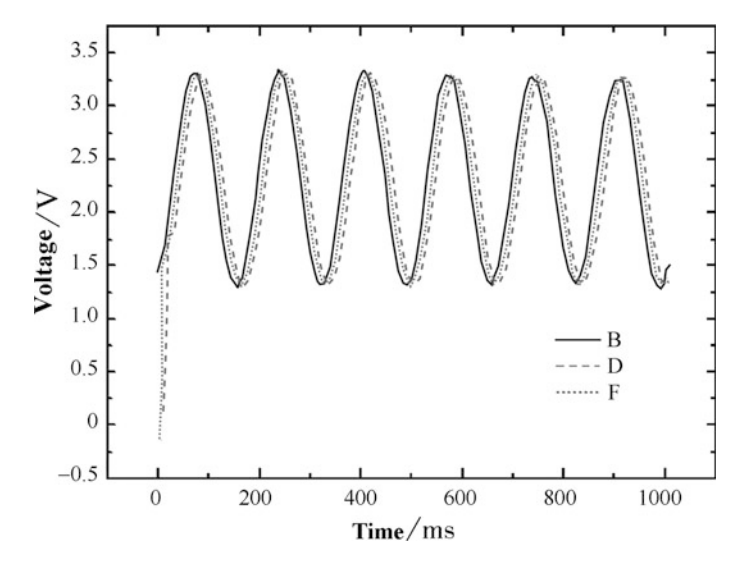


Fig. 10.23 IIR and FIR filtering result for the signal of the accelerometer

By using three kinds of the filtering methods the signal-to-noise ratio before and after filtering is shown in Table 10.11. It can be seen that after filtering the signal-to-noise ratios of the signal of the micromechanical gyroscope and the accelerometer are raised by 6 dB. However, for the IIR and FIR filtering algorithms there is a filtered phase shift and a large error at two ends of the filtering. These two drawbacks do not affect the zero phase shift filtering algorithm. Therefore, the zero

Method	The signal-to-noise ratios for the signal of the micromechanical gyroscope/db	The signal-to-noise ratios for the signal of the accelerometer/db	Method	The signal-to-noise ratios for the signal of the micromechanical gyroscope/db	The signal-to-noise ratios for the signal of the accelerometer/db
Before filtering	30.2	28.3	After FIR filtering	36.5	33.8
After IIR filtering	36.4	34.1	After zero phase shift filtering	37.6	34.7

Table 10.11 Signal-to-noise ratios of three filtering algorithms before and after filtering

phase shift filtering algorithm is utilized in the signal filtering of the micromechanical gyroscope.

2. Algorithm for the rolling angular velocity and angular position

The signal peak algorithm is to find the peak value of the de-noised signal of the micromechanical gyroscope and the accelerometer through three points and record the time value of the wave crest. The rolling angular velocity is obtained by the time difference of the adjacent peak values as follows

$$\dot{\varphi} = \frac{1}{t_2 - t_1} \cdot 360^{\circ} \tag{10.36}$$

The rolling angular position is obtained by

$$\phi = \sum_{i=1}^{n} \dot{\varphi}_{i} t_{i} + \phi_{o} \tag{10.37}$$

where ϕ_o is the initial angular position; and $\dot{\phi}_i$ is the angular velocity at time t_i .

3. Calculation of the signal envelope

The amplitude of the signal envelope of the micromechanical gyroscope is proportional to the combined pitch and yaw angular velocities. The envelope information is solved by using the Hilbert transformation method.

Given a continuous time signal x(t) whose Hilbert transformation $\hat{x}(t)$ is defined as

$$\hat{x}(t) = H[x(t)] = \frac{1}{\pi} \int_{-\infty}^{+\infty} \frac{x(\tau)}{t - \tau} d\tau = \frac{1}{\pi} \int_{-\infty}^{+\infty} \frac{x(t - \tau)}{\tau} d\tau = x(t) \times \frac{1}{\pi t}$$
(10.38)

 $\hat{x}(t)$ in Eq. (10.38) is regarded as the output of x(t) through a filter and the Fourier transformation of the unit impulse response $h(t) = 1/\pi t$ of this filter is a sign function $\text{sgn}(\Omega)$. Thus the frequency response of the Hilbert converter is

$$H(j\Omega) = -j\operatorname{sgn}(\Omega) = \begin{cases} -j, & \Omega > 0\\ j, & \Omega < 0 \end{cases}$$
 (10.39)

Denote $H(j\Omega) = |H(j\Omega)|e^{j\varphi(\Omega)}$, thus $H(j\Omega) = 1$

$$\varphi(j\Omega) = \begin{cases} -\frac{\pi}{2}, & \Omega > 0\\ \frac{\pi}{2}, & \Omega < 0 \end{cases}$$
 (10.40)

In other words, the Hilbert converter is an all pass filter with the amplitude 1. After the signal x(t) passes through the Hilbert converter, its negative frequency component has a +90° phase shift, while its positive frequency component has a -90° phase shift.

Assume that z(t) is the analytic signal of the signal x(t), thus there holds

$$z(t) = x(t) + j\hat{x}(t) \tag{10.41}$$

Applying the Fourier transform to both sides of Eq. (10.41) obtains

$$Z(j\Omega) = X(j\Omega) + j\hat{X}(j\Omega) = X(j\Omega) + jH(j\Omega)X(j\Omega)$$
 (10.42)

that is,

$$Z(j\Omega) = \begin{cases} 2X(j\Omega), & \Omega > 0\\ 0, & \Omega < 0 \end{cases}$$
 (10.43)

In this way, the analytic signal is obtained by the Hilbert transform, which contains the positive frequency component only and is twice the positive frequency component of the original signal.

For the discrete time signal x(n), its analytic signal z(n) can be obtained by the same method and the detailed steps are as follows:

(1) x(n) is performed by FFT and the negative frequency of X(k), k = 0, 1, ..., N-1, k = N/2, ..., N-1 can be obtained.

(2)
$$Z(k) = \begin{cases} X(k) & k = 0 \\ 2X(k) & k = 1, 2, \dots, \frac{N}{2} - 1 \\ 0 & k = \frac{N}{2}, \dots, N - 1 \end{cases}$$
 (10.44)

- (3) Z(k) is performed by inverse FFT and the analytic signal z(n) of x(n) can be obtained.
- (4) |z(n)| is the envelope of x(n).

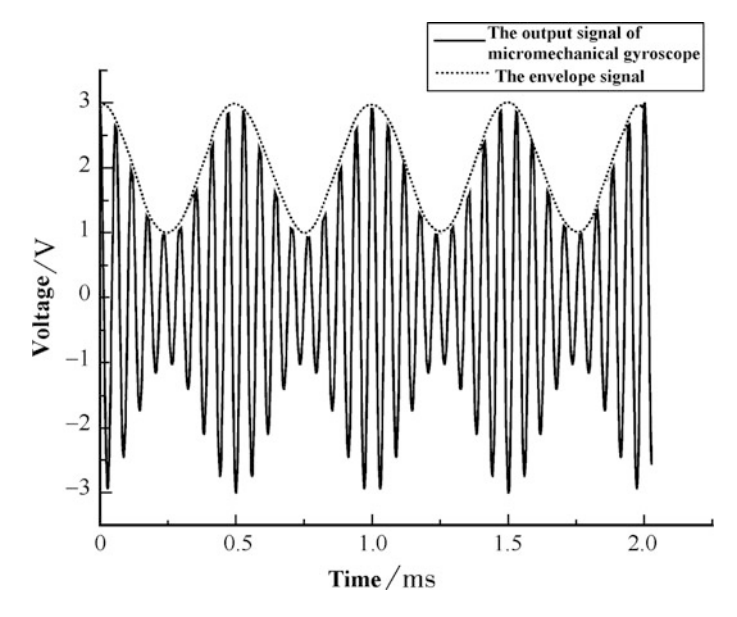


Fig. 10.24 The signal and its envelope of the micromechanical gyroscope

The micromechanical gyroscope is installed on the three-axis turntable. The inner frame of the turntable is set at 17 Hz and the frequencies of the middle frame and the outer frame are set as 2 Hz. The amplitude is a 5° angular vibration. The output signal of the micromechanical gyroscope is collected by the acquisition system and the Hilbert envelope program is written using Matlab7.0. The diagram for the output signal and the envelope of the micromechanical gyroscope is shown in Fig. 10.24.

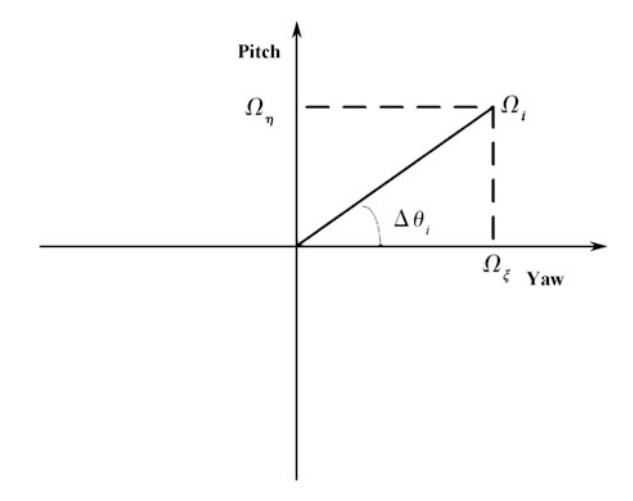
The input angular velocity (the combined angular velocity of the pitch angular velocity and the yaw angular velocity) is proportional to the signal envelope, but because of the influence of the change of the rolling angular velocity, the combined angular velocity of the pitch and the yaw can be obtained by the algorithm of attenuating the influence of the rolling change for the output signal.

4. Phase difference between the micromechanical gyroscope and the accelerometer

The phase difference reflects the deflection direction of the carrier space. By subtracting the wave peak positions of the micromechanical gyroscope and the accelerometer, the phase difference between the micromechanical gyroscope and the accelerometer can be obtained. However, the obtained phase difference is due to the difference between the peak value points and the distance between the wave peaks is 1/f, thus the points of the sampling rate with respect to 1 ms are too sparse. Here the Cubic Spline Interpolation method is adopted to complete the wave data and each 1 ms then corresponds to a phase difference. However, because of the influence of the input angular velocity and the rolling angular velocity on the phase

320 10 Signal Processing

Fig. 10.25 Decomposition diagram of the yaw angular velocity and the pitch angular velocity



difference, the initial phase difference is obtained by using the phase difference composite modeling compensating algorithm, and the final actual phase difference is obtained by their subtraction.

5. The yaw and pitch angular velocity and angular position

According to the envelope the input angular velocity Ω_i (the yaw and pitch composite angular velocity) can be obtained and the yaw and pitch instantaneous angular velocities are Ω_{ξ} and Ω_{η} respectively. According to the above theory the phase difference $\Delta\theta_i$ can be obtained as shown in Fig. 10.25. By using orthogonal decomposition the yaw angular velocity and the pitch angular velocity can be obtained.

$$\Omega_{\xi} = \Omega_i \cdot \cos(\Delta \theta_i) \tag{10.45}$$

$$\Omega_{\eta} = \Omega_i \cdot \sin(\Delta \theta_i) \tag{10.46}$$

where i = 1, 2, ..., n.

By integrating the yaw angular velocity and the pitch angular velocity in Eqs. (10.45) and (10.46), the yaw and pitch angular positions $\Omega_{j\xi}$ and $\Omega_{j\eta}$ can be obtained:

$$\Omega_{j\xi} = \sum \Omega_{\xi} \cdot 0.001 + \Omega_{\xi o} \tag{10.47}$$

$$\Omega_{j\eta} = \sum \Omega_{\eta} \cdot 0.001 + \Omega_{\eta o} \tag{10.48}$$

where $\Omega_{\xi o}$ and $\Omega_{\eta o}$ are the initial yaw and pitch angular positions.

10.3.2 Simulation Experiment

The rolling angular velocity of the inner ring of the three-axis turntable is set at 20 Hz and the outer ring and the middle ring move by means of the angular vibration motion whose frequency is 1 Hz and whose amplitude is 10°. The position of the three-axis turntable, the output signal of the micromechanical gyroscope and the output signal of the accelerometer are recorded by the collecting card. By using the above algorithm, the angular velocity and the angle information are demodulated and compared. The comparison of the rolling angular velocity and the demodulated angular velocity of the turntable is shown in Fig. 10.26. The comparison of the actual yaw angular velocity and the angle of the turntable and the comparison of the actual yaw angular velocity and the angle of the turntable are shown in Figs. 10.27 and 10.28. The comparison of the demodulated pitch angular velocity and the angle of the turntable and the comparison of the actual pitch angular velocity and the angle of the turntable are shown in Figs. 10.29 and 10.30.

The maximum relative error between the demodulated rolling angular velocity of the turntable and the actual rolling angular velocity of the turntable in 5 s is less than 0.3%. The maximum absolute error between the demodulated yaw angular velocity of the turntable and the actual yaw angular velocity of the turntable in 5 s is $5.2^{\circ}/s$; the maximum absolute error between the yaw angle and the demodulated yaw angle is 4° ; the maximum absolute error between the demodulated pitch angular velocity of the turntable and the actual pitch angular velocity of the turntable in 5 s is $4.1^{\circ}/s$ and the maximum absolute error between the pitch angle and the demodulated pitch angle is 3° .

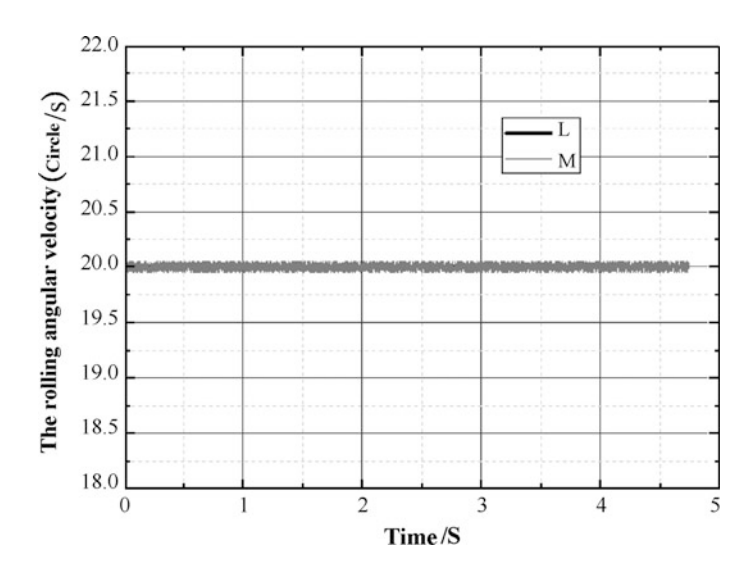
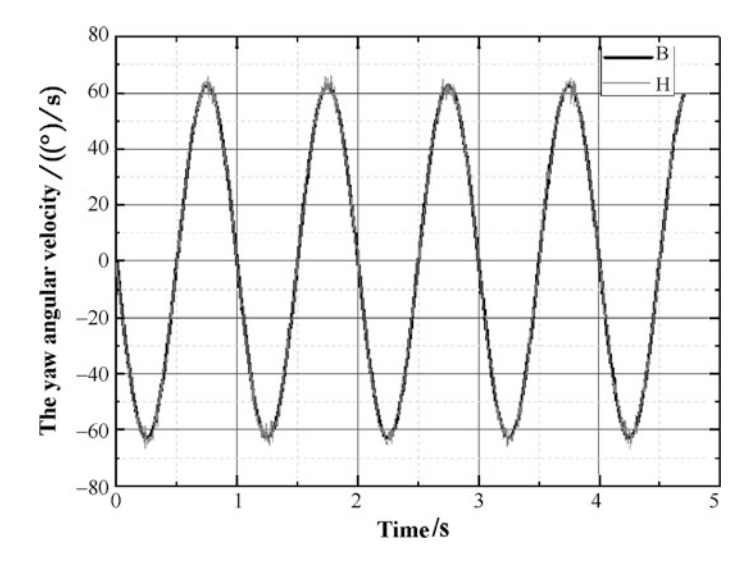


Fig. 10.26 Comparison of actual rolling angular velocity (L) and demodulated rolling angular velocity (M) of the turntable



 $\begin{tabular}{ll} Fig. \ 10.27 & Comparison of actual yaw angular velocity (B) and demodulated yaw angular velocity (H) of the turntable \\ \end{tabular}$

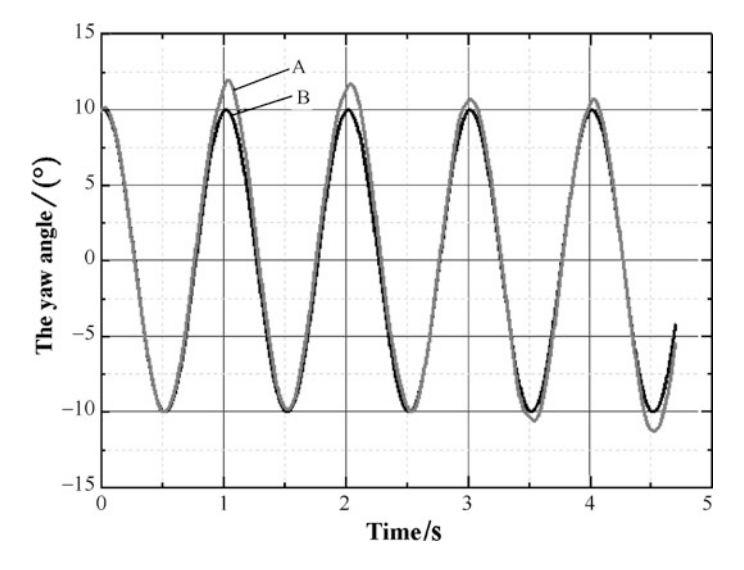


Fig. 10.28 Comparison of yaw angle (B) and demodulated yaw angle (A)

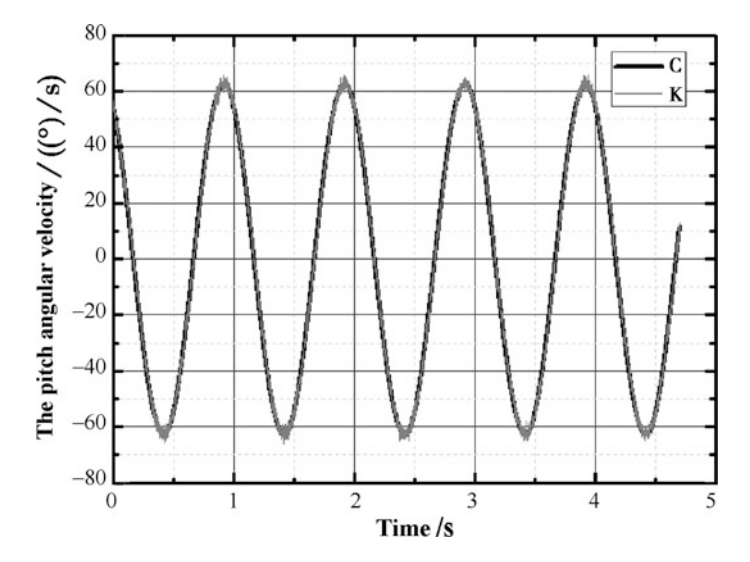


Fig. 10.29 Comparison of actual pitch angular velocity (C) and demodulated pitch angular velocity (K)

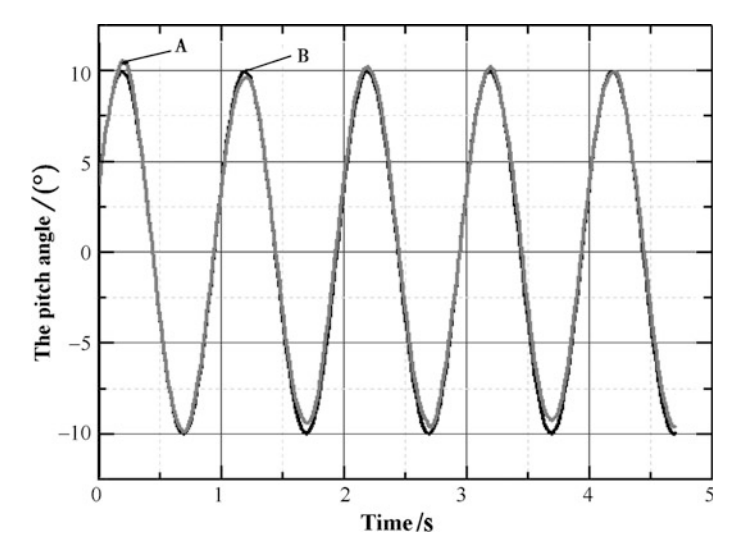


Fig. 10.30 Comparison of actual pitch angle (B) and demodulated pitch angle (A)

For this demodulating algorithm of the micromechanical gyroscope three angular velocities can be calculated. When the angle (angle position) is calculated it is necessary to know the initial position information of the rotating carrier. The angle information is obtained by the integral of the angular velocity, thus the angular velocity error will directly affect the accuracy of the angular position.

Chapter 11 Applications in the Flight Attitude Control System

11.1 Calculation Method Design and Software Creation

11.1.1 Calculation Method and Software

Due to the breakthrough provided by the calculation method and software, the output of multi-information from a "non-driven structure silicon micromechanical gyroscope" can be realized. The function of the software is shown in Fig. 11.1.

Figure 11.1 shows the output voltage signal of the "non-driven structure silicon micromechanical gyroscope" top left; the position (angle) graphic of the vertical axis endpoint (the laser spot on the inner ring of three-axis turntable) that moves in flight is top right; the yaw angle curve $\Omega(t)$ (the angle vibration change of the outer ring of the three-axis turntable) is bottom right; and the yaw angle curve that is calculated from the output of the "non-driven structure silicon micromechanical gyroscope" is bottom left.

The position (angle) graphic of the vertical axis endpoint that moves in flight has a great significance. Its long radius presents the maximum deviation angle and direction, but the composite angular velocity is minimal. This shows that the rotating carrier moves in an ellipse from the long radius to the short radius (convected motion), but the rotating direction of the absolute motion is generally the same (when the rolling is not reversed).

11.1.2 Computer Software Design

1. Wavelet function and transformation

The wavelet transform calculates the inner product of the basic wavelet that is scaling transformed and shifted with the signal to be analyzed.

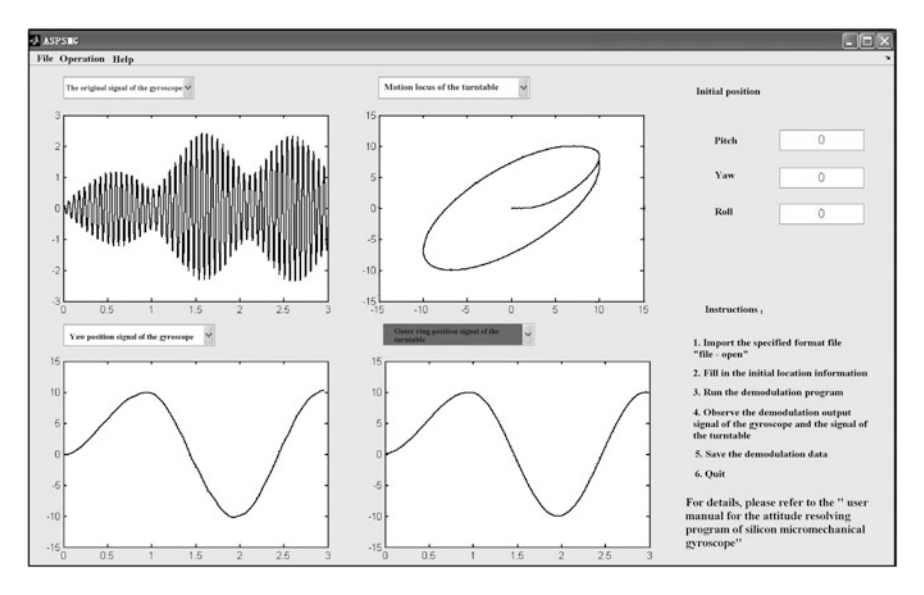


Fig. 11.1 The function of the software

The wavelet is a function family generated by panning and zooming a function that satisfies $\int_{\mathbb{R}} \varphi(t) dt = 0$, i.e.,

$$\varphi_{a,b}(t) = \frac{1}{\sqrt{a}} \varphi\left(\frac{t-b}{a}\right), \quad a, b \in R, \ a \neq 0$$
 (11.1)

Given an energy-limited signal x(t), whose continuous wavelet transform is defined as

$$CWT_{x}(a,b) = \frac{1}{\sqrt{a}} \int_{-\infty}^{+\infty} x(t) \dot{\varphi}\left(\frac{t-b}{a}\right) dt, \quad x(t) \in L^{2}(R)$$
 (11.2)

where $\dot{\varphi}$ is the conjugate of the wavelet function φ .

 $\varphi(t)$ is called the basic wavelet (the mother wavelet), and the non-zero real scalar a is called the scale factor which is the scale expansion parameter of the basic wavelet $\varphi(t)$ on the time axis. The real scalar b is called the time shift parameter and the different value of b indicates that the wavelet moves along the time axis to a different position. The function of the coefficient $1/\sqrt{a}$ is normalization. The change of the scale factor a determines the change of the function shape, but the size of the time/frequency window does not change. Thus when the low frequency (smaller a) is analyzed the time resolution of the wavelet transform is low and the frequency resolution is high. When the high frequency (higher a) is analyzed the time resolution of the wavelet transform is high and the frequency resolution is low,

which is consistent with the characteristics that the low frequency signal changes slowly and the high frequency signal changes rapidly.

When a smaller a is used to analyze the high frequency of the signal the high frequency wavelet is actually used to observe the signal. When a larger a is used to analyze the low frequency of the signal the low frequency wavelet is actually used to observe the signal. This characteristic of the wavelet transform is consistent with the law by which the signal is actually analyzed.

Although the Fourier transform is very widely used it gives the time domain (spatial domain) integrated information and cannot express the time/frequency domain of the signal. In order to give the local time-frequency information of the signal, a sliding "time window" can be added on the Fourier transform to analyze the signal. Assume that the non-stationary signal f(t) is stable within a short time of the analysis window function g(t), the analysis window function is moved such that $g(\tau)f(t-\tau)$ is a stable signal in the different finite time width and the power spectrums at different moments can be calculated. In essence, this method is still a single resolution method which cannot describe the detailed information of the signal at different scales.

Wavelet analysis is the development and the extension of the Fourier analysis method. It no longer uses the fixed window function to locally process the signal, instead it uses the wavelet function to process the signal. The essence of the wavelet function is similar to that of the time frequency window whose size is fixed and whose shape can be changed, while the widths of the time window and the frequency window can also change the window function.

2. Multi-resolution analysis

Because the wavelet transform can analyze the signal at the different scales it can be used to for multi-resolution analysis of the signal. The idea of multi-resolution is that the square integral function $x(t) \in L^2(R)$ is regarded as the limit case of a gradual approach and each level approximation uses a low-pass smoothing function $\varphi(t)$ to smooth x(t), but in the case of the gradual approach the smooth function $\varphi(t)$ is also gradually expanded, that is, the different resolution is used to gradually approach the analyzed function. The most important aspect is the construction of a series of orthogonal wavelet basis functions. The required wavelet basis function can be constructed by the scaling function.

In the digital signal processing system the signal envelope usually has three extraction methods: Hilbert amplitude demodulation the method, demodulation-filtering method and the high pass absolute value demodulation method. The real part of the analytical signal obtained by the Hilbert transform is the signal itself and the imaginary part is the Hilbert transform. The amplitude of the analytic signal is the envelope of the signal. The demodulation-filtering method is to demodulate the original signal with the non-zero mean and then normalize it by the zero mean and set the band pass filter with the center frequency f to obtain the envelope signal with the main component f. The high pass absolute value method is to apply high pass filtering to the time domain signal with the zero mean,

take the absolute value and apply the low pass filter. The selection of the low pass frequency determines the frequency components of the signal envelope.

The high pass absolute value method is the envelope of the signal center line and the demodulation-filtering method is the envelope of the signal positive half cycle center line. These two amplitude demodulations are not the actual amplitude envelopes. However, the absolute value of the signal can be demodulated by the Hilbert method where the demodulation amplitude is the actual envelope and the Hilbert transform can be realized easily by FFT.

The specific implementation can not be realized by the Hilbert transform directly, but it can be realized by FFT. The derivation procedure is as follows:

Given a continuous time signal x(t) whose Hilbert transform $\hat{x}(t)$ is defined as

$$\hat{x}(t) = H[x(t)] = \frac{1}{\pi} \int_{-\infty}^{\infty} \frac{x(\tau)}{t - \tau} d\tau = \frac{1}{\pi} \int_{-\infty}^{\infty} \frac{x(t - \tau)}{\tau} d\tau = x(t) * \frac{1}{\pi t}$$
(11.3)

where $\hat{x}(t)$ is regarded as a filter output of x(t) and the unit impulse response of this filter is $h(t) = 1/\pi t$.

From the theory of the Fourier transform, the Fourier transform of $jh(t) = j/\pi t$ is a sign function $sgn(\Omega)$. Thus the frequency response of the Hilbert converter is

$$H(j\Omega) = -j \operatorname{sgn}(\Omega) = \begin{cases} -j, & \Omega > 0\\ j, & \Omega < 0 \end{cases}$$
 (11.4)

Denote $H(j\Omega) = |H(j\Omega)|e^{j\varphi(\Omega)}$, thus $|H(j\Omega)| = 1$, i.e.,

$$\varphi(\Omega) = \begin{cases} -\frac{\pi}{2}, & \Omega > 0\\ \frac{\pi}{2}, & \Omega < 0 \end{cases}$$
 (11.5)

That is to say, the Hilbert converter is an all pass filter with amplitude characteristics 1. The signal x(t) passes through the Hilbert converter and its negative frequency component has a phase shift of $+90^{\circ}$ and its positive frequency component has a phase shift of -90° .

Assume that z(t) is an analytic signal of the signal x(t). Then there holds

$$z(t) = x(t) + j\hat{x}(t) \tag{11.6}$$

Apply the Fourier transform to both sides of the above formula and obtain the following result from Eq. (11.4)

$$Z(j\Omega) = X(j\Omega) + j\hat{X}(j\Omega) = X(j\Omega) + jH(j\Omega)X(j\Omega)$$
(11.7)

that is

$$Z(j\Omega) = \begin{cases} 2X(j\Omega), & \Omega > 0\\ 0, & \Omega < 0 \end{cases}$$
 (11.8)

In this way, the analytic signal is composed by the Hilbert transform, contains the positive frequency component only and is twice the original signal.

For the discrete time signal x(n) the same method can be applied to obtain its analytic signal z(n) and the detailed procedure is as follows:

(1) x(n) is applied by FFT to obtain X(k), k = 0, 1, ..., N - 1, where k = N/2, ..., N - 1, corresponds to the negative frequency.

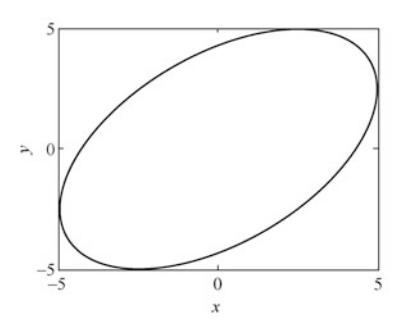
(2)
$$Z(k) = \begin{cases} X(k), & k = 0\\ 2X(k), & k = 1, 2, \dots, \frac{N}{2} - 1\\ 0, & k = \frac{N}{2}, \dots \frac{N}{2} - 1 \end{cases}$$

- (3) z(k) is applied by inverse FFT and obtains the analytic signal z(n) of x(n).
- (4) |z(n)| is the envelope of x(n).

11.2 Influence Connected Motion (Angular Vibration) as Three Axes Move Simultaneously

When the three axes of the three-axis turntable work simultaneously (the inner loop rotation, the middle loop and the outer loop angular vibration), the angular velocity (frequency) of the inner loop is always different from the given frequency.

As shown in Fig. 11.2, the self-spin is 17 Hz, the angle vibration of the middle loop is 1 Hz and $\pm 5^{\circ}$, the angle vibration of the outer loop is 1 Hz and $\pm 5^{\circ}$, and the space motion trajectory (angular position) is an ellipse. When the motion trajectory is elliptical there are two frequencies (16 and 18 Hz) in the FFT analysis (implicated motion). This is an important discovery. Using the Matlab FFT software, two frequencies can be observed. The appearance of the above phenomenon



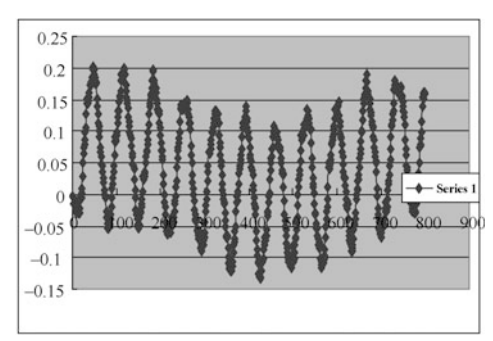
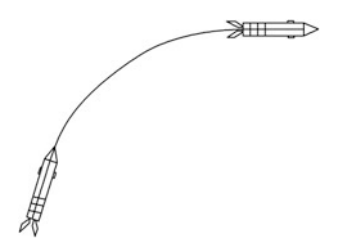


Fig. 11.2 Implicated motion phenomenon

Fig. 11.3 Flight trajectory of the rotating body



can be understood in flight, but it is not clear whether this phenomenon exists in the controlled rotating carrier.

The single channel control shows that the rotating body flies with a "straight line" and without a "circle" movement phenomenon as shown in Fig. 11.3. Whether the control result is a "closed circuit" needs to be studied.

For the experiment of the three-axis turntable the gyroscope is an open loop and is not controlled by the three-axis turntable. In the experiment, the above phenomenon is real (the phase between the yaw angular vibration and the pitch angular vibration determines that the motion trajectory is either an ellipse, circle or linear angular vibration).

If the three-axis turntable can be used as a gyroscope to control the (closed circuit) experiment, it will be a leap in the experiment and the experimental equipment, and the domestic and foreign information has not been reported.

11.3 DSP Digital Output of the Gyroscope

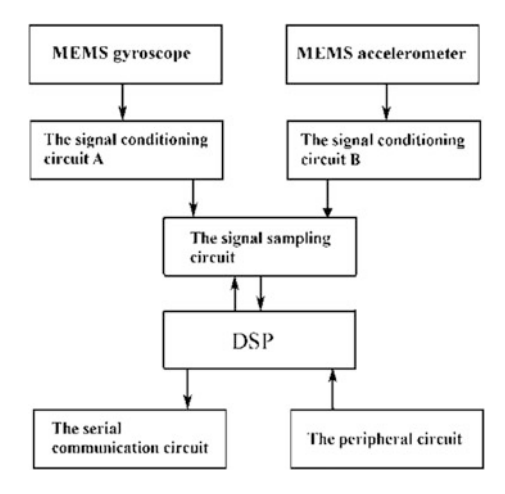
11.3.1 Hardware Circuit Design

Figure 11.4 shows the signal processing circuit diagram of the micromechanical gyroscope with a core processing circuit based on DSP.

The core of the signal processing circuit is the digital signal processor. This contains the sensitive components, the signal conditioning circuit module, the signal sampling circuit module, the serial communication circuit module and the peripheral circuit. The gyroscope and the accelerometer make up of some sensitive components and the gyroscope signal contains the rolling, pitching and yaw angular rates of the high speed rotating aircraft. The gravity accelerometer is a benchmark of the signal decomposition.

The signal conditioning circuit A is mainly to detect, filter and amplify the weak signal of the gyroscope as the core of MS3110. The signal conditioning circuit B is mainly composed of the amplifier OP27 and a filter circuit to pre-process the signal of the accelerometer. The signal sampling circuit is mainly composed of CD4051B, TLP281-4 and AD977a. Through controlling the control switch of TLP281-4, two channel signals of the gyroscope and the accelerometer can be alternately sampled, consistent with the characteristics of the one channel input of AD977a. The peripheral circuit is composed of the power module, the reset circuit, EPROM and the crystal

Fig. 11.4 Signal processing circuit diagram of the micromechanical gyroscope



oscillator circuit, etc. The power module is composed of LM2576_5.0V, LM1117_3.3V and LM1117_1.8V, which provides power supplies of 5, 3.3 and 1.8 V for this circuit. The serial communication circuit is composed of MAX232, which transfers three angular rates of the sensor to the host computer. The detailed circuit design is shown in Fig. 11.5. Finally the corresponding real object is shown in Fig. 11.6.

11.3.2 Algorithm and Software Realization

A flow chart diagram of the signal decomposition is shown in Fig. 11.7. The angular velocity signal (frequency) of the MEMS gyroscope is equal to the rolling angular velocity of the aircraft, while the amplitude envelope is proportional to the pitch and yaw composite rate.

The phase difference between the signals of the MEMS accelerometer and the gyroscope reflects the space attitude of the rotating aircraft. According to the phase difference, the pitch and yaw angular rate can be decomposed to obtain the three axial angular velocities in real time. Based on this, the signal is filtered and operated by the non-phase shift filtering method and the signal envelope is obtained by using the Hilbert transform method. The frequency is obtained by using the fast Fourier transform method.

The detailed algorithm is as follows:

- (1) After the signals of the gyroscope and the accelerometer are filtered, their smooth signals can be obtained.
- (2) Calculate the peak value of the gyroscope signal and its corresponding time, the peak value of the accelerometer signal and its corresponding time are obtained along with the envelope of the gyroscope signal.

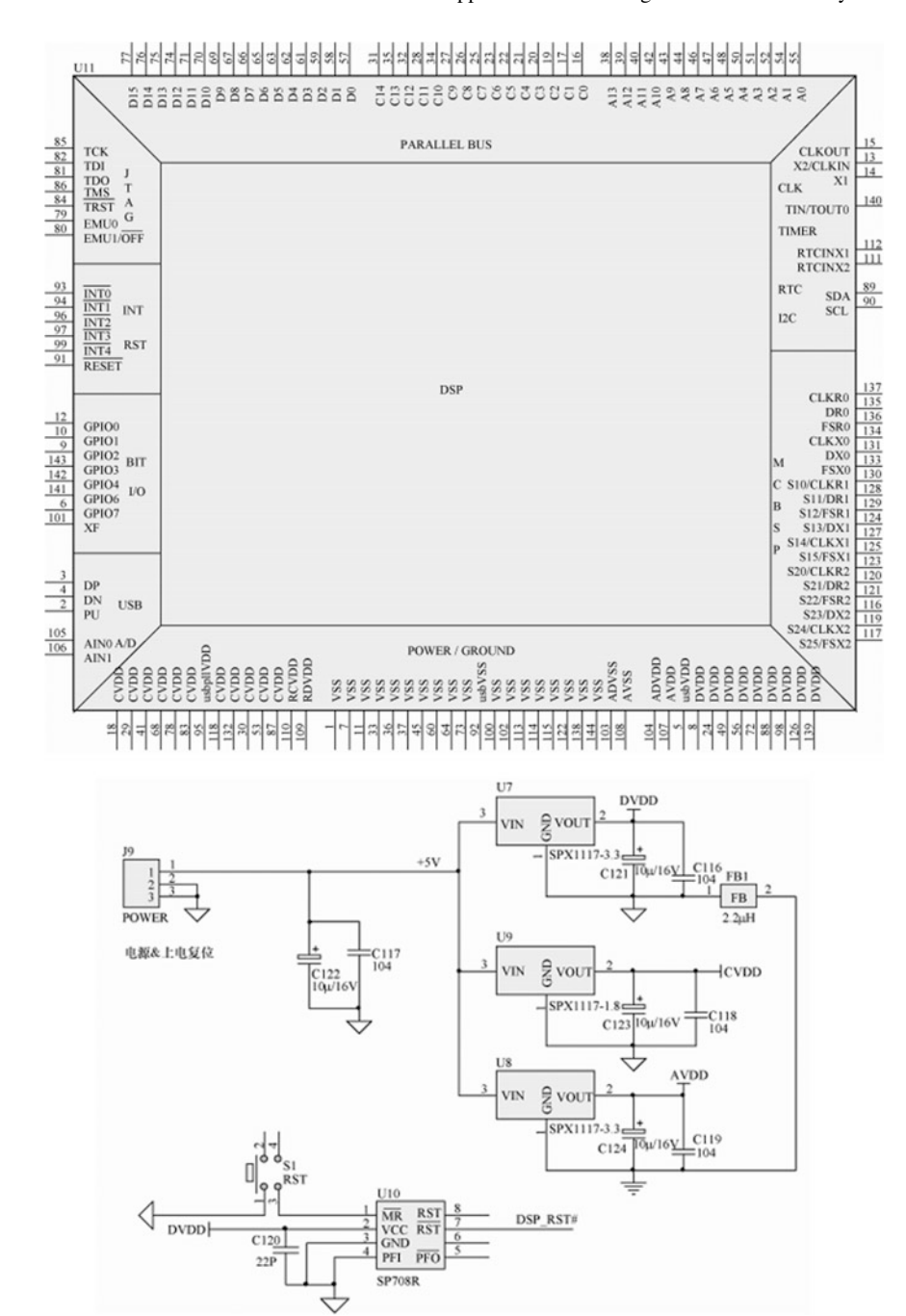


Fig. 11.5 DSP signal processing circuit

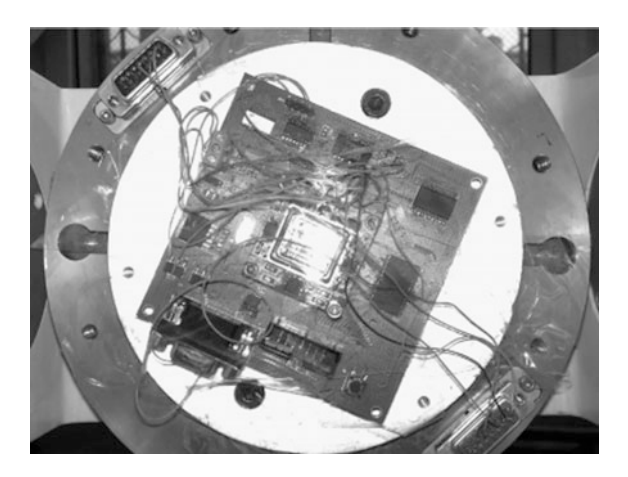


Fig. 11.6 DSP signal processing circuit system

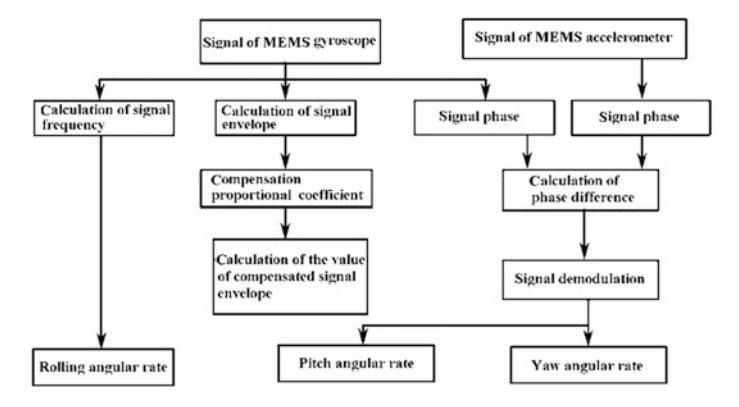
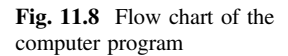
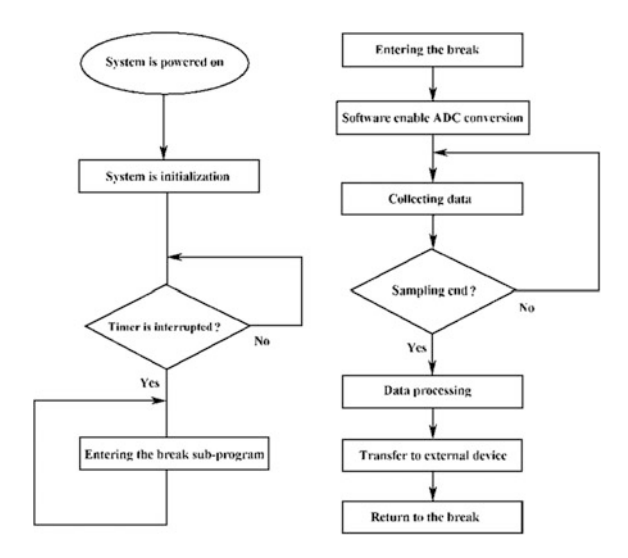


Fig. 11.7 Flow chart diagram of the signal decomposition

- (3) From the times corresponding to the peak points of the gyroscope signal and the accelerometer signal, calculate the phase difference between the signals of the gyroscope and the accelerometer. From the peak value of the accelerometer signal, calculate the self-spin frequency of the gyroscope, and calculate the self-spin angular velocity and the angular position of the rotating body.
- (4) Calculate the scaling factors of the yaw and the pitch.
- (5) From the envelope of the gyroscope signal the phase difference between the gyroscope signal and the accelerometer signal, and the scaling factors of the yaw and the pitch of the gyroscope, calculate the angular velocities and the angular positions of the yaw and the pitch of the rotating carrier.





The function of the hardware system is realized by the software system. The software design of this system is mainly the data acquisition and the processing part, which is written in *C* language and assembly language. The data acquisition and the processing program is the core of the software program, whose flow chart is shown in Fig. 11.8. According to Fig. 11.8, the data acquisition and the processing program consists of the following parts:

- 1 System is initialized.
- ② The software initiates the DSP sequence generator for data conversion and the data is stored in the data storage area.
- 3 When the acquisition is completed, the DSP will collect data for data processing.
- 4 After the processing is complete the data are sent to the external device.

11.3.3 Test Results

The attitude sensor of the micromechanical gyroscope based on DSP is installed on the three-axis turntable and the three-axis turntable is set to work under different working conditions. The results can be directly transmitted to the PC display.

The inner frame of the three-axis turntable is set at 10 Hz, the external frame (yaw angular velocity) is set at 100° /s, the middle frame (the pitch angular velocity) is 0° /s, and the test results are shown in Fig. 11.9. The first column, the second column and the third column represent the rolling angular velocity, the yaw angular velocity and the pitch angular velocity respectively.

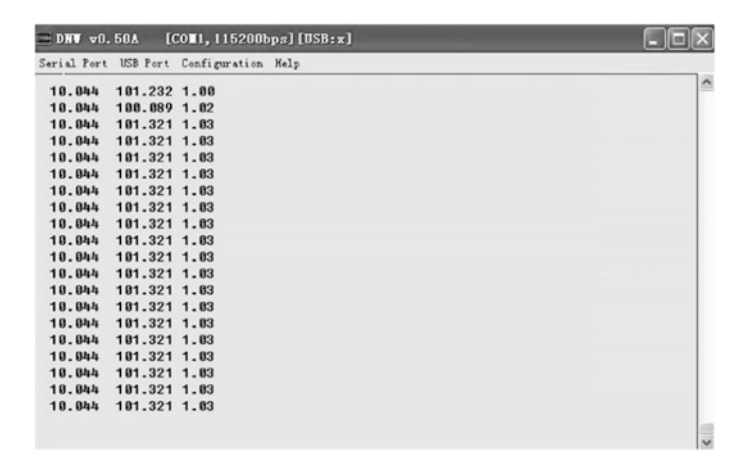


Fig. 11.9 Output results of the yaw motion

According to the DSP processing system, the signals of the micromechanical gyroscope can be decomposed into three angular velocities: the rolling angular velocity, the yaw angular velocity and the pitch angular velocity. From the output results, the maximum relative error of the rolling angular velocity is 0.44%, while the maximum absolute error of the pitch and the yaw angular velocity is less than 2°/s.

The self-spin angular velocity of the inner frame of the three-axis turntable is set as 9000°/s, the vibration frequency of the external and the middle frames is set as 1 Hz, and the vibration amplitude is set as 5°. The acquisition card records the angular position of the turntable and the output signal of micromechanical gyroscope is compared with the angular velocity of the turntable and the actual angular velocity of the turntable. Figures 11.10, 11.11 and 11.12 present a comparison of the actual yaw angular velocity, the pitch angular velocity and the rolling angular velocity with the corresponding angular velocities of the micromechanical gyroscope output signal respectively.

Fig. 11.10 Calculated yaw angular velocity of the turntable and actual yaw angular velocity of the turntable. A—Angular velocity of the turntable external frame; B—Measured yaw angular velocity

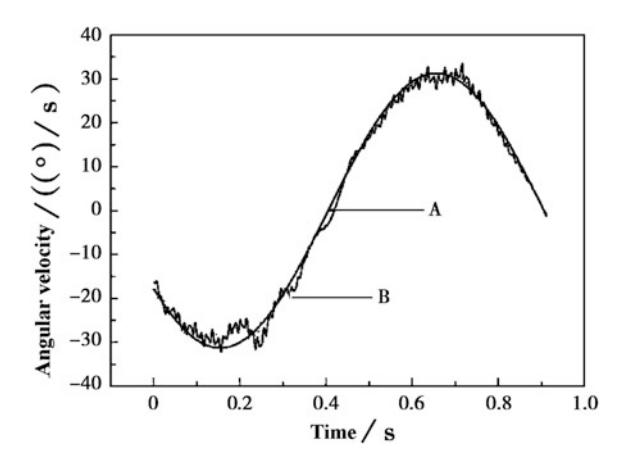


Fig. 11.11 Calculated pitch angular velocity of the turntable and actual pitch angular velocity of the turntable. A—Angular velocity of the turntable middle frame; B—Measured pitch angular velocity

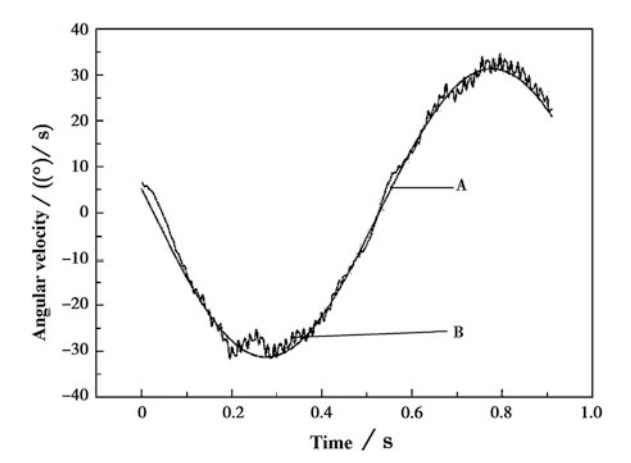
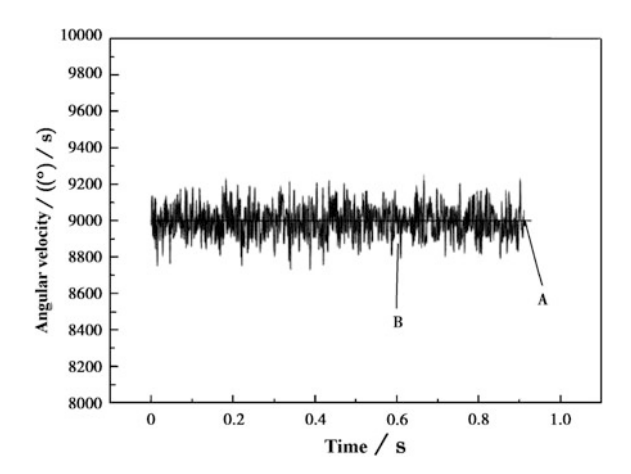


Fig. 11.12 Comparison of actual rolling angular velocity and measured rolling angular velocity. A—Angular velocity of the turntable inner frame; B—Measured rolling angular velocity



This experiment shows that the three angular velocities of rolling, pitch and the yaw can be obtained from the signal of the micromechanical gyroscope. The relative error of the obtained rolling angular velocity is less than 1% and the maximum relative error of the pitch and yaw angular velocity is 17%. The demodulation accuracy of the rolling angular velocity is relatively high such that the demodulation precision error of the pitch and the yaw is mainly the phase difference between the micromechanical gyroscope and the accelerometer. The calculation effect is directly affected by the phase difference.

11.4 Attitude Sensing System for Single Channel Control of the Rotating Flight Carrier

Relay control is a simple and reliable method used in the attitude control application of the rotating flight carrier and is also widely used in the control of the rotating flight carrier. The control scheme is different from the three channel attitude control scheme and has the advantages of high efficiency, low cost and good real-time performance.

The "non-driven silicon micromechanical gyroscope" in Fig. 11.13 is applied to the rotating flight carrier in Fig. 11.14, which replaces the liquid floating pendulum in Fig. 11.15. Both of them can get the output waveform (carrier and envelope) in Fig. 11.16 such that the cost performance of the rotating flight carrier is substantially increased.

The single channel control of the rotating flight carrier uses the "CJS–DR–WB01 type non-driven silicon micromechanical gyroscope", whose output signal is shown in Fig. 11.17 and whose control method is shown in Fig. 11.18. The control equation is as follows:

$$U_k = U_t + U_s = A_h \sin(\omega t + \varphi) + U_s \sin(2\pi\omega_o t)$$
(11.9)

$$U_{dk} = \operatorname{sgn}[A_{h}\sin(\omega t + \varphi) + U_{s}\sin(2\pi\omega_{o}t)]$$
 (11.10)

Fig. 11.13 Silicon micromechanical gyroscope

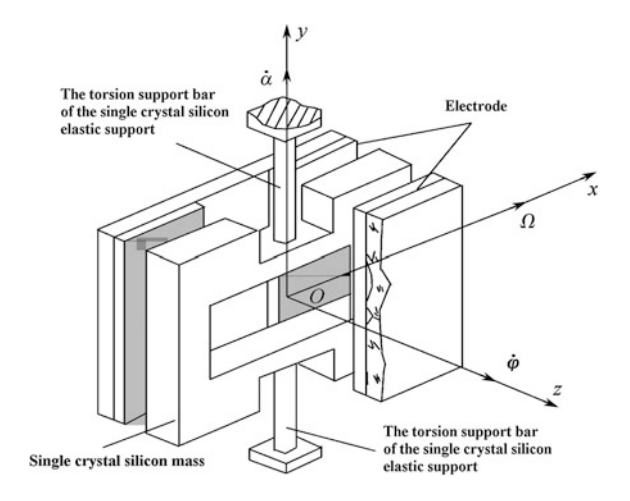


Fig. 11.14 Rotating flight carrier



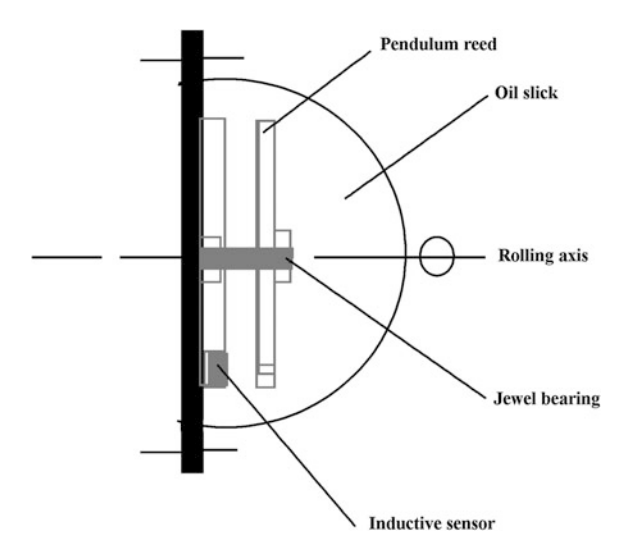


Fig. 11.15 Liquid floating pendulum

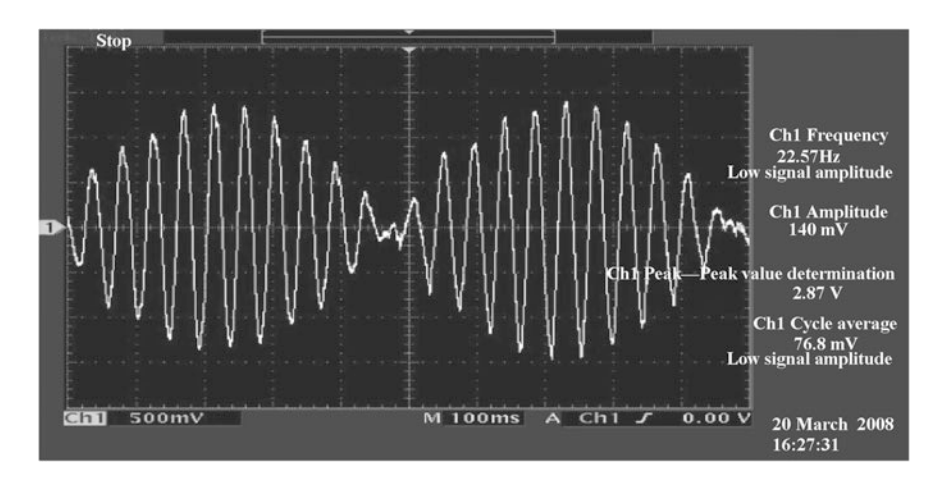


Fig. 11.16 Outputs of the non-driven silicon micromechanical gyroscope and the liquid floating pendulum

The different transverse angular velocities generate pulse width modulation control signals which have constant amplitudes and inconstant widths (Fig. 11.19). There is a linear relationship between the width of the pulse signal and the transverse angular velocity. Therefore, when the output signal of the gyroscope meets the above formula, the linear relationship between the pulse width modulation control signal and the transverse angular velocity can be established by introducing the linear signal. When the rotating flight carrier spins one circle, the phase of the rudder surface shifts four times such that the pitch control and the yaw control of

Fig. 11.17 Output signal of the non-driven micromechanical gyroscope. a Carrier signal; b Envelope signal; c Modulation signal

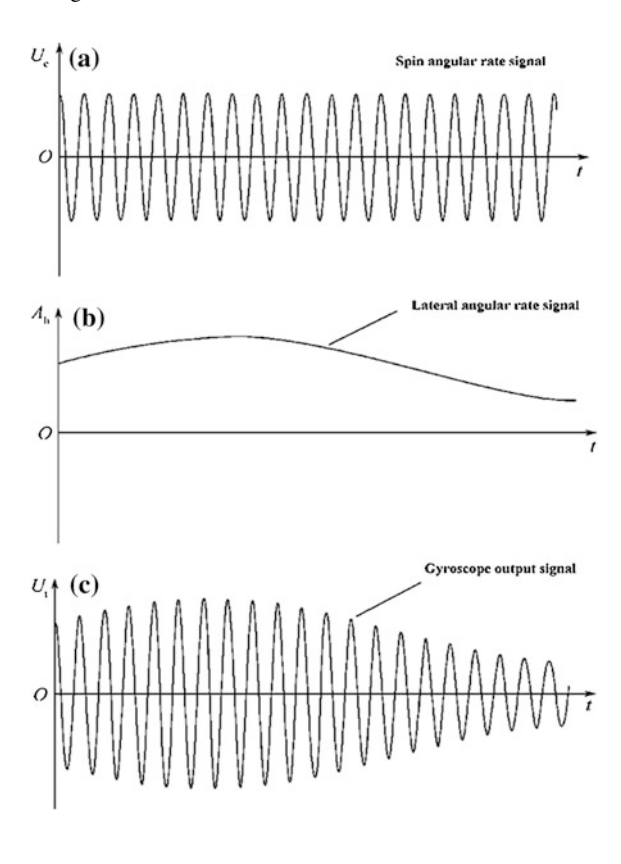
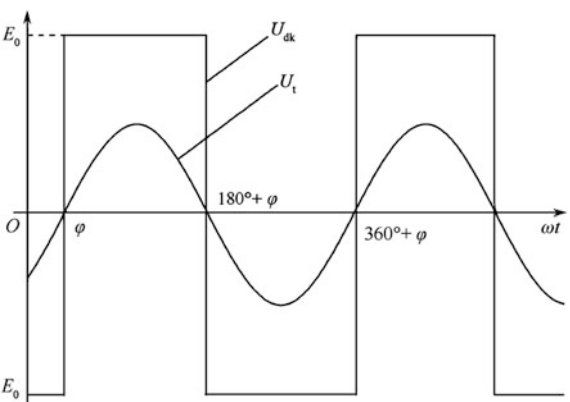


Fig. 11.18 Control method



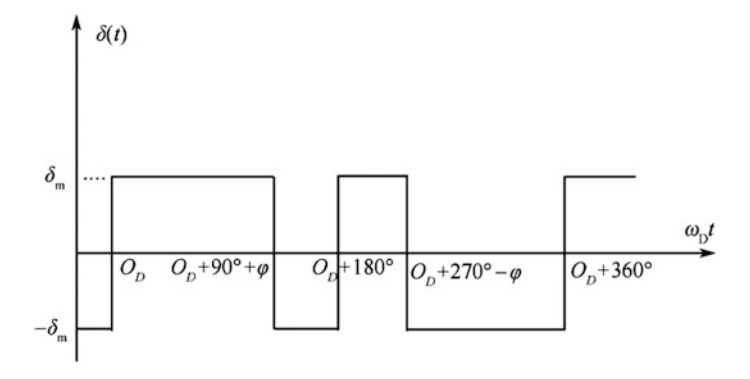


Fig. 11.19 Pulse width modulation control signal

the rotating flight carrier can be simultaneously achieved through a pair of rudder surfaces, that is, the single channel control of the rotating flight vector.

The analog output angular velocity of the gyroscope controls the rudder surface by the linearization of the function such that the attitude of the rotating flying carrier is controlled. The control signal is shown in Fig. 11.19.

11.5 Three Channels Attitude Sensing System of the Rotating Flight Carrier Through the Rectangular Coordinate Transformation

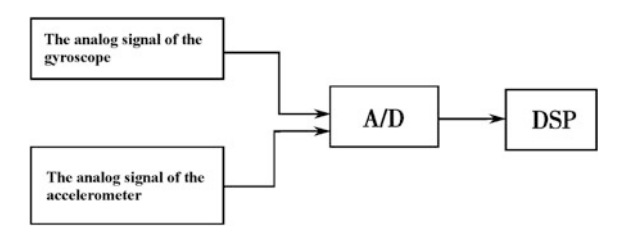
1. Calculation of Attitude Parameters of the Rotating Flight Carrier

By using the output signal of a "CJS-DR-WB01 type non-driven silicon micromechanical gyroscope" with geographic coordinate reference, six attitude parameters of the rotating flight carrier in the space can be calculated (three angular velocities and three accelerations).

The non-driven silicon micromechanical gyroscope is a type of angular velocity gyroscope whose angular velocity can be measured as long as it changes.

Design of the signal processing block diagram is shown in Fig. 11.20 and the calculation process is shown in Fig. 11.21.





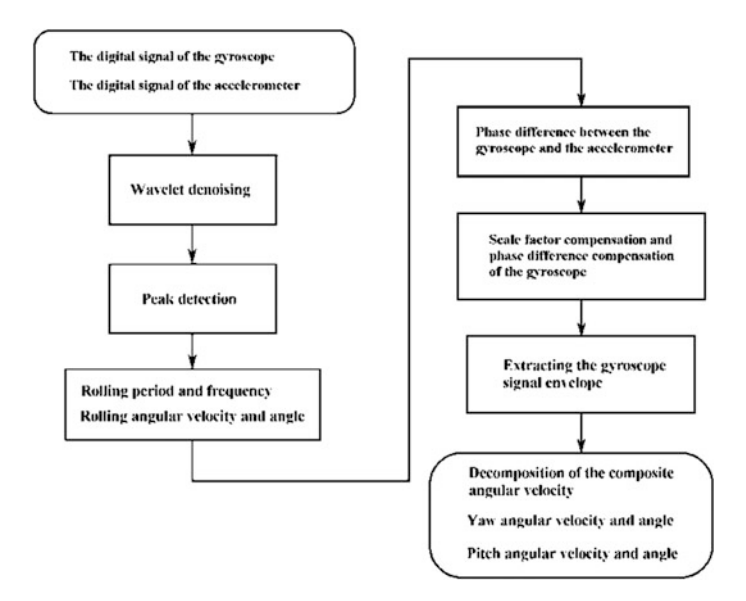
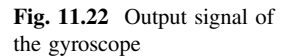
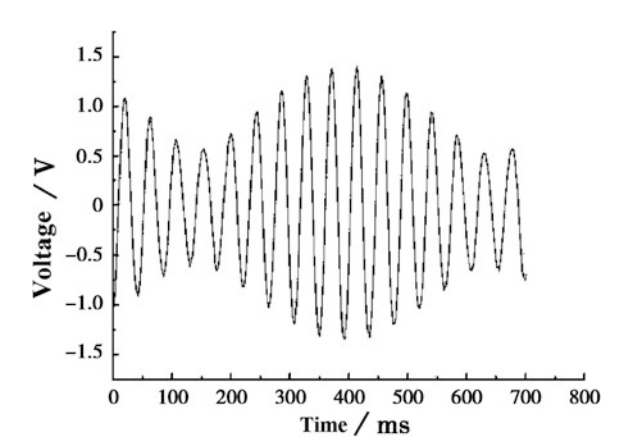


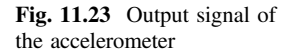
Fig. 11.21 Calculation process of the DSP software





The gyroscope is installed for testing on the inner loop workbench of the three-axis turntable. The experimental conditions are: the rolling frequency of the turntable inner loop is 24 Hz; the angular vibration frequency of the middle loop is 1 Hz and its amplitude is 5° ; the angular vibration frequency of the outer loop is 1 Hz and its amplitude is 5° .

The signals of the gyroscope and the accelerometer are shown in Figs. 11.22 and 11.23.



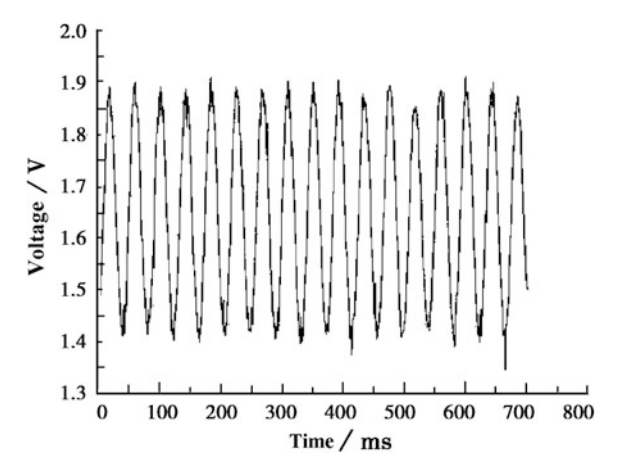
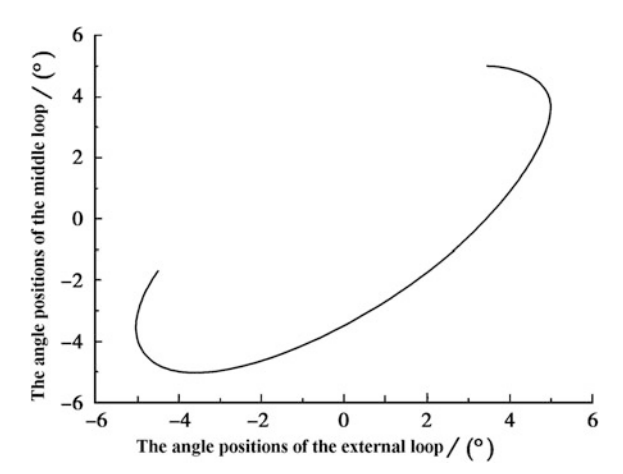


Fig. 11.24 Angle positions of the middle and external loops of the three-axis turntable



The laser space position of the inner loop of the three-axis turntable is shown in Fig. 11.24 and the calculated spatial attitude (angle) position of the vertical axis endpoint of the rotating flight carrier is shown in Fig. 11.25.

By comparison, the output yaw and pitch angular velocities of the gyroscope as well as the angular position error are shown in Table 11.1. The rolling frequency $f = 10.987 \,\text{Hz}$, and the relative error is 0.135%.

2. Test of the three-axis turntable

The flying state of the rotating flight carrier is simulated by the three-axis turntable: a gyroscope (with an accelerometer) is installed on the inner loop platform, the inner loop rotates (rolling of the rotating flight carrier), the angle vibrations of the middle loop the external loop are synthesized into an elliptical or a

Fig. 11.25 Calculated yaw and pitch angle position of the gyroscope

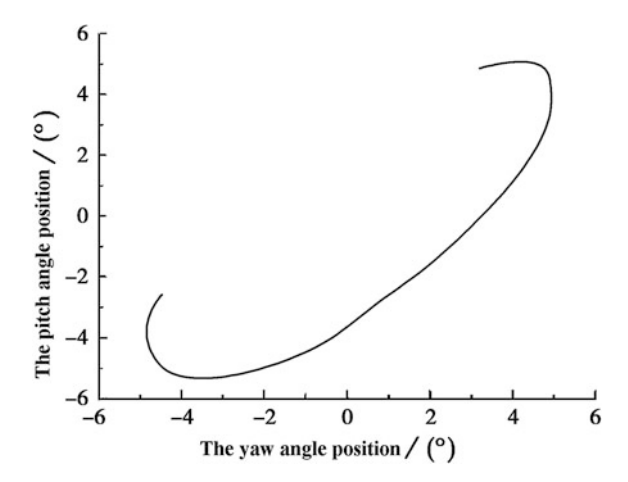


Table 11.1 Calculated error of the gyroscope signal

External loop position	0.997025	External loop velocity	0.988534
Middle loop position	0.99096	Middle loop velocity	0.996228

circular motion (or an angular vibration), and the real-time signals of the gyroscope and the accelerometer are extracted.

- (1) Simultaneously extract and process the three axial outputs of the three-axis turntable and get the "roll, pitch and yaw signals (angle and angular velocity)" of the "rotating flight carrier".
- (2) Process the output signal of the gyroscope and calculate the roll, pitch and yaw signals (the angle and the angular velocity).
- (3) Perform the whole calculation and compare the above steps and test the degree of compliance (accuracy) and real-time performance.
- (4) Add the test of the pitch angle and perform the complete calculation.
- 3. Synchronous acquisition, processing and comparison

The rotating angular velocity of the inner axis of the three-axis turntable represents the rolling angular velocity of the rotating flight carrier. The vibration angular velocity of the middle loop represents the pitch angular velocity and the vibration angular velocity of the external loop represents the yaw angular velocity. The signal of the accelerometer provides the geographic coordinate reference. The light on the wall (generated by the laser which is installed on the inner loop of the turntable) represents the attitude angle position of the longitudinal axis endpoint of the rotating flight carrier in flight.

The signal of the gyroscope, the signal of the accelerometer, and the signal of the three-axis turntable (the analog rotating flight carrier) are synchronously acquired and processed in real time, and then compared.

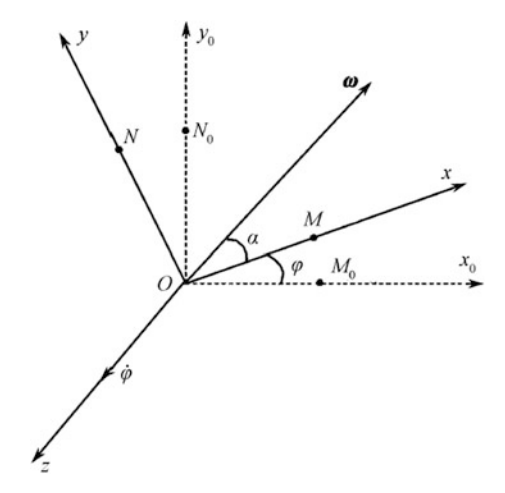
By using the attitude calculation software for the silicon micromechanical gyroscope (computer software copyright: 2009 5R030870), the yaw, pitch and roll angular velocities and the angles (incremental) can be obtained, and the angle measuring precision can reach $2^{\circ}/25$ s, $0.1^{\circ}/7$ s and $1^{\circ}/60$ s.

11.6 Attitude Sensing System of the Rotating Flight Carrier Through the Polar Coordinate Transformation

As shown in Fig. 11.26, where O is a fixed point on the longitudinal axis of the rotating flight carrier, OZ is fixed on the longitudinal axis of the rotating flight carrier, and two points are selected on the rotating flight carrier such that $OM \perp ON$ and the plane $OMN \perp OZ$. The coordinate system Oxyz of the rotating flight carrier is established through OM, ON and OZ, where the directions of the axis x and OM are the same, the directions of the axis y and ON are the same, and the directions of the axis z and OZ are the same.

When the rotating flight carrier in Fig. 11.26 rotates around the axis z with the rolling angular velocity $\dot{\varphi}$, the coordinate plane Oxy will also rotate around the axis z with the rolling angular velocity $\dot{\varphi}$. Assume that the rotating flight carrier begins to rotate and the points M and N are M_0 and N_0 on the axes OM_0 and ON_0 respectively. The coordinate system Ox_0y_0z is established through OM_0 , ON_0 and OZ, where the directions of Ox_0 and OM_0 are the same, the directions of Oy_0 and ON_0 are the same and the directions of Oz and OZ are the same. If the coordinate system Ox_0y_0z is defined as the coordinate system of the quasi-rotating flight carrier, there exists the following relationship between the coordinate system Oxyz of

Fig. 11.26 Coordinate system transformation of the rotating flight carrier



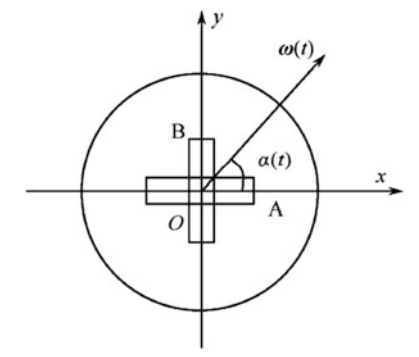
the rotating flight carrier and the coordinate system Ox_0y_0z of the quasi-rotating flight carrier:

$$\begin{pmatrix} x_0 \\ y_0 \\ z \end{pmatrix} = \begin{pmatrix} \cos \varphi & -\sin \varphi & 0 \\ \sin \varphi & \cos \varphi & 0 \\ 0 & 0 & 1 \end{pmatrix} \begin{pmatrix} x \\ y \\ z \end{pmatrix}$$
(11.11)

that is, the coordinate system Ox_0y_0z of the quasi-rotating flight carrier rotates around the axis z counterclockwise with angle $\varphi(t)$, and the coordinate system of the rotating flight carrier can be obtained.

The positional relationship between the sensitive elements A and B of the non-driven silicon micromechanical gyroscope is shown in Fig. 11.27. The sensitive axes of the sensitive elements A and B are perpendicular to each other, the sensitive axis of the sensitive element A is in the y axis, and the sensitive axis of the sensitive element B is in the x axis. The coordinate plane Oxy of the coordinate system Oxyz of the rotating flight carrier (Fig. 11.26) is connected to the sensitive element, that is, Oxy is connected to the rotating flight carrier, and the rotates by the angular velocity $\dot{\varphi}$. Therefore, assume that the angle of the transverse angular velocity $\omega(t)$ relative to the x axis of the coordinate system of the rotating flying carrier is $\alpha(t)$ and the angle of the transverse angular velocity relative to the axis x_0 of the coordinate system Ox_0y_0z of the quasi-rotating flight carrier (Fig. 11.26) is $\varphi(t) + \alpha(t)$. Therefore, in order to obtain the transverse angular velocity and its direction relative to the coordinate system of the quasi-rotating flight carrier, it is necessary to get $\omega(t)$, the azimuth angle $\alpha(t)$ relative to the coordinate system of the rotating flight carrier and the rolling angle $\varphi(t)$ relative to the coordinate system of the quasi-rotating flight carrier.

Fig. 11.27 Positional relationship diagram between the sensitive elements A and B of the non-driven silicon micromechanical gyroscope



11.6.1 Method for Obtaining the Transverse Angular Velocity Relative to the Rotating Coordinate System of the Rotating Flight Carrier

When there is an arbitrary transverse angular velocity $\omega(t)$ as shown in Fig. 11.27 and the coordinate system Oxyz is the reference coordinate system, the output voltage signals of the non-driven silicon micromechanical angular velocity sensitive elements A and B are as follows:

$$V_{\rm A}(t) = k_{\rm A}\omega(t)\sin\alpha(t) \tag{11.12}$$

$$V_{\rm B}(t) = k_{\rm B}\omega(t)\cos\alpha(t) \tag{11.13}$$

where $V_A(t)$ and $V_B(t)$ are the output voltage signals of the sensitive elements A and B; k_A and k_B are the scale factors of the sensitive elements A and B; and $\alpha(t)$ is the angle between the transverse angular velocity $\omega(t)$ and the axis x.

It is easy to find that $V_{\rm A}(t)$ and $V_{\rm B}(t)$ are orthogonal (Fig. 11.28). Thus by using the orthogonal envelope detection method in Fig. 11.29, the transverse angular velocity and the azimuth angle of the relative coordinate system Oxyz can be obtained.

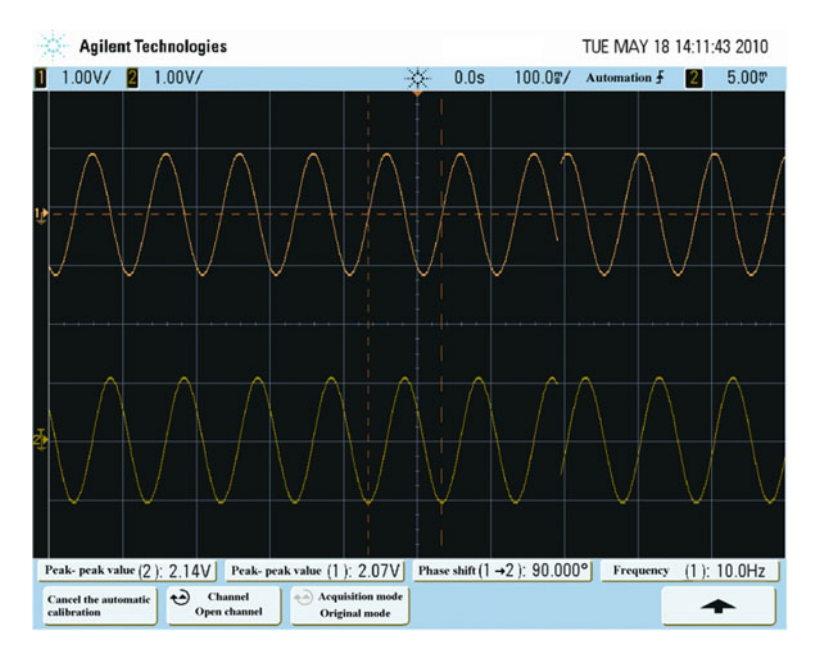


Fig. 11.28 Phase relationship between output voltage signals of sensitive elements A and B

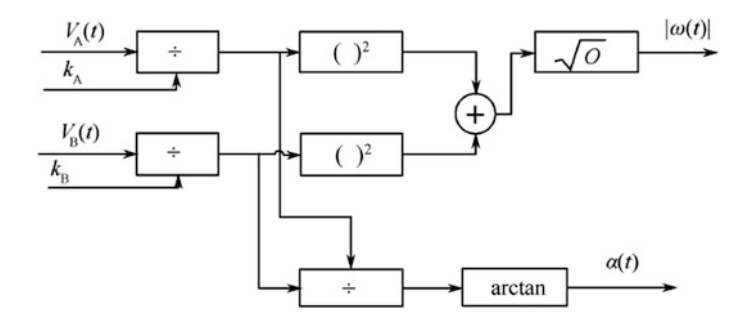


Fig. 11.29 Theory of orthogonal envelope detection

From Eqs. (11.12) and (11.13), obtains

$$\omega^{2}(t) = (V_{A}(t) / k_{A})^{2} + (V_{B}(t) / k_{B})^{2}$$
(11.14)

$$\tan \alpha(t) = \left(V_{\mathbf{A}}(t)k_{\mathbf{B}}\right) / \left(V_{\mathbf{B}}(t)k_{\mathbf{A}}\right) \tag{11.15}$$

From Eq. (11.14) the transverse angular velocity is obtained as

$$|\omega(t)| = \sqrt{(V_{\rm A}(t)/k_{\rm A})^2 + (V_{\rm B}(t)/k_{\rm B})^2}$$
 (11.16)

From Eq. (11.15) the azimuth angle is obtained as

$$\alpha(t) = \arctan(V_{A}(t)k_{B}) / (V_{B}(t)k_{A})$$
(11.17)

Therefore, from Eq. (11.16) the transverse angular velocity $\omega(t)$ can be determined and from Eq. (11.17) the azimuth angle $\alpha(t)$ can be determined.

If the scale factors of the sensitive elements A and B are the same, that is,

$$k_{\mathsf{A}} = k_{\mathsf{B}} = k \tag{11.18}$$

Substituting Eq. (11.18) into Eqs. (11.16) and (11.17) the transverse angular velocity $\omega(t)$ can be expressed as

$$|\omega(t)| = \sqrt{V_{\rm A}^2(t) + V_{\rm B}^2(t)} / k$$
 (11.19)

The azimuth angle $\alpha(t)$ can be expressed as

$$\alpha(t) = \arctan V_{\rm A}(t) / V_{\rm B}(t) \tag{11.20}$$

Therefore, for the silicon micromechanical gyroscope with scale factor $k_A = k_B = k$, the transverse angular velocity $\omega(t)$ relative to the coordinate system

Oxyz of the rotating flight carrier can be determined by Eq. (11.19) and the azimuth angle $\alpha(t)$ can be determined by Eq. (11.20).

11.6.2 Method for Obtaining the Rolling Angular Velocity Relative to the Coordinate System of the Ouasi-Rotating Flight Carrier

The scale factors of the sensitive elements A and B are adjusted to be the same such that $k_A = k_B = k$. The angle of the transverse angular velocity $\omega(t)$ relative to the axis x_0 of the coordinate system of the quasi-rotating flight carrier is $\varphi(t) + \alpha(t)$, while it is assumed that the rolling axis rotates with a rolling frequency f, then the azimuth angle induced by rolling at time t is $\varphi(t) = 2\pi ft$. Because $\dot{\varphi}(t) = 2\pi f \gg \dot{\alpha}(t)$, $\varphi(t) + \alpha(t)$ can be expressed by $\varphi(t) = 2\pi ft$. Thus Eqs. (11.12) and (11.13) can be expressed as

$$V_{\rm A}(t) = k\omega(t)\sin\left(2\pi ft\right) \tag{11.21}$$

$$V_{\rm B}(t) = k\omega(t)\cos\left(2\pi f t\right) \tag{11.22}$$

The voltage output signals $V_A(t)$ and $V_B(t)$ are proportional to the transverse angular velocity which is modulated by the carrier with frequency f, and scaling factor is k. From the characteristics of the modulation signal it can be known that the frequency of the modulated signal contains the two main frequencies of f_1 and f_2 respectively,

$$f_1 = f - f_{\omega} \tag{11.23}$$

$$f_2 = f + f_{\omega} \tag{11.24}$$

In order to obtain the frequency f of the rolling axis in real time, it is necessary to eliminate the frequency f_{ω} of the low frequency signal $\omega(t)$. The carrier frequency is usually extracted by using the orthogonal frequency detection method and its principle block diagram is shown in Fig. 11.30.

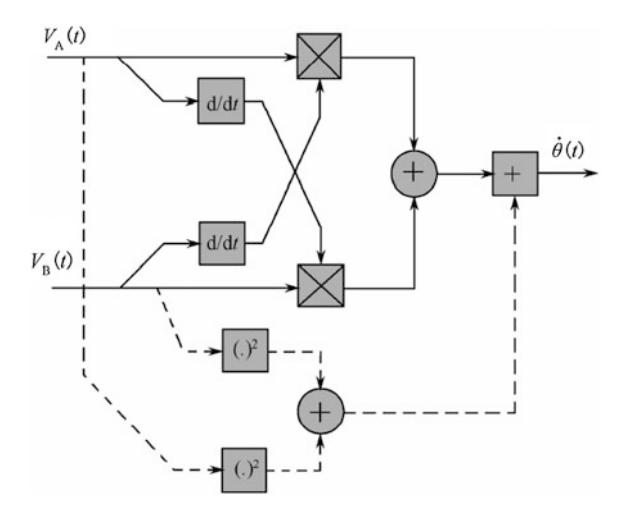
Firstly, calculate the derivatives of $V_A(t)$ and $V_B(t)$ respectively,

$$\dot{V}_{A}(t) = k\dot{\omega}(t)\sin\left(2\pi f t\right) + k2\pi f\omega(t)\cos\left(2\pi f t\right) \tag{11.25}$$

$$\dot{V}_{\rm B}(t) = k\dot{\omega}(t)\cos\left(2\pi f t\right) - k2\pi f\omega(t)\sin\left(2\pi f t\right) \tag{11.26}$$

$$\dot{V}_{A}(t)V_{B}(t) = k^{2}\omega(t)\dot{\omega}(t)\sin(2\pi f t)\cos(2\pi f t) + k^{2}2\pi f\omega^{2}(t)\cos^{2}(2\pi f t) \quad (11.27)$$

Fig. 11.30 Theory of orthogonal frequency detection



$$V_{\rm A}(t)\dot{V}_{\rm B}(t) = k^2\omega(t)\dot{\omega}(t)\sin{(2\pi f t)}\cos{(2\pi f t)} - k^22\pi f\omega^2(t)\sin^2(2\pi f t) \quad (11.28)$$

From Eqs. (11.27) and (11.28) obtain

$$\dot{V}_{A}(t)V_{B}(t) - V_{A}(t)\dot{V}_{B}(t) = k^{2}2\pi f\omega^{2}(t)$$
(11.29)

Because

$$V_{\rm A}^2(t) + V_{\rm B}^2(t) = k^2 \omega^2(t) \tag{11.30}$$

When $V_A^2(t) + V_B^2(t) \neq 0$, from Eqs. (11.29) and (11.30) obtains

$$\frac{\dot{V}_{A}(t)V_{B}(t) - V_{A}(t)\dot{V}_{B}(t)}{V_{A}^{2}(t) + V_{B}^{2}(t)} = 2\pi f$$
(11.31)

Thus the rolling frequency is obtained as

$$f = \frac{\dot{V}_{A}(t)V_{B}(t) - V_{A}(t)\dot{V}_{B}(t)}{2\pi[V_{A}^{2}(t) + V_{B}^{2}(t)]}$$
(11.32)

According to the rolling frequency f in Eq. (11.32) the effect of the transverse angular velocity frequency f_{ω} is eliminated and the rolling angular velocity $\dot{\varphi} = 360^{\circ} \times f_o$. Because all the values in the above calculation can be obtained at a certain time, the delay of the actual process is only the inevitable operation time.

11.6.3 Method for Obtaining the Pitch Angular Velocity and the Yaw Angular Velocity Relative to the Coordinate System of the Quasi-Rotating Flight Carrier

By using the mentioned methods for obtaining the transverse angular velocity and the rolling angular velocity, the transverse angular velocity $\omega(t)$ and the azimuth angle $\alpha(t)$ relative to the coordinate system of the rotating flight carrier can be obtained in real-time, and the rolling angular velocity $\dot{\varphi}$ relative to the coordinate system of the quasi-rotating flight carrier is obtained. According to the coordinate transformation in Eq. (11.11), the yaw angular velocity ω_{ph} and the pitch angle velocity ω_{fy} relative to the coordinate system Ox_0y_0z of the quasi-rotating flight carrier can be calculated as follows

$$\omega_{ph} = |\omega(t)| * \cos[\alpha(t) + \varphi(t)]$$
(11.33)

$$\omega_{fy} = |\omega(t)| * \sin[\alpha(t) + \varphi(t)]$$
 (11.34)

where a(t) is the azimuth angle of the transverse angular velocity $\omega(t)$ relative to the coordinate system of the rotating flight carrier, and $\varphi(t)$ is the rotating angle of the rotating carrier.

$$\varphi(t) = \int_{0}^{t} \dot{\varphi}(t) dt$$
 (11.35)

By integrating Eqs. (11.33) and (11.34) with respect to t, the yaw angle Ω_{ph} and the pitch angle Ω_{fy} can be obtained as

$$\Omega_{ph} = \int_{0}^{t} \omega_{ph} dt \tag{11.36}$$

$$\Omega_{fy} = \int_{0}^{t} \omega_{fy} dt \tag{11.37}$$

11.7 Applications in the Non-rotating Flight Carrier

The silicon micromechanical gyroscope has no driven structure, and its invisible driving force is provided by the rotating flight carrier to produce the gyroscope effect. For the non-rotating flight carrier, the rotating flight carrier cannot provide the driving force, thus it is necessary that the micromechanical gyroscope is driven by a motor. The schematic diagram of the silicon micromechanical gyroscope with a motor drive is shown in Fig. 11.31.

The performance of the active rotating micromechanical gyroscope can satisfy the requirements of the rotating flight carrier. The appearance of the product with the installation benchmark is shown in Fig. 11.32.

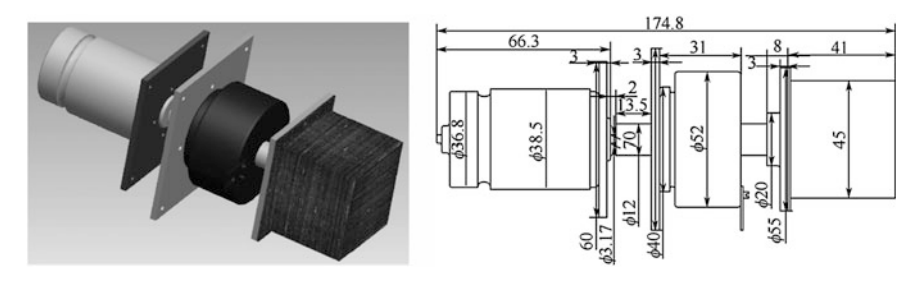
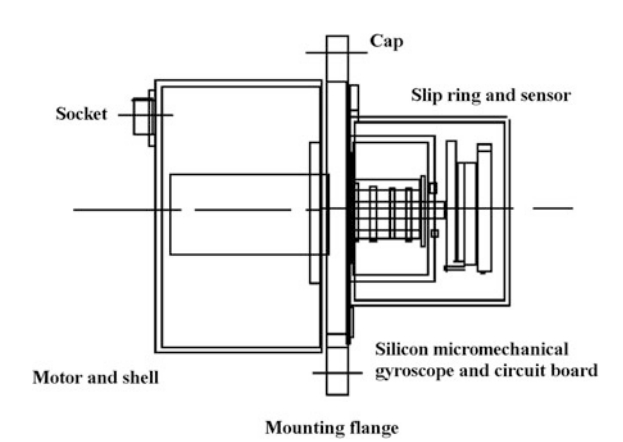
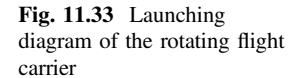
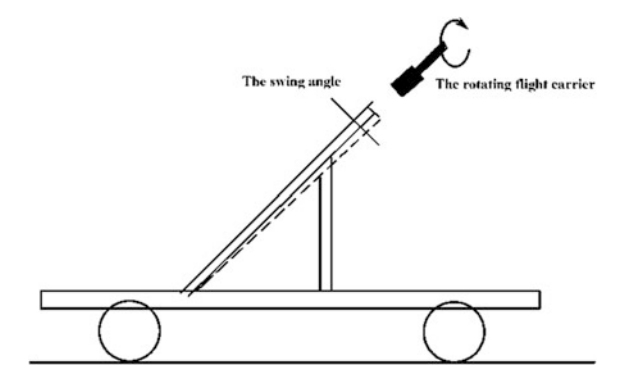


Fig. 11.31 Photo and assembly sketch of the motor-driven silicon micromechanical gyroscope

Fig. 11.32 Active rotating silicon micromechanical gyroscope







The "active rotating silicon micromechanical gyroscope" is applied to the rotating flight carrier such that the swing angle and other technical requirements of the detection launch are satisfied before the rotating flight carrier leaves the cartridge (Fig. 11.33).

- Konovalv, S.F., A.V. Kuleshov, V.P. Podtchezertsev et al. 2003. Vibrating angular rate sensor. In *Integrated Navigation Systems Proceedings, of 10th International Conference*. St Petersburg, 107–117.
- 2. Wang Hong-wei, Jia-lin Zhu, Wei Zhang, and Fu-xue Zhang. 2003. Angular rate sensor for rotating carrier. *Journal of Transducer Technology* 9 (22): 47–49, 55.
- 3. Wang Hong-wei, Jia-lin Zhu, Wei Zhang, Chao-min Zhang, and Fu-xue Zhang. 2003. A model of angular rate sensor for circumrotated carrier. *Journal of Chinese Inertial Technology* 3 (11): 56–58, 63.
- Zhang Fuxue, Hongwei Wang, Wei Zhang, et al. 2005. A silion micromachined gyroscope driven by the rotating carrier's angle velocity. In *Proceedings of the 2005 IEEE* International Conference on Information Acquisition, Hong Kong and Macau, China, 128–133.
- Zhang, Fuxue, Hongwei Wang, Wei Zhang, et al. 2005. The structure principle of silicon micromachined gyroscope driven by the rotating carrier. *International Journal of Information Acquisition* 2 (3): 203–216.
- 6. Mao Xu, Yu Liu, Wei Zhang, and Fu-xue Zhang. 2005. Cu/Si films grown by magnetron sputtering. *Electronic Components and Materials* 10 (24): 1–3.
- Zhang Fu-xue, Hong-wei Wang, Wei Zhang, Xu Mao, and Nang Zhang. 2005. Silicon micromachined gyro driving by angular rate of the rotating substrate. *Piezoelectrics & Acoustooptics* 2 (27): 109–117.
- 8. Zhang Fuxue, Hongwei Wang, Wei Zhang, et al. 2005. A silicon micromachined gyroscope driven by the rotating carrier's angle velocity. In *Proceedings of the 2005 IEEE International Conference on Information Acquisition*, 128–133.
- 9. Zhang Fu-xue, Hong-wei Wang, Wei Zhang, Xu Mao, and Nan Zhang. 2006. Design and performance test of a silicon micro-machined gyro driving by rotating carrier. *Electronic Components and Materials* 12 (25): 20–26.
- 10. Liu, Yu., Xu Mao, Ping Yue, and Fu-xue Zhang. 2006. Research on KOH etching Si by the thermostatic magnetic mixer. *Electronic Components and Materials* 12 (25): 41–46.
- Wang, Hong-wei, Xu Mao, Wei Zhang, and Fu-xue Zhang. 2006. The sense organ of silicon micro-machined gyroscope using for circumrotation carrier. *Piezoelectrics & Acoustooptics* 2 (28): 170–172.
- 12. Zhang, Fuxue, Xu Mao, and Wei Zhang. 2006. Si micromachined gyroscope driven by the rotating carrier. *Engineering Science* 8 (8): 23–27.
- 13. Zhang, Nan, Jiang-chuan Wen, and Fu-xue Zhang. 2006. Research on electrical model of silicon micromachined gyroscope driven by carrier. *Journal of Shihezi University (Natural Science)* 3 (24): 325–328.
- 14. Mao Xu, Liang Ming, Fuxue Zhang, et al. 2006. A kind of shock resistance method on silicon micromachimed gyroscope. In *Proceedings of the 2006 IEEE International Conference on Information Acquisition*, 101–105.

References References

 Liang, Ming, Yin-nian Wang, Jia-guang Wang, and Fu-xue Zang. 2006. Design of a signal detection circuit of silicon micromachined gyroscope. *Journal of Beijing Institute of Machinery* 4 (21): 20–25.

- Zhang Fuxue, Xu Mao, Liu Yu, et al. 2006. A silicon micromachined gyroscope driven by the rotating carrier self. *Rare Metal Materials and Engineering*, supplement 3 (35): 519–521.
- 17. Mao Xu, Yingxia Jin, Zhou Zhenlai, et al. 2006. The research on growth temperature of ge/si thin films grown by magnetron sputtering. *Rare Metal Materials And Engineering*, supplement 3 (35): 564–566.
- 18. Zhang Fuxue, and Xu Mao. 2006. Designed and fabricated a novel micromachined gyroscope. In *Asia-Pacific Conference of Transducers and Micro–Nano Technology, APCOT2006 Marina Mandarin Hotel*, Singapore, 1–4.
- 19. Mao Xu, Liu Yu, Mingqing Ding, et al. 2006. The performance of a new silicon micromachined gyroscope. In *Asia-Pacific Conference of Transducers and Micro–Nano Technology, APCOT2006 Marina Mandarin Hotel*, Singapore, 1–4.
- Zhang Fuxue, Ling Wang, and Jiangchuan Wen. 2007. Silicon micromachined angular rate sensor. In *Proceeding of 2007 International on Information Acquisition. Jeju, Korea*, IEEE, 2007. 17–24.
- 21. Fuxue, Zhang, and Wei Zhang. 2007. Si micromachined gyroscope driven by the rotating carrier. *Engineering Sciences* 5 (2): 148–152.
- Wang Ling, and Fuxue Zhang. 2007. Research on principle and phase of silicon micromachined gyroscope using for rotating carrier. In *Proceedings of the 2007 International Conference on Information Acquisition*, 10–16.
- 23. Fu-xue, Zhang, and Wei Zhang. 2007. Measuring error caused by spin angular velocity of rotating carrier. *Journal of scientific research (Hongkong)* 8: 21–34.
- Fu-xue, Zhang, and Wei Zhang. 2007. Influence of the rotator's spinning instability on the stability of Si micromachined gyroscope. *Journal of Chinese Inertial Technology* 5 (15): 585–588.
- Xu, Mao, Liu Yu, Yin-nian Wang, Ming-qing Ding, and Fu-xue Zhang. 2007. Research on two-dimensional silicon micro-machined gyroscope. *Piezoelectrics & Acoustooptics* 29 (3): 298–301.
- Ye Qing, Yangmeng Tian, Fuxue Zhang. 2008. Research on non-linearity compensation technology for the output signal of silicon micromachined gyroscope. In *Proceedings of the* 2008 IEEE International Conference on Information and Automation, 1503–1507.
- Zhang W, F.X. Zhang, Q.W. Yan. 2008. The study of signal processing technology for the no-driven silicon micromachined gyro. In *The 4th Asia Pacific Conference on Transducers* and Micro/Nano Technologies APCOT.
- 28. Zhang W, F.X. Zhang, Q.W. Yan. 2008. Multifunction silicon micromachined gyro. In *The* 4th Asia Pacific Conference on Transducers and Micro/Nano Technologies APCOT.
- Xu Xiao-song, Jing Fan, Hai-lin Liu, Jian-ming Xiao, and Fu-xue Zhang. 2008. Phase research of silicon micro-machined gyroscope using for rotating carrier. *Journal of Beijing Institute of Machinery*, 2 (23): 1–4.
- Xiao, Jian-ming, Jing Fan, Hai-lin Liu, Xu Xiao-song, and Fu-xue Zhang. 2008. Research
 on the signal of micro-machined silicon gyroscope for rotating carrier. *Journal of Beijing Institute of Machinery* 2 (23): 5–9.
- 31. Zhang, Fuxue. 2008. Influence of the instability of angular velocity of the rotating carrier itself on the stability of silicon micromachined gyroscope. *Engineering Sciences* 3 (6): 27–30.
- 32. Zhang, Fu-xue, Wei Zhang, and Qing-wen Yan. 2008. Non-driven silicon micro-mechanical gyroscope. *Piezoelectrics & Acoustooptics* 6 (30): 660–663.
- 33. Ye, Qing, Yang-meng Tian, and Fu-xue Zhang. 2008. Non-linearity compensation algorithm for the output signal of silicon micro-machined gyroscope. *Journal of Beijing Institute of Machinery* 3 (23): 5–10.

 Liu Hai-lin, Xiao-song Xu, and Jian-ming Xiao, Fu-xue Zhang. 2008. Signal process for the non-drive silicon micro-machined gyroscope. Journal of Beijing Institute of Machinery, 3 (23): 11–14, 33.

- 35. Liu Hailin, Xiaosong Xu, and Fuxue Zhang. 2008. Signal process for the non-drive silicon micro-machine gyroscope. In 2008 Pacific-Asia Workshop on Computational Intelligence and Industrial Application, 731–735.
- Xiao Jianming, Xiaosong Xu, and Fuxue Zhang. 2008. Research on the signal of silicon micro-machined gyroscope for rotating carrier. In 2008 Pacific-Asia Workshop on Computational Intelligence and Industrial Application, 846–851.
- 37. Xu Xiaosong, Hailin Liu, and Fuxue Zhang. 2008. Phase processing of non-drive structure silicon micromachined gyroscope. In 2008 Pacific-Asia Workshop on Computational Intelligence and Industrial Application, 987–991.
- 38. Feng, W.L., and F.X. Zhang. 2008. Research on fast calibration method for scale factor of micro-machined gyroscope. In 2008 3rd IEEE Conference on Industrial Electronics and Applications.
- Feng, W.L., and F.X. Zhang. 2008. Effect of the temperature on the performance of silicon micro-machined gyroscope using for rotating carrier. In 2008 Chinese Control and Decision Conference.
- Feng, W.L., and F.X. Zhang. 2008. The study of the scale factor of micro-machined gyroscope. IEICE Electronics Express, 5 (19): 840–845.
- Zhang Wei, Chen Chen, Shiyu Jiang, et al. 2008. Signal processing technique of omnidirectional gasflow style horizontal posture sensor. In 2008 IEEE International Conference on Information and Automation, ICIA, 1317–1321.
- Zhang, F.X. 2011. 2009/2010 Sensor and actuator collections. Beijing: Publishing House of electronics industry.
- 43. Chen Chen, Qiushi Han, Shiyu Jiang, et al. 2008. Research and design of micro-machined gas-pendulum dual-Axis tilt sensors common-mode restraining acceleration interference. *International Conference on Information and Automation*, 1485–1489.
- 44. Yan, Q.W., J.L. Zhu, and F.X. Zhang. 2008. The preparation of the single crystal pbti powder by sol-gel. In *The 4th Asia Pacific Conference on Transducers and Micro/Nano Technologies APCOT*.
- 45. Jiang, Shi-yu, Wei Zhang, Chen Chen, and Fu-xue Zhang. 2008. Signal processing technique of anti-acceleration disturb gasflow style inclination sensor. *Journal of Beijing Institute of Machinery* 23 (2): 10–13.
- Zhang, Wei, and Fu-xue Zhang. 2008. The structure and signal processing technology of the omnidirectional gasflow style obliquity sensor. *Electronic Components and Materials* 27 (10): 16–19.
- 47. Zheng, Yong-hong, Shi-liu Peng, Ying-xia Jing, Ying-xia Huang, and Fu-xue Zhang. 2008. Method of eliminating influence of environmental temperature on tilt sensor property. *Piezoelectrics & Acoustooptics* 30 (1): 33–35.
- 48. Jin, Ying-xia, Jing Zhou, Bin Zhang, Yong-hong Zheng, and Fu-xue Zhang. 2008. Study on distribution of fluidic velocity and force analysis of the airflow angle velocity sensor. *Piezoelectrics & Acoustooptics* 30 (5): 564–567.
- Jiang Shiyu, and Fuxue Zhang. 2008. The organ design and signal processing technique of anti-acceleration disturb gasflow style inclination sensor. Pacific-Asia Workshop on Computational Intelligence and Industrial Application, 736–740.
- Zhang Wei, Qingwen Yan, and Fuxue Zhang, et al. 2009. Design and realization for high dynamic silicon micromachined gyroscope. In 2009 IEEE International Conference on Information and Automation, ICIA, 1293–1297.
- Yan, Q.W., W. Zhang, L.F. Wu, et al. 2009. Measurement of rotation and angular vibration frequencies of spinning projectile in coning motion by a silicon micromachined gyro. In 2009 IEEE International Conference on Information and Automation, ICIA, 1018–1022.

 Zhang Fuxue, Qingwen Yan, Wei Zhang, et al. 2009. Determination of attitude of rotating carrier using a silicon micromachined gyroscope. In 2009 IEEE International Conference on Information and Automation, ICIA, 665–669.

- Zhang Fuxue, Qingwen Yan, Wei Zhang. 2009. Experiments and results of the silicon micromachined gyroscope. *Journal of Micro/Nanolithography, MEMS, and MOEMS* 8 (2): 1–6.
- Yan Qingwen, Fuxue Zhang, and Lifeng Wu. 2009. Silicon micromechanical gyroscope suitable for single channel control of rotating flight carrier. *Journal of Chinese Inertial Technology* 17 (5): 599–603.
- 55. Ye, Qing, Yang-meng Tian, Fu-xue Zhang, and Juan Zheng. 2009. Non-linearity compensation algorithm and realization for the output signal of silicon micromachined gyroscope. *Piezoelectrics & Acoustooptics* 31 (5): 633–635.
- Wu Li-feng, Fu-xue Zhang, Qing-wen1 Yan, and Yu Liu. 2009. Mechanism analysis on micromachined gyroscope's detecting rotator's spin. *Journal of Chinese Inertial Technology* 17 (2): 214–217.
- 57. Fan Jing, and Rong Yang. 2009. Bluetooth wireless network and A/D converter for data acquisition. Instrument Technique and Sensor, supplement, 261–263.
- 58. Yan Qing-wen, Zong-kai Zhang, Qing-chen Liu, Li-feng Wu, and Fu-xue Zhang. 2009. Silicon micromachined gyroscope for autopilot of rotating carrier. Instrument Technique and Sensor, supplement, 302–305.
- Zhang Fuxue, Qingwen Yan, and Lifeng Wu. 2009. Principle analysis and performance test of non-driven silicon micromechanical gyroscope. Instrument Technique and Sensor, supplement, 16–24.
- Xu Hong-zhuo, Li-feng Wu, Qing-wen Yan, Cheng-xiang Sun, and Fu-xue Zhang. 2009.
 Temperature effects on the phase difference of non-driven constructor silicon micro-machined gyroscope. Instrument Technique and Sensor, supplement, 309–312.
- Wen, Jiang-chuan, Ling Wang, Jia-guang Wang, and Fu-xue Zhang. 2009. Errors analysis
 of silicon micro-machined gyroscope driven by rotating carrier. *Piezoelectrics & Acoustooptics* 31 (2): 172–174.
- Sun Cheng-xiang, Yang-meng Tian, Qing-wen Yan, Li-feng Wu, Hong-zhuo Xu, and Fu-xue Zhang. 2009. Application of gravity accelerometer in signal demodulation silicon of micro-machined gyroscope. Instrument Technique and Sensor, supplement, 306–308.
- 63. Chen Chen, Qiushi Han, and Fuxue Zhang. 2009. Scaling effect research on micro-machined gas-pendulum dual-axis tilt sensors. In *International Conference on Sensing Technology*, 301–306.
- 64. Piao, Lin-hua, Xia Ding, Yan-jie Li, and Fu-xue Zhang. 2009. Effect of natural convection on the gas-flow angular rate sensor. *Piezoelectrics & Acoustooptics* 31 (2): 182–185.
- 65. Zhang, Fu-xue. 2009. Gas pendulum accelerometer and laminar jet angular rate gyroscope. Journal of Beijing Information Science & Technology University 24 (2): 1–8.
- 66. Liang, Fu-ping, Xiao-li Xu, Fu-xue Zhang, Zhong Su, Guo-xing Wu, and Qiu-shi Han. 2009. Sensor technology in the building of flexible development platform for modern instrument manufacture. *Journal of Beijing Information Science & Technology University* 24 (3): 22–26.
- Song Jia, Lin-hua Piao, Yu-jie Liu, Yan-jie Li, and Fu-xue Zhang. 2009. Sensitive mechanism of micromachined airflow omnibearing posture sensor. Piezoelectrics & Acoustooptics 31 (6): 797–799, 810.
- 68. Chen Chen, Qiu-shi Han, Fu-xue Zhang. 2009. Overview on micro-machined tilt sensors based on gas convection. *Journal of Beijing Information Science & Technology University* 24 (4): 35–38.
- Wu, L.F., Zh Peng, Q.W. Yan, et al. 2010. Design and implement of attitude sensor for high-speed-speed-spin vehicle. In *Applied Mechanics and Materials* (2010). Switzerland: Trans Tech Publications.

 Zhang Fuxue, Qingwen Yan, and Lifeng Wu. 2010. Research on vibration and shock-proof technology of silicon micro-machined gyroscope. In *Applied Mechanics and Materials* (2010). Switzerland: Trans Tech Publications.

- Yan Qingwen, Fuxue Zhang, Lifeng Wu, et al. 2010. Research on signal demodulation method of silicon micro-machined gyroscope. In *Applied Mechanics and Materials* (2010). Switzerland: Trans Tech Publications.
- Sun Chengxiang, Yangmeng Tian, Qingwen Yan, et al. 2010. Analyses on output signal of silicon micro-machined gyroscope. In Applied Mechanics and Materials (2010). Switzerland: Trans Tech Publications.
- Zhao Qifeng, Fuxue Zhang, Wei Zhang, et al. 2010. The Research of micromachined gas pendulum accelerometer's structrue. In *Applied Mechanics and Materials* (2010). Switzerland: Trans Tech Publications, 7–10.
- Wu Lifeng, Qingwen Yan, Hongzhuo Xu, et al. 2010. The theory analysis of non-driven micromechanical gyroscope. *Chinese Journal of Sensors and Actuators* 23 (2): 196–200.
- Zhang Fuxue, Qifeng Zhao, Ping Yue, et al. 2010. Two-dimension micromachined gas pendulum accelerometer and tilt sensor. *Piezoelectrics & Acoustooptics* 32 (1): 27–30.
- Yan Qingwen, Fuxue Zhanf, and Lifeng Wu. 2010. Theoretical and experimental study of silicon micro-machined gyroscope for measuring attitude of spinning projectile. Piezoelectrics & Acoustooptics 32 (2): 210–214,218.
- 77. Zheng, Yonghong, Shiliu Peng, and Fuxue Zhang. 2010. Designs for temperature compensation circuit based on fluid similarity. *Piezoelectrics & Acoustooptics* 32 (2): 223–225.
- 78. Wu Li-feng, Qing-wen Yan, Hong-zhuo Xu, Wei Zhang, and Fu-xue Zhang. 2010. Signal demodulation method of attitude sensor for high-speed-rotating aircraft. *Transducer and Microsystem Technologies* 29 (6): 28–31.
- Wu Lifeng, Qingwen Yan, and Hongzhuo Xu. 2010. Development of attitude sensor for rotating flight carrier based on MEMS gyroscope. *Piezoelectrics & Acoustooptics* 32 (5): 742–745.
- 80. Wu Lifeng, and Fuxue Zhang. 2010. A novel non-driven structural MEMS-based gyroscope. *JDCTA International Journal of Digital Content Technology and its Applications* 4 (6): 85–88.
- Wu Lifeng, Zhen Peng, Fuxue Zhang. 2010. Design and implementation of a digital angular rate sensor. Open Access sensors ISSN1424-8220, 9581-9589.
- 82. Shan Yanfeng, Fuxue Zhang, and Ling Wang. 2010. Real-time demodulation of the output signal of non-driven silicon micromechanical gyroscope. In *International Symposium on Inertial Technology and Navigation*, 134–142.
- 83. Wang Ling, Fuxue Zhang, Yanfeng Shan, et al. A novel silicon micromechanical gyroscope can be used in non-rotating or rotating flight carriers. In *International Symposium on Inertial Technology and Navigation*, 215–225.
- 84. Zhang Fuxue, Lifeng Wu, Wei Zhang. 2010. Attitude detection technique for a rotating flying object. In *International Symposium on Inertial Technology and Navigation*, 366–372.
- Liu Yu, Baisheng Sun, Fuxue Zhang, et al. 2010. Research of a MEMS gyroscope simulate and process. In *International Symposium on Inertial Technology and Navigation*, 373–377.
- 86. Zhang Wei, Liu Yu, and Fuxue Zhang. 2010. Research of anti-acceleration disturbance for the micro-machined airflow inclinometer. In *International Conference on Information and Automation*, 212–215.
- 87. Wang ling, and Fuxue Zhang. Analyses output signal of MEMS gyroscope applied to low speed rotating carrier. In *International Conference on Information and Automation*, 960–964.
- 88. Liu Yu, Baisheng Sun, Fuxue Zhang, et al. 2010. Research of etching a novel MEMS gyroscope sensing pendulum. In *International Conference on Information and Automation*, 1516–1519.

89. Zhang Fuxue, Lifeng Wu, Wei Zhang. 2010. Attitude detection technique for a rotating flying object. In *International Symposium on Inertial Technology and Navigation*, 366–372.

- Liu Yu, Baisheng Sun, Fuxue Zhang, et al. 2010. Research of a MEMS gyroscope simulate and process. In *International Symposium on Inertial Technology and Navigation*, 373–377.
- 91. Guo, Heng, Fu-xue Zhang, Hui Zhao, and Lin-xia Tan. 2011. Restraining acceleration interference in mircomachined two-dimension tilt sensor. *Journal of Beijing Information Science & Technology University* 26 (2): 53–57.
- 92. Qin Shengjie, Fuxue Zhang, Lin Xia Tan. 2011. Micromechanical pendulum and its application in the attitude control system of rotating flight carrier. *Conference on the Development Direction of Inertial Technology* (13): 1–13.
- 93. Tan, Linxia, Fuxue Zhang, and Hui Zhao. 2011. Acceleration interference suppression method for dynamic horizontal attitude sensor. *Conference on the Development Direction of Inertial Technology* 13: 106–111.
- 94. Zhang, Wei, Hui Zhao, and Pinjun Wan. 2011. Structure and performance of a high speed piezoelectric fluidic gyroscope. *Conference on the Development Direction of Inertial Technology* 13: 112–115.
- 95. Zhang, Fuxue, and Shengjie Qin. 2011. Micromechanical gyroscope assembly for attitude control of a rotating flying carrier. *Conference on the Development Direction of Inertial Technology* 13: 116–122.
- Tan, Linxia, and Fuxue Zhang. 2011. The system design for high-precision dynamic level attitude sensor. *Piezoelectrics & Acoustooptics* 33 (6): 910–914.
- Fan Jing, Siqin Guo, and Fuxue Zhang. 2011. Signal amplitude estimation technique for microsilicon gyroscope. Computer Engineering and Applications 47(8): 35–37,49.
- 98. Zhang, Fuxue, Linxia Tan, Liu Yu, et al. 2011. Mechanism analysis on micro-machined gyroscope's detecting rotator's spin. *The Proceedings of the China Association for Science and Technology* 7 (1): 37–41.
- Zhang Fuxue, Shengjie Qin, Yu Liu, et al. 2011. Silicon micromachined gyroscope for single-channel control of rotary missile. The Proceedings of the China Association for Science and Technology 7 (2): 581–586.
- Tan Linxia, and Fuxue Zhang. Research on acceleration disturbance suppression for dynamic detection of level attitude. *International Conference on Physics Science and Technology (ICPST 2011)* 22: 325–332.
- Zhang Wei, Yu Liu, and Fuxue Zhang. 2011. Research of structure and technology for the micro machined airflow inclinometer. *International Conference on Physics Science and Technology (ICPST 2011)* 22: 397–402.
- Zhang Fuxue, Shengjie Qin, Linxia Tan, et al. Micro-machined pendulum and non-driven micro-machined gyroscope. *International Conference on Physics Science and Technology* (ICPST 2011) 22: 487–492.
- Qin Shengjie, and Fuxue Zhang. A combination of silicon micro-gyroscope that application rotary missile attitude control system. *International Conference on Physics Science and Technology (ICPST 2011)* 22: 517–523.
- 104. Ma Tao, Fuxue Zhang, and Pinjun Wan. 2012. Effect of jet cavity structure on the performance of piezoelectric fluidic gyroscope. In Proceedings of the Twelfth National Conference on Sensitive Components and Sensors, 105–107.
- Gao Xing, Hui Zhao, Fuxue Zhang. 2012. Method for restraining acceleration interference of horizontal attitude sensor. In *Proceedings of the Twelfth National Conference on Sensitive Components and Sensors*, 108–111.
- 106. Zhang Fuxue, Zengping Zhang, and Hui Zhao. 2012. Mechanism and application of micromechanical pendulum sensitive rotating body posture. In *Proceedings of the Twelfth* National Conference on Sensitive Components and Sensors, 121–123.

 Zhang Fuxue, and Qingwen Yan. 2012. Signal solution for micromechanical gyroscope driven by the carrier. In *Proceedings of the Twelfth National Conference on Sensitive* Components and Sensors, 141–144.

- 108. Meng Dong, Fuxue Zhang, Wei Zhang. 2012. Signal processing and performance of a fast response level attitude sensor. In *Proceedings of the Twelfth National Conference on Sensitive Components and Sensors*, 343–345.
- Xu Zhicheng, Siqin Guo, Dongying Ke. 2012. Parallel seam welding technology and method of improving air tightness. In Proceedings of the Twelfth National Conference on Sensitive Components and Sensors, 528–530.
- Gao Yinjuan, Fuxue Zhang, and Zengping Zhang. 2012. Circuit design of non-driven silicon micromechanical gyroscope. In *Proceedings of the Twelfth National Conference on* Sensitive Components and Sensors, 553–556.
- 111. Zhang Wei, Hui Zhao, and Zengping Zhang. 2012. Principle structure and signal processing technology of non-driven silicon micromechanical gyroscope. In *Proceedings of the Twelfth National Conference on Sensitive Components and Sensors*, 557–560.
- 112. Wan Pinjun, Fuxue Zhang, and Tao Ma. 2012. The working principle and signal processing of the piezoelectric fluidic gyroscope. In *Proceedings of the Twelfth National Conference on Sensitive Components and Sensors*, 561–563.
- 113. Ji Gang, Ping Yue, and Yue Zou. 2012. Construction and practice of quality management model for micromechanical gyroscope chip batch production. In *Proceedings of the Twelfth* National Conference on Sensitive Components and Sensors, 691–693.
- 114. Zhang Zengping, Fuxue Zhang, Wei Zhang, et al. 2012. The research of vibration suppression method for silicon micro-machined gyro driven by the rotation aircraft. *Electronic & Mechanical Engineering and Information Technology*, 80–87.
- 115. Yan Qingwen, Fuxue Zhang, and Wei Zhang. 2012. A multi-functional micro-machined gyroscope for rotating aircraft. *Electronic & Mechanical Engineering and Information Technology*, 88–92.
- 116. Zhang Fuxue, Zengping Zhang, Qingwen Yan, et al. 2012. Micro-mechanical pendulum and application technology in the attitude control system of the rotating body. *Electronic & Mechanical Engineering and Information Technology*, 119–126.
- Zhao Hui, Fuxue Zhang, Qingwen Yan, et al. Anti-acceleration disturbance method for pendulum tiltmeter. *Electronic & Mechanical Engineering and Information Technology*, 127–132.
- 118. Yan Qingwen, Fu-xue Zhang, Yu1 Liu, Hui Zhao, and Zhen-ping Zhang. 2012. Analysis of shock-response signal of non-driven structure silicon micro-machined gyro. *Journal of Chinese Inertial Technology* 20 (5): 611–616.
- Yan, Qingwen, Fuxue Zhang, and Wei Zhang. 2012. A micro-machined gyroscope for rotating aircraft. Sensors ISSN 1424–8220: 9823–9828.
- 120. Zhang, Zengping, and Shuhua Li. 2012. The design and implementation of the embedded system based on ARM7. *Advanced Materials Research* 433: 5607–5610.
- 121. Zhang, Zengping, and Shuhua Li. 2012. Research of video tracking algorithm based on the blob analysis. *Advanced Materials Research* 383: 1185–1189.
- Zhang Zengping, Fuxue Zhang, Wei Zhang. 2013. Measurement of phase difference for micromachined gyros driven by rotating aircraft. Sensors 13(8): 11051–11068.
- 123. Zhang, Zeng-ping, Fu-xue Zhang, and Yin-juan Gao. 2013. Amplitude-frequency characteristics of a silicon micromachined gyro driven by rotating body. *Journal of Chinese Inertial Technology* 2: 245–263.
- Zhang Fuxue, Hongwei Wang, and Wei Zhang. Silicon micromechanical gyroscope. China invention patent: ZL 200410029089.0.

 Zhang Fuxue, Hongwei Wang, and Wei Zhang. Carrier-driven silicon micromechanical gyroscope. China invention patent: ZL 200410029228.X.

- Zhang Fuxue, Nan Zhang, Xu Mao. Two dimensional silicon micromechanical gyroscope. China invention patent: ZL 200510134858.8.
- Zhang Fuxue, Nan Zhang, and Xu Mao. Anti impact silicon micromechanical gyroscope.
 China invention patent: ZL 200510134857.3.
- 128. Zhang Wei, Linhua Pu, and Wenjie Tian. Air flow type small gyroscope. China invention patent: ZL 200510134860.5.
- Zhang Wei, and Fuxue Zhang. A novel silicon micromechanical gyroscope. China invention patent: ZL 200710105849.5.
- Zhang Wei, and Fuxue Zhang. Gas pendulum inertial sensor. China invention patent: ZL 200710105848.0.
- 131. Zhang Wei, and Fuxue Zhang. Novel piezoelectric quartz accelerometer. China invention patent: ZL 200710118526.X.
- 132. Zhang Wei, and Fuxue Zhang. Novel piezoelectric quartz horizontal attitude sensor. China invention patent: ZL 200710118525.5.
- 133. Zhang Fuxue. Horizontal attitude sensitive chip and its manufacturing method of the horizontal attitude sensor. China invention patent: ZL 200810116231.3.
- 134. Zhang Wei, Fuxue Zhang, and Qiushi Han. Gas flow type omnidirectional horizontal attitude sensor. China invention patent: ZL 200910120512.0.
- Zhang Fuxue, Ling Wang, and Wei Zhang. A silicon micromechanical gyroscope. China invention patent: ZL 201010517788.5.
- Zhang Fuxue, Yanfeng Dan, and Wei Zhang. A signal processing circuit and method of non-driven micromechanical gyroscope. China invention patent: ZL 201110023627.5.
- Zhang Fuxue, and Wei Zhang. Piezoelectric quartz level sensor. American invention patent: US 7603786B2.
- 138. Zhang Fuxue, and Wei Zhang. Piezoelectric quartz accelerometer. American invention patent: US 7716985B2.
- Zhang Fuxue, and Wei Zhang. Gas pendulum inertial sensor. American invention patent: US 7730781B2.
- Zhang Fuxue, and Wei Zhang. Novel silicon micromechanical gyroscope. American invention patent: US 7 805 994 B2.
- 141. Zhang Fuxue. Level posture sensing chip and its manufacturing methods, level posture sensor. American invention patent: US 7950161B2.
- 142. Zhang Fuxue. Level posture sensing chip and its manufacturing methods, level posture sensor. American invention patent: US 8198164B2.
- Zhang Fuxue, and Wei Zhang. Gas pendulum inertial sensor. British invention patents: GB 2449731.
- 144. Zhang Fuxue, and Wei Zhang. Silicon micromechanical gyroscope without driving structure. British invention patents: GB 2449955B.
- Zhang Fuxue, and Wei Zhang. Piezoelectric quartz accelerometer. British invention patents: GB 2450952.
- 146. Zhang Fuxue, and Wei Zhang. Piezoelectric quartz level snesor. British invention patents: GB 2450953.
- Zhang Fuxue. Level posture sensing chip and its manufacturing methods, level posture sensor. British invention patents: GB 2461736.
- Zhang Fuxue, and Wei Zhang. Capteur d attitude à quartz piézoélectrique. French invention patent: 07/08880.

149. Zhang Fuxue, and Wei Zhang. Nouveau type d'accélérométre à quartz. French invention patent: 2918758.

- 150. Zhang Fuxue, and Wei Zhang. Puce de detection de posture de niveau et son procede de fabrication, capteur de posture de niveau. French invention patent: 2933533.
- 151. Zhang Fuxue, and Wei Zhang. Gattungsbildender mikromechanischer siliziumkreisel. German invention patent: 10 2007 051 879.1.
- 152. Zhang Fuxue, and Wei Zhang. Gas-Trägheitssensor. German invention patent: 102007054456.3.